# On the Design and Characterization of Exotic Phases in One Dimension

Inaugural-Dissertation zur Erlangung des Doktorgrades der Mathematisch-Naturwissenschaftlichen Fakultät der Universität zu Köln

vorgelegt von

## Niklas Tausendpfund

aus

Mainz



Berichterstatter: Prof. Dr. Matteo Rizzi (Gutachter): Prof. Dr. Achim Rosch

Vorsitzender: Prof. Dr. Joachim Hemberger

Tag der mündlichen Prüfung: 08.10.2025

Dissertation durch die Mathematisch-Naturwissenschaftliche Fakultät der Universität zu Köln 2025 angenommen.

## Abstract

State-of-the-art quantum simulators – ranging from ultracold atoms and trapped ions to Rydberg arrays and superconducting qubits – have rapidly evolved into powerful platforms for investigating complex quantum many-body phenomena. In this thesis, we discuss various models and their static and non-equilibrium properties that can be realized on near-term quantum devices. We conduct comprehensive studies on the phases of these models, spanning novel symmetry-protected topological and critical gapless phases in one dimension to the non-equilibrium behavior of localized excitations in one-dimensional quantum chains and extended one-dimensional quantum objects embedded in a two-dimensional quantum magnet. On the technical side, we employ extensive tensor network simulations to validate our findings and introduce new algorithms to determine the lifetime of edge excitations emerging in the symmetry-protected topological phase of fermionic chains. Furthermore, we propose a new variational ansatz to directly search for these novel edge modes in the topological phase. By integrating analytical tools and tensor network simulations, this thesis contributes to the roadmap for establishing quantum simulators as promising tools for investigating complex quantum systems.

## List of Publications

The results presented in this thesis are based on the following list of publications:

- Chapter I Majorana zero modes in fermionic wires coupled by Aharonov-Bohm cages
  Niklas Tausendpfund, Sebastian Diehl, Matteo Rizzi
  Phys. Rev. B 107, 035124 (2023)
- Chapter II Quantum Simulation of the Tricritical Ising Model in Tunable Josephson Junction Ladders

  Lorenzo Maffi\*, Niklas Tausendpfund\*, Matteo Rizzi, Michele Burrello

  Phys. Rev. Lett. 132, 226502 (2024)
- Chapter III Roughening dynamics of interfaces in the two-dimensional quantum Ising model

  Wladislaw Krinitsin\*, Niklas Tausendpfund\*, Matteo Rizzi, Markus Heyl, Markus Schmitt

  Phys. Rev. Lett. 134, 240402 (2025)
- Chapter IV Almost Strong Zero Mode at Finite Temperature

  Niklas Tausendpfund, Aditi Mitra, Matteo Rizzi

  Phys. Rev. Research 7, 023245 (2025)

<sup>\*</sup>Both first authors have contributed equally.

## Contents

A	bstra	$\mathbf{ct}$		i
Li	st of	Public	cations	iii
A	bbre	viation	s	ix
In	trod	uction		1
$\mathbf{T}$	heor	etical [	Background	7
1	Pha	ses Of	Quantum Matter in One Dimension	7
	1.1		um Spin Chains	8
	1.1	1.1.1	Many-Body Hilbert Space	8
		1.1.2	Many-Body Operators	9
		1.1.3	Hamiltonian	11
		1.1.4	Symmetries	12
		1.1.5	Bosons and Fermions	13
		1.1.6	Translation Invariance and Fourier Transformation	18
		1.1.7	Experimental Realizations	21
	1.2		d Phases	21
	1.2	1.2.1	Spontaneous Symmetry Broken Phases	23
		1.2.2	Symmetry Protected Topological Phases	28
		1.2.3	Kitaev Chain and Unpaired Majorana Zero Modes	34
	1.3		ss Phases	45
	1.0	1.3.1	Luttinger Liquid and Bosonization	45
		1.3.2	Sine-Gordon Model and Opening of a Gap	54
		1.3.3	Basics of Conformal Field Theory	56
	1.4		glement	60
	1.1	1.4.1	Reduced Density Matrix and Entanglement Spectrum	60
		1.4.2	Entanglement Entropy and Boundary Law	63
		1.4.3	Excited States and Higher Dimensions	65
	1.5		t Strong Zero Mode	67
	1.0	1.5.1		68
		1.5.2	Away from Integrability	71
		v. <b>_</b>		• •
2	Ten	sor Ne	tworks	77
	2.1	Tensor	Network Description of Spin Chains	78
		2.1.1	Matrix Product State of Finite Systems	80
		2.1.2	Matrix Product Operator	83
		2.1.3	Uniform Matrix Product States	85

vi CONTENTS

	2.2	Entanglement and Correlations	88
		2.2.1 Entanglement Properties	88
		2.2.2 Correlation Functions	89
		2.2.3 Symmetries in Tensor Networks	92
	2.3	Numerical Minimization of Matrix Product States	93
	2.4	Other Tensor Networks	96
$\mathbf{R}$	esult	s	101
Ι		orana zero modes in fermionic wires coupled by Aharonov-	
		am cages	101
	I.1	Authors Contribution	101
	I.2	Data Availability	101
	I.3	Summary	102
II	•	entum Simulation of the Tricritical Ising Model in Tunable	
		ephson Junction Ladders	<b>121</b>
		Authors Contribution	121
		Data Availability	122
	11.3	Summary	122
II		ighening dynamics of interfaces in the two-dimensional quan-	
		Ising model	147
		Authors Contribution	147
		Data Availability	147
	III.3	Summary	148
ΙV		nost Strong Zero Mode at Finite Temperature	169
	IV.1	Authors Contribution	169
	IV.2	Data Availability	169
	IV.3	Summary	170
$\mathbf{V}$	Alm	nost Strong Zero Mode in Number Conserving Kitaev Chains	191
	V.1	Introduction	191
	V.2	Results	193
	V.3	Conclusion	196
$\mathbf{V}$	[Var	iational Ansatz for Strong Zero Modes	197
	VI.1	Introduction	197
	VI.2	Matrix Product Operator Ansatz	198
	VI.3	Exact Solution in the Integrable Limits	200
	VI.4	Numerical Minimization	201
		VI.4.1 Integrable Points	202
		VI.4.2 General Case	203
	VI.5	Conclusion	207

*CONTENTS* vii

C	onclu	asion	209
$\mathbf{A}$	ppen	ndix	215
$\mathbf{A}$	Bas	ics of Linear Algebra	215
	A.1	Linear Maps	215
		A.1.1 Vector Spaces	
		A.1.2 Linear Maps	216
	A.2	Matrix Decomposition	216
		A.2.1 QR Decomposition	217
		A.2.2 Singular Value Decomposition	218
		A.2.3 Eigenvalue decomposition	218
В	Der	ivation of the Jordan-Wigner Transformation	219
$\mathbf{C}$	Der	ivation of the Majorana Zero Modes	<b>22</b> 1
$\mathbf{D}$	Stro	ong Zero Mode from Quantum Circuit	223
	D.1	Case I: $U = 0$	224
		D.1.1 Algebraic Derivation	224
		D.1.2 Derivation Using a Matrix Product Operator	225
	D.2	Case II: $\mu = 0$	226
$\mathbf{E}$	Mat	trix Product Operator from Finite State Machines	<b>22</b> 9
Bi	bliog	graphy	233
A	cknov	wledgement	257

## Abbreviations

```
ACF Autocorrelation Function 70–76, 194, 195, 205
ASZM Almost Strong Zero Mode 67, 72, 73, 75, 76, 169, 170, 191–193, 195–198,
     202-207, 210, 211
BdG Bogoliubov-de-Gennes 38, 39
BKT Berezinski-Kosterlitz-Thouless 149, 150
CAR Canonical Anti-Commutation Relations 15, 16, 219
CCR Canonical Commutation Relations 13, 15
CFT Conformal Field Theory 56, 57, 59, 62, 64, 65, 89, 91
DMRG Density-Matrix Renormalization Group 78, 93, 95, 96, 103, 198
EDOS Edge Density of States 73–76, 194, 195
FOPT First-Order Phase Transition 59, 122, 123
JJA Josephson Junction Array 14, 15, 21, 122
KHM Kitaev-Hubbard Model 43, 62, 63, 74, 75, 170, 191–198, 200, 202, 203, 207,
     223
MPO Matrix Product Operator 84, 85, 93, 170, 193, 196, 198–204, 225, 226, 229–231
MPS Matrix Product State 77, 78, 80–85, 87–89, 91–97, 101, 122, 124
MZM Majorana Zero Mode 35, 37, 40, 43-45, 62, 67, 71, 102, 103, 170, 191, 192,
     196, 209, 210, 221, 222
PEPS Projected Entangled Pair States 97
SOS Solid-On-Solid 148–150
SPTP Symmetry-Protected Topological Phase 22, 23, 28–30, 33, 34, 37, 38, 43, 62,
     63, 69, 71–75, 102, 103, 170, 191, 192, 198, 204, 207, 209–211
SSHM Su–Schrieffer–Heeger Model 29–34, 38, 73–75, 194
SVD Singular-Value Decomposition 61, 79, 80, 95, 97, 218
SZM Strong Zero Mode 67–72, 74, 197, 198, 200–204, 207, 211, 223–227
```

 ${\it x}$   ${\it ABBREVIATIONS}$ 

TCI Tricritical Ising 59, 87, 89, 122–124, 209

**TFIM** Transverse Field Ising Model 23, 24, 26–28, 42, 64, 65, 85, 89, 97, 148, 209, 224, 229–231

TFXYM Transverse Field XY Model 41, 42

TLL Tomonaga-Luttinger Liquid 45, 47–49, 51–57, 123, 124, 149, 192

TTN Tree Tensor Network 96, 97

uMPS Uniform Matrix Product State 85–87, 89, 96, 123

VUMPS Variational Uniform Matrix Product State 96

## Introduction

"It always seems impossible until it's done."

— Nelson Mandela

In the era of noisy quantum computers, the underlying quantum systems are rapidly developing with an increasing number of available qubits. Although the individual components are increasingly controlled, the overall error in the qubit gates is still too large to implement fault-tolerant digital quantum computing and quantum algorithms, such as Shor's factoring algorithm [1]. Instead, recent advances in fabrication and measurement techniques allow the use of these noisy quantum computers as direct simulators for highly correlated quantum matter, in line with the ideas originally proposed by Feynman in 1982 [2]. Examples of such quantum simulators can be ultracold atoms in optical lattices [3–7], Rydberg arrays [8–10], or collective excitations in superconducting islands coupled by Josephson junctions [11–16].

In this context, the quantum system forming the simulator is designed to mimic the behavior of a different complex quantum system. Measuring this simulator allows us to gain insights into complex processes that are inaccessible to classical computers. One aspect of this is the study of exotic phases of matter that have not yet been experimentally observed in natural systems. Realizing these phases could help gain a deeper understanding of their properties and has been successfully employed in the past [17, 18]. When driven to a specific phase, a quantum simulator can also serve as a building block for more complicated scenarios or even the realization of a quantum computer that is more robust than existing platforms [19, 20].

Another interesting aspect is the non-equilibrium properties of complex quantum systems following a local or global quench [21]. On general grounds, it is conjectured that generic quantum systems should thermalize locally such that the time average of any local observable approaches its thermal equilibrium value [22]. However, there are several exceptions to this general rule [23–27], and identifying new mechanisms to prevent local thermalization is an active area of research. Although the dynamical behavior of a many-body quantum system is notoriously complicated owing to the large entanglement created, a quantum simulator can naturally be used to follow the time trajectory of a quantum system, an idea that has been successfully demonstrated in recent studies [10, 28–30]. Thus, designing and characterizing new promising models that can realize novel phases of matter or show non-trivial many-body dynamics on a state-of-the-art quantum platform is a thriving quest.

In this thesis, we contribute to this quest by studying the static and dynamic properties of various lattice models in one and two dimensions. To this end, we propose two one-dimensional lattice models that realize two different novel phases of quantum 2 INTRODUCTION

matter: a symmetry-protected topological phase of fermions exhibiting a fractionalized fermion in the ground state manifold, and a critical phase that serves as a building block for a topological quantum computer in two dimensions. We introduce two algorithms that allow us to study the coherence time of this fractionalized fermion at finite temperatures, an important question for future experimental applications, and to variationally search for new localized long-lived modes in generic models. Additionally, we explore the non-equilibrium behavior of a straight domain wall, a one-dimensional quantum object embedded in a two-dimensional quantum magnet, and discuss a new mechanism that prevents local thermalization of the many-body quantum state.

This thesis is organized as follows: In the first part, *Theoretical Background*, we provide a short survey of one-dimensional lattice models, including the general definitions and possible phases of matter occurring in such quantum chains in Chapter 1, and an introduction to tensor networks in Chapter 2, which are the main numerical tool used throughout this thesis. In the second part, *Results*, the results of this thesis are presented in Chapters I–VI with the following content:

The first model discussed in Chapter I is motivated by cold-atom experiments and realizes a symmetry-protected topological phase of fermionic chains. This phase has two unpaired Majorana zero modes localized at the edge, which could be used to realize nearly fault-tolerant quantum computation. Despite recent claims [31], there is no convincing evidence for the experimental realization of this novel phase [32] in solid-state systems. The approach proposed in this thesis circumvents the typical problems that arise in traditional implementations but comes with its own difficulties. In particular, it is necessary to fine-tune some parameters at the edges to achieve a symmetry-protected topological phase. Moreover, the model exhibits gapless density-wave excitations that may couple to the Majorana zero modes at higher energies. Our results have been published in [33].

The second model presented in Chapter II is inspired by recent advances in the fabrication of superconducting islands connected by Josephson junctions and aims to realize the tricritical Ising model. This exotic phase is an example of a critical theory in which multiple phases compete, leading to a rich particle content in the low-energy theory. In particular, one of the particles emerging in the low-energy theory can be used to build two-dimensional topologically ordered matter with non-Abelian anyonic excitations that can be used as a fault-tolerant quantum computer [34]. Our results have been published in [35].

In Chapter III we study the dynamics of the transverse-field Ising model in two dimensions, and in particular, of a straight domain wall state. We find that the non-equilibrium behavior is highly influenced by the emergence of a one-dimensional phase transition of the domain wall embedded in the two-dimensional quantum magnet. The dynamics of the two-dimensional quantum Ising model, which are highly limited in terms of system size for numerical simulations, can be explored using state-of-the-art Rydberg atom platforms. A realization on a Rydberg atom simulator would further allow the study of more complicated scenarios, such as a curved domain wall or bubbles, which are currently not accessible in numerical simulations. Our results have been published in [36].

In Chapter IV, we revisit the symmetry-protected topological phase of unpaired Ma-

jorana zero modes, a subject also addressed in Chapter I. Specifically, we study the influence of temperature on the stability of these edge-localized modes. To achieve this, we develop a new tensor-network algorithm that allows us to study the interplay between temperature and interactions on the lifetime of the Majorana zero modes. In particular, we find that these modes exhibit a finite, but still orders of magnitude larger lifetime than any bulk excitation. Based on the exact diagonalization results, we conjecture that this prolonged lifetime is due to an extended degeneracy in the many-body spectrum that emerges in the symmetry-protected topological phase. These findings demonstrate that, if realized in an experimental setup, the Majorana zero modes are resilient over long time scales, even at intermediate temperatures, allowing operations to be performed on them. Our results have been published in [37].

Finally, we discuss two yet unpublished extensions of the results from Chapter IV, namely: In Chapter V we return to the class of models that realizes the symmetry-protected topological phase of unpaired Majorana zero modes while conserving the particle number, also considered in Chapter I. Specifically, we apply our algorithm to study the lifetimes of the emergent Majorana zero modes. We find that the lifetime of the Majorana zero modes is drastically reduced at intermediate temperatures in the presence of a gapless mode, which is always present in this class of models. In Chapter VI, we propose a variational approach to identify long-lived edge excitations in fermionic models. In contrast to earlier approaches, such as in [38], the ansatz is tailored to respect all constraints for proper Majorana operators and thus lives in the correct variational manifold.

All additional data, including the unpublished results from Chapters IV and VI, presented in this thesis are publicly available under [39].

Theoretical Background

CHAPTER 1

# Phases Of Quantum Matter in One Dimension

One-dimensional quantum systems exhibit behavior that is distinct from that of their higher-dimensional counterparts. While two- and three-dimensional metals are often described by the concept of a Fermi liquid, a phase with long-lived fermionic quasiparticles [40–43], the one-dimensional analog is the Tomonaga-Luttinger liquid [44–47]. In a Tomonaga-Luttinger liquid, the fundamental excitations are collective charge and spin waves that can move independently from each other, also known as the charge-spin separation of the microscopic degrees of freedom. In addition to the characteristics of metallic phases, gapped phases are notably distinct, as one-dimensional systems are prohibited from breaking continuous symmetries owing to the Mermin-Wagner-Hohenberg theorem [48–50]. Consequently, all gapped phases either in a trivial phase with a unique ground state, break a finite symmetry group, such as a  $\mathbb{Z}_2$  parity symmetry, or form a non-trivial symmetry-protected topological phase where the ground state degeneracy depends on the topology of the underlying quantum system [51–54].

The special behavior of one-dimensional models is rooted in the fact that every position in the chain has a unique predecessor and successor, which allows for the definition of a natural order that is absent in higher dimensions. Consequently, quantum fluctuations are greatly enhanced owing to the reduced number of neighbors and entanglement monogamy [55, 56]. Additionally, the reduced connectivity and existence of a unique order allow for the formulation of powerful tools to solve one-dimensional quantum systems, both analytically [57–59] and numerically [60–64]. The reduced connectivity also leads to a fundamental equivalence between bosons, fermions, and spins. This allows for rewriting every local model as a spin model with each spin described by a finite-dimensional Hilbert space,  $\mathcal{H}_{loc} \cong \mathbb{C}^d$ . While this mapping is exact in the case of fermions, bosonic particles are only described effectively owing to the infinite-dimensional local Hilbert space of bosons.

The first part of this chapter, Section 1.1, introduces the general concepts of quantum chains, including the construction of the many-body Hilbert space and the operators acting on it. This general introduction is followed by a more detailed discussion of possible gapped phases of matter in Section 1.2 and gapless phases of matter in Section 1.3. The following Section 1.4 reviews of the concept of quantum entanglement and how the different phases of matter lead to different footprints in

the structure of entanglement. In last Section 1.5, the concepts of strong zero mode and almost strong zero mode are introduced. This concept extends the notion of Majorana Zero Modes, which are fractionalized fermions localized at the edge of a finite-sized quantum chain, to the entire many-body spectrum.

### 1.1 Quantum Spin Chains

Spin chains form the foundation of all models and their phases discussed in the results of this thesis. Therefore, understanding the notation and basic properties of these quantum mechanical systems is important and will be discussed in this section. To start, Subsection 1.1.1 gives a general definition of the many-body Hilbert space of spin chains, followed by the definition of the algebra of operators acting on this Hilbert space in Subsection 1.1.2, the Hamiltonian in Subsection 1.1.3, and the definition of symmetries and their implications in Subsection 1.1.4. Subsection 1.1.5 explains the duality between bosons, fermions, and spins, which are the typical degrees of freedom encountered in physical systems. This is followed by Subsection 1.1.6 which discusses the consequences of closing the chain to a ring by introducing periodic boundary conditions in the underlying quantum system. Finally, this section concludes in Subsection 1.1.7 with a discussion of the experimental platforms that allow the realization of quantum chains.

#### 1.1.1 Many-Body Hilbert Space

The quantum spin chain is constructed by taking a chain of N sites indexed by  $\mathcal{I} = \{1, \dots, N\}$  and associating a copy of the same Hilbert space<sup>1</sup> of dimension d,  $\mathcal{H}^{j}_{loc} \cong \mathbb{C}^{d}$ , to each lattice site, as illustrated in Fig. 1.1. The full many-body Hilbert

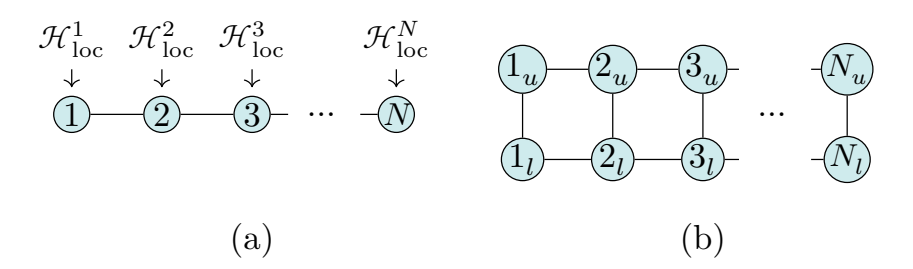


Figure 1.1: Examples of (quasi-)one dimensional lattice systems. (a) Simple spin chain of local quantum systems placed along a line. Each site is associated with a local Hilbert space  $\mathcal{H}_{loc}$ . (b) Quasi-one-dimensional system forming a ladder. The ladder is equivalent to the chain in (a) with  $\mathcal{H}_{loc} = \mathcal{H}_u \otimes \mathcal{H}_l$  where the sites u and l are blocked into a super-site.

space of the quantum spin chain is then given by the direct tensor product of the local Hilbert spaces

$$\mathcal{H} = \bigotimes_{j=1}^{N} \mathcal{H}_{\text{loc}}^{j}, \quad \dim(\mathcal{H}) = d^{N}. \tag{1.1}$$

Note that in a real physical system, the different sites j are separated by a physical length  $\alpha$ , where  $x_j = j\alpha$  denotes a real physical coordinate.

By choosing an appropriate basis in the local Hilbert space, a many-body basis can be generated based on the tensor product in Eq. (1.1). Let the local basis be

<sup>&</sup>lt;sup>1</sup>The requirement that every copy  $\mathcal{H}_{loc}^{j}$  is isomorphic to the same Hilbert space  $\mathcal{H}_{loc}$  is not necessary in general but is sufficient for this thesis.

enumerated by an integer number  $m \in \{1, ..., d\}$  such that  $|m\rangle \in \mathcal{H}_{loc}$ , a general state  $|\psi\rangle \in \mathcal{H}$  of the many-body Hilbert space is given by

$$|\psi\rangle = \sum_{\{m\}} \psi_{m_1,\dots m_N} \, |m_1,\dots,m_N\rangle \;,\; \psi_{m_1,\dots m_N} \in \mathbb{C} \,, \tag{1.2}$$

where

$$|m_1, \dots, m_N\rangle := |m_1\rangle \otimes \dots \otimes |m_N\rangle .$$
 (1.3)

#### 1.1.2 Many-Body Operators

A many-body operator is a linear map acting on the previously defined Hilbert space

$$\hat{O}|\psi\rangle \in \mathcal{H} \quad \forall |\psi\rangle \in \mathcal{H}.$$
 (1.4)

Analogous to the construction of a generic many-body state, a general operator can be expressed as a sum of products of local operators that act exclusively within the local Hilbert space  $\mathcal{H}_{loc}^j$ . Thus, it is beneficial to first define the operator algebra for a single spin described by  $\mathcal{H}_{loc}$ . Since  $\mathcal{H}_{loc} \cong \mathbb{C}^d$ , the set of all operators on  $\mathcal{H}_{loc}$  is given by the set of all complex  $d \times d$  matrices, denoted by  $\mathrm{Mat}(\mathbb{C},d,d)$ . In the local basis  $|m\rangle \in \mathcal{H}_{loc}$ , the operator  $\hat{O}$  can be written as

$$\hat{O} = \sum_{n,m} O_{m,n} |m\rangle \langle n| , \qquad (1.5)$$

where the matrix elements are defined by

$$O_{m,n} = \langle m|\hat{O}|n\rangle \in \mathbb{C}. \tag{1.6}$$

Given a state  $|\psi\rangle \in \mathcal{H}_{loc}$  and an operator  $\hat{O}$  acting on  $\mathcal{H}_{loc}$ , the expectation value of the operator with respect to the state  $|\psi\rangle$  is defined in the local basis as

$$\langle \psi | \hat{O} | \psi \rangle = \sum_{m,n} \bar{\psi}_m O_{m,n} \psi_n , \quad | \psi \rangle = \sum_{m=1}^d \psi_m | m \rangle .$$
 (1.7)

The complex transpose of an operator  $\hat{O}$  is defined by

$$\hat{O}^{\dagger} = \sum_{m,n} \bar{O}_{n,m} |m\rangle \langle n| , \qquad (1.8)$$

where  $\bar{z} = a - ib$  denotes the complex conjugate of the complex number z = a + ib. An operator that is invariant under complex transpose,  $\hat{O}^{\dagger} = \hat{O}$ , is called a Hermitian operator. Since

$$\overline{\langle \psi | \hat{O} | \psi \rangle} = \langle \psi | \hat{O}^{\dagger} | \psi \rangle ,$$

the expectation value of a Hermitian operator  $\langle \psi | \hat{O} | \psi \rangle$  is a real number. Therefore, Hermitian operators are naturally associated with the physical properties of a quantum system.

Together with the Frobenius scalar product

$$\langle \hat{O}, \hat{K} \rangle = \frac{1}{d} \operatorname{Tr} \left[ \hat{O}^{\dagger} \hat{K} \right] = \frac{1}{d} \sum_{j,k} \bar{O}_{jk} K_{jk} ,$$
 (1.9)

the algebra of all linear maps naturally forms a Hilbert space itself. Using this scalar product, it is possible to construct  $d^2$  orthogonal, normalized and Hermitian basis operators  $\sigma^{\alpha}$ , such that every operator can be expanded as

$$\hat{O} = \sum_{\alpha=1}^{d^2} O_{\alpha} \sigma^{\alpha} \,, \quad O_{\alpha} \in \mathbb{C} \,.$$

Typically,  $\sigma^1$  is set as the identity on  $\mathcal{H}_{loc}$ .

For example, consider a spin-1/2 degree of freedom with local Hilbert space dimensions d=2. In this case, the local Hilbert space is described by only two state which are typically denoted by the spin-up and spin-down state

$$|1\rangle \cong |\downarrow\rangle , \quad |2\rangle \cong |\uparrow\rangle . \tag{1.10}$$

An orthonormal and Hermitian basis for operators acting on this spin-1/2 Hilbert space is given by the Pauli matrices

$$\sigma^x = \begin{pmatrix} 0 & 1 \\ 1 & 0 \end{pmatrix}, \ \sigma^y = \begin{pmatrix} 0 & -i \\ i & 0 \end{pmatrix}, \ \sigma^z = \begin{pmatrix} 1 & 0 \\ 0 & -1 \end{pmatrix}$$
 (1.11)

together with the identity 1, as can be checked by explicitly evaluating the Frobenius scalar product, Eq. (1.9), between all operator pairs

$$\frac{1}{2}\operatorname{Tr}\left[\sigma^{\alpha}\sigma^{\beta}\right]=\delta_{\alpha,\beta}\,,\quad \sigma^{\alpha},\,\sigma^{\beta}\in\left\{\mathbb{1},\sigma^{x},\sigma^{y},\sigma^{z}\right\}.$$

Embedded in the many-body spin chain, an operator acting only on the Hilbert space  $\mathcal{H}^j_{loc}$  of the jth site is defined by

$$\hat{O}_j \coloneqq \underbrace{\mathbb{1} \otimes \mathbb{1} \otimes \cdots \otimes \mathbb{1}}_{i-1 \text{ times}} \otimes \hat{O} \otimes \underbrace{\mathbb{1} \otimes \cdots \otimes \mathbb{1}}_{N-i \text{ times}},$$

where  $\hat{O}$  denotes a single-site operator, as defined above. Note that operators acting on different sites  $j \neq k$  are naturally commuting

$$\left[\hat{O}_{i},\hat{K}_{k}\right] \coloneqq \hat{O}_{i}\hat{K}_{k} - \hat{K}_{k}\hat{O}_{i} = 0. \tag{1.12}$$

The local Hermitian basis  $\sigma_j^{\alpha}$  can be used to construct a full basis of many-body operators

$$\sigma^{\{\alpha\}} = \sigma_1^{\alpha_1} \sigma_2^{\alpha_2} \dots \sigma_N^{\alpha_N} \coloneqq \sigma^{\alpha_1} \otimes \sigma^{\alpha_2} \otimes \dots \otimes \sigma^{\alpha_N} \,. \tag{1.13}$$

This basis naturally forms an orthonormal basis set of Hermitian operators with respect to the many-body generalization of the Frobenius scalar product

$$\langle \sigma^{\{\alpha\}}, \sigma^{\{\beta\}} \rangle = \frac{1}{d^N} \operatorname{Tr} \left[ \sigma^{\alpha_1} \sigma^{\beta_1} \right] \dots \operatorname{Tr} \left[ \sigma^{\alpha_N} \sigma^{\beta_N} \right] = \delta_{\alpha_1, \beta_1} \dots \delta_{\alpha_N, \beta_N},$$

where  $\text{Tr}(\sigma^{\alpha}\sigma^{\beta}) = d\delta_{\alpha,\beta}$  was used. A generic many-body operator can now be expressed in terms of the many-body operator basis, Eq. (1.13), as

$$\hat{O} = \sum_{\{\alpha\}} O_{\alpha} \sigma^{\{\alpha\}} \,. \tag{1.14}$$

The complex transpose, expectation value, and other properties are naturally extended from single-site operators to many-body operators.

An important concept for many-body operators is the interaction range of a given operator  $\hat{O}$ . This range is defined as the length of a connected subset of indices on which the operator  $\hat{O}$  acts non-trivially while acting only with the identity on the complement. For example, consider the operator  $\hat{M} = \hat{O}_j \hat{O}_{j+l}$  which is the product of two local operators acting on sites j and j+l. The interaction range of this operator is l+1.

#### 1.1.3 Hamiltonian

The Hamiltonian H of the quantum spin chain of N sites is a special Hermitian operator that defines all the physical properties of the quantum spin chain. The Hamiltonian measures the energy of a given quantum state  $\langle \psi | H | \psi \rangle = E$ . Analogous to classical Hamiltonian mechanics, the quantum Hamiltonian is responsible for the time evolution of spin systems. Typically, the Hamiltonian is required to be local and includes only interactions that decay sufficiently rapidly with distance.

The models considered in this thesis have a stronger requirement that the Hamiltonian consists only of finite-range interactions. In this case, H can be written as

$$H = \sum_{j=1}^{N} h_j \,, \tag{1.15}$$

where  $h_j$  acts non-trivially only in a finite region around the jth site. The interaction radius is independent of the system size when N is sufficiently large.

For a given many-body quantum state  $|\psi\rangle$ , the Schrödinger equation describes how this state evolves over time

$$i\partial_t \left| \psi \right\rangle_t = H \left| \psi \right\rangle_t \ . \tag{1.16}$$

Solving the Schrödinger equation is equivalent to find the eigenstates  $|n\rangle$  and eigenvalues  $E_n$  of the Hamiltonian H defined by

$$H\left|n\right\rangle = E_n\left|n\right\rangle \;, \quad E_0 \leq E_1 \leq \ldots \leq E_{\max} \,. \tag{1.17} \label{eq:1.17}$$

Because the Hamiltonian only has interaction terms of finite size, the energy is bounded  $(E_0 > -\infty$  and  $E_{\rm max} < \infty)$  for a finite chain.

If unique, the state with the lowest energy  $|\Omega\rangle$  is called the ground state of the Hamiltonian. In this case, the system-size-dependent spectral gap is defined as the difference in energy between the ground state and first excited state

$$\Delta(N) := E_1(N) - E_0(N). \tag{1.18}$$

In the thermodynamic limit, this quantity becomes

$$\lim_{N \to \infty} \Delta(N) = \begin{cases} \Delta > 0 \\ 0 \end{cases} . \tag{1.19}$$

If the many-body gap is finite in this limit, the system is said to be gapped, whereas for  $\Delta(N)$  approaching zero, the system is called gapless. The existence of a many-body gap strongly influences the structure of ground-state correlations, as it has been shown that the correlation functions of any pair of local operators decay exponentially [65, 66].

Conversely, the low-energy regime of a gapless system is typically characterized by a conformal field theory, in which the correlation functions decay according to universal power laws. These exponents are determined exclusively by the algebraic structure of the underlying conformal field theory [67]. See Subsection 1.3.3 for further details.

If the ground state in the thermodynamic limit becomes degenerate, as in the case of symmetry breaking or topological degeneracy, the gap must be defined between the energy difference of the ground-state multiplet and the first true excited state.

#### 1.1.4 Symmetries

Symmetries play a crucial role for the properties of a quantum system, such as the existence of non-trivial observables that are invariant under time evolution, Eq. (1.16), or the existence of degeneracies in the energy spectrum. A symmetry is a group G that acts globally<sup>2</sup> on the quantum spin chain through unitary or anti-unitary<sup>3</sup> representations  $g \to U(g)$  on the many-body Hilbert space  $\mathcal{H}$  [68]. The action of the symmetry group preserves the Hamiltonian H of the spin chain

$$[H, U(g)] = 0, \forall g \in G, \qquad (1.20)$$

ensuring that the eigenstates of the Hamiltonian form irreducible representations of the group G. An irreducible representation is a subspace that contains no smaller subspace mapped into itself under the action of G.

Correspondingly, the Hamiltonian decomposes into smaller blocks [69]

$$H = \begin{pmatrix} H_1 & 0 & 0 & \dots & 0 \\ 0 & H_2 & 0 & \dots & 0 \\ \vdots & & \ddots & & \vdots \end{pmatrix} \,,$$

where each block  $H_{\alpha}=V_{\alpha}\otimes R_{\alpha}$  contains a part  $V_{\alpha}$  that carries the non-trivial irreducible representation of the symmetry group and  $R_{\alpha}$  which transforms trivially under G, called the degeneracy space. The space  $V_{\alpha}$  is completely fixed by the group representation labeled by the main quantum number  $\alpha$ 

$$|\alpha,\beta\rangle \in V_\alpha\,, \quad U(g)\,|\alpha,\beta\rangle = \sum_{\beta'} u^\alpha_{\beta,\beta'}(g)\,|\alpha,\beta'\rangle \in V_\alpha\,,$$

where  $\beta$  enumerates the basis of the representation  $V_{\alpha}$ . As  $R_{\alpha}$  has no further restriction, every eigenstate of the Hamiltonian satisfies  $H | \alpha, \beta \rangle \otimes | n \rangle = E_{\alpha,n} | \alpha, \beta \rangle \otimes | n \rangle$ , where  $| n \rangle \in R_{\alpha}$ . The energy  $E_{\alpha,n}$  is independent of the secondary quantum number  $\beta$ . This leads to the emergence of energy multiplets in the spectrum when  $\dim(V_{\alpha}) > 1$ .

If all elements of the group commute with each other, that is, [g, g'] = 0, the group is called an Abelian group; otherwise, it is non-Abelian. The irreducible representations of an Abelian group are one-dimensional and have the general form

$$u^{\alpha}(g) = e^{i\varphi_{\alpha}(g)}, \quad \varphi_{\alpha}(g) \in [0, 2\pi). \tag{1.21}$$

<sup>&</sup>lt;sup>2</sup> A unitary U that acts on all constituents of the spin chain is called a global unitary. By contrast, if the unitary U acts only on a few sites of the spin chain, it is called a local unitary transformation. If the spin chain is invariant under an extensive group G of local unitaries, then this group is called a gauge symmetry. In this thesis, only symmetries of global groups are considered.

<sup>&</sup>lt;sup>3</sup>An anti-unitary transformation is the concatenation of a unitary transformation and complex conjugation.

In this case, every eigenstate of the Hamiltonian can be chosen as a simultaneous eigenstate of the entire group U(g) with eigenvalue  $\exp(i\varphi_{\alpha}(g))$ . A non-Abelian group allows for higher-dimensional representations, and thus, a greater dimensional reduction.

The symmetries encountered in this thesis are Abelian and represented by point-wise operations of the form

$$U(g) = \prod_{i=1}^{N} u_j(g)$$
 (1.22)

where  $u_j(g) \neq 1$  is a unitary that acts only on the local Hilbert space  $\mathcal{H}_{loc}^j$ . The conservation of the total spin moment  $\hat{N} = \sum_j \sigma_j^z$  of a spin-1/2 quantum chain is an example of such a point-wise symmetry given by

$$U(g) = e^{ig\hat{N}} = \prod_{j=1}^N e^{ig\sigma_j^z}\,, \quad g \in [0,2\pi)\,.$$

#### 1.1.5 Bosons and Fermions

There is a natural equivalence between fermions and bosons with spin degrees of freedom. The necessary mappings are discussed in this subsection, starting with the case of bosons. For bosons, this requires truncating the full infinite-dimensional bosonic Hilbert space to include only a finite number of states. In the case of fermions, the mapping requires a non-local unitary transformation of the fermionic Hilbert space. While the mapping of bosons to spins can be readily extended to higher dimensions, the fermionic mapping results in long-range Hamiltonians, gauge theories, or the need for auxiliary sites [70–72].

The mappings presented in this subsection are used throughout the results presented in Chapters I–VI to efficiently simulate the models using tensor network algorithms formulated for spin chains.

#### **Bosons**

The many-body Hilbert space of a chain populated by bosons is constructed using bosonic ladder operators  $b_j^{\dagger}$  and  $b_j$ , which create and annihilate a bosonic particle at site j. These ladder operators fulfill the Canonical Commutation Relations (CCR)

$$[b_j, b_k^{\dagger}] = \delta_{j,k} \,, \tag{1.23}$$

and the number operator counting the total occupation of particles at site j is defined as

$$\hat{n}_{j} = b_{j}^{\dagger} b_{j} \,, \quad [\hat{n}_{j}, b_{j}] = -b_{j} \,. \tag{1.24}$$

The local Hilbert space  $\mathcal{H}_{\text{loc}}^j$  at site j is constructed as the eigenstates of the Hermitian operator  $\hat{n}_j$ .

For simplicity, consider first a single bosonic site described by only one pair of ladder operators b and  $b^{\dagger}$ .

Given the existence of a vacuum state,  $b|0\rangle = 0$ , and the commutation relations of the operator  $\hat{n}$  with b and  $b^{\dagger}$ , it can be shown that the spectrum of  $\hat{n}$  is the set of all natural numbers [42]

$$\hat{n} |n\rangle = n |n\rangle$$
,  $n \in \mathbb{N} \cup \{0\}$ .

The ladder operators act on these eigenstates as

$$b |n\rangle = \sqrt{n} |n-1\rangle$$
,  $b^{\dagger} |n\rangle = \sqrt{n+1} |n+1\rangle$ .

The many-body Hilbert space is a direct tensor product of N copies of the local bosonic Hilbert space, similar to Eq. (1.1).

The resulting many-body Hilbert space has a structure that is very similar to that of the spin chains discussed previously. In particular, the operators acting on different sites commute naturally. Given that the bosonic Hilbert space cannot be finite [73], the bosonic chain effectively represents a spin chain with  $d \to \infty$ . Therefore, mapping the bosonic chain to a spin chain with a finite number of local states requires truncation of the local Hilbert spaces to allow for a maximal occupation. There are multiple ways to perform such truncation, two of which are presented below.

The first truncation is natural in the dilute limit, with only a few strongly interacting bosonic particles populating the chain. In this case, the Hamiltonian H typically involves a Hubbard-like interaction term [74]

$$H_{\rm Hubbard} = V_{\rm Hubbard} \sum_{i} \hat{n}_{j} (\hat{n}_{j} - 1) \tag{1.25}$$

that penalizes large occupations when the interaction becomes the dominant energy scale of H. Consequently, only a few states with low occupations play a role in the ground state. This allows an effective description of the bosonic chain as a spin chain with a local Hilbert space dimension d by including only the vacuum state  $|0\rangle$  and d-1 additional bosons in the local Hilbert space. In the extreme limit  $V_{\text{Hubbard}} \to \infty$ , the only allowed states are the vacuum state  $|0\rangle$  and one additional boson  $|1\rangle$ . This situation is called a hardcore boson and is equivalent to a spin-1/2 degree of freedom.

While this first mapping works well in the dilute limit, the second mapping targets the opposite limit of a macroscopic number of bosons in the chain. This situation naturally occurs in an array of superconducting patches connected by Josephson junctions, also known as Josephson Junction Array (JJA) [75]. Each of these islands is described by a macroscopic condensation of Cooper pairs [75–77]. In this scenario, it is useful to define the reference state  $|0\rangle$  as the ground state of the superconducting island at site j. The number operator  $\hat{n}_j$  is redefined to measure the difference in occupation with respect to the reference state  $|0\rangle$ .

Further, it is useful to define the vertex operators  $\exp(\pm i\varphi_i)$  by

$$e^{-i\varphi_j} = \left(\hat{N}_j\right)^{-\frac{1}{2}} b_j \,, \quad e^{i\varphi} = b_j^\dagger \left(\hat{N}_j\right)^{-\frac{1}{2}} \tag{1.26}$$

where  $\hat{N}_j$  is the number operator that measures the absolute number of Cooper pairs on the jth island. The vertex operators acting on different islands naturally commute. The commutator of operators at the same island becomes in the limit of  $\hat{N}_j \to \infty$ 

$$[e^{-i\varphi_j},e^{i\varphi_j}] = \left(\hat{N}_j\right)^{-1}b_jb_j^\dagger - \left(\hat{N}_j-1\right)^{-1}b_j^\dagger b_j = 0\,.$$

Similar, the commutator of the vertex operator and the relative number operator  $\hat{n}_j$  is calculated as

$$[\hat{n}_j, e^{\pm i\varphi_j}] = \pm e^{\pm i\varphi} \,. \tag{1.27}$$

This equation indicates the interpretation of  $\varphi_j$  as the canonical conjugated operator of  $\hat{n}_j$ . It is important to note that owing to the discrete nature of the spectrum of  $\hat{n}_j$ ,

the commutator  $[\varphi_j, \hat{n}_j]$  is ill-defined, and only its exponential form has a rigorous definition [78–80]. Similar to the Hubbard interaction in Eq. (1.25), JJAs have a term penalizing large differences of the number of Cooper pairs with respect to the average filling

$$H_{\rm C} = V_{\rm C} \sum_{i} \hat{n}_j^2$$
.

Again, for  $V_{\rm C}$  being large compared to the natural energy scale of the JJA, one can truncate the effective Hilbert space to only allow for m additional excess bosons. In this case, the local Hilbert space dimension is d=2m+1.

#### Fermions

Spinless fermions populating the chain are described by their ladder operators  $a_j^{\dagger}$  and  $a_j$ . These operators create and annihilate a local fermion at site j, similar to the bosonic case discussed previously<sup>4</sup>. In contrast to the bosonic ladder operators which fulfilled the CCR (1.23), the fermionic operators have to fulfill the Canonical Anti-Commutation Relations (CAR)

$$\{a_j, a_k^{\dagger}\} = \delta_{j,k} \,, \tag{1.28}$$

with all other combinations being zero. Here,  $\{\hat{A}, \hat{B}\} = \hat{A}\hat{B} + \hat{B}\hat{A}$  denotes the anti-commutator of the two operators  $\hat{A}$  and  $\hat{B}$ . The CAR from (1.28) encodes the fundamental anti-symmetric properties of fermionic wave functions and is rooted in the Pauli principle [40, 42, 81] which states that two fermions cannot occupy the same quantum state. In fact, using the CAR it is found

$$(a_j^{\dagger})^2 = (a_j)^2 = 0$$
.

As a consequence, the local Hilbert space at site j can only consists out of two possible states: The fermionic vacuum state  $|0\rangle_j$  and the single occupied state  $|1\rangle_j$  with

$$a_{j}^{\dagger}\left|0\right\rangle _{j}=\left|1\right\rangle _{j}\,,a_{j}\left|1\right\rangle _{j}=\left|0\right\rangle _{j}\,.$$

These are the only two eigenstates of the fermionic number operator  $\hat{n}_j=a_j^\dagger a_j,$  which follows from

$$\begin{split} &(\hat{n}_j)^2 = a_j^\dagger a_j a_j^\dagger a_j = a_j^\dagger \{a_j, a_j^\dagger\} a_j - (a_j^\dagger)^2 (a_j)^2 = \hat{n}_j \\ &\Rightarrow \hat{n}_j (\hat{n}_j - 1) = 0 \,. \end{split}$$

If there is only a single fermionic site, the total Hilbert space comprises only two states, and can be naturally identified with the Hilbert space of a spin-1/2 degree of freedom<sup>5</sup>

$$|0\rangle \cong |\downarrow\rangle$$
,  $|1\rangle \cong |\uparrow\rangle$ . (1.29)

This identification of states also implies a representation of the ladder operators a and  $a^{\dagger}$  in terms of the Pauli matrices

$$a^\dagger = \frac{1}{2}(\sigma^x + i\sigma^y) \coloneqq \sigma^+ \,, \quad a = \frac{1}{2}(\sigma^x - i\sigma^y) \coloneqq \sigma^-$$

<sup>&</sup>lt;sup>4</sup>Typically, fermions are electrons that also carry a spin degree of freedom. This requires an additional index for the ladder operators. The spinless case is chosen to reduce the complexity of the notation.

<sup>&</sup>lt;sup>5</sup>The identification is not unique and other choices are equally valid and appear in the literature.

obeying the correct anti-commutation relations, and the Pauli matrix  $\sigma^z$  measures the parity of the fermionic site

$$\hat{p} \coloneqq -\sigma^z = e^{i\pi\hat{n}} = \mathbb{1} - 2\hat{n} .$$

At the level of the states, this mapping is readily extended to the full many-body quantum chain by performing the identification from Eq. (1.29) for all basis states in the occupation basis. This identification implies the mapping of the local fermion number operator

$$\hat{n}_j = \frac{1}{2} (\mathbb{1} + \sigma_j^z) \,, \tag{1.30}$$

similar to the case of one fermionic site. Performing the same extension from the single site to the chain for the creation and annihilation operators

$$\tilde{a}_j^\dagger = \frac{1}{2}(\sigma_j^x + i\sigma_j^y) \coloneqq \sigma_j^+ \,, \quad \tilde{a}_j = \frac{1}{2}(\sigma_j^x - i\sigma_j^y) \coloneqq \sigma_j^- \tag{1.31}$$

results in operators that commute on different lattice sites. Consequently, the  $\tilde{a}_{j}^{(\dagger)}$  operators do not fulfill the CAR from (1.28), and they do not represent proper fermionic operators on the quantum chain.

To define operators which have the proper anti-commuting properties, it is necessary to dress the improper ladder operators (1.31) by a non-local unitary

$$a_j^{(\dagger)} = \mathcal{J}_j \, \tilde{a}_j^{(\dagger)} = \prod_{k < j} \, e^{i \pi \hat{n}_j} \, \tilde{a}_j^{(\dagger)} = \prod_{j < k} \left( -\sigma_j^z \right) \, \tilde{a}_j^{(\dagger)} \,. \tag{1.32} \label{eq:aj}$$

This transformation is known as the Jordan-Wigner transformation [82], where  $\mathcal{J}_j$  is the Jordan-Wigner string operator that measures the partial parity of the sub-chain to the left of site j. A detailed derivation can be found in Appendix B.

The string operators have the properties

$$\mathcal{J}_{j}^{\dagger}=\mathcal{J}_{j}\,,\quad \mathcal{J}_{j}^{2}=\mathbbm{1}\,,\quad \mathcal{J}_{j+1}=\mathcal{J}_{j}e^{i\pi\hat{n}_{j}}\,, \tag{1.33}$$

which are useful for mapping local fermionic models to local spin models. For example, all the nearest neighbor terms for j < N are mapped to the spin chain according to

$$\begin{split} a_j^{\dagger} a_{j+1}^{} + \text{h.c.} &= \sigma_j^{+} \sigma_{j+1}^{-} + \text{h.c.} = \frac{1}{2} (\sigma_j^x \sigma_{j+1}^x + \sigma_j^y \sigma_{j+1}^y) \\ a_j^{\dagger} a_{j+1}^{\dagger} + \text{h.c.} &= \sigma_j^{+} \sigma_{j+1}^{+} + \text{h.c.} = \frac{1}{2} (\sigma_j^x \sigma_{j+1}^x - \sigma_j^y \sigma_{j+1}^y) \,. \end{split}$$

If the system has periodic boundary conditions, the operators connecting the first and last site of the chain acquire an additional term that depends on the global parity [83] of the fermionic chain and is given by

$$\hat{P} = \prod_{j=1}^{N} e^{i\pi \hat{n}_j} = \prod_{j=1}^{N} (-\sigma_j^z).$$
 (1.34)

The corresponding term in the Hamiltonian reads

$$a_N^{\dagger} a_1 + \text{h.c.} = \hat{P}(\sigma_1^+ \sigma_N^- + \sigma_1^- \sigma_N^+),$$

and similar for  $a_N^{\dagger} a_1^{\dagger}$ .

An important consequence of the existence of the Jordan-Wigner string is that a term like

$$H_{\mathrm{sp}} = V_{\mathrm{sp}} \sum_{j} a_{j}^{\dagger} + a_{j}$$

is forbidden, as it violates the principle of locality. Loosely speaking, the term  $a_j + a_j^{\dagger}$  is sensitive to the existence of a fermion, even if the fermion is infinitely far away. Consequently, the only allowed terms in the Hamiltonian are operators involving an even number of fermionic operators, and the fermionic parity of the entire chain is an unbreakable symmetry in all systems. In contrast, such a term is not forbidden in bosonic chains, and it is a common feature that appears, for example, in Rydberg systems [8–10]. Because the parity is a fundamental symmetry of fermionic chains, the extra parity operator  $\hat{P}$  that appears in fermionic chains with periodic boundary conditions can be incorporated into the boundary condition of the states on the spin chain, as the model can be solved separately in the even and odd parity sectors.

Based on the fermionic operators  $c_j$  it is possible to define a set of two independent Majorana operators

$$\gamma_{j,a} = c_j + c_j^{\dagger}, \quad \gamma_{j,b} = i \left( c_j - c_j^{\dagger} \right). \tag{1.35}$$

These Majorana operators are Hermitian  $\gamma_{j,\alpha}^{\dagger} = \gamma_{j,\alpha}$ , squaring to the identity  $\gamma_{j,\alpha}^2 = 1$ , and fulfill the anti-commutation relation

$$\{\gamma_{i,\alpha}, \gamma_{k,\beta}\} = 2\delta_{\alpha,\beta}\delta_{i,k}. \tag{1.36}$$

Rather than expressing the Majorana operators through the fermionic operators  $c_j$ , one can alternatively begin with a pair of independent Majorana operators,  $\gamma_{j,a}$  and  $\gamma_{j,b}$ . By pairing one a and b Majorana on the same site j results in a local two-dimensional fermionic Hilbert space described by the fermion

$$c_j = \frac{\gamma_{j,a} - i\gamma_{j,b}}{2} \,. \tag{1.37}$$

The occupation of this fermionic degree of freedom is measured by the local parity

$$\hat{p}_j = e^{i\pi\hat{n}_j} = i\gamma_{j,a}\gamma_{j,b}. \tag{1.38}$$

with the global parity of the state given by a product over all sites j

$$\hat{P} = \prod_{j=1}^{N} (i\gamma_{j,a}\gamma_{j,b}). \tag{1.39}$$

This construction is not limited to the pairing of two Majorana operators at the same site. In fact, any pairing of two independent Majorana operators can be chosen to construct the fermionic many-body Hilbert space. While the local parity operators may change for different pairings, the global parity operator is independent of the pairing and is always given by Eq. (1.39).

A particularly interesting scenario is the pairing of Majorana operators, which results in two unpaired Majorana operators localized at the opposite edges of the chain. In this case, the chain forms a symmetry-protected topological phase [84], which is the subject of Subsection 1.2.3.

#### 1.1.6 Translation Invariance and Fourier Transformation

To reduce the complexity of the notation, this subsection assumes that the quantum system describes either fermionic or bosonic particles populating a ring with N lattice sites. This type of geometry can be modeled by imposing (twisted) periodic boundary conditions on the quantum states. Let  $\beta_j^{(\dagger)}$  be either a set of fermionic or bosonic creation and annihilation operators building the many-body Hilbert space, and let  $\hat{T}$  be the many-body operator that shifts each lattice site by one, as shown in Fig. 1.2.

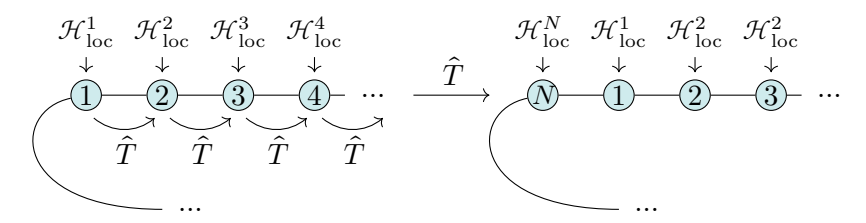


Figure 1.2: Action of the shift operator  $\hat{T}$  on a quantum system defined on a ring geometry.

Consequently, acting with  $\hat{T}$  on any quantum state on the ring N times should result in the same many-body quantum state, up to a global phase. Since the basis states are defined as repeated actions of the creation operators on the vacuum, this can be achieved by imposing that  $\hat{T}$  acts on the lattice operators as

$$\hat{T}\beta_{j}\hat{T}^{\dagger} = \beta_{j+1} , \quad \text{for } j < N$$

$$\hat{T}\beta_{N}\hat{T}^{\dagger} = e^{i\varphi}\beta_{1} .$$

$$(1.40)$$

The angle  $\varphi$  is known as the twisting angle. If the Hamiltonian of such a ring with twisted boundary conditions commute with the shift operator  $\hat{T}$ 

$$\left[\hat{T}, H\right] = 0\,,$$

the Hamiltonian is called translational invariant, and the eigenstates of the Hamiltonian can be selected as the simultaneous eigenstates of the shift operator  $\hat{T}$ . This is known as Bloch's theorem [43, 85].

The eigenstates of the shift operator  $\hat{T}$  can be created from the lattice creation and annihilation operators after applying the Fourier transformation

$$\beta_k := \frac{1}{\sqrt{N}} \sum_{i=1}^N e^{-ik\alpha j} \beta_j \,, \tag{1.41}$$

where  $\alpha$  is the length scale separating two adjacent lattice sites<sup>6</sup>. By calculating the adjoint action of the shift operator and using Eq. (1.40) these operators are found to be invariant under the action of  $\hat{T}$  for special values of the momentum k

$$\begin{split} \hat{T}\beta_{k_n}\hat{T}^\dagger &= e^{ik_n\alpha}\beta_{k_n} \\ k_n &= \frac{2\pi n + \varphi}{\alpha N} \,, \quad n = 0, \dots, N-1 \,. \end{split} \tag{1.42}$$

Thus, the twisting angle can be used to investigate different sets of momentum states.

<sup>&</sup>lt;sup>6</sup>The Fourier transformation is a unitary transformation that respects the canonical (anti)-commutations. Therefore, the new operators  $\beta_k$  are proper bosons or fermions.

If the system is translation-invariant, the contribution of the twist angle vanishes in the thermodynamic limit, and the bulk properties are independent of the twisting angle. There are two special twisting angles,  $\varphi=0$  resulting in standard periodic boundary conditions, and  $\varphi=\pi$  resulting in anti-periodic boundary conditions. The inverse transformation from the momentum operators to the position operators is given by

$$\beta_j = \frac{1}{\sqrt{N}} \sum_{k_n} e^{ik_n \alpha j} \beta_{k_n} \,, \tag{1.43}$$

where the sum runs over all allowed momenta from the set in Eq. (1.42).

The twisting angle can be implemented by starting from a Hamiltonian with periodic boundary conditions  $\varphi = 0$  and applying a magnetic field through the ring, as shown in Fig. 1.3. A particle (boson or fermion) encircling the magnetic field acquires a

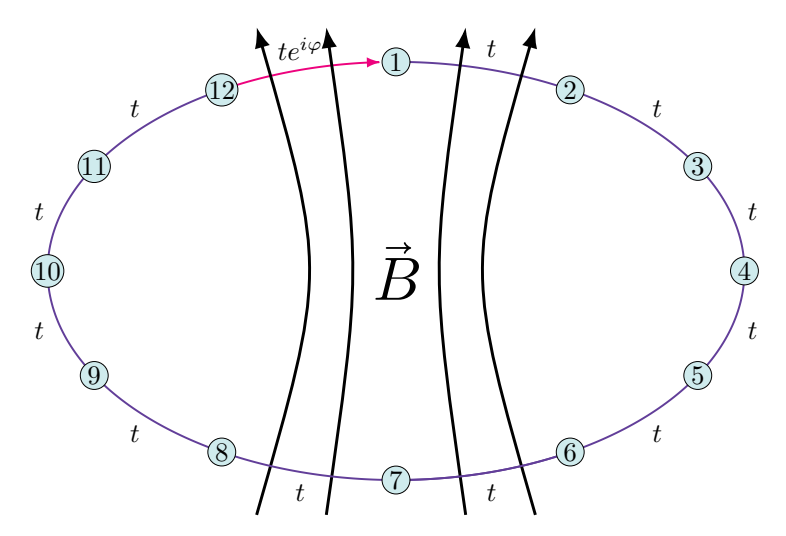


Figure 1.3: A quantum system defined on a ring of 12 lattice sites. The particles can tunnel from site j to j+1 with strength t and the tunneling from site 12 to site 1 has an additional complex phase owing to the presence of a magnetic field  $\vec{B}$ . This is highlighted in light red, with an arrow indicating the direction of tunneling.

geometric phase proportional to the magnetic flux [86, 87]. This geometric phase can be introduced in the Hamiltonian by modifying every term that leads to a current of particles through the bond (N,1), known as the Peierls substitution [88, 89]. For example, a single particle tunneling term becomes

$$-t\left(\beta_N^\dagger\beta_1+\mathrm{h.c.}\right)\rightarrow -t\left(e^{i\varphi}\beta_N^\dagger\beta_1+\mathrm{h.c.}\right)$$

and the single particle Hamiltonian

$$H = -t \sum_{i=1}^{N-1} \left( \beta_j^{\dagger} \beta_{j+1} + \text{h.c.} \right) - t \left( e^{i\varphi} \beta_N^{\dagger} \beta_1 + \text{h.c.} \right)$$

is invariant under the action of  $\hat{T}$  defined in Eq. (1.40). The Fourier transform (1.41) is straightforwardly extended to the case of the ring being populated by multiple independent fermionic or bosonic species, with each species labeled by an additional flavor index  $\sigma$  ranging from 1 to M. In this case, the Fourier transform acts independently on each flavor.

As an example, consider a generic non-interacting Hamiltonian quadratic in the  $\beta_{\sigma,j}$  variables

$$H = \sum_{j=1}^{N} \sum_{l=1}^{N} \sum_{\sigma,\tau} \beta_{\sigma,j}^{\dagger} \mathcal{H}_{\sigma,\tau}(j-l) \beta_{\tau,l} , \ \mathcal{H}_{\sigma,\tau}(r) = \overline{\mathcal{H}}_{\tau,\sigma}(-r) , \qquad (1.44)$$

where  $\sigma$  and  $\tau$  denote the flavor indices ranging from 1 to M. The matrix-valued function  $\mathcal{H}(r)$  also encodes the twisted boundary conditions such that H commutes with the shift operator  $\hat{T}$ .

Passing to the Fourier basis, this Hamiltonian becomes

$$H = \sum_{k_n} \sum_{\sigma,\tau} \beta_{\sigma,k_n}^\dagger \mathcal{H}_{\sigma,\tau}(r) \beta_{\tau,k_n} \ , \ \mathcal{H}_{\sigma,\tau}(k_n) = \sum_{r=-N+1}^{N-1} \mathcal{H}_{\sigma,\tau}(r) e^{-ik_n\alpha \, r}$$

which defines the Hermitian Bloch Hamiltonian  $\mathcal{H}(k_n)$ . The Hamiltonian is block diagonal in the momentum basis, and by further diagonalizing the Bloch Hamiltonian, this quadratic model becomes

$$H = \sum_{m} \sum_{k_{-}} \epsilon_{m}(k_{n}) \beta_{m,k_{n}}^{\dagger} \beta_{m,k_{n}}$$

$$\tag{1.45}$$

which defines the energy-momentum dispersion relation of the mth band  $\epsilon_m(k_n)$ .

Now, assuming a single flavor model M=1. If the system is loaded with  $n_{\rm B}$  bosons, the many-body ground state would be formed by placing all bosons in the single particle state with momentum minimizing the energy

$$k_{\min} = \operatorname{argmin}(\epsilon(k))$$
.

This naively indicates the formation of a Bose-Einstein condensate [90]. However, the condensation of all  $n_{\rm B}$  in the state of minimal energy is not stable against interactions or temperature. For example, adding a small but finite interaction term to Eq. (1.44), the interacting ground state of the bosonic system is instead a Tonks-Girardeau gas [91, 92].

If the system is instead populated by  $n_{\rm F}$  fermions, the many-body ground state is obtained by successively filling the  $n_{\rm F}$  lowest energy levels based on the Pauli exclusion principle [81]. The last occupied energy  $\epsilon_{\rm F}$  is called the Fermi energy, and the momenta with  $\epsilon(k_{\rm F})=\epsilon_{\rm F}$  forming the Fermi surface. Assuming  $\epsilon(-k)=\epsilon(k)$ , the Fermi surface only consists of the two points  $\{-k_{\rm F},k_{\rm F}\}$  and  $k_{\rm F}$  is called the Fermi momentum, which is related to the density  $\nu=n_{\rm F}/N$  of fermions by

$$k_{\rm F} = \pi \frac{n_{\rm F}}{\alpha N} = \pi \frac{\nu}{\alpha} \,. \tag{1.46}$$

The derivative of the dispersion relation of the fermions at the Fermi momentum defines the Fermi velocity

$$v_{\rm F} = \frac{\epsilon(k)}{\partial k} \bigg|_{k=k_{\rm F}} . \tag{1.47}$$

Similar to the case of bosons, this Fermi surface is not stable against small interactions, and the interacting ground state forms instead a Tomonaga-Luttinger liquid, which will be discussed in more detail in Subsection 1.3.1.

Unless stated otherwise, the length scale  $\alpha$  is assumed to be one, which simplifies the notation throughout the remainder of this thesis.

#### 1.1.7 Experimental Realizations

Although fairly simple to formulate as a mathematical theory, realizing a one-dimensional fermion or boson gas can be quite challenging owing to the intrinsically three-dimensional nature of every material. In a traditional condensed matter system, this requires strong confinement of the particles in two of the three dimensions, with the effective low-energy theory being one-dimensional [47, 93]. Examples include the fabrication of nanowires [94–96] of small diameters or carbon tubes [97]. While it has been demonstrated that such a system has the characteristics of one-dimensional quantum matter [98–101], recent developments have made it possible to directly formulate quasi-one-dimensional many-body systems in an artificial way, allowing for precise control of microscopic parameters.

The most prominent methods are the use of cold atoms with either bosonic or fermionic statistics loaded into an optical lattice [3–7]. These artificial lattice systems allow for high control of the interactions [102, 103], leading to the realization of highly interacting bosonic models [104], artificial fluxes with periodic boundary conditions [105, 106] and more. In particular, the model considered in Chapter I is inspired by these cold atom experiments to realize a topological phase with unpaired Majorana states localized at the edge.

Another promising approach is the use of highly excited Rydberg states of atoms that are optically confined to one dimension [8–10]. The strong interaction of atoms in the excited states while the atoms in the ground state are nearly non-interacting leads to a natural realization of Ising-like Hamiltonians, which are important in the study of many-body scars [26, 27] and the dynamical behavior of quantum matter [30]. A particular application is discussed in Chapter III, where the dynamic melting of a domain wall state is studied.

Instead of directly using fermions or bosons, a different approach is to realize them as effective excitations in composite systems. For example, the elementary excitations of superconductors are related to the creation and annihilation of Cooper pairs and thus obey bosonic statistics. This inspired the construction of arrays of small superconducting islands coupled by Josephson junctions, leading to the exchange of Cooper pairs between different superconducting islands in the array. With advanced fabrication methods and precise design of JJAs, it is possible to realize various strongly interacting bosonic many-body Hamiltonians [11–16]. The model proposed in Chapter II is inspired by these recent experimental improvements and adds a promising candidate to the existing literature for observing the tricritical Ising phase; see also Subsection 1.3.3.

In the case of fermions, a promising approach is to connect single quantum dots [107–110] or to place single magnetic atoms, called adatoms, to form a chain on the surface of a superconductor [111–113]. These adatoms form low-energy bound states in the gap of the host superconductor [114, 115] which leads to the formation of one-dimensional fermionic bands in the chain geometry.

### 1.2 Gapped Phases

The previous section introduced the basic notion necessary to describe a quantum many-body system on a chain. A crucial part of this description is the Hamiltonian H which defines the static and dynamic features of this quantum chain. These features are highly influenced by the existence or absence of a finite many-body gap  $\Delta$  as defined in Eqs. (1.18) and (1.19). This section aims to provide a short summary of

the possible phases of matter that can be realized by a one-dimensional quantum chain with a finite many-body gap.

Physically, the existence of a finite gap implies that every local excitation has a finite mass bounded from below by the gap  $\Delta$ . As a result, the gap introduces a natural length scale known as the correlation length of the system

$$\xi = \frac{1}{\Delta},$$

and ground state correlations on the size of this correlation length are exponentially decaying [65, 66]

$$C^{O,K}(j,k) \coloneqq \langle \hat{O}_j \hat{K}_k \rangle - \langle \hat{O}_j \rangle \, \langle \hat{K}_k \rangle \sim \frac{e^{-|j-k|/\xi}}{|j-k|} \,. \tag{1.48}$$

The existence of a finite correlation length, and the associated exponential clustering of correlations, implies that the ground state resembles a product state on length scales larger than  $\xi$ . Indeed, by defining a renormalization procedure that blocks neighboring sites into a super-site, similar to the Kadanoff block-spin transformation [116], it has been demonstrated that every ground state on a quantum chain flows to a product state in the presence of this length scale  $\xi$  [117, 118]. In contrast to quantum matter in higher dimensions, there is no possibility of a hidden topological order that is stable under this renormalization flow in quantum chains. From a quantum information perspective, this statement is equivalent to the existence of a short-range quantum circuit that, when applied to the quantum chain, results in a trivial product state [119].

However, this general statement overlooks the potential symmetries that may influence the quantum system, and the situation becomes more intriguing when these symmetries are considered. Throughout this section, the main object of interest is a quantum chain of N sites, either populated by bosons, fermions, or spins, which is described by the many-body Hamiltonian H. The Hamiltonian is assumed to be invariant under a global symmetry group G as explained in Subsection 1.1.4

$$U(g)HU(g)^{\dagger} = H \quad \forall \ g \in G \,, \quad U(g)^{\dagger}U(g) = U(g)U(g)^{\dagger} = \mathbb{1} \,\,.$$

The representation U(g) is acting point-wise by (anti-)unitary transformations on the quantum chain

$$U = \hat{K} \prod_{j=1}^{N} u_j,$$

and  $\hat{K}$  is either the identity or time-reversal operator, with U being unitary or antiunitary, respectively [68]. The local unitary  $u_j$  only acts non-trivially on the local Hilbert space  $\mathcal{H}_{\text{loc}}^j$  and with an identity on every other site  $k \neq j$ .

A gapped quantum chain invariant under a group G can be in one of three different phases: A trivial phase in which the ground state is unique and forms a trivial representation of the symmetry group, a symmetry-broken phase with a degenerate ground state, and a Symmetry-Protected Topological Phase (SPTP) in which the degeneracy of the ground state depends on the topology of the chain itself.

This section begins with a short review of symmetry-broken states in Subsection 1.2.1 focusing on finite Abelian symmetry groups, which are of special importance for

quantum models in one dimension. For example, the models considered in Chapters II and III exhibit a phase with spontaneously broken  $\mathbb{Z}_2$  symmetry. A more general review of this topic, including also higher dimensions, can be found in [120]. This is followed by a brief discussion of SPTPs in Subsection 1.2.2. More details on this topic can be found, for example, in [121, 122]. A special instance of an SPTP, the Kitaev chain, is discussed in detail in Subsection 1.2.3. This phase is of particular interest as it appears in the Chapters I, IV, V, and VI.

#### 1.2.1 Spontaneous Symmetry Broken Phases

The Mermin-Wagner-Hohenberg theorem [48–50] prohibit the possibility of spontaneously breaking a continuous symmetry group in one-dimensional quantum systems, except at fine-tuned points [123].

An example of this is the conservation of particles in typical fermionic chains with the symmetry group G being the  $\mathrm{U}(1)$  group generated by the total number of fermions

$$U(\phi) = e^{i\varphi \hat{N}}, \quad \varphi \in [0, 2\pi).$$

Based on the Mermin-Wagner-Hohenberg theorem, every ground state has a fixed number of fermions, and even the presence of attractive interactions does not lead to an instability, formation of Cooper pairs, and superconductivity [75–77].

While the Mermin-Wagner-Hohenberg theorem prevents the spontaneous breaking of a continuous group, it allows the quantum chain to break finite symmetry groups. In the simplest scenario, the symmetry group is Abelian, with all group elements commuting with each other, which is assumed in the following. Every finite Abelian group can be generated by one element  $\hat{P}$  and is given by

$$\mathbb{Z}_M \coloneqq \mathbb{Z}/M\mathbb{Z} \coloneqq \{\hat{P}^k \,, \ k = 0, \dots, n-1 \ : \ \hat{P}^M = \mathbb{1}\} \,. \tag{1.49}$$

From  $\hat{P}^M = 1$ , the possible eigenvalues of the generator  $\hat{P}$  are found as

$$\hat{P}|p\rangle = e^{-i\frac{2\pi}{M}p}|p\rangle , \quad p = 0, \dots M - 1.$$
 (1.50)

These eigenstates form the irreducible representations of the group  $\mathbb{Z}_M$ .

In the simplest non-trivial case, M=2, the group consists of only two elements: The identity  $\mathbbm{1}$  and one additional non-trivial element  $\hat{P}^2=\mathbbm{1}$ . A model implementing such a  $\mathbbm{Z}_2$  symmetry is the Transverse Field Ising Model (TFIM) [83, 124, 125]. Assuming open boundary conditions, the TFIM describes a chain of N spin-1/2 degrees of freedom interacting through the Hamiltonian

$$H_{\text{Ising}} = -J \sum_{j=1}^{N-1} \sigma_j^x \sigma_{j+1}^x - g \sum_{j=1}^{N} \sigma_j^z.$$
 (1.51)

Here,  $\sigma^{\alpha}$  denotes the Pauli matrices defined in Eq. (1.11). The Pauli matrix  $\sigma^{x}$  transforms odd under adjoint application of the  $\sigma^{z}$  matrix

$$\sigma^z \sigma^x \sigma^z = -\sigma^x \,. \tag{1.52}$$

Based on this transformation property, it is found that the TFIM has a global symmetry given by the parity of spins in the spin-up state<sup>7</sup>

$$\hat{P} = \prod_{j=1}^{N} (-\sigma_j^z), \quad P^2 = 1, \quad \hat{P}H_{\text{Ising}}\hat{P} = H_{\text{Ising}}.$$
 (1.53)

This operator forms the representation of the non-trivial element that generates the  $\mathbb{Z}_2$  symmetry group of the TFIM. Because the Hamiltonian commutes with  $\hat{P}$ , the eigenstates of  $H_{\text{Ising}}$  can be chosen as states with a fixed parity of spins in the spin-up state. A suitable set of basis states is given by

$$\hat{P}\left|s_{1},\ldots,s_{N}\right\rangle = (-1)^{\sum_{j=1}^{N}\left(m_{j}-1\right)}\left|s_{1},\ldots,s_{N}\right\rangle\,,\quad m_{j} = \begin{cases} 1\,,\text{ for }s_{j} = \downarrow\\ 2\,,\text{ for }s_{j} = \uparrow \end{cases}$$

and every eigenstate of H is a linear combination of these states with a fixed parity eigenvalue.

#### Consequences of Spontaneously Symmetry Breaking

If a given model spontaneously breaks the finite symmetry group  $\mathbb{Z}_M$ , the ground state is M times degenerated in the thermodynamic limit. The set of states forming the ground-state manifold is denoted by GS. This set forms an M-dimensional Hilbert space, with every element being a valid ground state of H. A simple basis of GS is given by states which are transformed into each other by applying the operator  $\hat{P}$ 

$$\hat{P} |\Omega_n\rangle = |\Omega_{n+1}\rangle , \quad n = 0, \dots M - 1, \quad M \cong 0.$$
 (1.54)

Because the operator  $\hat{P}$  is a global product of N local unitary operators, the states defined by this equation are macroscopically distinct

Since the Hamiltonian H is assumed to contain only interactions of finite range, an operator such as  $\hat{P}$  which acts on all sites at the same time, can only be generated in perturbation theory at an order equal to the system size itself. Thus, projecting the Hamiltonian to GS gives at any finite system size

$$H_{\rm GS} \approx A e^{-BN} (\hat{P} + \hat{P}^{\dagger}),$$
 (1.55)

with two constants A and B of order one. As expected, the true eigenstates for any finite system size are the symmetric states invariant under the action of  $\hat{P}$ , with a gap that closes exponentially fast with N.

The symmetry restoring states can be written in terms of the states defined in Eq. (1.54) as

$$|\omega_p\rangle = \frac{1}{\sqrt{M}} \sum_{m=0}^{M-1} e^{i\frac{2\pi}{M}mp} |\Omega_m\rangle = \frac{1}{\sqrt{M}} \sum_{m=0}^{M-1} e^{i\frac{2\pi}{M}mp} \hat{P}^m |\Omega_0\rangle$$
 (1.56)

with eigenvalue

$$\hat{P}\left|\omega_{p}\right\rangle = e^{-i\frac{2\pi}{M}p}\left|\omega_{p}\right\rangle$$

<sup>&</sup>lt;sup>7</sup> The transformation in Eq. (1.52) requires only the symmetry operator to be a product of all  $\sigma_j^z$  leaving out an undefined global phase. As the non-trivial symmetry operator  $\hat{P}$  should square to the identity, this fixes the global phase to a simple sign. The reason to choose the sign as in Eq. (1.52) is to be consistent with the Jordan-Wigner transformation and the fermionic parity operator; see also Eq. (1.34).

as required in Eq. (1.50). One way to detect whether a system spontaneously breaks symmetry is to define a local order parameter

$$\hat{O} = \sum_{j=1}^{N} \hat{o}_j \,, \quad \hat{O}^{\dagger} = \hat{O} \,,$$
 (1.57)

where  $\hat{o}_j$  acts only on a small neighborhood of site j.

The operators  $\hat{o}_j$  have to transform non-trivially under the action of the symmetry operator

$$\hat{P}^{\dagger}\hat{o}_{j}\hat{P} = e^{i\varphi}\hat{o}_{j}, \quad \varphi \neq 0. \tag{1.58}$$

As a consequence, this operator has a zero expectation value with respect to any symmetric state

$$\langle p|\hat{O}|p\rangle = \langle p|\hat{P}^{\dagger}\hat{O}\hat{P}|p\rangle = e^{i\varphi}\langle p|\hat{O}|p\rangle = 0$$
 (1.59)

and the operator  $\hat{O}$  is not allowed to appear in the perturbation series at any order. This statement is also true for the local operators  $\hat{o}_i$  that appear in the sum of  $\hat{O}$ .

Since the basis states of Eq. (1.54) are not symmetric, they are allowed to have a non-trivial expectation value

$$\frac{\langle \Omega_m | \hat{O} | \Omega_n \rangle}{N} \xrightarrow{N \to \infty} \delta_{m,n} \, c_m \, .$$

Here, it is assumed that  $\hat{O}$  is diagonal in the symmetry-breaking basis. By adding a small symmetry breaking perturbation to the Hamiltonian

$$H_{\rm sb} = h\hat{O}$$
,

the ground-state degeneracy splits, and the state minimizing  $hc_m$  is selected as the true ground state of the slightly perturbed system. Imagine turning off the perturbation after selecting the symmetry-breaking ground state. Because the coupling to the other states is exponentially small, Eq. (1.55), the system remains frozen in this symmetry-broken state for N sufficiently large.

Another way to formulate this is to consider a preparation protocol that attempts to steer the system into one of the symmetric ground states. However, these states are fragile, and a small fluctuation or imperfection in the preparation protocol leads to the collapse of the system in one of the symmetry-breaking states.

Although the expectation value of the order parameter  $\hat{O}$  evaluated with respect to the symmetry-restoring states is zero, their relation to the basis that breaks the symmetry, Eq. (1.56), can be used to probe the spontaneous breaking of the symmetry directly on the symmetry-restoring basis. For this, assume that in the thermodynamic limit

$$\langle \Omega_m | \hat{o}_i | \Omega_n \rangle = \delta_{mn} c_m$$

independent of the site<sup>8</sup> j. Since the operators  $\hat{o}_j$  are acting locally, their correlation function separates for large distances with respect to the symmetry-broken states

$$\langle \Omega_m | \hat{o}_j \hat{o}_k | \Omega_n \rangle \xrightarrow{|j-k| \to \infty} \sum_n \langle \Omega_m | \hat{o}_j | \Omega_n \rangle \langle \Omega_n | \hat{o}_j | \Omega_m \rangle = c_m^2.$$
 (1.60)

This result is based on inserting a resolution of the identity between the two operators  $\hat{o}_j$  and  $\hat{o}_k$  and exploiting the fact that the states outside the ground-state

<sup>&</sup>lt;sup>8</sup>This is the typical case as the lattice Hamiltonian is assumed to be translational invariant in the thermodynamic limit.

manifold are separated by an energy gap  $\Delta$  and thus only contribute to an exponential background decay [65].

Calculating the correlation function of the  $\hat{o}_j$  operators in the symmetry restoring basis results in a long distance limit of

$$\langle \omega_p | \hat{o}_j \hat{o}_k | \omega_p \rangle = \frac{1}{M} \sum_{m,n} e^{-i\frac{2\pi}{M}(m-n)p} \langle \Omega_m | \hat{o}_j \hat{o}_k | \Omega_n \rangle \xrightarrow{|j-k| \to \infty} \frac{1}{M} \sum_{m=0}^{M-1} c_m^2 , \qquad (1.61)$$

which modifies the general behavior described by Eq. (1.48). The onset of a constant limit is also known as an off-diagonal long-range order [126] which can serve as a tool to detect spontaneous symmetry breaking.

## Spontaneous Symmetry Breaking in the Transverse Field Ising Model

Again, consider the TFIM introduced in Eq. (1.51). There are two simple limits that allow for a direct solution of the model. For J = 0, the TFIM model reduces to

$$H_{\text{Ising}} = -g \sum_{j=1}^{N} \sigma_j^z. \tag{1.62}$$

The ground state is unique and found by minimizing all  $\sigma_i^z$  individually

$$|\Omega\rangle = |\uparrow, \dots, \uparrow\rangle , \quad H|\Omega\rangle = -gN|\Omega\rangle .$$
 (1.63)

This state is also an eigenstate of the parity operator  $\hat{P}$  with an eigenvalue depending on the total size of the chain

$$\hat{P} |\Omega\rangle = (-1)^N |\Omega\rangle .$$

On the other hand, for g = 0 the TFIM becomes

$$H_{\text{Ising}} = -J \sum_{i=1}^{N-1} \sigma_j^x \sigma_{j+1}^x$$

and there are two ground states defined by the eigenstates of the  $\sigma_i^x$  operator

$$\begin{split} |\pm\rangle \coloneqq \frac{1}{\sqrt{2}}(|\uparrow\rangle \pm |\downarrow\rangle) \\ |\Omega_{\pm}\rangle = |\pm,\dots,\pm\rangle \,, \quad H \, |\Omega_{\pm}\rangle = -J(N-1) \, |\Omega_{\pm}\rangle \;. \end{split} \tag{1.64}$$

The two states  $|\Omega_{\pm}\rangle$  are not eigenstates of the parity operator  $\hat{P}$  but get transformed into each other by

$$\hat{P} \left| \Omega_{+} \right\rangle = \left| \Omega_{-} \right\rangle \,, \tag{1.65}$$

and are thus the two states forming the symmetry-broken local basis from Eq. (1.54). The two symmetry restoring states are, following Eq. (1.56),

$$\begin{split} |\omega_{e/o}\rangle &= \frac{1}{\sqrt{2}}(|\Omega_{+}\rangle \pm |\Omega_{-}\rangle) \\ \hat{P} \, |\omega_{e/o}\rangle &= \pm |\omega_{e/o}\rangle \; . \end{split} \tag{1.66}$$

These states are linear combinations of macroscopically distinct product states, as discussed in the general setting. A suitable order parameter is given by the total magnetization in x direction

$$\hat{O} = \frac{1}{N} \sum_{j=1}^{N} \sigma_j^x \tag{1.67}$$

which transforms under the action of the parity operator as

$$\hat{P}\hat{O}\hat{P} = -\hat{O}$$
.

The expectation value of this order parameter with respect to the symmetry broken basis  $|\Omega_{+}\rangle$  is given by

$$\langle \Omega_{\pm} | \hat{O} | \Omega_{\pm} \rangle = \pm 1 \,, \quad \langle \Omega_{\pm} | \hat{O} | \Omega_{\mp} \rangle = 0 \,. \tag{1.68} \label{eq:equation:equation:1.68}$$

This follows from the expectation value of the local  $\sigma_j^x$  operator and the fact that  $|\Omega_+\rangle$  is a product state of eigenstates of  $\sigma^x$ 

$$\langle \Omega_{\pm} | \sigma_{j}^{x} | \Omega_{\pm} \rangle = \langle \pm | \sigma^{x} | \pm \rangle = \pm 1$$
 .

Using this result, the expectation value with respect to the symmetry restoring basis  $|\omega_{e/o}\rangle$  is straight forward to evaluate

$$\langle \omega_{e/o} | \hat{O} | \omega_{e/o} \rangle = \frac{\langle \Omega_+ | \hat{O} | \Omega_+ \rangle + \langle \Omega_- | \hat{O} | \Omega_- \rangle}{2} = \frac{1 - 1}{2} = 0 \tag{1.69}$$

which equals zero, as expected from Eq. (1.59). The two point correlation function of the local  $\sigma_i^x$  operators gives a non-trivial result

$$2 \left\langle \omega_{e/o} \middle| \sigma_j^x \sigma_k^x \middle| \omega_{e/o} \right\rangle = \underbrace{\left\langle \Omega_+ \middle| \sigma_j^x \sigma_k^x \middle| \Omega_+ \right\rangle}_{=1} + \underbrace{\left\langle \Omega_- \middle| \sigma_j^x \sigma_k^x \middle| \Omega_- \right\rangle}_{=1} = 2. \tag{1.70}$$

For finite values of g > 0, the ground states of the TFIM are no longer given by the product states in Eq. (1.64), but are dressed with short-range correlations. However, it was found that the ground state remains double-degenerated for all g < J. In general, these quantum corrections lead to a reduction of the order parameter in the symmetry broken basis

$$|\left\langle \Omega_{+}|\hat{O}|\Omega_{+}\right\rangle |\coloneqq m(g)\leq 1\,. \tag{1.71}$$

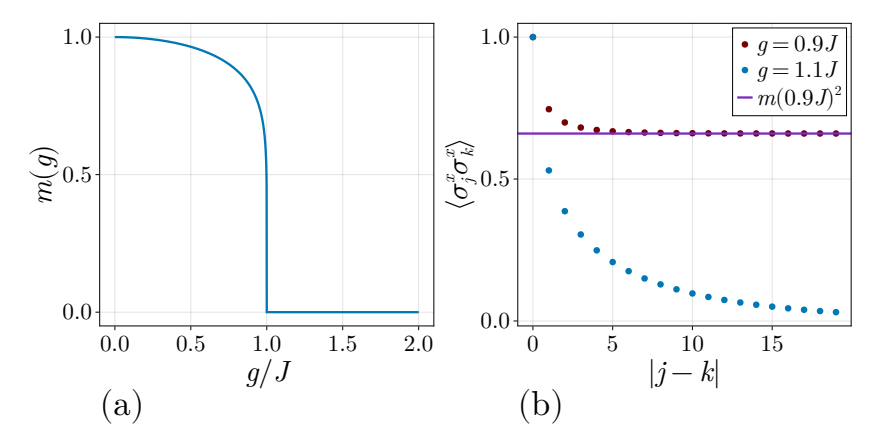


Figure 1.4: (a) Magnetization m(g) from Eq. (1.71) for varying the transverse field through the quantum phase transition at g = J. (b) Correlation function  $\langle \sigma_j^x \sigma_k^x \rangle$  for the two selected points g = 0.9J and g = 1.1J. In the symmetry-broken region (g = 0.9J), the ground states are selected as the symmetry-respecting ground states, as in Eq. (1.72). The purple line denotes the squared value of the magnetization  $m(0.9J)^2$  referred from panel (a).

Figure 1.4(a) shows the magnetization curve of the TFIM. For small values of g/J, the magnetization is close to 1 as predicted by Equations (1.68) and (1.70), and by approaching the quantum phase transition at g = J it starts to drop to zero.

Similar, the quantum corrections lead to an exponential decay at short distance for the correlation functions in the symmetry restoring basis before reaching the plateau value

$$\langle \omega_{e/o} | \sigma_j^x \sigma_k^x | \omega_{e/o} \rangle \approx e^{-\lambda |j-k|} + |m(g)|^2$$
 (1.72)

where the decay constant  $\lambda$  is related to the spectral gap of the system [65] and m(g) is the magnetization value from Eq. (1.71). This expected behavior of the correlation function in the symmetry-restoring basis is shown in Fig. 1.4(b) for g = 0.9J (red dots). After a transient short-distance exponential decay, the correlation function reaches a plateau value equal to  $m(0.9J)^2 \approx 0.66$  (purple line).

For g > J the TFIM has a unique symmetric ground state, compare also the J=0 limit in Eqs. (1.62) and (1.63). In this case, the expectation value of the order parameter must be zero, as shown in Fig. 1.4(a), and the correlation functions decay exponentially without reaching a non-zero plateau value. This is illustrated in Fig. 1.4(b) for g=1.1J (blue dots). At exactly g=J the TFIM undergoes a smooth quantum phase transition, and the model is described by the critical Ising model, which is a conformal field theory with correlations that decay algebraically. A more detailed discussion of this critical point can be found in Subsection 1.3.3.

In conclusion, a symmetry-broken state can be detected by a local order parameter  $\hat{O}$  that acquires a non-trivial value for symmetry-broken states but is zero for symmetry-restoring states. This is done by varying the parameters of the system and monitoring the onset of a non-trivial value for  $\langle \hat{O} \rangle$  or equivalently, the onset of an off-diagonal long-range order in the correlation functions. The next subsection discusses a different scenario for finite symmetry groups in one dimension: a Symmetry-Protected Topological Phase. In contrast to symmetry breaking, the different (topological) phases of such a system cannot be distinguished by a local order parameter and differ only in terms of global properties.

## 1.2.2 Symmetry Protected Topological Phases

In mathematics, topology classifies the properties of a system that remain invariant under continuous deformations, also known as topological invariants. Continuous deformations include any form of local change, such as stretching and deformation, but exclude any rapid changes, such as cutting or gluing. One of the most famous examples of this is the transformation of a cup into a donut (torus). During this transformation, the number of holes, also known as the genus, remains unchanged. However, further transformation of the torus into a figure eight with two holes requires gluing the torus together at some point.

In condensed matter physics, the concept of describing the properties of physical systems under the paradigm of topology was introduced by David J. Thouless, F. Duncan M. Haldane, and J. Michael Kosterlitz [127]. They adapted the mathematical concepts to explain phenomena, such as quantum Hall states or superfluid phase transitions. Nowadays, topological properties are ubiquitous in modern condensed matter physics. One example is the use of topological quantum matter as the basis for quantum computers. The idea behind this concept is the existence of a new type of collective low-lying energy excitation present in these quantum states, known as anyons<sup>9</sup>. The braiding of anyons can lead to logical quantum gatters and thus a po-

<sup>&</sup>lt;sup>9</sup>The name anyon originates from their exchange statistics. While bosons and fermions have either commuting or anti-commuting statistics, an anyon can have any possible exchange statistics.

tential universal gate set. Microscopically, an anyon arises from the fractionalization of the underlying microscopic degrees of freedom over a large distance [128, 129]. This makes these quasi-particles very robust against local perturbations, fully in line with the ideas of topology presented previously. Moreover, the existence of anyons leads to long-range order in the correlations of the quantum state. The existence of this hidden topological order makes it impossible to smoothly deform this quantum state into a product state [119]. Examples of such topological ordered states are the Moore-Read state [130, 131] closely related to the fractional quantum Hall state at  $\nu = 5/2$  [132] or general quantum spin liquids [133, 134].

In the presence of global symmetries, it is possible to define a Symmetry-Protected Topological Phase (SPTP). The SPTP shares some similarities with a topologically ordered state, such as the dependency of the ground state degeneracy on the boundary conditions of the physical system and the existence of zero-energy excitations emerging on the surface between two different SPTPs. However, unlike the topologically ordered state, an SPTP does not have non-trivial anyonic excitations and no intrinsic topological order. The simplest form of an SPTP is that of a topological insulator, which is very similar to an ordinary insulator described by two bands with a finite energy gap  $\Delta$  separating the valence band, which is completely filled with fermions, from the conductance band, which is completely empty. In an SPTP, the system hosts gapless states that are exponentially localized to its surface under open boundary conditions. The existence of such gapless surface states is also linked to a topological index  $\nu \in \mathbb{Z}$  or  $\nu \in \mathbb{Z}_m$  defined for the bulk of the system. This is known as the bulk-edge correspondence [135]. In the case of non-interacting fermionic models, a full classification in any dimensions was achieved [136, 137] according to the ten symmetry classes defined by A. Altland and M. Zirnbauer [138]. Interactions can have dramatic effects on the non-interacting classification [139] making it difficult to find a simple general classification for arbitrary dimensions. An exception is given by one-dimensional systems, where a full classification of interacting SPTPs has recently been achieved [52, 54].

### Su-Schrieffer-Heeger Model

A simple example of a model allowing for the existence of a non-trivial SPTP is the Su–Schrieffer–Heeger Model (SSHM) [140], which will reappear as an effective model in Chapter IV.

The SSHM was proposed to describe the electronic ground state of polyacetylene, a polymer chain consisting of alternating double and single electronic bonds between the carbon atoms, as shown in Fig. 1.5(a). This alternating structure motivates the formulation of a non-interacting lattice Hamiltonian  $H_{\rm SSH}$  shown in Fig 1.5(b). The Hamiltonian consists of an alternating structure of hopping amplitudes between neighboring lattice sites and reads

$$H_{\text{SSH}} = -t \sum_{j=1}^{N} (1 + (-1)^{j} \delta) c_{j}^{\dagger} c_{j+1} + \text{h.c.} = -\sum_{j=1}^{\lfloor \frac{N}{2} \rfloor} v a_{j}^{\dagger} b_{j} + w b_{j}^{\dagger} a_{j+1} + \text{h.c.}$$
 (1.73)

assuming periodic boundary conditions. The second equal sign follows after enlarging the unit cell to include two neighboring lattice sites followed by the identification

$$\begin{split} a_j &\coloneqq c_{2j-1} \,, \quad b_j \coloneqq c_{2j} \\ v &\coloneqq t(1-\delta) \,, \quad w \coloneqq t(1+\delta) \,. \end{split}$$

In the following,  $\tilde{N} = \lfloor \frac{N}{2} \rfloor$  denotes the number of unit cells in the system. The SSHM

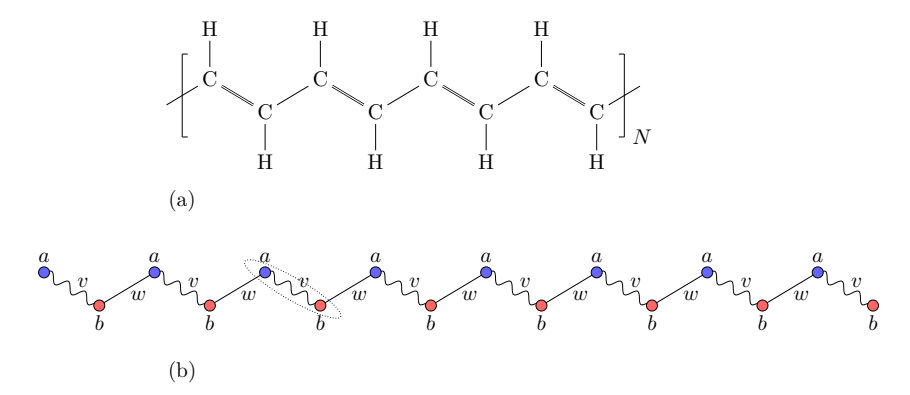


Figure 1.5: (a) Structure of Polyacetylene, which consists of alternating double and single bonds of carbon atoms. An additional hydrogen atom is attached to each carbon atom. (b) Lattice structure of the SSHM given by the Hamiltonian in Eq. (1.73). The dotted ellipse denotes an enlarged unit cell that includes two neighboring sites. This defines two independent fermionic species, a and b for the odd and even sites of the original lattice.

is symmetric under an anti-unitary transformation, which acts on the fermionic creation/annihilation operators as

$$\hat{\Gamma}a_{j}\hat{\Gamma}^{\dagger} = a_{j}^{\dagger}, \quad \hat{\Gamma}b_{j}\hat{\Gamma}^{\dagger} = -b_{j}^{\dagger}, \quad \hat{\Gamma}i\hat{\Gamma}^{\dagger} = -i. \tag{1.74}$$

This symmetry, also known as chiral or sublattice symmetry, can be seen as a combined action of a time-reversal operation followed by an interchange between particles and holes. Following the classification of SPTPs [136, 137], the SSHM is in class AIII, which is characterized by an integer topological index  $\nu \in \mathbb{Z}$  known as the winding number [141].

The non-interacting nature of the SSHM allows for diagonalization in the momentum basis, as discussed in Subsection 1.1.6. Using Eq. (1.43) the SSHM becomes

$$\begin{split} H_{\text{SSH}} &= \sum_{n=0}^{\tilde{N}} \left( a_{k_n}^{\dagger} \quad b_{k_n}^{\dagger} \right) \mathcal{H}_{\text{SSH}}(k_n) \begin{pmatrix} a_{k_n} \\ b_{k_n} \end{pmatrix} \,, \quad k_n = \frac{2\pi}{\tilde{N}} n \\ \mathcal{H}_{\text{SSH}}(k) &= \begin{pmatrix} 0 & -v - w e^{-ik} \\ -v - w e^{ik} & 0 \end{pmatrix} = d_x(k) \sigma^x + d_y(k) \sigma^y \,. \end{split} \tag{1.75}$$

After diagonalizing the  $2 \times 2$  Bloch Hamiltonian  $\mathcal{H}_{\text{SSH}}(k)$ , the two bands are described by the energy-momentum dispersion relations

$$\epsilon(k)_{\pm} = \pm \sqrt{d_x(k)^2 + d_y(k)^2} = \pm \sqrt{v^2 + w^2 + 2vw\cos(k)} \,. \tag{1.76}$$

The chiral symmetry of Eq. (1.74) is represented in the momentum basis by the matrix  $\gamma = \sigma^z$  which anti-commutes with  $\mathcal{H}_{\text{SSH}}(k)$ 

$$\gamma \mathcal{H}_{\text{SSH}}(k) \gamma = -\mathcal{H}_{\text{SSH}}(k)$$
. (1.77)

Chiral symmetry requires that for every eigenstate with energy  $\epsilon(k)$  a second eigenstate with energy  $-\epsilon(k)$  exists, and the dispersion relation is mirror-symmetric with respect to zero energy.

As shown in Fig. 1.6, the two bands are well separated by a finite gap  $\Delta = |v - w|$  except for v = w where the two bands touch each other. At this point, the system undergoes a quantum phase transition.

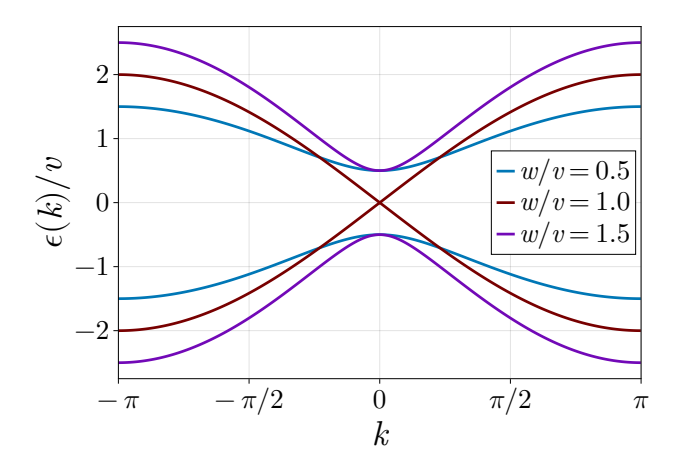


Figure 1.6: Band structure of the SSHM. The band structure is shifted by  $\pi$  with respect to Eq. (1.76) to place the band minimum at k = 0.

Both bands have  $\tilde{N}$  number of available states. Thus, filling the system with  $n_{\rm F} = \lfloor N/2 \rfloor = \tilde{N}$  number of fermions results in an insulating state with a unique ground state for either v < w or v > w.

Next, consider the same system with open boundary conditions. The SSHM can still be exact diagonalized by finding new single particle orbitals as linear combinations of the original fermions

$$\begin{split} H_{\text{SSH}} &= \sum_{n=1}^{\tilde{N}} \epsilon_{n} \left( c_{+,n}^{\dagger} c_{+,n} - c_{-,n}^{\dagger} c_{-,n} \right) \,, \quad U^{\dagger} U = U U^{\dagger} = \mathbb{1} \\ c_{+,n} &= \sum_{j=1}^{\tilde{N}} \bar{U}_{2j-1,n} \, a_{j} + \bar{U}_{2j,n} \, b_{j} \,, \quad c_{-,n} = \sum_{j=1}^{\tilde{N}} \bar{U}_{2j-1,n+\tilde{N}} \, a_{j} + \bar{U}_{2j,n+\tilde{N}} \, b_{j} \,, \end{split} \tag{1.78}$$

where the chiral symmetry of Eq. (1.74) again forces the bands to be symmetric around zero energy. As shown in Fig. 1.7(a) and (b), the system has a finite gap separating the two bands. This results in an insulating phase for  $v \neq w$  at half-filling with  $n_{\rm F} = \tilde{N}$ .

However, for w < v, the ground state is unique, whereas for w > v, two additional single-particle states are present in the gap at exactly zero energy. The existence of these additional states also reduces the number of states in the valence and conductance band by one.

Because occupying these states does not require additional energy, the half-filled chain has a doubly degenerate ground state in which either of the two zero-energy states is occupied. Furthermore, the zero energy states have a wave function which is exponentially localized to the two boundaries of the system and only involve one of the two species a or b

$$c_{0,1} = \sum_{j=1}^{\tilde{N}} \varphi_j^a a_j, \quad c_{0,2} = \sum_{j=1}^{\tilde{N}} \varphi_j^b b_j$$

$$\varphi_j^a = \mathcal{N}e^{-\lambda j}, \quad \varphi_j^b = \mathcal{N}e^{-\lambda(\tilde{N}-j)},$$

$$(1.79)$$

as shown in Fig. 1.7(c). The appearance of these edge localized zero energy modes is connected to a topological bulk index known as the winding number  $\nu \in \mathbb{Z}$  [141]

$$\nu = \frac{1}{2\pi} \int_{-\pi}^{\pi} dk \, \frac{d_x(k)\partial_k d_y(k) - \partial_k d_x(k)d_y(k)}{d_x(k)^2 + d_y(k)^2} \in \mathbb{Z}$$
 (1.80)

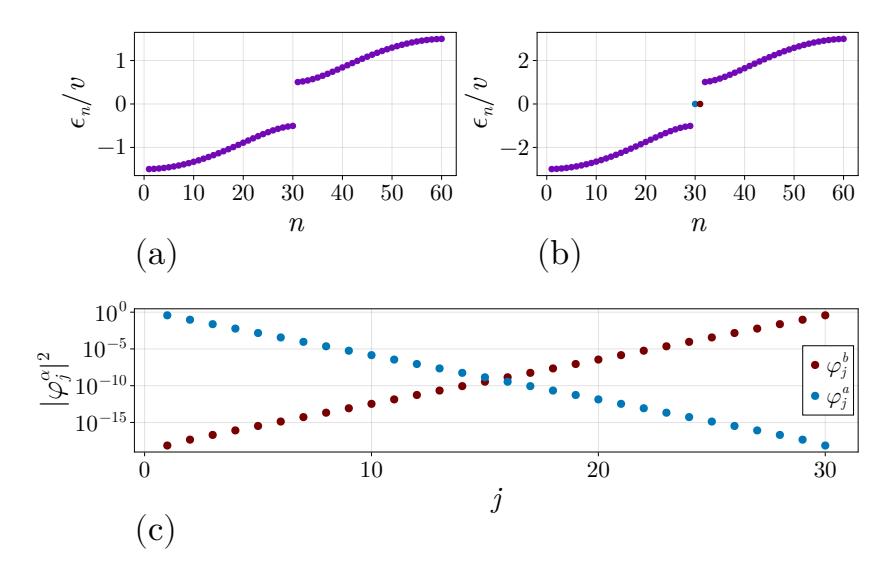


Figure 1.7: Eigenenergies of the SSHM with open boundary conditions for  $\tilde{N}=30$  unit cells for the topological trivial regime with w=v/2, panel (a), and the topological non-trivial regime with w=2v, panel (b). Panel (c) displays the single-particle wave functions, Eq. (1.79), of the zero-energy modes for w=2v with the color matching the state in panel (b). As both states have only support on one of the two species a or b, only the non-zero component is shown.

which for the SSHM evaluates to

$$\nu = \begin{cases} 0, & \text{for } v > w \\ 1, & \text{for } v < w \end{cases}$$
 (1.81)

This winding number measures how often the vector  $\vec{d}(k) = (d_x(k), d_y(k))^T$  defined in Eq. (1.75) winds around the origin when varying k, as shown in Fig. 1.8. Because the energy bands are given as the norm of this vector  $\epsilon_{\pm} = \pm |\vec{d}(k)|$ , crossing the origin is equivalent to a gap closing, and thus, a quantum phase transition occurs. Furthermore, the chiral symmetry from Eq. (1.77) forces the vector  $\vec{d}(k)$  to be in a two-dimensional plane. Consequently, the winding number can only be changed by either closing the gap or breaking the chiral symmetry.

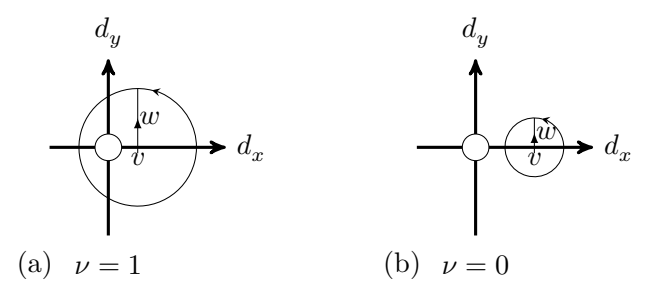


Figure 1.8: Path traced out by the planar vector function  $\vec{d}(k) = (d_x(k), d_y(k))^T$  for  $k \in [-\pi, \pi)$  for the topologically non-trivial regime v < w, panel (a), and the topologically trivial regime v > w, panel (b). The origin is indicated by a large white circle.

Breaking the chiral symmetry is achieved by adding a small  $\sigma^z$  contribution to the momentum Hamiltonian  $\mathcal{H}_{\text{SSH}}(k)$  in Eq. (1.75)

$$\mathcal{H}'(k) = \mathcal{H}_{SSH}(k) + \delta \sigma^z. \tag{1.82}$$

In real space, this term corresponds to a staggered potential

$$H_{\text{pot}} = \delta \sum_{j=1}^{\tilde{N}} (a_j^{\dagger} a_j - b_j^{\dagger} b_j). \tag{1.83}$$

Since the edge localized state have only support on one of the two species a or b, such a term directly lifts the degeneracy of the edge mode leading to a splitting proportional to the coupling  $\delta$ 

$$\Delta = 2\delta, \tag{1.84}$$

as demonstrated in Fig. 1.9. It is now possible to merge the previous zero-energy states with the valence and conductance bands, and the previous topological non-trivial phase can be deformed into a trivial state without closing the bulk gap.

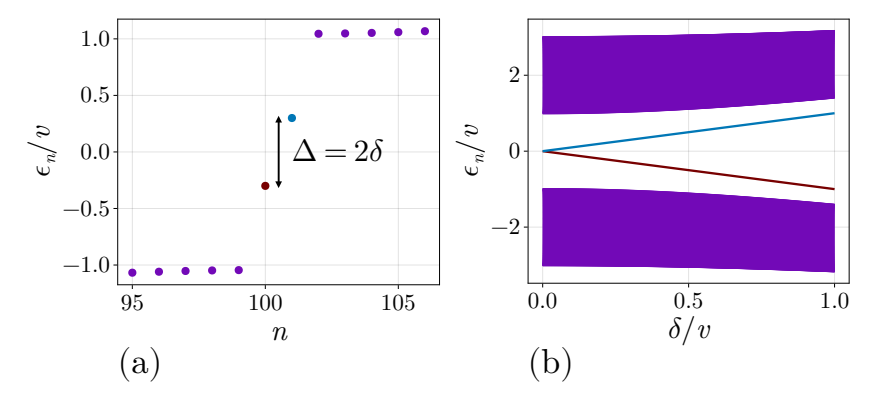


Figure 1.9: Splitting of the zero energy states under the influence of the staggered potential from Eq. (1.83) for  $\tilde{N}=100$  unit cells and w=2v for (a) fixed  $\delta=0.3v$  and (b) for varying  $\delta/v \in [0,1]$ .

The SSHM in Eq. (1.73) allows only one pair of zero-energy edge modes. By adding longer-ranged terms that respect the chiral symmetry from Eq. (1.74), it is possible to achieve larger winding numbers  $\nu$ , and thus a larger number of zero-energy states. In Fig. 1.10 this is shown exemplary for the deformed SSHM

$$H'_{\text{SSH}} = H_{\text{SSH}} - w_2 \sum_{j=1}^{\tilde{N}-2} b_j^{\dagger} a_{j+2} + \text{h.c.}$$
 (1.85)

where, for the correct choice of parameters, the system has four zero-energy states.

In general, topological insulators and SPTPs are very fragile, as small symmetry-breaking perturbations remove the gapless edge states, destroying the topological order. However, there is one physical system in one dimension that allows for a robust SPTP that cannot be destroyed by any physical deformation of the Hamiltonian that preserves the gap. As discussed in Subsection 1.1.5, the fermionic parity  $\hat{P}$  is a global  $\mathbb{Z}_2$  symmetry which can only be broken by non-local operators such as a term that creates/annihilates a single fermion

$$H = \Omega \sum_{i} c_{j} + c_{j}^{\dagger} \,.$$

Such a term violates the law of locality because a fermion placed at  $+\infty$  is sensitive to the action of this Hamiltonian at  $-\infty$  owing to the anti-commutation relations obeyed by fermions. Therefore, an SPTP protected by fermionic parity is stable

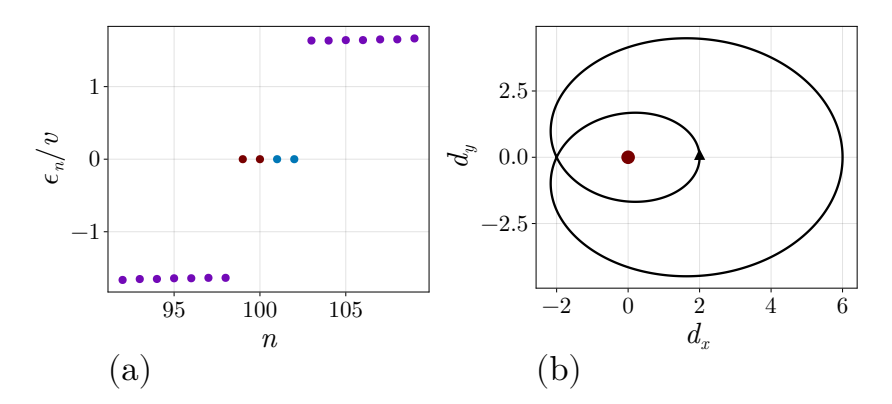


Figure 1.10: (a) Energy spectrum of the deformed SSHM according to Eq. (1.85) around zero energy for w=2v and  $w_2=3v$  for open boundary conditions and N=100 unit cells. There are four zero-energy states corresponding to the four states that are exponentially localized at the edge. At half-filling, two of the four zero-energy states are occupied, leading to a ground-state degeneracy of  $\binom{4}{2}=6$ . (b) Corresponding path of the planar vector  $(d_x(k),d_y(k))$  for the deformed SSHM with the same parameters as in (a). The path encircles the origin (red dot) twice while going from  $k=-\pi$  to  $k=\pi$  leading to a winding number of  $\nu=2$ .

against all local perturbations and can be considered a truly topologically ordered phase in one dimension. To see the physical consequences of this SPTP, the next subsection discusses a simple model Hamiltonian realizing this non-trivial SPTP: the Kitaev chain model [84].

## 1.2.3 Kitaev Chain and Unpaired Majorana Zero Modes

In his seminal paper [84] of 2001, Alexei Kitaev demonstrated that a chain populated by spinless fermions, described by the creation/annihilation operators  $c_j^{(\dagger)}$  allows for the existence of a non-trivial topological SPTP protected by the fermionic parity

$$\hat{P} = \prod_{i=1}^{N} \hat{p}_{j} = \prod_{i=1}^{N} e^{i\pi \hat{n}_{j}} = \prod_{i=1}^{N} (1 - 2\hat{n}_{j}) . \tag{1.86}$$

The key ingredient for the realization of this phase is to include a p-wave coupling term  $c_j^{\dagger}c_l^{\dagger}$  + h.c. between the fermions, which explicitly breaks the conservation of particles down to a residual  $\mathbb{Z}_2$  parity symmetry.

A particular simple model Hamiltonian meeting all the requirements is given by the Kitaev chain model

$$H_{\rm Kitaev} = \sum_{j=1}^{N-1} \left( -w \, c_j^\dagger c_{j+1}^{\phantom{\dagger}} - \Delta_p \, c_j^\dagger c_{j+1}^\dagger + {\rm h.c.} \right) - \frac{\mu}{2} \sum_{j=1}^{N} \hat{p}_j \, . \tag{1.87}$$

Since any phase of the pairing coupling  $\Delta_p$  can be removed by a redefinition of the fermionic operators [84], and the sign of the chemical potential can be flipped  $\mu \to -\mu$  by a particle-hole transformation  $c_j^\dagger \to c_j$ , it is sufficient to consider all parameters to be positive  $\mu, w, \Delta_p \geq 0$ .

To understand the behavior of this model and the appearance of the SPTP, it is useful to rewrite the Hamiltonian using the Majorana fermions defined in Eq. (1.35). For the sake of completeness, the definition is restated here

$$\gamma_{j,a} = c_j + c_j^{\dagger}, \quad \gamma_{j,b} = i \left( c_j - c_j^{\dagger} \right).$$
 (1.88)

In terms of the Majorana operators, the Kitaev chain model in Eq. (1.87) becomes

$$\begin{split} H_{\text{Kitaev}} &= -\frac{1}{2} \sum_{j=1}^{N-1} \left[ \left( w + \Delta_p \right) i \gamma_{j,b} \gamma_{j+1,a} - \left( w - \Delta_p \right) i \gamma_{j,a} \gamma_{j+1,b} \right] \\ &- \frac{\mu}{2} \sum_{i=1}^{N} i \gamma_{j,a} \gamma_{j,b} \,. \end{split} \tag{1.89}$$

## **Sweet Spot Limits**

Consider the limit  $w = \Delta_p = 0$ . The Hamiltonian simply reduces to

$$H_{\text{Kitaev}} = -\frac{i\mu}{2} \sum_{j=1}^{N} \gamma_{j,a} \gamma_{j,b} = -\frac{\mu}{2} \sum_{j=1}^{N} \left( 1 - 2c_j^{\dagger} c_j \right)$$
 (1.90)

and the original fermions defined by  $c_j$  diagonalizing the Hamiltonian. The ground state is given as the state where every local parity  $\hat{p}_j$  is evaluated to 1 which is the empty fermionic vacuum state. Local excitations are simply given by placing a fermion somewhere in the chain with an energy cost of  $\Delta = 2\mu$  as the local parity changes from  $1 \to -1$ .

Another particular simple limit is given by  $w = \Delta_p$  and  $\mu = 0$  for which the Hamiltonian becomes

$$H_{\text{Kitaev}} = -w \sum_{j=1}^{N-1} i \gamma_{j,b} \gamma_{j+1,a} \,.$$
 (1.91)

Instead of pairing the Majorana operators sharing the same site index j, the Hamiltonian is diagonalized by pairing the Majorana operators on adjacent sites. This leads to the definition of new fermions for  $j=1,\ldots,N-1$ 

$$\begin{split} H_{\text{Kitaev}} &= -w \sum_{j=1}^{N-1} \left( 1 - 2f_j^{\dagger} f_j \right) \\ f_j &= \frac{1}{2} \left( \gamma_{j,b} - i \gamma_{j+1,a} \right) = \frac{i}{2} \left( c_j - c_j^{\dagger} - c_{j+1} - c_{j+1}^{\dagger} \right) \,. \end{split} \tag{1.92}$$

The Hamiltonian probes the local parity of the new  $f_j$  fermions given by

$$e^{i\pi f_j^\dagger f_j} = (1 - 2f_j^\dagger f_j) = i\gamma_{j,b}\gamma_{j+1,a} \,. \tag{1.93} \label{eq:1.93}$$

Thus, the ground state is given by the vacuum of all  $f_j$  fermions, with excitations describing particle-hole pairs defined on neighboring lattice sites. At the boundaries, there are two Majorana operators  $\gamma_{1,a}$  and  $\gamma_{N,b}$  that do not appear in  $H_{\text{Kitaev}}$  and commute with the Hamiltonian. Pairing these two edge Majorana operators into the non-local fermion

$$f_E = \frac{1}{2} \left( \gamma_{N,b} - i \gamma_{1,a} \right) = \frac{i}{2} \left( c_N - c_N^\dagger - c_1^\dagger - c_1 \right)$$

results in a zero-energy excitation. The two Majorana edge operators are also known as Majorana Zero Mode (MZM).

As a result, there are two degenerated ground states

$$|\Omega_e\rangle = f_E \prod_{i=1}^{N-1} f_j \; |0\rangle \; , \quad |\Omega_o\rangle = f_E^\dagger |\Omega_e\rangle \; .$$

There is no local bulk observable that can distinguish between the two ground states, as they only differ in the occupation of the non-local fermion  $f_E$ .

There is an alternative way to interpret the double degeneracy of the ground state. For this, consider the global parity operator  $\hat{P}$  from Eq. (1.39) and rewrite it in terms of the new fermionic operators

$$\hat{P} = \prod_{j=1}^{N} \left( i \gamma_{j,a} \gamma_{j,b} \right) = i \gamma_{1,a} \tilde{P} \gamma_{N,b} , \quad \tilde{P} = \prod_{j=1}^{N-1} e^{i \pi f_j^{\dagger} f_j} . \tag{1.94}$$

The operator  $\tilde{P}$  measures the parity of the bulk of the chain and is the same for both degenerated ground states  $|\Omega_{e/o}\rangle$ . Thus, the parity operator projected on the ground state manifold fractionalizes to the ends of the chain with only the occupation of the non-local fermion  $f_E$  defining the parity of the ground state

$$\hat{P} = -i\gamma_{1,a}\gamma_{N,b} = \hat{P}_L\hat{P}_R. \tag{1.95}$$

The two operators  $\hat{P}_L = i\gamma_{1,a}$  and  $\hat{P}_R = \gamma_{N,b}$  defined by this equation individually commute with the Hamiltonian. Because they are also fermionic in nature and anti-commute  $\{\hat{P}_L,\hat{P}_R\}=0$ , they form two independent symmetries of the system. The existence of this pair of anti-commuting symmetries also requires the ground state to be doubly degenerate.

Considering the trivial limit of  $w=\Delta_p=0$  given by Eq. (1.90), the total parity operator fractionalizes to

$$\hat{P} = \hat{p}_1 \tilde{P} \, \hat{p}_N \,.$$

The two local parities  $\hat{p}_1$  and  $\hat{p}_N$  that appear at the edge commute again with the Hamiltonian. However, they are bosonic, commute with each other, and do not lead to independent symmetries. Consequently, the ground state has no non-trivial protected degeneracy. The two atomic limits  $(w = \Delta_p = 0 \text{ and } w = \Delta_p, \mu = 0)$  are illustrated in Fig. 1.11.

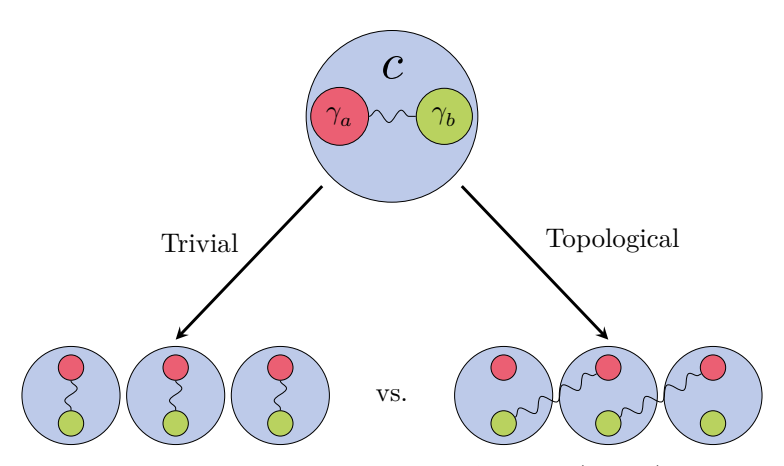


Figure 1.11: Sketch of the two atomic limits  $t=\Delta_p=0$  (trivial) and  $\mu=0,\ t=\Delta_p$  (topological). The fermion c is the result of pairing two independent Majorana operators  $\gamma_a$  (red) and  $\gamma_b$  (green). In a many-body setup, it is either possible to pair the Majorana operators on site, leading to the trivial limit of Eq. (1.90), or between adjacent sites, which results in the topological limit represented by Eq. (1.91). In the latter case, two unpaired Majorana operators exist at the left and right ends of the chain, which form a non-local fermion shared between the two endpoints.

By closing the chain to a ring, the Hamiltonian contains an additional contribution  $-w\,i\gamma_{N,b}\gamma_{1,a}$  and the zero mode disappears from the spectrum. The ground state becomes unique, with a well-defined fermionic parity.

#### General Parameters

Away from the sweet points defined above in Eq. (1.90) and Eq. (1.91), it is found that the ground-state degeneracy and the existence of the fractionalized fermionic excitation are stable for all  $\mu < 2w$  and  $\Delta_p > 0$ . For  $\mu > 2w$  the ground state is unique. The two regions are separated by a critical line for  $\mu = 2w$ , as illustrated in Fig. 1.12(a). The Hamiltonian is still diagonalized by particle-hole excitations similar to Eq. (1.92)

$$H_{\text{Kitaev}} = \sum_{n=1}^{N} E_n f_n^{\dagger} f_n + E_0 ,$$
 (1.96)

where  $E_0$  is an irrelevant constant. The  $f_j$  are general linear combinations of the annihilation and creation operators

$$f_n = \sum_{j=1}^N U_{n,j} c_j + V_{n,j} c_j^{\dagger} .$$

The  $N \times N$  matrices U and V can be combined to form a unitary  $2N \times 2N$  matrix

$$\mathcal{W} = \begin{pmatrix} U & V \\ \bar{V} & \bar{U} \end{pmatrix} , \quad \mathcal{W}^\dagger \mathcal{W} = \mathcal{W} \mathcal{W}^\dagger = \mathbb{1} .$$

The conditions imposed by  $\mathcal{W}$  being unitary on the matrices U and V are required for the  $f_n$  fermions to have the correct anti-commutation relations. A detailed calculation [84] shows that for  $\mu < 2w$ , one of the fermionic operators in Eq. (1.96) has an energy approximately equal to zero  $E_1 \approx 0$ . Moreover, this fermion  $f_1 = \Gamma_a - i\Gamma_b$  is a non-local object, as it is the result of pairing two Majorana operators which are exponentially localized to the edges given by

$$\begin{split} \Gamma_{a} &= \mathcal{N} \sum_{j=1}^{N} \left( \rho_{+}^{j} - \rho_{-}^{j} \right) \gamma_{j,a} \,, \quad \Gamma_{b} = \mathcal{N}' \sum_{j=1}^{N} \left( \rho_{+}^{N-j+1} - \rho_{-}^{N-j+1} \right) \gamma_{j,b} \\ \rho_{\pm} &= \frac{\mu \pm \sqrt{\mu^{2} - 4w^{2} + 4\Delta_{p}^{2}}}{2(w + \Delta_{p})} \,, \quad |\rho_{\pm}| < 1 \,, \end{split} \tag{1.97}$$

The two constants  $\mathcal{N}$  and  $\mathcal{N}'$  ensure the normalization  $\Gamma_{\alpha}^2 = \mathbb{1}$ , see also Appendix C for a derivation. These Majorana operators are the MZM in the topological regime of the Kitaev chain.

Similar to the topological atomic limit  $w=\Delta_p$  and  $\mu=0$ , the projection of the fermionic parity operator on the low-energy subspace results in a fractionalization [53] similar to Eq. (1.95)

$$\hat{P} \approx i\Gamma_a \Gamma_b = \hat{P}_L \hat{P}_R \,. \tag{1.98}$$

Because the Majorana operators are localized to the edge, it is expected that the two anti-commuting operators  $\hat{P}_L$  and  $\hat{P}_R$  implement independent symmetries, thereby forcing the existence of a double-degenerated ground state. Crossing the quantum phase transition for  $\mu=2w$ , the fractionalization of the parity operator into two independent fermionic-like symmetries becomes trivial, and the double degeneracy vanishes. In this sense, the SPTP is protected by the fermionic parity operator  $\hat{P}$ .

## Topological Invariant

To formulate a topological index for the bulk, consider the Kitaev chain Hamiltonian with periodic boundary conditions. In the Fourier basis, the Hamiltonian becomes

$$H_{\rm Kitaev} = \frac{1}{2} \sum_{k} \Psi_{k_n}^{\dagger} \mathcal{H}_{\rm BdG}(k_n) \Psi_{k_n} \,, \quad k_n = \frac{2\pi}{N} n \,, \ n = 0, \dots, N-1 \eqno(1.99)$$

where  $\Psi_{k_n}^\dagger=(c_{k_n}^\dagger,c_{-k_n}^{})$  is known as the Nambu spinor and

$$\begin{split} \mathcal{H}_{\mathrm{BdG}}(k) &= d_z(k)\sigma^z + d_y(k)\sigma^y \\ d_z(k) &= \mu - 2w\cos(k) \,, \ d_v(k) = -2\Delta_p\sin(k) \end{split} \tag{1.100}$$

is the Bogoliubov-de-Gennes (BdG) Hamiltonian [43, 126, 142, 143]. Note that the BdG Hamiltonian formally has a chiral symmetry very similar to the SSHM from Eq. (1.75) given by the chiral operator

$$\hat{\gamma} = \sigma^x \,. \tag{1.101}$$

Acting on the Nambu spinor, this operator interchanges the holes defined at momentum k with the particles defined at momentum -k and can again be interpreted as a combined particle-hole and time-reversal transformation acting on spinless fermions. It is this pairing induced by the p-wave coupling  $c_j^{\dagger}c_{j+1}^{\dagger} + \text{h.c.}$  that is responsible for the occurrence of the non-trivial SPTP. A direct diagonalization of the BdG Hamiltonian  $\mathcal{H}_{\text{BdG}} = WDW^{\dagger}$  results in

$$\begin{split} H_{\text{Kitaev}} &= \sum_{k} E(k) f_{k}^{\dagger} f_{k} \,, \quad f_{k} = \alpha(k) c_{k} + \beta(k) c_{-k}^{\dagger} \\ E(k) &= \sqrt{d_{z}(k)^{2} + d_{y}(k)^{2}} = \sqrt{(2w \cos(k) - \mu)^{2} + 4|\Delta_{p}|^{2} \sin(k)^{2}} \,. \end{split} \tag{1.102}$$

The ground state is defined as the vacuum of the new  $f_k$  quasi-particles, which are particle-hole pairs of the original fermions. The energy-momentum dispersion relation E(k) obeys a gap  $\Delta = |2w - \mu|$  separating the quasiparticle excitations from the ground state, as shown in Fig. 1.12(b).

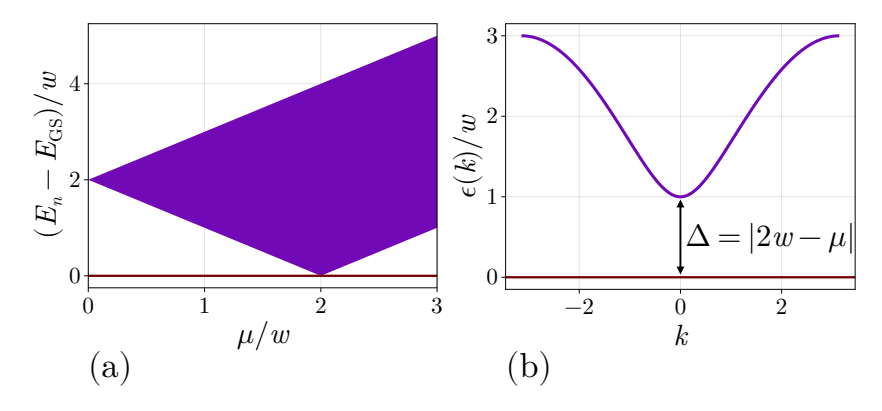


Figure 1.12: (a) Energy spectrum of the Kitaev chain model in Eq. (1.87) for  $w = \Delta_p$  and varying the chemical potential  $\mu$  from 0 to 3w. The gap between the ground state (red line) and the quasi-particle continuum (purple) closes at  $2w = \mu$ . (b) Energy-momentum dispersion relation of the Bogoliubov quasi-particles.

To define a topological bulk index, consider the two special points<sup>10</sup> k=0 and  $k=\pi$ . The BdG Hamiltonian at these points reads

$$\begin{split} \mathcal{H}_{\mathrm{BdG}}(0) &= (\mu - 2w)\sigma^z = m_0\sigma^z \\ \mathcal{H}_{\mathrm{BdG}}(\pi) &= (\mu + 2w)\sigma^z = m_\pi\sigma^z \,. \end{split}$$

The corresponding contribution to the Kitaev chain Hamiltonian is given by

$$H_{\text{Kitaev}} = \sum_{k_n \neq 0, \pi} E(k_n) f_{k_n}^{\dagger} f_{k_n} + m_0 c_0^{\dagger} c_0 + m_{\pi} c_{\pi}^{\dagger} c_{\pi} .$$

The ground state  $|\Omega\rangle$  is defined as the state that is annihilated by all operators that annihilate a quasi-particle with a positive excitation energy. In particular, focusing on  $w, \mu \geq 0$ , the ground state is annihilated by the  $c_{\pi}$  operator since  $m_{\pi} \geq 0$ 

$$c_{\pi} |\Omega\rangle = 0$$
.

The same is found for the k=0 contribution for the trivial region  $\mu>2w$  as  $m_0>0$  in this case. Consequently, the ground state does not have a mode at k=0 and  $k=\pi$ .

However, in the topological regime  $\mu < 2w$  the sign of  $m_0$  changes, and the ground state is annihilated by the  $c_0^{\dagger}$  operator. Thus, in the topological regime, the k=0 mode is occupied.

Taking the remaining N-2 contributions with  $k \neq 0, \pi$  into account, the ground state in both cases is given by

$$|\Omega\rangle = (c_0^{\dagger})^{p_0} \prod_{k \neq 0, \pi} \beta(-k) c_k^{\dagger} |0\rangle , \quad p_{\pi} = \begin{cases} 0 & \text{for } \mu > 2w \\ 1 & \text{for } \mu < 2w \end{cases}$$
 (1.103)

The quasiparticles for  $k \neq 0$ ,  $\pi$  are always a superposition of the creation and annihilation operators independent of  $\mu > 2w$  or  $\mu < 2w$ . Because N was chosen to be an even number, the action of the annihilation operators on the fermionic vacuum therefore always leads to a state that is a superposition of even-parity states.

A similar result is found for negative  $\mu$  where  $m_{\pi}$  changes sign and  $m_0$  is negative. As a consequence, the parity of the ground state only depends on the relative sign of the two  $m_0$  and  $m_{\pi}$  parameters

$$\langle \Omega | \hat{P} | \Omega \rangle = \operatorname{sign}(m_0 m_\pi)$$

where sign(a) denotes the sign of the number a. This parameter dependent parity allows for the definition of a topological  $\mathbb{Z}_2$  invariant given by

$$Q = \operatorname{sign}(m_0 m_{\pi}) \tag{1.104}$$

with Q = -1 indicating a topological non-trivial phase [84].

<sup>&</sup>lt;sup>10</sup> For periodic boundary conditions k=0 is always an allowed momentum, while  $k=\pi$  only appears in the set of allowed momenta for N even, compare Eq. (1.42). This is why N is fixed, even at the beginning of this subsection.

#### Some Consequences of Majorana Zero Modes

If the system is in the topological phase with a pair of MZM, it has various effects on its physical properties. First, the k=0 mode is only a valid momentum mode for periodic boundary conditions. If the system obeys anti-periodic boundary conditions  $c_{j+N} = -c_j$ , this mode merges with the trivial  $f_k$  excitations of the model. Consequently, the parity of the ground state in the topological regime is different for anti-periodic boundary conditions compared to periodic boundary conditions. The two cases can be connected using general twisted boundary conditions, as discussed in Subsection 1.1.6,

$$c_{j+N}=e^{i\varphi}c_j\,,\quad \varphi\in[0,2\pi)$$

implemented by deforming the two contributions to the Hamiltonian

$$c_N^\dagger c_1 \to e^{i\varphi} c_N^\dagger c_1 \,, \quad c_N^\dagger c_1^\dagger \to e^{i\varphi} c_N^\dagger c_1^\dagger \,.$$

Note that the Kitaev chain Hamiltonian at arbitrary twisting angles  $H_{\rm Kitaev}(\varphi)$  is not translation invariant  $\hat{T}H_{\rm Kitaev}(\varphi)\hat{T}^{\dagger}\neq H_{\rm Kitaev}(\varphi)$  because of the complex p-wave pairing term. However, translation invariance is restored for  $\varphi=0,\pi,$  that is, for periodic or anti-periodic boundary conditions. This breaking of translation invariance allows for a gap closing, which occurs at  $\varphi=\pi/2$ . At this point, a single state from the continuum touches zero energy, as shown in Fig. 1.13(a), and the parity of the ground state changes. This phenomenon is known as a parity switch and is related to the well-known  $4\pi$  Josephson current [95, 144].

In contrast, if the system is topologically trivial and the  $m_0$  mode is not occupied, the ground states at periodic and anti-periodic boundary conditions have the same parity, and there is no level crossing by twisting the boundary conditions, as shown in Fig. 1.13(b).

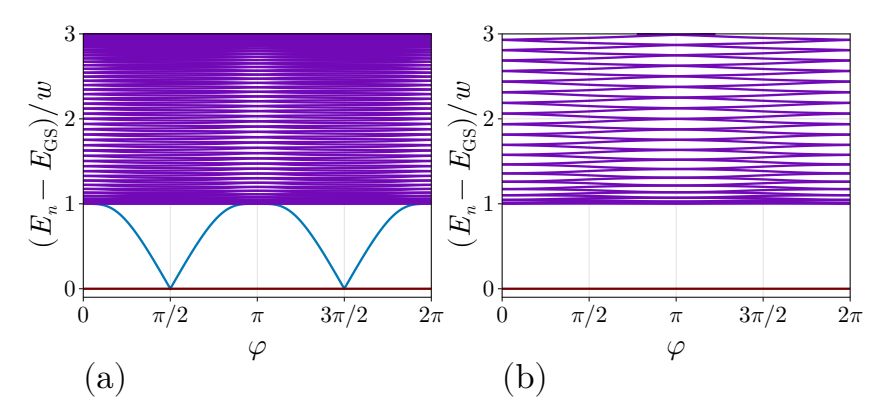


Figure 1.13: Energy spectrum of the Kitaev chain plotted against the twisting angle  $\varphi$  for  $w = \Delta_p = \mu$  in panel (a), and  $w = \Delta_p$ ,  $\mu = 3w$  in panel (b). In both cases, N = 100.

Another interesting property is the existence of non-local end-to-end correlations in the topological region for the single-particle correlation function  $\langle \Omega_{e/o}|c_1c_j^\dagger|\Omega_{e/o}\rangle$ . For simplicity consider the case  $w=\Delta_p$  for which the expression of the MZM in Eq. (1.97) can be written as a simple exponential

$$\Gamma_a = \mathcal{N} \sum_{j=1}^N e^{-\lambda(j-1)} \gamma_{j,a} \,, \quad \Gamma_b = \mathcal{N} \sum_{j=1}^N e^{-\lambda(N-j+1)} \gamma_{j,b} \,, \quad \lambda = -\log\left(\left|\frac{\mu}{2w}\right|\right) \ \, (1.105)$$

with normalization  $\mathcal{N}^2=e^{2\lambda}-1$ . The fermionic operator  $c_j$  can be expanded in terms of the  $f_n$  operators diagonalizing the Kitaev Hamiltonian

$$c_j = A \left( \Gamma_a e^{-\lambda j} - i \Gamma_b e^{-\lambda (N-j+1)} \right) + \tilde{c}_j$$

where  $\tilde{c}_j = \sum_{n=2}^N \psi_n(j) f_n + \xi_n(j) f_n^\dagger$  collects the contribution from the gapped quasi-particles and A is a constant.

Using this expansion in the correlation function is evaluated as

$$\begin{split} \langle \Omega_{e/o} | c_1 c_j^\dagger | \Omega_{e/o} \rangle = & 2A^2 e^{-\lambda(N-j+2)} \left< \Omega_{e/o} | i \Gamma_a \Gamma_b | \Omega_{e/o} \right> \\ & + A^2 \left( e^{-\lambda(j+1)} + e^{-\lambda(2N-j+1)} \right) \\ & + \langle \Omega_{e/o} | \tilde{c}_1 \tilde{c}_j | \Omega_{e/o} \rangle \ . \end{split}$$

The second line of this equation vanishes for  $j \gg 1$  and  $N \gg 1$  and the third line is a correlation function that only involves gapped quasi-particles and thus should decay exponentially as  $\exp(-\Delta j)$  where  $\Delta$  is the gap of the system.

The expectation value of the first line is nothing but the global parity, following Eq. (1.98). Taking the  $j \to N$  limit, results in a non-local correlation function whose revival depends on the parity of the ground state

$$\lim_{j \to N} \langle \Omega_{e/o} | c_1 c_j^{\dagger} | \Omega_{e/o} \rangle = 2A^2 e^{-2\lambda} P_{e/o} \,, \quad P_{\sigma} = \begin{cases} 1 & \text{for } \sigma = e \\ -1 & \text{for } \sigma = o \end{cases} . \tag{1.106}$$

This behavior is illustrated in Fig. 1.14.

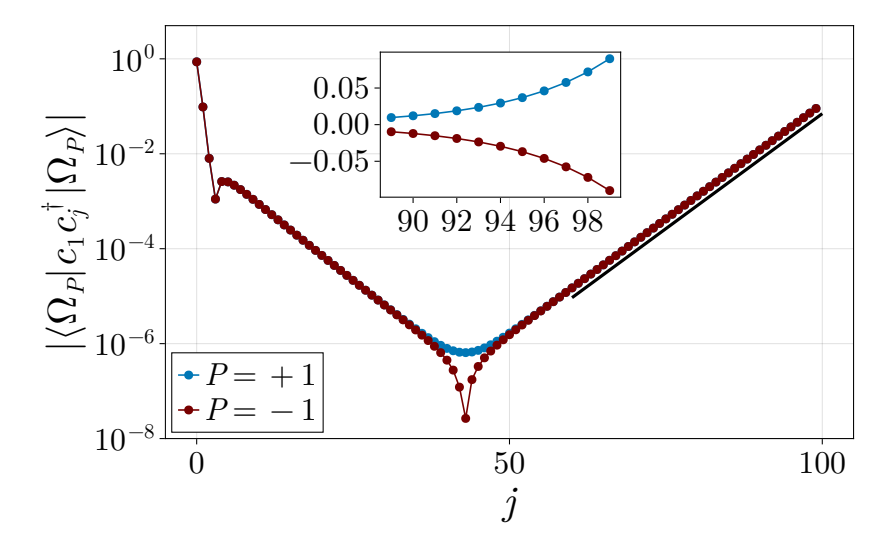


Figure 1.14: Single particle correlation function  $\langle c_1 c_j^\dagger \rangle$  between the first site and the jth site for  $w = \Delta_p$  and  $\mu = 1.6w$ . The blue (red) line is the correlation with respect to the even (odd) parity ground state, and the black line is an exponential of the form  $f(j) = A \exp(-\lambda (N-j))$  with  $\lambda = -\log(\mu/(2w)) \approx 0.22$  as predicted by Eq. (1.106). In the inset, a zoom around the right edge of the chain is shown, highlighting the relative  $\pi$  phase of the revival between the two ground states. The early transient decay is due to the overlap of the edge operator with bulk excitations, and the drop in the correlation function in the odd-parity sector is due to the relative sign change in the revival of the correlator.

By taking the Jordan-Wigner transformation, as defined in Eq. (1.32), the Kitaev chain is transformed to a Transverse Field XY Model (TFXYM). For open boundary

conditions, the equivalence is given by

$$\begin{split} H_{\text{Kitaev}} &\cong \sum_{j=1}^{N-1} J_x \sigma_j^x \sigma_{j+1}^x + J_y \sigma_j^y \sigma_{j+1}^y + g \sum_{j=1}^{N} \sigma_j^z \\ J_x &= -\frac{w + \Delta_p}{2} \,, \quad J_y = -\frac{w - \Delta_p}{2} \,, \quad g = \frac{\mu}{2} \,. \end{split} \tag{1.107}$$

In particular, for  $J_y=0$ , this model reduces to the TFIM discussed in Subsection 1.2.1. Similar to the TFIM, the TFXYM shows a spontaneous breaking of the  $\mathbb{Z}_2$  symmetry given by the spin parity operator

$$\hat{P} = \prod_{j=1}^{N} (-\sigma_j^z)$$

for  $|g| < |J_x + J_y|$ . Under the Jordan-Wigner transformation, the topological phase appearing in the fermionic model at  $\mu < 2w$  is mapped to the symmetry-breaking phase of the TFXYM. The two degenerate fermionic ground states are mapped to the symmetry-restoring basis defined in Eq. (1.66) in the ground-state manifold. This equivalence also allows the definition of a new order parameter for the Kitaev model by considering the  $\sigma_j^x$  correlation function in the TFXYM. Again, similar to the TFIM, the TFXYM shows off-diagonal long range order in the correlation function of the Pauli-X operators

$$\lim_{|j-k|\to\infty} \langle \sigma_j^x \sigma_k^x \rangle = m(g)^2 \,,$$

where the expectation value is taken with respect to the symmetry-restoring basis, as in Eq. (1.72).

By performing the inverse Jordan-Wigner transformation, the correlation function of the Pauli-X operators becomes a string order parameter

$$\lim_{|j-k|\to\infty} i \langle \gamma_{j,b} \prod_{l=j+1}^{k-1} e^{i\pi \hat{n}_l} \gamma_{k,a} \rangle = m(g)^2.$$
 (1.108)

While the correlation function in the TFXYM is related to the existence of a local observable, the string operator is a highly non-local observable probing the global structure of the ground state.

For periodic boundary conditions, the ground state of the Kitaev chain is unique, whereas the TFXYM still exhibits double degeneracy stemming from symmetry breaking. This is not a paradox, since the Jordan-Wigner transformation of the periodic Kitaev chain is sensitive to the total parity of the chain by the mapping of the operators

$$i\gamma_{N,b}\gamma_{1,a}\cong -\hat{P}\sigma_N^x\sigma_1^x\,,\quad i\gamma_{N,a}\gamma_{1,b}\cong -\hat{P}\sigma_N^y\sigma_1^y\,.$$

The Kitaev chain with an even parity is thereby mapped to the TFXYM with anti-periodic boundary conditions with an additional projection to the even parity sector, and the Kitaev chain at odd parity to the TFXYM with periodic boundary conditions projected onto the odd-parity sector. In both cases, the ground states are unique. Note that the symmetry-breaking basis, defined in Eq. (1.64) are not allowed in the fermionic picture because they represent a superposition of two fermionic states with different parities.

It was found that the topological ground-state degeneracy is stable against the addition of interactions to the Kiteav chain [145–148]. In general, these interactions spoil

the possibility of performing an exact diagonalization of the Hamiltonian, and the system has to be solved numerically using, for example, tensor network algorithms, as introduced in Chapter 2.

If the model is in the SPTP, it is still possible to define a non-trivial MZM wave function in terms of the overlap between the two degenerate ground states, existing for open boundary conditions, with the single Majorana operator

$$\Gamma_{a,j} = \frac{1}{2} \left( \langle \Omega_e | \gamma_{j,a} | \Omega_o \rangle + \langle \Omega_o | \gamma_{j,a} | \Omega_e \rangle \right)$$
 (1.109)

that is found to exhibit localization towards the edge of the system [149]. In contrast to the Kitaev chain, where the MZM is a many-body operator that commutes with the full Hamiltonian, the MZM in Eq. (1.109) is only guaranteed to exist in the degenerate ground-state manifold in the presence of interactions. A generalization of the concept of MZM in this case is presented in Section 1.5.

For periodic boundary conditions, the integrability-breaking nature of general interactions spoils the definition of the topological invariant in terms of the Bogoliubov Hamiltonian at the two momenta  $k = 0, \pi$ . However, it is found that the parity of the ground state interchanges by twisting the boundary conditions with a gap closing at  $\varphi = \pi/2$ , similar to the non-interacting case.

Figure 1.15 demonstrates this for the Kitaev-Hubbard Model (KHM) [148], a minimal extension of the Kitaev chain with nearest neighbor Hubbard like interactions

$$H_{\text{KH}} = H_{\text{Kitaev}} + U \sum_{j=1}^{N} \hat{p}_{j} \hat{p}_{j+1} .$$
 (1.110)

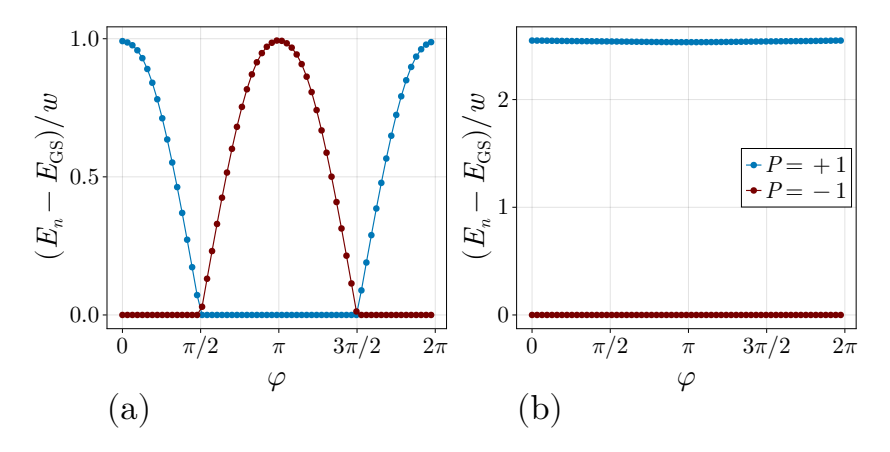


Figure 1.15: Ground state energy of the KHM in the even (P=+1) and odd (P=-1) parity sectors plotted against the twisting angle  $\varphi$ . For both plots, N=50,  $w=\Delta_p$  and  $\mu/w=1.6$ . In panel (a), U/w=0.6 places the model in a non-trivial SPTP with a degenerate ground-state manifold. As the twisting angle is varied from 0 to  $2\pi$ , the many-body gap closes at  $\varphi=\pi/2$  and  $\varphi=3\pi/2$ , which is accompanied by a change in the parity of the ground state. In panel (b), the interaction is chosen as U/w=2 which results in a trivial phase with no gap closing.

### Some Words on Experimental Realizations

The non-local nature of the fermion state  $f_E$  leads to intrinsic resilience against noise. This motivates the formulation of a topological quantum memory based on the two parity states [84, 150, 151]. As Majorana fermions are also an example of

non-Abelian anyons [152], coupling multiple chains in the topological regime can be used to define a set of logical gates that transform the global state of the system. However, a realization of the Kiteav chain in a real condensed matter system turns out to be complicated and has not been convincingly achieved so far.

There are multiple challenges: the Kiteav chain requires a spinless fermionic gas in a one-dimensional wire and p-wave superconducting correlations. The standard way of creating a spinless one dimensional fermionic gas is by using a semiconductor nanowire with a strong spin-orbit coupling, often of Rashba type [153, 154], and a strong magnetic field orthogonal to the direction of the wire [95, 96, 152, 155]. The spin-orbit coupling breaks the spin degeneracy by locking the spin with momentum, and the magnetic field results in the opening of the gap between these two bands, as shown in Fig. 1.16. By projecting onto the lower band, the effective low-

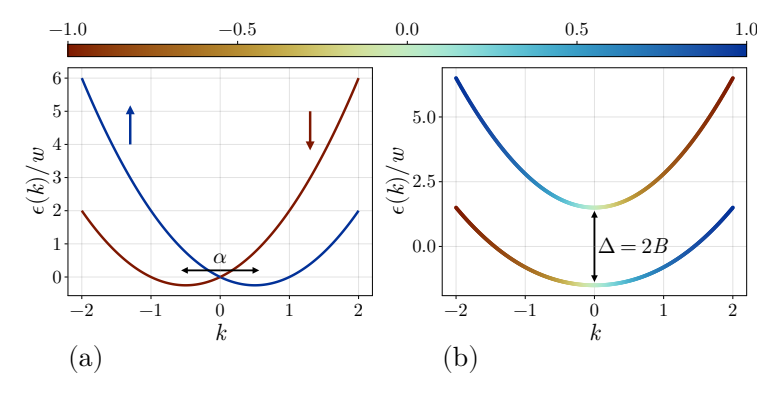


Figure 1.16: (a) Spin-orbit coupling  $\alpha$  results in the formation of two bands with locked spin and momentum, where red represents a spin-down and blue a spin-up state. The two bands touch at k=0 and the system has no gap. (b) Introducing a magnetic field perpendicular to the locked spin states leads to the opening of a gap at k=0 proportional to the magnetic field. Around zero momentum, the spin states are mixed; however, for large momenta, the spin-momentum locking is preserved. By projecting the model on the lower band, an s-wave superconducting coupling between the spin-up and spin-down states becomes an effective p-wave coupling of (k, -k) spinless modes.

energy theory describes a gas of spinless fermions. In a final step, the semiconductor nanowire is coupled with a host s-wave superconductor, which serves as a reservoir for Cooper pairs and induces s-wave superconducting correlations in the semiconductor nanowire through the proximity effect [152, 156, 157]. In the effective spinless low-energy theory, this s-wave correlation becomes a p-wave correlation as required for the Kitaev chain. This setup has some problems, as the interface between the nanowire and host superconductor can lead to the creation of trivial Andreev bound states with signatures similar to true MZMs [158]. In addition, the host superconductor requires a large critical field to survive the strong magnetic fields necessary to open a sufficiently large gap.

Alternative approaches include placing adatoms on a host superconductor [111–113] or quantum dots [107–109] where recently a Kitaev chain with N=2 sites was realized [159]. It has even been theoretically proposed that a topological phase with unpaired MZMs can appear in strongly interacting nanowires without coupling to a superconductor [33, 160–164]. The main idea is to replace the p-wave coupling term with a coherent pair-hopping term between two fermionic species [160], but no term that induces a direct transmission between the two species. Therefore, the total symmetry group of the system is  $\mathrm{U}(1) \times \mathbb{Z}_2$  consisting of the total particle number

of the two species and a sub-species parity symmetry.

Consequently, the parity symmetry is not as robust as in the Kitaev chain, and these models require fine-tuning of the parameters [165]. In Chapter I, a model inspired by recent cold atom experiments [106] is proposed, which implements the required symmetry group by an artificial flux imposing twisted boundary conditions along the short direction of a fermionic tube. The additional U(1) also leads to the existence of gapless density excitations, which may spoil the stability of the MZM away from the ground-state manifold. This question is addressed in Chapter V. However, if such a system is in the topological phase, the MZM has the same properties as the Kitaev chain [166].

# 1.3 Gapless Phases

The previous Section 1.2 focused on possible gapped phases of quantum matter in one dimension. As a reminder, the many-body gap  $\Delta$  is defined as the difference in energy between the ground-state manifold and the first excited state in the thermodynamic limit. The existence of a finite gap  $\Delta > 0$  implies a finite correlation length  $\xi = 1/\Delta$  on which the correlation function of local operators decays exponentially  $\langle \hat{O}_j \hat{K}_k \rangle \sim \exp(-|j-k|/\xi)$  [65, 66]. This exponential decay implies that quantum fluctuations occur mainly at length scales below  $\xi$ .

If the gap vanishes, the correlation length diverges,  $\xi \to \infty$ , resulting in the absence of any characteristic length scale other than the overall size of the system. Consequently, fluctuations can manifest at any length scale, with the system becoming self-similar. This phenomenon causes the correlation functions to decay at a rate slower than exponential. Indeed, self-similarity causes the correlation functions to follow an algebraic decay.

This section provides a brief review of the possible gapless phases of matter in one-dimensional chains. The first Subsection 1.3.1 begins with an introduction to Tomonaga-Luttinger Liquids (TLLs), an important class of models describing a large variety of gapless one-dimensional interacting models, and the solution of this model using the bosonization technique. In particular, the low-energy properties of the models proposed in Chapters I and II are partially described by such a TLL. In the second Subsection 1.3.2, a deformation of the TLL is considered. Based on the system parameters, this deformation leads to the opening of a spectral gap. The methods described in this subsection are also used in similar models to obtain analytical insights into the phases in Chapters I and II, and the phase transition is again encountered in Chapter III. The final Subsection 1.3.3 will review the basics of conformal field theory, a powerful tool for understanding gapless phases in one-dimensional quantum matter.

## 1.3.1 Luttinger Liquid and Bosonization

In two and higher dimensions, interacting fermions usually form a Fermi liquid characterized by a stable Fermi surface with a sharp momentum cutoff in the fermionic distribution function [40]. The situation is drastically different for interacting one-dimensional fermionic chains. In this case, the Fermi surface of a non-interacting system consists of only two points at the Fermi momenta  $\pm k_{\rm F}$ ; see also the discussion at the end of Subsection 1.1.6. This leads to a large phase space for resonant scattering processes. As a consequence, the Fermi surface collapses even for infinites-

imal small interactions and the fermion distribution function becomes

$$n(k) \sim |k - k_{\rm F}|^{\delta}$$

at zero temperature, with an interaction-dependent exponent.

## Effective Field Theory

The starting point is a ring of N sites separated by the physical length  $\alpha$  and populated by spinless fermions defined by the annihilation (creation) operators  $a_j^{(\dagger)}$ . The properties of the quantum ring are described by the non-interacting quadratic Hamiltonian, compare also Eq. (1.45),

$$H = \sum_k \epsilon(k) a_k^\dagger a_k \,, \quad \epsilon(-k) = \epsilon(k) \eqno(1.111)$$

where the operator  $a_k$  is the Fourier transform of  $a_j$  as defined in Eq. (1.43)

$$a_j := \frac{1}{\sqrt{N}} \sum_k e^{ikj\alpha} a_k \,. \tag{1.112}$$

The chain is loaded with  $n_{\rm F}$  number of fermions, which fill the dispersion relation up to the two Fermi momenta  $\pm k_{\rm F}$  related to the density  $\nu = n_{\rm F}/N$  by

$$\alpha k_{\rm F} = \pi \frac{n_{\rm F}}{N} := \pi \nu. \tag{1.113}$$

The main goal is to find an effective theory that describes the low-energy, long-wavelength excitations of this general model. These long-wavelength excitations are of particle-hole type, involving only states close to the Fermi energy  $\epsilon_{\rm F}=\epsilon(k_{\rm F})$ . There are two possible types of particle-hole excitations: the first type excites a fermion from a particle state to a hole state at the same site of the Fermi surface resulting in a momentum transfer of  $Q\approx 0$ , while the second type involves a particle-hole pair from across the two Fermi points with a momentum transfer of  $Q\approx 2k_{\rm F}$ . Both processes are illustrated in Fig. 1.17.

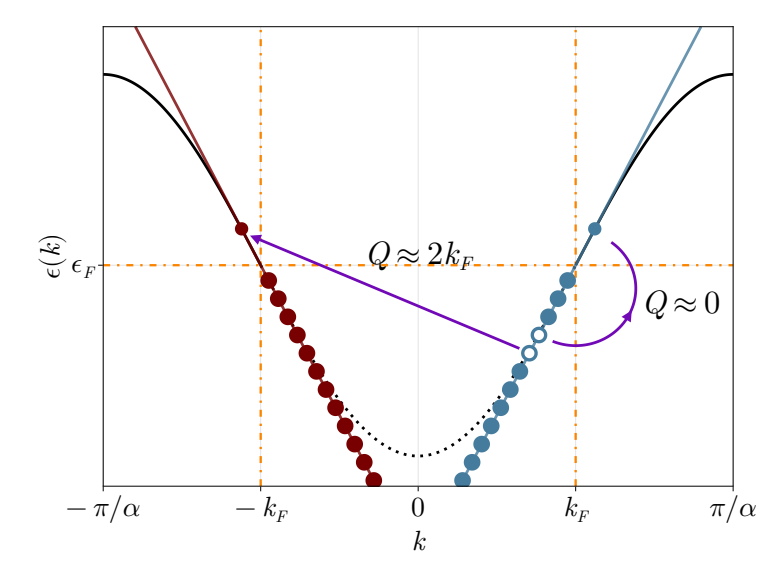


Figure 1.17: Approximation of the lattice model using a linear dispersion relation. The two particle-hole excitations represent the two possible low-energy excitations.

By linearizing the dispersion relation for momenta close to the two Fermi points  $|k\pm k_{\rm F}| \le \Lambda \ll k_{\rm F}$ 

$$\begin{split} \epsilon_{\pm}(k) &= v_{\mathrm{F}} \left( \pm k - k_{\mathrm{F}} \right) + \mathcal{O} \left( (k \pm k_{\mathrm{F}})^2 \right) \\ v_{\mathrm{F}} &\coloneqq \left. \frac{\partial \epsilon(k)}{\partial k} \right|_{k_{\mathrm{F}}} \end{split} \tag{1.114}$$

it is derived that the energy of a particle-hole excitation with momentum  $|q| \leq \Lambda$  depends only linearly on the relative momentum

$$\Delta E_q \coloneqq \epsilon(k_1) - \epsilon(k_2) \approx v_{\rm F} \left( k_1 \pm k_2 \right) = v_{\rm F} q \,. \tag{1.115} \label{eq:delta_Eq}$$

In this equation, the minus sign refers to a particle-hole excitation around the same Fermi point, and the plus sign refers to an excitation across the two Fermi points.

To describe the long-wavelength properties, it is sufficient to project the quadratic non-interacting Hamiltonian (1.111) on the states with  $|k \pm k_{\rm F}| \le \Lambda$ 

$$\begin{split} H &\approx \sum_{|q| \leq \Lambda} v_{\mathrm{F}} q a_{q-k_{\mathrm{F}}}^{\dagger} a_{q-k_{\mathrm{F}}} - v_{\mathrm{F}} q a_{q+k_{\mathrm{F}}}^{\dagger} a_{q+k_{\mathrm{F}}} \\ &\approx \sum_{|q| \leq \Lambda; r=R,L} \epsilon_r v_{\mathrm{F}} \, q \, c_{r,q}^{\dagger} c_{r,q} \\ c_{r,q} &= a_{q-\epsilon_r k_{\mathrm{F}}} \, , \quad \epsilon_r = \begin{cases} +1 & \text{for } r=R \\ -1 & \text{for } r=L \end{cases} \, , \end{split}$$

which implicitly defines the left/right-moving fermions  $c_{r,q}$ . This approximately reproduces the correct low-energy excitations of the original model. To simplify the model further, the allowed momenta are expanded to positive and negative infinity. By this, the model becomes the Tomonaga-Luttinger Liquid (TLL) [44–47] model of two left and right moving spinless fermions with linear dispersion relation and described by the Hamiltonian

$$H_{\text{TLL}} = \sum_{q:r=R} \int_{L} \epsilon_r v_{\text{F}} q c_{r,k}^{\dagger} c_{r,k}. \qquad (1.116)$$

The ground state  $|\Omega\rangle$  of the TLL is the filled Fermi sea, a state where all negative eigenstates are occupied by an infinite number of fermions

$$c_{R,-|q|}^{\dagger} |\Omega\rangle = c_{L,|q|}^{\dagger} |\Omega\rangle = 0.$$

The linearization process is illustrated in Fig. 1.17.

The projection of the long-wavelength degrees of freedom is equivalent to taking the continuum limit defined by sending the separation between two sites to zero,  $\alpha \to 0$ , while keeping the total length of the chain constant,  $L := \alpha N = \text{const.}$  This limit is understood to be taken at the end of the calculation, but with  $\alpha$  fixed at every intermediate step. As only the slow varying modes are contributing to the properties of the system, the left and right moving fermionic lattice operators can be approximated by smooth varying operator valued functions

$$\frac{1}{\sqrt{\alpha}}c_{r,j}\approx \psi_r(x_j)\,,\quad x_j=j\alpha\,.$$

In this projected space, the bare operators can be represented by the continuum fields as

$$\frac{1}{\sqrt{\alpha}}a_{j} = \frac{1}{\sqrt{L}}\sum_{k}e^{ik\,\alpha}a_{k} \approx \frac{1}{\sqrt{L}}\sum_{|q|\leq\Lambda}e^{-ik_{\mathrm{F}}\,\alpha}e^{iq,\alpha}a_{q-k_{\mathrm{F}}} + e^{ik_{\mathrm{F}}\,\alpha}e^{iq,\alpha}a_{q+k_{\mathrm{F}}}$$

$$\approx \left(e^{-ik_{\mathrm{F}}x_{j}}\psi_{R}(x_{j}) + e^{ik_{\mathrm{F}}x_{j}}\psi_{L}(x_{j})\right).$$
(1.117)

By performing the continuum limit, the sums in the Hamiltonian become an integral

$$\alpha \sum_{j} \dots \rightarrow \int_{L/2}^{L/2} \mathrm{d}x \dots$$

and the Fourier transformation is modified to

$$c_{r,k} = \frac{1}{\sqrt{L}} \int_{-L/2}^{L/2} \mathrm{d}x \, e^{-ikx} \psi_r(x) \,, \quad \psi_r(x) = \frac{1}{\sqrt{L}} \sum_k e^{ikx} c_{r,k} \,. \tag{1.118}$$

The continuum version of the TLL reads in position space

$$H_{\rm TLL} = -iv_{\rm F} \int_{-L/2}^{L/2} \mathrm{d}x \left\{ \psi_R^{\dagger}(x) \partial_x \psi_R(x) - \psi_L^{\dagger}(x) \partial_x \psi_L(x) \right\}, \qquad (1.119)$$

and the density operator of the left and right moving fermions can be written as<sup>11</sup>

$$\rho_r(x) := \psi_r^{\dagger}(x)\psi_r(x). \tag{1.120}$$

Note that the projection on long-wavelength excitations relies heavily on the existence of a linear regime in the energy-momentum dispersion relation  $\epsilon(k)$ . As such, it is expected to fail in the flat-band limit or if the interactions become comparable to the bandwidth of the system. In this case, the effects of non-linearity must be incorporated into the low-energy description [167].

#### Bosonization of the Tomonaga-Luttinger Liquid

The operator which creates particle-hole pairs of right (r = R) or left (r = L) moving fermions of momentum  $q \neq 0$  in the TLL model (1.116) is given by the Fourier components of the local density operator  $\rho_r(x)$ 

$$\rho_{r,q}^{\dagger} = \sum_{k} c_{r,k+q}^{\dagger} c_{r,k} \,. \tag{1.121}$$

The zero momentum (q = 0) density operator can be identified with the total number of fermions added (missing) from the TLL vacuum

$$\rho_{r,0}^{\dagger}\coloneqq\hat{N}_{r}\,,\quad\hat{N}_{r}\left|\Omega\right\rangle=0\,. \tag{1.122}$$

Because the dispersion relation of the TLL model is linear, the states created by applying  $\rho_{r,q}$  to the vacuum state  $|\Omega\rangle$  depend only on the momentum q. Therefore,

 $<sup>^{11}</sup>$ Formally, the product of two continuum operators at the same point x is ill-defined and needs some sort of regularization, which is implicitly assumed throughout this section.

they can be interpreted as stable quasi-particle excitations for each value of  $-\infty < q < \infty$ .

The commutator of the  $\rho_{r,q}$  operators, projected to the vacuum state  $|\Omega\rangle$ , is given by

$$[\rho_{r,q}^{\dagger}, \rho_{r',-p}^{\dagger}] = -\delta_{r,r'}\delta_{q,p}\frac{\epsilon_r q L}{2\pi}. \tag{1.123}$$

This result shows that the particle-hole operators have, up to a trivial normalization, the commutation relations of bosonic ladder operators, as in Eq. (1.23). By rescaling, it is possible to define proper bosonic ladder operators for  $q \neq 0$ 

$$b_{q}^{\dagger} = \left(\frac{2\pi}{L|q|}\right)^{1/2} \begin{cases} \rho_{R,q}^{\dagger}, \ q > 0 \\ \rho_{L,q}^{\dagger}, \ q < 0 \end{cases}, \quad b_{q} = \left(\frac{2\pi}{L|q|}\right)^{1/2} \begin{cases} \rho_{R,-q}^{\dagger}, \ q > 0 \\ \rho_{L,-q}^{\dagger}, \ q < 0 \end{cases}. \quad (1.124)$$

Furthermore, it can be shown that the operators in Eq. (1.124) form a complete set that can be used to span the full many-body Hilbert space of the TLL [58]. This implements the idea of rewriting the TLL Hamiltonian and fermionic operators  $\psi_r(x)$  in terms of these particle-hole excitations.

By calculating the commutator

$$[b_q, H] = v_F |q| b_q$$

it is shown that the Hamiltonian (1.116) is equivalently expressed in the bosonic variables as  $^{12}$ 

$$H_{\rm TLL} \cong \sum_{q \neq 0} v_{\rm F} |q| b_q^{\dagger} b_q = \sum_{q \neq 0} \omega_q b_q^{\dagger} b_q \tag{1.125}$$

because both representations have the same set of commutation relations with the bosonic ladder operators  $b_q$ . This result demonstrates that the TLL describes a set of uncoupled harmonic oscillators with a frequency  $\omega_q = v_{\rm F} |q|$ .

Instead of working with the momentum ladder operators  $b_q$ , it is convenient to change the variables by introducing two conjugated fields  $[\hat{\varphi}(x), \hat{\Pi}(y)] = i\delta(x-y)$  defined in terms of the ladder operators as

$$\hat{\varphi}(x) = -\frac{i\pi}{L} \sum_{q \neq 0} \left(\frac{L|q|}{2\pi}\right)^{1/2} \frac{e^{-iqx}}{q} \left(b_q^{\dagger} + b_{-q}\right)$$

$$\hat{\Pi}(x) = \frac{1}{L} \sum_{q \neq 0} \left(\frac{L|q|}{2\pi}\right)^{1/2} e^{-iqx} \operatorname{sign}(q) \left(b_q^{\dagger} + b_{-q}\right).$$
(1.126)

Physically, these two fields measure the fluctuations in the local density and the current in the quantum wire

$$-\frac{1}{\pi}\partial_x\hat{\varphi}(x)=\rho_R(x)+\rho_L(x)\,,\quad \hat{\Pi}(x)=\rho_R(x)-\rho_L(x)\,. \tag{1.127}$$

<sup>&</sup>lt;sup>12</sup> The bosonization formula for the TLL Hamiltonian (1.125) neglects the total charging effects of the wire proportional to  $N_r^2/L$ , which is subleading in 1/L. While crucial for studying the finite-size effect, this contribution is irrelevant in the thermodynamic limit.

In terms of these field variables, the bosonization of the Hamiltonian becomes

$$H_{\text{TLL}} = \frac{v_{\text{F}}}{2\pi} \int_{-L/2}^{L/2} dx \left(\pi \hat{\Pi}(x)\right)^{2} + \left(\partial_{x} \hat{\varphi}(x)\right)^{2}$$

$$= \frac{v_{\text{F}}}{2\pi} \int_{-L/2}^{L/2} dx \left(\partial_{x} \hat{\vartheta}(x)\right)^{2} + \left(\partial_{x} \hat{\varphi}(x)\right)^{2}, \qquad (1.128)$$

where in the second line, the field  $\partial_x \hat{\vartheta}(x) := \pi \hat{\Pi}(x)$  is defined. In this form, the Hamiltonian is self-dual by interchanging  $\hat{\varphi}$  and  $\hat{\vartheta}$  and represents the Hamiltonian of a massless bosonic field in one dimension with the speed of sound given by  $v_{\rm F}$ .

Similar to the bosonization formula for the Hamiltonian itself, it is possible to derive an operator identity connecting the fermionic fields to the bosonic variables in form of a vertex operator [47, 59]

$$\psi_r(x) = \frac{\hat{U}_r}{\sqrt{2\pi\alpha}} e^{-i(\epsilon_r \hat{\varphi}(x) - \hat{\vartheta}(x))}. \tag{1.129}$$

The operator  $\hat{U}_r$  is known as the Klein operator and removes a fermion from the Fermi sea that is equally spread throughout the entire system. The Klein operators are unitary  $\hat{U}_r^{\dagger}\hat{U}_r = \hat{U}_r\hat{U}_r^{\dagger} = 1$  have the following commutation relations

$$\left\{\hat{U}_r^\dagger,\hat{U}_{r'}\right\} = \delta_{r,r'}\,,\quad \left\{\hat{U}_r,\hat{U}_{r'}\right\} = 0\,, \text{ for } r \neq r'\,,\quad \left[\hat{N}_r,\hat{U}_{r'}\right] = -\delta_{r,r'}\hat{U}_{r'}$$

ensuring the correct anti-commutation relations of fermionic operators of different species and ensuring the correct commutation with the total density operator

$$[\hat{N}_r, \psi_{r'}(x)] = -\delta_{r\ r'}\psi_{r'}(x)$$
.

The equation for the bosonization of the non-interacting Hamiltonian (1.128), the identity for the local density and current (1.127) and the operator identity for the fermionic fields (1.129) completes the bosonization of the non-interacting model.

#### **Calculation of Correlation Functions**

The bosonization formula in Eq. (1.129) can be used to calculate the correlation functions of the fermion field  $\psi_r(x)$ . First, the correlation function of the bosonic fields at large distances is given by [47, 59]

$$\langle \hat{\varphi}(x)\hat{\varphi}(y)\rangle = \langle \hat{\vartheta}(x)\hat{\vartheta}(y)\rangle \sim -\frac{1}{2}\log\left(\frac{|x-y|}{\alpha}\right).$$
 (1.130)

The off-diagonal correlator  $\langle \hat{\varphi}(x) \hat{\vartheta}(y) \rangle = -i \operatorname{sign}(x-y)\pi/4$  is a constant [47] and will be ignored in the following. Next, for a quadratic Hamiltonian of the form given in Eq. (1.128), the following identity holds [47, 59]

$$\langle e^{i\alpha\hat{\phi}(x)}e^{i\beta\hat{\phi}(y)}\rangle = \delta_{\alpha+\beta,0}e^{\alpha^2\langle\hat{\phi}(x)\hat{\phi}(y)\rangle}, \qquad (1.131)$$

and similar for the other combinations of bosonic fields. Thus, the fermionic correlator can be calculated to

$$\begin{split} \langle \psi_r(x) \psi_{r'}^{\dagger}(y) \rangle &\sim \delta_{r,r'} \frac{1}{2\pi\alpha} \left\langle e^{-i(\epsilon_r \hat{\varphi}(x) - \hat{\vartheta}(x))} e^{i(\epsilon_r \hat{\varphi}(x) - \hat{\vartheta}(x))} \right\rangle \\ &\sim \delta_{r,r'} \frac{1}{2\pi\alpha} e^{\langle \hat{\varphi}(x) \hat{\varphi}(y) \rangle} e^{\langle \hat{\vartheta}(x) \hat{\vartheta}(y) \rangle} \sim \delta_{r,r'} \frac{1}{2\pi} \frac{1}{|x-y|} \,. \end{split} \tag{1.132}$$

#### Interactions

A typical interaction which can be added to the non-interacting model of Eq. (1.111) is a Fermi-Hubbard density-density interaction

$$H_V = V \sum_{j=1}^{N} \hat{n}_j \hat{n}_{j+1} \,. \tag{1.133}$$

To bosonizes this interaction, the density operator  $\hat{n}_j$  is projected on the long-wavelength degrees of freedom

$$\begin{split} n_j &\approx \alpha \left\{ \rho_R(x_j) + \rho_L(x_j) + e^{-2ik_{\rm F}x_j} \psi_R^\dagger(x_j) \psi_L(x_j) + e^{2ik_{\rm F}x_j} \psi_L^\dagger(x_j) \psi_R(x_j) \right\} \\ &\approx \alpha \left[ -\frac{1}{\pi} \partial_x \hat{\phi}(x_j) + \frac{1}{\alpha\pi} \cos(2\hat{\phi}(x_j) - 2k_{\rm F}x_j) \right] \,. \end{split} \tag{1.134}$$

With help of this equation, the Fermi-Hubbard interaction becomes

$$\begin{split} H_{V} &= H_{V,0} + \dots \\ H_{V,0} &= V\alpha \int\limits_{-L/2}^{L/2} \mathrm{d}x \, (\rho_{R}(x) + \rho_{L}(x))^{2} - 2\cos(k_{\mathrm{F}}\alpha)\rho_{R}(x)\rho_{L}(x) \end{split} \tag{1.135}$$

where the ellipsis collects all the terms which are irrelevant  $^{13}$ , and the limit  $x_j \approx x_{j+1}$  is taken.

The only remaining relevant contribution  $H_{V,0}$  is quadratic in the density operators and can readily be bosonized using Eq. (1.127)

$$H_{V,0} = \int_{L/2}^{L/2} dx \frac{g_4 + g_2}{(2\pi)^2} \left(\partial_x \hat{\varphi}(x)\right)^2 + \frac{g_4 - g_2}{(2\pi)^2} \left(\partial_x \hat{\vartheta}(x)\right)^2$$
(1.136)

with the two parameters

$$g_2 = 2V\alpha(1 - \cos(\pi\nu))\,,\quad g_4 = 2V\alpha\,,$$

which is expressed in terms of the density  $\alpha k_{\rm F} = \pi \nu$  using Eq. (1.113). In fact, it can be shown [47] that these are the only possible relevant interactions in the TLL model at low-energies<sup>14</sup>.

Since the interaction is quadratic in the bosonic variables, the interacting TLL Hamiltonian becomes

$$H_{\rm TLL} + H_V \approx \frac{u}{2\pi} \int_{L/2}^{L/2} \mathrm{d}x \, K \left( \partial_x \hat{\vartheta}(x) \right)^2 + \frac{1}{K} \left( \partial_x \hat{\varphi}(x) \right)^2 \tag{1.137}$$

 $<sup>^{13}</sup>$  One of these irrelevant terms is a contribution oscillating with  $\cos(4k_{\rm F}x)$ , arising from an Umklapp process. For generic densities, this term oscillates rapidly and averages to zero. However, for half-filling, the oscillation vanishes, and this term leads to a potentially relevant interaction that is similar to the interaction discussed in Subsection 1.3.2.

 $<sup>^{14}</sup>$  In the standard notation, the relevant low-energy interactions are the forward scattering of r type fermions  $(g_4\text{-process})$  and density-density interactions involving fermions of both species  $(g_2\text{-process}).$ 

which is again describing a free bosonic field, but with modified parameters

$$K^{2} = \frac{2\pi + g_{4} - g_{2}}{2\pi + g_{4} + g_{2}}, \quad u^{2} = \frac{v_{F}^{2}}{(2\pi)^{2}} \left( (2\pi + g_{4})^{2} - g_{2}^{2} \right). \tag{1.138}$$

The parameter K is known as the Luttinger parameter.

The form of the interacting TLL in Eq. (1.137) is expected to be universal. Independent of the microscopic nature of the interactions, the only effective parameters entering the description of the long-wavelength behavior of the quantum wire are the velocity of the sound waves u and the Luttinger parameter K. If the wire is dominated by repulsive interactions, then K < 1, and for attractive interactions K > 1. The non-interacting point K = 1 separates the two regimes.

Using the quadratic nature of the TLL Hamiltonian, the correlation functions of the fermionic fields can directly be calculated

$$\langle \psi_r(x)\psi_{r'}^{\dagger}(y)\rangle \sim \delta_{r,r'} \frac{1}{2\pi\alpha} \left(\frac{\alpha}{|x-y|}\right)^{\frac{K+1/K}{2}}$$
 (1.139)

similar to the non-interacting case in Eq. (1.132). Thus, the interacting ground state has algebraically decaying fermionic correlation functions, with the interaction tuning the decay constant.

#### **Multi Flavor Bosonization**

The bosonization can be extended along the above-discussed lines to cases with fermions carrying additional flavor quantum numbers, such as spin or fermions on a ladder [47]. In this case, all objects that appeared previously now carry an additional flavor index s. For example, the TLL Hamiltonian in the case of n flavors becomes

$$H_{\mathrm{TLL}} = \sum_{s=1}^{n} \frac{u_s}{2\pi} \int\limits_{L/2}^{L/2} \mathrm{d}x \, K_s \left( \partial_x \hat{\vartheta}_s(x) \right)^2 + \frac{1}{K_s} \left( \partial_x \hat{\varphi}_s(x) \right)^2$$

with all density-density interactions involving the same flavor type already absorbed in the flavor-dependent Luttinger parameter  $K_s$  and sound velocity  $u_s$ . In contrast to the spinless (single-flavor) case, where a generic interaction results in the universal TLL Hamiltonian, a multi-flavor fermionic system allows for additional possible relevant interactions.

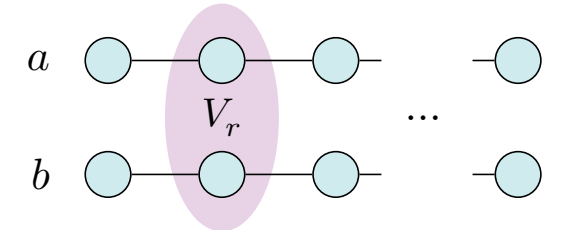


Figure 1.18: Ladder system of two spinless fermions a and b. Each species is described by a TLL, and both wires are coupled with a rung density-density interaction  $V_r$ .

For this, consider a two-leg ladder, as shown in Fig. 1.18. The fermions on the upper leg are denoted by  $a_i$ , and those populating the lower leg are denoted by  $b_i$ . The

density operator associated with the a (b) species is denoted by  $\hat{n}_{j}^{a}$  ( $\hat{n}_{j}^{b}$ ). Assuming the Luttinger parameters and sound velocity of the two species to be equal, the ladder system is described by the TLL Hamiltonian

$$H_{\text{Ladder},0} = \frac{u_s}{2\pi} \sum_{s=a,b} \int_{L/2}^{L/2} dx K \left(\partial_x \hat{\vartheta}_s(x)\right)^2 + \frac{1}{K} \left(\partial_x \hat{\varphi}_s(x)\right)^2. \tag{1.140}$$

A new intra-species interaction possible in this ladder setup is a density-density rung interaction

$$H_{\text{rung}} = V_r \sum_{j=1}^{N} \hat{n}_j^a \hat{n}_j^b \,. \tag{1.141}$$

Going through the bosonization process, the continuum version of the rung interaction becomes

$$\begin{split} H_{\rm rung} &\approx \int\limits_{-L/2}^{L/2} \mathrm{d}x \frac{g_1}{(2\pi)^2} \partial_x \hat{\varphi}_a(x) \partial_x \hat{\varphi}_b(x) + \frac{2g_2}{(2\pi\alpha)^2} \cos\left(2\hat{\varphi}_a(x) - 2\hat{\varphi}_b(x)\right) + \dots \,, \\ g_1 &= (2\pi)^2 V_r \alpha \,, \quad g_2 = V_r \alpha \,, \end{split} \tag{1.142}$$

where the ellipsis denotes irrelevant contributions. While the first term is quadratic in the bosonic fields and can thus be absorbed in a redefinition of the Luttinger parameters, the second term represents a new interaction that is not quadratic in the bosons. By passing to the bonding and anti-bonding variables<sup>15</sup>

$$\hat{\varphi}_{\pm} = \frac{1}{\sqrt{2}} \left( \hat{\varphi}_a(x) \pm \hat{\varphi}_b(x) \right) , \quad \hat{\vartheta}_{\pm} = \frac{1}{\sqrt{2}} \left( \hat{\vartheta}_a(x) \pm \hat{\vartheta}_b(x) \right) , \tag{1.143}$$

the full interacting ladder Hamiltonian becomes

$$\begin{split} H_{\text{Ladder}} &= \sum_{s=\pm} \frac{u_s}{2\pi} \int\limits_{-L/2}^{L/2} \mathrm{d}x \, K_s \left(\partial_x \hat{\vartheta}(x)\right)^2 + \frac{1}{K_s} \left(\partial_x \hat{\varphi}(x)\right)^2 \\ &+ \int\limits_{-L/2}^{L/2} \mathrm{d}x \, \frac{2g_2}{(2\pi\alpha)^2} \cos\left(2\sqrt{2}\hat{\varphi}_-(x)\right) \,, \end{split} \tag{1.144}$$

with the new parameters

$$u_{\pm}^2 = uK\left(\frac{u}{K} \pm \frac{g_2}{\pi\alpha^2}\right), \quad K_{\pm}^2 = \frac{uK}{\frac{u}{K} \pm \frac{g_2}{\pi\alpha^2}}.$$

Equation (1.144) shows that the bonding (charge) sector separates from the anti-bonding (spin) sector with different sound velocities and Luttinger parameters. While the bonding sector is described by a pure TLL, the anti-bonding sector has an additional cosine interaction. This perturbed TLL with an additional cosine potential is also known as the sine-Gordon model [168]. The next subsection 1.3.2 discusses when this perturbation becomes relevant and opens a gap in the spectrum.

<sup>&</sup>lt;sup>15</sup> If the two legs of the ladder represent the two spin states of an electron, the bonding sector measures the charge excitations, and the anti-bonding sector measures the spin excitations.

## 1.3.2 Sine-Gordon Model and Opening of a Gap

The starting point is the sine-Gordon model for  $L \to \infty$  of one bosonic field defined by

$$H = \frac{u}{2\pi} \int dx K \left(\vartheta(\hat{x})\right)^2 + \frac{1}{K} \left(\hat{\varphi}(x)\right)^2 + \frac{2g}{(2\pi\alpha)^2} \cos\left(2\sqrt{2}\hat{\varphi}(x)\right). \tag{1.145}$$

As discussed in the previous subsection, this model, for example, describes the lowenergy effective field theory of excitations in the anti-bonding sector of an interacting ladder system. The non-quadratic nature of the model precludes a direct solution. To determine whether the cosine potential is a relevant perturbation of the  $\overline{\text{TLL}}$ leading to the opening of a gap can be answered for small values of g in terms of a renormalization group flow.

The main idea is that the for g = 0, the model is free and correlations of the vertex operator are algebraic functions

$$R(x-y) = \langle e^{ia\sqrt{2}\hat{\varphi}(x)}e^{-ia\sqrt{2}\hat{\varphi}y}\rangle \sim \left(\frac{\alpha}{|x-y|}\right)^{a^2K}.$$
 (1.146)

This correlator is invariant under the rescaling of the physical length scale,  $\alpha' = \alpha e^{\delta l}$ , which induces an equivalent rescaling of the positions  $x' = e^{\delta l}\alpha$ . By adding a small interaction g, it can be studied how this property of the correlation function remains unchanged. In particular, if the interaction is irrelevant, the properties of the model at long distances should be similar to those of the unperturbed TLL model with possible renormalized Luttinger parameters, K'. However, if the interaction is relevant, the quantum field becomes pinned to the classical minima of the cosine potential at long distances  $\langle \hat{\varphi}(x \to \infty) \rangle \approx \varphi_0$  and the system has a finite gap. In this case, the correlation function in Eq. (1.146) decays exponentially and is no longer scale invariant.

Studying the influence of a small g requires an expansion of the exact correlation function in orders of g. This is typically performed using the Euclidean path integral formalism [40], and details can be found in [47]. After a lengthy calculation, the expansion of the correlation function up to second order in g is given by

$$R(x-y) = e^{-a^2KF(x-y)} \left( 1 + a^2F(x-y) \frac{g^2K^2}{2\pi^2u^2} \int\limits_{\alpha}^{\infty} \frac{\mathrm{d}r}{\alpha} \left( \frac{r}{\alpha} \right)^{3-4K} \right)$$

where F(x-y) is the bosonic correlation function

$$F(x-y) = \frac{2}{K} \langle \hat{\varphi}(x) \hat{\varphi}(y) \rangle .$$

For small g, this becomes

$$R(x-y) \approx e^{-a^2 K_{\rm eff} F(x-y)} \,, \quad K_{\rm eff} = K - \frac{g^2 K^2}{2\pi^2 u^2} \int\limits_{\alpha}^{\infty} \frac{{\rm d}r}{\alpha} \left(\frac{r}{\alpha}\right)^{3-4K} \,. \label{eq:Reff}$$

which is of the same form as for g=0 in Eq. (1.146), but with  $K_{\rm eff}$  replacing K. Requiring the correlation function to stay invariant under a rescaling of the length scale  $\alpha \to \alpha' = \alpha e^{\delta l}$  for small  $\delta l \ll 1$ , it is found that the coupling parameters K and g have to transform according to

$$K(\alpha') = K(\alpha) - \frac{g(\alpha)^2 K(\alpha)^2}{2\pi^2 u^2} \delta l \,, \quad g(\alpha')^2 = g(\alpha)^2 \left(1 + (4 - 4K(\alpha))\delta l\right) \,. \label{eq:Kappa}$$

Defining the dimensionless coupling  $y = g/(\pi u)$  and  $\rho = 2(K-1)$ , and assuming  $y, \rho \ll 1$ , this transformation implies the renormalization flow equations

$$\frac{\mathrm{d}\rho(l)}{\mathrm{d}l} = -y(l)^2, \quad \frac{\mathrm{d}y(l)}{\mathrm{d}l} = -\rho(l)y(l) \tag{1.147}$$

which defines the coupling parameters at the scale  $\alpha(l) = \alpha_0 e^l$ .

The renormalization flow has the following interpretation: if the cosine potential is an irrelevant perturbation of the TLL, the coupling y(l) should flow to zero at a length scale  $l^*$ . Because the flow of  $\rho(l^*)$  stops when  $y(l^*) = 0$ , the system behaves similarly to an unperturbed TLL with a renormalized Luttinger parameter  $K(l^*)$  at distances greater than  $l^*$ .

However, if the perturbation is relevant, the coupling y(l) increases and eventually violates the assumption of  $y \ll 1$  and the flow breaks down for  $y(l^*) \sim 1$ . In the strong coupling limit with  $|y| \to \infty$ , the true ground state has to be an approximate eigenstate of the  $\hat{\varphi}(x)$  operator with eigenvalue minimizing the cosine potential,

$$y\cos(\hat{\varphi})|\varphi_0\rangle \approx y\cos(\varphi_0)|\varphi_0\rangle$$
,  $y\cos(\varphi_0) < 0$ ,

By expanding the quantum field around this semi-classical value  $\hat{\varphi}(x) = \varphi_0 + \delta \hat{\varphi}$ , the cosine potential can be approximated by

$$\frac{yu}{2\pi\alpha^2}\int\!\mathrm{d}x\cos(\sqrt{8}\hat{\varphi}(x))\approx\frac{2yu}{\pi\alpha^2}\int\!\mathrm{d}x\,\delta\hat{\varphi}^2(x)\,.$$

Thus, the sine-Gordon model becomes a massive bosonic field with a gap  $\Delta \sim u\sqrt{y}/\alpha$ .

The gap of the system also flows under renormalization according to  $\Delta(l) = e^l \Delta(l = 0)$ . Using  $y(l^*) \sim 1$  as the scale of where the strong coupling limit becomes valid, the gap at the original scale with l = 0 is given by

$$\Delta(l=0) = e^{-l^\star} \Delta(l) \sim e^{-l^\star} \frac{u}{\alpha} \sqrt{y(l^\star)} \sim e^{-l^\star} \Delta_0 \,.$$

Returning to the renormalization equations (1.147), the flow trajectories are shown in Fig. 1.19. If  $\rho > 0$  and  $|y| < \rho$ , the coupling y flows to zero, and the sine-Gordon model is effectively a gapless free boson. However, for  $|y| > \rho$  and  $\rho < 0$ ,  $y \neq 0$ , the coupling y always flows to the strong coupling limit. The line  $0 < \rho = |y|$  is a special line with the parameters flowing to the self-dual point of  $\rho = y = 0$ .

In the case of interacting fermions on the quantum ladder, the sine-Gordon model describes the anti-bonding sector  $\sqrt{2}\hat{\varphi}_- = \hat{\varphi}_a(x) - \hat{\varphi}_b(x)$ . A pinning of the field  $\hat{\varphi}_- = \varphi_0$  implies an ordering of the relative density  $\rho_-(x) = \rho_a(x) - \rho_b(x)$  of the a and b fermions in the ladder [47]

$$\rho_-(x) \sim \rho_0 \cos(2k_{\rm F}x - 2\varphi_0) \,. \label{eq:rho}$$

This ordering breaks the translation invariance of the lattice but not the other global symmetry of the system. In particular, the global U(1) symmetry is unbroken even with strong attractive interactions, in accordance with the Mermin-Wagner-Hohenberg theorem [48–50].

In Chapters I and II extensions of the sine-Gordon model appear as effective descriptions of the ground state. By performing a renormalization group analysis similar to the one presented here, relevant parameters are identified for a first classification of the phase diagram.

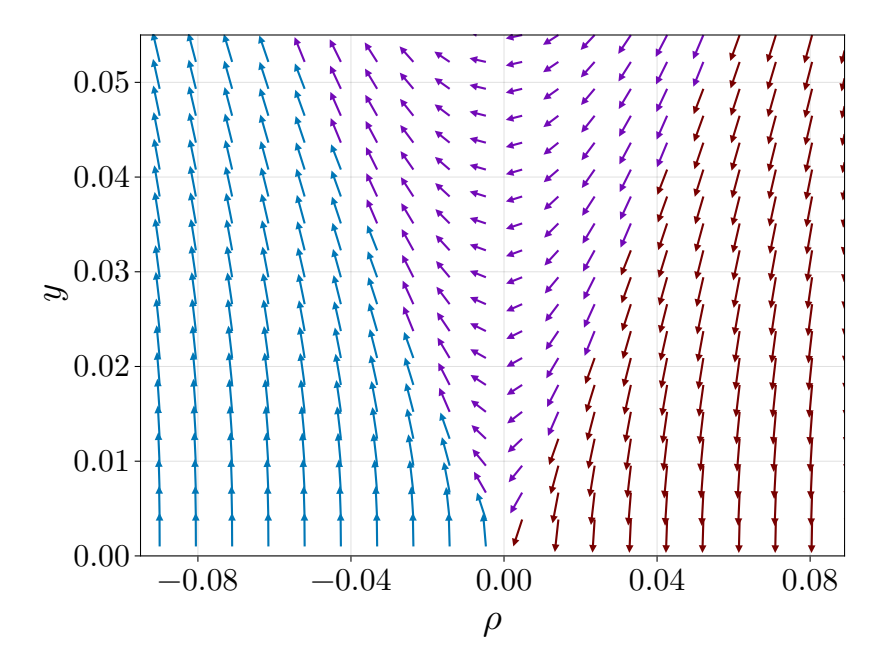


Figure 1.19: Flow field of the renormalization equations (1.147). The red-colored region flows to the gapless point with y = 0. The blue-colored region flows to the strong coupling limit. The violet-colored region first flows towards weak coupling, but ultimately flows to the strong coupling limit, similar to the blue region.

## 1.3.3 Basics of Conformal Field Theory

The TLL discussed in the previous subsection is an example of a Conformal Field Theory (CFT) [67]. A CFT is a gapless quantum model that is invariant under the large class of conformal transformations. On the two-dimensional Euclidean world sheet, which generally describes one-dimensional quantum matter, the conformal group is generated by an infinitely large algebra. Let z = x + iy the complex, holomorphic coordinate of the two-dimensional world sheet, and  $\bar{z} = x - iy$  the (independent) anti-holmorphic variable, every holomorphic function f(z) generates a proper conformal transformation

$$w = f(z) \text{ and } \bar{w} = \bar{f}(\bar{z}) \,, \quad \partial_{\bar{z}} f(z) = \partial_z \bar{f}(\bar{z}) = 0 \,.$$

Simple examples of conformal transformations are rotation and scaling with  $f(z) = \zeta z$  with  $0 \neq \zeta \in \mathbb{C}$ , or translations f(z) = z + a.

The conformal group induces a representation on the quantum fields of the theory, which also has an infinite number of generating operators. In general, this set of operators is very restricted and is known as the Virasoro algebra [67, 169]. The existence of the Virasoro algebra allows the extraction of many exact statements regarding the low-energy theory of the quantum system. For example, it is found that the theory can be described in terms of highly symmetric quantum fields, known as primary fields  $\hat{\psi}_n(z,\bar{z})$  and every other quantum field can be generated from these primary fields by the application of the Virasoro algebra.

At the level of correlation functions, conformal invariance is reflected by special transformation rules of the correlator under conformal symmetry. Taking a simple scaling w = bz with  $b \in \mathbb{R}$ , the correlation function of a set of operators transforms as

$$\langle \psi_1(z_1,\bar{z}_1)\dots \psi_n(z_n,\bar{z}_n)\rangle = |b|^{\Delta_1}\dots |b|^{\Delta_n} \, \langle \psi_1(bz_1,b\bar{z}_1),\dots,\psi_n(bz_n,b\bar{z}_n)\rangle$$

where  $\Delta_n$  is the scaling dimension of the quantum field  $\psi_n$ . For a two point function, this is already enough to be completely fixed to

$$G(z_1,z_2)\coloneqq \langle \psi_1(z_1,\bar{z}_1)\psi_2(z_2,\bar{z}_2)\rangle = \delta_{\Delta_1,\Delta_2} \frac{C_{12}}{|z_1-z_2|^{2\Delta_1}}\,.$$

Every n-point function is generally a homogeneous function, which is further fixed by invariance under additional conformal transformations.

Because every quantum field can be generated from the primary fields in a CFT, the scaling dimensions of such descendants are fixed by the scaling dimension of the primary field and the algebraic structure of the Virasoro algebra. In addition to the scaling dimensions, the Virasoro algebra defines the central charge c, which is an anomaly of the quantum field theory. This number has no influence on the structure of the correlation functions, but its existence permits the ground state to be invariant under the full conformal group. The central charge appears, for example, in the final size correction of the energy density or in the entanglement structure of the ground state, as discussed in Subsection 1.4.2.

Thus, one of the main aspects of a  $\overline{\text{CFT}}$  is identifying the primary fields and their associated scaling dimensions as well as the central charge c. In the following, three simple examples that are important for this thesis are presented.

#### Free Boson

The TLL encountered in Subsection 1.3.1 is described by a free bosonic field with a Hamiltonian given by Eq. (1.137). This theory is gapless and thus invariant under conformal transformations [169] as discussed above. However, the correlation function of the bosonic field  $\hat{\varphi}(z,\bar{z})$  is logarithmic

$$\langle \hat{\varphi}(z,\bar{z})\hat{\varphi}(w,\bar{w})\rangle \sim -\log\left((z-w)(\bar{z}-\bar{w})\right)$$
,

compare also Eq. (1.130), and the bosonic field is not a primary field. By taking the holomorphic derivative, the correlation function becomes algebraic and one finds

$$\langle \partial_z \hat{\varphi}(z,\bar{z}) \partial_w \hat{\varphi}(w,\bar{w}) \rangle \sim \frac{1}{(z-w)^2}$$

and similar for the anti-holomorphic derivative. Thus, the primary fields are  $\partial_z \hat{\varphi}(z, \bar{z})$  and  $\partial_{\bar{z}} \hat{\varphi}(z, \bar{z})$  both with scaling dimension  $\Delta = 1$ . In addition, it is found that every vertex operator  $e^{ia\hat{\varphi}(z,\bar{z})}$  is a primary field with a scaling dimension  $Ka^2/4$  and the free boson has infinitely many primary fields. To complete the CFT data, the central charge is c = 1 [67, 169].

#### Critical Ising model

Another simple CFT is the critical Ising model. The critical Ising model emerges in the transverse field Ising model discussed in Subsection 1.2.1 at the interface between the two gapped phases at J=g. This CFT has a central charge of c=1/2. In contrast to the free bosonic field, the Ising CFT has only two non-trivial primary fields. The first is the energy density  $\epsilon$  which has a scaling dimension of  $\Delta_{\epsilon}=1$  and the second field is the local magnetization  $\sigma$ , which has a scaling dimension of  $\Delta_{\sigma}=1/8$ . Under the  $\mathbb{Z}_2$  symmetry of the Ising model, the energy operator  $\epsilon$  transforms trivially, whereas the magnetization  $\sigma$  changes sign. In terms of the

macroscopic theory, this transformation implies the following identification of the microscopic variables with the primary fields

$$\epsilon \sim \sigma_j^x \sigma_{j+1}^x + \frac{\sigma_j^z + \sigma_{j+1}^z}{2} \,, \quad \sigma \sim \sigma_j^x \,.$$

Based on this identification, it is expected that the correlation function of the Pauli-X operators decay as

$$\langle \sigma_j^x \sigma_k^x \rangle \sim \frac{1}{|j-k|^{2\Delta_\sigma}} = \frac{1}{|j-k|^{1/4}}.$$
 (1.148)

This expected decay behavior is shown in Fig. 1.20.

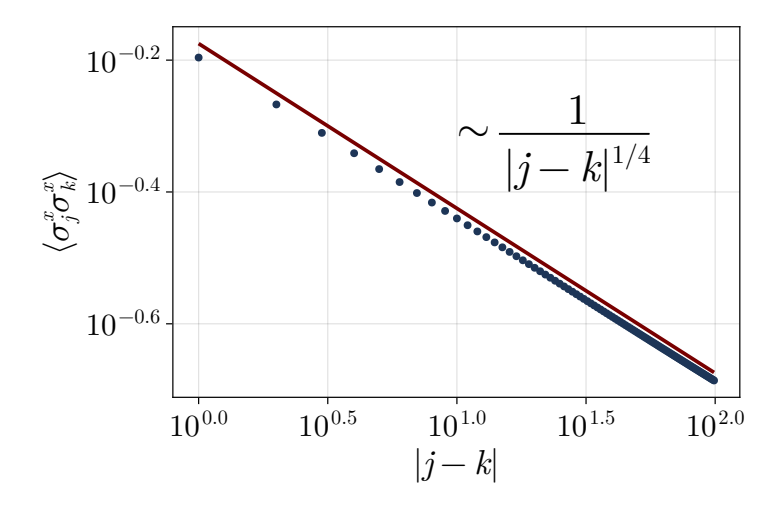


Figure 1.20:  $\sigma_i^x$  correlation function in the Ising model at the critical point J=g.

An explicit effective low-energy Hamiltonian describing the critical Ising model is the  $\hat{\varphi}^4$  theory. In particular, the Ising model appears at the massless point g=0 of the Hamiltonian

$$H = \int dx \left(\partial_x \hat{\varphi}(x)\right)^2 + g\hat{\varphi}(x)^2 + \lambda \hat{\varphi}(x)^4, \qquad (1.149)$$

where  $\hat{\varphi}(x)$  is real quantum field, and  $\lambda > 0$ . The  $\mathbb{Z}_2$  Ising symmetry is implemented by the transformation  $\hat{\varphi}(x) \to -\hat{\varphi}(x)$  which leaves the Hamiltonian invariant.

In a semi-classical picture, the potential  $V(\varphi)=m^2\varphi^2+\lambda\varphi^4$  is minimized by  $\varphi=0$ , if g>0, which is invariant under Ising symmetry. In the quantum picture, the ground state obeys  $\hat{\varphi}(x)|0\rangle\approx 0$  which is a unique symmetry-respecting state. For g<0, the potential has two minima at  $\varphi_{\pm}=\pm\sqrt{-2\lambda/g}$ , which are transformed into each other by the Ising symmetry. At the quantum level, these two minima correspond to two ground states with the property  $\hat{\varphi}(x)|\varphi_{\pm}\rangle\approx\varphi_{\pm}|\varphi_{\pm}\rangle$ , and the system breaks the Ising symmetry. At g=0, the two minima merge at  $\varphi=0$  and the critical Ising model emerges. The two primary fields are given in this representation as  $\epsilon=\hat{\varphi}^2$  and  $\sigma=\hat{\varphi}$  and are relevant perturbations of the critical Ising model.

## Tricritical Ising Model

Adding a  $\hat{\varphi}^6$  term to the low-energy effective Hamiltonian in Eq. (1.149)

$$H = \int dx \left(\partial_x \hat{\varphi}(x)\right)^2 + g\hat{\varphi}(x)^2 + \lambda \hat{\varphi}(x)^4 + \lambda_2 \hat{\varphi}(x)^6, \qquad (1.150)$$

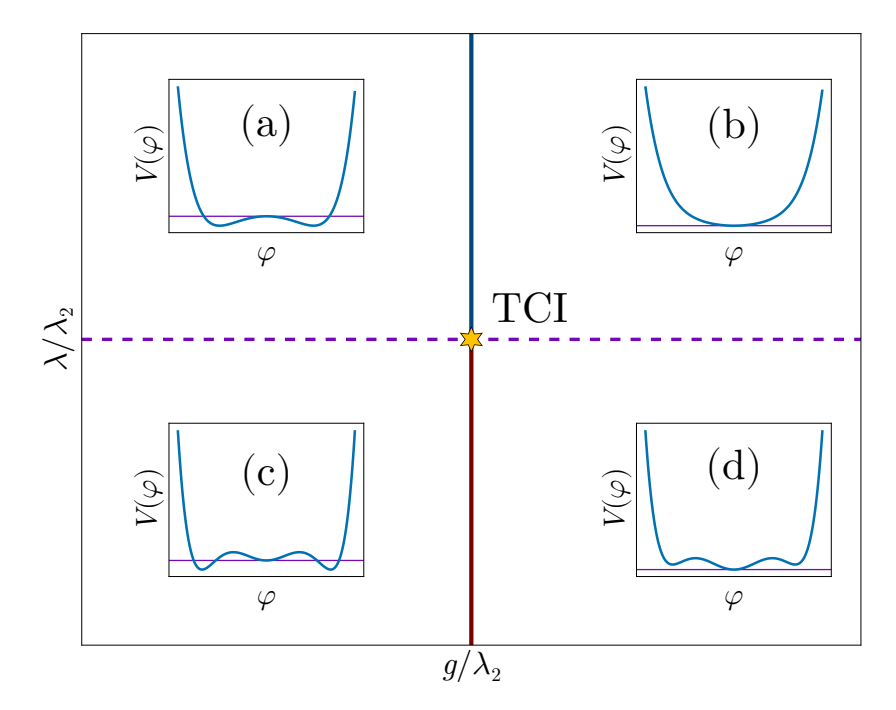


Figure 1.21: Sketch of the TCI phase diagram. At the purple dashed line  $\lambda=0$ , the blue and red lines are the symbolic lines where the model has a critical Ising transition and FOPT, respectively. (a) For  $\lambda>0$  and g<0 there are two minima of the potential  $V(\varphi)$  that break the Ising symmetry. (b) Crossing the blue line, the two minima merge at g=0 forming a unique symmetry restoring minimum at  $\varphi=0$ . At g=0, the model becomes the critical Ising model. (c) For  $\lambda, g<0$ , the model also breaks Ising symmetry with two local minima. (d) By crossing the red line, a FOPT, the two minima increase in energy, and the minimum at  $\varphi=0$  becomes the new global minimum. At the point where the blue and red lines merge  $(g=\lambda=0)$ , a triple point emerges, with three different minima merging, hosting the TCI model.

where  $\lambda_2>0$  and  $g,\lambda\in\mathbb{R}$ , allows for a richer phase diagram. A semi-classical analysis of the minima structure of the potential  $V(\varphi)$  reveals that, for  $\lambda>0$ , the system behaves similarly to the Ising case. In particular, for g>0 the system has a unique, symmetry-respecting minimum, whereas for g<0 there are two minima  $\varphi_\pm$  that break Ising symmetry. At g=0, the two minima merge and the critical Ising model emerges.

The situation is different when  $\lambda < 0$ . For  $g < g_c$ , the potential still exhibits two minima at  $\varphi_{\pm} \neq 0$ . However, by approaching the point  $g_c$ , these two minima increase in energy, and at  $g = g_c$  the potential has three minima at  $\varphi_{\pm}$  and  $\varphi_0 = 0$ . A further increase in g leads to  $\varphi_0$  being the unique symmetry-restoring ground state, with the previous minima  $\varphi_{\pm}$  becoming local minima with higher energy. This form of transition is called a First-Order Phase Transition (FOPT) with no CFT emerging at  $g = g_c$ . The phase diagram is sketched in Fig. 1.21. At the point  $g = \lambda = 0$ , the three local minima merge, and the Tricritical Ising (TCI) model emerges [170]. As a CFT, this model has a central charge of c = 7/10 and four non-trivial primary field operators: two energy operators  $\epsilon$  and  $\epsilon'$  and two magnetization operators  $\sigma$  and  $\sigma'$ . For example, the scaling dimension of the magnetization  $\sigma$  is given by  $\Delta_{\sigma'} = 3/40$ .

In Chapter II, a model based on Josephson Junction arrays is presented that realizes a combination of the free bosonic field and the TCI model.

# 1.4 Entanglement

The previous Sections 1.2 and 1.3 discussed the different phases that appear in one-dimensional quantum matter and introduced tools to determine the phase of a given model. These tools include local observables, such as the order parameter for symmetry-broken phases and the algebraic decay of correlation functions for gapless phases. This section introduces another tool that can be used to gain additional insights into the state of a quantum chain: quantum entanglement.

Quantum entanglement is a resource that defines how different regions of a quantum mechanical system are correlated with each other and is one of the key properties of quantum matter that distinguishes it from classical systems. This correlation results in uncertainty about the state of sub-region A after measuring the state of the rest of the system. The remaining part of the quantum state defined on A is described by a density matrix  $\rho$  which defines the distribution of the possible states of the reduced system. Although similar to a classical thermodynamic ensemble, this distribution has some fundamentally different properties [171–177].

As bosons and fermions are equivalent to spins in one-dimensional systems, see Subsection 1.1.5, this section focuses mainly on the case of spin chains.

## 1.4.1 Reduced Density Matrix and Entanglement Spectrum

Consider a spin chain with a local Hilbert space dimension  $\dim(\mathcal{H}_{loc}) = d$  and length N. The indices of the chain are denoted by  $\mathcal{I} = \{1, \dots, N\}$ . The chain can either describe a chain with open boundary conditions at the end or closed to a ring with periodic (twisted) boundary conditions.

Splitting the set of indices  $\mathcal{I}$  into two consecutive parts A and B

$$\mathcal{I} = A \cup B$$
,  $A := \{1, \dots, l\}$ ,  $B := \{l+1, \dots N\}$ . (1.151)

defines a bipartition of the chain. The length of the bipartition is measured as the length of sub-region A given by |A| = l. In the case of open boundaries, this bipartition cuts the chain along the bond (l, l + 1), whereas for a ring, it results in two cuts at (N, 1) and (l, l + 1), as shown in Fig. 1.22.

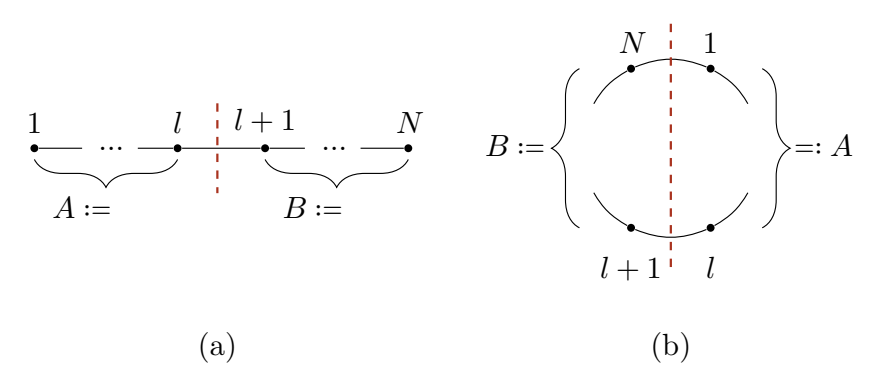


Figure 1.22: Bipartition on a one-dimensional chain. (a) Cutting an open chain at the bond (l, l+1). (b) Cutting a ring at two bonds (N, 1) and (l, l+1). In both cases, the two constituents have lengths |A| = l and |B| = N - l.

The bipartition (1.151) induces a decomposition of the many-body Hilbert space as

$$\mathcal{H} = \mathcal{H}_{A} \otimes \mathcal{H}_{B}$$

where the states defined on  $\mathcal{H}_A$  have support only on the sites contained in subregion A and are similar for  $\mathcal{H}_B$ . A generic many-body quantum state  $|\psi\rangle \in \mathcal{H}$  can be represented with respect to this bipartition as

$$|\psi\rangle = \sum_{a,b} \Psi_{a,b} |\psi_a^A\rangle \otimes |\psi_b^B\rangle = \sum_{\alpha=1}^{\alpha_{\text{max}}} \sigma_\alpha |\tilde{\psi}_\alpha^A\rangle \otimes |\tilde{\psi}_\alpha^B\rangle . \tag{1.152}$$

where  $|\psi_{a(b)}^{A(B)}\rangle$  forms an orthonormal basis set on the two sub-Hilbert spaces  $\mathcal{H}_A$  and  $\mathcal{H}_B$ . This equation is known as the Schmidt decomposition [61, 178, 179] and the singular values  $\sigma_{\alpha}$  are positive and real. The second equal sign in Eq. (1.152) is obtained by performing a Singular-Value Decomposition (SVD), see also Appendix A, on the coefficient matrix  $\Psi = U\Sigma V^{\dagger}$  followed by absorbing the unitiaries U and V in a redefinition of the basis states  $|\psi_a^A\rangle$  and  $|\psi_b^B\rangle$ . Assuming the state to be normalized  $\langle\psi|\psi\rangle=1$ , it follows  $\mathrm{Tr}[\Psi^{\dagger}\Psi]=\sum_{\alpha}\sigma_{\alpha}^2=1$ .

The bipartition  $\mathcal{I}=A\cup B$  in Eq. (1.151) allows for the definition of the reduced density matrix  $\rho_G$  where G=A,B, which is obtained by forming the pure density matrix  $\rho=|\psi\rangle\langle\psi|$  followed by tracing out the states of the Hilbert space defined on the complementary part  $\bar{G}=\mathcal{I}\setminus G$ 

$$\rho_G = \operatorname{Tr}_{\bar{G}} \left[ |\psi\rangle \langle \psi| \right] = \sum_{a,a'} (\rho_G)_{a,a'} |\psi_a^G\rangle \langle \psi_{a'}^G| . \tag{1.153}$$

Using the Schmidt decomposition (1.152), the reduced density matrix in equation (1.153) can be written in terms of the coefficient matrix  $\Psi$  as

$$\rho_A = \Psi \Psi^\dagger = U \Sigma^2 U^\dagger \,, \quad \rho_B = \Psi^\dagger \Psi = V \Sigma^2 V^\dagger \label{eq:rhoA}$$

and the two reduced density matrices are connected by a unitary transformation

$$\rho_A = W \rho_B W^{\dagger}, \quad W = U V^{\dagger}.$$

Based on this equivalence, the remainder of this section considers only the reduced density matrix of region A. Since the reduced density matrix is positive definite, it is possible to define an entanglement Hamiltonian

$$\rho_A \cong \exp\left(-H_{\text{ent}}\right) \,. \tag{1.154}$$

Following this definition, the quantum fluctuations in the remaining quantum state on region A described by the reduced density matrix  $\rho_A$  are interpreted as thermal fluctuations of a thermal ensemble described by the entanglement Hamiltonian at temperature T=1 [180]<sup>16</sup>. The entanglement spectrum  $\lambda_{\alpha}$  is defined by the eigenvalues of the entanglement Hamiltonian. Using equation (1.152), the entanglement spectrum is related to the singular values of the quantum coefficient matrix  $\Psi$  by

$$0 \le \sigma_{\alpha} = \exp(-\lambda_{\alpha}/2). \tag{1.155}$$

Note that the reduced density matrix and the entanglement Hamiltonian have the same symmetries as the quantum state  $|\Psi\rangle$ . In particular, let  $U = \prod_j u_j$  be a global unitary Abelian symmetry operator consisting of the product of local unitaries, and

 $<sup>^{16}{</sup>m This}$  is to be understood only as an analogy as quantum fluctuations are fundamentally different from thermal fluctuations.

let  $U|\psi\rangle = e^{i\phi}|\psi\rangle$  for some phase  $\phi$ . The reduced density matrix of  $|\psi\rangle$  becomes block diagonal and can be written as

$$\rho_A = \sum_{n} \sum_{a,a'} \left(\rho_A^n\right)_{a,a'} \left| \psi_{n,a}^A \right\rangle \left\langle \psi_{n,a'}^A \right| .$$

The states  $|\psi_{n,a}^A\rangle$  form representations of the symmetry  $U_A = \prod_{i \in A} u_i$ 

$$U_A |\psi_{n,a}^A\rangle = e^{i\phi_n} |\psi_{n,a}^A\rangle$$
.

# Properties of the Entanglement Hamiltonian

The entanglement Hamiltonian provides deep insights into the correlations of the many-body quantum state  $|\psi\rangle$  and can be used to determine the different phases of a quantum spin chain [181]. For example, if the chain is described by a CFT, the low-energy part of the entanglement spectrum becomes universal and is completely determined by the universal properties of the CFT [182, 183].

If the state  $|\Psi\rangle$  is the ground state of a gapped Hamiltonian, the entanglement Hamiltonian becomes concentrated at the boundary of the bipartition [184]. Although not universal in general for gapped states, the existence of additional degeneracies in the spectrum can be used to detect SPTPs that where discussed in Subsection 1.2.2 [51–54]. For example, consider the SPTP phase of unpaired MZM emerging in spinless fermionic chains subjected to p-wave superconducting correlations [84] as discussed in Subsection 1.2.3. Since the two MZMs are localized at the opposite edges of the chain, their existence is reflected in a fractionalization of the fermionic parity operator

$$\hat{P} = \prod_{j=1}^{N} \hat{p}_{j} \approx \hat{P}_{L} \hat{P}_{R}, \quad \{\hat{P}_{L}, \hat{P}_{R}\} = 0.$$

The parity symmetry of the Hamiltonian induces the same symmetry on the entanglement Hamiltonian which can be written in general as

$$H_{\mathrm{ent}} = \sum_{\alpha} \left( \lambda_{\alpha,+1} \left| \alpha, +1 \right\rangle \left\langle \alpha, +1 \right| + \lambda_{\alpha,-1} \left| \alpha, -1 \right\rangle \left\langle \alpha, -1 \right| \right)$$

where  $|\alpha,p\rangle$  denotes the eigenstate of  $H_{\rm ent}$  with parity p. In [53] it was shown that the fractionalization of the parity operator is a generic feature of this SPTP of fermionic quantum chains, and leads to an exact double degeneracy of the entanglement spectrum  $\lambda_{n,+1} = \lambda_{n,-1}$ , whereas this degeneracy is absent if the system is trivial. Figure 1.23 shows the entanglement spectrum for the KHM from Eq. (1.110), repeated here for completeness

$$H_{\text{KH}} = \sum_{j=1}^{N-1} \left( -w \, c_j^{\dagger} c_{j+1} - \Delta_p \, c_j^{\dagger} c_{j+1}^{\dagger} + \text{h.c.} \right) - \frac{\mu}{2} \sum_{j=1}^{N} \hat{p}_j + U \sum_{j=1}^{N-1} \hat{p}_j \hat{p}_{j+1} \,, \quad (1.156)$$

where  $c_j^{(\dagger)}$  annihilates (creates) a spinless fermion at site j. This model enters the SPTP for the correct choice of parameters; see also Figure (1) of [148]. In general, such degeneracy can also appear for symmetry-broken states if the entanglement Hamiltonian is calculated with respect to the symmetry-restoring basis from Eq. (1.56). However, the degeneracy can be removed by passing to the symmetry-breaking basis.

In Chapter I the double degeneracy of the entanglement spectrum is used to identify the non-trivial SPTP in an interacting fermion ladder.

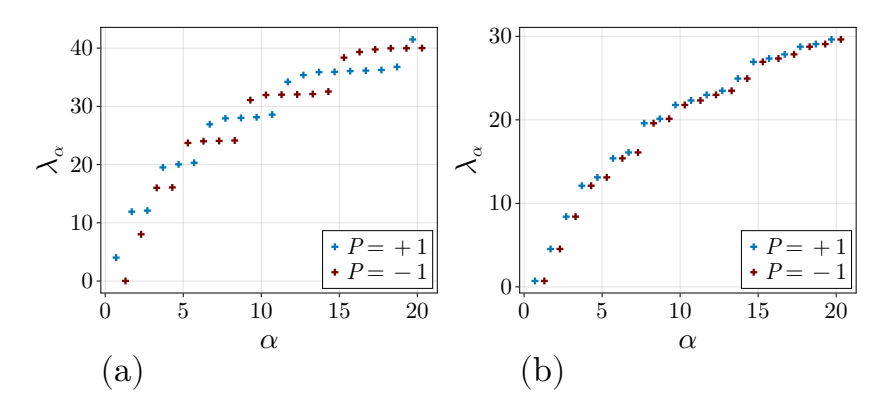


Figure 1.23: The first twenty values of the entanglement spectrum of the KHM, Eq. (1.156), measured at half the system size. In both panels, the size of the chain is N=100 and  $w=\Delta_p$ ,  $\mu=1.6w$  with U=2w in panel (a), and U=0.6w in panel (b). The eigenvalues are labeled by the parity of the eigenstate of the entanglement Hamiltonian, with blue denoting an even parity and red denoting an odd parity of the state. The large interaction in panel (a) leads to the formation of an insulating trivial state with a unique ground state and no degeneracy in the entanglement Hamiltonian. In contrast, the interaction in panel (b) is chosen to place the system in the fermionic SPTP, leading to a doubly degenerate entanglement spectrum.

# 1.4.2 Entanglement Entropy and Boundary Law

Various measures of entanglement can be defined based on the entanglement Hamiltonian and the entanglement spectrum. These measures are scalars that can be used to quantify the entanglement between two sub-regions and can be used as a tool for distinguishing different phases of matter. As a prominent example, the von-Neumann entanglement entropy, or simply entanglement entropy in the following, of the sub-region G is defined by

$$S(G) = -\operatorname{Tr}\left[\rho_G \log\left(\rho_G\right)\right] = \sum_{\alpha=1}^{\alpha_{\text{max}}} \lambda_\alpha e^{-\lambda_\alpha}, \qquad (1.157)$$

where the second equation follows from rewriting the sum in terms of the entanglement spectrum  $\lambda_{\alpha}$  introduced in Eq. (1.155). For the bipartition considered in Eq. (1.151), it follows from the unitary equivalence of the two reduced density matrices  $\rho_A$  and  $\rho_B$  that the entanglement entropy of both subsystems is equal

$$S(A) = S(B)$$
.

Consequently, the entanglement entropy depends only on the length of the subsystem |A| = l and the total length of the chain N. In this case, the entanglement entropy is denoted by S(l).

The entanglement entropy is maximized by a many-body state with a flat distribution of possible Schmidt vectors along a given cut (l, l + 1). For a quantum spin chain of length N with local Hilbert space dimension d, a flat distribution of Schmidt values, Eq. (1.152), means

$$\sigma_{\alpha} = d^{-l}$$
,

where the state  $|\psi\rangle$  is assumed to be normalized, and  $l \leq N/2$ . This follows from the fact that the coefficient matrix  $\Psi$  in Eq. (1.152) has a maximum rank of  $d^l$ . Inserting this flat entanglement spectrum into the formula of the entanglement entropy (1.157) gives

$$S(A) = l\log(d). \tag{1.158}$$

It was conjectured by D. Page [185], and later proven [186–188], that a normalized quantum state drawn randomly from the full many-body Hilbert space  $\mathcal{H}$  has an entanglement entropy close to this maximal possible value, at least if  $1 \ll l \ll N/2$ . Thus, a random quantum many-body state has an entanglement entropy which is expected to growth with the length of the subsystem A

$$S(A) \sim |A| \,. \tag{1.159}$$

It is expected that the eigenstates of a many-body Hamiltonian from the middle of the spectrum behave chaotically and therefore realize this volume law, except for special cases [25]. In contrast, the ground states and low-lying excitations of a typical one-dimensional Hamiltonian exhibit vastly different behaviors for the entanglement spectrum and, thus, the entanglement entropy. As introduced in Subsection 1.1.3, a

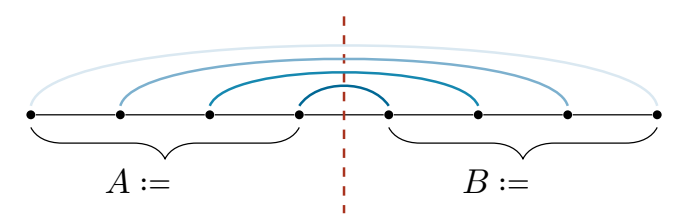


Figure 1.24: Bipartition of a quantum chain, similar to Fig. 1.22(a). The blue lines represent the entanglement between pairs of spins in the ground state of a short-range Hamiltonian, with the opacity denoting its strength. The contribution to the entanglement entropy of spins close to the cut is larger than that of spins that are more distant.

typical Hamiltonian H in one-dimensional quantum chains can either have a spectral gap  $\Delta > 0$  or be gapless and described by a CFT [67].

If the spectrum has a finite gap, the ground state is only short-range correlated, with all correlation functions decaying exponentially [65, 66]. The property of being only short-range correlated also implies that such a ground state has only short-range entanglement [52, 54, 119, 189, 190], where the entanglement through a cut at (l, l+1) can only be created by spins that are close to the cut, as illustrated in Fig. 1.24.

As a consequence, the entanglement entropy converges to a constant with respect to the size of the sub-region  $\cal A$ 

$$S(l) \approx \text{const}$$
, for  $1 \ll l \ll N$ . (1.160)

This is known as the boundary law of entanglement entropy [191–193] because S(l) is not proportional to the volume of the block A, as in the case of a random state, but rather to the size of the boundary  $\partial A$ , which is a simple constant in one-dimensional systems. It also demonstrates that the states realizing the ground states of gapped Hamiltonians are very special and different from the vast majority of generic states in the many-body Hilbert space, a situation visualized in Fig. 1.25.

Taking as an example the  $\overline{\text{TFIM}}$  introduced in Eq. (1.51)

$$H_{\text{Ising}} = -J \sum_{j=1}^{N-1} \sigma_j^x \sigma_{j+1}^x - g \sum_{j=1}^N \sigma_j^z \,. \label{eq:HIsing}$$

As discussed in Subsection 1.2.1, the TFIM is in a gapped phase with a unique ground state for g/J > 1. This results in an entanglement entropy that initially

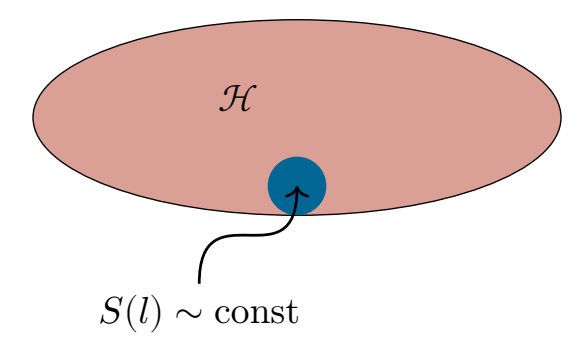


Figure 1.25: The states fulfilling the boundary law of entanglement Eq. (1.160) only occupy a small region in the full many-body Hilbert space.

increases with the length l of sub-region A until it reaches a system-size-independent plateau, as demonstrated in Fig. 1.26(a).

If the Hamiltonian is gapless and the low-energy sector is described by a CFT, the entanglement entropy violates the boundary law (1.160). However, the violation is in the weakest possible way by adding only a logarithmic correction [194, 195]

$$S(l) \approx \frac{c \cdot n_{\text{cut}}}{6} \log \left( \frac{d(l, N)}{n_{\text{cut}}} \right) + s_0.$$
 (1.161)

Here, c is the central charge of the underlying CFT, and  $n_{\rm cut}$  is the number of cuts necessary to perform the bipartition  $\mathcal{I} = A \cup B$ , with  $n_{\rm cut} = 1$  for an open chain, as shown in Fig. 1.22(a), and  $n_{\rm cut} = 2$  for a ring, as shown in Fig. 1.22(b). The function d(l, N) is called the chord distance

$$d(l,N) = \frac{2N}{\pi} \sin\left(\frac{\pi}{N}l\right), \qquad (1.162)$$

which appears when mapping the CFT from a plane on a finite cylinder [195].

Figure 1.26(b) shows the entanglement entropy for the TFIM at the critical point g = J. At this point, the low-energy part of the spectrum is described by a CFT with a central charge of c = 1/2, known as the critical Ising model. By plotting the entanglement entropy against the chord distance, the different system sizes collapse to the universal logarithmic law (1.161) with the correct prefactor of  $1/12 = 1/2 \cdot 1/6$ .

The reason for the boundary law in Eq. (1.160) for gapped ground states or the logarithmic law in Eq. (1.161) for a CFT lies in the structure of the entanglement spectrum. For a random quantum state, the distribution of the Schmidt values  $\sigma_{\alpha}$  and thus the distribution of the entanglement spectrum, is nearly flat, while the Schmidt values are expected to decay exponentially in the case of ground states. The crucial difference between the gapped and gapless cases is that the Schmidt values for a gapped system decay rapidly and become nearly system-size-independent with non-universal values. However, for a gapless chain, the entanglement spectrum becomes dense for  $N \to \infty$  with a universal structure encoding further data of the underlying CFT [182, 183].

#### 1.4.3 Excited States and Higher Dimensions

The final part of this section considers the generalization of the ideas presented previously to higher dimensions and excited states. For excited states, one finds that

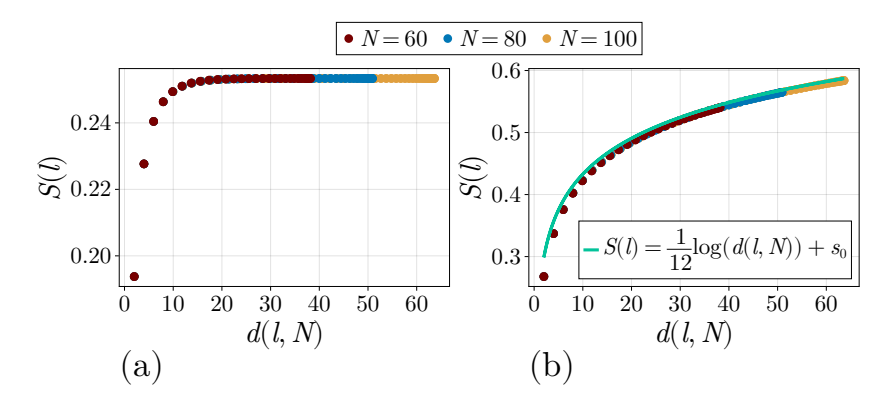


Figure 1.26: Entanglement entropy of the transverse field Ising model plotted against the chord distance d(l,N) from Eq. (1.162). (a) For g/J=1.2 the model is gapped with a unique ground state. As expected, the entanglement entropy converges to a small constant for all system sizes. (b) For g=J the model is gapless with the long wavelength fluctuations being described by the critical Ising model with a central charge c=1/2. In this case the entanglement entropy follows the universal logarithmic behavior of Eq. (1.161). The light-blue curve is a fit by the eye with  $s_0\approx 0.24$ .

low-lying excitations have an entanglement entropy that grows logarithmically [196, 197] in the length of block A similar to the entanglement entropy of a critical system in Eq. (1.161). This result is based on the idea that a low-lying excitation can be generated by the application of local operators from the ground state [64, 198], which is similar to the Fourier sum proposed by Bijl, Feynman, and Cohen [199–201].

In higher dimensions, some of the ideas presented previously have appropriate counterparts. The bipartition considered in a D-dimensional quantum many-body system is typically a region A with volume |A| and a closed boundary of length  $|\partial A|$ , as illustrated in Fig. 1.27. A result which directly generalizes to the D dimensional case is the volume law of Eq. (1.159) for random states [185–188]

$$S(A) \sim |A|$$
.

The boundary law for gapped systems is more subtle. Here it was conjectured, and proven for the related quantity of the mutual information, that the entanglement entropy of a gapped quantum many-body system fulfills the modified boundary law [189, 191–193, 202, 203]

$$S_A \approx C |\partial A| + \frac{n_B}{2} \log \left( |\partial A| \right) \,, \tag{1.163}$$

where  $n_B$  represents the number of Goldstone bosons [204–206] appearing in symmetrically broken systems in  $D \ge 2$  dimensions. For gapless systems, it was conjectured, and actually proven for Fermi surfaces [207, 208], that the area law obtains a multiplicative logarithmic correction [192]

$$S_A \sim \log(|A|)|\partial A|$$
.

Another exotic behavior that is absent in one dimension is the formation of topologically ordered states [128, 129]. These states are gapped phases without symmetry breaking. Thus, they follow the boundary law in Eq. (1.163) with  $n_B = 0$ . However, these states also allow for fractionalized quasi-particles with non-trivial braiding

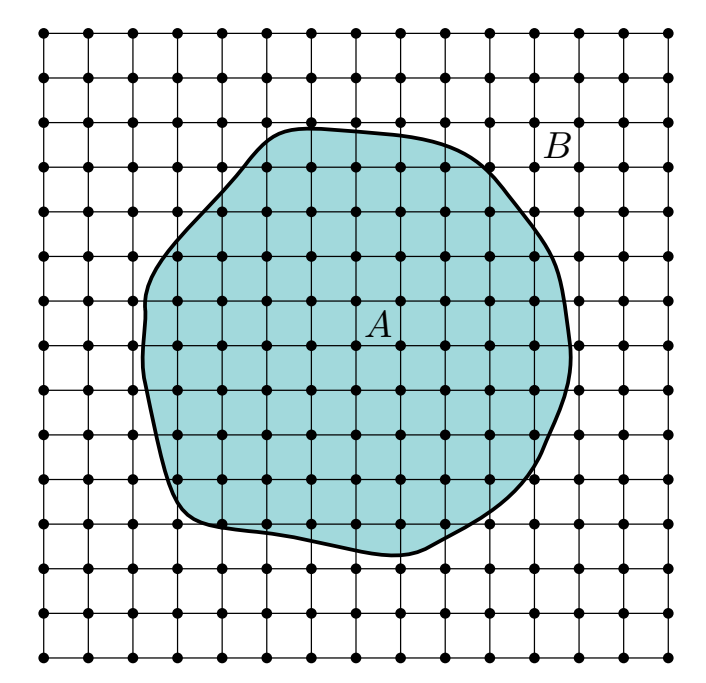


Figure 1.27: Bipartition on a two-dimensional lattice defined by the area shaded in blue, separating region A from B. The boundary of region A is  $\partial A$ .

statistics, also known as anyons [128, 129]. As a result, the boundary law is corrected by a negative constant  $\gamma_{\text{topo}}$ , which depends only on the possible anyons of the topological ground state [209]. On the level of the entanglement Hamiltonian, this amounts to an additional universal boundary theory living on the virtual cut separating region A from B [210] and investigating the properties of this boundary theory can help in understanding the topological nature of the phase [211, 212].

# 1.5 Almost Strong Zero Mode

Subsection 1.2.3 discusses the appearance of MZMs in the topological regime of the Kitaev chain model. These MZMs, denoted by  $\Gamma_{a/b}$ , are Majorana operators exponentially localized to the edges of the chain, as expressed in Eq. (1.97), and represent a non-local fermionic degree of freedom  $c_E = \Gamma_a - i\Gamma_b$ .

The existence of a non-local fermion leads to a double degeneracy of the ground state in the Kitaev chain. Moreover, based on the exact commuting properties of the MZMs  $[\Gamma_{\alpha}, H_{\text{Kitaev}}] = 0$ , the degeneracy is not limited to the ground state but applies to the entire spectrum. Any eigenstate of the system with a given parity can be created from one of the two ground states using arbitrary applications of the Bogoliubov quasi-particle creation operators  $f_n^{\dagger}$  defined in Eq. (1.96). Owing to the non-interacting nature of the Kitaev Hamiltonian, these quasi-particles are not influenced by the occupation of the fractionalized fermion  $c_E = \Gamma_a - i\Gamma_b$ .

At finite interactions, the quasi-particles begin to interact, and the MZM hybridizes with the bulk. If these interactions do not drive the system through a quantum phase transition, the ground state remains topologically degenerate. However, this is not necessarily the case for higher-excited states.

The aim of this section is to provide a brief introduction to the concepts of the Strong Zero Mode (SZM) and Almost Strong Zero Mode (ASZM), which will be the main topic of Chapters IV–VI. While the SZM is a generalization of the Majorana Zero Modes (MZMs) found in the Kitaev chain, the ASZM is the smooth connection

of the  $\overline{\text{SZM}}$  to interacting, non-integrable systems. The basic setting is a quantum chain of N lattice sites populated by spinless fermions described by a many-body Hamiltonian that only commutes with the fermionic parity<sup>17</sup>

$$\hat{P}H\hat{P} = H, \quad \hat{P} = \prod_{j=1}^{N} e^{i\pi \hat{n}_j},$$

defining a  $\mathbb{Z}_2$  symmetry.

# 1.5.1 Strong Zero Modes – Definitions and Results

A Strong Zero Mode (SZM) is a Hermitian operator  $\Gamma$  acting on the many-body Hilbert space  $\mathcal{H}$  of the quantum chain which has the following properties [213–220]

- C.1 Normalizability:  $\Gamma^2 = 1$
- C.2 Anti-commutation with the parity operator:  $\{\Gamma, \hat{P}\} = 0$
- C.3 Localized at position j
- C.4 Commuting with the Hamiltonian for  $N \to \infty$ :  $[H, \Gamma] = \hat{R}, ||\hat{R}|| \sim e^{-\lambda N}$

Condition C.1 and C.2 implies that  $\Gamma$  is a Majorana operator connecting a state with a given parity p with a state of flipped parity  $\bar{p}=-p$  and the two states are orthogonal

$$\langle \psi_p | \Gamma | \psi_p \rangle = 0$$
.

The localization property C.3 requires that there exists a local operator  $\hat{o}_j$  acting only at site j which can be expanded as

$$\hat{o}_j = A(N)\Gamma + \sum_n \Phi_{n,j} \hat{O}_j \,, \quad \lim_{N \to \infty} A(N) = A > 0$$
 (1.164)

where  $\hat{O}_j$  together with  $\Gamma$  form a complete set of operators acting on the many-body Hilbert space  $\mathcal{H}$ . Assuming this set to be orthogonal with respect to the Frobenius scalar product from Eq. (1.9)

$$\langle \hat{O}_k, \hat{O}_j \rangle := \frac{1}{\dim(\mathcal{H})} \operatorname{Tr} \left[ \hat{O}_k \hat{O}_j^{\dagger} \right] = \delta_{j,k} \,, \quad \langle \Gamma, \hat{O}_j \rangle = 0 \,,$$
 (1.165)

the constant A(N) can be obtained by calculating

$$A(N) = \langle \hat{o}_i, \Gamma \rangle$$
.

The final condition C.4 imposes a pairing of eigenstates of odd and even parity. Given an eigenstate  $|n,p\rangle$  with energy  $E_n$  and of parity p it follows

$$\begin{split} H\Gamma \left| n,p \right\rangle &= \Gamma H \left| n,p \right\rangle - \left[ H,\Gamma \right] \left| n,p \right\rangle = E_n \Gamma \left| n,p \right\rangle - \hat{R} \left| n,p \right\rangle \\ &\xrightarrow{N \to \infty} E_n \Gamma \left| n,p \right\rangle \;. \end{split} \tag{1.166}$$

Thus, in the thermodynamic limit  $N \to \infty$ , the state  $\Gamma | n, p \rangle := | n, \bar{p} \rangle$  is a valid eigenstate of opposite parity  $\bar{p} = -p$  with the same energy  $E_n$  and the spectrum of H consists of two degenerated towers.

The ideas presented in this section generalize to arbitrary finite-symmetry groups  $\mathbb{Z}_n$ . The case n=2 was chosen to reduce the complexity of the notation and also because of its connection the Majorana Zero Modes (MZMs) of Subsection 1.2.3.

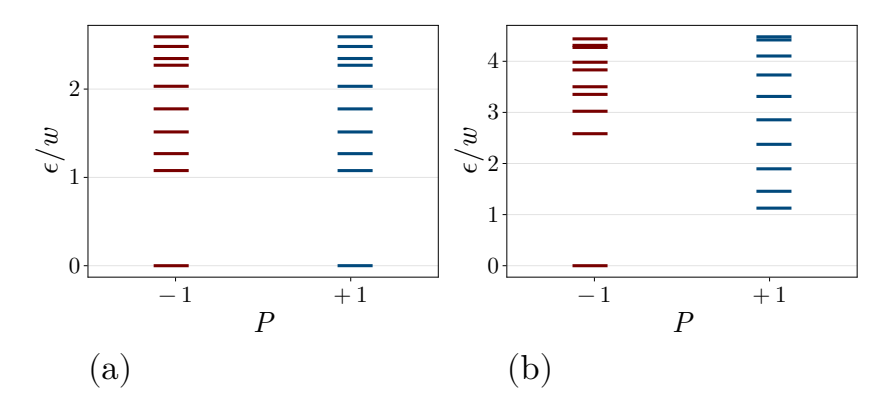


Figure 1.28: First ten excitation energies of the Kitaev chain model, Eq. (1.167), for (a) in the SPTP with  $\mu = w$ , and (b) in the trivial phase with  $\mu = 3w$ . The energies are sorted with respect to the parity P of the corresponding eigenstate, with red (blue) representing states of odd (even) parity.

Take as an example the Kitaev chain model in Eq. (1.87) with  $w=\Delta_p$ , repeated here for completeness

$$H_{\text{Kitaev}} = -w \sum_{j=1}^{N-1} \left( c_j^{\dagger} - c_j \right) \left( c_{j+1} + c_{j+1}^{\dagger} \right) - \frac{\mu}{2} \sum_{j=1}^{N} \hat{p}_j . \tag{1.167}$$

If  $|\mu| < 2w$  the chain is in an SPTP. Figure 1.28 shows the eigenstates of the Kitaev chain for a parameter point in the SPTP (panel (a)) and for a parameter in the trivial phase (panel (b)). While the trivial region has no degeneracy in the spectrum, the energies in the topological regime are degenerate for all states owing to the existence of the two edge-localized Majorana operators. Focusing on the left end of the chain and sending  $N \to \infty$ , the relevant operator is given by

$$\Gamma_a = \mathcal{N} \sum_{j=1}^{\infty} e^{-\lambda j} \gamma_{j,a} , \quad \lambda = -\log\left(\left|\frac{\mu}{w}\right|\right) , \quad \mathcal{N}^2 = e^{2\lambda} - 1 .$$
 (1.168)

which commutes with  $H_{
m Kitaev}$  and is localized to the left edge of the chain with

$$\gamma_{1,a} = \mathcal{N}\Gamma_a + (\tilde{c}_1 + \tilde{c}_1^{\dagger}). \tag{1.169}$$

The fermion operator  $\tilde{c}_j$  is a linear combination of all the gapped Bogoliubov quasiparticle states and was defined below Eq. (1.105). Since the normalization constant  $\mathcal{N}$  is finite in the thermodynamic limit,  $\Gamma_a$  is a valid SZM localized to the left edge of the chain<sup>18</sup>.

In the remainder of the section it is assumed that the SZM, if existent, is localized to the left site of the chain such that

$$\gamma_{1,a} = A\Gamma + \tilde{c}_1 + \tilde{c}_1^\dagger \tag{1.170}$$

holds, with  $\tilde{c}_1$  representing the contributions from bulk excitations, similar to the Kitaev chain example.

Note that an equal conclusion is possible for the right edge of the system by replacing  $\Gamma_a$  with  $\Gamma_b$  and  $\gamma_{1,a}$  with  $\gamma_{N,b}$ .

#### Autocorrelation function

The existence of the SZM and the induced towers of degenerate eigenstates have strong implications for the dynamics of specific operators. A useful tool in this context is the Autocorrelation Function (ACF), a physical property that, for example, appears in the study of response functions [221, 222]. The ACF of an operator  $\hat{O}$  with respect to the energy eigenstate  $|n, p\rangle$  of parity p is defined as

$$C_{n,p}(\hat{O},t)\coloneqq\langle n,p|\hat{O}\hat{O}^{\dagger}(t)|n,p\rangle \tag{1.171}$$

where  $\hat{O}(t) = e^{itH} \hat{O} e^{-itH}$  denotes the Heisenberg time evolution. In the following, it is assumed that the operator  $\hat{O}$  anti-commutes with the parity symmetry  $\hat{P}$  and that only overlaps of the type  $\langle n,p|\hat{O}|m,\bar{p}\rangle$  with  $\bar{p}=-p$  are non-zero.

Inserting a resolution of the unity  $\mathbb{1} = \sum_r \sum_{p=\pm 1} |r, p\rangle \langle r, p|$ , the equation for the ACF becomes

$$C_{n,p}(\hat{O},t) = \sum_{r} \left| \langle n, p | \hat{O} | r, \bar{p} \rangle \right|^2 e^{it(E_{n,p} - E_{r,\bar{p}})} \,. \tag{1.172}$$

For a generic operator and state  $|n,p\rangle$  a large number of matrix elements  $\langle n,p|\hat{O}|r,\bar{p}\rangle$  are non-zero, and the sum in Eq. (1.172) results in a fast exponential decay  $C_{n,p}(t)\sim e^{-t/\tau}$  with the lifetime  $\tau$  of the order of unity, owing to the incoherent addition of all these terms. The situation is different if an SZM exists, where  $\langle n,p|\Gamma|n,\bar{p}\rangle=1$  and  $E_{n,p}-E_{n,\bar{p}}=\Delta E_n\sim e^{-\lambda N}$  holds. In this case, the ACF for  $\Gamma$  evaluates to

$$\begin{split} C_{n,p}(\Gamma,t) &= \left| \langle n,p | \Gamma | n,\bar{p} \rangle \right|^2 e^{it\Delta E_n} + \sum_{n \neq r} \left| \langle n,p | \Gamma | r,\bar{p} \rangle \right|^2 e^{it(E_{n,p} - E_{r,\bar{p}})} \\ &\xrightarrow{N \to \infty} 1 + \tilde{C}_{n,p}(t) \,, \end{split} \tag{1.173}$$

where  $\tilde{C}(n,p)(t) \sim e^{-t/\tau}$  collects all  $r \neq n$  contributions that add up incoherently. It is found that the ACF saturates to one in the long-time limit, independent of the state  $|n,p\rangle$ .

The single state ACF defined in Eq. (1.171) is extended to finite temperatures by

$$C_{\beta}(\hat{O}, t) = \frac{1}{\mathcal{Z}(\beta)} \sum_{n} \sum_{p=\pm 1} e^{-\beta E_{n,p}} \mathcal{R}\left(C_{n,p}(\hat{O}, t)\right) := \langle \hat{O} | \hat{O}(t) \rangle_{\beta} . \tag{1.174}$$

Here,  $\beta = 1/T$  is the inverse temperature,  $\mathcal{R}(z)$  denotes the real part of the complex number z and  $\langle \hat{A} | \hat{B} \rangle_{\beta}$  is the finite temperature scalar product of operators [221–223]

$$\langle \hat{A} | \hat{B} \rangle_{\beta} = \frac{1}{2 \operatorname{Tr} e^{-\beta H}} \operatorname{Tr} \left[ e^{-\beta H} \left\{ \hat{A}^{\dagger}, \hat{O} \right\} \right] , \quad \left\{ \hat{A}^{\dagger}, \hat{O} \right\} \coloneqq \hat{A}^{\dagger} \hat{O} + \hat{O} \hat{A}^{\dagger} . \tag{1.175}$$

Calculating the temperature dependent ACF for the SZM follows directly from Eq. (1.173)

$$\lim_{N \to \infty} C_{\beta}(\Gamma, t) = 1 + \underbrace{\tilde{C}_{\beta}(t)}_{\sim e^{-t/\tau}} \xrightarrow{t \to \infty} 1.$$
 (1.176)

It is found that the long-time limit is independent of the temperature of the system. For finite sizes, the equation exhibits long-time oscillations induced by the exponentially small finite-size splitting between the two parity towers.

Using the relation between the SZM and the edge Majorana operator  $\gamma_{1,a}$  from Eq. (1.170) together with Eq. (1.176), the long time limit of the ACF for  $\gamma_{1,a}$  becomes

$$\lim_{N \to \infty} C_{\beta}(\gamma_{1,a}, t) = |A|^2 + \underbrace{\tilde{C}_{\beta}(t)}_{\text{out}^{-t/\tau}} \xrightarrow{t \to \infty} |A|^2, \qquad (1.177)$$

where  $\tilde{C}_{\beta}(t)$  collects all contributions from bulk excitations. Figure 1.29 shows the ACF for infinite temperature  $\beta=0$  of the edge Majorana operators  $\gamma_{1,a}$  and  $\gamma_{1,b}$  for the Kitaev chain in the topological and trivial regimes, respectively. In the topo-

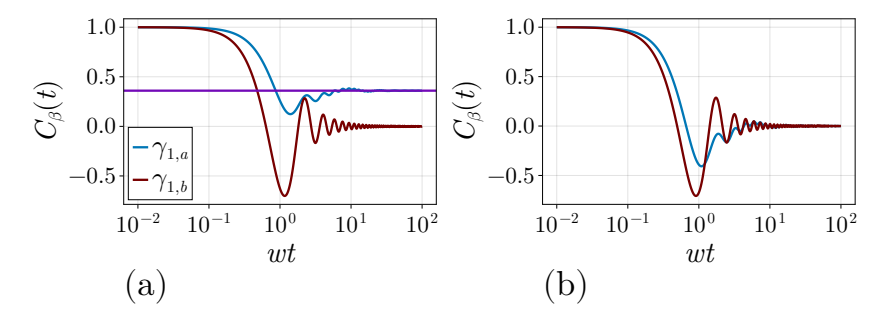


Figure 1.29: ACF at infinite temperature of the two edge Majorana operators  $\gamma_{1,a}$  and  $\gamma_{1,b}$  with  $w = \Delta_p$  for  $\mu/w = 1.6$  (topological) in panel (a) and  $\mu/w = 2.6$  (trivial) in panel (b). The purple line in panel (a) represents the theoretical limit  $\lim_{t\to\infty} C_{\beta=0}(\gamma_{1,a},t) = \mathcal{N}^2$ .

logical regime,  $\gamma_{1,a}$  receives a finite contribution from the SZM, thereby satisfying Eq. (1.170), while  $\gamma_{1,b}$  only has contributions from bulk excitations. As illustrated in Fig. 1.29(a), within this regime, the ACF of  $\gamma_{1,b}$  shows a rapid exponential decay on a timescale approximately equal to  $t_{\star} \sim w$ . Conversely, the ACF of  $\gamma_{1,a}$  stabilizes at a constant value determined by  $\mathcal{N}^2$  defined in Eq. (1.168). By contrast, in the trivial regime, Fig. 1.29(b), the ACF for either of the two Majorana operators decays exponentially at times of  $t_{\star} \sim w$ .

# 1.5.2 Away from Integrability

The existence of the SZM has only been demonstrated in integrable systems [84, 224]. In this case, the SZM can always be related to the MZMs that appear if the model is in a non-trivial SPTP. Adding small terms that break the integrability preserves the topological order, as long as no quantum phase transition is crossed. This implies a stable degeneracy of the ground-state manifold with two ground states of opposite degeneracy  $|\Omega_{e/o}\rangle$ . Consequently, the ACF still saturates in the zero temperature limit  $(\beta \to \infty)$  to a constant value for  $t \to \infty$ . To arrive at this conclusion, note that the finite temperature scalar product from Eq. (1.175) projects on the ground-state manifold for  $\beta \to \infty$ 

$$\langle \hat{A}, \hat{O} \rangle_{\beta = \infty} = \frac{\langle \Omega_e | \hat{A}^\dagger \hat{O} + \hat{O} \hat{A}^\dagger | \Omega_e \rangle + \langle \Omega_o | \hat{A}^\dagger \hat{O} + \hat{O} \hat{A}^\dagger | \Omega_o \rangle}{4} \,,$$

and the operator  $\gamma_{a,1}$  can be written as

$$\gamma_{a,1} = A\left(\left|\Omega_e\right\rangle\left\langle\Omega_o\right| + \left|\Omega_o\right\rangle\left\langle\Omega_e\right|\right) + \tilde{\gamma}_{a,1} \; , \label{eq:gamma_alpha_alpha}$$

where  $\tilde{\gamma}_{a,1}$  collects contributions from the higher excited states. Combining the two equations leads to

$$C_{\beta=\infty}(\gamma_{1,a},t)=|A|^2+\dots$$

where the ellipses denote incoherent contributions from higher-excited states.

In contrast to the integrable case, the degeneracy of the ground state does not imply the degeneracy of the higher excited states. In general, the ACF becomes zero  $C_{\beta}(\gamma_{1,a},t_{\star})\approx 0$  at a finite coherence time  $t_{\star}$ . One limit often considered in the literature is the infinite temperature limit, where the finite-temperature scalar

product in Eq. (1.175) is reduced to the Frobenius scalar product in Eq. (1.165). In this limit, it was found that the coherence time of the edge Majorana operator  $\gamma_{1,a}$  becomes finite, but still exceeds the coherence time of any bulk operator by orders of magnitude if the system is in a topologically non-trivial SPTP. It was conjectured that in this case the system has only an Almost Strong Zero Mode (ASZM)  $\Gamma$  which fulfills the conditions C.1–C.3 of the SZM but only nearly commutes with the Hamiltonian [214]

$$[\Gamma, H] = E, \quad ||E|| \sim e^{-n^*}$$

where  $n^*$  denotes a constant proportional to the integrable breaking term. This is related to the existence of an emergent U(1) symmetry, leading to long coherence times  $t_* \sim e^{n^*}$  and the ASZM is given by a local unitary rotation of  $\gamma_{1,a}$ .

# Mapping to Single Particle Dynamics

An alternative approach for understanding the behavior of an ASZM was proposed by Yates et al. [217, 218] who mapped the Heisenberg time evolution to the dynamics of a single particle on a semi-infinite chain. This mapping is based on the generation of a series of operators that are orthogonal with respect to the finite-temperature scalar product, Eq. (1.175). The series of operators is generated using the Lanczos algorithm [221] applied to the commutator  $\mathcal{L}(\hat{O}) := [H, \hat{O}]$ , which is the generator of the Heisenberg time evolution. In this basis, the commutator becomes a tri-diagonal matrix, where the non-zero elements in this matrix can be interpreted as the tunneling weights of a non-interacting artificial Hamiltonian.

Before considering the case of a system with an ASZM, consider a general one-dimensional chain described by the Hamiltonian H. The aim is to calculate the ACF of a generic operator  $\hat{O}$ . Without loss of generality, assume that the operator is Hermitian  $\hat{O}^{\dagger} = \hat{O}$  and normalized  $\langle \hat{O} | \hat{O} \rangle_{\beta} = 1$ . By setting  $\mathcal{O}_0 = \hat{O}$ ,  $\mathcal{O}_{-1} = 0$  and  $b_0 = 0$ , the Lanczos algorithm iteratively generates the new basis operators  $\mathcal{O}_n$  by the sequence

$$\begin{split} \hat{A}_n &:= \mathcal{L}\mathcal{O}_{n-1} - b_{n-1}O_{n-2} \,, \\ b_n &= \sqrt{\langle \hat{A}_n | \hat{A}_n \rangle_{\beta}} \,, \\ \mathcal{O}_n &= \hat{A}_n/b_n \,. \end{split} \tag{1.178}$$

Note that  $\mathcal{O}_n$  is an hermitian (anti-hermitian) operator if n is even (odd) and the superoperator  $\mathcal{L}$  is hermitian as a map from operators to operators

$$\langle \mathcal{L}\hat{O}|\hat{W}\rangle_{\beta} = \langle \hat{O}|\mathcal{L}\hat{W}\rangle_{\beta}$$
.

The orthogonality is readily checked by induction.

The time evolved operator  $\hat{O}(t)$  can be expanded in this orthogonal basis 19

$$\hat{O}(t) = \sum_{n=0}^{\infty} \varphi_n(t) i^n \mathcal{O}_n , \quad \varphi_j(0) = \delta_{j,0} . \tag{1.179}$$

By identifying the Lanczos operators with a single-particle basis  $i^n \mathcal{O}_n \cong |n\rangle$ , the superoperator  $\mathcal{L}$  can be written in terms of an artificial single-particle Hamiltonian

$$H_{\rm sp} = \sum_{n=0}^{\infty} i b_{n+1} |n+1\rangle \langle n| + \text{h.c.}.$$
 (1.180)

The reason to choose the factor  $i^n$  is that the combination  $i^n\mathcal{O}_n$  is a hermitian operator and  $\varphi_n(t)$  can be chosen as real valued functions.

Under this mapping, the seed operator  $\hat{O}$  becomes the boundary state  $|0\rangle$ . Thus, the ACF becomes the time-evolution of a wave-package localized at the first site of the artificial single-particle chain

$$C_{\beta}(\hat{O}, t) = \varphi_0(t) = \langle 0|e^{-itH_{\rm sp}}|0\rangle . \tag{1.181}$$

The complexity of the Heisenberg time evolution is now hidden in the exact sequence of the Lanczos coefficients  $b_n$ , which is highly dependent on the seed operator  $\hat{O}$ , the Hamiltonian H and the inverse temperature  $\beta$ .

It is useful to recast the exponential Eq. (1.181) in terms of the Edge Density of States (EDOS) defined as

$$\nu_{\beta}^{E}(\omega) = \langle 0|\delta(\omega - H_{\rm sp}|0\rangle . \tag{1.182}$$

Using the EDOS, the ACF becomes a simple integral

$$C_{\beta}(\hat{O}, t) = \int_{-\infty}^{\infty} d\omega \, \nu_{\beta}^{E}(\omega) \cos(\omega t) \,. \tag{1.183}$$

For infinite temperatures, the artificial Hamiltonian  $H_{\rm sp}$  has been extensively studied in the context of quantum chaos and scrambling [223]. There it was found that the Lanczos sequence follows a universal growth [222, 223]

$$b_n \approx A \frac{n}{\log(n)} + b_0 \tag{1.184}$$

for generic non-integrable one-dimensional systems and large n. In case of integrable systems, the growth of the Lanczos coefficients becomes sub-linear or even saturates to a constant

$$b_n \approx An^{\delta} + b_0 \,, \quad \delta < 1 \,. \tag{1.185}$$

In the artificial Hamiltonian  $H_{\rm sp}$ , the universal growth results in an exponentially fast delocalization of wave packages originally localized to the first lattice site [222]; thus, the ACF for generic operators and models decays rapidly.

#### Lanczos Series for Almost Strong Zero Modes

After discussing the general case, consider again a fermionic chain possessing an ASZM represented by  $\gamma_{1,a}$ . In particular, consider the case of infinite temperature  $(\beta=0)$ . In this limit, Yates et al. [217, 218] found that the artificial single-particle Hamiltonian calculated with respect to  $\gamma_{1,a}$  obeys a staggering of the hopping amplitudes  $b_n$ 

$$b_n \approx h_n + (-1)^n \tilde{h}_n \tag{1.186}$$

with  $h_n$  following the universal law in Eq. (1.184) for non-integrable systems and Eq. (1.185) for integrable systems [217]. The staggered component  $\tilde{h}_n$  is positive for small n, eventually decays to zero, and changes sign for some  $n^\star$ . Compared to Subsection 1.2.2, particularly Eq. (1.73), the artificial single-particle Hamiltonian represents an SSHM in a topological non-trivial SPTP of length  $n^\star$  dressed with a background increase in the tunneling amplitudes and attached to a conducting semi-infinite reservoir. However, when calculating the single-particle Hamiltonian based on the (trivial) Majorana operator  $\gamma_{1,b}$  only a trivial staggering was found, and the artificial single-particle Hamiltonian is in a trivial phase.

In contrast to a pure SSHM in the topological limit, which supports exponentially localized edge modes, the attachment to a conducting semi-infinite chain leads to a finite overlap between the left edge state and the metallic bulk states. Originally pinned to exactly zero energy, this hybridization leads to a continuum energy states that are close to zero and the EDOS from Eq. (1.182) can be written as

$$\nu_{\beta=0}^{E} = A \frac{\gamma/\pi}{\omega^2 + \gamma^2} + (1 - A)\tilde{\nu}(\omega), \qquad (1.187)$$

where  $\tilde{\nu}(\omega)$  denotes an incoherent background. This behavior is demonstrated in Fig. 1.30 in the simple case of attaching an SSHM of length  $n^*$  to a homogeneous semi-infinite chain described by

$$H = \sum_{j=1}^{n^{\star}-1} -va_{j}^{\dagger}b_{j} - wb_{j}^{\dagger}a_{j+1} + \text{h.c.} - va_{n^{\star}}^{\dagger}b_{n^{\star}} - vb_{n^{\star}}^{\dagger}a_{n^{\star}}$$

$$- ub_{n^{\star}}^{\dagger}c_{n^{\star}+1} - uc_{n^{\star}+1}^{\dagger}b_{n^{\star}} - u\sum_{j=n^{\star}+1}^{\infty} c_{j}^{\dagger}c_{j+1} + \text{h.c.}.$$
(1.188)

Based on this general consideration, it is found that the ACF of  $\gamma_{1,a}$  decays exponentially, where the lifetime  $\tau$  is defined by the width parameter  $\gamma$  of the Lorentzian peak in the EDOS

$$C_{\beta=0}(\gamma_{1,a},t) \sim Ae^{-t/\tau}, \quad \tau = 1/\gamma.$$

In this picture, the limit of an SZM is understood as  $\gamma \to 0$  and the EDOS becomes  $\nu_{\beta=0}^E(\omega) \sim A\delta(\omega)$ .

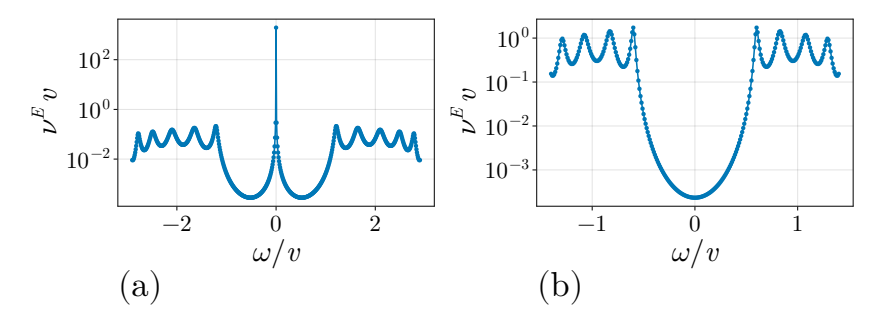


Figure 1.30: Edge density of states, Eq. (1.182), evaluated for an SSHM of  $n^* = 6$  unit cells attached to a homogeneous lead. In panel (a), w = 2v places the SSHM in a non-trivial SPTP with zero-energy states. The coupling to the lead with u = 1.5v results in a sharp peak around zero energy. In panel (b), w = 0.5v with the SSHM being trivial, without any zero-energy states. As a consequence, the coupling to the lead with u = 0.75v has no special features around zero energy.

Consider as an example the KHM as defined in Eq.(1.110), with  $w=\Delta_p$  given by

$$H_{\rm KH} = \sum_{j=1}^{N-1} -w \left( c_j^\dagger - c_j^{} \right) \left( c_{j+1}^{} + c_{j+1}^\dagger \right) + U \hat{p}_j \hat{p}_{j+1}^{} - \frac{\mu}{2} \sum_{j=1}^{N} \hat{p}_j^{} \,. \tag{1.189} \label{eq:KH}$$

Figure 1.31(a) shows the Lanczos series of the KHM for U = 0.3w,  $\mu = 0.2w$ , and varying system sizes. After an early increase that is almost linear, and thus compatible with the universal law in Eq. (1.184), the coefficients  $b_n$  saturate to a plateau value that is linearly dependent on the system size. This behavior is generally expected for a non-integrable Hamiltonian [223]. In addition to this overall shape, the series shows a clear staggering, as shown in Eq. (1.186) for small values of n; see also

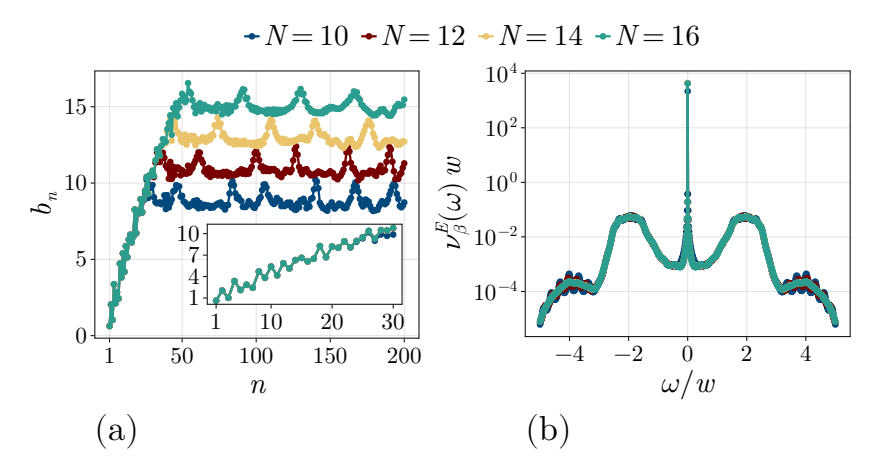


Figure 1.31: (a) Lanczos series of the KHM from Eq. (1.189) for U/w = 0.3,  $\mu/w = 0.2$  and varying the system size from N = 10 to N = 16. The inset plot shows a zoom of the first third values of the series. (b) Calculated EDOS from the different Lanczos series in panel (a).

the inset of Fig. 1.31(a). This staggering resembles the situation expected for the existence of an ASZM discussed above for the finite SSHM in the topological regime, attached to a semi-infinite conducting chain. In the EDOS associated with the different Lanczos series shown in Fig. 1.31(a), this staggering leads to the emergence of a sharp Lorentzian peak around zero energy that is dressed with a non-universal incoherent background, see Eq. (1.187). While the background has a strong dependence on the system size, the central Lorentzian peak converges for  $N \geq 12$ , as shown in Fig. 1.31(b).

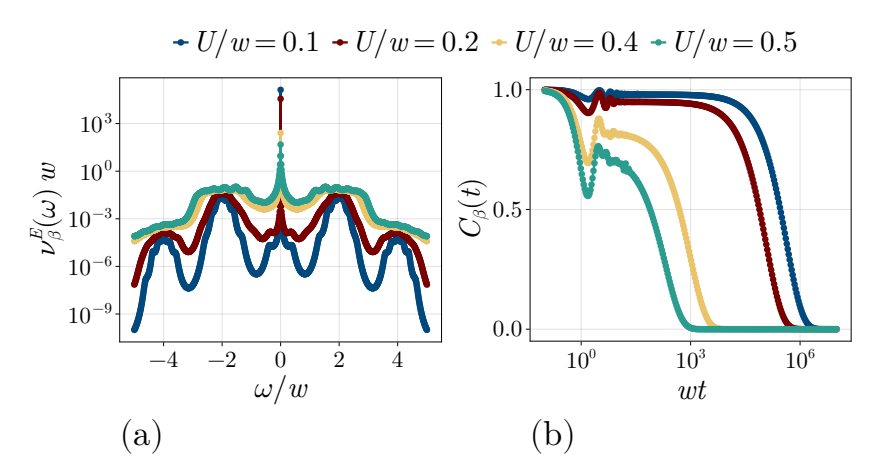


Figure 1.32: (a) EDOS calculated from the Lanczos series of the KHM, Eq. (1.189), for various values of the interaction U at a fixed chemical potential  $\mu/w = 0.2$  and size N = 16. (b) ACF Reconstructed from the EDOS in panel (a).

Figure 1.32(a) shows different EDOS obtained from the KHM at a fixed system size N=16 and chemical potential  $\mu=0.2w$ , but varying the interaction U. All values shown here are in the SPTP. Correspondingly, for every value of U the EDOS has a sharp Lorentzian peak, see Eq. (1.187), around zero energy, and thus, an emergent ASZM. The width of the Lorentzian peak increases with increasing interaction strength. This increase leads to a faster decay of the ACF, and thus a shorter lifetime of the ASZM. Figure 1.32(b) shows the ACF reconstructed from the EDOS

following Eq. (1.183). After an initial transient decay at time scales of  $t \sim w$ , which is completely determined by the incoherent part of the EDOS, the ACF saturates to an intermediate plateau value before decaying to zero at a time scale  $t_{\star} \sim 1/\gamma$ .

Finally, note that the Lanczos series  $b_n$  requires calculations with matrices of size  $2^{2L}$ , except for models that are quadratic in the fermionic operators. At infinite temperature, the scalar product in Eq. (1.175) can be reduced to the Frobenius scalar product in Eq. (1.165), and the calculation of the Lanczos series requires only the computation of commutators and traces. For generic temperatures, it is further necessary to calculate the full diagonalization of the Hamiltonian to gain access to the density matrix  $\rho(\beta) = \exp(-\beta H)/\operatorname{Tr}(\exp(-\beta H))$ . Because this is extremely expensive, previous studies have focused on the infinite-temperature case.

In Chapter IV, the concepts presented in this section are combined with a tensor network ansatz to extend the previously obtained results to finite temperatures. The temperature-dependent coherence time aids in understanding how the ASZM connects to the zero-temperature limit [37].

# Tensor Networks

The many-body Hilbert space  $\mathcal{H}$  of the quantum chain, as defined in the previous chapter, has a total dimension that grows exponentially with the system size N. This renders a direct calculation of the ground state of a generic many-body Hamiltonian for larger systems impossible, except for special integrable cases [57, 225]. On the other hand, as explained in Section 1.4, the ground state of a typical Hamiltonian has only very limited correlation between any two parts of the system. This is reflected in the boundary law of entanglement in Eq. (1.160), which states that the entanglement of a bipartition must saturate to a constant for the ground state of a gapped Hamiltonian. Compared to generic states, which have maximal possible entanglement, the class of states fulfilling the boundary law is a tiny corner in the full many-body Hilbert space.

In this perspective, tensor networks [61, 118] are a class of variational ansatz states that directly target this tiny corner of the boundary law entangled quantum states. By limiting the range of correlations of any bipartition, the tensor network reduces the exponential number of free parameters to a number that is linear in the system size at a fixed bond dimension, which controls the expressive power of the tensor network.

Furthermore, the special structure of the tensor networks allows the formulation of efficient contraction algorithms for calculating observables. This is required to formulate variational optimization and obtain a faithful approximation of the true quantum ground state [60–62]. Shortly after the formulation of tensor-network ansatz states for gapped one-dimensional systems, the idea was extended to ground states of gapless one-dimensional chains [226, 227], two-dimensional lattice systems [228, 229], dynamics [63, 230–232] and many more. Recently, the idea of using correlations between subsystems as an approximation resource was extended to fields outside of quantum mechanics, with applications of tensor networks to non-linear partial differential equations [233, 234] or even in financial marketing [235, 236]. However, tensor networks not only serve as a numerical tool but also provide analytical insights into the structure of highly correlated quantum states, allowing for the classification of quantum matter in low dimensions [52–54, 118].

The topic of this chapter is to give a brief introduction to tensor networks as a tool to solve numerical problems for one-dimensional quantum states, and is organized as follows: The first Section 2.1 discusses the construction of tensor network states, and in particular, the Matrix Product States (MPSs), for quantum systems in one

dimension, together with some important properties. In the second Section 2.2, the general correlation and entanglement structure of MPSs are discussed. This is followed by a short discussion of the Density-Matrix Renormalization Group (DMRG) algorithm in Section 2.3, which minimizes the energy of a finite-size Hamiltonian in the class of MPS to obtain approximations of the ground state. Finally, Section 2.4 concludes with a discussion on alternative tensor networks.

# 2.1 Tensor Network Description of Spin Chains

A tensor generalizes the concepts of scalars and vectors to higher dimensions. On a practical level, a tensor can be considered as a collection of complex numbers ordered in a multi-dimensional array  $C_{i_1,\dots,i_n}$ , where each index  $i_l$  runs from 1 to  $d_l$ . The number n of indices  $i_l$  denotes the rank of the tensor C, and the total number of elements is  $D = \prod_{l=1}^n d_l$ . For example, a scalar is a zero-rank tensor, a vector is a rank-1 tensor, and a matrix is a rank-2 tensor.

In the context of the quantum spin chains discussed in the previous Chapter 1, such a tensor appears as the coefficients  $\Psi_{s_1,\ldots,s_N}$  of a generic quantum state

$$|\psi\rangle = \sum_{s_1,\dots,s_N} \Psi_{s_1,\dots,s_N} \left| s_1,\dots,s_N \right\rangle \,. \tag{2.1}$$

This quantum tensor is of rank N, the length of the chain, and has a total dimension of  $d^N$  where d is the dimension of the local Hilbert space.

A common way to represent tensors and contractions among them is in the form of a graphical representation, as introduced by R. Penrose already in 1971 [237]. In this representation, a tensor is denoted by a 2d geometric object (square, triangle, or circle), and each index  $i_l$  is an open leg attached to this object. The contraction of two tensors over a shared index is denoted by joining the two open links that represent this index. For example, a simple matrix-matrix multiplication becomes

$$C_{jk} = \sum_{\alpha} A_{j\alpha} B_{\alpha k} = \stackrel{j}{-} A \stackrel{\alpha}{-} B \stackrel{k}{-} k . \tag{2.2}$$

While the notation may not be useful for simple matrix algebra, it becomes useful, especially when handling and manipulating larger networks of tensors. A more complicated example is the contraction of three tensors, each of rank-3, into a new tensor

$$D_{jkl} = \sum_{\alpha,\beta,\gamma} A_{j,\beta,\alpha} B_{\alpha,\gamma,k} C_{\beta,l,\gamma} = \begin{matrix} j & \alpha & B \\ \beta & \gamma \end{matrix} . \tag{2.3}$$

Here, the convention is used to label tensors counter-clockwise. When the summation index is clear from the context, it will be omitted in the following.

In addition to the process of contracting a network of tensors into a single tensor, the inverse operation of decomposing a tensor into a network of tensors is equally important. By fusing the individual indices of a tensor into two super-indices, such a decomposition can be inferred from standard matrix decompositions. For example, consider the Schmidt decomposition discussed in Subsection 2.2.1. At the level of

the quantum tensor, the Schmidt decomposition is an Singular-Value Decomposition (SVD) of the form

$$\Psi_{s_1,\dots,s_N} = \Psi_{(s_1,\dots,s_j),(s_{j+1},\dots s_N)} = \sum_{\alpha=1}^{\alpha_{\text{max}}} U_{(s_1,\dots,s_j),\alpha} \sigma_{\alpha} \bar{V}_{(s_{j+1},\dots,s_N),\alpha}$$
(2.4)

with the two isometries U and V, and where the singular values are real positive definite numbers  $\sigma_{\alpha} > 0$ . In this case, the isometry condition means that  $U^{\dagger}U = \mathbb{1}$ , but  $UU^{\dagger}$  is not necessarily the identity, but rather a projection operator on a sub-Hilbert space; see also Appendix A for more details about the SVD. In the graphical notation, this decomposition is written as

$$\begin{array}{c|c} \Psi \\ \hline \downarrow \\ s_1 \end{array} = \begin{array}{c|c} U \\ \hline \downarrow \\ s_1 \end{array} . (2.5)$$

The isometries are denoted by triangles, and the isometric property reads in the graphical notation

$$= \left( \begin{array}{c} \\ \\ \end{array} \right), \qquad (2.6)$$

where, by convention, the tensors in the lower row are complex conjugated, and the identity is represented as a simple line 1 := 1.

Given the high-dimensional quantum tensor  $\Psi$ , a tensor network is a low-rank approximation of this tensor, achieved by representing  $\Psi$  as a contraction network of lower-rank tensors  $M_j$ . The simplest example is a truncation of the Schmidt decomposition by restricting the sum in Eq. (2.4) to only include the  $\alpha'_{\text{max}} < \alpha_{\text{max}}$  largest Schmidt values

$$\Psi_{s_1,\dots,s_N} \approx \tilde{\Psi}_{s_1,\dots,s_N} = \sum_{s=1}^{\alpha'_{\max}} U_{(s_1,\dots,s_j),\alpha} \sigma_{\alpha} \bar{V}_{(s_{j+1},\dots,s_N),\alpha} \,.$$

Compared to the original  $d^N$  numbers required to store  $\Psi$ , the truncated tensor  $\tilde{\Psi}$  requires only  $(d^j + d^{N-j} + 1)\alpha'_{\text{max}}$  numbers to be stored, and the error of this approximation is given by the infidelity

$$\epsilon = 1 - \langle \psi | \tilde{\psi} \rangle = 1 - \sum_{\alpha = \alpha'_{\text{max}} + 1}^{\alpha_{\text{max}}} \sigma_{\alpha}^{2}.$$
 (2.7)

For generic states, the Schmidt values have a flat distribution [185–188], and this truncation requires  $\alpha'_{\rm max}$  to be of the order of the original  $\alpha_{\rm max}$  to have a small truncation error, and a significant compression is not possible. However, as discussed in Section 1.4, the ground states of a typical Hamiltonian have an exponential decay of the Schmidt values with respect to any bipartition of the system, and the truncation is expected to yield a good approximation, even if  $\alpha'_{\rm max} \ll \alpha_{\rm max}$ .

Furthermore, by iteratively performing this truncation for each bipartition of the ground state and storing the truncated isometries, as shown in Fig. 2.1, the exponentially large quantum tensor  $\Psi$  is decomposed into smaller rank-3 tensors, each

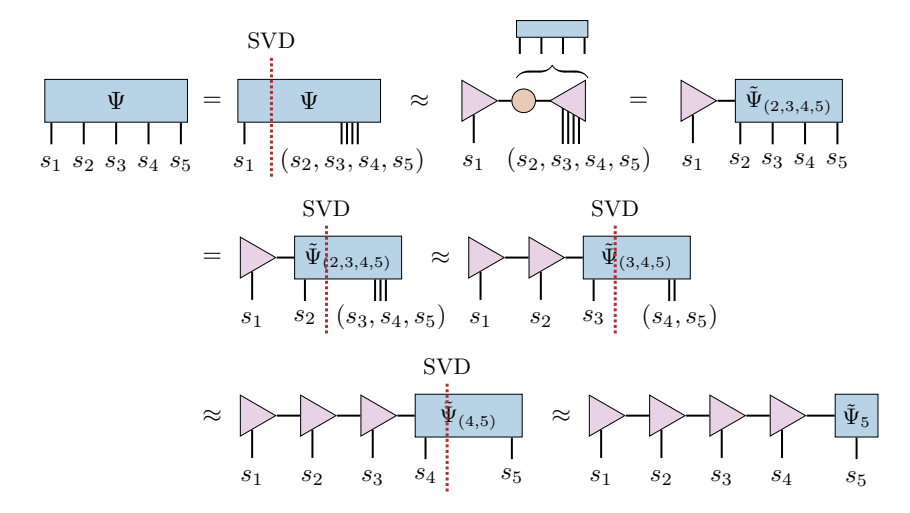


Figure 2.1: Decomposition of a rank-5 quantum tensor  $\Psi_{s_1,s_2,s_3,s_4,s_5}$  into an MPS. After performing the SVD on a given bipartition, the singular values are then truncated.

containing at most  $d(\alpha'_{\text{max}})^2$  elements. The exponential decay of the Schmidt values ensures that this low-rank approximation closely approximates the original full-rank tensor  $\Psi$  in terms of the infidelity defined in Eq. (2.7), thereby enabling an efficient compression to merely  $\mathcal{O}(N)$  parameters. Instead of compressing a known ground state, this exponential reduction of parameters motivates the use of such a tensor network of rank-3 tensors as a variational ansatz for the ground states. The properties of this class of tensor network states are the topic of the remainder of this section.

# 2.1.1 Matrix Product State of Finite Systems

Matrix Product States (MPSs) are a class of variational many-body states where the quantum tensor  $\Psi$  is represented as a contraction over rank-3 tensors<sup>1</sup>

$$|\psi(\{M^k\})\rangle \cong \boxed{\Psi(\{M^j\})} = \boxed{M^1} \qquad \boxed{M^2} \qquad \cdots \qquad \boxed{M^N} . \tag{2.8}$$

The  $\cong$  sign means that the right-hand side is only the numerical tensor that must be contracted with the local basis  $|s_1,\ldots,s_N\rangle$  to give a proper quantum state. By fixing the physical index  $s_j=s\in\{1,\ldots,d\}$ , the set of matrices  $M^{j,s}$  has dimension  $\chi_{j-1}\times\chi_j$  with the convention  $\chi_0=\chi_N=1$ . The quantity  $\chi=\max_j(\chi_j)$  is called the bond dimension of the MPS, and the total number of parameters is of the order  $\mathcal{O}(N\chi^2)$ .

The MPS not only achieves a reduction in the parameters but also allows for an efficient evaluation of expectation values. By performing the contraction of the network in the correct order, as shown in Fig. 2.2, expectation values of local observables  $\langle \psi(\{M^j\})|\hat{o}_k|\psi(\{M^j\})\rangle$  have a complexity of  $\mathcal{O}(N\chi^3d)$ .

<sup>&</sup>lt;sup>1</sup>The boundaries are of rank-2, but by attaching a dummy one-dimensional index to them, they also become tensors of rank-3.

Figure 2.2: Contraction representing the norm of an MPS. (a) Contracting the network starting from the left and alternatively absorbing a tensor from the upper and lower layers. This contraction sequence leads to a boundary tensor of maximal  $\chi^2$  elements and the complexity is  $\mathcal{O}(N\chi^3 d)$ . (b) First contracting all tensors in the upper and lower layer individually leads to two rank-N tensors with  $d^N$  elements and the complexity is  $\mathcal{O}(d^N)$ .

## Gauge Freedom of Matrix Product States

Given a set of rank-3 tensors  $M^j$ , the many-body state they represent as an MPS is not unique. In fact, performing the transformation

$$B^{j,s} = X_{j-1}^{-1} M^{j,s} X_j, \quad X^j \in GL_{\mathbb{C}}(\chi_j)$$
 (2.9)

for a set of invertible matrices  $X_j$ , the tensors  $B^j$  generate the same MPS. Here,  $\mathrm{GL}_{\mathbb{C}}(\chi_j)$  denotes the set of all invertible  $\chi_j \times \chi_j$  complex matrices. This transformation is illustrated in Fig. 2.3.

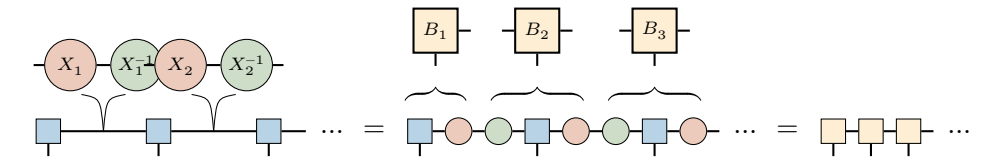


Figure 2.3: Gauge freedom of an MPS. Originally, the MPS is given by the  $M^j$  tensors, which are represented by the blue squares. By inserting a resolution of the identity  $\mathbbm{1} = X_j X_j^{-1}$  at every link, the MPS is given by the  $B^j = X_{j-1}^{-1} M^j X_j$  tensors, which are represented by orange squares.

Consequentially, not all parameters of the MPS are independent, and the dimension of the MPS manifold, denoted as  $\mathcal{MPS}(N, \{\chi_i\}, d)$ , is

$$\dim\left(\mathcal{MPS}(N,\{\chi_j\},d)\right) = d\sum_{n=1}^N \chi_{n-1}\chi_n - \sum_{n=1}^{N-1} \chi_n^2\,.$$

# Canonical Gauge

The existence of the gauge freedom allows to choose a representation of the MPS that is of particular use in practical calculations: the mixed canonical gauge [61, 62, 238]. In this gauge, the MPS is written as a set of left/right isometric tensors with an orthogonality center at position j

The left (right) isometries are represented by left (right) pointing red shaded triangles, a convention used for the rest of this thesis, and fulfill the condition

$$= \left( \begin{array}{c} \\ \\ \end{array} \right) = \left( \begin{array}{c} \\ \\ \end{array} \right) . \tag{2.11}$$

The canonical gauge can be obtained from a general representation given by a set of rank-3 tensors  $M^j$  by iteratively performing a QR decomposition. Starting from the left (right), the tensors  $M^j$  are decomposed into an isometry and a residual tensor by fusing the left (right) index with the physical leg. The left (right) isometry replaces the tensor at position j, and the residual tensor is absorbed in the next tensor to the left (right) of site j. The entire procedure is illustrated in Fig. 2.4. This procedure

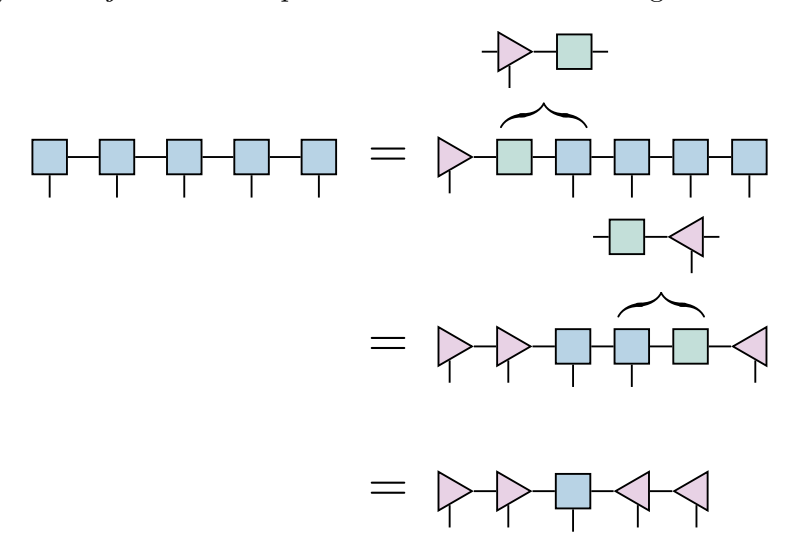


Figure 2.4: Gauging of a general MPS. Starting from the left, the first tensor  $M^1 = Q^1R$  is decomposed in a left isometry  $Q^1$ , which carries the physical index  $s_1$ , and a residual tensor R. The residual tensor is contracted with the next MPS tensor  $M^2$ , and the result is decomposed again in a left isometry  $Q^2$  which carries the left link and physical link, and a residual link tensor R. This procedure is repeated until the target site j. By performing the same steps from the right, the final MPS is in the mixed canonical form.

can also be used to shift the orthogonality center from position j to position k by subsequently performing a QR decomposition of the current orthogonality center in the direction of the new target position, keeping the isometry, and absorbing the residual tensor with the next tensor in line.

Representing an MPS in the mixed canonical form allows for fast evaluation of local observables. Taking the example of a local operator  $\hat{o}_j$ , by moving the orthogonality center to position j, the expectation value is given by

$$\langle \psi | \hat{o}_j | \psi \rangle =$$

$$(2.12)$$

owing to the isometric properties of the triangles left and right of the orthogonality center. In particular, by setting  $\hat{o} = 1$ , the norm of an MPS is simply given by the

Frobenius norm of the orthogonality center  $M^{j}$ 

$$\langle \psi | \psi \rangle = \sum_{s=1}^{d} \operatorname{Tr} \left[ \left( M^{j,s} \right)^{\dagger} M^{j,s} \right].$$

#### Reduced Density Matrix

The left and right isometries in Eq. (2.10) can be interpreted as a transformation of the basis from the physical indices to the virtual space. Therefore, the mixed canonical form can be interpreted as a tri-partition

$$|\psi\rangle = \sum_{\alpha_1,\alpha_2,s_j} \left(M^j\right)_{\alpha_1,\alpha_2}^{s_j} |\varphi_{\alpha_1}^L\rangle \otimes |s_j\rangle \otimes |\varphi_{\alpha_2}^R\rangle \ ,$$

where the two set of states  $|\varphi_{\alpha}^{L(R)}\rangle$ 

$$|\varphi_{\alpha}^{L}\rangle\cong \longrightarrow \cdots \longrightarrow \alpha , \quad |\varphi_{\alpha}^{R}\rangle\cong \alpha \longrightarrow \cdots \longrightarrow s_{j+1} \qquad (2.13)$$

are defined on the lattice sites to the left (right) of site j and are orthonormal by the properties of the isometries.

This partition allows for an efficient calculation of the reduced right density matrix, introduced in Subsection 1.4.1, at the cut (j, j + 1)

$$\rho_{R} = \sum_{\alpha,\beta} \sum_{\rho,s_{j}} (M^{j})_{\rho,\alpha}^{s_{j}} (\bar{M}^{j})_{\rho,\beta}^{s_{j}} |\varphi_{\alpha}^{R}\rangle \langle \varphi_{\beta}^{R}| \cong \begin{pmatrix} M^{j} \\ \bar{M}^{j} \end{pmatrix} . \tag{2.14}$$

Consequently, the entanglement spectrum and entanglement entropy can be efficiently calculated for an MPS by performing an eigenvalue decomposition of the  $\chi \times \chi$  Hermitian matrix  $\rho_R$  obtained solely from the orthogonality center.

#### 2.1.2 Matrix Product Operator

The construction of the MPS is based on a low-rank approximation of the quantum tensor  $\Psi$  which appears in the expansion of a general quantum state  $|\psi\rangle$  in the local basis 2.1. Similar to the expansion of a general quantum state, a general many-body quantum operator  $\hat{O}$  can be expanded as a weighted sum in an operator basis, as discussed in Subsection 1.1.2

$$\hat{O} = \sum_{\alpha_1, \dots, \alpha_N} O_{\alpha_1, \dots, \alpha_N} \sigma^{\alpha_1} \otimes \sigma^{\alpha_2} \otimes \dots \otimes \sigma^{\alpha_N}. \tag{2.15}$$

The operators  $\sigma^{\alpha}$  are Hermitian and orthonormal with respect to the Frobenius scalar product  $\text{Tr}[\sigma^{\alpha}\sigma^{\beta}] = d\delta_{\alpha,\beta}$ , and the index  $\alpha$  runs from  $1,\ldots,d^2$ . In this formulation, the operator  $\hat{O}$  can be interpreted as a many-body quantum state  $|O\rangle$  with local Hilbert space dimension  $d^2$  and the local basis<sup>2</sup>  $|\alpha\rangle$ 

$$\hat{O} = \sum_{\alpha_1, \dots \alpha_N} O_{\alpha_1, \dots, \alpha_N} \sigma^{\alpha_1} \otimes |\alpha_1, \dots, \alpha_N\rangle \ .$$

<sup>&</sup>lt;sup>2</sup> Interpreting operators as states within a Hilbert space is also referred to as the *Third Quantization* [239]. Operators that act on other operators are called super-operators. The commutator  $\mathcal{L}_A |B\rangle = |[A,B]\rangle$  is an example of such a super-operator.

This allows to express the expansion tensor  $O_{\alpha_1,\dots,\alpha_N}$  directly as an MPS with N legs

A more common way to represent the operator is in the form of a Matrix Product Operator (MPO). For this, the local basis is written explicitly as a map on the local Hilbert space

$$\sigma^{\alpha} = \sum_{s,s'} \left(\sigma^{\alpha}\right)_{s,s'} \left|s\right\rangle \left\langle s'\right| \cong \int_{s-s'}^{\alpha}$$

and the weights  $(\sigma^{\alpha})_{s,s'}$  are absorbed into the MPS tensors  $M^j$  defining the new rank-4 tensors

$$-\frac{W^{j}}{s} - = (W^{j})_{s,s'} = \sum_{\alpha} M_{\alpha}^{j} \left(\sigma^{\alpha}\right)_{s,s'} = -\frac{M^{j}}{s} - \frac{M^{j}}{s} -$$

The full MPO form of the many-body operator is given by

$$\hat{O} \cong W^{1} - W^{2} - \cdots - W^{N}$$

$$s_{1} \quad s_{2} \quad s_{N}$$

$$(2.16)$$

In this form, the application of an MPO to an MPS is a simple tensor network

which defines the new MPS tensors  $\tilde{M}^j$ . If the bond dimensions of the MPS and MPO are denoted as  $\chi_{\psi}$  and  $\chi_O$ , respectively, the bond dimension of the resultant MPS is generally given by  $\chi = \chi_{\psi}\chi_O$ . To maintain the bond dimension of the resulting MPS at  $\chi_{\psi}$ , the MPS–MPO product must be truncated [62]. In Chapter I, this MPO-MPS product, together with a truncation based on the reduced density matrix [240] is employed to generate the Lanczos series of the commutator algebra for the almost strong zero modes, as described in Section 1.5.

# Matrix Product Operator of a Local Hamiltonian

As discussed in Section 1.1, a typical Hamiltonian H has only interactions that are of finite range. Moreover, the number of independent interactions in the Hamiltonian is small, and the MPO representation of H has a small bond dimension. A general strategy for building an MPO representation of a Hamiltonian is in terms of a finite state machine [241–243], which is briefly reviewed in Appendix E.

Taking the Transverse Field Ising Model (TFIM) from Eq (1.51) as an example

$$H_{\mathrm{Ising}} = -J \sum_{j=1}^{N-1} \sigma_j^x \sigma_{j+1}^x - g \sum_{j=1}^N \sigma_j^z \,. \label{eq:HIsing}$$

The MPO representation is given by

$$W^{j} = \begin{pmatrix} \mathbb{1} & -J\sigma^{x} & -g\sigma^{z} \\ 0 & 0 & \sigma^{x} \\ 0 & 0 & \mathbb{1} \end{pmatrix}, \quad W^{1} = \begin{pmatrix} \mathbb{1} & -J\sigma^{x} & -g\sigma^{z} \end{pmatrix}, \quad W^{N} = \begin{pmatrix} -g\sigma^{z} \\ \sigma^{x} \\ \mathbb{1} \end{pmatrix}. \tag{2.18}$$

The action in the vertical direction of the MPO is defined by the operators appearing in the matrix  $W^{j}$ .

Similar to the MPS, every MPO has a gauge degree of freedom, as defined in Eq. (2.9). This gauge freedom can be used to transform every MPO into an upper-triangular structure, as in Eq. (2.18), called the canonical form of the MPO [244].

# 2.1.3 Uniform Matrix Product States

The previous subsections focused mainly on the case of finite-size systems. To study the pure bulk properties of a system, it is useful to formulate the MPS ansatz directly in the thermodynamic limit. In the case of a translation invariant state  $|\psi\rangle$ , a reasonable ansatz is to repeat the same rank-3 tensor M infinitely many times

$$|\psi(M)\rangle\cong \cdots \qquad \boxed{M} \boxed{M} \boxed{M} \boxed{M} \cdots \quad , \qquad (2.19)$$
 
$$s_{j-2} \quad s_{j-1} \quad s_{j} \quad s_{j+1} \quad s_{j+2}$$

called a Uniform Matrix Product State (uMPS) [63, 232, 245, 246].

Similar to the finite case, a uMPS possess a gauge degree of freedom

$$B^s = XM^sX^{-1},$$

which can be exploited to obtain a canonical form of the uMPS

$$|\psi(A_L,A_C,A_R)\rangle\cong \cdots - A_L - A_L - A_C - A_R - A_R - \cdots , \quad (2.20)$$

which defines the quantum state  $|\psi(A_L,A_C,A_R)\rangle$  in terms of three matrices; the left isometry  $A_L$ , the right isometry  $A_R$  and the orthogonality center  $A_C$ . Translation invariance is ensured by imposing the pull-through equations

$$A_L - A_C = A_C - A_R - . (2.21)$$

## Transfermatrix

The most important object in the context of uMPS is the transfer matrix  $\mathcal{T}_L$  defined as

In fact, all properties of the uMPS can be derived from the transfer matrix. The transfer matrix can be interpreted as a map from the left to the right indices. As such, the eigenvalue decomposition of  $\mathcal{T}_L$  is given as

$$\mathcal{T}_{L} = \sum_{n \geq 0} \lambda_{n} \left| R_{n} \right\rangle \left\langle L_{n} \right| = R - \lambda - L \qquad (2.23)$$

where the left and right eigenvectors  $|L_n\rangle$  and  $|R_n\rangle$  form a biorthogonal basis  $\langle L_n|R_m\rangle=\delta_{n,m}$ . In the graphical representation, the left and right eigenvectors are represented by a rank-3 tensor, and the eigenvalues are collected in the diagonal matrix  $\lambda$ .

For a generic uMPS, there exists exactly one eigenstate  $\lambda_0 = 1$  and  $|\lambda_n| < 1$  for all the remaining eigenvalues [118, 238]. The left eigenvector  $|L_0\rangle$  is the identity acting on the left indices, and the right eigenvector  $|R_0\rangle$  is the reduced density matrix  $\rho_L$  of the left semi-infinite system acting on the right indices. The remaining eigenvalues define the correlation structure of the uMPS, see Subsection 2.2.2 for more details, and are related to the spectrum of local excitations [247].

There is an exception to the uniqueness of the largest eigenvalue of the transfer matrix. If the uMPS can be written as the sum of individual uMPS

$$|\psi\rangle = \sum_{n} \mu_n |\varphi_n\rangle ,$$

the transfer matrix becomes block diagonal, and multiple eigenvalues with  $|\lambda_n|=1$  can emerge. This situation appears, for example, if the states  $|\varphi_n\rangle$  spontaneously break a symmetry, while  $|\psi\rangle$  is a symmetry-restoring state, as discussed in Subsection 1.2.1. For illustration, consider the translation invariant state given by

$$|\psi\rangle = \frac{1}{\sqrt{2}} \left( |\cdots\uparrow\downarrow\uparrow\downarrow\ldots\rangle + |\cdots\downarrow\uparrow\downarrow\uparrow\ldots\rangle \right)$$

which is an equal linear combination of the two product states  $|\varphi_{1(2)}\rangle$  with an alternating order of spin-1/2 in the up and down states. The two states are not translation invariant, and the state  $|\varphi_2\rangle$  can be obtained from  $|\varphi_1\rangle$  and vice versa by shifting each lattice site by one unit. Because  $|\psi\rangle$  is translationally invariant, it can be represented by a uMPS with bond dimension  $\chi=2$ , and the transfer matrix is given by

$$\mathcal{T}_L = \begin{pmatrix} 0 & 0 & 0 & 1 \\ 0 & 0 & 0 & 0 \\ 0 & 0 & 0 & 0 \\ 1 & 0 & 0 & 0 \end{pmatrix} \,.$$

This transfer matrix has eigenvalues  $\lambda_n = \{1, -1, 0, 0\}$ , and thus, there exist two eigenvalues of magnitude one.

The definition of the uMPS can be naturally extended to allow for larger unit cells and translation invariance over the unit cell. In the previous example, the states  $|\varphi_n\rangle$  are translation invariant over two sites. In this case, it is natural to define a uMPS with a two-sited unit cell defined by  $\{A_L^j, A_C^j, A_R^j\}$  for j=1,2. The total transfer matrix of the state  $|\varphi_n\rangle$  over a full unit cell is now a simple scalar,  $\mathcal{T}_L=1$ .

The transfer matrix can also be defined for the right isometries  $A_R$ , with properties similar to those of  $\mathcal{T}_L$ . However, in this case, the left eigenvector with the largest eigenvalue is the reduced density matrix of the semi-infinite right half of the system, and the right eigenvector is the identity. The transfer matrix can also be extended to include an additional operator insertion,  $\hat{o}$ , on the physical leg

$$\mathcal{T}_L^O = := \sum_{s,s'=1}^d (\hat{o})_{s',s} A_L^{s'} \otimes \bar{A}_L^s = \begin{array}{c} & & \\ & \hat{o} & \\ & & \end{array}$$
 (2.24)

which appears, for example, in the calculation of correlation functions as boundary operators or for string operators in general.

# Fidelity per Site

The existence of the gauge freedom in the uMPS raises the interesting question of how one can decide whether two sets of tensors generate the same uMPS. In fact, the fundamental theorem of translational invariant matrix product states that two uMPS are the same if and only if their tensors are related by a general gauge transformation [238]. Consider two uMPS generated by  $\{A_L, A_C, A_R\}$  and  $\{B_L, B_C, B_R\}$ , the fundamental theorem implies that their mixed transfer matrix

$$\tilde{\mathcal{T}}_L = \sum_{s=1}^d A_L^s \otimes \bar{B}_L^s \tag{2.25}$$

has the same spectral properties as  $\mathcal{T}_L$ , which is the transfer matrix defined only with  $A_L$ . In particular, if the two uMPS are the same, the mixed transfer matrix  $\tilde{\mathcal{T}}_L$  has exactly one eigenvalue of size one, and all others have a magnitude smaller than one

On the other hand, if the two uMPS are not the same, the largest eigenvalue will be strictly less than one  $|\lambda_0| < 1$ . This motivates the definition of the log-fidelity density<sup>3</sup>

$$\mathcal{F} = -\log(|\lambda_0|). \tag{2.26}$$

It was shown, that this quantity has a universal behavior for states close to a quantum phase transition [248, 249], and is used in Chapter II to determine the phase transition in the phase diagram of the Tricritical Ising (TCI) model.

Note that the same conclusions also hold when  $(A_L, B_L)$  is replaced with  $(A_R, B_R)$ .

 $<sup>^3</sup>$  One way to understand this quantity is by considering two finite MPS,  $|\psi(A_L)\rangle$  and  $|\psi(B_L)\rangle,$  of length N generated by the  $A_L$  and  $B_L$  tensors placed at every site. A direct calculation of the fidelity of this finite system shows that  $\langle \psi(A_L)|\psi(B_L)\rangle\approx e^{-N\mathcal{F}}$  for  $N\to\infty.$ 

# 2.2 Entanglement and Correlations

The previous section introduced MPSs as a class of many-body states characterized by a number of parameters that scale linearly with the system size. In contrast to the exponentially large number of parameters required to describe a generic state in the many-body Hilbert space, this raises the question of what class of states an MPS can represent. It has been shown that MPS exhibit a highly restricted correlation structure [118, 238], similar to that of the ground states of typical Hamiltonians. Consequently, it has been demonstrated that every MPS with a finite bond dimension  $\chi$  is the unique ground state of a gapped Hamiltonian with only finite-range interactions [238, 250]. Consequently, the ground state of any arbitrary one-dimensional lattice model with a spectral gap can be approximated by an MPS with an error  $\epsilon(\chi)$  that becomes exponentially small as  $\chi \to \infty$  [251, 252], regardless of the system size. Even for gapless models, good approximations can be found; however, the bond dimension  $\chi(\epsilon, N)$  required to achieve an error of  $\epsilon$  also depends on the system size.

This section discusses some of the basic entanglement and correlation properties of general MPS and demonstrates why MPS are good approximations of general ground states for one-dimensional quantum matter.

#### 2.2.1 Entanglement Properties

Consider an MPS of bond dimension  $\chi$  and length N in the mixed canonical gauge described by a set of left and right isometries and an orthogonality center at position j, as defined in Eq. (2.10). The right reduced density matrix of the bipartition  $(s_1, \ldots, s_j) \cup (s_{j+1}, \ldots, s_N)$  is given solely in terms of the center tensor

$$\rho_{R} = \sum_{\alpha,\beta} \sum_{\rho,s_{j}} (M^{j})_{\rho,\alpha}^{s_{j}} (\bar{M}^{j})_{\rho,\beta}^{s_{j}} |\varphi_{\alpha}^{R}\rangle \langle \varphi_{\beta}^{R}| \cong \begin{pmatrix} M^{j} \\ \bar{M}^{j} \end{pmatrix}, \qquad (2.27)$$

compare also Eq. (2.14). The entanglement spectrum can be obtained from the diagonalization of the  $\chi \times \chi$  matrix  $\rho_R$ , and the entanglement entropy is simply given by

$$S(j) = -\operatorname{Tr}\left[\rho_R \log(\rho_R)\right] = -\sum_{n=1}^{\chi} \lambda_n e^{-\lambda_n}$$
 (2.28)

where  $\lambda_n$  are the entanglement spectrum values of  $\rho_R$ , and the notation of Subsection 2.2.1 is used. Because  $\rho_R$  is a  $\chi \times \chi$  Hermitian matrix, the size of the entanglement spectrum is at most  $\chi$ .

Maximizing the entanglement entropy requires a flat distribution of  $\lambda_n$ , and the matrix  $\rho_R$  which maximes S(j) is given by

$$\rho_R = \frac{1}{\chi} \, \mathbb{1} \ .$$

As a consequence, the entanglement entropy of such a bipartition is bounded from above by a size independent constant

$$S(j) \le \log(\chi) \tag{2.29}$$

for every MPS of bond dimensions  $\chi$ . Compared to the boundary law of entanglement for gapped ground states from Eq. (1.160)

$$S(j) \approx \text{const} := S_0, \quad 1 \ll j \ll N,$$

the upper bound for the MPS entanglement is similar to the general boundary law. As long as  $\chi$  is sufficiently large, it is expected that the MPS can approximate any ground state with  $S_0 < \log(\chi)$ . Further increasing the bond dimensions leads to exponentially small corrections, as the additional states correspond to highly excited states in the entanglement Hamiltonian.

In the case of a ground state of a gapless Hamiltonian with open boundary conditions, the entanglement entropy has a logarithmic correction, see also Eq. (1.161). The maximal entanglement entropy for system of size N is obtained at half-system size and reads

$$S(N/2) \approx \frac{c}{6} \log \left(\frac{2N}{\pi}\right)$$
.

By using the upper bound (2.29), it is found that the bond dimension of an MPS has to scale with the system size to achieve the same precision for all system sizes

$$\chi(N) \sim N^{c/6}$$
.

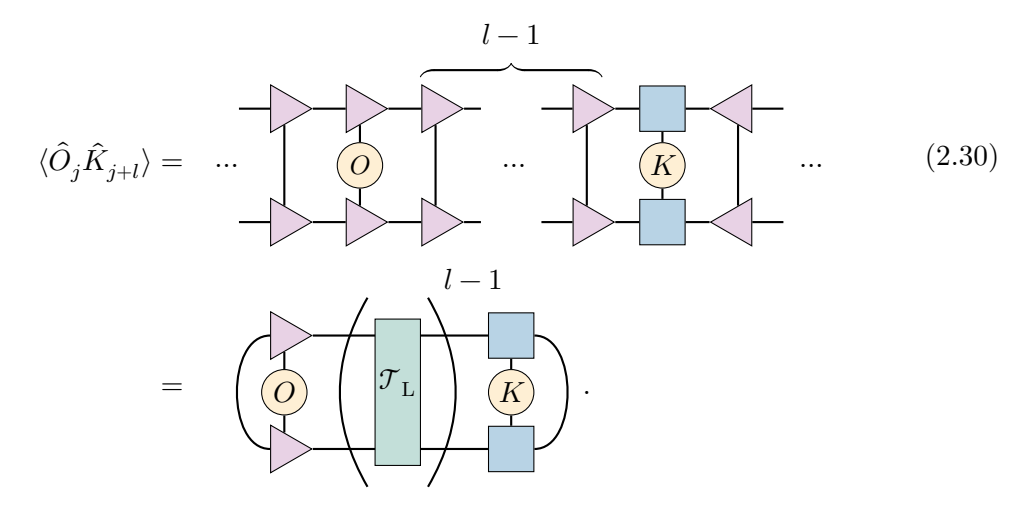
Therefore, for models with a small central charge c, the required bond dimension to reach a desired precision is relatively small, even for large chains. For example, the TFIM at the critical point realizes a Conformal Field Theory (CFT) with c = 1/2. Thus, obtaining a ground state with the same precision as that for a length  $N_1$  for  $N_2 = 10N_1$  requires a bond dimension  $\chi_2$  which is only 1.2 times larger than the bond dimension  $\chi_1$ .

However, if the central charge is large, the required bond dimension to obtain reasonable results quickly grows out of size. In Chapter II, the central charge at the phase transition is  $c_1=1+1/2$  and  $c_2=1+7/10$ , corresponding to a critical Ising and TCI model, together with a background gapless boson field. In this case, making the system ten times bigger would require a scaling of the bond dimension of  $\chi_2/\chi_1\approx 1.8$  in the first case and  $\chi_2/\chi_1\approx 1.9$  in the second case. This large scaling limits the achievable system size to a few unit cells.

# 2.2.2 Correlation Functions

This subsection discusses the general correlation properties of MPSs in the bulk. For simplicity, a uMPS is considered an ansatz. The uMPS is described by the set of three matrices  $\{A_L, A_C, A_R\}$ , where  $A_L$   $(A_R)$  is a left (right) isometry and  $A_C$  is a center tensor; see also Section 2.1.3.

For a pair of local operators  $\hat{O}_j$  and  $\hat{K}_{j+l}$ , the correlation function is given by

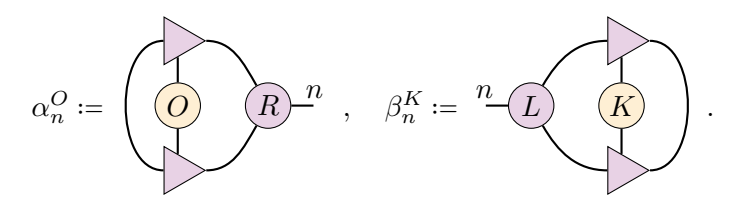


To go from the first line to the second, the isometric properties (2.11) are used, and  $\mathcal{T}_{L}$  is the transfer matrix from Eq. (2.22).

Inserting the eigenvalue decomposition from Eq. (2.23) of the transfer matrix, this becomes

$$\langle \hat{O}_j \hat{K}_{j+l} \rangle = \sum_{n \geq 0} \lambda_n^{l-1} \alpha_n^O \, \beta_n^K \, , \label{eq:constraint}$$

where the weights are defined as



The two rank-3 tensors R and L collect all right and left eigenvectors of  $\mathcal{T}_L$  with eigenvalues  $\lambda_n$  and are introduced in Eq. (2.23). It should be noted that these eigenvectors are not uniquely defined. Assuming no degeneracies in the transfer matrix spectrum, they can be redefined by arbitrary complex numbers

$$|\tilde{R}_n\rangle = z \, |R_n\rangle \ , \quad |\tilde{L}_n\rangle = \frac{1}{z} \, |L_n\rangle \ , \label{eq:relation}$$

in the notation of Eq. (2.23). However, because the transformation is reciprocal between the left and right eigenvectors, the combination  $c_n^{O,K} := \alpha_n^O \beta_n^K$  is gauge invariant. The complex number  $c_n^{O,K}$  are called the form factors of the correlation function<sup>4</sup>.

Putting everything together, and splitting the  $\lambda_0=1$  contribution from the sum, the correlation function becomes

$$\langle \hat{O}_{j} \hat{K}_{j+l} \rangle = c_{0}^{O,K} + \sum_{n>0} e^{-\frac{|l-1|}{\xi_{n}}} c_{n}^{O,K} \,, \quad \xi_{n} = -\frac{1}{\log(\lambda_{n})} \,. \tag{2.31}$$

<sup>&</sup>lt;sup>4</sup> If there are degeneracies in the spectrum, the transformation is generally a complex matrix that is block diagonal in the degenerate subspaces. Because the rank-3 tensor L transforms with the inverse of the transformation R, the combination appearing in the correlation function is still gauge invariant. However, the form factors  $c_n^{O,K}$  are not well-defined individually in the degenerate subspace.

The n=0 contribution,  $c_0^{O,K}$ , is the product of the expectation values  $\langle O \rangle \langle K \rangle$ , and the correlation lengths are strictly positive,  $\xi_n>0$ . For long distances, the correlation function is given by the smallest correlation length  $\xi_{n_\star}$  for which the form factor  $c_{n_\star}^{O,K}$  is non-zero

$$\langle \hat{O}_j \hat{K}_{j+l} \rangle \xrightarrow{l \to \infty} c_0^{O,K} + e^{-\frac{l}{\xi_{n_*}}} c_{n_*}^{O,K}$$
 (2.32)

By choosing  $\hat{O} = \hat{K}^{\dagger}$ , this behavior can be used to extract information about the gap in the spectrum of local excitations generated by the operator  $\hat{O}$ . This strategy is used in Chapter II to explicitly target the gap of a specific low-energy sector that was otherwise hidden in a gapless spectrum of charge excitations.

In practice, the calculation of the left and right eigenvectors of the transfer matrix is performed by solving the two equations

$$\mathcal{T}_{\mathrm{L}}\left|R_{n}\right\rangle = \lambda_{n}\left|R_{n}\right\rangle\,,\quad \mathcal{T}_{\mathrm{L}}^{T}\left|L_{n}\right\rangle = \lambda_{n}\left|L_{n}\right\rangle$$

independently of each other, where  $\mathcal{T}_{L}^{T}$  is the transpose of  $\mathcal{T}_{L}$  obtained by swapping the left and right indices in Eq. (2.22)

$$\mathcal{T}_{\mathbf{L}}^T \coloneqq \mathcal{T}_{\mathbf{L}}^T =$$

To calculate the form factors  $c_n^{O,K}$ , it is necessary to correctly identify the correct pairs of left and right eigenvectors. Moreover, if the spectrum is degenerated, re-biorthogonalization is required to ensure the correct orthogonality relations  $\langle R_n | L_m \rangle = \delta_{n,m}$ .

#### Correlation length in critical systems

Equation (2.32) states that every MPS (finite or in the thermodynamic limit) always has a finite correlation length given by the largest eigenvalue of the transfer matrix  $\mathcal{T}_{\rm L}$  which is smaller than one. While this gives good approximations of gapped states, a critical system has a divergent correlation length  $\xi \to \infty$ . For the transfer matrix, a dense spectrum ranging from one to zero is required. Every finite-bond-dimension approximation necessarily introduces an artificial correlation length  $\xi(\chi)$  which diverges for  $\chi \to \infty$  in a universal way [253]

$$\xi(\chi) \sim \chi^{\kappa}$$
,

where the exponent  $\kappa$  decreases monotonically with the central charge [254].

In a finite system, this is not a problem as long as the artificial correlation length is larger than the system size. For an infinite system, this scaling limit cannot be reached, and the finite bond dimension acts as a relevant perturbation of the CFT. However, the system is expected to behave as practiced by the CFT for scales smaller than the correlation length but much larger than one. To measure the critical exponents, it is therefore necessary to increase the bond dimension to have  $\xi(\chi) \sim 10^4$  such that the universal algebraic decay can be fitted using linear regression.

#### 2.2.3 Symmetries in Tensor Networks

If the quantum many-body state  $|\psi\rangle$  is symmetric under a global symmetry group G, the tensors forming the MPS have a non-trivial representation of this symmetry group [69]. Assuming, similar the Subsection 1.1.4, that the global symmetry  $\hat{U}(g)$  for  $g \in G$  is Abelian and generated by a product of local unitary operators  $\hat{u}_i$  as

$$\hat{U}(g) = \prod_{j=1}^N u_j(g) \,.$$

If the state  $|\psi\rangle$  is invariant under U

$$e^{i\varphi(g)}\left|\psi\right\rangle = \hat{U}\left|\psi\right\rangle = \sum_{s_1,\dots,s_N} \Psi_{s_1,\dots,s_N} \prod_{j=1}^N u_j \left|s_1,\dots,s_N\right\rangle\,,$$

the quantum tensor has to fulfill the equation

$$\Psi_{s_1,\dots,s_N} = e^{-i\varphi(g)} \sum_{s_1',\dots,s_N'} \Psi_{s_1',\dots,s_N'} \prod_{j=1}^N \left(u_j\right)_{s_j,s_j'}.$$

Expressing the tensor  $\Psi$  by an MPS as in (2.8), this implies that every tensor  $M^j$  has to transform according to

where  $\sum_{j=1}^N \varphi_j = \varphi(g)$  and the arrows on the links indicate whether the unitary acting on that link must be conjugated. The matrix  $\tilde{u}_j$  forms a representation of the global symmetry group G acting on the horizontal legs. Typically, one chooses  $\varphi_1 = \varphi(g)$  and  $\varphi_j = 0$  for all  $j \neq 1$ .

Because the irreducible representations of an Abelian group are one dimensional, the tensors  $M^j$  decomposes into independent blocks

where  $\delta_{\alpha}$  is a tensor carrying the one-dimensional irreducible representations on its links, and  $R_{\alpha,j}$  is a degeneracy tensor that transforms trivially under the symmetry group. In particular, the representations acting on  $\delta_{\alpha}$  are given by

$$\tilde{u}^\alpha_{j-1}(g) = e^{i\varphi^l_\alpha(g)}\,, \quad \tilde{u}^\alpha_j(g) = e^{i\varphi^r_\alpha(g)}\,, \quad u^\alpha_j(g) = e^{i\varphi^d_\alpha(g)}\,,$$

as in Eq. (1.21). The invariance equation (2.33) requires that

$$\varphi_{\alpha}^l(g) + \varphi_{\alpha}^r(g) - \varphi_{\alpha}^d(g) - \varphi_j(g) = 0 \,.$$

This can easily be extended to tensors with arbitrary number of legs, and also to non-Abelian symmetries, where the symmetry tensor  $\delta_{\alpha}$  can carry non-trivial higher-dimensional representations [255]. In this case, the invariance Equation (2.33) is still

valid and requires all the representations on the links of the symmetry tensor  $\delta_{\alpha}$  to combine to the trivial representation.

The existence of symmetries in the tensor network can be used to reduce the computational time for algorithms for tensor networks, as each block of the tensor can be handled separately. As an example, consider the case of a  $\mathbb{Z}_2$  symmetry representing, for example, the parity symmetry of a fermionic chain. In this case, there are only two irreducible representations represented by  $\varphi(g) = 0$  and  $\varphi(g) = \pi$ , resulting in two independent blocks. If both blocks are approximately equally sized, there is an expected speedup of at least two for every operation.

# 2.3 Numerical Minimization of Matrix Product States

The previous section introduced the MPS as a low-rank approximation of the full quantum tensor  $\Psi$ . This low-rank approximation is controlled by the amount of possible entanglement for a fixed bond dimension  $\chi$  in the state, making MPS very similar to the typical ground states of many-body Hamiltonians in one dimension. This section discusses how actual ground-state approximations in terms of an MPS are found numerically, mainly in the context of finite-size systems and the famous DMRG [60, 62] algorithm.

# Density Matrix Renormalization Group

The starting point is a quantum chain of size N and local Hilbert space dimension d, described by a Hamiltonian H containing only finite-range interactions. As discussed in Subsection 2.1.2, this Hamiltonian can be represented as an MPO

of bond dimension  $\chi_H$ . The aim is to find the best approximation of the ground state of H within the class of quantum states  $|\psi\rangle$  represented by an MPS of bond dimension  $\chi_{\psi}$ 

$$|\psi\rangle\cong M^1 \longrightarrow M^2 \longrightarrow M^N \ .$$
 $s_1 \qquad s_2 \qquad s_N$ 

The best approximation of the ground state obtained by using such an MPS is obtained by finding the variational minimum of the energy functional

$$E(\{M^j, \overline{M}^j\}) := \frac{\langle \psi | H | \psi \rangle}{\langle \psi | \psi \rangle} \tag{2.34}$$

with respect to the MPS tensors  $M^j$  and their complex conjugated  $\overline{M}^j$ . Formulated in this way, the variational minimization is a global optimization of all  $\mathcal{O}\left(N\chi_{\psi}^2\right)$  parameters of the MPS. This global optimization is very expensive and suffers from the large gauge freedom of the MPS.

One way to solve this problem is to use the mixed canonical gauge in combination with a fixed-point iteration. The resulting algorithm is known as the Density-Matrix

Renormalization Group (DMRG), and was originally introduced by S. White in 1992 [60]. Using the canonical gauge serves two purposes: first, it largely reduces the redundancy in the ansatz, and second, the fixed-point iteration is formulated as a local eigenvalue problem of a small Hermitian matrix in the canonical gauge.

The denominator of the energy functional from Eq. (2.34) can be discarded by restricting to all states of norm  $\langle \psi | \psi \rangle = 1$ , and the minimization problem can be restated using a Lagrange multiplier

$$E(\{M^j, \overline{M}^j\}, \lambda) := \langle \psi | H | \psi \rangle - \lambda \left( \langle \psi | \psi \rangle - 1 \right) . \tag{2.35}$$

By writing the MPS in the mixed canonical form with the orthogonality center  $M^j$  at site j, this energy functional becomes in the graphical notation

As discussed in Eq. (2.13), the left/right isometries define an effective reduced basis set for the spins at sites  $(1, \ldots, j-1)$  and  $(j+1, \ldots, N)$ . By keeping this basis fixed, the global minimization problem reduces to a local problem with the energy functional of Eq. (2.36) only depends on  $M^j$  and  $\lambda$ .

The tensor  $M^j$  that minimizes this local problem is found by taking the derivative of Eq. (2.36) with respect to the conjugated tensor  $\overline{M}^j$  and setting the result to zero. In the graphical notation, this becomes

This equation is an eigenvalue problem with respect to the linear operator  $H_{\text{eff}}^{j}$  acting on the orthogonality center  $M^{j}$ , and can be interpreted as the full many-body eigenvalue problem projected into the basis defined by the left and right isometries. Further, the Lagrange multiplier requires  $M^{j}$  to be normalized

$$\begin{pmatrix} M^j \\ \hline M^j \end{pmatrix} = 1 \, .$$

The tensor minimizing the local optimization problem is therefore the normalized eigenvector of  $H_{\text{eff}}^{j}$  with the smallest eigenvalue  $\lambda_{0}$ , and by replacing the old orthogonality center with this optimal solution, the whole MPS gets lowered in energy.

To find the global optimum, the projection on the local basis is performed iteratively for every site  $j \in \{1, ..., N\}$ . In particular, the steps are as follows:

1. Initialize the MPS, for example, in a random state, j = 1, and  $\sigma = +1$ .

- 2. Move the orthogonality center to j.
- 3. Solve the local problem with respect to the projected Hamiltonian  $H^j_{\text{eff}}$ , and obtain the lowest eigenvector  $\tilde{M}^j$ .
- 4. Replace the old orthogonality center with the optimal local solution  $M^j \to \tilde{M}^j$ .
- 5. If j = N, set  $\sigma = -1$ , else if j = 1, set  $\sigma = 1$ .
- 6. Set  $j \to j + \sigma$  and repeat from Step 2.

Because the energy is lowered in every step, this procedure iteratively moves towards a minimum of the energy functional in Eq. (2.34). Performing one full circle from j=1 to j=N and back to j=1 is called a full sweep, and performing a total number of  $N_{\rm Sweep}$  sweeps is the DMRG algorithm.

To be precise, the sweeping presented here is the single-site DMRG, where only one site of the MPS is optimized at every step [256]. The overall complexity of the single-site DMRG is  $\mathcal{O}\left(\chi_H\chi_\psi^3d + \chi_H^2\chi_\psi^2d^2\right)$ . This algorithm is prone to becoming stuck in a local minimum, and it is necessary to include educated noise terms to improve convergence [256].

In a similar fashion, it is possible to define a two-site DMRG by considering the local problem with respect to two neighboring sites in the MPS. Contracting two neighboring tensors into a super-block spanning over two sites enlarges the variational subspace from  $\chi^2 d \to \chi^2 d^2$ . This allows for better convergence, but the additional factor of d also increases the computational complexity, and the two-site algorithm is expected to be d-times slower. After the optimal two-site tensor is found, it has to be decomposed into two single site tensors to restore the shape of the MPS

$$\begin{array}{c|c} \hline M^{j,j+1} \\ \hline \\ s_j & s_{j+1} \end{array} \approx \begin{array}{c|c} \hline A_L^j \\ \hline \\ s_j & s_{j+1} \end{array}.$$

This decomposition can be performed, for example, using the SVD. An exact decomposition would lead to a connecting link between  $A_j^L$  and  $M^{j+1}$  of size  $d\chi$ . This allows for either dynamically increase the bond dimension, or to truncate the singular values back to the  $\chi$  most relevant ones<sup>5</sup>. To achieve better convergence or allow for a dynamical increase in the bond dimension in the single-site DMRG, it is necessary to implement a subspace expansion [69, 257] that allows for an interpolation between the single-site and two-site algorithms, followed by a truncation of the singular values of the enlarged matrix, similar to the two-site scheme.

The DMRG can also be formulated without choosing the mixed canonical gauge. In this case, only optimizing a single tensor while keeping the rest fixed can be interpreted as a projection of the full Hamiltonian onto a general, non-orthonormal basis. The non-orthogonality renders the eigenvalue problem from Eq. (2.37) into a generalized eigenvalue problem of the form

$$H_{\text{eff}}^{j} \left| M^{j} \right\rangle = \hat{N}^{j} \left| M^{j} \right\rangle \,,$$

where  $\hat{N}^j$  is the norm matrix. Such a generalized eigenvalue problem is more difficult to solve numerically. Choosing the mixed-orthogonal form for the MPS therefore leads to a much simpler and stable numerical problem.

<sup>&</sup>lt;sup>5</sup> Truncating the singular values of this super-block tensor is equivalent to truncating the reduced density matrix of the cut (j, j+1). Therefore, the algorithm selects the most relevant density matrix contribution to the ground state, explaining the name Density-Matrix Renormalization Group.

# Infinite Systems

The sweeping procedure of the DMRG only works in finite-sized systems, and finding the variational optimal uMPS that minimize a Hamiltonian directly in the thermodynamic limit is not simple. Because the energy is extensive, operating in the thermodynamic limit always leads to an infinite energy  $\langle \psi | H | \psi \rangle = \infty$  for generic quantum states. This infinity arises from the existence of a finite energy density e associated with the state  $|\psi\rangle$ , and a proper variational minimization aims to minimize this density instead of the total (infinite) energy of  $|\psi\rangle$ . If  $|\psi\rangle$  is an uMPS, this energy density can be calculated using only the right eigenvector of the transfer matrix  $\mathcal{T}_L$  defined in Eq. (2.22) [258]. By removing the density contribution from the Hamiltonian  $\tilde{H} = H - e \sum_{j=1}^{\infty} \mathbb{1}$ , it is possible to define a proper variational minimization of the uMPS<sup>6</sup> This algorithm is called Variational Uniform Matrix Product State (VUMPS), and it operates directly on the manifold of all uMPS [63, 232]. Because VUMPS ensures that the uMPS is translation invariant at every iteration, it is more evolved than the simple DMRG algorithm, and an in-depth discussion is out of reach for this thesis. A detailed explanation of VUMPS can be found, for example, in [258].

In Chapters II and III, the VUMPS is used to find the ground states of onedimensional models directly in the thermodynamic limit, allowing for the determination of the general phase diagram of the models considered in these chapters.

# 2.4 Other Tensor Networks

The previous sections introduced the MPS, which is a class of variational ansatz states. Based on their entanglement structure, this class is identified as a good approximation of the ground states of gapped Hamiltonians in one dimension. In other scenarios, such as gapless states or higher dimensions, the MPS is prone to failure because the entanglement in the ground state rapidly outgrows the possible entanglement captured by the MPS. This section briefly discusses the extensions of the MPS to more general tensor network states that can capture the entanglement in higher dimensions.

A straightforward generalization of the MPS, which shares most of its properties, is in the form of a Tree Tensor Network (TTN) [259–261]. This is a state with a hierarchical structure that mimics the renormalization flow from the microscopic to the macroscopic scale, as shown in Fig. 2.5(a) for a sketch. The main advantage of the structure of the TTN is that it preserves the local nature of Hamiltonians in arbitrary dimensions, as shown in Fig. 2.5(b) in two dimensions. In contrast, using an MPS for the simulation of a two-dimensional quantum system leads to long-ranged interactions in the linear index of the MPS. Furthermore, the TTN has the property that by removing one tensor from the network, the remaining part decomposes into unconnected pieces. This property, which is also shared with the MPS, allows for the definition of a mixed canonical gauge similar to the MPS. Therefore, calculating local observables using a TTN is efficient, and sweeping algorithms that minimize the energy can be defined in analogy to the DMRG algorithm for MPS.

<sup>&</sup>lt;sup>6</sup>Formally, this sum is infinite, and the expression should be considered as shifting a finite size Hamiltonian, and taking the thermodynamic limit of expectation values of this finite-size Hamiltonian with the uMPS.

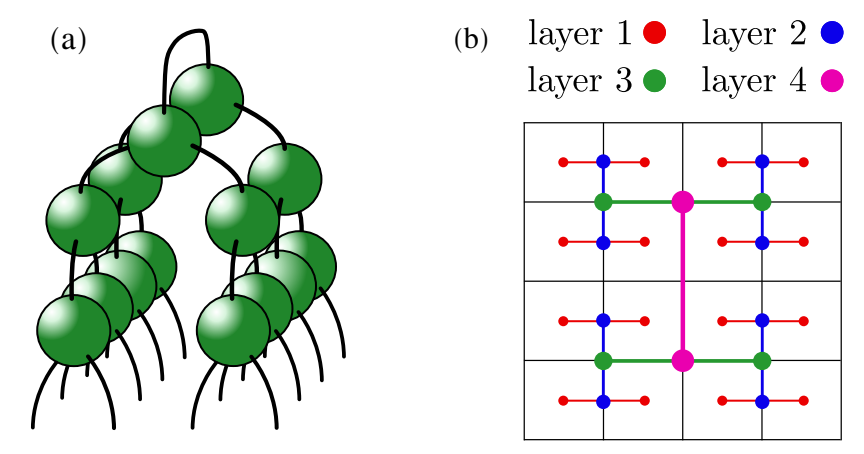


Figure 2.5: (a) A binary TTN for a two-dimensional system. Every tensor has a unique parent tensor (going up in the tree) and two child tensors, except for the layer connecting to the physical lattice. (b) Top-down view of the physical lattice and how the TTN fuses two sites into one super-site, alternating in the x and y directions.

In the past, TTN were successfully applied to approximate the ground state of highly correlated quantum systems in two dimensions [260–265], and recently, to simulate the dynamics of quantum matter [36, 266–268]. A TTN is also used in Chapter III to simulate the dynamics of a two-dimensional TFIM. However, the renormalization character of the tree leads to a significant increase in computational complexity. Consider a binary tree in which each tensor has a unique parent node and two child nodes, as illustrated in Fig. 2.5(a). The tensors in the higher layers are rank-3 tensors, where each leg has the dimension  $\chi$ , the bond dimension of the TTN. Performing a decomposition of such a tensor, either with SVD or QR decomposition, has a complexity of  $\mathcal{O}(\chi^4)$ . The same decomposition scales only  $\mathcal{O}(\chi^2 d)$  in the case of the MPS, and the expected increase in the computational time by a factor of  $\chi$  limits the reachable bond dimensions for the TTN. However, recent developments in the overall performance of modern graphics cards have allowed the limits to be pushed, allowing the study of complex quantum systems in two dimensions. See also [268] for a recent survey on TTN on graphics cards.

Although TTN are quite successful for certain two-dimensional models, they are not the perfect ansatz state to simulate general two-dimensional ground states. This is because of the boundary law of entanglement  $S(A) \sim \partial A$  expected in twodimensions [189, 191–193, 202, 203], see also Subsection 1.4.3 The TTN cannot reproduce this scaling, as cutting the single connection at the top of the tree divides the two-dimensional lattice into two halves, and the bond dimension  $\chi$  must scale exponentially with the system size to capture the boundary law. A more direct approach is to place a tensor at every site of the underlying lattice, and connect these tensors along nearest neighbor, also known as a Projected Entangled Pair States (PEPS) [228, 229] Cutting along a closed line now breaks a number of links that is proportional to the length of this line. Every broken link contributes a maximal amount of entanglement, and this ansatz reproduces the boundary law. Compared to the TTN and MPS, the PEPS has loops that spoil the existence of a canonical form. Consequently, the contraction of a PEPS network is not efficient, and additional approximations are necessary. However, recent advances [269, 270] have demonstrated that PEPSs are powerful numerical tools for simulating two-dimensional quantum matter.

# Results

CHAPTER

# Majorana zero modes in fermionic wires coupled by Aharonov-Bohm cages

Authors: Niklas Tausendpfund, Sebastian Diehl, Matteo Rizzi

**Year:** 2023

Journal: Physical Review B

Volume/Issue: 107, 3

**DOI:** 10.1103/PhysRevB.107.035124

### I.1 Authors Contribution

The initial idea of realizing Majorana Zero Modes (MZMs) using coupled Aharonov-Bohm cages was developed by Sebastian Diehl and Matteo Rizzi. After being introduced to the idea, Niklas Tausendpfund carried out the analytical and numerical treatment of the model, including the design of the simulation code. He wrote the first draft of the manuscript, which was revised by Matteo Rizzi and Sebastian Diehl, who contributed helpful comments. During this project, he received guidance from his supervisor Matteo Rizzi in form of regular discussions and help with conceptual problems by Sebastian Diehl.

## I.2 Data Availability

The analytical calculations, including the derivation of the effective model and the renormalization group analysis are performed on paper and are available upon request from the author. The numerical results presented in this study were obtained by performing Matrix Product State (MPS) simulations. The code and data are stored on the PGI-8 backed-up data server at Forschungszentrum Jülich. Upon request, the data can be made available by the Institute for Optimal Quantum Control.

## I.3 Summary

Realizing the fermionic Symmetry-Protected Topological Phase (SPTP) supporting unpaired Majorana fermions localized to the edge of a quantum chain remains an open problem and has not been convincingly achieved to date. As explained in Subsection 1.2.3, the typical setup requires breaking the particle number conservation in an effective spinless fermionic wire. This is achieved, for example, by creating semiconductor-superconductor heterostructures in a strong magnetic field [95, 96, 152, 155].

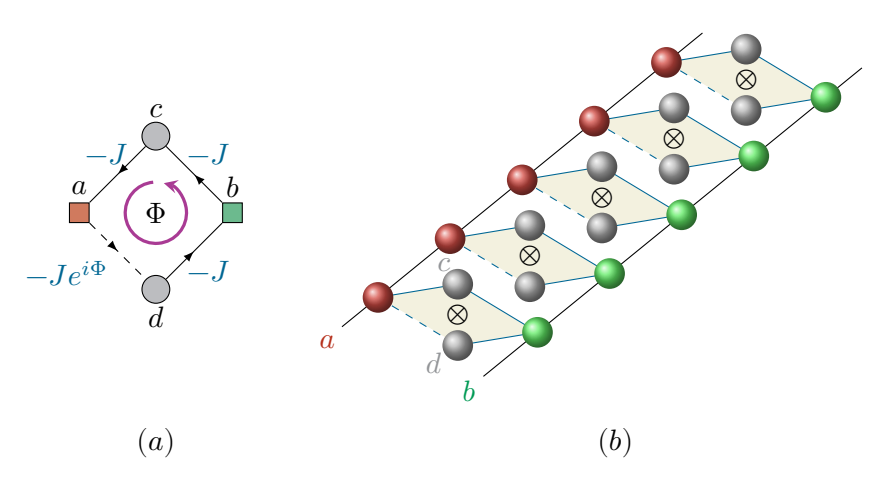


Figure I.1: (a) Single diamond defined by the Hamiltonian  $h_{\Diamond}$ . (b) Ladder system defined by coupling the diamonds along one direction.

In this study, we follow an alternative approach that does not require a host superconductor to induce p-wave superconducting correlations in nanowires. Earlier works [160, 162, 166, 271] discovered that the same SPTP can be engineered by a global  $U(1) \times \mathbb{Z}_2$  symmetry, where the U(1) is the conservation of the total particle number and  $\mathbb{Z}_2$  is a partial parity. The idea of this realization is to engineer a ladder system with coherent pair-hopping between the two fermionic species described by the  $a^{(\dagger)}$  and  $b^{(\dagger)}$  fermionic ladder operators. A minimal Hamiltonian is given by [160]

$$H = \sum_{j=1}^{N-1} -t \, a_{j+1}^{\dagger} a_j - t \, b_{j+1}^{\dagger} b_j + W a_j^{\dagger} a_{j+1}^{\dagger} b_{j+1} b_j + \text{h.c.} \,. \tag{I.1}$$

From a mean-field perspective, one species plays the role of the superconductor, with the pair-hopping term playing the role of p-wave pair creation and annihilation. The Hamiltonian (I.1) has the desired  $U(1) \times \mathbb{Z}_2$  symmetry, where the total particle number  $N_{\text{tot}} = N^a + N^b$  and the partial parity of one of the two species  $P_a = (-1)^{N^a}$  are conserved. As long as there is no single particle hopping  $a_j^{\dagger}b_k + \text{h.c.}$  between the two legs of the ladder, this model can be driven into the SPTP with emergent Majorana Zero Modes (MZMs). However, the existence of the additional U(1) symmetry leads to the existence of gapless density wave excitations, which can be seen from the effective low-energy field theory as described in Subsection 1.3.1.

In contrast to earlier studies that depended on the desired symmetry group emerging through perturbative methods, our study introduces an exact engineering approach using the negative interference of complex hopping amplitudes, resulting in Aharonov-Bohm Cages [272, 273]. The fundamental component is a four-site diamond, as illustrated in Fig. I.1(a), which is pierced by a magnetic flux  $\Phi$ . As the

I.3. SUMMARY 103

fermions encircle the magnetic flux, they acquire a geometric phase, as detailed in Subsection 1.1.6. The Hamiltonian that characterizes this diamond is given by

$$h_{\Diamond} = -J(a^{\dagger}c + c^{\dagger}b + b^{\dagger}d + e^{i\Phi}d^{\dagger}a + \text{h.c.}). \tag{I.2}$$

The transition amplitude for a fermion initially located at the a site to the b site is given by

 $\langle b|a(t)\rangle\coloneqq\langle 0|b\ e^{-ih_{\diamondsuit}t}a^{\dagger}|0\rangle=\left|\sin\left(2Jt\cos\left(\Phi/2\right)\right)\right|^{2}\ .$ 

When  $\Phi$  is set to  $\pi$ , this transition becomes zero for all times t.

Building on this result, by arranging N of such diamonds on a line pierced by a flux  $\Phi = \pi$  as illustrated in Fig I.1(b), there is no single-particle transition from any  $a_j$  fermion to any  $b_k$  fermion. This remains true even when adding general inter-species coupling terms, such as nearest-neighbor tunneling or density-density interactions. The coupled wire system has a global U(1) × U(1) symmetry, and the desired breaking to a U(1) ×  $\mathbb{Z}_2$  group is achieved by adding generic inter- and intra-particle interactions on the c and d fermions.

In the present study, we demonstrated that this model simplifies to an extended version of the pair-hopping Hamiltonian in Eq. (I.1) when considered in a perturbative limit. The desired pair-hopping term emerges in the fourth order in the perturbation series. Through a renormalization group analysis of the bosonized Hamiltonian, we discovered that the model supports the formation of an SPTP with MZMs when the parameters are appropriately chosen. This expectation is confirmed using Density-Matrix Renormalization Group simulations and by verifying the fingerprints presented in Subsection 1.2.3 of unpaired edge-localized Majorana operators.

In the final part of our study, we extended the analysis to the full four-wire model, illustrating the presence of the SPTP within a broader parameter range without resorting to perturbative arguments The existence of this extended region allows the proposed model to be realized using synthetic dimensions on cold atom platforms. However, it remains uncertain whether the MZMs manifest solely in the ground state or form an almost strong zero mode, as discussed in Section 1.5. Specifically, it is unclear how the gapless mode couples to the Majorana operators at higher energies, thereby reducing their lifetime. First results on this issue are presented in Chapter V, where the methodology developed in Chapter IV is applied to the class Hamiltonians that realize this SPTP in a number-conserving setup, determining the lifetime of Majorana operators localized at the edges.

### Majorana zero modes in fermionic wires coupled by Aharonov-Bohm cages

Niklas Tausendpfund, 1,2 Sebastian Diehl, 2 and Matteo Rizzi, 1,2

<sup>1</sup>Forschungszentrum Jülich GmbH, Institute of Quantum Control, Peter Grünberg Institut (PGI-8), 52425 Jülich, Germany <sup>2</sup>Institute for Theoretical Physics, University of Cologne, D-50937 Köln, Germany



(Received 8 September 2022; revised 16 December 2022; accepted 23 December 2022; published 17 January 2023)

We devise a number-conserving scheme for the realization of Majorana zero modes in an interacting fermionic ladder coupled by Aharonov-Bohm cages. The latter provide an efficient mechanism to cancel single-particle hopping by destructive interference. The crucial parity symmetry in each wire is thus encoded in the geometry of the setup, in particular, its translation invariance. A generic nearest-neighbor interaction generates the desired correlated hopping of pairs. We exhibit the presence of an extended topological region in parameter space, first in a simplified effective model via bosonization techniques, and subsequently in a larger parameter regime with matrix-product-states numerical simulations. We demonstrate the adiabatic connection to previous models, including exactly solvable ones, and we briefly comment on possible experimental realizations in synthetic quantum platforms, like cold atomic samples.

#### DOI: 10.1103/PhysRevB.107.035124

#### I. MOTIVATION

In the last decade, the quest for topological states of matter has arguably been one of the driving directions in condensed matter physics [1–3], partially motivated also by their envisioned usage as platforms for quantum computation [4]. Among all possible topological states, Majorana zero modes (MZMs) are one of the simplest examples realizing an anyonic excitation, i.e., not obeying either fermionic or bosonic statistics [4–6]. Despite them being conceptually quite simple, an ongoing quest is being pursued towards an unambiguous measurement of their existence. While they do not enable a universal set of gates, they have been proposed to serve as a topological protected quantum memory [7,8].

Stemming from the cornerstone paper by Kitaev [9], most efforts have focused on a one-dimensional realization of Majorana zero modes via coupling some semiconducting nanowire to a bulk superconductor [10–16]. The superconductor serves as a reservoir inducing p-wave superconductivity into the nanowire via the proximity effect resulting in an effective breaking of the U(1) symmetry of number conserving down to a residual fermionic parity symmetry  $\mathbb{Z}_2$ .

In recent years, alternative proposals for realizing MZMs without breaking the number conservation were put forward [17,18]. These schemes are based on the field-theoretical observation that a minimal  $U(1) \times \mathbb{Z}_2$  model of two (fermionic) Luttinger liquids coupled exclusively by a pair-hopping term indeed leads to the same topological signatures [19]. Noticeably, even some exactly solvable instances were found [20,21], giving deep insights into the nature of this phase. Moreover, a number-conserving scheme is particularly appealing for synthetic quantum matter platforms like cold atoms [22]. However, a perfect cancellation of single-particle tunnelings between the chains is needed to ensure the  $\mathbb{Z}_2$  protection of MZMs. In previous works, this was only achievable in an approximate fashion via some perturbative suppression. Here, we present an alternative scheme which makes use of exact interference terms of complex hopping amplitudes, also known as Aharonov-Bohm cages [23,24], and perfectly cancels all single-particle poisoning. These cages are arranged in a translation-invariant sequence across the two target fermionic chains, and a generic nearest-neighbor interaction term enables the sought-after correlated hopping of particles.

The paper is structured as follows: First in Sec. II we introduce our model which involves four spinless fermionic species. After discussing the basic properties of that model, we integrate out two of these spinless fermions using a Schrieffer-Wolff (SW) transformation [25], and show that the obtained effective Hamiltonian falls into the same class as those of previous proposals. This effective Hamiltonian is first investigated in Sec. III by using bosonization [26,27], in order to find the most favorable parameter regime for realizing the MZM phase. In this section we also review the basic indicators used for detecting the MZM phase: the nonlocal behavior of the end-to-end correlation function together with a relative sign between the ground states of the two parity sectors and the exact double degeneracy of the entanglement spectrum [28]. Next, in Sec. IV, we show numerical results using tensor network techniques [29], exhibiting all defining features of the MZM phase, not only for the effective model but also for the full four-flavor setup in regimes very far from the perturbative expansion conducted before. Finally, in Sec. V we summarize our findings and give a short outlook of open questions.

#### II. MODEL INTRODUCTION

Let us consider two (lattice) wires a and b, populated by spinless fermions, and connected to each other via additional sites c and d in a rhomboidal configuration pierced by a  $\pi$  phase, as described by the following Hamiltonian:

$$H_{\Diamond} = -J \sum_{j} (a_{j}^{\dagger} c_{j} + c_{j}^{\dagger} b_{j} + b_{j}^{\dagger} d_{j} - d_{j}^{\dagger} a_{j} + \text{H.c.})$$
 (1)

$$= -J\sqrt{2} \sum_{j} (a_{j}^{\dagger} m_{j} + b_{j}^{\dagger} p_{j} + \text{H.c.}), \qquad (2)$$

where  $\alpha_j^{(\dagger)}$  annihilates (creates) a fermion in the site of kind  $\alpha=a,b,c,d$  at the jth lattice position, and  $p=(c+d)/\sqrt{2}$  ( $m=(c-d)/\sqrt{2}$ ) are the (anti)symmetric superposition of the intermediate modes. For the sake of simplicity, we picked up a gauge where the whole  $\pi$  phase has been collected on

a single link; however, any redistribution along the rhombi would, of course, lead to the same Aharonov-Bohm caging effect in the end. As made explicit by Eq. (2), indeed, destructive interference prohibits single-particle motion between the (decorated) wires; i.e., the two charges

$$N_{\pm} = (N^a + N^m) \pm (N^b + N^p),$$
 (3)

with  $N^{\alpha}=\sum_{j}n_{j}^{\alpha}=\sum_{j}\alpha_{j}^{\dagger}\alpha_{j}$ , are separately conserved and denoted as the U(1)<sub>±</sub> symmetries in the following.

In order to let Majorana physics emerge, we need to partially break the  $U(1)_-$  associated to the  $N_-$  charge into a residual  $\mathbb{Z}_2$  symmetry for each dressed chain. We could naturally achieve it by considering nearest-neighbor density-density interaction terms of the kind

$$H_{\text{int}} = \sum_{j=1}^{L-1} \left[ V_1 \left( n_j^c n_{j+1}^c + n_j^d n_{j+1}^d \right) + V_2 \left( n_j^c n_{j+1}^d + n_j^d n_{j+1}^c \right) \right]$$

$$= \sum_{j=1}^{L-1} \left[ \frac{V_1 + V_2}{2} \left( n_j^p + n_j^m \right) \left( n_{j+1}^p + n_{j+1}^m \right) + \frac{V_1 - V_2}{2} \left( p_j^{\dagger} m_j + m_j^{\dagger} p_j \right) \left( p_{j+1}^{\dagger} m_{j+1} + m_{j+1}^{\dagger} p_{j+1} \right) \right], \tag{4}$$

which does not preserve  $N^p$  and  $N^m$  (but still preserves their parity) away from the fine-tuned point  $V_1 = V_2$ . The residual unbroken symmetry is actually  $(\mathbb{Z}_4)_-/(\mathbb{Z}_2)_+$ , since the parity of the conserved overall population fixes the parity of the relative population, too: as a convention, we decide to look at the parity in the dressed a chain, i.e.,

$$P = e^{i\pi(N^a + N^m)} = e^{\frac{i\pi}{2}N_+} e^{\frac{i\pi}{2}N_-}.$$
 (5)

Actually, we show in Appendix C that our model is adiabatically connected to a regime where the  $U(1)_+$  symmetry is further broken and the residual group is an even simpler  $\mathbb{Z}_2 \times \mathbb{Z}_2$ , i.e., the same symmetry class as two individual Majorana chains. Later we will abuse this relation to derive the signatures of the topological regime in the single-particle correlation functions.

Any additional generic intrawire Hamiltonian  $H_{\alpha=a,b}$  and any Hamiltonian of the kind

$$H_{c,d} = \sum_{j} \left[ \mu \left( n_{j}^{c} + n_{j}^{d} \right) + t_{\parallel} (c_{j}^{\dagger} c_{j+1} + d_{j}^{\dagger} d_{j+1}) + t_{\perp} (c_{j}^{\dagger} d_{j+1} + d_{j}^{\dagger} c_{j+1}) + \text{H.c.} \right]$$
(6)

acting on the intermediate sites would still fall in the same  $U(1)_+ \times (\mathbb{Z}_2)_-$  symmetry class. We initially set  $t_{\parallel} = t_{\perp} = 0$  for the sake of keeping most calculations analytically feasible, but in Appendix A we provide some estimate on their utility for making the desired topological signatures even more evident.

A pictorial sketch of the generic Hamiltonian,

$$H = H_a + H_b + H_{c,d} + H_{\Diamond} + H_{\text{int}}, \tag{7}$$

is given in Fig. 1(b). Once we integrate out the intermediate sites (c, d) via a Schrieffer-Wolff transformation along the lines of Ref. [25], we are left with a low-energy description

of the dressed wires (a, b), illustrated in Fig. 1(c):

$$H_{\text{eff}} = \widetilde{H}_a + \widetilde{H}_b + U_{\text{nn}} \sum_{j} (n_j^a + n_j^b) (n_{j+1}^a + n_{j+1}^b)$$

$$- \sum_{j} (W_1 a_j^{\dagger} a_{j+1}^{\dagger} b_{j+1} b_j + W_2 b_j^{\dagger} a_{j+1}^{\dagger} b_{j+1} a_j$$

$$+ W_3 b_j^{\dagger} a_i^{\dagger} a_{j+1} b_{j+1} + \text{H.c.}). \tag{8}$$

The form of Eq. (8) allows for a direct comparison with the model of Ref. [17] and the exactly solvable one of Ref. [20], as discussed in Appendix C. The two pair-hopping terms have rather different effects: The interchain one,  $W_1$ , embodies the original Kitaev-chain model per each wire separately, and it is indeed the one responsible for the desired topological effect [17,19,20]. The intrachain one,  $W_2$  and  $W_3$ , instead promotes a (pseudo-)spin-density-wave ordering in the wire-label degree of freedom, as we will discuss after considering the bosonized version of Hamiltonian (8) below Eq. (13). The attainable couplings with the presented microscopic derivation are

$$\frac{W_1}{\mu} = \frac{W_2}{\mu} = \left(\frac{J}{\mu}\right)^4 \frac{8\mu(V_2 - V_1)}{(2\mu + V_1)(2\mu + V_2)},$$

$$\frac{U_{nn}}{\mu} = \left(\frac{J}{\mu}\right)^4 \frac{8(\mu(V_1 + V_2) + V_1V_2)}{(2\mu + V_1)(2\mu + V_2)},$$
(9)

and  $W_3 = 0$ . Due to the similar effect of  $W_2$  and  $W_3$ , we set  $W_3 = 0$  for the rest of the main text. We will show in the following, via a combination of field-theoretical calculations and numerical simulations, that  $W_2 = W_1$  does not impair the formation of the wished topological order, at least in an extended region of the parameter space.

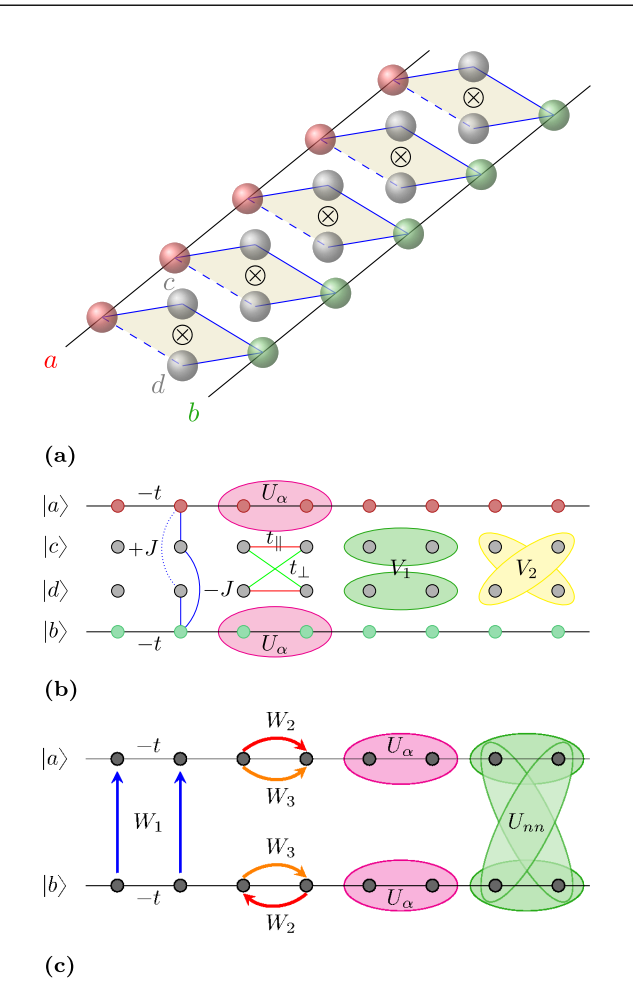


FIG. 1. Pictorial representation of the main Hamiltonians of this work: (a) Translation-invariant coupling of the two wires, a and b, via the rhombi Hamiltonian  $H_{\Diamond}$  encompassing a  $\pi$  flux, here denoted via a single hopping with opposite sign to the rest (dashed line). (b) Full model of Eq. (7), with intrachain hopping elements (black), interchain ABC hoppings (blue) as in panel (a), and bubbles indicating the density-density interactions. (c) Effective low-energy model of Eq. (8), with the blue arrows standing for the correlated interchain pair hopping, and the red and orange ones for the cross-correlated hopping terms. From the microscopic derivation one finds  $W_1 = W_2$  and  $W_3 = 0$ ; however, we considered all three couplings for comparison to the exact solvable model of Ref. [20] (see Appendix C).

The dressed Hamiltonians  $\tilde{H}_{\alpha}$  ( $\alpha = a, b$ ) read

$$\widetilde{H}_{\alpha} = H_{\alpha} + t \left(\frac{J}{\mu}\right)^{2} \sum_{j} \left[ (\alpha_{j}^{\dagger} \mathcal{K}_{\alpha,j} + \text{H.c.}) - \frac{2t}{\mu} \mathcal{K}_{\alpha,j}^{\dagger} \mathcal{K}_{\alpha,j} \right],$$
(10)

where we used the abbreviation for the commutator  $\mathcal{K}_{\alpha,j} := [H_{\alpha}, \alpha_j]/t$ . Equation (10) is formulated for generic oneparticle Hamiltonians  $H_a$  and  $H_b$ . For making concrete statements we will fix them to  $(H_a = H_b \cong H_{\alpha})$ 

$$H_{\alpha} = \sum_{j} \left( -t(\alpha_{j}^{\dagger} \alpha_{j} + \text{H.c.}) + U_{\alpha} n_{j}^{\alpha} n_{j+1}^{\alpha} \right). \tag{11}$$

In this case the commutator  $\mathcal{K}_{\alpha,j}$  amounts to a simple renormalization of the bare parameters in Eq. (11) along with some three-body interactions, density-supported and next-nearest-

neighbor hoppings. From a renormalization point of view these terms can be safely considered to be less relevant. Therefore, we decide to drop them henceforth to keep the model simpler, and leave details for the interested reader in Appendix B.

#### III. BOSONIZATION

We now proceed with a field-theoretical analysis of the toy Hamiltonian (8) via bosonization along the notation of Ref. [26]. After having introduced density and phase fluctuating fields,  $\varphi_{\alpha}$  and  $\vartheta_{\alpha}$ , for both fermionic species,  $\alpha=a,b$ , and their (anti)symmetric combinations  $\varphi_{\pm}=1/\sqrt{2}(\varphi_{a}\pm\varphi_{b})$  (same for  $\vartheta_{\pm}$ ), we find the following Hamiltonian:

$$H_{\text{bos}} = \sum_{\tau = \pm} \frac{v_{\tau}}{2} \int dx K_{\tau} (\partial_{x} \vartheta_{\tau}(x))^{2} + \frac{1}{K_{\tau}} (\partial_{x} \varphi_{\tau}(x))^{2}$$
$$+ \beta_{1} \int dx \cos(\sqrt{8\pi} \vartheta_{-}(x))$$
$$+ \beta_{2} \int dx \cos(\sqrt{8\pi} \varphi_{-}(x)), \tag{12}$$

where  $K_{\tau}$  and  $v_{\tau}$  denote the Luttinger parameter and Fermi velocity in the  $\tau=\pm$  sectors, and we already dropped less relevant terms (see Appendix B), including those becoming resonant only at half filling. We notice that a similar bosonized Hamiltonian appears when considering spinful fermions with anisotropic spin interactions [30], and moreover with  $\beta_2=0$  in other discussions of number-preserving models for Majorana zero modes [17,19].

Besides an ordinary Tomonaga-Luttinger liquid in the symmetric (charge) sector,  $\tau = +$ , which is therefore always gapless, the antisymmetric (spin) sector,  $\tau = -$ , exhibits a double sine-Gordon interaction with bare couplings and scaling dimensions:

$$\beta_1 \propto W_1, \ \Delta_{\beta_1} = \frac{2}{K}; \quad \beta_2 \propto W_2 - U_{nn}, \ \Delta_{\beta_2} = 2K_-.$$
 (13)

It is therefore apparent that a gap will arise whenever  $K_- \neq 1$  [31]: while for  $K_- < 1$  the  $\varphi_-$  field is pinned and the phase is trivially a charge-density-wave or singlet pairing, depending on the sign of the  $\beta_2$  coupling [32], the  $\beta_1$  term causes instead the appearance of unpaired Majorana edge modes for  $K_- > 1$  [19]. Furthermore, the refermionization argument for  $K_- = 2$  given in Ref. [19] also shows that this mode has to be identified with single-particle transitions from one of the two chains to the other.

Therefore, one expects certain overlaps like  $\langle \Omega_{oo} | a_i^{\mathsf{T}} b_j | \Omega_{ee} \rangle$  to be nonzero at the edges with an exponential decay to a possible nonzero bulk value. Otherwise said, the degenerate ground states in the topological phase are related to the ground states of two independent Kitaev-Majorana chains, once projected on a fixed total charge  $N_{+}$  [20]. Thus, using the standard classification of topological insulators, one expect two pairs of MZM to be present in the system, for the unconstrained model, corresponding to the two independent Kitaev-Majorana chains. However, after fixing the total particle number we do not observe  $4 = 2 \times 2$  Majorana modes, but—depending on the total parity  $P_+$ —only two out of the four possible combinations.

The picture of two unconnected chains is particularly useful to get a grasp of some fundamental behavior of single-particle correlation functions, which we will employ as a fingerprint of the desired edge physics. Let us consider the (four) ground states to be connected to

$$\begin{split} |\Omega_{\rm ee}\rangle &= |\Omega\rangle \,, \quad |\Omega_{\rm oo}\rangle = c_{a,E}^{\dagger} c_{b,E}^{\dagger} \, |\Omega\rangle \,, \text{ if } N_{+} \text{ even,} \\ |\Omega_{\rm oe}\rangle &= c_{a,E}^{\dagger} \, |\Omega\rangle \,, \quad |\Omega_{\rm eo}\rangle = c_{b,E}^{\dagger} \, |\Omega\rangle \,, \text{ if } N_{+} \text{ odd,} \end{split} \tag{14}$$

with  $|\Omega\rangle$  being the vacuum of the theory, and  $c_{\alpha,E}$  the fermionic operator formed by two Majorana edge modes,  $c_{\alpha,E}=\gamma_{\alpha,L}-i\gamma_{\alpha,R},\{\gamma_{\alpha,r},\gamma_{\beta,s}\}=2\delta_{\alpha,\beta}\delta_{s,r}$ . The mode expansion reads

$$\alpha_i = A(\gamma_{\alpha,L}e^{-(j-1)/\ell} - i\gamma_{\alpha,R}e^{-(L-j)/\ell}) + \cdots, \qquad (15)$$

with  $\cdots$  denoting the (gapped) excitations of the system,  $\ell$  the correlation length, and A being a normalization factor. For each single chain then holds

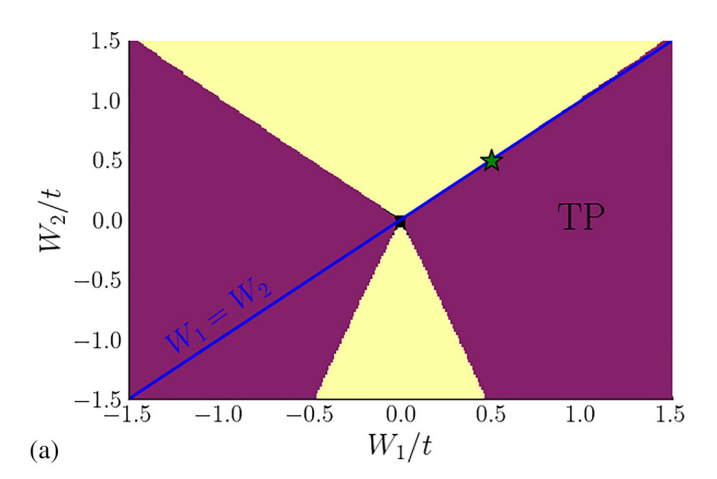
$$\langle \Omega_P | a_1 a_j^{\dagger} | \Omega_P \rangle \sim i A^2 e^{-(L-j)/\ell} \langle \Omega_P | \gamma_L \gamma_R | \Omega_P \rangle + \tilde{G}(j)$$

$$= -P A^2 e^{-(L-j)/\ell} + \tilde{G}(j), \tag{16}$$

where  $P=\pm$  for the even or odd sector, and  $\tilde{G}(j)$  is the exponentially decaying correlation function coming from the residual (gapped) excitations of the spectrum. In Sec. IV we will use this exponential revival of the end-to-end correlation function together with this characteristic relative sign between the two parity sectors as one of the indicators for having a MZM phase. Closely related to that behavior of the correlation function is the vanishing of the energy gap between the two parity sectors:  $\Delta E = |E_- - E_+| \sim e^{-2L/l}$ . A second indicator is provided by studying the entanglement spectrum [33], which should be exactly double degenerate in the case of being in a Majorana-like phase [28].

While working at fixed particle number might circumvent the formation of a charge gap by forbidding hybridization of different fillings (as it is indeed the case in our setup), the spin sector remains instead gapped (see Appendix B). Therefore, we expect an exponentially decaying behavior to the middle of the system, followed by an exponential revival with a  $\pi$ phase difference between the two ground states. The same holds true for matrix elements of interchain operators like the so-called Majorana wave function [20],  $\langle \Omega_{ee} | a_i b_i^{\dagger} | \Omega_{oo} \rangle$ . Since the characteristics are similar for both observables, we decide to only present results for the single-particle correlation functions. This is also motivated from the fact that, in a generic interacting model, the overlap  $\langle \Omega_{\rm ee} | a_i b_i^{\dagger} | \Omega_{\rm oo} \rangle$ may have a nonzero bulk value, making it harder to uniquely identify the edge contribution. This problem is absent for the single-particle correlation function, since  $\langle a_i \rangle$  is fundamentally zero.

In order to determine the most favorable regime of the microscopic parameters for achieving the topological phase, we consider the perturbative renormalization group (RG)



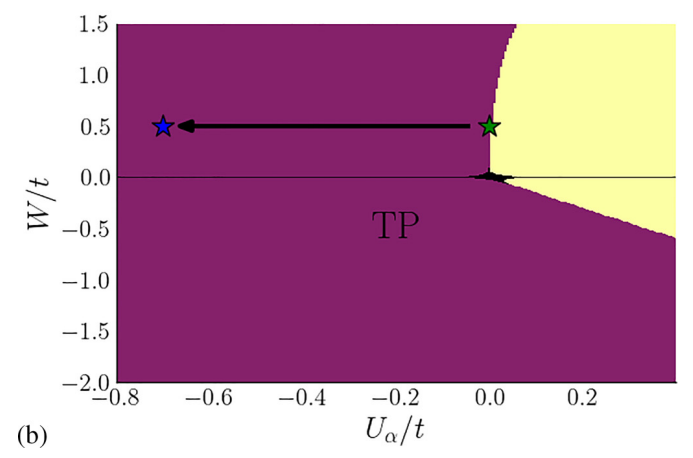


FIG. 2. RG-based estimates of the phase diagram of the bosonized Hamiltonian (12) at  $\nu=1/3$  in different, orthogonal planes, according to the flow equations (17): magenta refers to the dominance of  $\beta_1$  (topological phase), while yellow indicates the dominance of  $\beta_2$  (trivial charge density wave or spin density wave phase). (a)  $W_1$ - $W_2$  plane with  $U_{nn}=U_{\alpha}=0$ : The blue line,  $W_1=W_2=W$ , indicates the effective Hamiltonian (9), for which the prediction depends strongly on cutoff details and, possibly, further orders in the flow. (b) W- $U_{\alpha}$  plane with  $U_{nn}=0$ : by choosing a finite negative  $U_{\alpha}$ , we can move deep inside the topological phase, where RG predictions are unambiguous, as represented by the shift from the green to the blue star. The latter set of parameters is what is used in the main text for the most simulations.

equations (strictly valid only around  $K_{-} \approx 1$ ) [32]:

$$\frac{d\beta_{1}}{dl} = 2\left(1 - \frac{1}{K_{-}}\right)\beta_{1},$$

$$\frac{d\beta_{2}}{dl} = 2(1 - K_{-})\beta_{2},$$

$$\frac{dK_{-}}{dl} = \frac{4\pi^{2}\mathcal{A}}{v_{-}^{2}}\left(\beta_{1}^{2}\frac{1}{K_{-}} - \beta_{2}^{2}K_{-}^{3}\right).$$
(17)

We now have to integrate these differential equations starting from the bare values of  $K_{-}$  and  $\beta_{j}$  on the original lattice couplings, Eq. (B17) (see Appendix B for details). Thereby we get a rough estimation of the phase diagram, presented in Fig. 2: The exact position of the phase boundaries is (highly) dependent on the nonuniversal constant  $\mathcal{A}$ .

Interestingly, anyway, both the very asymmetric role played by  $W_2$  and the strikingly almost straight critical lines in the  $(W_1, W_2, U_\alpha = 0)$  plane can be predicted by the equation

$$|W_1| = D W_2(\operatorname{sgn}(W_2) - C),$$
 (18)

with two nonuniversal constants *D* and *C*. This equation represents the linearized version of the criticality condition found in Ref. [30] (see also Appendix B 1 for more details).

By inspecting Fig. 2, we notice that, in the absence of intrawire interactions ( $U_{\alpha}=0$ ), the line  $W_1=W_2=W$  dictated by Eq. (9) is well inside the topological phase for W<0, while no definite conclusion can be reached on the boundary for W>0. Noticeably, for  $U_{\alpha}<0$  the bare parameters for the RG flow are sensibly pushed away from the boundary, thus making the topological phase observable also for W>0 [see Fig. 2(b)].

We stress here that the extra terms in  $H_{c,d}$  of Eq. (6) are foreseen to contribute to stabilize the topological phase, too. Including nonvanishing couplings  $t_{\parallel}$  and  $t_{\perp}$ , indeed, a regime with  $W_1 > W_2$  can be achieved, which pushes the model deeper into the topological region even for  $U_{\alpha} = 0$ , as can be seen from Fig. 2(a) (see Appendix A for more details).

#### IV. NUMERICAL RESULTS

Next, we validate the cutoff-dependent predictions of bosonization against unbiased numerical simulations on the lattice, performed via matrix product states (MPSs), not only for the effective Hamiltonian (8) but also for the full model (7), i.e., without introducing any perturbative description. We focus on two pristine indicators of the emergence of unpaired Majorana modes at the edges, i.e., (i) finite end-to-end single-particle correlations with an exponential decay in the bulk, with relative  $\pi$ -phase between the two parity sectors, and (ii) double degeneracy of the entanglement spectrum, dictated by the  $\mathbb{Z}_2$  protecting symmetry.

We conduct our numerical investigations at a fixed density of  $v = N_+/(2L) = 1/3$ , so that additional resonances arising at half filling are avoided. As an exemplary parameter set for the effective model we choose

$$\frac{W}{J} = 0.5, \ \frac{U_{\alpha}}{J} = -0.7, \ \frac{U_{nn}}{J} = 0.0,$$
 (19)

with a chain of length L=256 and  $N_+=170$  fermions in the system. The specific choice of  $U_{nn}=0$  was made to simplify the number of parameters to a minimum, without affecting the qualitative picture, as we verified for a wide range of  $U_{nn}$ . Indeed, from a RG point of view, the operator coupled to  $U_{nn}$  only has a minimal influence by slightly detuning the bare Luttinger parameter  $K_-$  and decreasing the bare coupling strength  $\beta_2$  of the bosonized Hamiltonian (see Appendix B). Moreover, this choice is always reachable, at least in this fourth-order effective Hamiltonian description, by suitably tuning the bare interaction parameters  $V_1$  and  $V_2$  relative to  $\mu$  and J.

First, Fig. 3 illustrates the decay of the single-particle terms  $\langle a_1 a_x^\dagger \rangle_\pm$  with correlation length  $\ell \approx 7.35$  and their strong revival at the opposite edge  $r \approx \mp 0.5$ , with the sign depending on the parity sector, as discussed in Sec. III and predicted in Eq. (16). The quantity r is thereby defined as the amplitude of

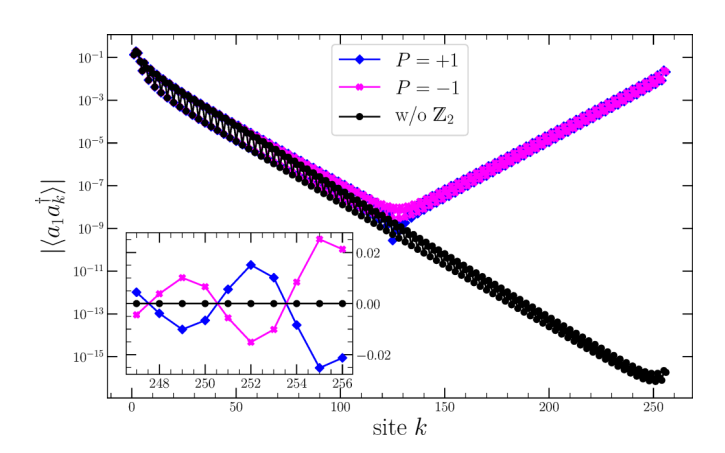
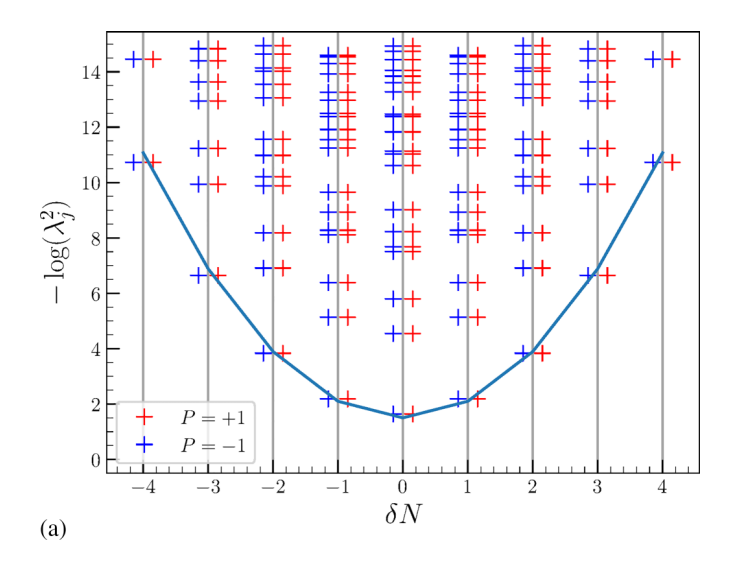


FIG. 3. Single-particle correlation function  $\langle a_1 a_k^{\dagger} \rangle$  between the leftmost site of the chain and the kth one. The magenta and blue lines represent the expectation value to the ground state in the parity sector  $P=\pm$ . The black line displays a simulation neglecting the parity conservation, allowing a superposition between the two different sectors. The inset zooms around the right edge of the chain, revealing the relative  $\pi$  phase between the recovery of the correlation function in the two parity sectors.

an exponential fit performed on both ends of the correlation function. Ignoring the underlying  $\mathbb{Z}_2$  symmetry in the density matrix renormalization group (DMRG) simulation results in a pure exponential decay, indicating an equal weighted superposition of the two (nearly) degenerated ground states of the two parity sectors (see black line in Fig. 3). Such a scenario is confirmed by examining the parity expectation value in this setup,  $\langle P \rangle \approx 0$ . This is an expected behavior, since DMRG favors the least entangled ground state [34–36].

Second, Fig. 4(a) shows the entanglement spectrum [33], i.e.,  $-\ln \lambda_j^2$  with  $\lambda_j$  the Schmidt values of a L/2 bipartition of the system, as a function of the quantum numbers  $\delta N_+ = n_+ - N_+/2$  and  $P_- = (-1)^{n_a}$ . On one hand, the perfect double degeneracy between the two parity sectors is a clear fingerprint of the symmetry-protected topological nature of the antisymmetric channel  $(\tau = -)$  [28]. On the other hand, the parabolic shape (with particle-hole symmetry) indicates the gapless nature of the symmetric channel  $(\tau = +)$  [37,38], with the curvature giving back a Luttinger parameter  $K_+ \simeq 0.97$  [39], pretty close to the bare value of Eq. (B17),  $K_+^{(\text{bare})} \simeq 0.85$ .

Noticeably, from Fig. 5 it can be seen that, even in the presence of this gapless channel, the energy difference between the even and the odd sectors vanishes exponentially, as one would expect for a system with two topological ground states. The finite-size gap inside each parity sector, instead, vanishes algebraically with  $\simeq L^{-1}$  as expected for a standard Luttinger liquid with a linear dispersion relation  $\epsilon_+(q) = v_+|q|$ . Additionally, in Appendix C we show that an adiabatic path exists between our effective model and the exactly solvable one of Ref. [20]. In this article, a path is called adiabatic if the U(1)  $\times \mathbb{Z}_2$  symmetry group is preserved all along that path and the single particle gap, as defined by the antisymmetric sector, stays finite. This is analogous to requiring that we observe a finite correlation length of the single-particle correlation function smaller than the system size along that



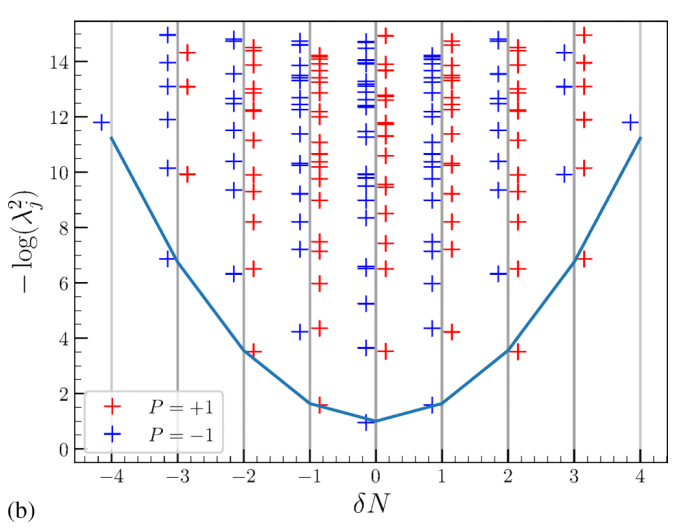


FIG. 4. Entanglement spectrum for a bipartition cutting the system exactly in the middle for a system with 256 sites at filling v=1/3. (a) The system being in the Majorana-like phase with  $W_1/t=W_2/t=0.5$ ,  $U_\alpha/t=-0.7$ , and  $U_{nn}/t=0$ . The spectrum was extracted from the ground state found in the even-parity sector; however, taking the odd-parity-sector ground state is analogous. (b) The system is in the trivial state with  $W_1/t=0.3$ ,  $W_2/t=0.7$ , and  $U_\alpha/t=U_{nn}/t=0$ . The spectrum was extracted from the true ground state given by the odd-parity sector.

path. Constructing such a path requires the insertion of some extra operators, but its cartoon projection in the  $W_1$ - $W_2$ - $U_{nn}$  parameter space is illustrated as a dashed line in Fig. 8. The energy gap, extracted via fitting the exponential decay of single-particle correlation in the bulk, is plotted in Fig. 9(a), and is evidently nonvanishing.

In the same Appendix C, we also demonstrate numerically the adiabatic connection to the two uncoupled Majorana chains by further breaking the residual conservation of the total particle number down to a total parity and only requiring a residual global symmetry group of  $\mathbb{Z}_2 \times \mathbb{Z}_2$ .

After reporting the topological fingerprints found in the effective model, we also studied the full model of Eq. (7) with the single-particle Hamiltonians fixed according to Eq. (11) and showed that the topological phase persists once the full

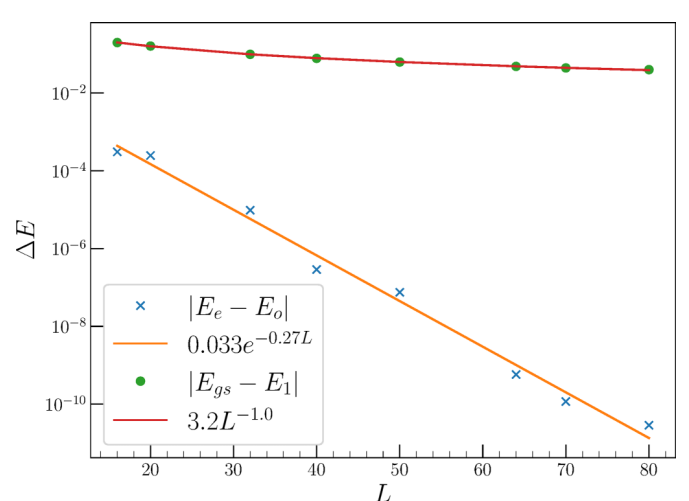


FIG. 5. Scaling of the energy difference between and inside the parity sectors for the parameter set  $W_1/J = W_2/J = 0.5$ ,  $U_\alpha/J = -0.7$ ,  $U_{nn} = 0$  for lengths from 16 to 80 sites and a filling of v = 1/3, i.e.,  $n_e = 2L/3$  particles. The degeneracy split closes exponentially in system size, with a decay length roughly equal to twice the single-particle correlation length l since this splitting originates in the exponential small overlap between the two Majorana wave functions localized at the two ends of the chain [9]. On the other hand, the energy gap to the first excited state vanishes as 1/L originating from the discretization of the momentum in a finite-size system as expected for a well-behaved Luttinger liquid [32] having a linear dispersion relation.

four-flavor Hilbert space is taken into account. For this, we studied at the same indicators as reported above, namely, the nonlocal correlation functions with the characteristic relative sign between the two parity sectors as predicted by Eq. (16) and the double degeneracy of the low-lying entanglement spectrum. As a warmup we treated the model with a set of parameters deep inside the perturbative regime of the effective Hamiltonian. The results are reported in Appendix E, where we indeed find the full model to have nonlocal correlation functions as expected. Nonetheless, the parameters in this regime are not so appropriate to experimental realizations with interaction strengths of several orders of magnitude in difference.

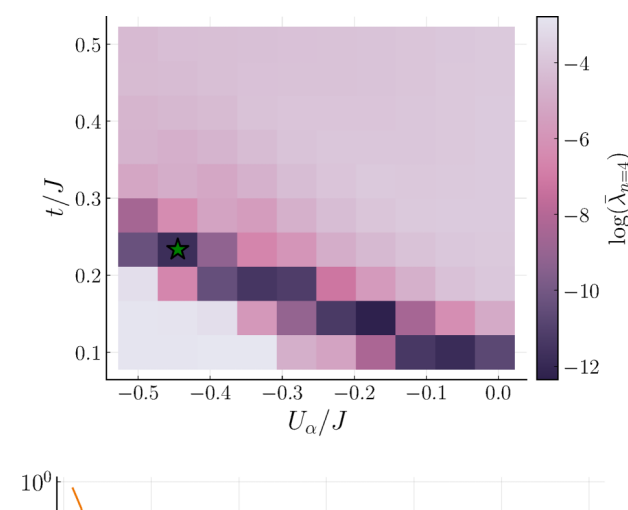
However, we can do better by going away from the perturbative regime. Indeed, we showed that the Majorana-like phase is not bounded to the perturbative regime, but is considerably extended to a more realistic parameters, where we find a double degenerated entanglement spectrum and non-local correlation functions for a large range of parameters.

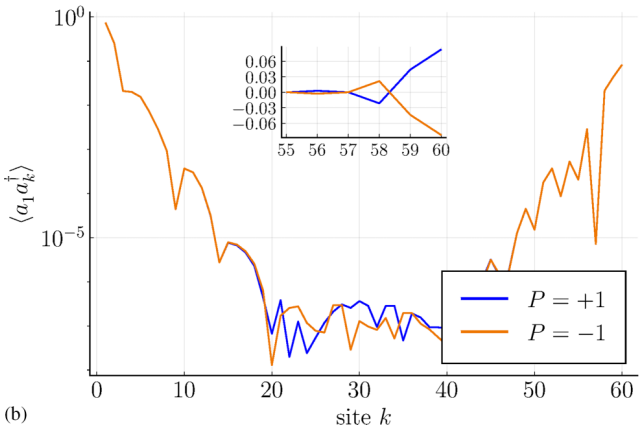
As an example consider Fig. 6(a). In this figure we computed the average degeneracy of neighboring Schmidt values of the low-lying entanglement spectrum for a cut at half of the system of length L=60,

$$\bar{\lambda} = \frac{1}{n} \sum_{i=1}^{n} |\lambda_{2j-1} - \lambda_{2j}|,\tag{20}$$

computed by fixing the following set of parameters:

$$n_e = 80, \quad \mu/J = 2, \quad V_1/J = -1,$$
  
 $V_2/J = 1.25, \quad t_{\parallel} = 0.1t, \quad t_{\perp} = 0,$ 





(a)

FIG. 6. Analysis of the full model. (a) Logarithm of the average degeneracy of neighboring Schmidt values of the low-lying entanglement spectrum from Eq. (20) taking n=4. Taking the logarithm was motivated to highlight values near zero. (b) One example end-to-end correlation function plotted for t= and  $U_{\alpha}=$  [green star in panel (a)]. The inset shows a zoom onto the last few sites showing the relative  $\pi$  phase for the revival of both symmetry sectors.

$$t/J = \in [0.1, 0.5], \quad U_{\alpha}/J \in [-0.5, 0].$$

Noticeably, there seems to be an overall separatrix region of nearly vanishing  $\bar{\lambda}$  between two regions having a finite splitting between the neighboring entanglement values. Along that set of parameters we expect the Majorana-like phase to appear: This is confirmed by the end-to-end correlation function showing the characteristic  $\pi$ -phase revival [see Fig. 6(b) as one example]. Furthermore, we stress here that this result is not sensitive to the concrete choice of the chemical potential and the filling. We have explicitly checked it for all  $\mu/J \in [2,5]$  and also for  $n_e=40$ , which corresponds to the 1/3 filling in the effective model.

As a final remark we want to discuss possible experimental platforms. We emphasize that the crucial ingredient in realizing our proposal is the cylindrical-like structure defined by the rhombi Hamiltonian  $H_{\Diamond}$ , Eq. (1). The requirement of having periodic boundary conditions along one direction together with imprinting an effective phase is usually a hard task in physical setups. Recently this task was achieved by using the internal degrees of freedom of cold atoms as synthetic dimensions and imprinting arbitrary gauge fluxes to the atoms [40,41]. Together with the good controllability of hopping

transition by loading the cloud of atoms to an optical lattice [42–45] and the reliability of species with sizable nearest-neighbor interactions such as polar atoms [46–48], cold atoms are suggested as the perfect platform, but also other synthetic platforms could be valid. However, a concrete realization goes beyond the scope of this article.

#### V. CONCLUSION AND OUTLOOK

Motivated by the ongoing search for an unambiguous detection of topological Majorana zero modes, we have put forward a new number-conserving realization of a Majorana-like phase. Our proposal uses the geometry of the underlying lattice together with the Aharonov-Bohm effect to achieve exact cancellation of all possible single-particle processes and only allow for pair transitions.

Starting from a perturbative analysis, we found clear fingerprints of a Majorana-like phase with Majorana zero modes being present in an extended parameter regime. We also showed that this is still true in the full model far away from the perturbative regime, thus raising the hope for realizations using synthetic dimensions in a cold-atom platform. Due to the large amount of possible parameters to tune, we postpone the development of a concrete scheme together with an experimentally reachable parameter space to future work.

Among the important open questions for all possible quasione-dimensional number-conserving setups, the influence of finite temperature on the Majorana zero modes plays an important role. To be concrete, it is unclear how possible higher-order terms in the bosonization may couple the symmetric gapless sector to the antisymmetric gapped sector hosting the Majorana zero modes. Such effects could lead to a much smaller lifetime of the MZM than expected from the limit of two unconnected Kitaev-Majorana chains. This will be the subject for future investigations.

#### **ACKNOWLEDGMENTS**

We thank M. Burello, R. Egger, A. Haller, and M. Köhl for inspiring discussions about theoretical and experimental aspects of this work. We also want to warmly acknowledge a fruitful exchange with F. Lisandrini and C. Kollath, working on a different scheme for the same scope [49]. This work has been funded by the Deutsche Forschungsgemeinschaft (DFG, German Research Foundation) under Germany's Excellence Strategy–Cluster of Excellence Matter and Light for Quantum Computing (ML4Q) EXC 2004/1 – 390534769, and under Project Grant No. 277101999, within the CRC network TR 183 (Subproject No. B01).

## APPENDIX A: DERIVATION OF THE EFFECTIVE HAMILTONIAN

In this Appendix, we briefly recall the basics of the Schrieffer-Wolff (SW) transformation in the version of Ref. [25], which we used to derive the effective model of Eqs. (8) and (9). Furthermore, we discuss the effect of the extra terms  $(t_{\parallel}, t_{\perp})$  of Eq. (6), showing that they may lead to an even more convenient regime for the topological phase to arise.

In the SW formalism, the Hamiltonian is considered to be divided between a block-diagonal noninteracting part  $H_0$  with a clear energy-scale separation, and some small interaction V, i.e.,

$$H = H_0 + V,$$
  

$$H_0 = P_{\mathcal{P}} H_0 P_{\mathcal{P}} + P_{\mathcal{Q}} H_0 P_{\mathcal{Q}},$$
  

$$V = P_{\mathcal{P}} V P_{\mathcal{O}} + P_{\mathcal{O}} V P_{\mathcal{P}} + P_{\mathcal{O}} V P_{\mathcal{O}},$$

where  $\mathcal{H}=\mathcal{P}\oplus\mathcal{Q}$  denotes the division of the Hilbert space such that

$$||P_{\mathcal{P}}H_0P_{\mathcal{P}}|| \ll ||P_{\mathcal{Q}}H_0P_{\mathcal{Q}}||,$$
  
 $||V|| \ll (||P_{\mathcal{O}}H_0P_{\mathcal{O}}|| - ||P_{\mathcal{P}}H_0P_{\mathcal{P}}||),$ 

in the sense that all eigenvalues from the  $\mathcal{P}$  subspace are much smaller than the eigenvalues from the  $\mathcal{Q}$  subspace, and that the matrix elements of the V operator are much smaller than the energy separation between the two subspaces. We recall that a possible term  $P_{\mathcal{P}}VP_{\mathcal{P}}$  can be set to zero without loss of generality. The target SW transformation is a rotation X of the Hilbert space, such that the Hamilton operator is brought back to a block-diagonal form under its action:

$$H' = X^{-1}(H_0 + V)X = P_{\mathcal{P}}H'P_{\mathcal{P}} + P_{\mathcal{O}}H'P_{\mathcal{O}}.$$
 (A1)

The desired effective low-energy Hamilton operator is then given by

$$H_{\text{eff}} = P_{\mathcal{P}} H' P_{\mathcal{P}}. \tag{A2}$$

While X, and thus  $H_{\rm eff}$ , are only known exactly for a few special cases, there exists a perturbative solution in terms of powers of the interaction V, with terms in the typical form

$$\hat{O}^{(n)} = P_{\mathcal{P}}V \left(P_{\mathcal{Q}} \frac{1}{E_0 - P_{\mathcal{Q}}H_0P_{\mathcal{Q}}} P_{\mathcal{Q}}V\right)^n P_{\mathcal{P}},\tag{A3}$$

and variations thereof, especially in case the original lowenergy subspace is not exactly degenerate, i.e., if not all states in  $\mathcal{P}$  share the same eigenvalue  $E_0$  under  $H_0$ . Anyway, we can easily identify the Green operator  $\hat{G}(\omega)$  restricted to the high-energy space  $\mathcal{Q}$  and evaluated at  $E_0$ :

$$\hat{G}_{\mathcal{Q}}(E_0) = P_{\mathcal{Q}} \frac{1}{E_0 - P_{\mathcal{Q}} H_0 P_{\mathcal{Q}}} P_{\mathcal{Q}}, \tag{A4}$$

a fact which will come in handy in the following.

In our specific setup, we chose

$$H_0 = H_{\text{c.d}} + H_{\text{int}},\tag{A5}$$

i.e., the Hamiltonian acting on the auxiliary sites. Thereby, it is easy to identify the low-energy space  $\mathcal P$  as the one containing all states with empty c and d sites, while the high-energy configurations  $\mathcal Q$  are all the remaining ones with at least one fermion placed on these auxiliary sites. As a consequence,  $E_0=0$  and the energy separation is of the order of  $\mu$ . As long as  $t_\parallel=t_\perp=0$ ,  $H_0$  is already diagonal in the Fock basis, and this allows for an exact evaluation of  $\hat G_{\mathcal Q}(E_0)$ , leading to the compact expressions of Eqs. (8) and (9).

If we now include such terms, i.e.,  $t_{\parallel}$ ,  $t_{\perp} \neq 0$ , this is not true anymore since a fermionic excitation on the c and d states is now allowed to delocalize across the auxiliary sites. Fortunately, we can still evaluate  $\hat{G}_{\mathcal{Q}}(E_0)$  if we restrict for a

moment to the case in which at most one fermionic state in the c and d sites can be occupied. The matrix elements of this operator decay exponentially in real space. This in turn leads to an additional exponentially decaying hopping in the a,b chains of the form

$$H_{t,\exp} = \sum_{j,l,\alpha} -t'_{\alpha} \gamma_{\alpha}^{|j-k|} \alpha_{j}^{\dagger} \alpha_{k} + \text{H.c.}, \ \gamma_{\alpha} < 1,$$

$$t'_{\alpha} = \frac{2J^{2}}{\sqrt{\mu^{2} - 4(t_{\parallel} \pm t_{\perp})^{2}}},$$

$$\gamma_{\alpha} = \frac{1}{2(t_{\parallel} \pm t_{\perp})} \{\mu - \sqrt{\mu^{2} - 4(t_{\parallel} \pm t_{\perp})^{2}}\}, \tag{A6}$$

where the - (+) holds for  $\alpha=a$  (b). However, the fourth-order term in the Schrieffer-Wolff transformation, which generates the desired pair-hopping term, requires to deal with two fermions on the c and d sites, and therefore to solve the full interacting problem. However, an analytic solution is not that easy any more. Anyway, in the limit of  $t_{\parallel}$ ,  $t_{\perp} \ll \mu$  (consistently with all other energy scales of the setup), one can treat them as small perturbations and compute the Green operator perturbatively. The sizable diagonal elements are responsible for the generation of the pair-hopping terms, while the off-diagonal contributions are again exponentially suppressed. We finally arrive at the expression

$$W'_{j} = W(1 + (t_{\parallel}, t_{\perp})\Gamma_{j}(t_{\parallel}, t_{\perp})^{T}) + \mathcal{O}(t_{\parallel}^{4}, t_{\perp}^{4}), \tag{A7}$$

where  $\Gamma_j$  are  $2 \times 2$  matrices, depending on all other parameters, with  $\Gamma_1 \neq \Gamma_2$ , which allows for detuning  $W_1 \neq W_2$ . In Fig. 7 some examples for  $W_j(t_{\parallel}, t_{\perp})$  are shown. Moreover, a third pair coupling operator is generated:

$$H_{W_3} = (t_{\parallel}, t_{\perp}) \Gamma_3(t_{\parallel}, t_{\perp})^T \sum_j a_j^{\dagger} a_{j+1} b_j^{\dagger} b_{j+1} + \text{H.c.}$$
 (A8)

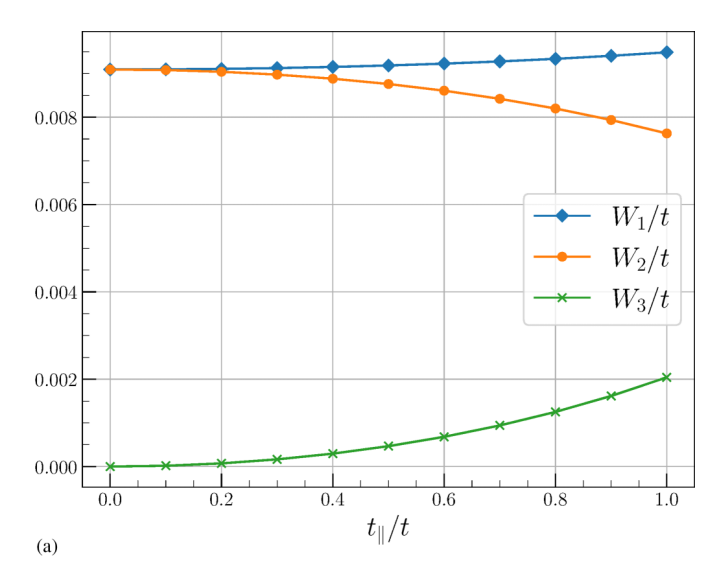
This was also one of the reasons to consider the slightly more general toy model of Eq. (8) where one finds the relation  $W_3 = (t_{\parallel}, t_{\perp}) \Gamma_3(t_{\parallel}, t_{\perp})^T$ . The possibility of detuning  $W_1$  relative to  $W_2$  and also the generation of  $W_3$  shifts the effective model near the vicinity of the exactly solvable model [20], for which the relation  $W_2 = W_3 = W_1/2$  holds. Comparing to Fig. 7, indeed, we see that introducing  $t_{\parallel}$  increases  $W_1$  relative to  $W_2$  and also introduces a positive  $W_3$ .

#### APPENDIX B: BOSONIZATION DETAILS

In this Appendix, we provide the details of the derivation of the bosonized low-energy theory and its bare couplings in terms of the microscopic parameters. The starting point is the effective Hamiltonian of Eq. (8). In order to keep the equations simple, we start here by using the simplified single-chain Hamiltonian from the main text:

$$\widetilde{H}_{\alpha} = \sum_{i} \left( -t(\alpha_{j}^{\dagger} \alpha_{j} + \text{H.c.}) + U_{\alpha} n_{j}^{\alpha} n_{j+1}^{\alpha} \right).$$
 (B1)

However, towards the end of this Appendix we will shortly discuss additional operators which are generated by the Schrieffer-Wolff transformation. The first step is to rewrite the lattice annihilation and creation operators  $\alpha^{(\dagger)}$  in terms of two (slowly varying) envelope functions  $\psi_{R/L,\alpha}$  defining the right



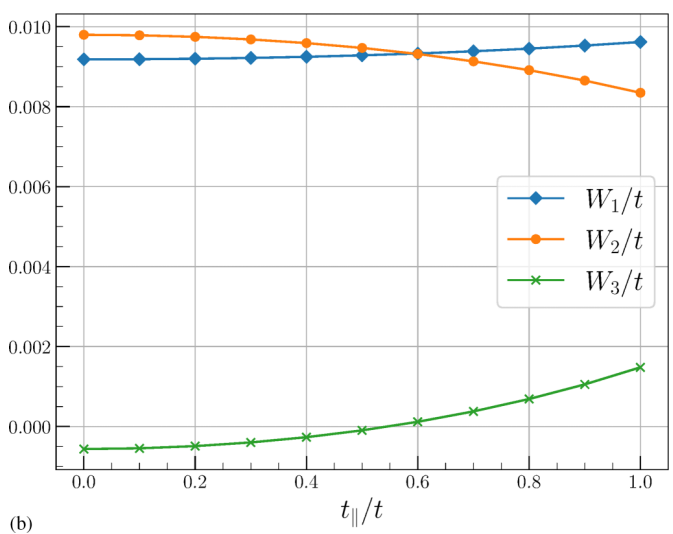


FIG. 7. Dependence of the effective parameters  $W_1$ ,  $W_2$ , and  $W_3$  for (a)  $t_{\perp}/t = 0$  and (b)  $t_{\perp}/t = 0.5$ . The other parameters are chosen to be  $V_1/t = 1$ ,  $V_2/t \approx -0.83$ .

and left moving fields:

$$\alpha_j = \sqrt{a} \left( \psi_{\alpha,R}(x_j) e^{ik_F x_j} + \psi_{\alpha,L}(x_j) e^{-ik_F x_j} \right).$$
 (B2)

The "continuum" position  $x_j$  is defined as  $x_j \coloneqq aj$ , with a the lattice spacing, in terms of which we will express all quantities (like lengths, energies, etc.) in the following. The Fermi momentum is defined by  $k_{\rm F} = \frac{N\pi}{2La}$ , with N being the number of fermions and L the number of lattice sites in the system. In order to formulate a theory in the continuum, we send  $a \to 0$  while keeping constant the product  $ak_{\rm F} \coloneqq \delta = \pi \, v$ , as well as all energies  $ta, U_{\alpha}a, \ldots$ . This also amounts to replacing sums by integrals according to the rule  $a\sum_j \to \int dx$ . Henceforth, we will also remove any residual explicit dependence on the lattice spacing by appropriately rescaling the fields and the coupling constants for better readability.

The next step is the assumption of linearity for the fermionic dispersion relation near the (two) Fermi points. The right- and left-moving fields become thus independent from each other, and the free fermion Hamiltonian is written as

$$H_0 = \sum_{\alpha=a,b} \int dx \, h_{0,\alpha}(x)$$
:

$$h_{0,\alpha}(x) = -iv_{\rm F}[\psi_{\alpha,R}^{\dagger}(x)\partial_x\psi_{\alpha,R}(x) - \psi_{\alpha,L}^{\dagger}(x)\partial_x\psi_{\alpha,L}(x)],$$
(B3)

where  $v_{\rm F}=2t\sin(\delta)$  defines the Fermi velocity. The independent left- and right-moving fields are then rewritten in terms of vertex operators of continuous bosonic fields  $\varphi_{\alpha}(x)$  and  $\vartheta_{\alpha}(x)$ , describing respectively the density and phase fluctuations:

$$\psi_{\alpha,\sigma} = \frac{\eta_{\alpha,\sigma}}{\sqrt{2\pi}} \exp(-i\sqrt{\pi}(\vartheta_{\alpha} + s_{\sigma}\varphi_{\alpha})),$$

$$n^{\alpha}(x) := \psi_{\alpha,R}^{\dagger}\psi_{\alpha,R} + \psi_{\alpha,L}^{\dagger}\psi_{\alpha,L} = -\frac{1}{\sqrt{\pi}}\partial_{x}\varphi_{\alpha}(x),$$

$$\partial_{x}\vartheta_{\alpha}(x,t) = -\partial_{v_{F}t}\varphi_{\alpha}(x,t),$$
(B4)

with  $s_{\sigma} = +1$  if  $\sigma = R$  (and -1 for L), and the latter relation defined in the Heisenberg picture with explicit time-dependent operators. It is particularly useful to recall also the expression for the current densities:

$$J_{\sigma}^{\alpha}(x) = -\frac{1}{\sqrt{4\pi}} \partial_x \{ \varphi_{\alpha}(x) + s_{\sigma} \vartheta_{\alpha}(x) \}.$$
 (B5)

The Klein factors  $\eta_{\alpha,\sigma}$ , forming a Clifford algebra (i.e.,  $\{\eta_{\alpha,\sigma},\eta_{\beta,\rho}\}=2\delta_{\alpha,\beta}\delta_{\sigma,\rho}$ ), are essential to obtain the correct anticommuting behavior of the fermionic operators [27]. However, thanks to the particle-number-preserving character of the Hamiltonian, we can simply treat them as simple Hermitian matrices and reorder their strings to be the same in all terms; henceforth, we consider to have already performed such a reordering and drop all Klein factors from our formulas

Subsequently, we rewrite the different lattice operators in terms of the bosonic fields, according to the dictionary presented in Eqs. (B4) and (B5), and taking care of normal ordered products along standard procedures [32]. One major consequence is that, in most cases, the algebra amounts to directly summing the exponents appearing in Eq. (B4) when dealing with products of  $\psi^{(\dagger)}$  fields. Since all terms turn out to be diagonal in the bosonic fields, and we are considering identical (a,b) species, it is convenient to resort to symmetric and antisymmetric combinations of the fields:

$$\varphi_{\pm}(x) = \frac{1}{\sqrt{2}}(\varphi_a(x) \pm \varphi_b(x)). \tag{B6}$$

The free Hamiltonian and the intrachain interactions are thereby well known to be mapped to a quadratic form:

$$H_0 = \sum_{\tau \to 1} \frac{v_{\tau}}{2} \int dx \, K_{\tau} (\partial_x \vartheta_{\tau}(x))^2 + \frac{1}{K_{\tau}} (\partial_x \varphi_{\tau}(x))^2, \quad (B7)$$

with  $v_{\tau}$  and  $K_{\tau}$  the Fermi velocity and the so-called Luttinger parameter in each sector. These are equal to  $v_F$  and 1 in the free case, and get renormalized by the interactions. Indeed, the representation of the lattice number operator reads

$$\alpha_i^{\dagger} \alpha_i / a = \dots \approx n^{\alpha}(x) + O_{\text{CDW}}^{\alpha} + O_{\text{CDW}}^{\alpha \dagger}$$
 (B8)

with  $O_{\text{CDW}}^{\alpha} = \psi_{\alpha,R}^{\dagger}(x_j)\psi_{\alpha,L}(x_j)e^{-i2k_{\text{F}}x_j}$  accounting for charge density waves. By integrating their product on neighboring sites over the whole lattice, all oscillating terms will average

out unless we are at half filling, and we are left with

$$U_{\alpha} \sum_{j} n_{j}^{\alpha} n_{j+1}^{\alpha} \longrightarrow U_{\alpha} \int dx \left( J_{R}^{\alpha} + J_{L}^{\alpha} \right)^{2} - 2\cos(2\delta) J_{R}^{\alpha} J_{L}^{\alpha}$$

$$= \frac{1}{2\pi} \int dx \, g_{U,\vartheta} (\partial_{x} \vartheta_{\alpha})^{2} + g_{U,\varphi} (\partial_{x} \varphi_{\alpha})^{2}$$
 (B9)

with the following coefficients:

$$g_{U,\vartheta} = U_{\alpha} \cos(2\delta),$$
  

$$g_{U,\varphi} = U_{\alpha}(2 - \cos(2\delta)).$$
(B10)

By applying the same procedure to the total unit-cell interaction, the interchain terms give rise to an extra sine-Gordon interaction involving the field  $\varphi_-$ , originating from scattering terms of the form

$$\hat{O}(x) = \psi_{a,R}^{\dagger}(x)\psi_{a,L}(x)\psi_{b,L}^{\dagger}(x)\psi_{b,R}(x) + \text{H.c.}$$
 (B11)

The bosonized expression reads

$$H_{\rm nn} \longrightarrow \frac{1}{2\pi} \sum_{\tau=\pm} \int dx \, g_{{\rm nn},\vartheta,\tau} (\partial_x \vartheta_\tau)^2 + g_{{\rm nn},\varphi,\tau} (\partial_x \varphi_\tau)^2$$
$$- \frac{U_{nn} \cos(2\delta)}{\pi^2} \int dx \, \cos(\sqrt{8\pi} \varphi_-) \tag{B12}$$

with coefficients

$$g_{\text{nn},\vartheta,+} = -g_{\text{nn},\varphi,-} = g_{\text{nn},\vartheta,-} = U_{nn}\cos(2\delta),$$
  
 $g_{\text{nn},\varphi,+} = U_{nn}(4 - \cos(2\delta)).$  (B13)

Finally, we can also translate the pair-hopping terms by similar algebra, and obtain

$$H_{W_1} \longrightarrow -\frac{2\sin^2(\delta)W_1}{\pi^2} \int dx \cos(\sqrt{8\pi}\vartheta_-), \qquad (B14)$$

$$H_{W_2} \longrightarrow \frac{1}{2\pi} \sum_{\tau=\pm} \tau \int dx \, g_{W,\vartheta} (\partial_x \vartheta_\tau)^2 + g_{W,\varphi} (\partial_x \varphi_\tau)^2 + \frac{W_2}{\pi^2} \int dx \, \cos(\sqrt{8\pi}\varphi_-), \qquad (B15)$$

with coefficients

$$g_{W,\vartheta} = 2W_2 \sin^2(\delta),$$
  

$$g_{W,\varphi} = 2W_2 \cos^2(\delta).$$
(B16)

Noticeably, the two kinds of pair hoppings give rise to sine-Gordon terms for the two conjugate bosonic fields: it will be the one in  $\vartheta_-$  which will be responsible for the topological phase, while the one in  $\phi_-$  is already present with other types of density interactions between the two chains. The sine-Gordon term involving  $\phi_-$  favors the formation of either a spin density wave or charge density wave, depending on the sign of the coupling [32].

By putting all these contributions together, we get to Eq. (12) with the bare couplings of the low-energy theory expressed in terms of those of the microscopic lattice

Hamiltonian:

$$\kappa_{\tau} = \frac{1}{2\pi} (\pi v_{F} + g_{U,\varphi} + g_{nn,\varphi,\tau} + \tau g_{W,\varphi}),$$

$$\xi_{\tau} = \frac{1}{2\pi} (\pi v_{F} + g_{U,\vartheta} + g_{nn,\vartheta,\tau} + \tau g_{W,\vartheta}),$$

$$K_{\tau}^{2} = \frac{\xi_{\tau}}{\kappa_{\tau}}, \quad v_{\tau}^{2} = 4\kappa_{\tau}\xi_{\tau},$$

$$\beta_{1} = -\frac{2W_{1}\sin^{2}(\delta)}{\pi^{2}}, \quad \beta_{2} = \frac{W_{2} - \cos(2\delta)U_{nn}}{\pi^{2}}.$$
(B17)

In order to determine the actual phase the system will end up in, such bare couplings should be analyzed from the renormalization group (RG) perspective, i.e., by integrating out short-distance degrees of freedom and retaining the long-distance ones only, thus moving from a full quantum action to a low-energy effective one.

#### 1. RG flow

The RG flow is controlled by the flow parameter l, representing the effective momentum cutoff in terms of the overall ultraviolet one via  $\Lambda_{\rm UV}/\Lambda \simeq 1+dl$ . At first order, the equations for the sine-Gordon couplings  $\beta_k$ , with k=1,2, are determined by their scaling dimension  $\Delta_k$ :

$$\frac{d\beta_k(l)}{dl} = (2 - \Delta_k)\beta_k(l). \tag{B18}$$

If a coupling flows to  $\infty$  for  $l \to \infty$ , then the theory acquires a gap, and the coupling is dubbed relevant: this happens if  $\Delta_k < 2$ . One should actually stop the flow when the value overcomes the cutoff, and one could then estimate thereby the value of the gap. If instead the scaling dimension is large,  $\Delta_k > 2$ , the coupling is irrelevant, since it flows to zero and disappears from the effective theory. In the limiting case,  $\Delta_k = 2$ , the coupling is labeled as marginal, and higher orders are required to find out its actual behavior. In our Eq. (12) we find the common result  $\Delta_1 = 2/K_-$  and  $\Delta_2 = 2K_-$  [32]: while  $K_+$  does not flow at all, and the symmetric sector remains gapless in all cases, we should resort to higher orders of perturbation theory to inspect the flow of  $K_-$ , at least around  $K_- \approx 1$ ,

$$\frac{dK_{-}}{dl} = \frac{4\pi^{2} \mathcal{A}}{v^{2}} \left( \beta_{1}^{2} \frac{1}{K_{-}} - \beta_{2}^{2} K_{-}^{3} \right), \tag{B19}$$

where  $\mathcal{A}$  is some cutoff-dependent constant. No additional contribution to the flow of the  $\beta_k$  couplings is generated at second order, and thus the set of Eqs. (B18) and (B19) is consistent.

Similar RG flow equations have been studied in the past, and it has been shown that all points on the plane defined by

$$\frac{v_{-}}{\pi\sqrt{A}}(K_{-}-1) - |\beta_{2}| + |\beta_{1}| = 0$$
 (B20)

flow to a critical model [30]. Upon inserting the bare values of  $K_{-}$  and  $\beta_{j}$  in terms of the original lattice couplings, Eq. (B17), and linearizing the dependence of  $v_{-}$  and  $K_{-}$  on small  $W_{2}$  values, the criticality condition can be recast, for  $U_{\rm nn}=0$ , as

$$|W_1| = D W_2(\operatorname{sgn}(W_2) - C)$$
 (B21)

with two nonuniversal constants  $D=\pi^2/(2\sin^2\delta)$  and  $C=\cos(2\delta)/(\pi^2\sqrt{\mathcal{A}})$  (in the case of  $U_\alpha=0$ ). Therefore, we expect a pretty different behavior depending on the sign of  $W_2$ , while a symmetry in  $W_1$  should appear. For example, inserting all numbers we would expect a slope  $\alpha_+=1$  ( $\alpha_-=-1/3$ ) in the case of  $W_2>0$  ( $W_2<0$ ), which perfectly matches the observed slope in Fig. 2(a). The same equation can also be used to predict the behavior of the critical lines in the  $W_1=W_2=W$  and  $U_\alpha$  phase diagram of Fig. 2(b). However, the equations are not compact and easy to write. But for the choice of the nonuniversal constant  $\mathcal A$  used for the numerical integration one finds a leading-order linear behavior for W<0 and a quadratic leading order for W>0, matching the numerical observations.

We tested these predictions by numerically integrating the differential equations (B18) and (B19) starting from the bare values of the couplings, up to a point where one of the two  $\beta_k$  coupling constants reaches a certain cutoff value  $\beta_k(l_*)=c$ . This indicates the formation of a spectral gap of one or the other kind, which can be estimated according to  $\Delta \sim e^{-l_*}$ . The precise predictions depend on the nonuniversal constant  $\mathcal A$  appearing in the flow equations, too; nevertheless, we can use them for a rough estimation of the phase diagram, presented in Fig. 2. The (asymmetric) linearity of the boundaries is evidently kept up to fairly large values of the W couplings.

#### 2. Two Kitaev chains

In the context of the adiabatic connection between our model and the situation of two independent Kitaev chains (which will be deepened in Appendix C), it is worth briefly mentioning the bosonization of the pair-hopping operator acting equally on the two chains:

$$H_{\Delta} = \sum_{j,\alpha} \Delta \alpha_j^{\dagger} \alpha_{j+1}^{\dagger} + \text{H.c.}$$
 (B22)

By using the recipe exposed above, one finds

$$H_{\Delta} \longrightarrow -g_{\Delta} \sum_{\alpha} \int dx \cos(\sqrt{4\pi} \vartheta_{\alpha}(x))$$

$$\sim \int dx \cos(\sqrt{2\pi} \vartheta_{+}(x)) \cos(\sqrt{2\pi} \vartheta_{-}(x))$$
(B23)

with  $g_{\Delta} = 2\Delta \sin(\delta)/\pi$ . In a situation where the  $\vartheta_{-}$  field is already locked, as in the topological phase through the  $H_{W_1}$  operator,  $H_{\Delta}$  is basically the operator  $\cos(\sqrt{2\pi}\vartheta_{+}(x))$ . The scaling dimension of this operator is given by  $\Delta = (2K_{+})^{-1}$ ; i.e., as long as  $K_{+} > 1/4$ , this operator becomes relevant and gaps out the charge sector.

#### 3. Irrelevance of additional effective terms

As promised at the beginning of this long Appendix, we want to justify our assumption of dropping all the additional terms which appear in the effective single-chain Hamiltonians  $\widetilde{H}_{\alpha}$ . As a starting point, the single-chain Hamiltonians of the full model are chosen as the usual spinless Fermi-Hubbard Hamiltonian consisting of a hopping term and a

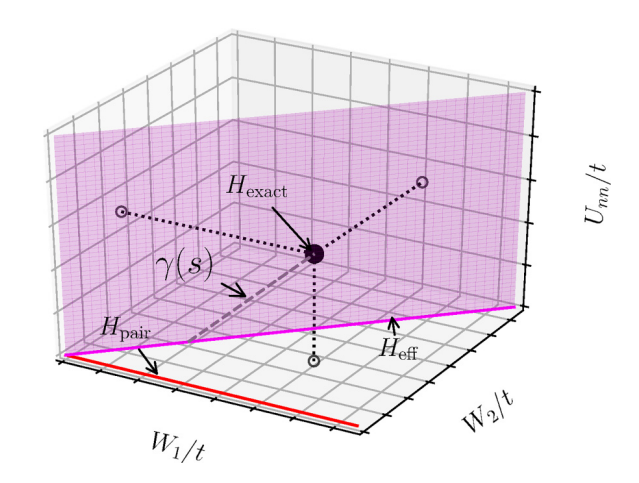


FIG. 8. Relation of the parameter space of Eq. (8) to some related works in the literature. The model of Ref. [17] spans the red line at  $W_2 = W_3 = U_{nn} = 0$ ; the effective model in Eq. (9) spans the magenta plane at  $W_2 = W_1$ ,  $W_3 = 0$ ; and the black dot indicates the exactly solvable model of Ref. [20] at  $W_2 = W_3 = U_{nn} = W_1/2$ . However, since the last lives in a higher-dimensional space, this is to be understood as a cartoon, rather than an exact statement.

nearest-neighbor interaction term:

$$H_{\alpha} = \sum_{j} \left( -t(\alpha_{j}^{\dagger} \alpha_{j} + \text{H.c.}) + U_{\alpha} n_{j}^{\alpha} n_{j+1}^{\alpha} \right).$$
 (B24)

The commutators  $\mathcal{K}_{\alpha,j} = [H_{\alpha}, \ \alpha_j]/t$  can be readily computed to be

$$\mathcal{K}_{\alpha,j} = \alpha_{j+1} + \alpha_{j-1} - \frac{U_{\alpha}}{t} \left( \alpha_j n_{j+1}^{\alpha} + n_{j-1}^{\alpha} \alpha_j \right)$$
 (B25)

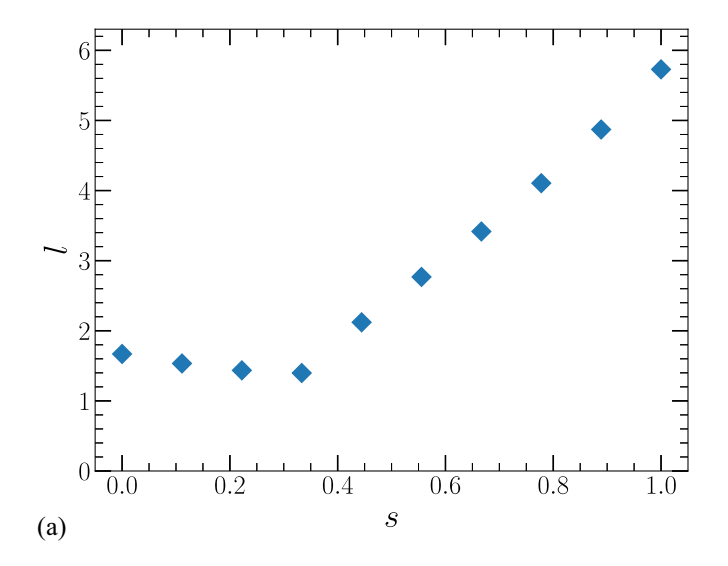
and inserted into Eq. (10): while  $\alpha_j^{\dagger} \mathcal{K}_{\alpha,j} + \text{H.c.}$  will only redefine the effective values of t and U, the product  $\mathcal{K}_{\alpha,j} \mathcal{K}_{\alpha,j}$  will also generate three-body terms  $(n_{j-1} n_j n_{j+1})$ .

In general, the lowest order of an operator consisting of N fermionic densities is given in bosonization by a power-N operator  $\sim (\partial_x \varphi_\alpha)^N$ . The scaling dimension of these operators can be shown to be  $\Delta_N = N$ ; i.e., their flow equations are of the form  $d\beta_N/dl = (2-N)\beta_N$ . Thus, these operators become surely irrelevant for all  $N \geqslant 3$ .

In addition to these N-power operators, also some higher-order harmonic cosine terms might appear, i.e.,  $\cos(n\sqrt{4\pi}\varphi_{\alpha})$ . However, their scaling dimension is a monotonic increasing function of n, meaning that the most relevant operator is given by the first harmonic n=1. Nevertheless, with increasing interaction strength these higher-order harmonics might become relevant, if  $K_{\pm} \ll 1$ ; however, this is by far not the scenario we are considering in this paper.

## APPENDIX C: ADIABATIC CONNECTION TO EXACTLY SOLVABLE MODELS

In this Appendix, we provide details about the two paths in parameter space we chose for illustrating the adiabatic connection between our effective model in Eq. (8) and (i) the exactly solvable one of Ref. [20] or (ii) the setup with two uncoupled noninteracting Majorana chains. In Fig. 8 we



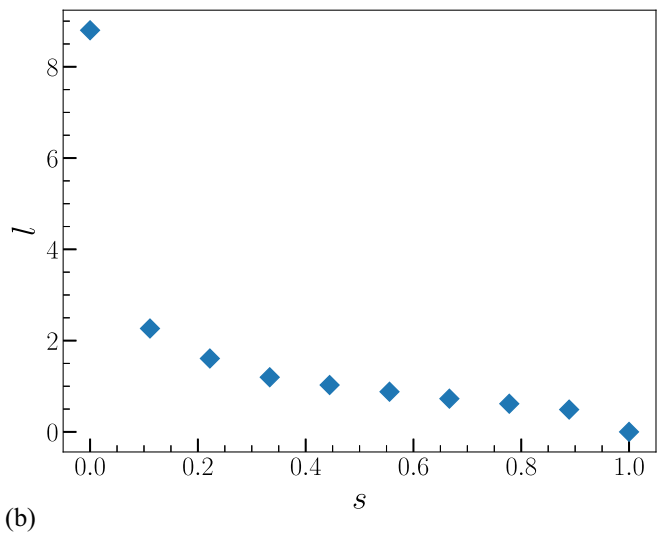


FIG. 9. Fitted single-particle correlation length l for the single-chain correlation function  $\langle a_1 a_1^{\dagger} \rangle$  along the two paths of Appendix C. (a) Interpolation between the effective model and the exactly solvable model of Ref. [20] via the path  $\gamma(s)$ . (b) Linear interpolation between the effective model with L=100,  $\nu=1/3$ ,  $W_1=W_2=0.5$ ,  $U_{\alpha}=-0.7$ , and  $U_{nn}=0$ . We chose different starting points of the effective model in both adiabatic paths. This was motivated by finding the shortest connection between our effective model and the target model. However, we explicitly checked that the effective model was in both cases in the Majorana-like phase, and that all other fingerprints of the MZM are present along the paths.

also show a cartoon picture of how all the different numberconserving models of this article are related.

For the first one, whose nonvanishing gap is plotted in Fig. 9(a), we chose

$$H_{\text{ext}} = \sum_{j;\alpha=a,b} \left( -t \, \alpha_{j+1}^{\dagger} \alpha_j + \frac{\mu}{2} \left( n_j^{\alpha} + n_{j+1}^{\alpha} \right) - U_{\alpha} \, n_j^{\alpha} n_{j+1}^{\alpha} - \frac{U_r}{2} \left( n_j^{a} n_j^{b} + n_{j+1}^{a} n_{j+1}^{b} \right) - U_{nn} \left( n_i^{a} + n_j^{b} \right) \left( n_{i+1}^{a} + n_{i+1}^{b} \right)$$

$$- W_{1} b_{j}^{\dagger} b_{j+1}^{\dagger} a_{j+1} a_{j} + W_{2} a_{j}^{\dagger} a_{j+1} b_{j}^{\dagger} b_{j+1} + W_{3} a_{j}^{\dagger} a_{j+1} b_{j+1}^{\dagger} b_{j} + \text{H.c.} , \qquad (C1)$$

where H.c. acts over every term which is not already explicitly Hermitian. In the Hamiltonian above, the chemical potential  $\mu$ , half of the strength for the very first and very last site compared to the bulk sites and compared to Eq. (8), an additional interaction term between the two chains  $U_r$  is introduced. This is necessary in order to solve the model exactly at the special point considered in Ref. [20]. However, we explicitly checked that the existence of the Majorana-like phase does not depend on the lowering of the on-site potential for the first and last sites, as one would expect for a topological phase.

The path (setting t = 1 for fixing the energy scale)

$$\gamma(s) = (W_2(s), W_3(s), U_\alpha(s), U_r(s)) 
= (0.8 - 0.4s, 0.4s, -0.7 + 0.3s, -0.8s),$$
(C2)

with  $W_1 = 0.8$ ,  $U_{nn} = -0.4$ , and  $\mu = 4$  kept constant, stretches from s = 0 at our model to s = 1 at  $\frac{1}{4}H_{\lambda=0.8}$  in the notation of Ref. [20].

For the second case, we define a simple linear interpolation,  $s \in [0, 1]$ , between the two limiting cases,

$$H(s) = (1 - s)H_{\text{eff}} + s(H_{\text{kitaev},a} + H_{\text{kitaev},b}), \tag{C3}$$

with  $H_{\text{eff}}$  the one in Eq. (8) and  $H_{\text{kitaev},\alpha}$  the Majorana chain for the  $\alpha = a, b$  species defined at the sweet spot:

$$H_{\text{kitaev},\alpha} = -t \sum_{j} (\alpha_{j}^{\dagger} - \alpha_{j})(\alpha_{j+1} + \alpha_{j+1}^{\dagger})$$

$$= -t \sum_{j} (\alpha_{j}^{\dagger} \alpha_{j+1} + \alpha_{j}^{\dagger} \alpha_{j+1}^{\dagger} + \text{H.c.}).$$
(C4)

The correlation length extracted from the single-particle correlation functions stays finite along the interpolation path, as shown in Fig. 9(b). The big drop in the beginning can be explained by the charge sector gapping out. This is supported by looking at the entanglement entropy (not shown here) which becomes asymptotically constant instead of following the logarithmic law of critical systems [50]. This behavior is expected since adding the pair potential terms allows for coupling of states with all possible particle numbers.

The existence of such an adiabatic connection, preserving the time-reversal symmetry and a  $(\mathbb{Z}_2)_+ \times (\mathbb{Z}_2)_-$  subgroup of the full symmetry group  $\mathrm{U}(1)_+ \times (\mathbb{Z}_2)_-$  of our model, is instrumental to understand and categorize the topological phase. Breaking the  $\mathrm{U}(1)$  symmetry leads to a fourfold degeneracy, differently from the case of preserving the  $\mathrm{U}(1)$  symmetry. This can be understood by recognizing that the four ground states split into two ground states for each parity of the total particle number. By conserving the total particle number, and therefore fixing the parity, we restrict the model to one of the two subspaces having either an even parity ( $N_{\mathrm{tot}}$  mod 2=0) or an odd parity. This results in an effective two-fold ground-state degeneracy as observed in the DMRG simulations (see Fig. 5).

Since the model we are dealing in this work is of an interacting nature and the interaction is crucial to obtain the desired Majorana-like phase, it should be noted that the general  $\mathbb{Z}$  classification of noninteracting fermionic systems in spatial dimension one breaks down to a  $\mathbb{Z}_8$  classification presence of interactions and time-reversal symmetry, as was shown in Ref. [51]. As long as we only couple two chains by the effective Hamiltonian (8) such a distinction is not relevant.

#### APPENDIX D: ENTANGLEMENT SPECTRUM ANALYSIS

In this Appendix we briefly discuss the form of the entanglement spectrum within the topological phase, as depicted in Fig. 4(a). From the bosonization analysis of our model we learned that the symmetric and antisymmetric sectors of the Hilbert space decouple. A similar decoupling is therefore also expected for the entanglement spectrum and the states corresponding to the Schmidt decomposition:

$$\epsilon_{\delta N, P, j} = -2 \log(\lambda_{\delta N, P, j}) \stackrel{!}{=} \epsilon_{\delta N, j}.$$
 (D1)

Here,  $\lambda_{\delta N,P,j}$  denotes the Schmidt values labeled by two quantum numbers associated to the symmetric  $(\delta N)$  and antisymmetric sector (P), namely, the excess charge with respect to average filling and the parity of one of the dressed chains. Since the symmetric sector is gapless and the antisymmetric one is in a gapped topological phase, we expect that the spectrum will show distinctive features of both.

The gapless charge sector is indeed displaying the universal behavior with entanglement levels arranged in parabolas as a function of the quantum number  $\delta N$ , whose details are determined by the underlying conformal field theory [37,38].

This special form of the entanglement spectrum is also useful for extracting the Luttinger parameter  $K_+$ , which was also used in the main text [39]:

$$\langle (N_{+,l} - \langle N_{+,l} \rangle)^2 \rangle = \frac{K_+}{2\pi} \log \left( \frac{2L}{\pi} \sin(\pi/Ll) \right).$$

Moreover, the curvature of the parabolas is also mainly determined by the Luttinger parameter  $K_+$  by [38]

$$-\log(\lambda(\delta N_+)^2) \sim \frac{K_+}{2}(\delta N_+)^2.$$

However, the exact numerical values of the entanglement spectrum and all correct degeneracies are hard to extract, since they are subject of strong finite bond dimension effects [37] and using the formula connecting the total number fluctuation to the Luttinger parameter is more stable.

The topological character of the gapped antisymmetric sector is dictating the presence of two copies of each level, transforming differently under the parity. This is in perfect agreement with the results of Ref. [28], and the degeneracy represents the fractionalization of the fermionic parity operator at the end of a finite subsystem, as is more generally known for symmetry-protected topological phases [52]. Comparing the results for the system in the topological phase, Fig. 4(a), with results from the system being in the trivial phase, Fig. 4(b), we indeed find that the parabolas originating from the gapless charge sector are still present; however, the nontrivial double degeneracy between the two different parity sectors is gone.

## APPENDIX E: THE FULL MODEL IN THE PERTURBATIVE REGIME

In this Appendix we report the results found for the full model deep inside the perturbative regime. The Schrieffer-Wolff transformation used for deriving the effective Hamiltonian (9) is valid in the limit of  $\mu$  (the chemical potential on the c and d states) being the dominant energy scale. Together with requiring the resulting parameters of the effective model defined by relation (9) being in the topological regime gives some additional constrains on the parameters of the full model.

For example, targeting the effective parameters  $U_{nn} \approx 0$ ,  $W \approx t/1.4$ , and  $U_{\alpha} = -0.5t$  while fixing

$$\mu/J = 5$$
,  $V_1/J = -1$ ,  $V_2/J = 1.25$ ,  $t = 0.01$ ,

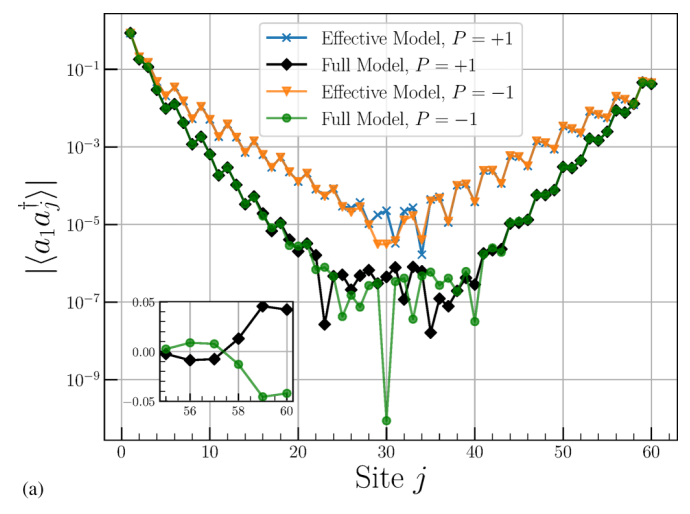
leads to  $W/J \approx 0.007$  and  $U_{\alpha}/J \approx -0.005$ . Thus, the intrawire interaction  $U_{\alpha}$  is several orders of magnitude smaller than the interactions on the c and d states ( $V_1$  and  $V_2$ ), which are not constrained to be small since they act exclusively on the c and d subspace. Further, we used  $t_{\parallel} = 0.05$  together with  $t_{\perp} = 0$ . This should lead to a slight detuning  $W_1 > W_2$ favoring the topological phase as expected from Appendix A. The results for a simulation of a system with 60 sites and a filling of  $n_e = 40$  ( $\nu = 1/3$  in the effective model) are shown in Fig. 10. First looking at the density profiles in Fig. 10(b), one sees a slight decrease of the population on the a and b sites compared to the effective model. However, this is expected due to the additional c and d states. Now looking at the end-to-end correlation function in Fig. 10(a), one sees the same characteristic behavior as in the effective model, i.e., an exponential decay towards the middle of the system together with an exponential revival showing a relative sign between the two parity sectors. Remarkably, the energy gap (correlation length) of the full four-flavor model seems to be larger (smaller) than in the effective model. This can be explained by the additional terms in Hamiltonian (8) which are discarded in the numerical simulations of the effective model, as discussed below Eq. (10).

#### APPENDIX F: DEVIATION FROM PERFECT $\pi$ FLUX

In this Appendix we shortly address the effects of having a small deviation from a perfect  $\pi$  flux  $\Phi = \pi - \epsilon$  through the rhombi building the chain, Fig. 1(a). This change amounts to adding a perturbation term to  $H_{\Diamond}$  according to

$$\begin{split} H_{\Diamond}(\epsilon) &= H_{\Diamond} + \delta H(\epsilon), \\ \delta H(\epsilon) &= J \sum_{j} i \epsilon \, d_{j}^{\dagger} a_{j} + \text{H.c.} \end{split} \tag{F1}$$

Perfect cancellation of single-particle processes between the (dressed) a and b wires only occurs at perfect  $\pi$  flux.  $\delta H(\epsilon)$  therefore explicitly breaks the exact  $\mathbb{Z}_2$  symmetry representing the fermionic parity in each (dressed) wire, and with it also the protection of the Majorana edge modes. Intuitively, we would expect the two parity ground states to hybridize and to form a ground-excited doublet, split by an energy amount proportional to the deviation from  $\pi$  flux.



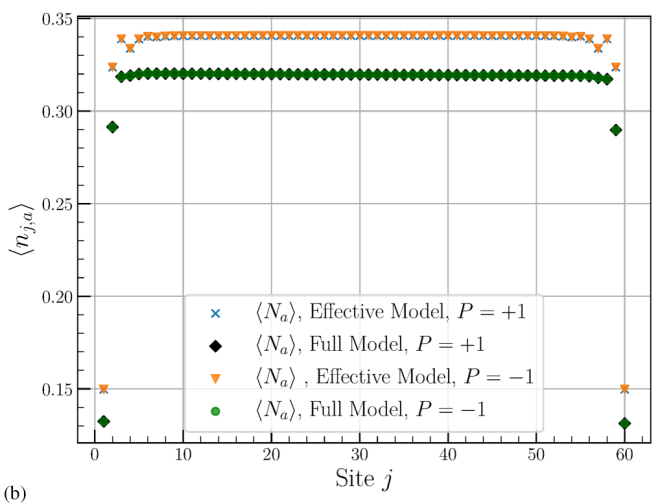


FIG. 10. Comparison of the results for the full model with couplings described in the text versus the effective model for an L=60 system: (a) single-particle correlations, (b) local density of a single species. Results obtained for the sites b are analogous.

By performing the Schrieffer-Wolff transformation similar to Appendix A it is possible to find the induced perturbation on the effective model (8) to lowest order,

$$\delta H_{\text{eff}}(\epsilon) = \frac{i\epsilon J^2}{\mu^3} \sum_{j} (a_j^{\dagger} b_j - b_j^{\dagger} a_j), \tag{F2}$$

which makes evident its  $\mathbb{Z}_2$ -breaking character. This leads to a direct coupling between the two parity sectors

$$\langle \Omega_{+} | \delta H_{\text{eff}}(\epsilon) | \Omega_{-} \rangle \propto \epsilon$$
 (F3)

and thus to a mixing of these states to form the true ground and first-excited states, with an energy splitting proportional to  $\epsilon$ .

While the above concerns a homogeneous violation of the  $\pi$ -flux condition, another interesting question revolves around a single flux impurity at site j:

$$\hat{O}_j = g_p a_i^{\dagger} b_j + \text{H.c.}$$

Cheng et al. [19] showed using bosonization that  $\hat{O}_j$  becomes irrelevant as long as j is deep inside the bulk. However, approaching the boundaries j=0 or j=L the operator  $\hat{O}_j$  essentially becomes the Majorana-mode operator of the left or right site of the system resulting exactly in the abovementioned coupling between the two ground states [Eq. (F3)].

We therefore expect that the larger is the window around the edges for which the  $\pi$ -flux condition can be exactly implemented, the smaller will be the splitting and thus the larger the lifetime of the Majorana bound states.

Verifying these statements numerically is technically very tedious. As mentioned in Sec. IV, even in the ideal case of  $\Phi=\pi$ , the DMRG calculations would tend to select an equal-weighted superposition of the two sectors if the parity conservation is not imposed at the tensor level. As a consequence, the edge-to-edge revival of correlations gets shadowed, as in Fig. 3; also features in the entanglement spectrum get lost, which are the main effects expected from a  $\pi$ -flux violation. Furthermore, the symmetry-breaking energy split proportional to  $\epsilon$  gets masked by the overall gapless nature of the model, which dictates a finite-size closing of the gap as  $L^{-1}$ . This limits quite severely the accessible system sizes and/or the maximal value of the  $\pi$ -flux violation according to  $\epsilon \ll L^{-1}$ .

A more reasonable way to study the fate of the Majorana modes in the presence of a  $\pi$ -flux violation would be to look at dynamical observables, like the autocorrelation function of an operator having a finite overlap with the Majorana edge modes [53]. This approach would be independent of imposing symmetries to the tensors and would give a direct access to the lifetime of the Majorana edge modes. However, studying dynamical quantities goes beyond the scope of this paper and is left for future studies.

J. K. Asbóth, L. Oroszlány, and A. Pályi, A Short Course on Topological Insulators (Springer, Berlin, 2016)

<sup>[2]</sup> Y. Ren, Z. Qiao, and Q. Niu, Topological phases in two-dimensional materials: A review, Rep. Prog. Phys. **79**, 066501

<sup>[3]</sup> J. Wang and S.-C. Zhang, Topological states of condensed matter, Nat. Mater. **16**, 1062 (2017).

<sup>[4]</sup> C. Nayak, S. H. Simon, A. Stern, M. Freedman, and S. D. Sarma, Non-Abelian anyons and topological quantum computation, Rev. Mod. Phys. 80, 1083 (2008).

<sup>[5]</sup> D. A. Ivanov, Non-Abelian Statistics of Half-Quantum Vortices in *p*-Wave Superconductors, Phys. Rev. Lett. 86, 268 (2001).

<sup>[6]</sup> S. Rao, Introduction to Abelian and non-Abelian anyons, in *Topology and Condensed Matter Physics*, edited by S. M. Bhattacharjee, M. Mj, and A. Bandyopadhyay (Springer, Singapore, Singapore, 2017), pp. 399-437.

<sup>[7]</sup> S. D. Sarma, M. Freedman, and C. Nayak, Majorana zero modes and topological quantum computation, npj Quantum Inf. 1, 15001 (2015).

- [8] M. Ippoliti, M. Rizzi, V. Giovannetti, and L. Mazza, Quantum memories with zero-energy Majorana modes and experimental constraints, Phys. Rev. A 93, 062325 (2016).
- [9] A. Y. Kitaev, Unpaired Majorana fermions in quantum wires, Phys. Usp. 44, 131 (2001).
- [10] Y. Oreg, G. Refael, and F. von Oppen, Helical Liquids and Majorana Bound States in Quantum Wires, Phys. Rev. Lett. 105, 177002 (2010).
- [11] R. M. Lutchyn, J. D. Sau, and S. Das Sarma, Majorana Fermions and a Topological Phase Transition in Semiconductor-Superconductor Heterostructures, Phys. Rev. Lett. 105, 077001 (2010).
- [12] J. Alicea, Y. Oreg, G. Refael, F. Von Oppen, and M. P. Fisher, Non-Abelian statistics and topological quantum information processing in 1D wire networks, Nat. Phys. 7, 412 (2011).
- [13] L. Fidkowski, R. M. Lutchyn, C. Nayak, and M. P. A. Fisher, Majorana zero modes in one-dimensional quantum wires without long-ranged superconducting order, Phys. Rev. B 84, 195436 (2011).
- [14] J. Alicea, New directions in the pursuit of Majorana fermions in solid state systems, Rep. Prog. Phys. 75, 076501 (2012).
- [15] A. Keselman and E. Berg, Gapless symmetry-protected topological phase of fermions in one dimension, Phys. Rev. B 91, 235309 (2015).
- [16] T. Li, M. Burrello, and K. Flensberg, Coulomb-interaction-induced Majorana edge modes in nanowires, Phys. Rev. B 100, 045305 (2019).
- [17] C. V. Kraus, M. Dalmonte, M. A. Baranov, A. M. Läuchli, and P. Zoller, Majorana Edge States in Atomic Wires Coupled by Pair Hopping, Phys. Rev. Lett. 111, 173004 (2013).
- [18] F. Iemini, L. Mazza, L. Fallani, P. Zoller, R. Fazio, and M. Dalmonte, Majorana Quasiparticles Protected by  $\mathbb{Z}_2$  Angular Momentum Conservation, Phys. Rev. Lett. **118**, 200404 (2017).
- [19] M. Cheng and H.-H. Tu, Majorana edge states in interacting two-chain ladders of fermions, Phys. Rev. B 84, 094503 (2011).
- [20] F. Iemini, L. Mazza, D. Rossini, R. Fazio, and S. Diehl, Localized Majorana-Like Modes in a Number-Conserving Setting: An Exactly Solvable Model, Phys. Rev. Lett. 115, 156402 (2015).
- [21] N. Lang and H. P. Büchler, Topological states in a microscopic model of interacting fermions, Phys. Rev. B 92, 041118(R) (2015).
- [22] F. Schäfer, T. Fukuhara, S. Sugawa, Y. Takasu, and Y. Takahashi, Tools for quantum simulation with ultracold atoms in optical lattices, Nat. Rev. Phys. 2, 411 (2020).
- [23] J. Vidal, R. Mosseri, and B. Douçot, Aharonov-Bohm Cages in Two-Dimensional Structures, Phys. Rev. Lett. 81, 5888 (1998).
- [24] J. Vidal, P. Butaud, B. Douçot, and R. Mosseri, Disorder and interactions in Aharonov-Bohm cages, Phys. Rev. B 64, 155306 (2001).
- [25] K. Suzuki and R. Okamoto, Degenerate perturbation theory in quantum mechanics, Prog. Theor. Phys. 70, 439 (1983).
- [26] D. Sénéchal, An introduction to bosonization, in Theoretical Methods for Strongly Correlated Electrons, edited by D. Sénéchal, A. M. Tremblay, and C. Bourbonnais, CRM Series in Mathematical Physics (Springer, New York, 2006).

- [27] J. von Delft and H. Schneller, Bosonization for beginners— Refermionization for experts, Ann. Phys. 510, 225 (1998).
- [28] A. M. Turner, F. Pollmann, and E. Berg, Topological phases of one-dimensional fermions: An entanglement point of view, Phys. Rev. B 83, 075102 (2011).
- [29] U. Schollwöck, The density-matrix renormalization group in the age of matrix product states, Ann. Phys. **326**, 96 (2011), january 2011 special issue.
- [30] T. Giamarchi and H. J. Schulz, Theory of spin-anisotropic electron-electron interactions in quasi-one-dimensional metals, J. Phys. France 49, 819 (1988).
- [31] P. Lecheminant, A. O. Gogolin, and A. A. Nersesyan, Criticality in self-dual sine-Gordon models, Nucl. Phys. B 639, 502 (2002).
- [32] T. Giamarchi, Quantum Physics in One Dimension (Oxford University Press, Oxford, UK, 2004).
- [33] H. Li and F. D. M. Haldane, Entanglement Spectrum as a Generalization of Entanglement Entropy: Identification of Topological Order in Non-Abelian Fractional Quantum Hall Effect States, Phys. Rev. Lett. 101, 010504 (2008).
- [34] E. Stoudenmire and S. R. White, Studying two-dimensional systems with the density matrix renormalization group, Annu. Rev. Condens. Matter Phys. 3, 111 (2012).
- [35] H.-C. Jiang, Z. Wang, and L. Balents, Identifying topological order by entanglement entropy, Nat. Phys. 8, 902 (2012).
- [36] T. G. Kiely and E. J. Mueller, Role of conservation laws in the density matrix renormalization group, Phys. Rev. B **106**, 235126 (2022).
- [37] A. M. Läuchli, Operator content of real-space entanglement spectra at conformal critical points, arXiv:1303.0741.
- [38] A. Roy, F. Pollmann, and H. Saleur, Entanglement Hamiltonian of the 1 + 1-dimensional free, compactified boson conformal field theory, J. Stat. Mech.: Theory Exp. (2020) 083104.
- [39] S. Rachel, N. Laflorencie, H. F. Song, and K. Le Hur, Detecting Quantum Critical Points Using Bipartite Fluctuations, Phys. Rev. Lett. 108, 116401 (2012).
- [40] J. H. Han, J. H. Kang, and Y. Shin, Band Gap Closing in a Synthetic Hall Tube of Neutral Fermions, Phys. Rev. Lett. **122**, 065303 (2019).
- [41] A. Fabre, J.-B. Bouhiron, T. Satoor, R. Lopes, and S. Nascimbene, Laughlin's Topological Charge Pump in an Atomic Hall Cylinder, Phys. Rev. Lett. 128, 173202 (2022).
- [42] L. D. Carr, D. DeMille, R. V. Krems, and J. Ye, Cold and ultracold molecules: Science, technology and applications, New J. Phys. 11, 055049 (2009).
- [43] M. Lewenstein, A. Sanpera, and V. Ahufinger, *Ultracold Atoms in Optical Lattices: Simulating Quantum Many-Body Systems* (Oxford University Press, Oxford, UK, 2012).
- [44] I. Bloch and P. Zoller, Ultracold atoms and molecules in optical lattices, in *Ultracold Bosonic and Fermionic Gases*, Contemporary Concepts of Condensed Matter Science Vol. 5, edited by K. Levin, A. L. Fetter, and D. M. Stamper-Kurn (Elsevier, Amsterdam, 2012), Chap. 5, pp. 121–156.
- [45] L. Mazza, A. Bermudez, N. Goldman, M. Rizzi, M. A. Martin-Delgado, and M. Lewenstein, An optical-lattice-based quantum simulator for relativistic field theories and topological insulators, New J. Phys. 14, 015007 (2012).
- [46] C. Menotti, M. Lewenstein, T. Lahaye, and T. Pfau, Dipolar interaction in ultra-cold atomic gases, in *Dynamics and Ther*modynamics of Systems with Long Range Interactions: Theory

- *and Experiments*, edited by A. Campa, A. Giansanti, G. Morigi, and F. S. Labini, AIP Conf. Proc. No. 970 (AIP, New York, 2008), p. 332.
- [47] K. Aikawa, S. Baier, A. Frisch, M. Mark, C. Ravensbergen, and F. Ferlaino, Observation of Fermi surface deformation in a dipolar quantum gas, Science **345**, 1484 (2014).
- [48] S. Baier, M. J. Mark, D. Petter, K. Aikawa, L. Chomaz, Z. Cai, M. Baranov, P. Zoller, and F. Ferlaino, Extended Bose-Hubbard models with ultracold magnetic atoms, Science 352, 201 (2016).
- [49] F. T. Lisandrini and C. Kollath, Majorana edge modes in a spinful-particle conserving model, Phys. Rev. B **106**, 245121 (2022).

- [50] P. Calabrese and A. Lefevre, Entanglement spectrum in one-dimensional systems, Phys. Rev. A 78, 032329 (2008).
- [51] L. Fidkowski and A. Kitaev, Effects of interactions on the topological classification of free fermion systems, Phys. Rev. B 81, 134509 (2010).
- [52] F. Pollmann, A. M. Turner, E. Berg, and M. Oshikawa, Entanglement spectrum of a topological phase in one dimension, Phys. Rev. B **81**, 064439 (2010).
- [53] D. J. Yates, A. G. Abanov, and A. Mitra, Lifetime of Almost Strong Edge-Mode Operators in One-Dimensional, Interacting, Symmetry Protected Topological Phases, Phys. Rev. Lett. 124, 206803 (2020).

# Quantum Simulation of the Tricritical Ising Model in Tunable Josephson Junction Ladders

Authors: Lorenzo Maffi, Niklas Tausendpfund, Matteo Rizzi,

Michele Burrello

**Year:** 2024

Journal: Physical Review Letters

**Volume/Issue:** 132, 22

**DOI:** 10.1103/PhysRevLett.132.226502

#### II.1 Authors Contribution

Michele Burrello and Lorenzo Maffi designed the concept of the triple junction and the quantum ladder and carried out the model's initial analysis in form of a semi-classical study of possible ground states. They further carried out the bosonization analysis to identify the parameter ranges of potential interest. Niklas Tausendp-fund designed and carried out the numerical experiments and led the analysis of the data. Specifically, he developed a technique to extract the correlation length of different emerging sectors, even in the absence of an explicit symmetry in the initial model. He received guidance from his supervisor, Matteo Rizzi, during regular meetings. The results were discussed with all the authors in weekly discussions. Michele Burrello and Lorenzo Maffi prepared the first draft of the manuscript, and Niklas Tausendpfund wrote the paragraphs discussing the numerical findings. The draft was subsequently modified by all the authors. Lorenzo Maffi and Niklas Tausendpfund share the first authorship on this publication.

## II.2 Data Availability

The simulation combined infinite and finite Matrix Product State (MPS) simulations based on the ITensor.jl [274] library. The code and final results are publicly available on ZENODO under [275]. The bare wave functions are stored on the PGI-8 backup data server at Forschungszentrum Jülich. Upon request, the data can be made available by the Institute for Optimal Quantum Control.

## II.3 Summary

The standard Ising model has two phases: a  $\mathbb{Z}_2$  symmetry broken phase and an unordered phase. Both phases are separated by a continuous phase transition of second order, described by the critical Ising model, see also Subsection 1.3.3. By extending the Ising model to allow for a First-Order Phase Transition (FOPT) between the two phases, a tricritical point emerges at the parameter where the continuous transition line merges with the FOPT line; see Subsection 1.3.3. At this point, multiple competing phases become critical, and new physics emerge.

This Tricritical Ising (TCI) model, generally described by a conformal field theory, has a rich particle content, with one of the fields being related to non-Abelian anyons in two-dimensional topologically ordered quantum matter [276] and fault-tolerant quantum computation [34] by coupling copies of the TCI model in a two-dimensional wire array. This coupling is designed to gap out all unwanted low-energy excitations, leaving only the field related to the non-Abelian anyons. A strategy we have recently employed to realize a Kalmayer-Luttinger spin liquid in a triangular lattice [277]. Moreover, it was conjectured that the TCI model can be used to observe emergent supersymmetry [278, 279].

Despite the rich physics expected at the TCI phase transition, there has been no experimental realization to date, to the best of our knowledge. In the present study, we propose a promising approach for experimentally accessing this exotic phase transition. The proposed quantum simulator is based on Josephson Junction Arrays (JJAs), where recent advances in the fabrication process [12, 13, 280–282] allow for the necessary high control of the coupling parameters to tune the system into the TCI transition. Furthermore, the JJA forms a natural platform for the direct simulation of strongly interacting bosonic field theories [168].

The main idea is to engineer the low-energy theory of the JJA to become a triple sine-Gordon model

$$H_{\text{eff}} \approx \int dx \left(\partial_x \hat{\varphi}(x)\right)^2 + \sum_{n=1}^3 \mu_n \cos\left(\sqrt{2}n\hat{\varphi}(x)\right)$$
 (II.1)

which has the same universality behavior as the standard  $\hat{\varphi}^6$  theory [283–285] from Eq. (1.150).

The basic building block used in the quantum ladder is designed to mimic this multi-frequency sine-Gordon model with individual control over the  $\mu_n$  amplitudes. In particular, this element consists of two superconducting islands joined by three individual Josephson junctions with transparencies  $T_1 = T_3$  and  $T_2$ , with an additional flux piercing the two loops formed by the triple junction, as shown in Figure 1(a) of the publication. Let  $\varphi$  be the difference in the superconducting phase of the

II.3. SUMMARY 123

two islands and  $\Delta$  the gap of the bulk superconductor, the energy-phase relation of the triple junction is given by [286]

$$\begin{split} V_J(\varphi) &= -\Delta \left( \sqrt{1 - T_1 \sin \left( \frac{\varphi - \Phi}{2} \right)^2} + \sqrt{1 - T_2 \sin \left( \frac{\varphi}{2} \right)^2} \right. \\ &+ \sqrt{1 - T_1 \sin \left( \frac{\varphi + \Phi}{2} \right)^2} \right) \, . \end{split}$$

This potential is symmetric under the transformation  $\varphi \to -\varphi \mod 2\pi$  which implements the  $\mathbb{Z}_2$  Ising symmetry. The non-sinusoidal character of this potential ultimately leads to the desired form of the low-energy theory in Eq. (II.1).

This is explicitly seen by performing an expansion in a Fourier sum

$$V_J(\varphi) = \sum_n \mu_n \cos(n\varphi)$$

where each potential,  $\cos(n\varphi)$ , represents the tunneling of n Cooper pairs from one island to the other, and the coefficients depend on the three free parameters  $T_1$ ,  $T_2$  and  $\Phi$ .

In the limit of no charging effect, the quantum mechanical state of the triple junction is completely defined in terms of the classical potential landscape of  $V_J(\varphi)$ , and in particular, the local and global minima defined by

$$\varphi_{\min}(T_1,T_2,\Phi) = \mathop{\rm argmin}_{\varphi \in [0,2\pi)} (V_J(\varphi)) \ . \tag{II.2} \label{eq:poisson}$$

If there is only one global minima  $\varphi_{\min}=0$ , the triple junction is in an unordered symmetry-restoring phase. On the other hand, if the solution space is double degenerated with  $\varphi_{\min,1}=-\varphi_{\min,2}\mod 2\pi$ , the triple junction spontaneously breaks the Ising symmetry. The transitions between the unordered phase and the symmetry-broken phase are classified either as a second-order transition of Ising criticality, where the two degenerate minima merge, or as a FOPT, where the minimum  $\varphi=0$  raises in energy and the two local minima become the new global minima. This semi-classical analysis leads to Figure 2 of our publication, which displays the single-particle Cooper-pair current  $\hat{J}_{\perp}^{(2e)}\sim\sin(\varphi)$  through the triple junction as an order parameter.

In a final step, we extended this semi-classical analysis to a full quantum ladder model by repeating the triple junction, coupling them with single Josephson junctions, and adding general charging effects between the two legs of the ladder. The full quantum chain is shown in Figure 1(b) of our publication. A first bosonization study of the model revealed that the anticipated multi-frequency sine-Gordon model from Eq. (II.1) emerges, along with an additional uncoupled Tomonaga-Luttinger Liquid (TLL), as a low-energy representation of the model. While the TLL characterizes the long-wavelength behavior of excitations in the total density, the multi-frequency sine-Gordon model describes excitations between the two legs of the ladder, akin to the anti-bonding sector in Eq. (1.143). Through a renormalization group analysis of the model, we identified a set of parameters for which the quantum ladder might exhibit a TCI point.

We verified these findings by an extensive numerical study of the quantum ladder model using Uniform Matrix Product State (uMPS). By measuring the local order

# CHAPTER II. QUANTUM SIMULATION OF THE TRICRITICAL ISING MODEL IN TUNABLE JOSEPHSON JUNCTION LADDERS

parameter  $\hat{J}_{\perp}^{(2e)}$ , we identified the bulk phases of the quantum ladder. The semiclassical phase diagram was qualitatively reproduced, as illustrated in Figure 3(a) of our publication. By further analyzing the transitions between the ordered and disordered phases, we identified the first-order transition line and the continuous Ising transition line, and extrapolated them to the point  $p_{\star}$  in the parameter space, where the two lines merge. Measuring the central charge, extracted from small finite-size MPS simulations with periodic boundary conditions, through the merging point reveals that the central charge is  $c \approx 1 + 1/2$  on the Ising site, becomes  $c \approx 1 + 7/10$  at  $p_{\star}$  and then rapidly drops to  $c \approx 1$ , as shown in Figure 3(e) of our publication. Because the low-energy theory predicts a background gapless TLL with a central charge of c = 1, this behavior leads to the conclusion that the remaining part of the low-energy theory enters the TCI phase, as expected.

However, it was not possible to measure the critical exponents of primary fields, such as the magnetization. The main challenge is the large bond dimension required to extract good data. A rough estimate given by the correlation length directly extracted for the anti-bonding sector using the technique described in Subsection 2.2.2 suggests that a bond dimension of approximately  $\chi \sim 20000$  is required to observe the algebraic decay over a few hundred lattice sites. This is mainly rooted in the large central charge and poor scaling of the correlation length with the bond dimension. Performing extended simulations at this huge bond dimension is beyond the scope of the present work.

### **Quantum Simulation of the Tricritical Ising Model** in Tunable Josephson Junction Ladders

Lorenzo Maffi<sup>®</sup>, <sup>1,2,3,\*</sup> Niklas Tausendpfund<sup>®</sup>, <sup>4,5,\*</sup> Matteo Rizzi<sup>®</sup>, <sup>4,5</sup> and Michele Burrello<sup>®</sup> <sup>1</sup>Center for Quantum Devices and Niels Bohr International Academy, Niels Bohr Institute, University of Copenhagen, DK-2100 Copenhagen, Denmark <sup>2</sup>Dipartimento di Fisica e Astronomia "G. Galilei," Università degli Studi di Padova, I-35131 Padova, Italy <sup>3</sup>Istituto Nazionale di Fisica Nucleare (INFN), Sezione di Padova, I-35131 Padova, Italy <sup>4</sup>Forschungszentrum Jülich GmbH, Institute of Quantum Control, Peter Grünberg Institut (PGI-8), 52425 Jülich, Germany <sup>5</sup>Institute for Theoretical Physics, University of Cologne, D-50937 Köln, Germany

(Received 5 December 2023; revised 17 March 2024; accepted 22 April 2024; published 28 May 2024)

Modern hybrid superconductor-semiconductor Josephson junction arrays are a promising platform for analog quantum simulations. Their controllable and nonsinusoidal energy-phase relation opens the path to implement nontrivial interactions and study the emergence of exotic quantum phase transitions. Here, we propose the analysis of an array of hybrid Josephson junctions defining a two-leg ladder geometry for the quantum simulation of the tricritical Ising phase transition. This transition provides the paradigmatic example of minimal conformal models beyond Ising criticality and its excitations are intimately related to Fibonacci non-Abelian anyons and topological order in two dimensions. We study this superconducting system and its thermodynamic phases based on bosonization and matrix-product-state techniques. Its effective continuous description in terms of a three-frequency sine-Gordon quantum field theory suggests the presence of the targeted tricritical point and the numerical simulations confirm this picture. Our results indicate which experimental observables can be adopted in realistic devices to probe the physics and the phase transitions of the model. Additionally, our proposal provides a useful one-dimensional building block to design exotic topological order in two-dimensional scalable Josephson junction arrays.

DOI: 10.1103/PhysRevLett.132.226502

The rapid advances in the fabrication of superconductorsemiconductor heterostructures [1,2] allow for the realization of Josephson junction arrays (JJAs) with unprecedented tunability of their physical parameters [3–5]. State-of-the-art electron beam lithography and etching techniques enable the realization of superconducting (SC) arrays with exquisite geometrical precision and scalability. Epitaxial growth consents to create pristine interfaces between a semiconducting substrate and SC islands, thus providing the possibility of controlling these setups through voltage gates. These fabrication developments are flanked by remarkable advances in measurement techniques that include microwave spectroscopy to study the strongly correlated systems emerging in Josephson junction chains [6–8] and transport measurements to investigate the intricate thermodynamic properties of these systems [3–5,8,9]. Such progresses brought JJAs right back into the arena of analog quantum simulation platforms, where they started their journey decades ago. The simultaneous tunability of the junction transparencies [2,10–13] and magnetic fluxes opens indeed the path to tailor models of interest, among them quantum field theories (QFTs) and integrable models [6,14–16]. In particular, the experimental achievement of multicritical points, with peculiar conformal field theories (CFTs) associated with them [17], becomes within reach [18].

In this Letter, we formulate a blueprint for the quantum simulation of the tricritical Ising (TCI) CFT in a tunable Josephson junction ladder. The reasons for interest in this model are multiple. It constitutes the simplest example of CFT beyond the Ising model, and its particle content includes excitations that share the same fusion properties of Fibonacci non-Abelian anyons. Successfully implementing this model will open the way to engineer exotic topological order in 2D arrays in the spirit of the wire constructions of Refs. [19-22]. Moreover, the TCI model stands as a strong potential candidate to observe the emergence of supersymmetry [23-25]. Notably, to our knowledge, no experimental realization of a quantum TCI phase transition in 1D has ever been observed, nor have its critical exponents been measured.

Indeed, the quantum simulations of CFTs beyond the Ising universality class face both experimental and theoretical challenges: the most recent theoretical proposals rely on advanced constructions based on Majorana modes [22,24–28], extended Hubbard models with staggering potentials [29,30], or nontrivial mappings between microscopic lattice operators and the field content of the CFTs [31]. In this context, the main mechanism to achieve a TCI point is to consider platforms like Rydberg atom systems [32,33] and ultracold atoms in tilted optical superlattices

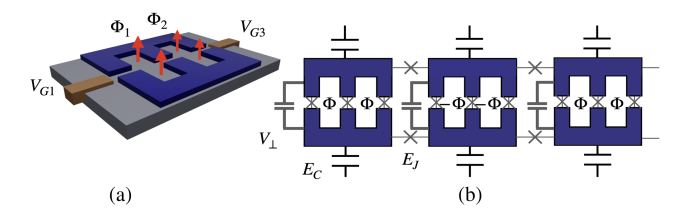


FIG. 1. (a) Two E-shaped SC islands are connected through three parallel junctions. An out-of-plane magnetic field (red arrows) dictates the Aharonov-Bohm phases  $\Phi_1$  and  $\Phi_2$  along the two loops. The external junctions are controlled by electrostatic gates at potential  $V_{G1}$ ,  $V_{G3}$ , which vary the carrier density in the surrounding semiconductor. This triple JJ element allows us to control the potential (2) at each rung of the ladder geometry (b). The fluxes of the triple JJ elements are staggered along the ladder [39]. Mutual rung capacitances and the island self-capacitances determine the electrostatic interactions  $V_{\perp}$  and  $E_{C}$ .

[34] that are described by discrete models with a continuous Ising phase transition turning into a first-order phase transition (FOPT) at the tricritical point.

JJAs offer a direct way to implement the scaling limit of interacting bosonic QFTs [15,18]. In the following we present a ladder system that embodies a three-frequency sine-Gordon model and can be tuned to naturally flow towards the TCI point at low energy. The chosen ladder geometry offers an alternative construction compared to previous works on SC chains [16,18] (see also the ladder construction in Ref. [6]), and opens a path toward 2D devices with exotic properties [33]. To achieve our goal, we utilize a blend of analytical techniques, including mean field analysis and bosonization [35], complemented by numerical results based on variational uniform matrix product states (VUMPS) [36–38].

The triple Josephson junction.—The building block of our 1D construction consists of two E-shaped SC islands facing each other and grown on a semiconducting substrate [Fig. 1(a)]. Schematically, we model this element as three parallel Josephson junctions (JJs) [39] where Andreev bound states induced in the semiconductor mediate the Cooper pair tunneling [51,52]. For simplicity, we assume that each junction is defined by a single transport channel with transparency  $T_p \in [0,1]$  (p=1,2,3) and energyphase relation [51]

$$\mathcal{E}_{J}^{(p)}(\varphi) = -\Delta\sqrt{1 - T_{p}\sin^{2}(\varphi/2)}. \tag{1}$$

See Refs. [13,53] for alternative realizations. In Eq. (1),  $\varphi$  is the phase difference between the two islands and  $\Delta$  is the SC gap induced by proximity in the semiconducting substrate. High-transparencies  $T_p$  lead to coherent tunneling events of multiple Cooper pairs [54] corresponding to higher harmonics contribution,  $\cos(n\varphi)$  with n > 1, to the dispersion (1). In the triple JJ geometry, the amplitudes of

such events can be tuned by inserting two magnetic fluxes in the resulting loops [Fig. 1(a)] [39].

We set  $\Phi_1 = \Phi_2 = \Phi$  and identical transparencies  $(T_1 = T_3)$  for the external junctions, controlled using electrostatic gates [Fig. 1(a)]. With these constraints, the exchange of the SC islands,  $\varphi \to -\varphi$ , corresponds to the required  $\mathbb{Z}_2$  symmetry for the multicritical Ising physics, which is reflected in the odd current-phase relation of the triple JJ. Multiple channels in the junctions or unequal plaquette areas may explicitly break this symmetry [39], hindering the observation of critical features whenever the corresponding energy gaps are larger than the experimentally achievable energy resolution due to the finite size L and the temperature. In the symmetric setup, the total Josephson potential can be expanded as

$$V_J(\varphi) = \sum_{n \in \mathbb{N}} \mu_n(\mathbf{X}) \cos(n\varphi). \tag{2}$$

The Fourier coefficients  $\mu_n$  [39] depend on the values of the external parameters  $\mathbf{X} = (T_1 \cos(\Phi), T_1 \sin(\Phi), T_2)$  which span a solid cylinder.

We will use many copies of this triple JJ to build a 1D ladder geometry, thus promoting the phase difference  $\varphi$  to a position-dependent field. In light of this, a preliminary mean field analysis allows us to qualitatively understand the onset of a TCI point by investigating the potential  $V_J(\varphi)$  as a function of **X**. In a semiclassical picture, a tricritical point arises when three potential minima merge [55–57]. In the landscape defined by  $V_J(\varphi)$  with  $\varphi \in (-\pi, \pi]$ , for any  $T_2$ , there exists a point  $(T_1, \Phi)_c$  where this merging occurs and  $V_J(\varphi)$  is approximated by a  $\varphi^6$  local potential; see Fig. 2. This suggests the first connection to the TCI model and its Ginzburg-Landau formulation [55–57].

1D model.—We design a 1D quantum simulator to achieve a TCI point by arranging a set of identical triple JJs with potential  $V_J$  in parallel, as depicted in Fig. 1(b), to implement a multiple-frequency sine-Gordon model at low energies. The Hamiltonian of the JJ ladder is

$$\hat{H} = \sum_{j=0}^{L-1} \left[ \sum_{\alpha = a,b} (E_C \hat{N}_{\alpha,j}^2 - E_J \cos(\hat{\varphi}_{\alpha,j+1} - \hat{\varphi}_{\alpha,j})) + V_{\perp} \hat{N}_{a,j} \hat{N}_{b,j} + V_J (\hat{\varphi}_{a,j} - \hat{\varphi}_{b,j}) \right],$$
(3)

where  $\hat{\varphi}_{\alpha,j}$  represents the phase operator of the jth island on the leg  $\alpha \in \{a, b\}$ . Along the legs, the SC islands are connected through JJs in a standard sinusoidal regime with Josephson energy  $E_J$ . This energy scale can vary from  $E_J \simeq h50$  GHz [11] down to  $E_J = 0$  for completely depleted junctions. The dynamics of the SC phases in Eq. (3) is dictated by charging effects, described by the charge operators  $\hat{N}_{\alpha,j}$ , canonically conjugated to the SC

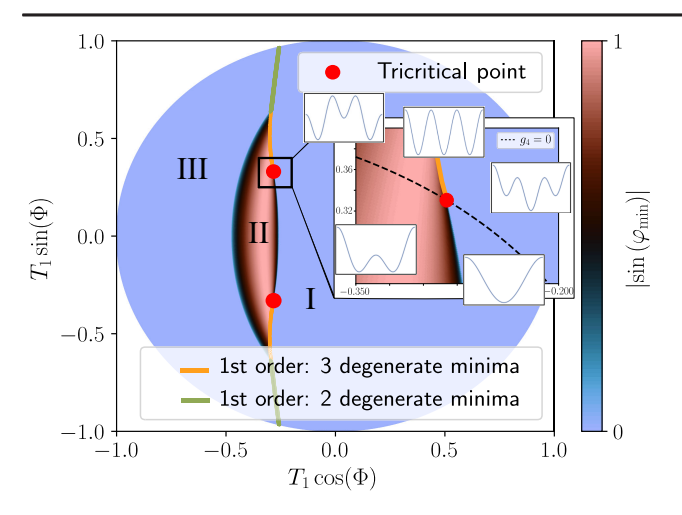


FIG. 2. Given  $\varphi_{\min}$  the global minimum of  $V_J$  in Eq. (2), we depict  $|\sin(\varphi_{\min})|$  in the parameter space at  $T_2=0.6$ . Regions I and III correspond to  $\mathbb{Z}_2$ -symmetric configurations with  $\varphi_{\min}=0,\pi$ , respectively. Region II presents two degenerate minima. Inset: the transition between Regions I and II can be either discontinuous with three degenerate minima (yellow line) or continuous with the merging of the two minima in  $\varphi_{\min}=0$ . The red dot labels a tricritical point where a three-well potential  $V_J=g_2\varphi^2+g_4\varphi^4+\varphi^6$  approximates Eq. (2). The dashed line corresponds to  $g_4=0$ .

phases,  $[\hat{N}_{\alpha,j}, e^{i\hat{\varphi}_{\alpha,j}}] = -e^{i\hat{\varphi}_{\alpha,j}}$ . We consider in particular an on-site electrostatic repulsion  $E_C$  and a rung repulsive interaction  $V_\perp$ .

To obtain the rung potentials  $V_J$  in Eq. (3), the pattern of magnetic fluxes in the system must be carefully considered: a uniform magnetic field breaks time-reversal invariance driving the system into Meissner chiral phases [58–64] and does not fulfill the  $\mathbb{Z}_2$  symmetry on each rung. We consider instead staggered fluxes alternating at each triple JJ [Fig. 1(b)]. This choice yields the local effective potential (2) and avoids additional fluxes between subsequent rungs [39].

The aimed multifrequency sine-Gordon model emerges when the rung potentials  $V_J$  and the Josephson energy  $E_J$  dominate over the charging effects  $E_C$  and  $V_\perp$ . In this Josephson-dominated regime, the system lies away from Mott insulating phases [61,65,66] and phase localization due to charge disorder [67–69] is strongly irrelevant. The effects of disorder in the potential  $V_J$  are discussed in [39]. In the continuum limit, the low-energy physics of the Cooper pairs can be described through bosonization [35] by introducing dual fields  $[\hat{\theta}_{\alpha}(x), \hat{\varphi}_{\alpha}(x)]$  for each leg  $\alpha$ , with  $[\hat{\theta}_{\alpha}(y), \hat{\varphi}_{\beta}(x)] = -i\pi\delta_{\alpha\beta}\Theta(y-x)$ .  $\hat{N}_{\alpha,j}/a \approx -\partial_x\hat{\theta}_{\alpha}(x)/\pi$  represents the charge of the island j=x/a and a the lattice spacing.

By defining the customary charge c and spin s sectors,  $\hat{\varphi}_{c/s}(x) = (\hat{\varphi}_{a}(x) \pm \hat{\varphi}_{b}(x))/\sqrt{2}$ , the Hamiltonian (3) is approximated by [39]

$$\hat{H} = \sum_{q=c,s} u_q \int \frac{dx}{2\pi} \left[ K_q (\partial_x \hat{\varphi}_q)^2 + \frac{1}{K_q} (\partial_x \hat{\theta}_q)^2 \right]$$

$$+ \int \frac{dx}{a} \sum_{r=1}^3 \mu_r \cos(\sqrt{2}n\hat{\varphi}_s).$$
(4)

Equation (4) describes the two branches of the model as Luttinger liquids (LLs), with Luttinger parameters  $K_{c/s} \approx \pi \sqrt{E_J/(2E_C \pm V_\perp)}$  [58,61]. The rung potential  $V_J$  affects only the spin branch and yields the targeted multiple sine-Gordon interactions. The three potential terms in Eq. (4) must be relevant in the renormalization group sense and induce order in the phase  $\hat{\varphi}_s$ , driving the spin sector away from the LL phase. This sets the constraint  $K_s > 9/4$ , which, indeed, is fulfilled for sufficiently large Josephson energies, when the semiclassical description is most accurate. Higher harmonics in Eq. (2), instead, are neglected as less relevant and characterized by smaller amplitudes [39].

The interplay of the three sine-Gordon terms  $\mu_n$  yields nontrivial phase transitions [18,70,71] between the low-energy massive phases of the spin sector. In particular, an Ising critical line meets a FOPT in a tricritical point characterized by the TCI CFT with central charge c=7/10 [18,71].

Observables and results.—We study the phase diagram of our model by using the VUMP ansatz [36–38] to find the ground state of the Hamiltonian (3) in the thermodynamic limit. The VUMP is based on a two-site elementary cell representing two SC islands on the same rung. The local Hilbert space is constructed from the charge basis defined by  $\hat{N}_{\alpha=a/b,j}$ . For numerical purposes, we truncate its basis by introducing a cutoff,  $|N_{\alpha,j}| < N_{\max}$ , with  $N_{\max} \ge 6$  [39]. We set  $E_C/E_J = 0.4$  and  $V_\perp/E_J = 0.65$ , corresponding

We set  $E_C/E_J = 0.4$  and  $V_\perp/E_J = 0.65$ , corresponding to  $K_s \approx 8$ . This favors the clean emergence of the transition lines as the interactions are strongly relevant, yielding sizeable energy gaps in the spin sector. The Fourier components  $\mu_n$  in Eq. (2) are determined from Eq. (1) with a SC gap  $\Delta/E_J = 50$  and  $T_2 = 0.6$ , consistent with Fig. 2.

We identify the phases of the model with labels I, II, and III as in Fig. 2, and, to distinguish them, we employ the local order operator  $\hat{J}_{\perp}^{(2e)}(x)=\sin\left(\sqrt{2}\hat{\varphi}_s(x)\right)$  representing the single-particle contribution to the rung current. In the VUMPS simulations, the symmetry-broken phase II is signaled by a finite  $\langle \hat{J}_{\perp}^{(2e)} \rangle$  [Fig. 3(a)], and it aligns with the mean field predictions in Fig. 2. The symmetric phases I and III broaden away from the semiclassical limit due to the dominant scaling behavior of the first-harmonic interaction. The order parameter allows us to investigate the boundary between the disordered phase I and the ordered phase II: a neat jump in  $\langle \hat{J}_{\perp}^{(2e)} \rangle$  marks a FOPT for  $X_2 = T_1 \sin(\Phi) \gtrsim 0.475$  [Fig. 3(b)], while a continuous change in the region  $|X_2| \lesssim 0.475$  indicates the onset of a second-order transition, as exemplified for  $X_2 = 0$  in Fig. 3(c).

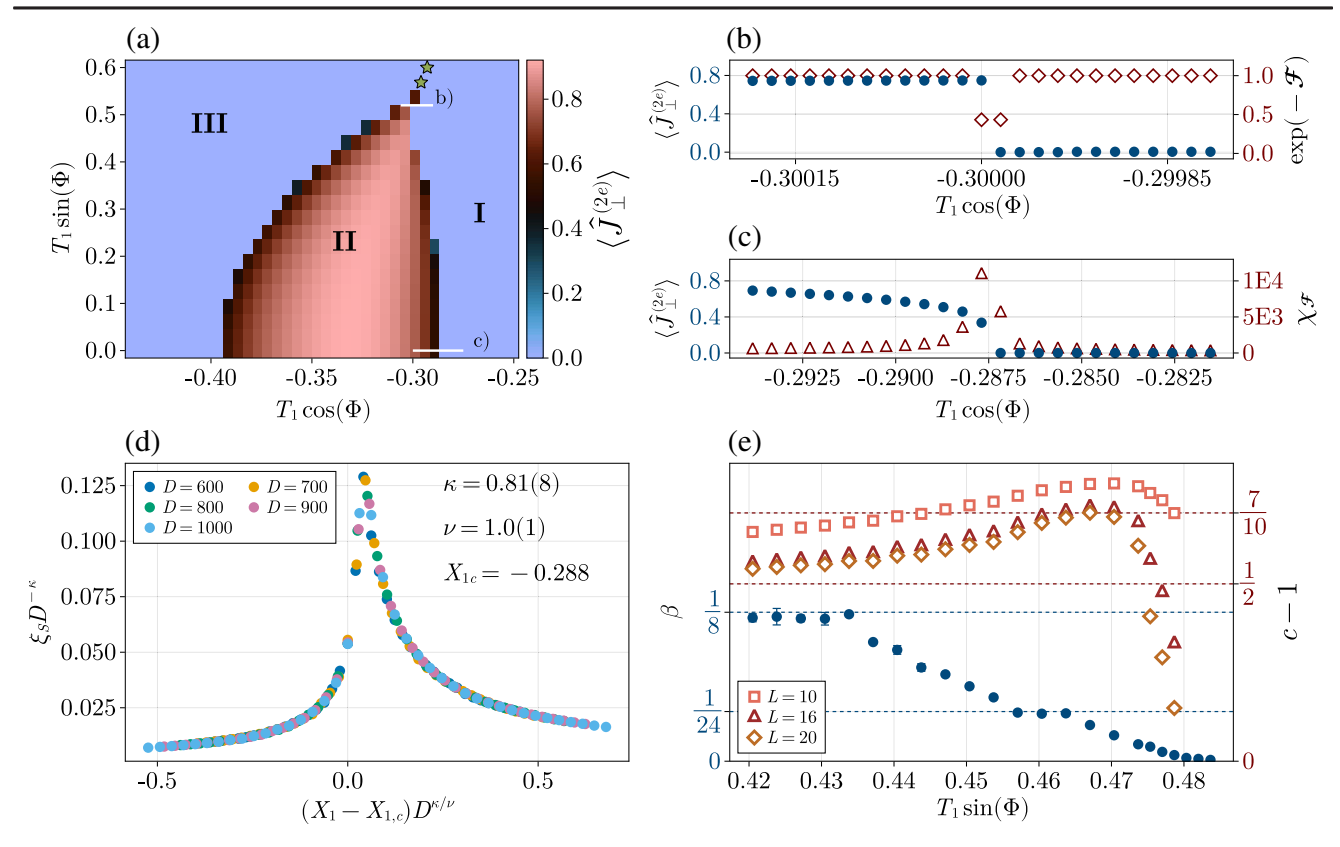


FIG. 3. (a) Expectation value of the order parameter  $\hat{J}_{\perp}^{(2e)}$  at  $T_2=0.6$ . Green stars mark a discontinuity of the log fidelity per site [Eq. (5)] denoting the FOPT between phases I and III, consistently with the mean field picture. (b) FOPT discontinuity of  $\exp(-\mathcal{F})$  and  $\langle \hat{J}_{\perp}^{(2e)} \rangle$  between phases II and I at  $X_2=0.52$  [cut (b) in panel (a)]. (c) Singular behavior of the fidelity susceptibility  $\chi_{\mathcal{F}}$  and order parameter along the cut (c) at  $X_2=0$ , both indicating a second-order phase transition. (d) Collapse of the correlation length  $\xi_s$  at  $X_2=0$  for five values of the bond dimension D by employing a finite-entanglement scaling [39,72]. (e) Critical exponent  $\beta$  obtained by fitting  $\langle \hat{J}_{\perp}^{(2e)} \rangle$  as a function of  $X_1$  for  $0.42 < X_2 < 0.49$  and bond dimension D=600 (blue dots). Two plateaus appear close to the Ising  $(\beta_{\rm IS}=1/8)$  and TCI  $(\beta_{\rm TCI}=1/24)$  predictions. The central charge (empty symbols), derived from finite-size density matrix renormalization group simulations [39], increases from  $c \simeq 1+1/2$  to  $c \simeq 1+7/10$  before dropping to  $c \simeq 1$ .

This picture is confirmed by the analysis of the ground state fidelities [73–76]. Given the abrupt change of the ground state  $|\psi(\mathbf{X})\rangle$  across the FOPT, the average log fidelity per site [75],

$$\mathcal{F}(\mathbf{X}, \delta) = -\lim_{N \to \infty} \frac{1}{N} \log \left( \langle \psi(\mathbf{X} - \delta) | \psi(\mathbf{X} + \delta) \rangle \right), \quad (5)$$

displays a clean discontinuity [Fig. 3(b)], at fixed  $\delta$ . On the other hand, across the lower cut the fidelity susceptibility  $\chi_{\mathcal{F}} = \mathcal{F}/\delta^2$  shows a more gradual singular behavior and exhibits the typical peak of a second-order phase transition in Fig. 3(c).

The universal collapse of the spin correlation length  $\xi_s$  according to finite-entanglement scaling ansatz [39,72] confirms that the continuous phase transition lies within the Ising universality class; see Fig. 3(d). For  $X_2 = 0$ , we located the critical point  $X_{1c}$  and extrapolated the infinite bond dimension estimate of the critical exponent  $\nu = 1.0(1)$ , matching the CFT prediction  $\nu_{\rm IS} = 1$ .

Additionally, our analysis reveals the scaling of the effective magnetization [39]  $\langle \hat{J}_{\perp}^{(2e)} \rangle \sim |X_1 - X_{1c}|^{\beta}$ , with the critical exponent  $\beta$  compatible with the Ising value  $\beta_{\rm IS} = 1/8$  for  $|X_2| < 0.43$  [Fig. 3(e)].

The latter confirms also the onset of the TCI point joining the Ising phase transition and the FOPT. By increasing  $X_2$  above 0.43,  $\beta$  decreases and, at  $X_2 \sim 0.46$ , it exhibits a plateau close to the expected TCI value  $\beta_{\text{TCI}} = 1/24$  [Fig. 3(e)]. Further increasing  $X_2$  results in a vanishing  $\beta$ , as expected for a FOPT. The error bars in Fig. 3(e) do not account for finite-entanglement effects, accentuated by the massless LL in the charge sector with c=1 throughout the entire phase diagram. Despite this, we observe a good convergence in scaling features away from the critical point.

Finally, along the transition line for  $X_2 > 0.42$ , finitesize density matrix renormalization group simulations reveal in Fig. 3(e) the nonmonotonic behavior of the central charge c [29,77], consistently with the presence of the TCI CFT (c - 1 = 7/10) amid the Ising regime (c - 1 = 1/2) and the FOPT (c-1=0). Finite-size effects yield large central charge estimates as expected and shift the tricritical point to larger  $X_2$  relative to the  $\beta = \beta_{TCI}$ .

Experimental observables.—Transport features can be used to explore the phase diagram of the model. Indeed, the thermal conductance across 1D systems at criticality is proportional to the central charge c of the related CFT at low temperature T [78,79]:  $G_Q = (\pi k_B^2 T c/6\hbar)$ . In our model, symmetric and symmetry-broken phases exhibit c=1 due to the charge sector, while along the transition line, the additional contribution of the spin sector yields the behavior shown in Fig. 3(e).

In thermal transport experiments [80,81], heat currents will be dominated by the QFT collective modes for temperatures considerably below the SC gap ( $\sim$ 2 K for Al). Finite size and temperature will affect the profile of the heat conductance as a function of the system parameters. Nevertheless, a nonmonotonic behavior of  $G_Q$  across the second-order phase transition line and in proximity of the TCI point would provide strong evidence of the emergence of the related CFTs.

Furthermore, as the rung currents exhibit quasi-long-range order at the phase transitions, the power spectrum of their noise provides a probe to detect the critical lines and measure the scaling dimension of the order parameter. Additionally, microwave spectroscopy of JJAs [6–8] allows for the study of the excitation spectra of the system and can be used to verify the predictions of the TCI CFT spectra [57,82–85].

Conclusions.—We designed a JJ ladder to realize a quantum simulator for the tricritical Ising CFT. Our construction is based on the properties of hybrid semi-conducting-superconducting JJs and their nonsinusoidal energy-phase relation. In particular, we engineered a triple JJ that allows us to tune the higher harmonics and we adopted them to realize the physics of a multifrequency sine-Gordon QFT [71].

We used bosonization and tensor-network simulations to investigate this JJA. Our analysis showed the presence of an ordered phase and highlighted the existence of a critical Ising plane connected to a first-order transition along a tricritical Ising line within a three-parameter space.

Our construction does not require the introduction of strong and fine-tuned interactions and relies on the adjustments of parameters that can be controlled in hybrid stateof-the-art platforms.

Our Letter poses the basis for further explorations of the connection between nontrivial interacting CFTs and hybrid JJ systems characterized by high harmonics terms. The ladder we devised, in particular, provides a tool to engineer systems with exotic topological order in two-dimensional setups: an array of these tricritical systems opens the way to realize Fibonacci topological superconductors [21,22] with universal non-Abelian anyons.

The data and code for this Letter are available at [87].

We thank L. Banszerus, A. Cappelli, C. Marcus, G. Mussardo, C. Schrade, and S. Vaitiekenas for fruitful discussions. We acknowledge support from the Deutsche Forschungsgemeinschaft (DFG) project Grant No. 277101999 within the CRC network TR 183 (subprojects B01 and C01). L. M. and M. B. are supported by the Villum Foundation (Research Grant No. 25310). N. T. and M.R. are further supported by the DFG under Germany's Excellence Strategy-Cluster of Excellence Matter and Light for Quantum Computing (ML4Q) EXC 2004/1 2013 390534769. The authors gratefully acknowledge the Gauss Center for Supercomputing e.V. for funding this project by providing computing time through the John von Neumann Institute for Computing (NIC) on the GCS Supercomputer JUWELS at the Jülich Supercomputing Centre (JSC) (Grant NeTeNeSyQuMa) and the FZ Jülich for JURECA (institute project PGI-8) [86].

\*These authors contributed equally to this work.

- [3] C. G. L. Bøttcher, F. Nichele, M. Kjaergaard, H. J. Suominen, J. Shabani, C. J. Palmstrøm, and C. M. Marcus, Superconducting, insulating and anomalous metallic regimes in a gated two-dimensional semiconductor– superconductor array, Nat. Phys. 14, 1138 (2018).
- [4] C. G. L. Bøttcher, F. Nichele, J. Shabani, C. J. Palmstrøm, and C. M. Marcus, The Berezinskii-Kosterlitz-Thouless transition and anomalous metallic phase in a hybrid Josephson junction array, arXiv:2210.00318.
- [5] C. G. L. Bøttcher, F. Nichele, J. Shabani, C. J. Palmstrøm, and C. M. Marcus, Dynamical vortex transitions in a gatetunable two-dimensional Josephson junction array, Phys. Rev. B 108, 134517 (2023).
- [6] M. T. Bell, B. Douçot, M. E. Gershenson, L. B. Ioffe, and A. Petković, Josephson ladders as a model system for 1D quantum phase transitions, C.R. Phys. 19, 484 (2018).
- [7] R. Kuzmin, R. Mencia, N. Grabon, N. Mehta, Y.-H. Lin, and V. E. Manucharyan, Quantum electrodynamics of a superconductor–insulator phase transition, Nat. Phys. 15, 930 (2019).
- [8] S. Mukhopadhyay, J. Senior, J. Saez-Mollejo, D. Puglia, M. Zemlicka, J. Fink, and A.P. Higginbotham, Superconductivity from a melted insulator in Josephson junction arrays, Nat. Phys. 19, 1630 (2023).

<sup>[1]</sup> P. Krogstrup, N. L. B. Ziino, W. Chang, S. M. Albrecht, M. H. Madsen, E. Johnson, J. Nygård, C. M. Marcus, and T. S. Jespersen, Epitaxy of semiconductor–superconductor nanowires, Nat. Mater. 14, 400 (2015).

<sup>[2]</sup> J. Shabani, M. Kjaergaard, H. J. Suominen, Y. Kim, F. Nichele, K. Pakrouski, T. Stankevic, R. M. Lutchyn, P. Krogstrup, R. Feidenhans'l, S. Kraemer, C. Nayak, M. Troyer, C. M. Marcus, and C. J. Palmstrøm, Two-dimensional epitaxial superconductor-semiconductor heterostructures: A platform for topological superconducting networks, Phys. Rev. B 93, 155402 (2016).

- [9] K. Cedergren, R. Ackroyd, S. Kafanov, N. Vogt, A. Shnirman, and T. Duty, Insulating Josephson junction chains as pinned Luttinger liquids, Phys. Rev. Lett. 119, 167701 (2017).
- [10] M. Kjaergaard, H. J. Suominen, M. P. Nowak, A. R. Akhmerov, J. Shabani, C. J. Palmstrøm, F. Nichele, and C. M. Marcus, Transparent semiconductor-superconductor interface and induced gap in an epitaxial heterostructure Josephson junction, Phys. Rev. Appl. 7, 034029 (2017).
- [11] L. Casparis, M. R. Connolly, M. Kjaergaard, N. J. Pearson, A. Kringhøj, T. W. Larsen, F. Kuemmeth, T. Wang, C. Thomas, S. Gronin, G. C. Gardner, M. J. Manfra, C. M. Marcus, and K. D. Petersson, Superconducting gatemon qubit based on a proximitized two-dimensional electron gas, Nat. Nanotechnol. 13, 915 (2018).
- [12] C. Ciaccia, R. Haller, A. C. C. Drachmann, T. Lindemann, M. J. Manfra, C. Schrade, and C. Schönenberger, Gatetunable Josephson diode in proximitized InAs supercurrent interferometers, Phys. Rev. Res. 5, 033131 (2023).
- [13] L. Banszerus, W. Marshall, C. W. Andersson, T. Lindemann, M. J. Manfra, C. M. Marcus, and S. Vaitiekėnas, Voltage-controlled synthesis of higher harmonics in hybrid Josephson junction circuits, arXiv:2402.11603.
- [14] A. Roy and H. Saleur, Quantum electronic circuit simulation of generalized sine-Gordon models, Phys. Rev. B 100, 155425 (2019).
- [15] A. Roy, D. Schuricht, J. Hauschild, F. Pollmann, and H. Saleur, The quantum sine-Gordon model with quantum circuits, Nucl. Phys. B968, 115445 (2021).
- [16] A. Roy and S. L. Lukyanov, Soliton confinement in a quantum circuit, Nat. Commun. 14, 7433 (2023).
- [17] P. Di Francesco, P. Mathieu, and D. Senechal, *Conformal Field Theory*, Graduate Texts in Contemporary Physics (Springer-Verlag, New York, 1997).
- [18] A. Roy, Quantum electronic circuits for multicritical ising models, Phys. Rev. B 108, 235414 (2023).
- [19] R. S. K. Mong, D. J. Clarke, J. Alicea, N. H. Lindner, P. Fendley, C. Nayak, Y. Oreg, A. Stern, E. Berg, K. Shtengel, and M. P. A. Fisher, Universal topological quantum computation from a superconductor-Abelian quantum Hall heterostructure, Phys. Rev. X 4, 011036 (2014).
- [20] E. M. Stoudenmire, D. J. Clarke, R. S. K. Mong, and J. Alicea, Assembling Fibonacci anyons from a Z<sub>3</sub> parafermion lattice model, Phys. Rev. B 91, 235112 (2015).
- [21] Y. Hu and C. L. Kane, Fibonacci topological superconductor, Phys. Rev. Lett. 120, 066801 (2018).
- [22] C. Li, H. Ebisu, S. Sahoo, Y. Oreg, and M. Franz, Coupled wire construction of a topological phase with chiral tricritical Ising edge modes, Phys. Rev. B 102, 165123 (2020).
- [23] D. Friedan, Z. Qiu, and S. Shenker, Conformal invariance, unitarity, and critical exponents in two dimensions, Phys. Rev. Lett. 52, 1575 (1984).
- [24] A. Rahmani, X. Zhu, M. Franz, and I. Affleck, Emergent supersymmetry from strongly interacting majorana zero modes, Phys. Rev. Lett. 115, 166401 (2015).
- [25] E. O'Brien and P. Fendley, Lattice supersymmetry and order-disorder coexistence in the tricritical Ising model, Phys. Rev. Lett. **120**, 206403 (2018).

- [26] A. Rahmani, X. Zhu, M. Franz, and I. Affleck, Phase diagram of the interacting Majorana chain model, Phys. Rev. B 92, 235123 (2015).
- [27] X. Zhu and M. Franz, Tricritical Ising phase transition in a two-ladder Majorana fermion lattice, Phys. Rev. B 93, 195118 (2016).
- [28] H. Ebisu, E. Sagi, and Y. Oreg, Supersymmetry in the insulating phase of a chain of Majorana cooper pair boxes, Phys. Rev. Lett. 123, 026401 (2019).
- [29] S. Ejima, F. H. L. Essler, F. Lange, and H. Fehske, Ising tricriticality in the extended Hubbard model with bond dimerization, Phys. Rev. B 93, 235118 (2016).
- [30] S. Ejima, F. Lange, F.H. Essler, and H. Fehske, Critical behavior of the extended Hubbard model with bond dimerization, Physica (Amsterdam) 536B, 474 (2018).
- [31] R. S. K. Mong, D. J. Clarke, J. Alicea, N. H. Lindner, and P. Fendley, Parafermionic conformal field theory on the lattice, J. Phys. A 47, 452001 (2014).
- [32] K. Slagle, D. Aasen, H. Pichler, R. S. K. Mong, P. Fendley, X. Chen, M. Endres, and J. Alicea, Microscopic characterization of Ising conformal field theory in Rydberg chains, Phys. Rev. B 104, 235109 (2021).
- [33] K. Slagle, Y. Liu, D. Aasen, H. Pichler, R. S. K. Mong, X. Chen, M. Endres, and J. Alicea, Quantum spin liquids bootstrapped from ising criticality in rydberg arrays, Phys. Rev. B 106, 115122 (2022).
- [34] A. S. Buyskikh, L. Tagliacozzo, D. Schuricht, C. A. Hooley, D. Pekker, and A. J. Daley, Spin models, dynamics, and criticality with atoms in tilted optical superlattices, Phys. Rev. Lett. 123, 090401 (2019).
- [35] T. Giamarchi, Quantum Physics in One Dimension (Clarendon Press, Oxford, England, UK, 2003).
- [36] J. Haegeman, J. I. Cirac, T. J. Osborne, I. Pižorn, H. Verschelde, and F. Verstraete, Time-dependent variational principle for quantum lattices, Phys. Rev. Lett. 107, 070601 (2011).
- [37] J. Haegeman, C. Lubich, I. Oseledets, B. Vandereycken, and F. Verstraete, Unifying time evolution and optimization with matrix product states, Phys. Rev. B 94, 165116 (2016).
- [38] V. Zauner-Stauber, L. Vanderstraeten, M. T. Fishman, F. Verstraete, and J. Haegeman, Variational optimization algorithms for uniform matrix product states, Phys. Rev. B 97, 045145 (2018).
- [39] See Supplemental Material at http://link.aps.org/ supplemental/10.1103/PhysRevLett.132.226502 for further data and technical details, which includes Refs. [40–50].
- [40] S. Hart, Z. Cui, G. Ménard, M. Deng, A. E. Antipov, R. M. Lutchyn, P. Krogstrup, C. M. Marcus, and K. A. Moler, Current-phase relations of InAs nanowire Josephson junctions: From interacting to multimode regimes, Phys. Rev. B 100, 064523 (2019).
- [41] C. W. J. Beenakker, Random-matrix theory of quantum transport, Rev. Mod. Phys. 69, 731 (1997).
- [42] F. Nichele, E. Portolés, A. Fornieri, A. M. Whiticar, A. C. C. Drachmann, S. Gronin, T. Wang, G. C. Gardner, C. Thomas, A. T. Hatke, M. J. Manfra, and C. M. Marcus, Relating andreev bound states and supercurrents in hybrid Josephson junctions, Phys. Rev. Lett. 124, 226801 (2020).

- [43] F. Arute *et al.*, Quantum supremacy using a programmable superconducting processor, Nature (London) **574**, 505 (2019).
- [44] G. Mussardo, *Statistical Field Theory* (Oxford University Press, Oxford, England, UK, 2020).
- [45] A. B. Harris and T. C. Lubensky, Renormalization-group approach to the critical behavior of random-spin models, Phys. Rev. Lett. 33, 1540 (1974).
- [46] T. Giamarchi and H. J. Schulz, Anderson localization and interactions in one-dimensional metals, Phys. Rev. B 37, 325 (1988).
- [47] P. Calabrese and J. Cardy, Entanglement entropy and quantum field theory, J. Stat. Mech. (2004), P06002.
- [48] F. Pollmann, S. Mukerjee, A. M. Turner, and J. E. Moore, Theory of finite-entanglement scaling at one-dimensional quantum critical points, Phys. Rev. Lett. **102**, 255701 (2009).
- [49] S. M. Bhattacharjee and F. Seno, A measure of datacollapse for scaling, J. Phys. A 34, 6375 (2001).
- [50] M. Fishman, S. R. White, and E. M. Stoudenmire, The ITensor software library for tensor network calculations, SciPost Phys. Codebases 4 (2022) 10.21468/SciPostPhysCodeb.4.
- [51] C. W. J. Beenakker, Universal limit of critical-current fluctuations in mesoscopic Josephson junctions, Phys. Rev. Lett. 67, 3836 (1991).
- [52] A. Kringhøj, L. Casparis, M. Hell, T. W. Larsen, F. Kuemmeth, M. Leijnse, K. Flensberg, P. Krogstrup, J. Nygård, K. D. Petersson, and C. M. Marcus, Anharmonicity of a superconducting qubit with a few-mode Josephson junction, Phys. Rev. B 97, 060508(R) (2018).
- [53] A. M. Bozkurt, J. Brookman, V. Fatemi, and A. R. Akhmerov, Double-Fourier engineering of Josephson energy-phase relationships applied to diodes, SciPost Phys. 15, 204 (2023).
- [54] T. T. Heikkilä, J. Särkkä, and F. K. Wilhelm, Supercurrent-carrying density of states in diffusive mesoscopic Josephson weak links, Phys. Rev. B 66, 184513 (2002).
- [55] A. B. Zamolodchikov, Conformal symmetry and multicritical points in two-dimensional quantum field theory, Sov. J. Nucl. Phys. 44, 529 (1986).
- [56] M. Lässig, G. Mussardo, and J. L. Cardy, The scaling region of the tricritical Ising model in two dimensions, Nucl. Phys. B348, 591 (1991).
- [57] L. Lepori, G. Mussardo, and G. Z. Tóth, The particle spectrum of the tricritical Ising model with spin reversal symmetric, J. Stat. Mech. (2008), P09004.
- [58] E. Orignac and T. Giamarchi, Meissner effect in a bosonic ladder, Phys. Rev. B **64**, 144515 (2001).
- [59] A. Petrescu and K. Le Hur, Bosonic Mott insulator with Meissner currents, Phys. Rev. Lett. **111**, 150601 (2013).
- [60] M. Piraud, F. Heidrich-Meisner, I. P. McCulloch, S. Greschner, T. Vekua, and U. Schollwöck, Vortex and Meissner phases of strongly interacting bosons on a two-leg ladder, Phys. Rev. B 91, 140406(R) (2015).
- [61] A. Petrescu and K. Le Hur, Chiral Mott insulators, Meissner effect, and Laughlin states in quantum ladders, Phys. Rev. B 91, 054520 (2015).
- [62] S. Greschner, M. Piraud, F. Heidrich-Meisner, I.P. McCulloch, U. Schollwöck, and T. Vekua, Spontaneous

- increase of magnetic flux and chiral-current reversal in bosonic ladders: Swimming against the tide, Phys. Rev. Lett. **115**, 190402 (2015).
- [63] S. Greschner, M. Piraud, F. Heidrich-Meisner, I.P. McCulloch, U. Schollwöck, and T. Vekua, Symmetry-broken states in a system of interacting bosons on a two-leg ladder with a uniform Abelian gauge field, Phys. Rev. A 94, 063628 (2016).
- [64] A. Haller, A. S. Matsoukas-Roubeas, Y. Pan, M. Rizzi, and M. Burrello, Exploring helical phases of matter in bosonic ladders, Phys. Rev. Res. 2, 043433 (2020).
- [65] R. Fazio and H. van der Zant, Quantum phase transitions and vortex dynamics in superconducting networks, Phys. Rep. 355, 235 (2001).
- [66] M. Goldstein, M. H. Devoret, M. Houzet, and L. I. Glazman, Inelastic microwave photon scattering off a quantum impurity in a Josephson-junction array, Phys. Rev. Lett. 110, 017002 (2013).
- [67] T. Giamarchi and H. J. Schulz, Localization and interaction in one-dimensional quantum fluids, Europhys. Lett. 3, 1287 (1987).
- [68] E. Orignac and T. Giamarchi, Weakly disordered spin ladders, Phys. Rev. B 57, 5812 (1998).
- [69] F. Crépin, N. Laflorencie, G. Roux, and P. Simon, Phase diagram of hard-core bosons on clean and disordered twoleg ladders: Mott insulator–Luttinger liquid–Bose glass, Phys. Rev. B 84, 054517 (2011).
- [70] G. Delfino and G. Mussardo, Non-integrable aspects of the multi-frequency sine-Gordon model, Nucl. Phys. B516, 675 (1998).
- [71] G. Z. Tóth, A nonperturbative study of phase transitions in the multi-frequency sine-gordon model, J. Phys. A 37, 9631 (2004).
- [72] L. Tagliacozzo, Thiago. R. de Oliveira, S. Iblisdir, and J. I. Latorre, Scaling of entanglement support for matrix product states, Phys. Rev. B 78, 024410 (2008).
- [73] P. Zanardi and N. Paunković, Ground state overlap and quantum phase transitions, Phys. Rev. E 74, 031123 (2006).
- [74] M. Cozzini, R. Ionicioiu, and P. Zanardi, Quantum fidelity and quantum phase transitions in matrix product states, Phys. Rev. B 76, 104420 (2007).
- [75] M. M. Rams and B. Damski, Quantum fidelity in the thermodynamic limit, Phys. Rev. Lett. 106, 055701 (2011).
- [76] D. Rossini and E. Vicari, Ground-state fidelity at first-order quantum transitions, Phys. Rev. E 98, 062137 (2018).
- [77] S. Ejima, T. Yamaguchi, F. H. L. Essler, F. Lange, Y. Ohta, and H. Fehske, Exotic criticality in the dimerized spin-1XXZ chain with single-ion anisotropy, SciPost Phys. 5, 059 (2018).
- [78] D. Bernard and B. Doyon, Conformal field theory out of equilibrium: A review, J. Stat. Mech. (2016), 064005.
- [79] K. Gawędzki, E. Langmann, and P. Moosavi, Finite-time universality in nonequilibrium CFT, J. Stat. Phys. **172**, 353 (2018).
- [80] M. Partanen, K. Y. Tan, J. Govenius, R. E. Lake, M. K. Mäkelä, T. Tanttu, and M. Möttönen, Quantum-limited heat conduction over macroscopic distances, Nat. Phys. 12, 460 (2016).
- [81] A. Gubaydullin, G. Thomas, D. S. Golubev, D. Lvov, J. T. Peltonen, and J. P. Pekola, Photonic heat transport in three

- terminal superconducting circuit, Nat. Commun. 13, 1 (2022).
- [82] A. Feiguin, S. Trebst, A. W. W. Ludwig, M. Troyer, A. Kitaev, Z. Wang, and M. H. Freedman, Interacting anyons in topological quantum liquids: The Golden chain, Phys. Rev. Lett. **98**, 160409 (2007).
- [83] Y. Zou, A. Milsted, and G. Vidal, Conformal data and renormalization group flow in critical quantum spin chains using periodic uniform matrix product states, Phys. Rev. Lett. **121**, 230402 (2018).
- [84] A. C. Cubero, R. M. Konik, M. Lencsés, G. Mussardo, and G. Takács, Duality and form factors in the thermally

- deformed two-dimensional tricritical Ising model, SciPost Phys. 12, 162 (2022).
- [85] M. Lencsés, G. Mussardo, and G. Takács, Confinement in the tricritical Ising model, Phys. Lett. B 828, 137008 (2022).
- [86] J. S. Centre, Jureca: Data centric and booster modules implementing the modular supercomputing architecture at Jülich supercomputing centre, J. Large-Scale Res. Facil. 7, A182 (2021).
- [87] L. Maffi, N. Tausendpfund, M. Rizzi, and M. Burrello, Data and Code associated to the paper "Quantum simulation of the tricritical Ising model in tunable Josephson junction ladders", 10.5281/zenodo.10225786 (2023).

# Supplemental materials for "Quantum simulation of the tricritical Ising model in tunable Josephson junction ladders"

### I. TRIPLE JOSEPHSON JUNCTION ELEMENT

### A. Higher harmonics expansion

In this section, we briefly analyze the decomposition of the energy-phase relation of the triple JJ into harmonic terms  $\mu_n$  that we introduced in Eq. (2) of the main text. Assuming that each semiconducting/superconducting junction is described by a single quantum channel, the potential of triple JJ element

$$V_{J}(\varphi) = -\Delta \left( \sqrt{1 - T_{1} \sin^{2} \left( \frac{\varphi - \Phi_{1}}{2} \right)} + \sqrt{1 - T_{2} \sin^{2} \left( \frac{\varphi}{2} \right)} + \sqrt{1 - T_{3} \sin^{2} \left( \frac{\varphi + \Phi_{2}}{2} \right)} \right), \tag{S1}$$

can be expanded as  $V_J = \sum_n \mu_n \cos(n\varphi)$ , where  $\varphi$  is the SC phase difference of the two islands and  $\Delta$  the superconducting gap induced in the semiconducting layer of the hybrid system. To maintain the reflection symmetry  $\varphi \to -\varphi$ , we impose  $\Phi_1 = \Phi_2 = \Phi$  and  $T_1 = T_3$ . The full expression of  $\mu_n$  involves the elliptic integrals

$$\mu_n = \int_{-\pi}^{\pi} \frac{d\varphi}{\pi} V_J(\varphi) \cos(n\varphi), \tag{S2}$$

which do not have an elementary analytical solution. However, for small transparencies  $T_i \ll 1$ , we can approximate them as follows:

$$\mu_{1}/\Delta = -\frac{1}{512} \left( T_{2} \left( 128 + 32T_{2} + 15T_{2}^{2} \right) + 2T_{1} \left( 128 + 32T_{1} + 15T_{1}^{2} \right) \cos \Phi \right) + O\left( T_{i}^{4} \right)$$

$$\mu_{2}/\Delta = \frac{1}{256} \left( T_{2}^{2} \left( 4 + 3T_{2} \right) + 2T_{1}^{2} \left( 4 + 3T_{1} \right) \cos 2\Phi \right) + O\left( T_{i}^{4} \right)$$

$$\mu_{3}/\Delta = -\frac{1}{512} \left( T_{2}^{3} + 2T_{1}^{3} \cos 3\Phi \right) + O\left( T_{i}^{4} \right)$$

$$\mu_{4}/\Delta = O\left( T_{i}^{4} \right).$$
(S3)

In this limit, it is evident that the potential  $V_J$  is mostly determined by the first harmonic term  $\cos \varphi$  with  $\mu_1 < 0$ , as long as the magnetic flux is such that  $\cos \Phi > 0$ . Numerical evaluation of the integrals (S2) shows that this is true also in the large transparencies limit.

The situation is different if we consider fluxes such that  $\cos \Phi < 0$ . In particular, one can fine-tune the external parameters to make  $\mu_1$  vanish. Moreover, for  $\Phi = 2\pi/3$  and  $T_1 = T_2$  both  $\mu_1$  and  $\mu_2$  vanish as a consequence of destructive interference of tunneling events of one and two Cooper pairs through the three junctions. In this case only triplet of Cooper pairs can jump between the two SC islands with amplitude  $|\mu_3|$ . One can also check that, in the considered geometry, the contribution  $\mu_4$  is always at least one order of magnitude smaller than the other terms as showed in Fig. S1. Therefore, given the ability of controlling both the transparencies of the hybrid junctions through external gates and the magnetic flux piercing the two loops, we can tune independently the ratios between the first three harmonics amplitudes in Eq. (S1). In particular, the results discussed in the main text require that only the transparencies of the external junctions,  $T_1$  and  $T_3$ , need to be tuned, whereas  $T_2$  does not qualitatively affect the appearance of the tricritical Ising point. This constitutes an advantage for experimental realizations since we envision that the external junctions can more easily be controlled via electrostatic gates.

Importantly, our approximations hold when each junction is sufficiently shorter than the (diffusive) coherence length of the superconducting regions induced in the semiconductor, allowing coherent tunneling process. This is achieved in [1] with a length of 150 nm. The width of the junction, instead, mostly affects the amount of active quantum channels in the junction: the limit of single-channel junction has been experimentally investigated in hybrid nanowire devices, with widths of about 100 nm [2, 3].

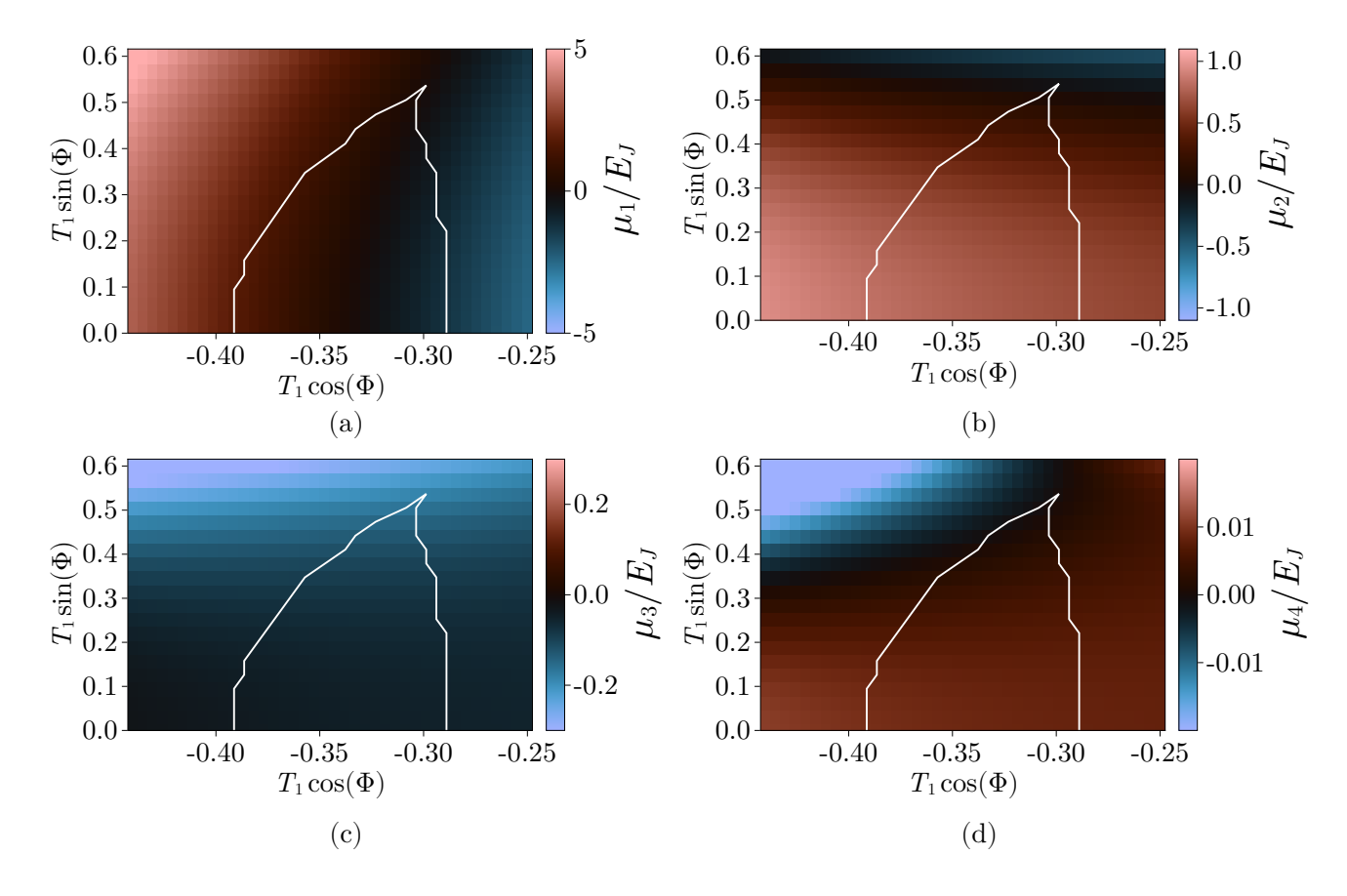


Figure S1. The amplitudes of the first four harmonics  $\mu_n$  with  $n=0,1,\ldots,4$  as a function of the triple JJ parameters. The white lines mark the boundary of the symmetry-broken regime. We set  $T_2=0.6$  and the SC gap  $\Delta$  induced by proximity in the semiconductors is fixed at  $\Delta=50$  in units of  $E_J$  and does not influence the ratio between the  $\mu$  coefficients (S2).

### B. Multichannel case

In the case of several transport channels in each of the junctions, the Josephson energy-phase relation is given by the sum of the related contributions:

$$\mathcal{E}_{J}^{(p)} = -\sum_{i=1}^{M_p} \Delta \sqrt{1 - T_p^{(i)} \sin^2(\phi/2)},\tag{S4}$$

where  $T_p^{(i)}$  represents the transparency of the *i*th channel in the JJ p, and  $M_p$  is the number of channels in the junction. For disordered multichannel junctions, these transport coefficients  $T_p^{(i)}$  follow a bimodal distribution [4], with a few high-transparency channels resulting in a nonsinusoidal current response. A complete generalization of our results to the multichannel case goes beyond the scope of this supplemental section. However, a qualitative analysis of its effects is needed. In particular, one essential feature of our triple JJs element is the symmetry between the two external junctions.

Experimental results for wide junctions (with width  $W \simeq 2-3\,\mu\mathrm{m}$ ) in gate-tunable device showed that the nonsinusoidal effects are overall well-approximated by one JJ with  $M^*$  high-transparency channels with the same average  $T^*$ , such that the current phase relation reads [1, 5]

$$I(\varphi) = \frac{e\Delta M^* T^*}{\hbar} \frac{\sin(\varphi)}{\sqrt{1 - T^* \sin^2(\varphi/2)}}.$$
 (S5)

Therefore, the nonlinear function in Eq. (1) in the main text well approximates the energy-phase relation also in the multichannel case. Equation (S5) represents a phenomenological approximation that effectively described the behavior of past experimental platforms [1], but it does not capture comprehensively the multichannel case.

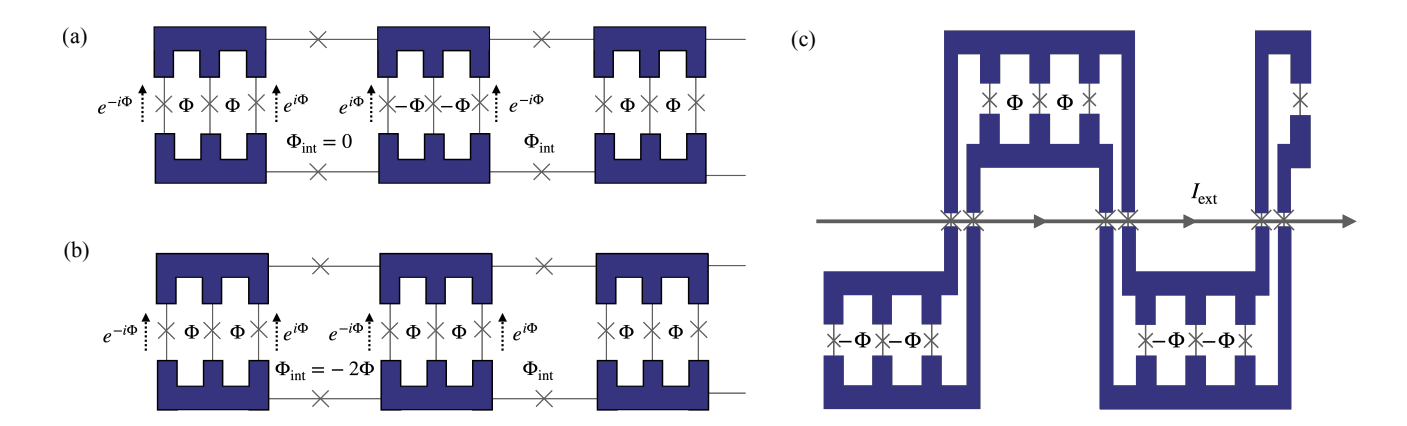


Figure S2. (a) and (b) illustrate the two configurations of nonuniform magnetic fluxes essential for preserving time-reversal invariance in the effective ladder description. In configuration (a), the fluxes are staggered within consecutive triple Josephson junction (JJ) elements, while in (b), the  $\Phi_{\rm int}=-2\Phi$  condition is implemented in the plaquettes of the effective ladder. Panel (c) shows the physical realization of configuration (a) achieved through a snake geometry and the insertion of a line with a tunable external current  $I_{\rm ext}$ .

In such approximation, one can assume that the external voltage gate  $V_G$  affects only the number of channels  $M^*$  and not the average transparency  $T^*$ , which mildly varies among the junctions [1]. In this case, the symmetry between the external JJs is lifted by the weak finite difference between the two average transparencies  $T_1^* - T_3^* \neq 0$ , which is almost independent of the voltage gates  $V_{G1}$  and  $V_{G3}$ . However, tuning the number of open channels  $M_1^*$  and  $M_3^*$  via the voltage gates provides a way to mitigate this explicit symmetry breaking. Finally, potential asymmetries in the magnetic fluxes cause a splitting in energy of the minima of the potential  $V_J$  which is linear in  $\Phi_1 - \Phi_3$ . However, this effect can also be used to mitigate the asymmetry caused by the mismatch of the transparencies  $T_1^* \neq T_3^*$  and restore the degeneracy of the minima of  $V_J$ .

Alternatively, as briefly mentioned in the main text, the non-sinusoidal current/phase relation can effectively be obtained by substituting each of the junctions with two sinusoidal multichannel JJs in series [6, 7]. For the external links, the effective transmissions  $T_{p,\text{eff}}$  with p=1,3 will depend on the critical currents flowing through such JJs and indeed can be tuned by external electrostatic gates.

### II. LADDER: FURTHER DETAILS

### A. Staggered magnetic fluxes

Interacting bosons on a ladder with uniform magnetic fields exhibit are characterized by the onset of several chiral many-body phases, including the Meissner phase. For our purposes the onset of the Meissner effect may be detrimental, because it breaks the emergent Lorentz invariance in the QFT and may compete with the phases and critical points discussed in the main text.

Additionally, to obtain a quantum simulation of the three-frequency sine-Gordon model, each rung triple JJ must be characterizes by the same  $V_J$ . This condition is, in the general case, fulfilled only by staggered patterns of magnetic fluxes.

We present two viable flux configurations which are schematically represented in Fig. S2(a) and (b). The solution (a) relies on the parity property of the local potential  $V_J$  under  $\Phi \to -\Phi$  and enables the engineering of a ladder geometry where the magnetic flux between two subsequent rungs, thus the related Aharonov-Bohm phase  $\Phi_{\rm int}$ , vanishes. This preserves time-reversal invariance in the effective QFT. However, this approach leads to the experimental challenge of controlling nonuniform magnetic fields along the ladder.

A convenient construction to realize the configuration (a) in experimental devices is depicted in Fig. S2(c). To stagger the magnetic fluxes within two subsequent triple JJ elements, we design the ladder in a 'snake' configuration and control the magnetic field by introducing a current  $I_{\text{ext}}$  through the line schematically represented in Fig. S2. Alternatively, a local control of multiple fluxes can be achieved with the techniques adopted by modern quantum processors based on transmon qubits [8].

An alternative flux configuration, Fig. S2(b) results in the same potentials  $V_J$  on each rung and relies on compensat-

ing the magnetic fluxes of the triple JJs with opposite fluxes in the ladder plaquettes, thus setting  $\Phi_{\rm int}=-2\Phi$  between each rung. The possibility of introducing additional integer fluxes in each loop, thus replacing  $\Phi_{\rm int}\to\Phi_{\rm int}+2\pi$  may also offer an alternative to implement the configuration (b) with uniform magnetic fluxes. To tune the system at the tricritical point in this scenario, however, it is required to known a priori the parameter  $T_2$  of the ladder: the critical flux of the trijunctions depends indeed on  $T_2$ ; therefore, its knowledge is necessary to designing superconducting circuits with a correct ratio between the areas of the loops inside the trijunctions and the areas of the loops between the ladder rungs to obtain the desired tunneling phases at constant magnetic field.

### B. Disorder

In the hybrid solid-state devices we consider, disorder is limited by the accurate epitaxial growth and lithographic techniques employed for their fabrication. Nevertheless, a certain amount of disorder is unavoidable due to the typical etching procedures adopted to define the Josephson junctions and it may prevent the emergence of the targeted many-body phases. In our physical device we envision two potential sources of disorder: (a) disordered-induced charges on the superconducting islands, and (b) disorder in the junction transmissions. Given the large values of the Luttinger parameter  $K_s$ , we expect to be protected against the charge disorder (a) that results in irrelevant operators in the low-energy limit of the model. On the other hand, the disorder (b) translates into a disordered local potential  $V_J$ , Eq. (2) in the main text, and requires a more careful analysis.

In our proposal, we assume that the transmission  $T_2$  of the central junction cannot be controlled, making it the primary source of this kind of disorder. A random distribution of  $T_2$  maintains the  $\mathbb{Z}_2$ -symmetry of the ladder, while inducing random variations in the parameters  $\mu_n$  in Eq. (2) of the main text. When assuming Gaussian random disorder, we can give a rough estimate of the threshold over which disorder dominates over the features studied in our model by comparing their standard deviations with the typical gaps observed in the system.

In particular, when considering the gapped symmetry-broken phase, the impact of disorder can be estimated in the following way. Given a certain amount of disorder  $\delta T_2/T_2$ , we compare the energy scale  $\Delta \delta T_2/T_2$  with the mass of the solitons interpolating between the two minima of  $V_J$  in the related field theory, which provides a good approximation of the spin gap  $\Delta_s$ . In the semiclassical approach, the local potential  $V_J$  approximately assumes the typical double well form  $g_2\varphi^2 + g_4\varphi^4$ , within the ordered phase II  $(g_2 < 0)$ . By following standard calculations [9], we determine the soliton mass to be

$$M_s = \frac{2\sqrt{2}}{3} \frac{|g_2|^{3/2}}{g_4} \sqrt{E_J},\tag{S6}$$

where we accounted for the Luttinger kinematics renormalization in spin sector (see the next subsection). The stability of the ordered phase hinges on whether the energy scale of the disorder in  $T_2$  remains below  $M_s$  and  $\Delta_s$ . By considering the input values of our simulations, we derive that a 10% disorder in  $T_2$  constitutes the threshold over which the ordered phase is obscured, possibly leading to glassy physics phenomena. Similar results are obtained by comparing the disorder energy scale with the numerical gaps derived from the transfer matrix eigenvalues within the spin sector (see Sec. IV ).

Notably, however, such effects can be mitigated by increasing the Josephson energy scale  $E_J$  along the legs of the ladder, thus  $M_s \sim \Delta_s$ . Larger values of  $E_J$  decrease indeed the occurrence of phase slips in the 1D system.

In recent experimental systems with long JJ chains [10], characterized by more than 30000 JJs, the estimated disorder in the Josephson energies was below 10%. In this context, carefully engineered ladders with a smaller number of junctions fabricated to specifically observe the physics of the TCI should allow us to achieve the most favorable energy hierarchy for mitigating disorder effects and observe the many-body phases discussed in the main text.

A further useful fabrication aspect to emphasize in order to optimize the construction of the ladder device is the following: suitable amplitudes and large energy scales for the higher harmonics in the potential  $V_J$  can be achieved by constructing triple junctions with a wider central junction with many low transmission channels, such that we approximate its energy-phase relation with the standard sinusoidal form  $E_{J2}\cos\varphi$ . By enlarging the size of the middle junctions, on one side we decrease the impact of geometric imperfections leading to disorder of the kind (b) and, on the other, we increase the energy gaps that characterize the gapped phases in our model, thus improving the resilience of the phase diagram against disorder.

Regarding the critical features of the ladder, they will remain clean below a characteristic disorder length that decreases with increasing disorder  $\delta T_2$ . If this disorder lengthscale becomes considerably smaller than the system size, however, unexpected critical scaling phenomena may emerge. A comprehensive understanding of disorder in conformal field theory (CFT) remains elusive, as does a systematic theoretical framework for its treatment. Nevertheless, we can apply symmetry reasoning to our system and make use of the Harris criterion [11] to provide qualitative insights.

According to the Harris criterion, a random quenched disorder that preserves the conformal symmetry becomes relevant only if it couples with a local operator of the CFT with scaling dimension D < 1 [11]; concerning disorder with a Gaussian distribution in general one-dimensional quantum systems, instead, the renormalization group analysis of Giamarchi and Schultz [12] shows that disorder is relevant if the related operator has dimension D < 3/2. At the TCI point, the disorder in  $T_2$  does not couple with the odd magnetizations  $\sigma$  and  $\sigma'$ , which explicitly break the  $\mathbb{Z}_2$ -symmetry. This fact ensures the preservation of the ordered phase in the low-energy limit, preventing the system from losing long range order, analogously to what happens in the Ising CFT. Moreover, the disorder in  $T_2$  couples with the less relevant thermal deformation  $\epsilon$ , with scaling dimension 1/5. This implies that weak disorder introduces an additional lengthscale in the system, which diverges for clean systems and must be sufficiently large to observe criticality; the TCI features can be observed for distances below this disorder lengthscale, whereas observables extending over this length will present features typical of disordered and gapped systems. To our knowledge, thermal disorder in TCI CFT has not been studied yet, in neither the classical nor the quantum case.

### C. Bosonization

In this section, we will review the main steps of the connection between the lattice Hamiltonian in (3) in the main text and the three-frequency sine-Gordon quantum field theory. At low temperature  $K_BT < \Delta_c$  each SC island of our lattice corresponds to a condensate of  $N_c$  Cooper pairs with gap  $\Delta_c$  and a well defined complex order parameter, the SC phase  $\hat{\varphi}_{\alpha,j}$ . The residual charge around  $N_c$  is represented by the operator  $\hat{N}_{\alpha,j}$  dual to the SC phase. In the long wavelength limit, we can use an effective continuum description in terms of the Bose fields  $\hat{\theta}_{\alpha}(x)$  and  $\hat{\varphi}_{\alpha}(x)$  [13], fulfilling commutation relations:

$$\left[\hat{\theta}_{\alpha}(y), \hat{\varphi}_{\beta}(x)\right] = -i\pi \delta_{\alpha\beta} \Theta(y-x) , \qquad (S7)$$

where  $\Theta$  indicates the Heaviside step function. The weak interactions case  $E_C$ ,  $V_{\perp}$ ,  $\ll E_J$  we considered allows us to neglect fast-oscillating contributions in the Cooper-pair density and write  $\hat{N}_{\alpha,j} \approx -a \frac{\partial_x \hat{\theta}_{\alpha}(x)}{\pi}$ , with j=xa. In the harmonic approximation for the Josephson interaction along the legs, the low-energy lattice Hamiltonian can be written as

$$\hat{H} = \sum_{\alpha = \mathsf{a}, \mathsf{b}} \left[ E_J \int dx \ a \left( \partial_x \hat{\varphi}_\alpha \left( x \right) \right)^2 + \frac{E_C a}{\pi^2} \int dx \ \left( \partial_x \hat{\theta}_\alpha \left( x \right) \right)^2 \right] + \frac{V_\perp a}{\pi^2} \int dx \ \left( \partial_x \hat{\theta}_a (x) \right) \left( \partial_x \hat{\theta}_b (x) \right) + \sum_{n=1}^3 \frac{\mu_n}{a} \int dx \ \cos \left( n \left( \hat{\varphi}_\mathsf{a} - \hat{\varphi}_\mathsf{b} \right) \right). \tag{S8}$$

By rotating the fields  $\hat{\varphi}_{c/s}(x) = (\hat{\varphi}_{\mathsf{a}}(x) \pm \hat{\varphi}_{\mathsf{b}}(x))/\sqrt{2}$  and the corresponding dual ones  $\hat{\theta}_{c/s}(x)$ , we obtain the Hamiltonian (4) in the main text with the perturbative relations

$$K_{c/s} = \pi \sqrt{\frac{E_J}{(2E_c \pm V_\perp)}}$$
 and  $u_{c/s} = a\sqrt{E_J(2E_C \pm V_\perp)}$ . (S9)

In general, a finite intra-leg capacitance  $C_L$  among adjacent islands leads to a long range interaction stemming from the inverse capacitance matrix [14] with screening length  $\lambda = a\sqrt{C_L/C_g}$ , where  $C_g$  is the self capacitance. However, this may be ignored as long as one is interested in the physics of modes with energies lower than  $u_{c/s}/\lambda$ .

From a perturbative point of view the plasma frequency of the spin sector  $u_s/a = \Lambda \simeq \sqrt{E_J (2E_c - V_\perp)}$  defines a UV cut-off that allows us to define the dimensionless coupling  $\tilde{\mu}_n = \mu_n/\Lambda$  in the sine-Gordon Euclidean action,

$$S\left[\varphi_s(x,\tau)\right] = \frac{1}{2\pi} \int dx d\tau \ K_s \left( \left(\partial_\tau \varphi_s\right)^2 + \left(\partial_x \varphi_s\right)^2 \right) - \sum_{n=1}^3 \frac{\tilde{\mu}_n}{a^2} \int dx d\tau \ \cos\left(\sqrt{2}n\varphi_s\right), \tag{S10}$$

where we have rescaled the imaginary time  $\tau \to u_s \tau$ . The operators  $\widehat{\mathcal{O}}_n = \cos\left(\sqrt{2}n\hat{\varphi}_s\right)$  correspond to primaries of the unperturbed free boson c=1 theory with scaling dimensions

$$\Delta_n = \frac{n^2}{2K_s}. (S11)$$

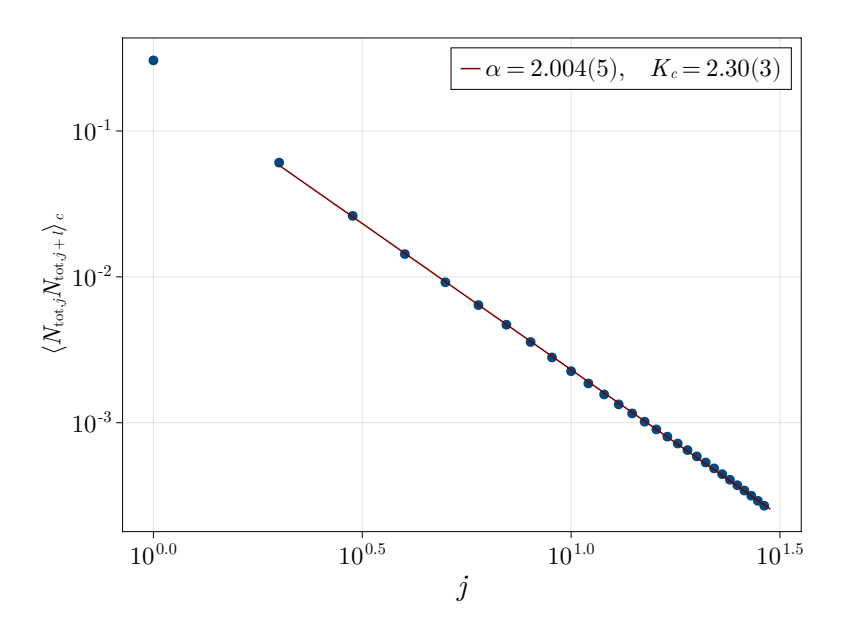


Figure S3. Connected part of the correlation functions of the total density operator  $\widehat{N}_{\text{tot},j} = \left(\widehat{N}_{\text{a},j} + \widehat{N}_{\text{b},j}\right)$  taken at a random position in the phase-diagram  $[X_1 \approx -0.3 \text{ and } X_2 \approx 0.47]$  with  $T_2 = 0.6$ . The red line is the result of a fit by a function  $f(j) = K_c/\pi^2 j^{-\alpha}$ . The fit result  $\alpha \approx 2$  well reproduces the predictions from bosonization theory, and also the obtained Luttinger parameter is close to the prediction from perturbation theory:  $K_c^{\text{pert}} \approx 2.61$ .

Therefore, such operators drive the LL to a massive phase, namely they are relevant, only when  $\Delta_n < 2$  inferring the lower bound  $K_s > 9/4$  considered in the main text to make  $\mathcal{O}_{n < 3}$  relevant.

Note that the charge sector remains massless as there is no sine-Gordon potential for  $\hat{\varphi}_c$ . We checked the validity of this statement in our lattice simulation. In the LL liquid phase the density correlation functions is expected to show the following power-law decay

$$\langle \widehat{\rho}_{\text{tot}}(x) \widehat{\rho}_{\text{tot}}(y) \rangle \sim \frac{2}{\pi^2} \langle \partial_x \theta_c(x, \tau) \partial_y \theta_c(y, \tau) \rangle = \frac{K_c}{\pi^2} \frac{1}{|x - y|^2}.$$
 (S12)

In the ladder model, the operator  $\hat{\rho}_{\text{tot}}(x)$  corresponds to the total rung density offset  $\hat{N}_{\text{tot},j} - \langle \hat{N}_{\text{tot},j} \rangle$  with  $\hat{N}_{\text{tot}} = \hat{N}_{a,j} + \hat{N}_{b,j}$ . We explicitly checked the decay of Eq. (S12) for each point of the phase diagram by fitting a power-law decay [Fig. S3]. The so found  $K_c$  parameters are in a good agreement with the perturbative approximations given by Eq. (S9). This confirms the validity of the field theoretical approach in the low energy regime of the ladder.

On the other hand, the spin sector (S10) is subject to the different relevant interactions in Eq. (S10) which tend to order the SC phase difference  $\hat{\varphi}_s$ . In Ref. [15] the author shows that this quantum field theory flows to a tricritical Ising point with central charge c = 7/10 for suitable values of the coupling constants  $\mu$ . Despite the absence of any non-perturbative mappings between our lattice operators and the massless excitations of this field theory, we can exploit the Ginzburg-Landau representation of the TCI CFT to gain insight about this relation.

The operator content of the CFT is split in the odd and even sector with respect to the  $\mathbb{Z}_2$ -symmetry and is characterized by 6 primary fields: the identity I, four relevant operators  $\sigma$ ,  $\epsilon$   $\sigma'$ ,  $\epsilon'$  ( $\Delta < 2$ ) and one irrelevant ( $\Delta > 2$ ) operator. The Ginzburg-Landau Lagrangian representation of the TCI corresponds to [9]

$$\mathcal{L} = \frac{K_s}{2\pi} \varphi_s \left( \partial_x^2 + \frac{\partial_\tau^2}{u_s^2} \right) \varphi_s - \lambda_2 : \varphi_s^2 : -\lambda_4 : \varphi_s^4 : -\lambda_6 : \varphi_s^6 :, \tag{S13}$$

where :: indicates the normal ordering with respect to the tricritical point CFT. In the mean-field limit  $K_s \gg 1$ , we

can build an approximate mapping bewteen local operators in our theory and the primary fields (see also Ref. [16]),

$$\varphi_{s}(x) \to \sigma(x), \quad (h_{\sigma}, \bar{h}_{\sigma}) = \left(\frac{3}{80}, \frac{3}{80}\right) 
: \varphi_{s}^{2}(x) : \to \epsilon(x), \quad (h_{\epsilon}, \bar{h}_{\epsilon}) = \left(\frac{1}{10}, \frac{1}{10}\right) 
: \varphi_{s}^{3}(x) : \to \sigma'(x), \quad (h_{\sigma'}, \bar{h}_{\sigma'}) = \left(\frac{7}{16}, \frac{7}{16}\right) 
: \varphi_{s}^{4}(x) : \to \epsilon'(x), \quad (h_{\epsilon'}, \bar{h}_{\epsilon'}) = \left(\frac{3}{5}, \frac{3}{5}\right),$$
(S14)

which implies the expansion of the local order operator  $\hat{J}_{\perp}$  in terms of the most relevant operator  $\sigma$  close to the critical point,

$$\hat{J}_{\perp}(x) = \sin\left(\sqrt{2}\hat{\varphi}_s(x)\right) \sim \hat{\varphi}_s(x) + \dots \to \sigma(x) + \dots$$
(S15)

In the previous expansion the dots indicate less relevant operator contributions.

### III. CHARGE BASIS

For the numerical simulations, we formulated the Hamiltonian (3) from the main text in the charge basis. In this basis the operator  $\hat{N}_{\alpha,j}$  is diagonal and defines how the number of Cooper pairs differs from the average occupation on the island  $(\alpha, j)$ :

$$\hat{N}_{\alpha,j} = \text{diag}(\dots, -2, -1, 0, 1, 2, \dots)$$
 (S16)

Using this choice, it is easy to show that  $e^{i\hat{\varphi}_{\alpha,j}}$  must to be of the form

$$e^{i\hat{\varphi}_{\alpha,j}} = \begin{pmatrix} \ddots & & & & \\ & 0 & 1 & & \\ & & 0 & 1 & \\ & & & 0 & 1 \\ & & & \ddots & \end{pmatrix}_{\alpha,j} \equiv \widehat{\Sigma}_{\alpha,j}^{-}$$
 (S17)

for the commutator  $[\hat{N}, \hat{\Sigma}^-] = -\hat{\Sigma}^-$  to hold. Further, in order to represent these operators in our simulations, we have to truncate the number of possible charge states

$$\widehat{N}_{\alpha,j} = \text{diag}(-N_{\text{max}}, -2, -1, 0, 1, 2, \dots, N_{\text{max}}),$$
(S18)

i.e. we adopt a truncated local Hilbert-space of dimension  $2N_{\max}+1$  per each SC island. We can control the error caused by this truncation by varying  $N_{\max}$  until we reach convergence in all observables. Alternatively, we can measure the probability  $\langle \hat{P}_{\alpha,j}^n \rangle$  of finding an excitation n on the island  $(\alpha,j)$ . By ensuring that  $N_{\max}$  is large enough to have negligible weight  $\langle \hat{P}_{\alpha,j}^{N_{\max}} \rangle < \epsilon$  we can claim to be converged in  $N_{\max}$ . In practice we found that  $N_{\max}=8$  gives

 $\langle \hat{P}_{\alpha,j}^{N_{\text{max}}} \rangle \sim 10^{-9}$ . The Hamiltonian used for the simulation finally reads  $\hat{H} = \sum_{j=0}^{L} \hat{h}_{j,j+1}$  with:

$$\hat{h}_{j,j+1} = \sum_{\alpha=a,b} \left[ E_c \left( \widehat{N}_{\alpha,j} \right)^2 - \frac{E_J}{2} \left( \widehat{\Sigma}_{\alpha,j}^+ \widehat{\Sigma}_{\alpha,j+1}^- + \widehat{\Sigma}_{\alpha,j}^- \widehat{\Sigma}_{\alpha,j+1}^+ \right) \right]$$

$$+ V \widehat{N}_{a,j} \widehat{N}_{b,j} + \frac{\mu_1}{2} \left( \widehat{\Sigma}_{a,j}^+ \widehat{\Sigma}_{b,j}^- + \widehat{\Sigma}_{b,j}^+ \widehat{\Sigma}_{a,j}^- \right)$$

$$+ \frac{\mu_2}{2} \left( \left( \widehat{\Sigma}_{a,j}^+ \right)^2 \left( \widehat{\Sigma}_{b,j}^- \right)^2 + \left( \widehat{\Sigma}_{b,j}^+ \right)^2 \left( \widehat{\Sigma}_{a,j}^- \right)^2 \right)$$

$$+ \frac{\mu_3}{2} \left( \left( \widehat{\Sigma}_{a,j}^+ \right)^3 \left( \widehat{\Sigma}_{b,j}^- \right)^3 + \left( \widehat{\Sigma}_{b,j}^+ \right)^3 \left( \widehat{\Sigma}_{a,j}^- \right)^3 \right)$$
(S19)

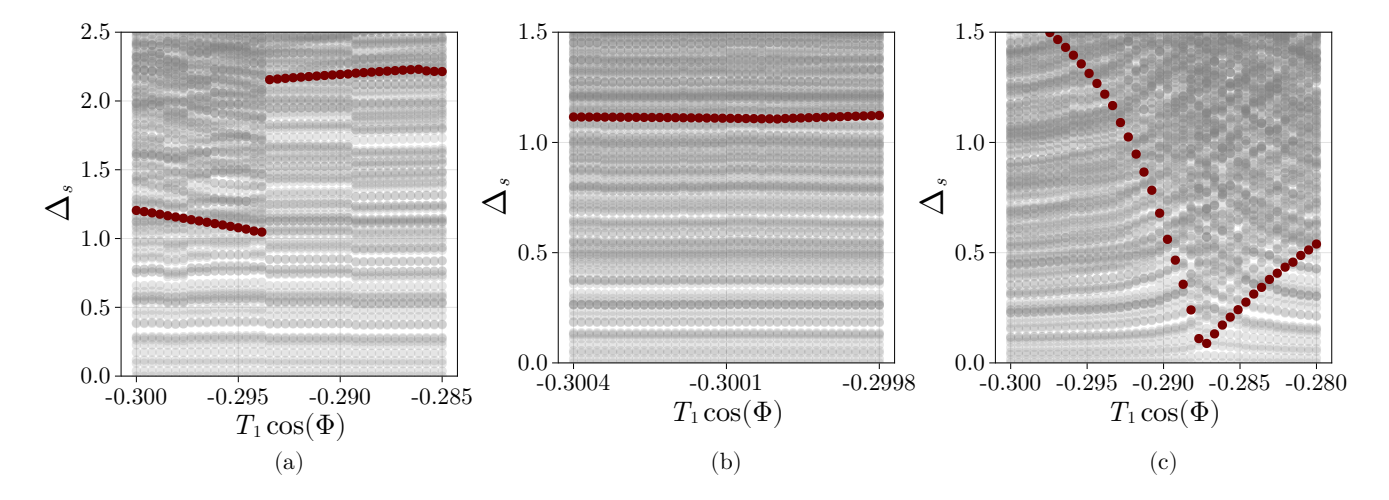


Figure S4. The gap in the spin sector  $\Delta_s$  is determined by tracking the second largest eigenvalue of the transfer matrix within the spin sector  $\lambda_1$ . The results are obtained for the three cuts shown in the main text: a)  $X_2 = 0.6$ , b)  $X_2 = 0.52$  and c)  $X_2 = 0$ . The red points correspond to the gap  $\Delta_s = -\log(\lambda_1)$  which remains finite across the FOPTs in panel (a) and (b), while displaying the gap-closing feature of a second-order phase transition in panel (c).

### IV. FURTHER NUMERICAL EVIDENCE FOR THE TRANSITIONS

In this section, we present additional numerical indications about the different nature of the transitions across the phase diagram. All the data in this section refer to a system with  $T_2 = 0.6$ , but variations of the parameter  $T_2$  do not affect qualitatively our results as long as  $T_2$  is sufficiently large to observe the symmetry-broken phase.

### A. Hysteresis and gap jump at the first-order transition

First of all, we present additional evidence of first-order phase transitions (FOPTs) along the horizontal cuts at  $X_2 = 0.52$  (between the disordered phase I and the ordered phase II) and at  $X_2 = 0.6$  (between phases I and III).

One significant indicator involves the distinct behavior of the lowest energy excitation in the spin sector. Its energy corresponds to the system's gap, which can be extracted (see Section V) from the transfer matrix spectrum as shown in Fig. S4. By following the corresponding eigenvalue of the transfer matrix  $\lambda_1$ , we can extract the gap of the spin sector  $\Delta_s = -\log \lambda_1$ . Across a second-order phase transition, the physical gap closes and, in the numerical VUMPS simulations, this is marked by a minimum in  $\Delta_s$  [panel (c)] which approaches zero by increasing the bond dimension. Across a FOPT, instead, the spin gap remains finite [panels (a) and (b)], although it may display a discontinuity when the mass of the spin excitations is different in the two phases. Panels (a) and (b) respectively depict the typical behaviors of the FOPT between the two disordered phases and between phase II and phase I. In the latter case, the related order parameter displays a very weak variation, resulting in an almost continuous behavior of  $\Delta_s$ .

This behavior is reflected also in the analysis of the hysteresis in the order parameter and the many-body ground state energy, as illustrated in Fig. S5.

A discontinuity in the first derivative of the energy density is observed in the FOPT cases, which is absent in the second-order transition at  $X_2 = 0$  and indicates the crossing of the lowest energy levels. Furthermore, by altering the minimization procedure at each point  $X_1$  and initializing the ground state with the result from  $X_1 \pm \delta$ , the variational algorithm follows the corresponding branch, even within the opposite phase. This can be interpreted as a hysteresis effect induced by the orthogonality of these two states around the crossing point.

Also in this case the features of the FOPT are stronger between the two disordered phases – panel S5 (b) is depicted with a magnified energy scales with respect to panel (a). The discontinuity of the derivative  $\partial \varepsilon / \partial X_1$  is around 30  $E_J$  in panel (a) and 22  $E_J$  in panel (b). This is physically related to the jump of the average loop current circulating around each triple JJs element, namely  $\hat{J}_{\text{loop}} = \partial \hat{H} / \partial \Phi$ .

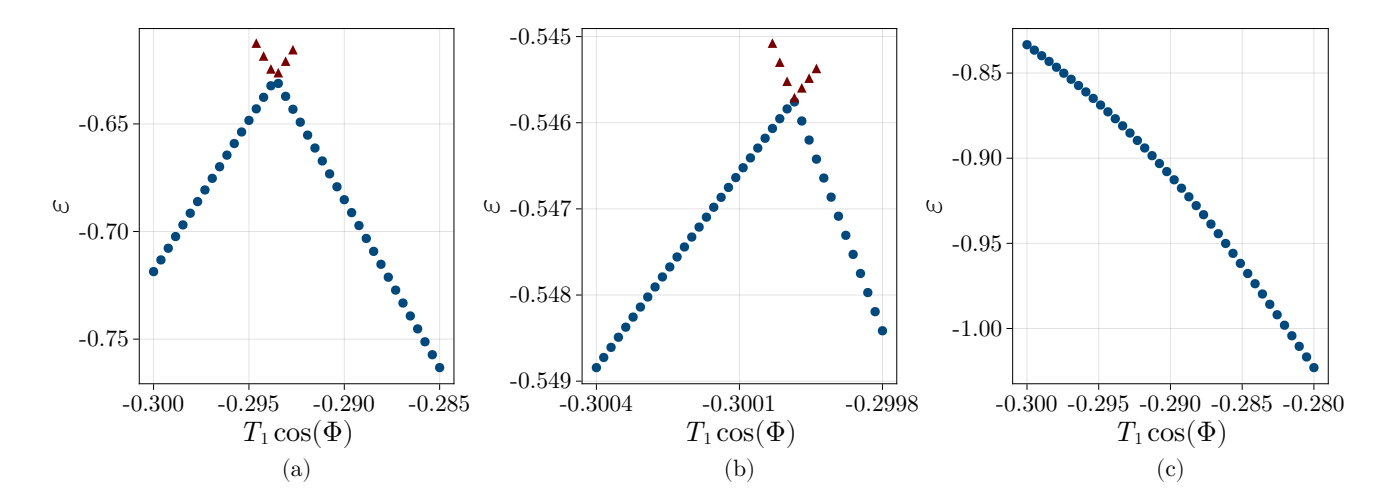


Figure S5. Energy density  $\varepsilon$  of the groundstate obtained at the three cuts from the main text: a)  $X_2 = 0.6$ , b)  $X_2 = 0.52$  and c)  $X_2 = 0$ . The red triangles in the case of a) and b) are obtained by minimizing the Hamiltonian  $H(\mathbf{X} + \delta)$  by starting from one of the two groundstates left/right of the meeting point of the two branches. The minimization procedure follows these branches instead of falling into the true ground state. The absence of such an effect for  $X_2 = 0$  is another indication for a FOPT in the case a) and b), but a second order phase transition for c).

### B. Scaling and critical exponents Ising phase transition

In this subsection, we focus on characterizing the critical exponents  $\nu$  and  $\beta$ , which describe how the correlation length diverges and the order parameter approaches zero across the continuous phase transitions. Concerning the Ising line, we will consider as main example the  $X_2 = T_1 \sin(\Phi) = 0$  cut corresponding to Fig. 3(c)-(d) of the main text. In this case, the measured values indicate indeed that the transition belongs to the Ising universality class with  $\nu_{\rm IS} = 1$  and  $\beta_{\rm IS} = 1/8$ . To extract these exponents, we relied on scaling properties of three different quantities: the log-fidelity per site  $\mathcal{F}$  (and its susceptibility  $\chi_{\mathcal{F}}$ ), the correlation length of the spin sector  $\xi_s$  and the order parameter  $\hat{J}_s^{(2e)}$ .

We determine the critical exponent  $\nu$  through two different methods based on the fidelity scaling, both yielding values near  $\nu_{\rm IS}=1$  [Fig. S6]. The first approach involves fitting the non-analytic behavior of the log-fidelity per site at the critical point, showing a consistent increase towards  $\nu=1$  as the bond dimension D grows [Fig. S6 a), inset], although the adopted bond dimensions were not sufficient to converge to  $\nu=1$ . The second approach, instead, provides more accurate results and relies on analyzing the divergence pattern of the fidelity susceptibility along a horizontal cut; in this way we obtain  $\nu=1.00(3)$  [Fig. S6 b)].

To take into account finite bond dimension corrections, we employed the finite entanglement scaling discussed in Ref. [17] for the spin correlation length  $\xi_s$ . Similarly to finite size effects, the finite bond dimension introduces an artificial length scale making all correlation functions exponential decaying even at critical points. This can be interpreted as the addition of a relevant perturbation of the underlying CFT. However, in the  $D \to \infty$  limit, the gapless nature of the model must be restored. This artificial length scale is associated with the critical exponent  $\kappa$ :

$$\xi_D \sim D'$$

and we use this relation to define the following scaling ansatz [17]

$$\xi_D = D^{\kappa} f\left(D^{\frac{\kappa}{\nu}} \frac{|X_1 - X_{1c}|}{X_{1c}}\right), \quad f(x) \sim \begin{cases} \text{const}, & x \to 0\\ \frac{1}{x^{\nu}}, & x \gg 1 \end{cases}$$
 (S20)

where  $\nu$  is the critical exponent of the correlation length in the infinite bond dimension case. We use this ansatz and the collapse procedure explained in [18] to determine the critical point  $X_{1c}$  and to extract the critical exponents  $\nu$  and  $\kappa$  discussed in the main text.

Additionally, to extract the critical exponent  $\beta$  we employ the scaling of the expectation value of the single-particle current  $\hat{J}_{\perp}^{(2e)}$  close to the critical point. Indeed, this operator plays the role of the Ising magnetization which is odd under the  $\mathbb{Z}_2$ -symmetry  $\hat{\varphi}_s \to -\hat{\varphi}_s$ . By fitting the expected scaling behaviour  $|X_1 - X_{1c}|^{\beta}$ , we obtain the critical

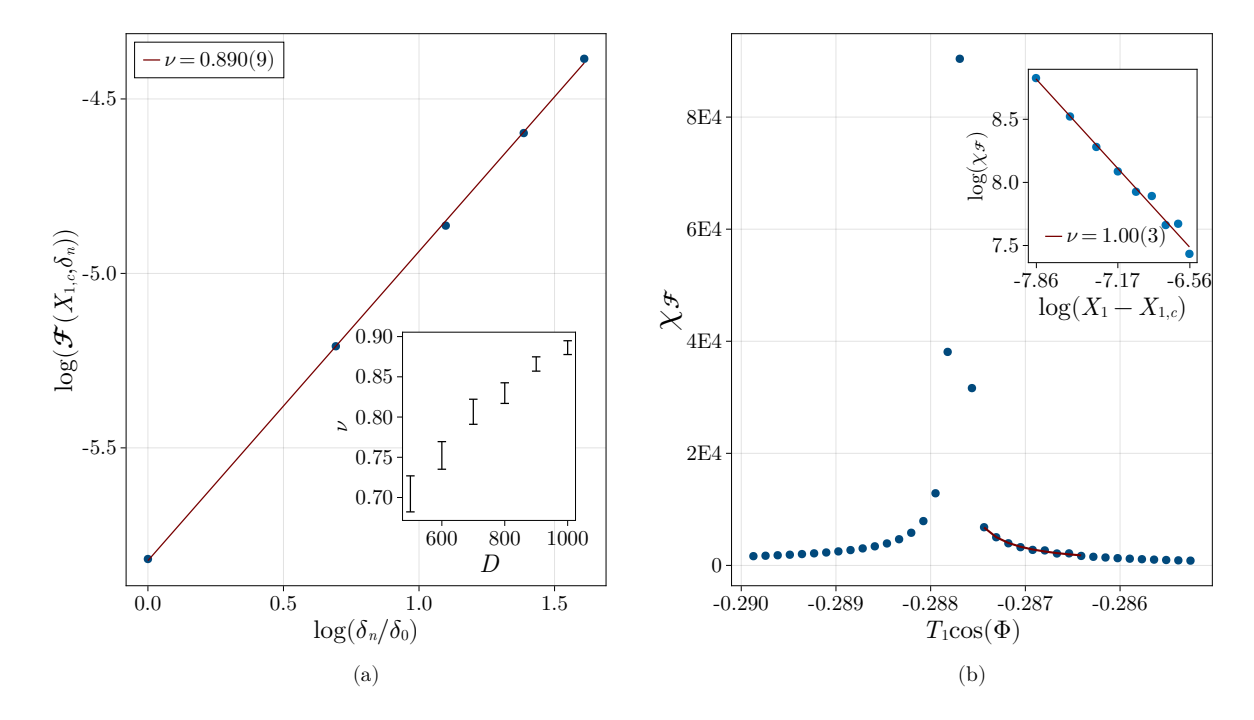


Figure S6. Extrapolation of the critical exponent  $\nu$  from the scaling features of the fidelity at  $X_2 = 0$ . (a): Two-parameter fit of the relation  $\mathcal{F}(X_{1c}, \delta) = a |\delta|^{\nu}$  at bond dimension D = 1000. The extracted values of  $\nu$  increase with the increasing bond dimension (inset). (b): Fit of the fidelity susceptibility  $\chi_{\mathcal{F}} = b |X_1 - X_{1c}|^{\nu-2}$  away from the critical point with a fixed  $\delta \ll |X_1 - X_{1c}|$ . The plot in log-log scale is shown in the inset. The position of the critical point  $X_{1c}$  is obtained from the collapse of the spin correlation length (S20).

exponent  $\beta = 0.125(3)$  [Fig. S7] at  $X_2 = 0$ , and analogous values are obtained for  $|X_2| \lesssim 0.435$ , as depicted in Fig. (3)(e) in the main text.

These results collectively indicate that our findings concerning the transition from the ordered to the disordered phase sufficiently far from the first order discontinuities are compatible with the Ising universality class with  $\nu_{\rm IS} = 1$  and  $\beta_{\rm IS} = 1/8$ .

The critical exponents  $\kappa$  extracted for the spin correlation length at the second order transitions are typically smaller than one. This implies that a considerable increase of the bond dimension is required in order to faithfully capture the algebraic decay of correlation functions over a long distance. Taking the example of the  $X_2=0$  cut from the main text with  $\kappa\approx 0.8$ . The largest correlation length obtained for  $X_2$  is  $\xi_s\approx 30$  for a bond dimension of D=1000. Using the scaling behavior  $\xi_s\sim D^{0.8}$  we estimate that a bond dimension  $D^*\approx 4500$  is necessary to get  $\xi_s\approx 100$  sites, and  $D^*\approx 18000$  for  $\xi_s\approx 300$  sites.

### C. Central charge

Given the separation of the two sectors in our model, in the thermodynamic limit the entanglement entropy of the system is predicted to display a typical divergence  $S = c_c/6\log(\xi_c) + c_s/6\log(\xi_s)$  [19] in proximity of the second-order phase transition, with  $c_{c/s}$  the central charge of the charge/spin sector. However, strong finite entanglement effects in the VUMPS simulations have a quantitative impact on the estimate of the latter and result in strong fluctuations. Moreover, the theory of finite-entanglement corrections [17, 20, 21] is less developed than the finite-size scaling and, in particular, doesn't cover the case of two gapless modes sharing the same finite bond dimension in the MPS representation. In particular, as already pointed out at the end of previous section, achieving a reliable description of the critical correlations of the system with  $\xi_s \to \infty$  requires a very large bond dimension D, given the sub-linear scaling of  $\xi_s \sim D^{\kappa}$ .

For these reasons, we determined the total central charge c from finite-size DMRG simulations with periodic boundary conditions by fitting the relation [19]

$$S(j) = \frac{c}{3}\log\left(d\left(j, L\right)\right) + s_1,\tag{S21}$$

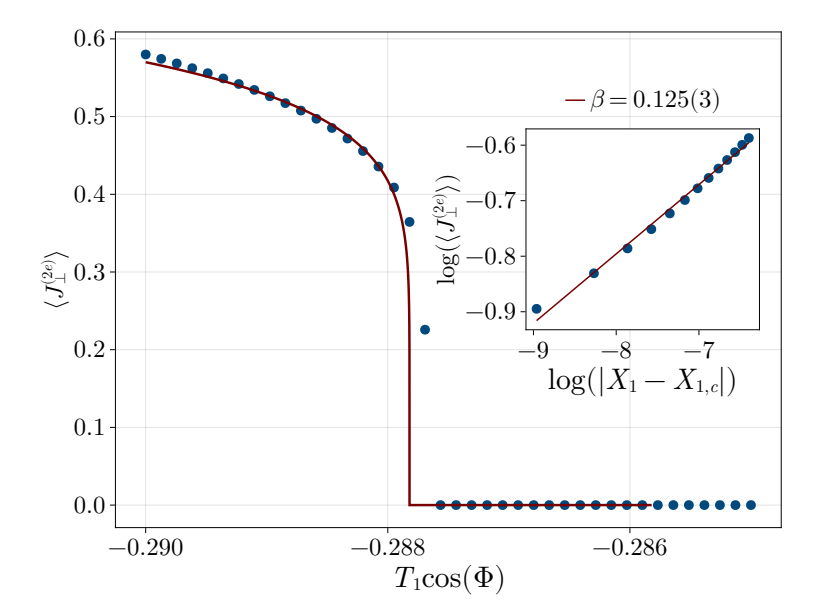


Figure S7. The single-particle current  $J_{\perp}^{(2e)}$  plays the role of the effective magnetization at the Ising critical point, displaying a scaling behavior  $|X_1 - X_{1c}|^{\beta}$  with the fitted value  $\beta = 0.125(3)$  (red curve). The critical point  $X_{1c}$  is fixed by the collapse of  $\xi_s$  obtained by using Eq. (S20). The discrepancy with the numerical points is due to finite entanglement effects that shifts the position of the critical point at finite bond dimensions.

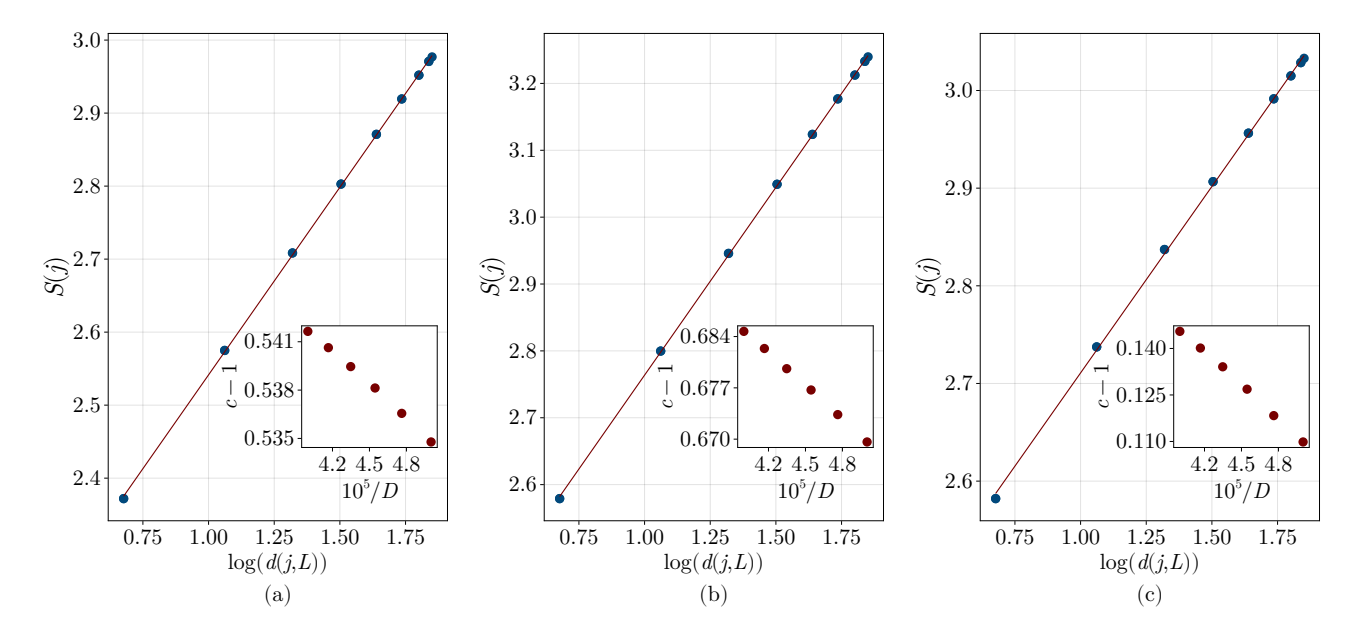


Figure S8. Fits of the entanglement entropy relation (S21) for L=20 and bond dimension D=2500 at three significant points along the transition line. The inset shows the slow convergence of the fitted value with respect to the inverse of the bond dimension, allowing for an extrapolation  $D \to \infty$ . For  $X_{2c} \simeq 0.42$  (a), this interpolation yields  $c \approx 0.57$ . At  $X_{2c} \simeq 0.464$  (b), the central charge increases,  $c \approx 0.74$  before dropping for  $X_{2c} \simeq 0.479$  (c).

where S(j) is the entanglement entropy at the site j,  $d(j,L) = L/\pi \sin(\pi j/L)$  is the chord distance, and  $s_1$  is a non-universal constant.

We specifically traced the transition line where the VUMPS spin correlation length  $\xi_s$  is maximal and the critical exponent  $\beta$  shows the CFTs predictions before vanishing at the FOPT, Fig. 3(e) in the main text. Figure S8 shows the excellent agreement of our data with the relation (S21) at three illustrative points along this line. Finite size effects are present in any case and lead to an overestimation of the value of the central charge. The measured estimate

is expected to decrease by increasing the size of the finite system.

### V. EXTRACTION OF CORRELATION LENGHTS

Most of the numerical results presented in this latter are obtained by the VUMPS algorithm presented in Ref. [22]. The concrete implementation uses the ITensor library [23]. This ansatz operates directly in the thermodynamic limit by enforcing translational invarance. The class of ansatz states is characterized by the set of matrices  $\{A_L^{\sigma}, A_C^{\sigma}, A_R^{\sigma}\}$ , with  $\sigma$  enumerating the physical local states. From this set of matrices, the state  $|\psi\rangle$  is represented as

$$|\psi\rangle = \sum_{\{\sigma\}} \operatorname{Tr} \left[ \dots A_L^{\sigma_{j-2}} A_L^{\sigma_{j-1}} A_C^{\sigma_j} A_R^{\sigma_{j+1}} A_L^{\sigma_{j+2}} \dots \right] |\dots \sigma_{j-2} \sigma_{j-1} \sigma_j \sigma_{j+1} \sigma_{j+2} \dots \rangle \ .$$

The matrices  $A_L^{\sigma}$  and  $A_R^{\sigma}$  fulfill  $\sum_{\sigma} (A_L^{\sigma})^{\dagger} A_L^{\sigma} = \sum_{\sigma} A_R^{\sigma} (A_R^{\sigma})^{\dagger} = \mathbb{1}$  and special equivariance relations to ensure the translational invariance of the ansatz, see Fig. S9. Using the transfer-matrix of the system, defined by

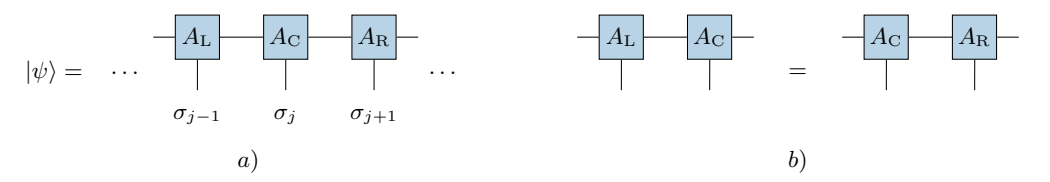


Figure S9. (a): VUMPS ansatz in the central gauge. (b): Equivariance property to ensure translational invariance

$$\mathcal{T}_L := \sum_{\Lambda} A_L^{\sigma} \otimes \bar{A}_L^{\sigma} \,, \tag{S22}$$

and the two transfer-matrices with operator insertion

$$\mathcal{T}_{L}^{O} := \sum_{\sigma,\tau} O_{\sigma,\tau} A_{L}^{\sigma} \otimes \bar{A}_{L}^{\tau}, \quad \mathcal{T}_{C}^{K} := \sum_{\sigma,\tau} K_{\sigma,\tau} A_{C}^{\sigma} \otimes \bar{A}_{C}^{\tau},$$
 (S23)

where  $\bar{z}$  denotes the complex conjugation of z, one can represent the correlation function of two arbitrary operators  $\hat{O}$  and  $\hat{K}$  as, Fig. S10:

$$\langle \hat{O}_{j} \hat{K}_{j+l} \rangle = \langle \mathbb{1} | \mathcal{T}_{L}^{O} (\mathcal{T}_{L})^{l-1} \mathcal{T}_{C}^{K} | \mathbb{1} \rangle = \sum_{n \geq 0} \lambda_{n}^{l-1} \alpha_{n}^{O} \beta_{n}^{K} = \sum_{n \geq 0} e^{-\frac{l-1}{\xi_{n}}} c_{n}^{O,K}$$

$$\alpha_{n}^{O} = \langle \mathbb{1} | \mathcal{T}_{O} | R_{n} \rangle, \ \beta_{n}^{K} = \langle L_{n} | \mathcal{T}_{K} | \mathbb{1} \rangle, \ \xi_{n} = -\frac{1}{\log(\lambda_{n})}.$$
(S24)

The second line in Eq. S24 is obtained after using the eigen decomposition of the transfer-matrix

$$\mathcal{T}_{L} = \sum_{n \geq 0} \lambda_{n} |R_{n}\rangle \langle L_{n}| , \quad \langle L_{n}|R_{m}\rangle = \delta_{m,n} .$$
 (S25)

Using Eq. S24, it is straightforward to extract the asymptotic behavior of any correlation function

$$\langle \hat{O}_j \hat{K}_{j+l}^\dagger \rangle \approx c_{n^\star}^{O,K} \, e^{\frac{l}{\xi_{n^\star}}} + c_0^{O,K} \, . \label{eq:constraint}$$

where  $n^*$  is the first n > 0 in the descending sequence  $\lambda_0 > |\lambda_1| \ge |\lambda_2| \dots$  with a non-zero operator weight  $c_n^{O,K}$  (assuming  $\lambda_{n^*}$  to be unique). The contribution  $c_0^{O,K}$  equals the product of expectation values  $\langle \hat{O}_j \rangle \langle K_j^{\dagger} \rangle$ . In the case of  $\hat{O} = \hat{K}$  this asymptotic behavior can be used to extract the smallest energy gap in the excitation spectrum generated by the operator  $\hat{O}$ . In the main text, we applied this analysis to the current operator

$$\hat{O} = \hat{J}_{\perp}^{(2e)} \coloneqq \frac{i}{2} \left( \Sigma_{\mathsf{a}}^{+} \Sigma_{\mathsf{b}}^{-} - \Sigma_{\mathsf{b}}^{+} \Sigma_{\mathsf{a}}^{-} \right) \,.$$

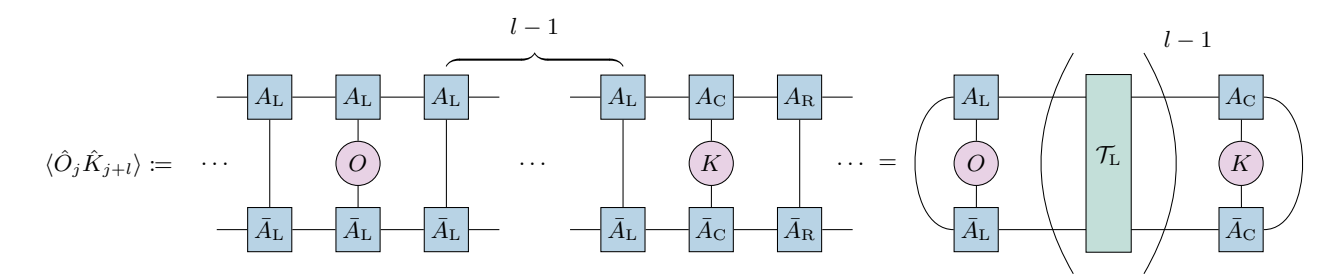


Figure S10. Correlation function in the infinite system.

which can be interpreted as the magnetization order parameter in the field theory  $\sin\left(\sqrt{2}\hat{\varphi}_s(x)\right)$  odd under the  $\varphi_s(x) \to -\varphi_s(x)$  symmetry transformation. Thus,  $\hat{J}_{\perp}^{(2e)}$  is naturally associated to excitations in the spin-sector exclusively.

Very similarly, one can extract the density of the logarithmic fidelity  $\mathcal{F}$  in the thermodynamic limit from the mixed transfer-matrix

$$\mathcal{T}_{L}^{\phi,\psi} \coloneqq \sum_{\sigma} A_{L}^{\phi,\sigma} \otimes \bar{A}_{L}^{\psi,\sigma}, \tag{S26}$$

where  $A_L^{\phi}$  defines the state  $|\phi\rangle$  and  $A_L^{\psi}$  the state  $|\psi\rangle$ . Define  $\lambda_0$  the smallest in maginutde eigenvalue of  $\mathcal{T}_L^{\phi,\psi}$ , it is straigthforward to show:

$$\mathcal{F} := -\lim_{N \to \infty} \frac{1}{N} \log \left( \langle \psi | \phi \rangle \right) = -\log(|\lambda_0|).$$

- C. Ciaccia, R. Haller, A. C. C. Drachmann, T. Lindemann, M. J. Manfra, C. Schrade, and C. Schönenberger, Phys. Rev. Res. 5, 033131 (2023).
- [2] A. Kringhøj, L. Casparis, M. Hell, T. W. Larsen, F. Kuemmeth, M. Leijnse, K. Flensberg, P. Krogstrup, J. Nygård, K. D. Petersson, and C. M. Marcus, Phys. Rev. B 97, 060508 (2018).
- [3] S. Hart, Z. Cui, G. Ménard, M. Deng, A. E. Antipov, R. M. Lutchyn, P. Krogstrup, C. M. Marcus, and K. A. Moler, Phys. Rev. B 100, 064523 (2019).
- [4] C. W. J. Beenakker, Rev. Mod. Phys. 69, 731 (1997).
- [5] F. Nichele, E. Portolés, A. Fornieri, A. M. Whiticar, A. C. C. Drachmann, S. Gronin, T. Wang, G. C. Gardner, C. Thomas, A. T. Hatke, M. J. Manfra, and C. M. Marcus, Phys. Rev. Lett. 124, 226801 (2020).
- [6] A. M. Bozkurt, J. Brookman, V. Fatemi, and A. R. Akhmerov, SciPost Phys. 15, 204 (2023).
- [7] L. Banszerus, W. Marshall, C. W. Andersson, T. Lindemann, M. J. Manfra, C. M. Marcus, and S. Vaitiekėnas, arXiv 10.48550/arXiv.2402.11603 (2024), 2402.11603.
- [8] F. Arute, K. Arya, R. Babbush, D. Bacon, J. C. Bardin, R. Barends, R. Biswas, S. Boixo, F. G. S. L. Brandao, D. A. Buell, B. Burkett, Y. Chen, Z. Chen, B. Chiaro, R. Collins, W. Courtney, A. Dunsworth, E. Farhi, B. Foxen, A. Fowler, C. Gidney, M. Giustina, R. Graff, K. Guerin, S. Habegger, M. P. Harrigan, M. J. Hartmann, A. Ho, M. Hoffmann, T. Huang, T. S. Humble, S. V. Isakov, E. Jeffrey, Z. Jiang, D. Kafri, K. Kechedzhi, J. Kelly, P. V. Klimov, S. Knysh, A. Korotkov, F. Kostritsa, D. Landhuis, M. Lindmark, E. Lucero, D. Lyakh, S. Mandrà, J. R. McClean, M. McEwen, A. Megrant, X. Mi, K. Michielsen, M. Mohseni, J. Mutus, O. Naaman, M. Neeley, C. Neill, M. Y. Niu, E. Ostby, A. Petukhov, J. C. Platt, C. Quintana, E. G. Rieffel, P. Roushan, N. C. Rubin, D. Sank, K. J. Satzinger, V. Smelyanskiy, K. J. Sung, M. D. Trevithick, A. Vainsencher, B. Villalonga, T. White, Z. J. Yao, P. Yeh, A. Zalcman, H. Neven, and J. M. Martinis, Nature 574, 505 (2019).
- [9] G. Mussardo, Statistical Field Theory (Oxford University Press, Oxford, England, UK, 2020).
- [10] R. Kuzmin, R. Mencia, N. Grabon, N. Mehta, Y.-H. Lin, and V. E. Manucharyan, Nat. Phys. 15, 930 (2019).
- [11] A. B. Harris and T. C. Lubensky, Phys. Rev. Lett. 33, 1540 (1974).
- [12] T. Giamarchi and H. J. Schulz, Phys. Rev. B 37, 325 (1988).
- [13] T. Giamarchi, Quantum Physics in One Dimension (Clarendon Press, Oxford, England, UK, 2003).
- [14] R. Fazio and H. van der Zant, Phys. Rep. 355, 235 (2001).
- [15] G. Z. Tóth, Journal of Physics A: Mathematical and General 37, 9631–9650 (2004).
- [16] S. Ejima, F. H. L. Essler, F. Lange, and H. Fehske, Phys. Rev. B 93, 235118 (2016).

- [17] L. Tagliacozzo, Thiago. R. de Oliveira, S. Iblisdir, and J. I. Latorre, Phys. Rev. B 78, 024410 (2008).
- [18] S. M. Bhattacharjee and F. Seno, J. Phys. A: Math. Gen. 34, 6375 (2001).
- [19] P. Calabrese and J. Cardy, J. Stat. Mech.: Theory Exp. **2004** (06), P06002.
- [20] F. Pollmann, S. Mukerjee, A. M. Turner, and J. E. Moore, Phys. Rev. Lett. 102, 255701 (2009).
- [21] M. M. Rams and B. Damski, Phys. Rev. Lett. 106, 055701 (2011).
- [22] V. Zauner-Stauber, L. Vanderstraeten, M. T. Fishman, F. Verstraete, and J. Haegeman, Phys. Rev. B 97, 045145 (2018).
- [23] M. Fishman, S. R. White, and E. M. Stoudenmire, SciPost Phys. Codebases , 4 (2022).

# Roughening dynamics of interfaces in the two-dimensional quantum Ising model

Authors: Wladislaw Krinitsin, Niklas Tausendpfund, Matteo Rizzi,

Markus Heyl, Markus Schmitt

**Year:** 2025

Journal: Physical Review Letters

Volume/Issue: 134, 24

**DOI:** 10.1103/9bsk-x9rw

### III.1 Authors Contribution

This project was initiated jointly by the authors after observing the long thermalization properties of a domain-wall state in the two-dimensional quantum Ising model. After the first numerical results, the authors jointly developed the idea of the effective one-dimensional bosonic model and the relevant order parameters. The simulation code was written and designed in a joint effort by the authors Niklas Tausendpfund and Wladislaw Krinitsin. Wladislaw Krinitsin designed and analyzed the numerical experiments for the two-dimensional quantum Ising model. Niklas Tausendpfund designed and analyzed the numerical experiments and analytical results of the one-dimensional model. The findings were discussed in weekly meetings. The first draft was prepared by Wladislaw Krinitsin and later modified by all authors. Wladislaw Krinitsin and Niklas Tausendpfund share the first authorship on this publication.

## III.2 Data Availability

The simulation of the two-dimensional quantum Ising model were performed with the publicly available Julia package TTN.jl [287]. This package, written by the au-

thors Niklas Tausendpfund and Wladislaw Krinitsin, is based on the ITensors.jl library [274]. The remaining code and extracted data are available on Zenodo under [288].

### III.3 Summary

As explained in Subsection 1.2.1, a system that spontaneously breaks the finite group  $\mathbb{Z}_M$  has a ground state that is M times degenerate. A natural basis used to describe this ground-state manifold is the symmetry-broken basis of Eq. (1.54), which transforms non-trivially under the action of the group. By joining two subsystems realizing a different symmetry-broken ground state, an interface is generated, and new physics can emerge.

While this interface has the character of a local particle in one-dimensional models, it becomes an extended object in  $d \ge 2$ , and understanding the static and dynamic behavior is a challenging but important task. Surprisingly, the extended nature of the interfaces allows them to undergo phase transitions independent of the bulk.

In this work, we study the dynamics of interfaces in the two-dimensional Transverse Field Ising Model (TFIM) on a square lattice of  $N_x \times N_y$  sites

$$H_{\text{Ising}} = \sum_{\langle \vec{j}, \vec{k} \rangle} -J \sigma_{\vec{j}}^x \sigma_{\vec{k}}^x - g \sum_{\vec{j}} \sigma_{\vec{j}}^z. \tag{III.1}$$

This model spontaneously breaks the  $\mathbb{Z}_2$  parity symmetry for  $|g| < g_c \approx 3.04J$  and temperatures  $T < T_c \approx 2.27J$ . Here,  $\vec{j} = (j_x, j_y)$  is the two-dimensional coordinate and  $\langle \vec{j}, \vec{k} \rangle$  denotes a pair of neighboring spin-1/2 degrees of freedom.

To this end, we consider a straight domain wall formed by initializing all spins for  $j_y \leq N_y/2$  in the  $|+\rangle$  eigenstates of the  $\sigma^x$  operator, and for  $j_y > N_y/2$  in the  $|-\rangle$  eigenstate<sup>1</sup>. We selected this particular scenario to remove all additional effects, such as curvature, that may influence the dynamics of the domain wall in a non-trivial way and to study the isolated dynamics of the domain wall. In addition, we chose the boundary conditions in the horizontal direction along the domain wall to be periodic, whereas the boundary conditions orthogonal to the domain wall were fixed to open boundary conditions.

By mapping the domain wall state onto an effective one-dimensional model, known as a Solid-On-Solid (SOS) model, it was found [289–291] that such a domain wall undergoes a static phase transition at  $g_r < g_c$  known as the roughening transition [292, 293]. The mapping assumes that the domain wall forms a well-defined one-dimensional subsystem that decouples from the bulk of the surrounding quantum magnet. By projecting the TFIM onto the relevant many-body states (see below for details), the SOS model is derived. This model contains two competing energy terms: a potential that pins the position of the domain wall relative to its neighbors, and a term that promotes local fluctuations of the domain wall. The relative strength of the two interaction terms is controlled by the original transverse field g.

Through a duality transformation, this model becomes the more familiar quantum rotor model [126]. For small values of the transverse field  $g < g_r$ , the pinning potential dominates, and the domain wall remains a well-defined, localized object with

<sup>&</sup>lt;sup>1</sup> For g=0, a product state is formed by setting all local Hilbert spaces to  $|+\rangle$  or  $|-\rangle$  where  $\sigma^x |\pm\rangle = \pm |\pm\rangle$  is the ground state of the system, compare also Subsection 1.2.1.

III.3. SUMMARY 149

only limited fluctuations in the vertical direction. As the transverse field is increased, the fluctuations start to diverge at  $g=g_r$  and the domain wall becomes a fuzzy delocalized object for all  $g>g_r$ . Because the SOS model is dual to the quantum rotor model, the transition at  $g=g_r$  is of the Berezinski-Kosterlitz-Thouless (BKT) type [289, 291], a transition also found in the sine-Gordon model considered in Subsection 1.3.2 in the context of the Tomonaga-Luttinger Liquid (TLL), and generally describes a gapless-to-gapped transition.

To study the dynamics of the domain wall state, we utilize large-scale tree-tensor network [261, 266, 267] simulations; see also our recent publication [268] for a comprehensive survey. While computing the non-equilibrium behavior of a general quench is notorious difficult in two-dimensional quantum systems and not possible in general owing to the creation of large entanglement, the situation considered here is different as we quench the system inside the same phase. This limits the amount of produced entanglement, especially through the domain wall allowing to reach large time scales. As a first result, we found that the imbalance defined by the expectation value of the  $\sigma^x$  operator in the upper half minus the lower half shows long-lived pre-thermal plateaus even for values of  $g \approx J$ , as shown in Figure 1(b) of our publication.

To explain the pre-thermal plateaus, we assumed that the dynamics of the domain wall were decoupled from the dynamics of the bulk, similar to the equilibrium case discussed above. By this, only the many-body states with exactly one domain wall per column contribute to the dynamics Assigning a positive number  $0 \le m_j \le N_y - 1$  counting the position of the domain wall in the y direction, the relevant many-body states are given by

$$|m_1,\dots,m_{N_r}\rangle\in\mathcal{H}$$
 .

The sub-Hilbert space formed by this set of states can be identified with the Hilbert space of a bosonic chain truncated to a maximum of  $N_y - 1$  occupations; see also Subsection 1.1.5. Projecting the Hamiltonian on this class of states leads to an SOS model

$$H_{\rm SOS} = -J \sum_{i=1}^{N_x-1} |\hat{N}_j - \hat{N}_{j+1}| - g \sum_{i=1}^{N_x} \left( \hat{E}_j + \hat{E}_j^{\dagger} \right) \,, \tag{III.2}$$

where  $\hat{N}_j$  is the operator which measures the bosonic occupation of the jth site in the chain and  $\hat{E}_j^{(\dagger)}$  is the vertex operator of Eq. (1.26) that removes (inserts) a boson at sites j

$$\begin{split} \hat{E}_j & \left| m_j \right\rangle = \left| m - 1 \right\rangle \,, \quad \hat{E}_j^\dagger \left| m \right\rangle = \left| m + 1 \right\rangle \\ & E_j & \left| 0 \right\rangle = E_j^\dagger \left| N_y - 1 \right\rangle = 0 \,. \end{split}$$

The two terms appearing in Eq. (III.2) compete with each other, with the first term pinning the occupation of neighboring sites and the second term promoting larger local fluctuations of the bosonic particles. In the language of the domain wall, this is exactly the competition between a smooth well-defined and a fuzzy delocalized domain wall. The duality transformation to the quantum rotor model is given by passing from the bosons defined on the site to new bosons defined on the link of the original lattice. The new number operator is thereby given by

$$\hat{L}_k\coloneqq \hat{N}_j - \hat{N}_{j+1} \,,$$

where k denotes the link between position j and j+1. Under this transformation, the vertex operator  $\hat{E}_j$  becomes a tunneling operator

$$\hat{E}_i = e^{i\hat{\varphi}_k} e^{-i\hat{\varphi}_{k+1}}$$

of the new  $\hat{L}_k$  bosons. Here  $\hat{\varphi}_k$  is a vertex operator canonically conjugated to the operator  $\hat{L}_k$ , see also the discussion below Eq. (1.26). The full SOS model becomes a quantum rotor model<sup>2</sup>

$$H_{\rm SOS} = -J \sum_k \left| \hat{L}_k \right| - 2g \sum_k \cos(\hat{\varphi}_k - \hat{\varphi}_{k+1}) \,. \label{eq:HSOS}$$

In our study, we compared the dynamics of the two-dimensional domain wall state with the non-equilibrium behavior of the effective one-dimensional model given by Eq. (III.2), where we found good agreement between the results.

In particular, from the static BKT transition of the SOS model it is known that the kink operator

$$K(\alpha, l) = \cos(\alpha(N_1 - N_l)), \quad \alpha \in [0, 2\pi)$$

is a good order parameter for measuring the onset of this transition. It saturates to a constant for  $l \to \infty$  if the domain wall is well-defined for  $g < g_r$ , and to zero if the domain wall becomes fuzzy for  $g > g_r$ . This behavior is understood by considering the height of a domain wall at position j being locked with respect to the neighbors in the  $g < g_r$  regime, and the kink operator has a finite expectation value for long distances. For  $g > g_r$ , the divergence of the vertical fluctuations destroys this locking, and the kink operator averages to zero.

By measuring the thermalization of the kink operator in the SOS model and the corresponding operator in the full two-dimensional model, we observed that in both cases, the expectation value saturates to the same constant, as shown in Figure 3 of our publication. For  $g > g_R$ , the SOS model thermalizes to zero, while the kink operator becomes ill-defined in the full two-dimensional model, indicating the breakdown of the initial assumption that the domain-wall dynamics are independent of the two-dimensional bulk.

It is possible to assign an artificial temperature to the system by matching the two expectation values

$$\langle \psi_0 | H | \psi_0 \rangle = \text{Tr} \left[ \rho(\beta) H \right],$$

where  $\beta=1/T$  is the inverse temperature,  $\rho(\beta)$  is the canonical density matrix, and  $|\psi_0\rangle$  is the initial domain wall state. This is used to interpret the quench and the emergence of the pre-thermal plateaus in the full T-g phase diagram.

Although there is no phase transition in a one-dimensional model at any finite temperature, there exists a transition temperature  $T_r(g,N_x,\alpha)$  for every finite system size N. For  $T\ll T_r$ , the kink operator saturates to a value close to one, whereas for  $T\gg T_r$  the kink operator averages zero. In the classical limit g=0, we show by an analytical calculation that the transition temperature vanishes slower than algebraic with the system size

$$T_r(0,N_x,\alpha)/J = 2\log\left(\frac{2(1-\cos(\alpha N_x)}{\log(2)}\right)^{-1} \,. \label{eq:Tr}$$

Thus, the BKT transition extends as a finite-size transition to the full T-g phase diagram, implying the existence of a roughening transition at some value of  $(T_r, g_r)$ . The breakdown of the single-domain wall assumption can then be interpreted as crossing this finite-temperature BKT-like transition line into an unordered region with unbounded vertical fluctuations.

<sup>&</sup>lt;sup>2</sup> The standard quantum rotor model has a potential of the form  $L_k^2$  instead of an absolute value potential. However, both models have the same symmetries and, thus, the same critical properties, which we also verified explicitly in our publication.

### Roughening Dynamics of Interfaces in the Two-Dimensional Quantum Ising Model

Wladislaw Krinitsin®, 1,2\*\*,† Niklas Tausendpfund®, 1,3,\* Matteo Rizzi®, 1,3 Markus Heyl®, 4,5 and Markus Schmitt® 1.2 Institute of Quantum Control (PGI-8), Forschungszentrum Jülich, D-52425 Jülich, Germany 2Faculty of Informatics and Data Science, University of Regensburg, D-93040 Regensburg, Germany 3Institute for Theoretical Physics, University of Cologne, D-50937 Köln, Germany 4Theoretical Physics III, Center for Electronic Correlations and Magnetism, Institute of Physics, University of Augsburg, D-86135 Augsburg, Germany 5Centre for Advanced Analytics and Predictive Sciences (CAAPS), University of Augsburg, Universitätsstraße 12a, 86159 Augsburg, Germany

(Received 8 January 2025; accepted 21 May 2025; published 20 June 2025)

The properties of interfaces are key to understanding the physics of matter. However, the study of quantum interface dynamics has remained an outstanding challenge. Here, we use large-scale tree tensor network simulations to identify the dynamical signature of an interface roughening transition within the ferromagnetic phase of the 2D quantum Ising model. For initial domain wall profiles we find extended prethermal plateaus for smooth interfaces, whereas above the roughening transition the domain wall decays quickly. Our results can be readily explored experimentally in Rydberg atomic systems.

DOI: 10.1103/9bsk-x9rw

Introduction—The static and dynamical properties of interfaces are fundamental to understanding the physics and to engineer the functionality of materials. Interfaces can even undergo their own unique phase transitions independently of the bulk matter. At a roughening transition, first identified in models for surface growth and classical magnetism [1–3], the nature of interfaces changes qualitatively from being smooth to rough. Intuitively these different phases can be characterized by their interface fluctuations, with small bounded fluctuations in the smooth phase and large unbound ones in the rough phase. The theoretical analysis of effective solid-on-solid (SOS) models revealed the Berezinskii-Kosterlitz-Thouless (BKT) nature of the transition [4,5], which was confirmed in numerical simulations [6]. For experimental studies, the interface between liquid and crystallized Helium-4 is a particularly suited model system [7]. At the involved low temperatures, however, quantum effects enter. It was found that quantum fluctuations can cause a roughening transition at vanishing temperature T = 0 in two-dimensional systems, but not in three dimensions [8,9]. Interface properties are relevant also in a broader scientific context beyond condensed matter. For instance, in high-energy physics, the flux tube connecting quarks realizes an interface that can

Published by the American Physical Society under the terms of the Creative Commons Attribution 4.0 International license. Further distribution of this work must maintain attribution to the author(s) and the published article's title, journal citation, and DOI. undergo roughening [10]. Signatures of which were recently observed via digital quantum simulation of a lattice gauge theory [11]. The exploration of such interface roughening in quantum matter *away from equilibrium* has, however, remained an outstanding challenge to date.

In this Letter, we study the nonequilibrium signatures of the roughening transition in the quantum Ising model. Based on large-scale Tree Tensor Network (TTN) simulations for real-time evolution [12–14], we find that the underlying quantum roughening transition is reflected in a qualitative change of dynamical behavior of domain wall initial conditions upon tuning the transverse field strength. In particular, we identify the independent equilibration of the interface in the smooth interface regime as an alternative cause of prethermal plateaus, which is distinct from the known mechanisms relying on approximate conservation laws or Hilbert space fragmentation [15,16]. The phenomenology can be readily explored in experiments with Rydberg atomic systems [17–31].

*Model*—For the central objective to study the dynamics of interfaces we consider the paradigmatic transverse-field Ising model (TFIM) on a square lattice, given by

$$H = -J \sum_{\langle i,j \rangle} \sigma_i^x \sigma_j^x - g \sum_i \sigma_i^z, \tag{1}$$

where the first sum runs over all neighboring spin pairs. The TFIM exhibits a ferromagnetic phase, which extends to nonzero temperatures, with a quantum phase transition at  $g_c/J \approx 3.04$  and a thermal transition temperature of  $T_c/J \approx 2.27$  at g=0 [32]. Importantly, the 2D quantum Ising model inherits a second quantum phase transition

<sup>\*</sup>These authors contributed equally to this work.

Contact author: w.krinitsin@fz-juelich.de

point of BKT type within the ferromagnetic phase, which is associated with a transition from smooth to rough interfaces [9]. A suited order parameter will be defined at a later point of this Letter, providing a quantitative description of the transition. In the quantum domain, when considering the limit  $J \gg g$ , the TFIM can be perturbatively linked to the PXP model, which shows strong dynamical constrains and Hilbert space fragmentation, leading to a slow relaxation of various domain wall initial conditions [13,14,33,34].

For the purpose of studying the dynamics of quantum interfaces, we will initialize the system with two oppositely polarized magnetic domains, separated by a straight domain wall; see Fig. 1(a). This is a natural choice for experimental platforms, while not introducing any additional effects stemming from, e.g., interface curvature. For weak enough transverse fields, i.e., within the PXP approximation, these states remain stable due to sectors of different interface lengths being dynamically disconnected from each other, preventing thermalization up to timescales that scale exponentially with J/g. (Eventual

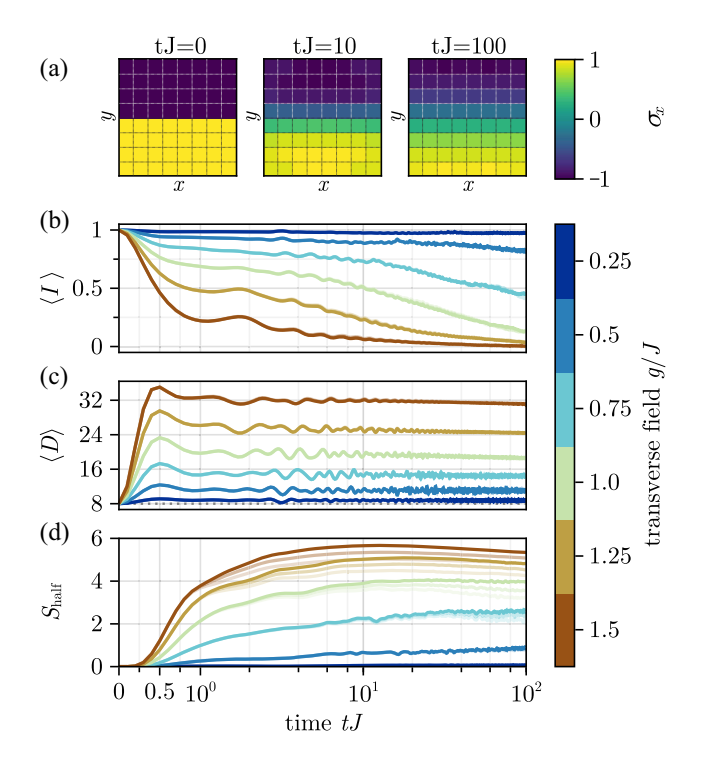


FIG. 1. Time evolution of a flat interface on an  $8 \times 8$  lattice with open boundary conditions. (a) Spatially resolved magnetizations at times tJ=0, 10, and 100 for a transverse field of g/J=0.75. The bottom three plots show (b) the imbalance, (c) the domain wall length, and (d) the entropy of entanglement across the initial interface for several transverse fields: the color coding is indicated in the color bar to the right. The imbalance shows the existence of long-lived plateaus, even at transverse fields  $g \approx J$ . All the results are shown for three different bond dimensions  $\chi=181,256,362$ , where the opacity increases with the bond dimension. For panels (a) and (b), almost all of the data points lie on top of each other.

thermalization is expected to happen for transverse fields  $g/J \ge 0.2$  as is revealed by an analysis of the level-spacing statistics of a 4 × 5 system; see SM for more details [35], which includes Refs. [36,37].)

In the following we depart from any such perturbative limit and target the dynamics in strongly correlated regimes  $g/J \sim 1$ . As will be shown later, we observe prethermal plateaus that cannot be explained by Hilbert space fragmentation. Instead, this nonperturbative effect is related to the thermalization of the interface below a roughening temperature.

Numerical methods—In order to comprehensively explore the quantum roughening dynamics, we employ a variety of complementary tensor network techniques. The simulations of the full dynamics on the 2D lattice were performed using TTNs and the time-dependent variational principle [12-14]. Being loop-free, TTNs are efficiently contractible and their hierarchical structure allows for a more natural covering of the 2D lattice than the widely used matrix product states (MPSs) [38]. MPSs will be used later in the text in order to solve time evolution of an effective 1D model. Furthermore, we utilize the variational uniform matrix product state (VUMPS) algorithm [39-41] to study the ground state properties of the effective model in the thermodynamic limit. Quantum Monte Carlo (QMC) simulations [42–44] are employed to estimate effective temperatures corresponding to the domain wall initial conditions. More details on the aforementioned methods are given in Supplemental Material (SM) [35].

*Interface dynamics*—A first indication for the slow thermalization dynamics is provided by the time evolution of the magnetization imbalance,

$$I = M_T - M_B, (2)$$

with  $M_{T/B} = (1/N) \sum_{i \in T/B} \sigma_i^x$  and T/B indicating the top and bottom halves of the system [see Fig. 1(a)]. The imbalance is maximal in the initial state  $\langle I(t=0)\rangle = 1$ and it has to vanish in a thermal state. Figure 1(b) shows  $\langle I(t)\rangle$  for a range of transverse fields; the spatially resolved magnetization  $\langle \sigma_i^x(t) \rangle$  at three time points is included exemplarily in Fig. 1(a). For the largest transverse fields we expect a rapid thermalization, which is reflected by the observed rapid drop in the imbalance on a timescale of  $tJ \approx 1$ . The subsequent slow decay of the remaining imbalance is attributed to the diffusive approach to a finally homogeneous energy density. The smallest field values conversely show extremely long-lived nonthermal states due to the aforementioned emergent constraints [33,34]. Noticeably, however, prethermal plateaus seem to dominate the dynamics even up to intermediate values of the transverse fields of up to  $g/J \approx 1$  and timescales of  $Jt \approx 10$ .

The fact that the domain wall length operator  $D = \frac{1}{2} \sum_{\langle i,j \rangle} (1 - \sigma_i^x \sigma_j^x)$  shown in Fig. 1(c) strongly departs from its initial value highlights, that the existence of

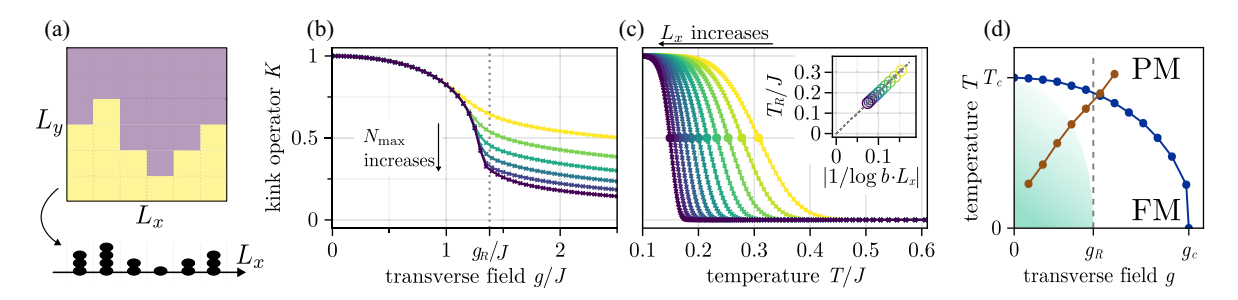


FIG. 2. (a) Mapping from a domain wall state in the full two-dimensional model to an effective one-dimensional bosonic state. (b) Expectation value of the kink operator, evaluated on the ground state of the effective model as a function of the transverse field. Different maximal occupation numbers  $4 \le N_{\text{max}} \le 14$  in steps of two are shown; as  $N_{\text{max}}$  increases, the kink operator starts exhibiting a jump at  $g_R/J \approx 1.38$  corresponding to the roughening transition; see also SM [35]. (c) Expectation value of the kink operator, evaluated on the thermal state of the effective model in the classical limit (g=0) as a function of temperature. We consider chain lengths  $L_x \in [500, 512 \times 10^3]$ , with exponentially increasing steps. The inset shows that the crossover temperature  $T_R$ , defined by  $\langle K(T_R/J) \rangle = 0.5$ , vanishes in the thermodynamic limit as the inverse logarithm of the system size, confirming the analytical prediction (5) that is indicated by the dashed gray line. The constant b in the x axis label is given by  $b = 2(1 - \cos 1)/\log 2$ . Data points in (b) and (c) are represented by crosses, with a linear interpolation between them. (d) Phase diagram of the 2D TFIM. The blue line represents the critical line separating the ferro- from the paramagnetic phase, the red line denotes the effective temperature of the initial state based on its energy, obtained from QMC simulations; see SM [35]. Our results point toward the existence of a roughening transition at a value of  $g_R/J \approx 1.38 < g_c/J$ . The green shaded region shows the extended smooth interface regime present in finite systems.

prethermal plateaus at intermediate transverse fields cannot be captured within the usual framework of Hilbert space fragmentation governed by restricted domain wall lengths. We will instead demonstrate in the following that an effective description can be formulated in terms of a single-domain-wall approximation.

Figure 1 includes a convergence check of the numerical results with different bond dimensions up to  $\chi=362$ . While late times and stronger transverse fields become challenging, the prominent prethermal plateaus are well within the regime of certain convergence. Most sensitive to varying bond dimension is the half-system entanglement entropy [Fig. 1(d)], when splitting the system into two equal partitions along the initial interface, which shows that the moderate amounts of entanglement generated up to the lifetime of the plateaus are well captured.

Effective model—In order to explain the observed nonperturbative prethermal effects, we formulate an effective, one-dimensional model that corresponds to the projection of Eq. (1) onto the subspace of domain wall states with exactly one horizontal interface segment per column (see SM for a more detailed derivation [35]),

$$\mathbf{H}_{\text{eff}} = 2J \cdot \sum_{i} |N_i - N_{i+1}| - g \cdot \sum_{i} (E_i + E_i^{\dagger}). \quad (3)$$

Here, we introduced height operators  $N_i$  measuring the perpendicular displacement of the domain wall; see Fig. 2(a). The raising (lowering) operators  $E_i^{\dagger}(E_i)$  are the projection of the  $\sigma_i^z$ , which in the manifold of single horizontal domain walls can only flip spins next to the domain wall. The raising and lowering operators obey the

commutation relations  $[E_i,N_j]=E_i\delta_{i,j}$  similar to the standard definition used in quantum rotor models [45]. Hence, the phase operator  $\varphi$  defined through  $E_j=\exp(i\varphi_j)$  is canonically conjugate to the height operator and the  $N_i$  can alternatively be viewed as bosonic occupation number operators. It is important to note that the model is not based on some low-order Schrieffer-Wolff transformation, but instead captures the relevant fluctuations of the initial domain wall.

The effective model (3) is also closely related to SOS-like models [4,5], in which roughening appears as a BKT transition [46]. The critical point of  $H_{\rm eff}$  has been argued to be upperbounded by the critical point of the quantum rotor model [47–49]. This is noticeably below the symmetry-breaking phase transition of the full TFIM.

Roughening is indicated by the kink operator

$$K_{\alpha}(l) = \cos[\alpha(N_1 - N_I)],\tag{4}$$

which probes the fluctuations of the interface in the direction perpendicular to its initial orientation. It is a suited order parameter because a value of  $\langle K_\alpha(l) \rangle = 1$  corresponds to a flat (smooth) interface, while a value of  $\langle K_\alpha(l) \rangle = 0$  corresponds to a highly fluctuating (rough) interface. A universal quantitative analysis would require taking the limits  $\lim_{\alpha \to 0} \lim_{l \to \infty} \langle K_\alpha(l) \rangle$  for the angle  $\alpha$  and distance l. In our numerical analysis of finite systems, we choose  $l = L_x$  maximal and we find that  $\alpha = 1$  is the minimal value, that sufficiently suppresses bulk contributions when considering the full TFIM; see SM [35] for more details. From now on we will drop the dependency on  $\alpha$  and l, i.e.,  $K \equiv K_{\alpha=1}(l=L_x)$ .

Figure 2(b) shows the ground state expectation value of the kink operator for varying g/J and different values of the occupation number truncation  $N_{\rm max}$ , obtained using the VUMPS algorithm. The drop of  $\langle K \rangle$  with increasing g/J clearly indicates the transition from a smooth to a rough interface regime. This drop becomes sharper as  $N_{\rm max}$  is increased, pointing toward the existence of a phase transition—a fit of the correlation length provides the critical value  $g_R/J \approx 1.38$ . Further analysis strengthens the hypothesis of a BKT transition in the SOS model; see End Matter and SM [35].

Next, we turn toward the question of whether its signatures survive even at nonzero temperatures T. Note that order at T>0 would not violate the Mermin-Wagner theorem due to the infinite local Hilbert space dimension [50]. We consider the classical limit of the effective model, i.e., g/J=0, and use a transfer matrix based method to calculate the expectation value of the kink operator in the thermal state; see End Matter and SM for more details [35]. The thermal expectation value of the kink operator shown in Fig. 2(c) exhibits an extended regime with a clear signature of smooth interfaces at low temperatures for system sizes up to  $L_x=5\times10^5$ . However, the turning point shifts with increasing system size and its location behaves perturbatively as

$$T_R/J = 2\log\left(\frac{2[1-\cos(\alpha)]L_x}{\log(2)}\right)^{-1}.$$
 (5)

See the inset of Fig. 2(c) as well as End Matter and SM [35], which includes Ref. [51]. Thus, in the thermodynamic limit  $L_x \to \infty$ , roughening occurs immediately for any T>0. Nonetheless, clear signatures of a smooth interface regime at nonzero temperature survive up to very large system sizes due to the logarithmic dependence of  $T_R$  on  $L_x$ , which has especial relevance for current experimental realizations in quantum simulators.

Figure 2(d) shows a sketch of the inferred phase diagram in the full two-dimensional Ising model, summarizing all the previously discussed results: The ferromagnetic phase encompasses an extended smooth interface regime delimited by a roughening quantum phase transition (OPT) and a system-size dependent crossover at nonvanishing temperatures. We include the effective temperatures fixed by the domain wall initial condition for the range of considered transverse fields g/J, indicating that signatures of a smooth interface regime will vanish already at field strengths below the critical  $g_R$ . Concerning the nonequilibrium dynamics, this phase diagram suggests that the effective model can thermalize in the smooth domain wall regime, implying stability of domain walls for long times. We will show next that this prediction is even quantitatively accurate for the full dynamics of the two-dimensional TFIM.

Dynamical signature of roughening—The effective model covers the subspace of single domain wall states

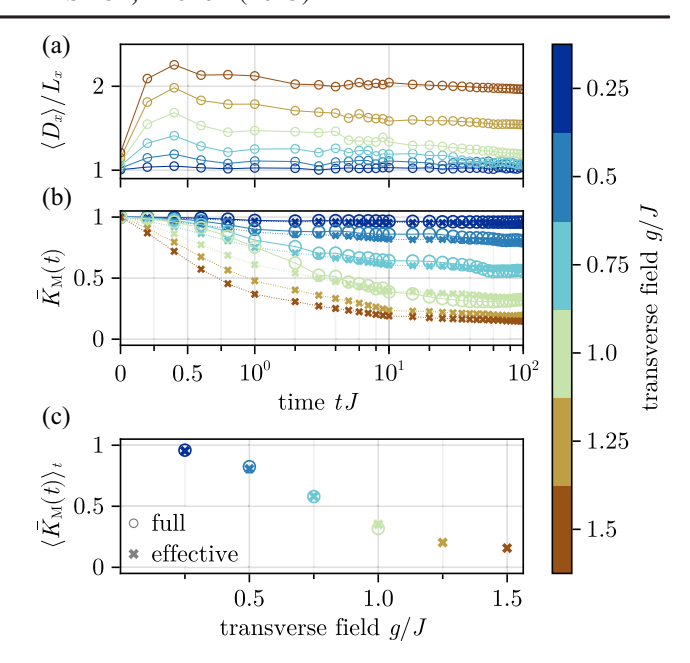


FIG. 3. (a) Time evolution of the horizontal contribution to the domain wall length divided by the horizontal lattice dimension. The plot shows that up until g/J = 1, each column has approximately one horizontal domain wall for the times considered, confirming the validity of the effective model (3) in that regime. (b) Comparison between the effective (dashed lines and crosses) and the full model (solid lines and circles) for the time evolution of the kink operator. In order to filter out the strong fluctuations of the data we show the running mean of the kink operator. For the full model, we calculate the modified kink operator  $K_{\rm M} = \langle K \rangle / \langle K_{\rm bulk} \rangle$ . We do not show data for transverse fields beyond g/J = 1, as bulk and interface contributions become increasingly difficult to disentangle. (c) Late-time averages of the kink operators shown in (b), taken over the interval  $tJ \in [20, 100]$ , as functions of the transverse field. The values agree well up to g/J = 1, once again confirming the quantitative predictive power of the effective model in that regime.

without bubbles or overhang. To check the validity of this description, we plot the time dependence of the horizontal domain wall length  $D_x = 1/2 \sum_{i,j} (\mathbb{1} - \sigma_{i,j}^x \sigma_{i,j+1}^x)$  in Fig. 3(a). The small deviations of  $\langle D_x \rangle / L_x$  from 1 for transverse fields up to  $g/J \approx 1$  support the validity of the effective model in that regime.

We now turn to a direct comparison between the dynamics of the full and the effective model—the latter simulated using MPS. In the full 2D TFIM, the operator probing the vertical position of the domain wall at site i is given by  $N_i = \sum_{j \perp i} j/2(1 - \sigma_{i,j}^x \sigma_{i,j+1}^x)$  with the sum running over all lattice sites j perpendicular to the domain wall. For a meaningful comparison with the effective model, however, we need to account for bulk contributions such as single spin flips away from the domain wall. For that purpose, we define a modified kink operator  $K_{\rm M} = \langle K \rangle / \langle K_{\rm bulk} \rangle$ , where  $\langle K_{\rm bulk} \rangle$  is obtained by calculating the kink operator for a system where the interaction

along the initial domain wall is removed, i.e., only bulk effects contribute to the time evolution. Since the time-dependent expectation values obtained from the full and the effective models differ in their high frequency fluctuations, we will moreover consider their running time averages  $\bar{K}(t) = (1/t) \int_0^t dt \langle K(t) \rangle$  instead for the direct quantitative comparison. See SM for more details [35].

The time evolution of the modified kink operator in comparison with the kink operator of the effective model is shown in Fig. 3(b). Data for the full model is restricted to transverse fields  $g/J \leq 1$ , since the separation of bulk from interface effects becomes infeasible for larger fields. We find very good quantitative agreement between these two models, meaning that the dynamics of interfaces in the TFIM can be understood in terms of the SOS model: for the considered intermediate values of the transverse field, the SOS model thermalizes within the smooth interface regime [cf. Fig. 2(d)] and the initially flat domain wall profile remains eternally stable. This stability of the domain wall manifests itself in the full TFIM in the form of prethermal plateaus with  $\bar{K}_{\rm M}(t) > 0$ . In contrast to the effective model, a subsequent decay of these prethermal states is to be expected in the full model, but these timescales seem out of reach for current numerical approaches. Figure 3(c) displays the late-time stationary values of the running, time-averaged kink operator by taking the mean over points lying in the interval  $tJ \in [20, 100]$ , which once more highlight the compelling quantitative agreement between the SOS model and the TFIM. Results obtained for a  $16 \times 16$  lattice confirm said agreement for larger system sizes, without the need to suppress temporal fluctuations via taking the running mean; see SM [35] for more details. Finally, notice that the imbalance in Fig. 1(b) and the kink operator in Fig. 3(b) exhibit different lifetimes of the prethermal plateaus. This indicates that restoring the rotational symmetries requires longer times than the restoration of translational symmetry.

Discussion—Our analysis establishes a connection between the roughening transition and the relaxation dynamics of quantum interfaces in the 2D TFIM. The stability of domain walls in the smooth interface regime constitutes a new mechanism for prethermalization beyond known ones like proximity to an integrable point [15] or Hilbert space fragmentation and quantum scars [16], highlighting a qualitative change within the dynamical phase diagram of the TFIM in two dimensions.

The domain wall dynamics of the quantum Ising model can be probed experimentally in state of the art Rydberg atomic systems [31,52–54]. Domain wall initial conditions can be prepared via programmable locally controlled light shifts, and recent experiments demonstrate the feasibility of a transversely oriented magnetic field of the required intermediate magnitude [31,53]. Our formulation of the effective model remains unchanged for the typical antiferromagnetic interactions. Since the imbalance and the

kink operator are immediately accessible through snapshot measurements, we expect that the described phenomenology is readily accessible in current Rydberg atom quantum simulators. An exciting prospect would be the possibility to probe longer timescales in this way.

Furthermore, it will be interesting to investigate other initial domain wall configurations in the light of roughening. Examples include the observed self-straightening dynamics of a initial zigzag configuration [31] and potential implications for false vacuum decay probed via bubble formation [55–58]. More generally, the impact of curvature on the phenomenology of the roughening dynamics remains to be explored in a future work. Another immediate question concerns the generalization to other symmetries, since the results presented here rely on a  $\mathbb{Z}_2$  symmetry-broken phase.

The TTN simulations presented in this Letter were produced with TTN.jl [59], a software package we developed based on the ITensor library [60]. The MPS simulations were performed with the help of ITensor. The QMC simulations were produced with the help of the ALPS software package [61] and a rust library [44].

Acknowledgments—We acknowledge fruitful discussions with A. Segner, J.-D. Urbina, M. Steinhuber, L. Behringer, S. Tomsovic, T. Mendes-Santos, A. Gambassi, and U.-J. Wiese. M. S. and W. K. were supported through the Helmholtz Initiative and Networking Fund, Grant No. VH-NG-1711. We acknowledge support from the Deutsche Forschungsgemeinschaft (DFG) under Germany's Excellence Strategy-Cluster of Excellence Matter and Light for Quantum Computing (ML4Q) EXC 2004/1-390534769 (NT, MR and MS), under Grant No. 277101999—CRC network TR 183 (NT and MR), under Project No. 499180199—FOR 5522 (MH). M. H. has received funding from the European Research Council (ERC) under the European Union's Horizon 2020 research and innovation programme (Grant Agreement No. 853443). M. R. and N. T. acknowledge funding under Horizon Europe programme HORIZONvia CL4-2022-QUANTUM-02-SGA the No. 101113690 (PASQuanS2.1). The authors gratefully acknowledge the Gauss Centre for Supercomputing e.V. [62] for funding this project by providing computing time through the John von Neumann Institute for Computing (NIC) on the GCS Supercomputer JUWELS [63] at Jülich Supercomputing Centre (JSC) under grant NeTeNeSyQuMa. They also gratefully acknowledge computing time on the supercomputer JURECA [64] at Forschungszentrum Jülich under grants NeTeNeSyQuMa and pgi8.

Data availability—The data that support the findings of this article are openly available [65].

W. K. Burton, N. Cabrera, and F. C. Frank, The growth of crystals and the equilibrium structure of their surfaces, Phil. Trans. R. Soc. A 243, 299 (1951).

- [2] R. L. Dobrushin, Gibbs state describing coexistence of phases for a three-dimensional Ising model, Theory Probab. Appl. 17, 582 (1973).
- [3] J. D. Weeks, G. H. Gilmer, and H. J. Leamy, Structural transition in the Ising-model interface, Phys. Rev. Lett. 31, 549 (1973).
- [4] S. T. Chui and J. D. Weeks, Phase transition in the twodimensional Coulomb gas, and the interfacial roughening transition, Phys. Rev. B **14**, 4978 (1976).
- [5] H. van Beijeren, Exactly solvable model for the roughening transition of a crystal surface, Phys. Rev. Lett. 38, 993 (1977).
- [6] M. Hasenbusch, S. Meyer, and M. Pütz, The roughening transition of the three-dimensional Ising interface: A Monte Carlo study, J. Stat. Phys. 85, 383 (1996).
- [7] S. Balibar, H. Alles, and A. Y. Parshin, The surface of helium crystals, Rev. Mod. Phys. 77, 317 (2005).
- [8] D. S. Fisher and J. D. Weeks, Shape of crystals at low temperatures: Absence of quantum roughening, Phys. Rev. Lett. 50, 1077 (1983).
- [9] E. Fradkin, Roughening transition in quantum interfaces, Phys. Rev. B **28**, 5338 (1983).
- [10] M. Lüscher, Symmetry-breaking aspects of the roughening transition in gauge theories, Nucl. Phys. B180, 317 (1981).
- [11] T. A. Cochran *et al.*, Visualizing dynamics of charges and strings in (2+1)D lattice gauge theories, arXiv:2409. 17142.
- [12] B. Kloss, D. R. Reichman, and Y. B. Lev, Studying dynamics in two-dimensional quantum lattices using tree tensor network states, SciPost Phys. 9, 070 (2020).
- [13] L. Pavešić, D. Jaschke, and S. Montangero, Constrained dynamics and confinement in the two-dimensional quantum Ising model, Phys. Rev. B 111, L140305 (2025).
- [14] W. Krinitsin, N. Tausendpfund, M. Heyl, M. Rizzi, and M. Schmitt, Time evolution of the quantum Ising model in two dimensions using tree tensor networks, arXiv:2505.07612.
- [15] M. Moeckel and S. Kehrein, Interaction quench in the Hubbard model, Phys. Rev. Lett. 100, 175702 (2008).
- [16] S. Moudgalya, B. A. Bernevig, and N. Regnault, Quantum many-body scars and Hilbert space fragmentation: A review of exact results, Rep. Prog. Phys. 85, 086501 (2022).
- [17] M. Greiner, O. Mandel, T. W. Hänsch, and I. Bloch, Collapse and revival of the matter wave field of a Bose–Einstein condensate, Nature (London) 419, 51 (2002).
- [18] I. M. Georgescu, S. Ashhab, and F. Nori, Quantum simulation, Rev. Mod. Phys. 86, 153 (2014).
- [19] T. Kinoshita, T. Wenger, and D. S. Weiss, A quantum Newton's cradle, Nature (London) 440, 900 (2006).
- [20] E. A. Martinez, C. A. Muschik, P. Schindler, D. Nigg, A. Erhard, M. Heyl, P. Hauke, M. Dalmonte, T. Monz, P. Zoller, and R. Blatt, Real-time dynamics of lattice gauge theories with a few-qubit quantum computer, Nature (London) 534, 516 (2016).
- [21] J.-Y. Choi, S. Hild, J. Zeiher, P. Schauß, A. Rubio-Abadal, T. Yefsah, V. Khemani, D. A. Huse, I. Bloch, and C. Gross, Exploring the many-body localization transition in two dimensions, Science 352, 1547 (2016).
- [22] C. Gross and I. Bloch, Quantum simulations with ultracold atoms in optical lattices, Science **357**, 995 (2017).

- [23] P. Jurcevic, H. Shen, P. Hauke, C. Maier, T. Brydges, C. Hempel, B. P. Lanyon, M. Heyl, R. Blatt, and C. F. Roos, Direct observation of dynamical quantum phase transitions in an interacting many-body system, Phys. Rev. Lett. 119, 080501 (2017).
- [24] H. Bernien, S. Schwartz, A. Keesling, H. Levine, A. Omran, H. Pichler, S. Choi, A. S. Zibrov, M. Endres, M. Greiner, V. Vuletić, and M. D. Lukin, Probing many-body dynamics on a 51-atom quantum simulator, Nature (London) 551, 579 (2017).
- [25] J. Zhang, G. Pagano, P. W. Hess, A. Kyprianidis, P. Becker, H. Kaplan, A. V. Gorshkov, Z.-X. Gong, and C. Monroe, Observation of a many-body dynamical phase transition with a 53-qubit quantum simulator, Nature (London) 551, 601 (2017).
- [26] M. Gärttner, J. G. Bohnet, A. Safavi-Naini, M. L. Wall, J. J. Bollinger, and A. M. Rey, Measuring out-of-time-order correlations and multiple quantum spectra in a trapped-ion quantum magnet, Nat. Phys. 13, 781 (2017).
- [27] S. Choi, J. Choi, R. Landig, G. Kucsko, H. Zhou, J. Isoya, F. Jelezko, S. Onoda, H. Sumiya, V. Khemani, C. von Keyserlingk, N. Y. Yao, E. Demler, and M. D. Lukin, Observation of discrete time-crystalline order in a disordered dipolar many-body system, Nature (London) 543, 221 (2017).
- [28] H. Levine, A. Keesling, A. Omran, H. Bernien, S. Schwartz, A. S. Zibrov, M. Endres, M. Greiner, V. Vuletić, and M. D. Lukin, High-fidelity control and entanglement of Rydbergatom qubits, Phys. Rev. Lett. 121, 123603 (2018).
- [29] S. Hild, T. Fukuhara, P. Schauß, J. Zeiher, M. Knap, E. Demler, I. Bloch, and C. Gross, Far-from-equilibrium spin transport in Heisenberg quantum magnets, Phys. Rev. Lett. 113, 147205 (2014).
- [30] D. Barredo, V. Lienhard, S. de Léséleuc, T. Lahaye, and A. Browaeys, Synthetic three-dimensional atomic structures assembled atom by atom, Nature (London) 561, 79 (2018).
- [31] T. Manovitz, S. H. Li, S. Ebadi, R. Samajdar, A. A. Geim, S. J. Evered, D. Bluvstein, H. Zhou, N. U. Koyluoglu, J. Feldmeier, P. E. Dolgirev, N. Maskara, M. Kalinowski, S. Sachdev, D. A. Huse, M. Greiner, V. Vuletić, and M. D. Lukin, Quantum coarsening and collective dynamics on a programmable quantum simulator, Nature (London) 638, 86 (2025).
- [32] H. W. J. Blöte and Y. Deng, Cluster Monte Carlo simulation of the transverse Ising model, Phys. Rev. E 66, 066110 (2002).
- [33] F. Balducci, A. Gambassi, A. Lerose, A. Scardicchio, and C. Vanoni, Localization and melting of interfaces in the two-dimensional quantum Ising model, Phys. Rev. Lett. 129, 120601 (2022).
- [34] F. Balducci, A. Gambassi, A. Lerose, A. Scardicchio, and C. Vanoni, Interface dynamics in the two-dimensional quantum Ising model, Phys. Rev. B **107**, 024306 (2023).
- [35] See Supplemental Material at http://link.aps.org/supplemental/10.1103/9bsk-x9rw for further details about the tree tensor network simulations, properties of the kink operator, the transfer matrix analysis, and the quantum Monte Carlo simulations.

- [36] A. A. Abul-Magd and A. Y. Abul-Magd, Unfolding of the spectrum for chaotic and mixed systems, Physica (Amsterdam) **396A**, 185 (2014).
- [37] Y. Y. Atas, E. Bogomolny, O. Giraud, and G. Roux, Distribution of the ratio of consecutive level spacings in random matrix ensembles, Phys. Rev. Lett. 110, 084101 (2013).
- [38] P. Silvi, F. Tschirsich, M. Gerster, J. Jünemann, D. Jaschke, M. Rizzi, and S. Montangero, The tensor networks anthology: Simulation techniques for many-body quantum lattice systems, SciPost Phys. Lect. Notes 8 (2019).
- [39] J. Haegeman, J. I. Cirac, T. J. Osborne, I. Pižorn, H. Verschelde, and F. Verstraete, Time-dependent variational principle for quantum lattices, Phys. Rev. Lett. 107, 070601 (2011).
- [40] J. Haegeman, C. Lubich, I. Oseledets, B. Vandereycken, and F. Verstraete, Unifying time evolution and optimization with matrix product states, Phys. Rev. B 94, 165116 (2016).
- [41] V. Zauner-Stauber, L. Vanderstraeten, M. T. Fishman, F. Verstraete, and J. Haegeman, Variational optimization algorithms for uniform matrix product states, Phys. Rev. B 97, 045145 (2018).
- [42] H. G. Evertz, G. Lana, and M. Marcu, Cluster algorithm for vertex models, Phys. Rev. Lett. 70, 875 (1993).
- [43] H. G. Evertz, The loop algorithm, Adv. Phys. 52, 1 (2003).
- [44] S. Hearth, IsingMonteCarlo (2024).
- [45] S. Sachdev, *Quantum Phase Transitions*, 2nd ed. (Cambridge University Press, Cambridge, England, 2011).
- [46] E. Fradkin and L. Susskind, Order and disorder in gauge systems and magnets, Phys. Rev. D 17, 2637 (1978).
- [47] A. Hasenfratz, E. Hasenfratz, and P. Hasenfratz, Generalized roughening transition and its effect on the string tension, Nucl. Phys. **B180**, 353 (1981).
- [48] S. L. Sondhi, S. M. Girvin, J. P. Carini, and D. Shahar, Continuous quantum phase transitions, Rev. Mod. Phys. 69, 315 (1997)
- [49] M. Hasenbusch, The two-dimensional XY model at the transition temperature: A high-precision Monte Carlo study, J. Phys. A 38, 5869 (2005).
- [50] J. A. Cuesta and A. Sánchez, General non-existence theorem for phase transitions in one-dimensional systems with short range interactions, and physical examples of such transitions, J. Stat. Phys. 115, 869 (2004).
- [51] W.-C. Yueh and S. S. Cheng, Explicit eigenvalues and inverses of tridiagonal toeplitz matrices with four perturbed corners, ANZIAM J. 49, 361 (2008).
- [52] J. Zeiher, J. Y. Choi, A. Rubio-Abadal, T. Pohl, R. van Bijnen, I. Bloch, and C. Gross, Coherent many-body spin

- dynamics in a long-range interacting Ising chain, Phys. Rev. X 7, 041063 (2017).
- [53] H. Bernien, S. Schwartz, A. Keesling, H. Levine, A. Omran, H. Pichler, S. Choi, A. S. Zibrov, M. Endres, M. Greiner, V. Vuletić, and M. D. Lukin, Probing many-body dynamics on a 51-atom quantum simulator, Nature (London) 551, 579 (2017).
- [54] P. Scholl, M. Schuler, H. J. Williams, A. A. Eberharter, D. Barredo, K.-N. Schymik, V. Lienhard, L.-P. Henry, T. C. Lang, T. Lahaye, A. M. Läuchli, and A. Browaeys, Quantum simulation of 2d antiferromagnets with hundreds of Rydberg atoms, Nature (London) 595, 233 (2021).
- [55] S. Coleman, Fate of the false vacuum: Semiclassical theory, Phys. Rev. D 15, 2929 (1977).
- [56] G. Lagnese, F. M. Surace, M. Kormos, and P. Calabrese, False vacuum decay in quantum spin chains, Phys. Rev. B 104, L201106 (2021).
- [57] A. Milsted, J. Liu, J. Preskill, and G. Vidal, Collisions of false-vacuum bubble walls in a quantum spin chain, PRX Quantum 3, 020316 (2022).
- [58] A. Zenesini, A. Berti, R. Cominotti, C. Rogora, I.G. Moss, T.P. Billam, I. Carusotto, G. Lamporesi, A. Recati, and G. Ferrari, False vacuum decay via bubble formation in ferromagnetic superfluids, Nat. Phys. 20, 558 (2024).
- [59] N. Tausendpfund, M. Rizzi, W. Krinitsin, and M. Schmitt, TTN—A tree tensor network library for calculating groundstates and solving time evolution (2024), available on Zenodo.
- [60] M. Fishman, S. R. White, and E. M. Stoudenmire, The ITensor software library for tensor network calculations, SciPost Phys. Codebases 4 (2022).
- [61] B. Bauer et al., The ALPS project release 2.0: Open source software for strongly correlated systems, J. Stat. Mech. (2011) P05001.
- [62] www.gauss-centre.eu
- [63] Jülich Supercomputing Centre, JUWELS cluster and booster: Exascale pathfinder with modular supercomputing architecture at JSC, J. Large-Scale Res. Facil. 7, A183 (2021).
- [64] Jülich Supercomputing Centre, JURECA: Data centric and booster modules implementing the modular supercomputing architecture at JSC, J. Large-Scale Res. Facil. 7, A182 (2021).
- [65] W. Krinitsin, N. Tausendpfund, M. Rizzi, M. Heyl, and M. Schmitt, Data and code associated to the paper roughening dynamics of interfaces in two-dimensional quantum matter, 10.5281/zenodo.14705609 (2025).

### **End Matter**

BKT transition of the SOS model—Here, we demonstrate that the nature of the transition in the effective SOS model (3) belongs to the BKT universality class. To this end, we use the VUMPS algorithm [39–41] to study the ground state properties of the effective model. This allows us to work directly in the thermodynamic limit with a fixed truncation of bosonic excitations  $N_{\rm max} \in 2\mathbb{Z}$ . In the two-dimensional model, this is equivalent to considering an infinitely long slab of width  $L_{\rm y} = N_{\rm max} + 1$  with the interface oriented along

the infinite direction. To observe the critical properties, it is necessary to scale the results against  $N_{\rm max} \to \infty$ .

In practice, we considered  $N_{\rm max} \leq 14$ . Since the local Hilbert space scales as  $\dim(\mathcal{H}_{\rm loc}) = N_{\rm max} + 1$ , a maximum bosonic occupation of 14 already leads to very long simulation times of  $13 \times 10^3$  s per iteration for a bond dimension of  $\chi = 600$ .

In contrast to continuous phase transitions described by the Landau-Ginzburg theory, the BKT transition cannot be detected by the divergence of any derivative of the energy

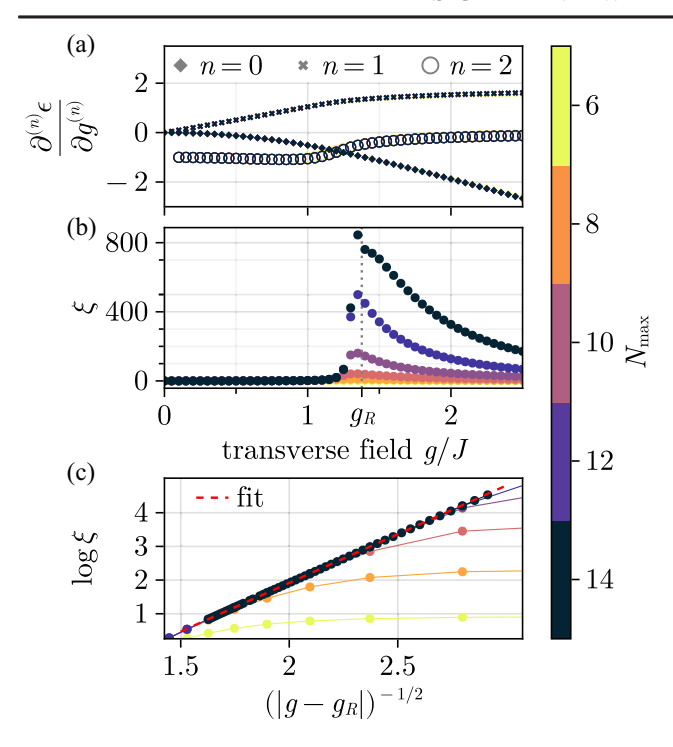


FIG. 4. (a) The energy density and its first two derivatives with respect to the transverse field g, as a function of g. All of the different orders do not show any sign of nonanalyticity around the transition point, excluding the possibility of it being a first or second order phase transition. (b) The correlation length shows a divergence at  $g=g_R$  when increasing the maximal bosonic occupation number. All results are obtained with a bond dimension of  $\chi=600$  and are converged for  $N_{\rm max}<14$ . For the  $N_{\rm max}=14$ , the points around the transition are not yet fully converged, showing numerical artifacts for  $g>g_R$ . (c) Fit of (A1) to the data, showing the correct BKT type divergence law of the correlation length. Increasing  $N_{\rm max}$  again leads to a better agreement between the data and the expected law. The critical transverse field obtained from the fit for the largest  $N_{\rm max}=14$  is  $g_R/J=1.38$ .

density  $\epsilon(g)$ , which is an analytical function of g. This is demonstrated in Fig. 4(a) via the example of the first and second derivative of  $\epsilon(g)$ . Moreover, we observe that  $\epsilon(g)$  and its derivatives are quickly converging in  $N_{\rm max}$ .

Characteristic of the BKT transition is the exponential divergence of the correlation length when approaching the critical value  $g_R$ ,

$$\xi(g) = \xi_0 \exp\left(\frac{B}{\sqrt{|g - g_R|}}\right), \text{ for } g < g_R.$$
 (A1)

Here,  $\xi_0$  and B are nonuniversal constants depending on the model and on the observable used to extract the correlation length. We observed the largest correlation length for the vortex-vortex correlation function

$$C(l) = \langle e^{-iN_0} e^{iN_l} \rangle^{\dagger \to \infty} A e^{-\frac{l}{\xi}} + C_{\infty},$$

which is closely related to the kink operator (4). The constant  $C_{\infty}$  is expected to be close to 1 in the  $g < g_R$  region, while we expect it to vanish after the BKT transition for  $N_{\max} \to \infty$ . In particular one has  $\langle K_{\alpha}(l) \rangle \to |C_{\infty}|$  for  $l \to \infty$ . The results are displayed in Fig. 4(b) for  $6 \le N_{\max} \le 14$ . For increasing  $N_{\max}$ , the correlation length shows a divergent behavior around  $g/J \approx 1.4$  with  $\xi \sim 800$  for  $N_{\max} = 14$ .

To quantify that  $\xi(g)$  has the correct behavior approaching  $g_R/J$ , we fit  $\xi(g)$  for  $N_{\rm max}=14$  for 1.1 < g/J < 1.385 with higher resolution using Eq. (A1). From this fit, we obtain  $g_R/J \approx 1.38$ . In Fig. 4(c) we plot the logarithmic correlation length as a function of  $1/\sqrt{|g-g_R|}$  for  $g < g_R$  and  $6 \le N_{\rm max} \le 14$  using the value of  $g_R$  obtained by the fit. Increasing  $N_{\rm max}$  leads to a better agreement between the data and the prediction for the correlation length, which should be exact in the limit  $N_{\rm max} \to \infty$ . For lower  $N_{\rm max}$  the curve starts flattening out and thus deviating sooner, illustrating the finite  $N_{\rm max}$  effects.

Finite temperature crossover in the classical limit—In the classical limit  $g \to 0$  the effective model (3) contains only commuting operators  $|N_j - N_{j+1}|$ . Thus, all eigenstates are simply given by product states  $|\{s_j\}\rangle$ , fixing the occupation on the jth site. To study the thermodynamic properties in this limit, it is sufficient to replace the number operator  $N_j$  by its eigenvalues  $s_j \in \{0, N_{\text{max}}\}$ ,

$$\mathcal{H}_{\text{class}}(\{s_j\}) = 2J \sum_{j=1}^{L_x - 1} |s_j - s_{j+1}| = \sum_{j=1}^{L_x - 1} h(s_j, s_{j+1}).$$
 (B1)

Let  $V_{s,s'}=\exp[-\beta h(s,s')]$  be the transfer matrix of the classical system and define the general  $\alpha$  twisted boundary vector  $|E(\alpha)\rangle=\sum_{s=0}^{N_{\rm max}}e^{i\alpha s}|s\rangle$ . The  $\alpha$  twisted partition function of a chain of length  $L_x$  with open boundary conditions can be written compactly as

$$\mathcal{Z}(\alpha) = \sum_{s_1=0}^{N_{\text{max}}} \dots \sum_{s_{L_x}=0}^{N_{\text{max}}} e^{-\beta \mathcal{H}_{\text{class}}(\{s_j\}) - i\alpha(s_1 - s_{L_x})}$$

$$= \langle E(\alpha) | V^{L_x - 1} | E(\alpha) \rangle. \tag{B2}$$

The standard partition function corresponds to zero twisting, i.e.,  $\mathcal{Z}=\mathcal{Z}(0)$ . We can now write down the expectation value of the string operator  $\langle K_l \rangle$ . For simplicity, we consider  $l=L_x$ , i.e., the end-to-end expectation value. Using the twisted partition function, we obtain

$$\langle K_{\alpha}(L_x)\rangle = \frac{\mathcal{Z}(\alpha)}{\mathcal{Z}(0)}.$$
 (B3)

The calculation can be further simplified by diagonalizing the transfer matrix  $V = U\Lambda U^{\dagger}$ . In this case, the

twisted partition function can be written as

$$\mathcal{Z}(\alpha) = \lambda_1^{L_x - 1} \sum_{s=0}^{N_{\text{max}}} f_n^{L_x - 1} |c_n(\alpha)|^2,$$
 (B4)

where  $\lambda_1$  is the largest eigenvalue,  $f_n = \lambda_n/\lambda_1$ , and  $c_n(\alpha)$  are the form factors obtained by calculating the overlap between the eigenstates  $|\psi_n\rangle$  of V and the twisted boundary vector  $|E(\alpha)\rangle$ .

Numerically we found the operator  $\langle K_{\alpha}(L_x) \rangle$  to rapidly converge in  $N_{\rm max}$ ; more specifically  $N_{\rm max}=200$  is large enough for our analysis (see SM [35] for more details).

It is also possible to understand the crossover behavior analytically and derive a functional form for the transition temperature  $T_R(L_x)$ . Using the exact eigenvectors and eigenvalues of the transfer matrix V of the classical

model (B1), we were able to find an approximation of the end-to-end string operator in the limit of large  $N_{\text{max}}, L_x \gg 1$ , and small  $q \ll 1$  [35],

$$\langle K_{\alpha}(L_x) \rangle \approx \exp\left(-2q(1-\cos(\alpha)L_x)\right).$$
 (B5)

By setting  $\langle K_{\alpha}(L_x) \rangle = 1/2$  and solving for  $T/J = -2/\log(q)$ , we find that the transition temperature  $T_R$  should vanish logarithmically with the system size  $L_x$ ,

$$T_R(L_x)/J = 2\log\left(\frac{2[1-\cos(\alpha)]L_x}{\log(2)}\right)^{-1},$$
 (B6)

which has been confirmed numerically; see inset of Fig. 2(c).

# Supplemental materials for "Roughening dynamics of interfaces in two-dimensional quantum Ising model"

### TREE TENSOR NETWORKS AND TIME DEPENDENT VARIATIONAL PRINCIPLE

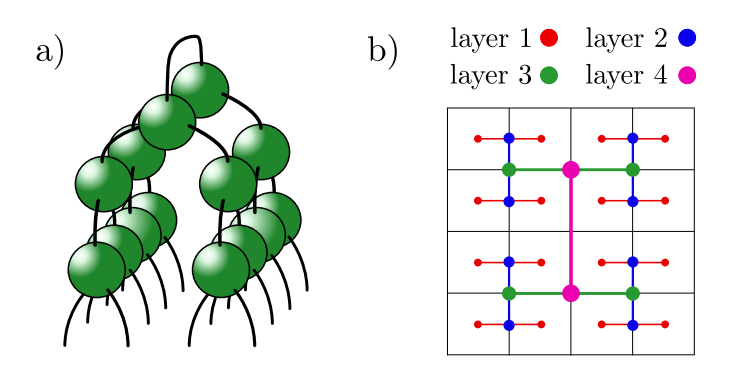


FIG. S1. a) Visualization of a binary tree tensor network and its connectivity on a 2D lattice. Going horizontally from layer to layer changes the direction of the connection. This is presented more clearly in b) which shows said direction as a top-down view on the lattice, with different colors representing different layers.

We use binary tree tensor networks, see Fig. S1 a for a graphical representation thereof, in order to simulate the dynamics of a quantum system on a two dimensional lattice. By alternating the x-/y-direction for the link connection in each layer of the tree one can achieve a more natural cover of the lattice, see Fig. S1 b. The orientation of the tree tensor network with respect to the lattice is such that the top node connects the two halves of the systems across the interface. The choice of the orientation might play an important role for rotationally asymmetric initial states such as ours. We checked the effect of that choice on the results by rotating the tensor network structure by 90 degrees. This did not have any effect for the system sizes and bond dimensions, for the intermediate transverse fields  $(g/J \le 1)$  considered.

An advantage of such a hierarchical structure lies in the fact that two spins at distance l on the two dimensional lattice are connected by at most  $O_{\rm ttn} \sim \log l$  tensors, in contrast to the  $O_{\rm mps} \sim l$  tensors needed in an MPS. The absence of loops means that one can define an isometry center and thus has access to efficient algorithms such as the TDVP algorithm [12] used here. Its 1-site version ensures that the energy and norm of the state are conserved. However as a downside, it doesn't allow for the bond dimension to be adapted throughout the algorithm. Thus, the desired bond dimension needs to be encoded in the initial state from the beginning, which is done by padding the product state with zeros. For the time step we chose dt = 0.1.

The TTN structure allows one to easily access the von Neumann entanglement entropy, by performing an SVD on the tensor which splits the system into the desired partitions — the entanglement entropy is given in terms of the singular values  $\lambda_i$ :  $S = -\sum_i \lambda_i^2 \log \lambda_i^2$ .

Convergence is checked by comparing results obtained at different bond dimensions. In our case, local observables often show rapid convergence in terms of bond dimensions, while the entanglement entropy carries information about all higher order correlations, and is a more sensitive measure for convergence, see Fig. 1d in the main text.

We work with open boundary conditions (OBC) in both lattice directions due to the slower buildup of entanglement compared to periodic boundary conditions (PBC). In principle, periodic boundary conditions would be preferable in the direction parallel to the interface to reduce boundary effects.

Another consequence of the binary tree structure is that the tensors appearing in the tree are of size  $\chi^2 \times \chi$  and thus of the skinny-tall type, which allows for an efficient parallelization of the QR decompositions on these tensors. Since tensor contractions are already naturally parallelizable, this means that the overall runtime of the simulations profit substantially from GPU acceleration. In our case, we observe a speedup of around  $70\times$  over CPU performance. More specifically, the most expensive simulation at a bond dimension  $\chi=362$ , at a time step dt=0.1 up to  $t_{\rm max}=100$  takes around two days on a single A100 GPU – on a CPU (Xeon~Gold) the same calculation would take around 145 days.

### EFFECTIVE MODEL

In the following section we present and motivate a derivation of the effective model. The domain wall length operator, introduced in the main text, can be split into a horizontal and vertical component, by performing the sum only over horizontally

$$D_x = \frac{1}{2} \sum_{i,j} \left( \mathbb{1} - \sigma_{i,j}^x \sigma_{i,j+1}^x \right)$$
 (S1)

or vertically

$$D_{y} = \frac{1}{2} \sum_{i,j} \left( \mathbb{1} - \sigma_{i,j}^{x} \sigma_{i+1,j}^{x} \right)$$
 (S2)

oriented bonds, respectively. With that, the transverse field Ising Hamiltonian can be rewritten as

$$H = 2JD_x + 2JD_y - g \cdot \sum_i \sigma_i^z,$$
 (S3)

which coincides with the original Hamiltonian up to an irrelevant, additive constant. The effective model is introduced as the projection onto the subspace of domain wall states that have exactly one horizontal domain wall per column, thus fixing  $D_x/L_x = 1$ . As a consequence these states cannot exhibit overhangs or bubbles of oppositely oriented spins within the bulk.

The vertical contribution to the domain wall length operator is determined by the difference of the vertical position  $N_i$ ,  $i \in \{1, ..., L_x\}$  of two neighboring segments

$$D_y \propto \sum_i |N_i - N_{i-1}|, \tag{S4}$$

while the absolute value reflects that the result is independent of the relative ordering in each pair.

### KINK OPERATOR

The kink operator measures by how much the interface fluctuates across its length. In the case of a smooth interface, the difference in the heights of the interface at different points of the domain wall will be close to 0, hence K=1, while for a rough interface, the cosine function ensures that large fluctuations add up to K=0. This behavior is reflected in Fig. S2 a, which shows how the kink operator stays close to K=1 during time evolution up to tJ=100 for small transverse fields, while for large ones it drops to zero on a timescale of  $0.1 \le tJ \le 1$ . This as well as all subsequent simulations in that section were performed on an  $8 \times 8$  lattice.

Since the expectation value of the kink operator is real, we can alternatively write it as the real part of the complex exponential instead of the cosine, i.e.

$$K_{\alpha}(l) = \exp(-i\alpha(N_1 - N_l)). \tag{S5}$$

From that, the modified kink operator  $K_{\rm M}=K/K_{\rm bulk}$ , introduced in the main text, can be understood as splitting the bulk and interface contributions in the exponent into a sum, which in turn allows one to factor out the bulk contribution in the calculation of the kink operator. This separation only works when neglecting cross terms introduced by the exponential function, i.e. when the bulk and interface contributions can be clearly separated. This becomes infeasible for transverse fields g/J>1 as can be seen in Fig. S2b, where the kink operator first drops and then goes up again in time for  $g/J \geq 1.25$ . We want to stress that the observed rising of the kink operator an artifact of the method and not a physical effect.

The angle  $\alpha$  and distance l, appearing in the calculation of the kink operator allow to tune its sensitivity. In Fig. S2c and d we show their influence on the time average of the running mean of the kink operator.

As expected,  $K \to 1$  for  $\alpha \to 0$ . For transverse fields g/J < 1 we observe little deviation between the results for the effective and full model. For g/J = 1 this is not the case anymore, which is to be expected as we are approaching the roughening transition. For the system sizes considered in this work, we found the value of  $\alpha = 1.0$  to provide the best agreement between the effective and full model across all transverse fields of interest, and thus the highest sensitivity

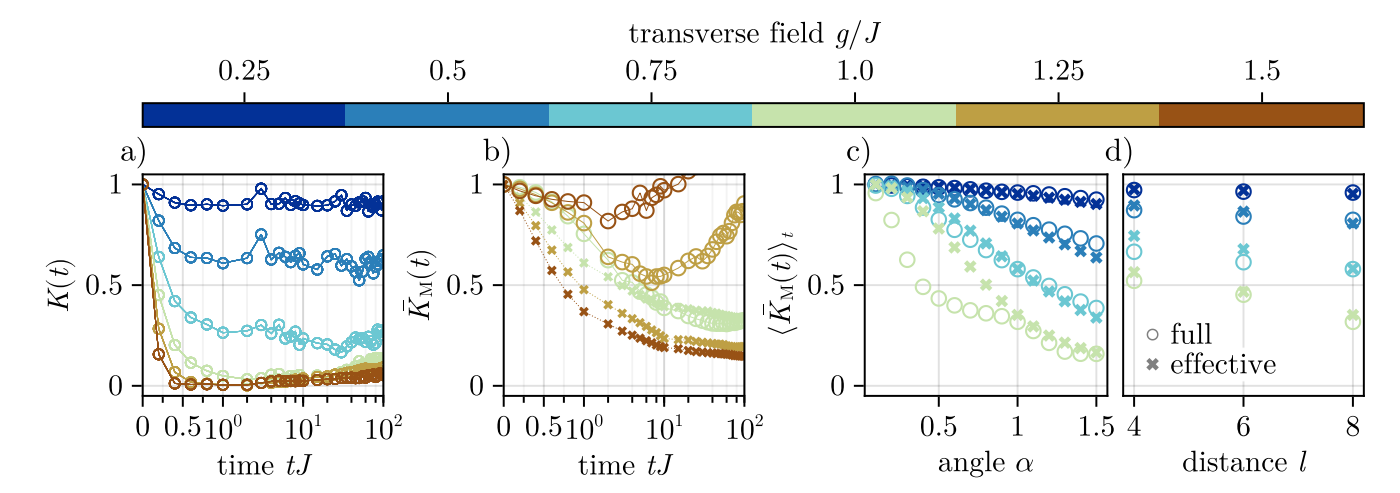


FIG. S2. a) Time evolution of the bare, i.e. unmodified kink operator in the 2D TFIM. b) Time evolution of the modified kink operator for transverse fields g/J=1,1.25,1.5, for both the 2D TFIM and 1D effective model. The plot shows unphysical growth of the modified kink operator for g/J>1, signaling the breakdown of the assumption that bulk and interface effects can be separated. Plots c) and d) show the modified, kink operator, averaged over the interval  $tJ \in [20,100]$ , as a function of c) the angle  $\alpha$  and d) the distance l. The distance does not have much influence on how well the effective and full model agree, which is why throughout the work we chose the largest distance possible for our lattice, i.e. l=8. This is different for the angle where we observe larger deviations for the largest transverse field g/J=1. The smallest angle which showed the smallest deviations across all values of the transverse fields considered is  $\alpha=1$ , which we used throughout this work.

to the roughening transition. This can be understood as smaller angles leading to an overall higher sensitivity to boundary and unwanted bulk effects, which due to their large vertical distance from the initial interface provide a big contribution to the kink operator, which in turn is detrimental for the system sizes considered. A larger value of  $\alpha$  enhances all contributions to the kink operator, while boundary effects are being "washed" out due to the cosine function, which will add up larger arguments to 0 due to the rapid sign changes. One thus needs to be careful to not make the angle too large, otherwise the contributions coming from the interface will be lost as well.

Figure S2 d shows the effect of changing the distance to l – the effective and full model agree for all transverse fields and distances l = 4, 6, 8 shown here.

Results for the kink operator on a 16 by 16 lattice are provided in Figure S3, in a similar fashion to what has been presented in the main text for an 8 by 8 lattice. Due to the larger overall entanglement, the simulations only provide reliable results up to a timescale of  $t_{\text{max}} = 30$ .

Figure S3 a) shows the domain wall length contribution coming from horizontally aligned interface lengths, normalized by the length of the lattice in x-direction. Once again this confirms that up to g/J=1, the number of domain walls per column does not scale extensively with the vertical lattice size. The agreement between the time evolution of the modified kink operator calculated in the full 2D and effective models is shown in Figure S3 b).

We want to emphasize that for that comparison we did not utilize the running mean of the modified kink operator as has been done in the main text for the 8 by 8 system. This is because compared to the 8 by 8 system, the kink operator calculated in the 16 by 16 system does not show strong temporal fluctuations, allowing for a direct comparison.

The agreement between the two models is made even more apparent when comparing the late time plateau values of the respective kink operators, obtained by taking the mean points within the region  $tJ \in [5, 30]$ , see Figure S3 c).

### EXACT SOLUTION OF THE CLASSICAL LIMIT AND APPROXIMATIONS

The thermodynamic properties at temperature  $T = 1/\beta$  of the SOS model in the classical limit  $g \to 0$  are defined by the transfer-matrix

$$V_{s,s'} = \exp(-\beta h(s,s')) = q^{|s-s'|},$$
 (S6)

with  $q = \exp(-2J\beta)$  and  $s \in \{1, ..., M\}$ . Here, we have shifted the range of values for s by one with respect to the main text and defined  $M = N_{\text{max}} + 1$  to simplify the notation in the following discussion. We are interested in

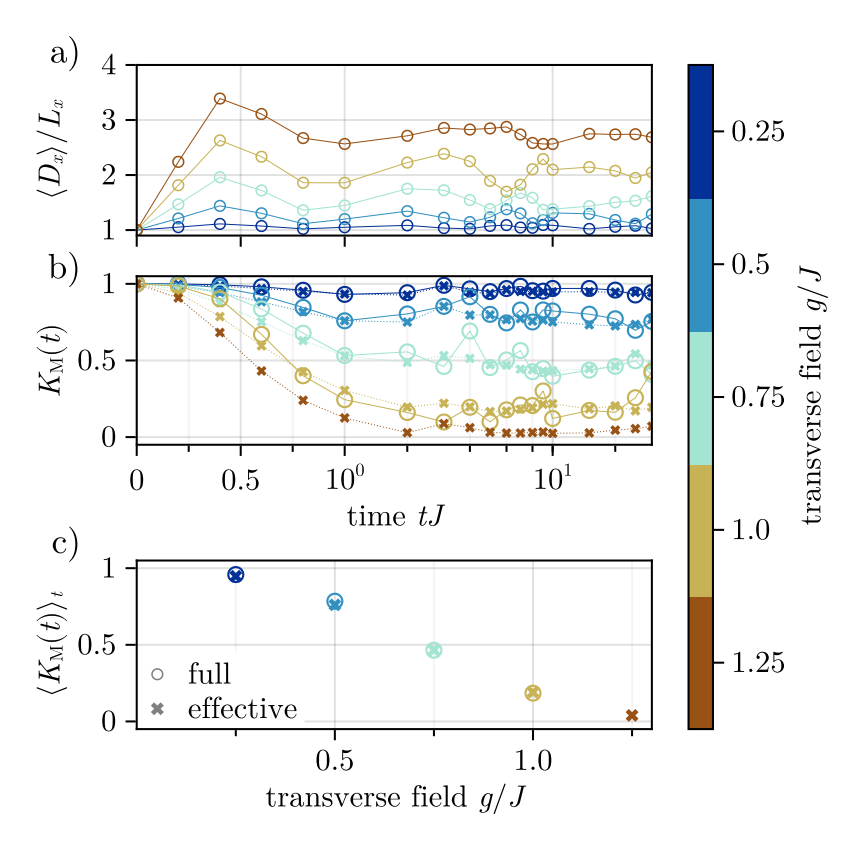


FIG. S3. Kink operator for a 16 by 16 system, evolved up to a time of  $t_{\text{max}} = 30$ . a) Time evolution of the horizontal contribution to the domain wall length divided by the horizontal lattice dimension. The plot shows that the number of horizontal domain walls in each column does not scale extensively with the vertical system size, confirming the validity of the effective model in that regime. (b) Comparison between the effective (dashed lines/crosses) and the full model (solid lines/circles) for the time evolution of the kink operator. For the full model, we calculate the modified kink operator  $K_{\rm M} = \langle K \rangle / \langle K_{\rm bulk} \rangle$ . We don't show data for transverse fields beyond g/J = 1, as bulk and interface contributions become increasingly difficult to disentangle. (c) Late-time averages over the interval  $tJ \in [5,30]$  of the kink operators shown in (b) as functions of the transverse field. The values agree well up to g/J = 1, once again confirming the quantitative predictive power of the effective in that regime.

evaluating the end-to-end kink correlation function given by

$$\langle K_{\alpha}(L_x) \rangle = \frac{\mathcal{Z}(\alpha)}{\mathcal{Z}(0)}$$

with the twisted partition function

$$\mathcal{Z}(\alpha) = \lambda_1^{L_x - 1} \sum_{n=1}^{M} f_n^{L_x - 1} |c_n(\alpha)|^2,$$

$$c_n(\alpha) = \sum_{s=1}^{M} e^{i\alpha s} \psi_n(s), \quad f_n = \frac{\lambda_n}{\lambda_1},$$
(S7)

where  $|\psi_n\rangle = \sum_{s=1}^M \psi_n(s) |s\rangle$  are the eigenvectors of V and  $\lambda_n$  the corresponding eigenvalues with  $\lambda_1$  being the largest eigenvalue.

The inverse of Eq. (S6) is connected to a single-particle tight-binding Hamiltonian  $H_{\rm sp}$  via

$$H_{\rm sp} = (1 - q^2)V^{-1} - (1 + q^2)\mathbb{1} = -q\sum_{s=1}^{M} (|s\rangle\langle s + 1| + \text{h.c.}) - q^2(|0\rangle\langle 0| + |M\rangle\langle M|),$$
 (S8)

which is a standard next nearest neighbor hopping Hamiltonian with additional edge potentials. The eigenvalue and eigenvectors of this tight binding model are known [42]

$$\psi_n(s) = \mathcal{N}\left\{\sin(s\theta_n) - q\sin((s-1)\theta_n)\right\}, \ \epsilon_n = -2q\cos(\theta_n), \tag{S9}$$

where  $|\psi_n\rangle = \sum_s \psi_n(s) |s\rangle$  are the eigenvectors,  $\mathcal{N}$  a normalization factor, and the  $\theta_n$  are defined by the roots of the equation

$$\sin((M+1)\theta_n) + q^2 \sin((M-1)\theta_n) - 2q \sin(M\theta_n) = 0,$$
 (S10)

with  $\theta_n \in [0, \pi]$ . For  $M \to \infty$  and  $q \to 0$ , the solutions of this equation become dense in the interval  $[0, \pi]$ , with the distance between two solutions vanishing as  $|\theta_{n+1} - \theta_n| \sim 1/M$ . In first order one finds  $\theta_n = n\pi/(M+1)$  similar to a homogeneous chain without the additional edge potentials.

By inverting Eq. (S8), the eigenvalues of V are given by

$$\lambda_n = \frac{1 - q^2}{1 + q^2 - 2q\cos(\theta_n)},$$

while the eigenvectors are still given by  $\psi_n(s)$  from Eq. (S9).

From the exact expression of the eigenvalues and eigenvectors, we can now proceed to calculate the form factors  $c_n(\alpha)$ . Note that due to the reflection symmetry of the Hamiltonian (S9) one has  $\psi_n(M-s) = (-1)^n \psi_n(s)$  and thus  $|c_n(\alpha)|^2 = |c_n(2\pi - \alpha)|^2$ . Thus it is sufficient to restrict the analysis to  $\alpha \in [0, \pi]$ .

Using the summation identity

$$\sum_{s=1}^{M} e^{i\alpha s} \sin(s\theta + \delta) = \frac{e^{i\alpha}}{2i} \left( e^{i\frac{\theta(M+1)+2\delta}{2}} g_M(\alpha + \theta) - e^{-i\frac{\theta(M+1)+2\delta}{2}} g_M(\alpha - \theta) \right), \ g_M(x) = \frac{\sin\left(\frac{x}{2}M\right)}{\sin\left(\frac{x}{2}\right)}$$

derived from the finite geometric sum, we find an exact expression for the form factors

$$|c_n(\alpha)|^2/\mathcal{N}^2 = \frac{g_M(\theta_n + \alpha)^2 + g_M(\theta_n - \alpha)^2}{4} \left(1 + q^2 - 2q\cos(\theta_n)\right) - \frac{g_M(\theta_n + \alpha)g_M(\theta_n - \alpha)}{2} \left(\cos(\theta_n(M+1)) + q^2\cos(\theta_n(M-1)) - 2q\cos(\theta_nM)\right).$$
(S11)

Note that  $c_n(\alpha)$  has a unique singularity at  $\theta_* = \alpha$  coming from the function  $g_M(\theta - \alpha)$  for  $\theta$ ,  $\alpha \in [0, \pi]$ . Let  $n_*$  be the solution to Eq. (S10) with  $\theta_{n_*}$  close to  $\theta_*$ .

The most dominant contribution to the twisted partition function  $\mathcal{Z}(\alpha)$  is thus given by the  $n_{\star}$  form factor in the large M limit

$$\mathcal{Z}(\alpha)/\lambda_1^{L_x-1} \approx f_{n_\star}^{L_x-1} |c_{n_\star}(\alpha)|^2 \,.$$

Since the distance between two solutions vanishes as 1/M in the large M limit, we expect  $|\theta_{n_{\star}} - \theta_{\star}| \approx \delta/M$ , where  $\delta$  is a constant of order one and independent of  $\alpha$ . Expanding  $c_{n_{\star}}$  for small  $\delta/M$  and keeping only the dominant part, we arrive at

$$|c_{n_{\star}}|^2/\mathcal{N}^2 \approx \frac{M^2}{4} \frac{\sin(\delta/2)^2}{(\delta/2)^2} (1 + q^2 - 2q\cos(\alpha)),$$

which diverges as expected for  $M \to \infty$ .

Next consider the weights  $f_n$  and expand them around  $n_{\star}$ 

$$f_{n_{\star}} = \frac{\lambda_n}{\lambda_1} = \frac{1 + q^2 - 2q\cos(\theta_1)}{1 + q^2 - 2q\cos(\theta_{n_{\star}})} \approx \frac{\Gamma}{(1 - \frac{2q}{1 + q^2}\cos(\alpha))}$$
.

Here,  $\Gamma=\frac{1+q^2-2q\cos(\theta_1)}{1+q^2}$  is a  $\alpha$  independent constant. Assuming q small one finds in the  $L_x\to\infty$  limit

$$f_{n_{\star}}^{L_x-1} \approx \Gamma \left( 1 + \frac{2q}{1+q^2} \cos(\alpha) \right)^{L_x} \approx \Gamma e^{\frac{2q}{1+q^2} \cos(\alpha)L_x} \,.$$

Combining the results, we obtain for the end-to-end kink correlator

$$\langle K_{\alpha}(L_x) \rangle = \frac{\mathcal{Z}(\alpha)}{\mathcal{Z}(0)} \approx \frac{1 + q^2 - 2q\cos(\alpha)}{(1 - q)^2} \exp\left(-\frac{2q}{1 + q^2}(1 - \cos(\alpha))L_x\right) \approx e^{-2q(1 - \cos(\alpha))L_x}, \quad (S12)$$

where the last approximation is valid in the small q and large  $L_x$  limit. Note that  $1 - \cos(\alpha) > 0$  for  $\alpha \in (0, \pi)$ , such that  $\lim_{L_x \to \infty} \langle K_\alpha(L_x) \rangle = 0$  for all values of  $\alpha \in (0, \pi)$ .

Fig. S4 a shows the agreement between numerical data and the analytical expectation (S12) for  $L_x = 512 \cdot 10^3$  and  $N_{\text{max}} = 200$ , confirming the approach presented here. In Fig. S4 b we numerically test the dependence of the results on the maximal bosonic occupation number  $N_{\text{max}}$  for different, color-coded system sizes, establishing that  $N_{\text{max}} = 200$  is sufficient to reliably calculate the kink operator for the system sizes considered here.

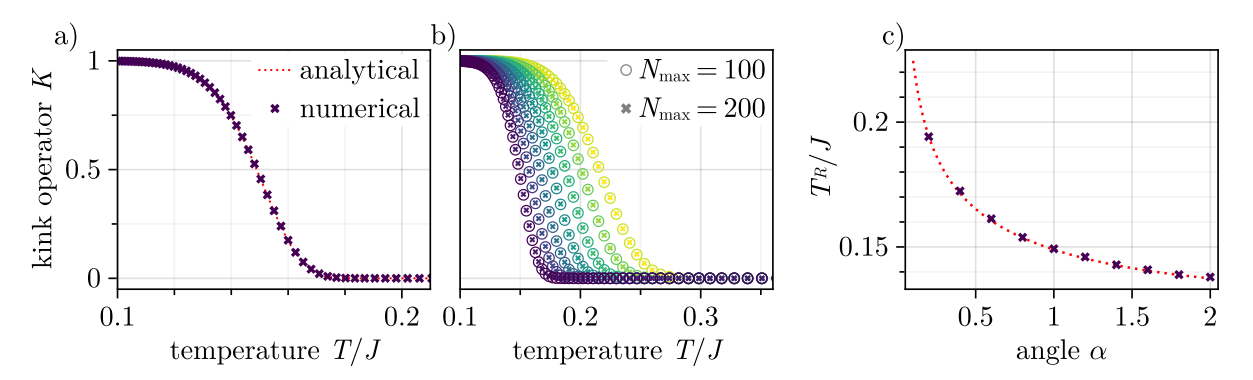


FIG. S4. a) Kink operator as a function of the temperature for system size  $L_x = 512 \cdot 10^3$  and  $N_{\rm max} = 200$ . The numerically obtained data points agree very well with the analytical prediction (S12). b) Results for the kink operator as a function of T for different system sizes and maximal bosonic occupation numbers. System sizes considered here lie in  $L_x \in [500, 512 \cdot 10^3]$ , with exponentially increasing steps. The data points for  $N_{\rm max} = 100, 200$  lie on top of each other, meaning results are converged in the maximal bosonic occupation number. c) Dependence of the transition temperature on the angle  $\alpha$  at  $L_x = 512 \cdot 10^3$ , following the dependence (S13) (grey, dotted line), obtained from analytical considerations on the transfermatrix.

We define the transition temperature in the classical limit by setting  $\langle K_{\alpha}(L_x) \rangle = 1/2$ , and solving for  $T/J = -2/\log(q)$ :

$$T_R(L_x) = 2\log\left(\frac{2(1-\cos(\alpha))L_x}{\log(2)}\right)^{-1}$$
 (S13)

This relation is tested numerically by calculating the end-to-end kink correlator both as a function of the system size for a fixed  $\alpha$ , see inset of Fig.2 c in the main text, as well as a function of the angle  $\alpha$  for fixed system size, see Fig. S4 c.

### THERMALIZATION AND LEVEL SPACING STATISTICS

In the main text, we implicitly assume eventual equilibration of the interface initial condition to a homogeneous spin state. To support this claim, which is not trivial and still under debate, we provide an analysis of the level spacing statistics of the exact eigenenergy spectrum  $E_i$  for a 4 by 5 lattice with PBC in x-direction and OBC in y-direction, analogous to what has been done in the main text for larger system sizes. The level spacing statistics provides a way to determine wether a system is chaotic or integrable, based on results from random matrix theory. An integrable system is characterized by its level spacing statistics following a Poisson distribution, while for a chaotic system it follows the one of a Gaussian orthogonal ensemble (GOE). In order to evaluate the level spacing statistics reliably, one has to first unfold the spectrum, i.e. separate the level spacing from overall changes in the energy scale. This is done via the relation

$$s_n = (E_{n+1} - E_n) \frac{\partial n(E)}{\partial E} |_{E=E_n}, \tag{S14}$$

where n(E) is the staircase or cumulative spectral function, returning the number of levels below or at the energy E [43].

In Figure S5 a) we show results of the unfolded spectrum for two different transverse fields g/J=0.15,0.75. The level spacing of the larger field clearly resembles the one of a GOE, indicating a chaotic system, which is true also for the smaller transverse field, even though the peak of the distribution starts to travel towards zero level spacing. To summarize, neither of the cases follows the level spacing distribution expected from an integrable system.

The mean over the distribution of ratios

$$\tilde{r}_n = \frac{\min(d_n, d_{n-1})}{\max(d_n, d_{n-1})},\tag{S15}$$

with  $d_n = E_n - E_{n-1}$ , assumes the value  $\langle \tilde{r}_n \rangle_{\text{Poisson}} \approx 0.38629$  or  $\langle \tilde{r}_n \rangle_{\text{GOE}} \approx 0.60266$  if the underlying distribution is of Poissonian or GOE type, respectively [44]. Figure S5 b) presents this quantity as a function of the transverse field, showing that in the considered system of finite size the underlying level spacing statistics closely follows the chaotic one, with minimal deviations towards smaller transverse fields. Hence, we expect eventual thermalization of the system in the non-equilibrium dynamics considered in the main text for all system sizes considered.

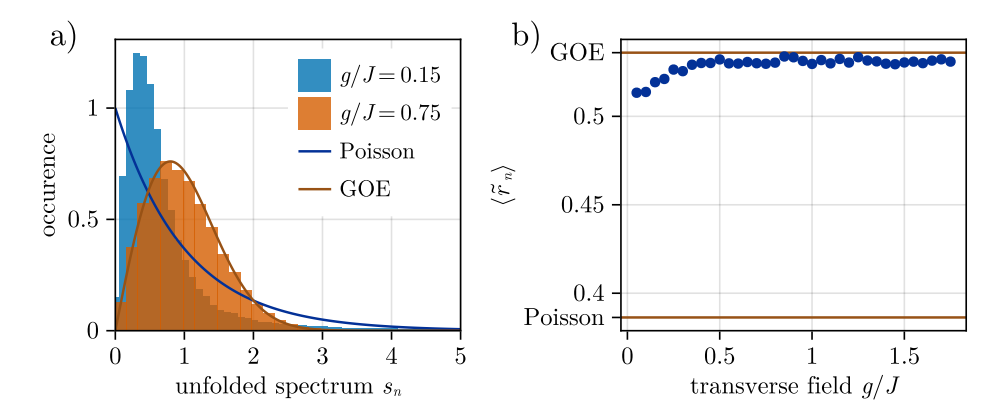


FIG. S5. a) Two examples of the unfolded level spacings at different g/J. The one corresponding to g/J=0.75 clearly agrees with the one predicted from random matrix theory for chaotic systems, while for the smaller g/J=0.15 it starts exhibiting features from both, i.e. the mean level spacing moves towards zero – however the characteristic peak at  $s_n=0$  is still missing, distinguishing it from a pure Poisson statistics. b) Mean level-spacing distribution ratio of a 4 by 5 system for different transverse fields. Across all transverse fields considered, the ratio corresponds to a GOE distribution and hence an chaotic system with slight deviations from that expected value at the smallest fields.

### QUANTUM MONTE CARLO

The data points in the phase diagram of Fig. 2d) are obtained using the QMC loop-algorithm [40, 41] provided in the ALPS package [61] for the critical temperatures (blue line) and using the QMC package written in Rust [45] for the effective temperature of the initial state (red line).

The points of the blue line are obtained by finding the crossing points of the binder cumulant of the magnetization as a function of temperature for lattice sizes L = 8, 12, 16, see Fig. S6 a.

The points of the red line correspond to the temperature associated with the initial domain wall state on an  $8 \times 8$  lattice at a transverse field g, i.e. the temperature  $T_{\rm cross}$  s.t. the energy  $E = {\rm Tr}\ H \rho_{\rm Gibbs}$  of the Gibbs state  $\rho_{\rm Gibbs} = \exp{(-H/T_{\rm cross})}$  corresponds to the energy of the initial state  $E_{\rm init}$ , see Fig. S6 b. Note, that in order to simulate the conditions for a domain wall state and get the correct effective temperature, we employ periodic boundary conditions on one edge and anti-periodic boundary conditions on the other within the QMC simulation.

Data points are obtained using  $5 \cdot 10^4 / 1 \cdot 10^5$  samples for the critical/actual temperatures, after  $1 \cdot 10^4$  thermalization steps are performed. These values where chosen such that the estimated error on all the observables considered here lies below 1%.

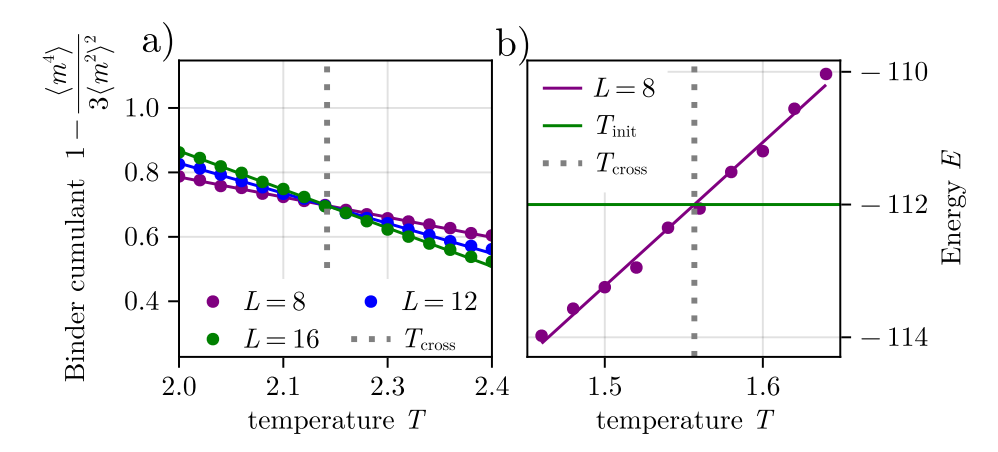


FIG. S6. a) Binder cumulant of the magnetization on a 2D square lattice for three different lattice dimensions. Shown is an example for a transverse field g/J=1. The crossing point of the three lines marks the critical temperature of the system at said transverse field. b) This plot shows how an effective temperature can be associated to a non-equilibrium state. For that, we find the temperature of an equilibrium state whose energy coincides with the energy of the state we are interested in. This is shown again on the example of g/J=1 for an  $8\times 8$  lattice.

# Almost Strong Zero Mode at Finite Temperature

Authors: Niklas Tausendpfund, Aditi Mitra, Matteo Rizzi

**Year:** 2025

Journal: Physical Review Research

Volume/Issue: 7, 2

**DOI:** 10.1103/PhysRevResearch.7.023245

### IV.1 Authors Contribution

This project was initiated after Aditi Mitra visited the University of Cologne, where she presented her work on Almost Strong Zero Mode (ASZM). Niklas Tausendpfund developed the idea of combining this technique with a tensor-network algorithm to open the door for studying the ASZM in more complicated cases, such as the number-conserving setup presented in Chapter I or including the effect of temperature. He designed the code and carried out the numerical experiments and data analysis. The results were shared in joint discussions with Matteo Rizzi and Aditi Mitra on a weekly basis. Niklas Tausendpfund prepared the first draft, which was revisioned by Matteo Rizzi and Aditi Mitra contributing helpful comments.

## IV.2 Data Availability

The tensor network code is based on the ITensors.jl library [274]. The code and extracted data are available on Zenodo under the reference [294].

### IV.3 Summary

In non-interacting integrable fermionic quantum chains, the existence of a topologically protected ground-state degeneracy implies a stable degeneracy of the entire many-body spectrum. This is associated with the existence of Majorana operators exponentially localized to the edge of the quantum chain with an infinite lifetime, even at infinite temperatures. As explained in Section 1.5, away from integrability, this property is destroyed in general, and these Majorana Zero Modes (MZMs) become an ASZM. Compared to the integrable case, the ASZM has a finite lifetime, which, in principle, depends on the temperature.

The presented work extends previous studies [214, 217, 218] that considered the ASZM exclusively at infinite temperatures by including the effect of finite temperature. In addition, this allows to study how the ASZM is connected to the MZM that are associated with the degenerated ground-state manifold for fermionic chains in the Symmetry-Protected Topological Phase (SPTP).

In earlier works, the ASZM was studied by mapping the Heisenberg time evolution of the edge operator on an artificial single-particle chain. This is done by performing a Lanczos iteration, which iteratively generates an orthonormal basis of operators, as explained in Section 1.5. In this present study, we approximate the basis operators by a Matrix Product Operator (MPO) with a maximal bond dimension  $\chi$ , and the Lanczos iteration is formulated with the help of these approximate basis states. While previous studies used exact methods to calculate the Lanczos iteration, using a tensor network ansatz has two major advantages. First, by using a fixed maximal bond dimension, the number of variational parameters is only linear in the system size compared to the exponentially many parameters in an exact approach. This allows the study of larger system sizes, which is crucial for obtaining the system size-converged lifetime of the ASZM. Second, the tensor network allows the temperature to be included directly by using a standard tensor network algorithm for calculating the canonical density matrix [295, 296]. Furthermore, the formulation can be extended to a semi-infinite chain by expanding the tensor network at each step. Although this is straightforward in the infinite temperature limit, the finitetemperature algorithm requires a formulation of the density matrix in a semi-infinite chain. To the best of our knowledge, such an algorithm has not yet been developed.

We apply this algorithm to the Kitaev-Hubbard Model (KHM) from Eq. (1.110) in the topological regime. We observe that the lifetime of the ASZM increases exponentially as T approaches zero, as shown in Figure 6(a) of our publication, and the ASZM is smoothly connected to the MZM defined in the ground-state manifold. Surprisingly, the energy scale associated with this exponential  $\Delta_{\rm eff}$  is greater than the many-body gap  $\Delta$  and depends non-trivially on the microscopic coupling parameters, as shown in Figure 6(b) in our publication.

In the final part of our work, we show that this effective energy scale is related to a prolonged degeneracy of the low-lying energy states in the many-body spectrum. Specifically, we demonstrate that the excitation energies for  $E_{n,p} - E_0 \leq \Delta_{\rm eff}$  show an extended degeneracy between the even and odd parity sectors, even away from the ground-state manifold, as shown in Figure (8) of our publication. Although not proven, this builds the idea of the existence of the ASZM, reflecting this extended degeneracy.

### Almost strong zero modes at finite temperature

Niklas Tausendpfund , <sup>1,2</sup> Aditi Mitra, <sup>3</sup> and Matteo Rizzi <sup>1,2</sup>

<sup>1</sup>Forschungszentrum Jülich GmbH, Institute of Quantum Control, Peter Grünberg Institut (PGI-8), 52425 Jülich, Germany 
<sup>2</sup>Institute for Theoretical Physics, University of Cologne, D-50937 Cologne, Germany 
<sup>3</sup>Center for Quantum Phenomena, Department of Physics, New York University, 726 Broadway, New York, New York 10003, USA

(Received 29 January 2025; accepted 7 May 2025; published 11 June 2025)

Interacting fermionic chains exhibit extended regions of topological degeneracy of their ground states as a result of the presence of Majorana or parafermionic zero modes localized at the edges. In the opposite limit of infinite temperature, the corresponding nonintegrable spin chains, obtained via generalized Jordan-Wigner mapping, are known to host so-called almost strong zero modes, which are long-lived with respect to any bulk excitations. Here we study the fairly unexplored territory that bridges these two extreme cases of zero and infinite temperature. We blend two established techniques for states, the Lanczos series expansion and a tensor network ansatz, uplifting them to the level of operator algebra. This allows us to efficiently simulate large system sizes for arbitrarily long timescales and to extract the temperature-dependent decay rates. We observe that for the Kitaev-Hubbard model, the decay rate of the edge mode depends exponentially on the inverse temperature  $\beta$ , and on an effective energy scale  $\Delta_{\rm eff}$  that is greater than the thermodynamic gap of the system  $\Delta$ .

### DOI: 10.1103/PhysRevResearch.7.023245

#### I. INTRODUCTION

Fractionalization of low-energy excitations is one of the most interesting properties of topological many-body systems, with the simplest example of this being the Majorana zero modes (MZMs) [1-5] that appear in fermionic chains protected only by the fermion parity P. These MZMs correspond to fractionalized fermions exponentially localized at the edges of a finite-size system. Because of this non-local nature, a (topological) ground-state degeneracy arises, as there is no local physical operator that couples to these fractionalized fermions. The appearance of edge modes can easily be understood in the noninteracting limit as the model formally belongs to the BDI symmetry class in the Altland-Zirnbauer classification [6,7]. For finite interaction strengths, it has been shown that the topological region—with the appearance of fractionalized edge modes within the degenerate ground-state manifold—persists for a wide range of parameters [8–11].

Away from the ground-state manifold, little is known about the spectral properties for generic interactions, and whether stable MZMs exist even for excited states. However, this is important because it strongly affects the finite temperature lifetime of local edge excitations that have overlap with the MZMs, and has ramifications on practical realization of topologically protected qubits. In the zero-temperature limit, where only the ground-state manifold contributes to the dynamics, the topological degeneracy leads to an infinite lifetime of these edge excitations. On the other hand, at infinite

Published by the American Physical Society under the terms of the Creative Commons Attribution 4.0 International license. Further distribution of this work must maintain attribution to the author(s) and the published article's title, journal citation, and DOI.

temperature, the same edge excitations were shown to have an unusually long lifetime compared to generic bulk excitations [12–19]. In integrable limits, this behavior can be explained by the appearance of a strong zero mode (SZM) [1,20–23], a generalization of the Majorana zero mode to the full spectrum. Here the existence of the SZM implies a protected degeneracy of the whole spectrum and not only of the ground-state manifold, and thus one recovers an infinite lifetime. Away from these special limits, the lifetime becomes strictly finite, with the edge mode often referred to as an almost strong zero mode (ASZM) [12]. Besides some phenomenological arguments [13], it is still an open question how the lifetime of the edge excitations behaves at finite temperatures. In particular, it is not known how the infinite lifetime emerges as the temperature is lowered from infinity to zero.

In this work, we explore this rather unchartered territory by employing a tensor network ansatz [24] to approximate the sequence of operators generated by the Lanczos algorithm for Heisenberg time evolution [25,26]. This procedure maps the operator dynamics to the time evolution of a single-particle problem on an artificial one-dimensional chain. Originally used to study the complexity growth of time-evolved operators, this method has been shown to be a useful tool for understanding the emergence of these long-lived ASZMs [16,17]. However, these earlier studies were highly limited in system size and, most importantly, to infinite temperatures. The formulation of the Lanczos algorithm for tensor networks removes the limitation of small system sizes by introducing a controlled approximation given by the bond dimension  $\chi$  of the tensor network. Moreover, an intrinsic tensor network formulation allows for the efficient inclusion of arbitrary temperatures  $T = 1/\beta$ , since the density matrix  $\rho(\beta)$  can also be approximated by a tensor network [27]. We emphasize that in contrast to direct integration schemes such as the time-dependent variational principle (TDVP) [28,29], the Lanczos method developed here converges quickly with the bond dimension in the case of a long-lived ASZM. In the former case, the bond dimension necessarily has to grow exponentially with time, while this is not the case for our Lanczos approach; see Appendix F 3 for details.

As an application, we explicitly calculate the lifetime of the Majorana edge mode in the nonintegrable Kitaev-Hubbard chain [30]. We find an exponential dependence of the lifetime on the inverse temperature  $\tau(\beta) = \exp(\Delta_{eff}\beta)$ . However, in contrast to generic bulk excitations where  $\Delta_{eff}$  is expected to be the energy gap in the many-body spectrum [31], we observe a nontrivial dependence of  $\Delta_{eff}$  on the interaction strength. In particular, we find that  $\Delta_{eff}$  is consistently larger than the many-body gap, hinting at a degenerate structure of the low-energy portion of the spectrum and not exclusively of the ground state.

The paper is organized as follows: In Sec. II we introduce the main concepts such as the finite temperature autocorrelation function from which the lifetime of an excitation can be extracted, and the Lanczos iteration for calculating the autocorrelation function. We also introduce our algorithm for evaluating the Lanczos series approximately using tensor networks. We close this section by reviewing the concept of ASZMs, which are the central object studied in this paper. In Sec. III we introduce the Kitaev-Hubbard chain: a toy model exhibiting an extended topological phase in its ground-state phase-diagram. The Majorana edge modes appearing in this topological phase serve as a perfect test for our algorithm. Finally in Sec. IV we present the numerical findings for the lifetime of these Majorana edge modes at various parameter points in the topological phase of the Kitaev-Hubbard chain. We close this paper with Sec. V that summarizes our findings and comments on possible extensions to other systems such as parafermions [32-34], Floquet circuits [20,22,35-37] and number-conserving realizations of MZMs [34,38–45].

### II. DEFINITIONS

### A. Autocorrelation functions at finite temperatures

We define the lifetime of an excitation generated by the operator  $\hat{O}$  by the decay of the autocorrelation function (ACF) defined as

$$C_{\beta}(\hat{O}, t) := \langle \hat{O} | \hat{O}(t) \rangle_{\beta}, \qquad (1)$$

with the temperature-dependent scalar product [25,26,46]

$$\langle \hat{A} | \hat{O} \rangle_{\beta} = \frac{1}{2} \text{Tr}[\rho(\beta) \{ \hat{A}^{\dagger} \hat{O} + \hat{O} \hat{A}^{\dagger} \}]. \tag{2}$$

Here  $\hat{O}(t) = e^{itH} \hat{O}e^{-itH}$  denotes the Heisenberg time evolution,  $\beta = 1/T$  is the inverse temperature, and  $\rho(\beta) = \exp(-\beta H)/\text{Tr}[\exp(-\beta H)]$  is the finite temperature density matrix.

Let us briefly discuss the two limiting cases of Eq. (2), namely, of zero and infinite temperature. In the infinite temperature limit  $\beta \to 0$ , the scalar product of Eq. (2) becomes proportional to the Frobenius scalar product on the vector space of operators

$$\langle \hat{A} | \hat{O} \rangle_{\beta=0} = \frac{1}{\dim(\mathcal{H})} \operatorname{Tr}[\hat{A}^{\dagger} \hat{O}].$$

The normalization is given by the dimension of the many-body Hilbert space  $\mathcal{H}$ .

On the other hand, for zero temperature  $\beta \to \infty$ , the density matrix projects onto the ground-state manifold, denoted by GS. Thus, the scalar product in Eq. (2) reduces to an equally weighted average over all ground states in GS:

$$\langle \hat{A} | \hat{O} \rangle_{\beta = \infty} = \frac{1}{2 \dim(\mathrm{GS})} \sum_{\Omega \in \mathrm{GS}} \langle \Omega | \hat{A}^\dagger \hat{O} + \hat{O} \hat{A}^\dagger | \Omega \rangle \; .$$

Before closing this subsection, let us comment on the fact that the temperature-dependent scalar product in Eq. (2) is not a unique choice; see Appendix A. However, our choice appears naturally in linear response theory and directly links the ACF to a measurable quantity [25,26].

#### B. Lanczos series evaluation of the autocorrelation function

To solve the Heisenberg time evolution, and thus calculate the ACF, we make use of the Lanczos algorithm [25]. As we detail below, this generates a tridiagonal superoperator that can be interpreted as a single particle hopping on a semi-infinite chain, where the sites are (orthonormal) operators. In fact, the edge density of states (EDOS) of this artificial single-particle problem carries all the information about the ACF.

Defining the superoperator  $\mathcal{L}\hat{O} := [H, \hat{O}]$ , the Heisenberg time evolution can be written as

$$\hat{O}(t) = e^{iHt} \hat{O}e^{-iHt} = \sum_{n=0}^{\infty} \frac{(it)^n}{n!} \mathcal{L}^n \hat{O}.$$
 (3)

The Lanczos algorithm now aims at constructing an operator basis  $\mathcal{O}_n$  to express the time evolution in a more efficient way. This basis is constructed to be orthonormal with respect to the temperature-dependent scalar product defined in Eq. (2). To this end, we assume w.l.o.g.  $\langle \hat{O} | \hat{O} \rangle_{\beta} = 1$  and require  $\hat{O}^{\dagger} = \hat{O}$ .

To iteratively construct this new basis, we start by setting  $\mathcal{O}_0 := \hat{O}$ ,  $\mathcal{O}_{-1} = 0$ , and  $b_0 = 0$ . The sequence of orthonormal operators then reads

$$\hat{A}_{n} = \mathcal{L}\mathcal{O}_{n-1} - b_{n-1}\mathcal{O}_{n-2},$$

$$b_{n} = \sqrt{\langle \hat{A}_{n} | \hat{A}_{n} \rangle_{\beta}},$$

$$\mathcal{O}_{n} = \hat{A}_{n}/b_{n}.$$
(4)

The time-evolved operator  $\hat{O}(t)$  can be expanded in this basis with real coefficients  $\varphi_n(t)$  as

$$\hat{O}(t) = \sum_{n=0}^{\infty} i^n \varphi_n(t) \mathcal{O}_n, \quad \varphi_n(0) = \delta_{n,0}.$$

Further, by defining the states  $|n\rangle = i^n \mathcal{O}_n$ , with  $\langle n|m\rangle = \delta_{m,n}$ , the ACF is now equivalently expressed by

$$C_{\beta}(\hat{O}, t) = \varphi_0(t) = \langle 0|e^{-itH_{\rm sp}}|0\rangle, \qquad (5)$$

$$H_{\rm sp} = \sum_{n=0}^{\infty} i \, b_{n+1} \, |n+1\rangle \, \langle n| + \text{H.c.},$$
 (6)

where  $H_{\rm sp}$  is the artificial single-particle Hamiltonian, solely defined by the Lanczos coefficients  $b_n$  [47]. In fact, these Lanczos coefficients  $b_n$  carry all the information about the seed operator  $\hat{O}$  used to construct the Lanczos series, the Hamiltonian H, and the temperature through the chosen scalar product.

Instead of computing the ACF directly by calculating the exponential of Eq. (6), it is simpler to reconstruct the ACF from the EDOS of the single-particle Hamiltonian  $H_{\rm sp}$ , defined as

$$\nu_{\beta}^{E}(\omega) = \langle 0|\delta(\omega - H_{\rm sp})|0\rangle. \tag{7}$$

The EDOS  $v_{\beta}^{E}(\omega)$  is connected to the ACF  $C_{\beta}(\hat{O},t)$  by a simple Fourier transform

$$C_{\beta}(\hat{O}, t) = \int_{-\infty}^{\infty} d\omega \, v_{\beta}^{E}(\omega) \cos(\omega t) \tag{8}$$

and equivalently carries all information about the dynamics. Note that the tridiagonal structure of  $H_{\rm sp}$ , Eq. (6), with zeros on the diagonal, implies  $\nu^E_\beta(\omega) = \nu^E_\beta(-\omega)$ .

In principle, to obtain the full time dynamics of a given operator  $\hat{O}$ , it is necessary to calculate a large number of the Lanczos coefficients  $b_n$ . To keep the computational effort to a minimum, we need to truncate the series at some point. This is possible because the Lanczos coefficients are expected to grow nearly linearly with n, saturating at some plateau value due to finite-size effects [26]. We therefore adopt a strategy similar to that used by one of us in Ref. [16]. For this, we compute the first N coefficients of the Lanczos series explicitly. After reaching the plateau value, we approximate the unknown values for n > N by setting  $b_{n>N} = b_N$ . In terms of the artificial single-particle Hamiltonian, this amounts to attaching a featureless semi-infinite homogeneous chain with a hopping parameter  $w = ib_N$ . This approximation also leads to an efficient calculation of the EDOS in terms of a continued fraction as explained in Appendix D.

Note that the details of the transition to the semi-infinite chain with uniform hopping is not that crucial; see also Appendix F 1 for a numerical demonstration. This can be understood in terms of the artificial Hamiltonian  $H_{\rm sp}$ . Since we are mainly interested in the edge properties of  $H_{\rm sp}$ , changing the parameters far away from the edge has only a small influence, as long as N is large enough and  $b_N$  is placed well inside the featureless plateau.

### C. Evaluation using a tensor network ansatz

The tridiagonal form of the artificial  $H_{\rm sp}$  of Eq. (6) does not imply that the exact calculation of the Lanczos series is an easy task overall. Indeed, since the Lanczos iteration involves nested commutators, the basis states  $\mathcal{O}_n$  quickly become fully dense matrices for any given system size. The exponential growth  $2^{2L}$  with system size of the number of elements, limits previous studies [16,17] to very small system sizes and infinite temperatures. Including finite temperatures would require a full diagonalization of the Hamiltonian to obtain the density matrix  $\rho(\beta)$ , a task impossible for L > 16. To overcome this limitation in system size and temperature, we introduce a tensor network approach that approximates the basis operators  $\mathcal{O}_n$ . In particular, we choose the operators  $\mathcal{O}_n$  to be

#### ALGORITHM 1. Lanczos iteration.

```
\begin{split} & \textbf{function} \ \text{LANCZOS\_STEP}(\mathcal{O}_n, \mathcal{O}_{n-1}, b_n, H, \beta, \chi) \\ & \hat{B}_{n+1} \leftarrow \texttt{commutator}(H, O_n, \chi) \\ & \hat{A}_{n+1} \leftarrow \texttt{add}(\hat{B}_{n+1}, -b_n \cdot \mathcal{O}_{n-1}, \chi) \\ & b_{n+1} \leftarrow \texttt{norm}(\hat{A}_{n+1}, \beta) \\ & \mathcal{O}_{n+1} \leftarrow \hat{A}_{n+1}/b_{n+1} \\ & \textbf{return}(\mathcal{O}_{n+1}, b_{n+1}) \\ & \textbf{end function} \end{split}
```

represented by a matrix product operator (MPO):

Here  $\chi$  is the bond dimension of the ansatz and is kept fixed. For a given bond dimension  $\chi$ , the number of elements grows algebraically with the system size  $\mathcal{O}(L\chi^2d^2)$ , in contrast to the exponential growth of dense matrices. Similarly, the Hamiltonian H and the density matrix  $\rho(\beta)$  can also be efficiently represented by an MPO [27,48]. To evaluate the Lanczos iteration of Eq. (4), we have to replace the normal matrix algebra by the corresponding tensor network algebra. For example, the application of the superoperator  $\mathcal{LO}_n = H\mathcal{O}_n - \mathcal{O}_n H$  can be expressed by two MPO-MPO applications followed by subtraction of the two resulting MPOs. In general, these tensor network operations lead to an increase in the bond dimension of the final MPO. To keep the bond dimension fixed at  $\chi$ , it is therefore necessary to truncate the bond dimension back to the target bond dimension  $\chi$ .

In this paper we choose to apply a truncation scheme based on the singular values of the MPO. More specifically, we use the reduced density matrix approach [49], analogously to matrix product states. Moreover, to make the application of the superoperator as exact as possible, we apply this truncation scheme in one shot to the full  $\mathcal{LO}_n$  and not separately after each intermediate step (i.e.,  $H\mathcal{O}_n$ ,  $\mathcal{O}_nH$  and their subtraction). Let us note that this truncation scheme maximizes the fidelity  $\langle \hat{M} | \mathcal{LO}_n \rangle_0$ , which corresponds to the infinite-temperature scalar product. In principle, one could also directly optimize the fidelity obtained from the finite-temperature scalar product via a variational optimization.

The complete Lanczos iteration step described by Eq. (4) using the tensor network approach is summarized in the pseudo-code (Algorithm 1). The core function LANC-ZOS\_STEP takes as input the current  $\mathcal{O}_n$  and the previous basis operator  $\mathcal{O}_{n-1}$ , the current Lanczos coefficient  $b_n$ , the system Hamiltonian H and the inverse temperature  $\beta$  together with the target bond dimension  $\chi$ . The function commutator calculates the application of  $\mathcal{L}$  to  $\mathcal{O}_n$  in MPO form with a direct truncation of the target bond dimension to  $\chi$ ; see Appendix G. Similarly, add takes the output of commutator, subtracts  $b_n\mathcal{O}_{n-1}$  as a MPO with a direct truncation and stores the result in  $\hat{A}_{n+1}$ . Finally norm calculates the norm of  $\hat{A}_{n+1}$  with respect to the temperature dependent scalar product of Eq. (2).

Note that the algorithm presented here can be directly applied in the thermodynamic limit, at least for infinite temperature where  $\rho=1$  independent of the system size. For example, for a seed operator  $\mathcal O$  originally localized at the edge of a semi-infinite chain and a Hamiltonian H with only nearest-neighbor interaction, the basis operators  $\mathcal O_n$  have a support on at most n+1 sites. Thus, by growing the operator in each step, it is possible to remove all finite-size effects. For finite temperatures one needs a good representation of the density matrix  $\rho(\beta)$  for an infinite system, which is beyond the scope of this article.

#### D. (Almost) strong zero modes

MZMs occur in gapped fermionic chains where the number conservation is broken to a  $\mathbb{Z}_2$  fermionic parity symmetry. They always appear in pairs, with one MZM at the left and the other at the right end of the chain. The appearance of a MZM is associated with a ground-state degeneracy of two, where the two ground states  $|\Omega_p\rangle$  have opposite parity  $p=\pm$ . As they differ only in the occupancy of the MZM, there is no local bulk operator that can distinguish between the two ground states and the degeneracy is topologically protected. To define the MZM, we assume that the chain is populated by spinless fermions described by the creation/annihilation operators  $c_j^\dagger/c_j$ . Equivalently, we can define the set of Majorana operators by  $c_j=(\gamma_{j,a}-i\gamma_{j,b})/2$ .

Now, given the two ground states, one typically defines the MZM as

$$\gamma_L := \sum_{i=1}^{N} \varphi_i \gamma_{j,a}, \quad \varphi_j := \text{Re}[\langle \Omega_+ | \gamma_{j,\alpha} | \Omega_- \rangle].$$
(9)

Above Re[z] denotes the real part of the complex number z. Here for simplicity, we focus on the left end of the chain and assume that only the  $\gamma_{j,a}$  Majorana operators contribute (in contrast to odd products of the Majoranas). A typical behavior is exponential localization with  $|\varphi_j| \sim e^{-\delta j}$ , with  $\delta$  depending on the coupling parameters of the model [1].

The existence of a MZM has strong consequences for the ACF for  $\gamma_{1,a}$  at zero temperature. As discussed in Sec. II A, the ACF reduces to an equally weighted average over correlation functions in the ground-state manifold,

$$C_{\beta=\infty}(\gamma_{1,a},t) = \frac{1}{2} \sum_{p=\pm 1} \text{Re}[\langle \Omega_p | \gamma_{1,a} e^{iHt} \gamma_{1,a} | \Omega_p \rangle],$$

where we have assumed  $H |\Omega_P\rangle = 0$ . From  $\bar{p} = -p$ , it follows from an insertion of the identity that

$$\begin{split} & \operatorname{Re}[\langle \Omega_{p} | \gamma_{1,a} e^{iHt} \gamma_{1,a} | \Omega_{p} \rangle] \\ & = |\langle \Omega_{p} | \gamma_{1,a} | \Omega_{\bar{p}} \rangle|^{2} + \sum_{n \notin \operatorname{GS}} |\langle \Omega_{p} | \gamma_{1,a} | n, \bar{p} \rangle|^{2} \operatorname{cos}(E_{n,\bar{p}}t) \\ & = |\varphi_{1}|^{2} + \tilde{C}(t) \xrightarrow[t \to \infty]{} |\varphi_{1}|^{2}, \end{split}$$

where  $\tilde{C}(t)$  represents the incoherent part coming from the states above the gap and is assumed to decay rapidly. It follows  $C_{\infty}(\gamma_{1,a},t) \to |\varphi_1|^2$  for  $t \to \infty$ .

In the previous discussion, the MZM was defined solely by the properties of the ground-state manifold. The SZM can be seen as a generalization of these ideas to the full many-body spectrum. In this perspective, a SZM [1,21,32,33,50] is defined as an operator  $\Gamma$  with the following properties:

- 1. Hermitian:  $\Gamma^{\dagger} = \Gamma$
- 2. Anticommuting with the fermionic parity:  $\{P, \Gamma\} = 0$
- 3. Commuting with the Hamiltonian:  $[\Gamma, H] \to 0$  for  $L \to \infty$ .

We also require the  $\Gamma$  to be localized at the edge of the system, so that the SZM has an exponentially decaying weight on operators with support away from the edge of the chain, similar to the MZM.

It follows that a system possessing a SZM has an exact double degeneracy of the spectrum in the thermodynamic limit: Every energy eigenstate of defined parity p has a partner state of the opposite parity -p [1,21,32,33,50]. As a direct consequence, it is easy to show that for any operator with  $\langle \hat{O}, \Gamma \rangle_{\beta} = \alpha$  the long-time thermodynamic behavior of the ACF is given by  $C_{\beta}(\hat{O},t) \rightarrow |\alpha|^2$  for arbitrary temperatures  $T=1/\beta$ . In contrast, the existence of a MZM only guarantees the double degeneracy in the ground-state manifold and thus an infinite lifetime of  $\gamma_{1,a}$  only at exactly zero temperature.

The construction of a SZM in an exact way has only been achieved in a few cases of integrable Hamiltonian models [1,21]. Apart from integrability, it is still an open question whether it is possible to find a SZM and whether it is possible to have an exact double degeneracy in the spectrum even in a perturbative regime [11,51,52]. Still, it has been found numerically [12–17] that  $\gamma_{1,a}$  has a long lifetime at infinite temperature. Unlike a SZM, in this case the lifetime saturates with the system size and is strictly finite in the thermodynamic limit. This behavior has been linked to the existence of an ASZM. More precisely, an ASZM shares all properties of a SZM except that the commutator with the Hamiltonian saturates to a nonzero operator with increasing system size [13]. This error term then necessarily leads to a finite lifetime of the edge excitation  $\gamma_{1,a}$ .

In a prethermal regime, the authors of [13] connected the appearance of such a nearly commuting operator to an approximately conserved U(1) symmetry. In their formulation, the ASZM is given by a local unitary rotation of  $\gamma_{1,a}$ . A different approach to understanding the ASZM was proposed by Yates *et al.* [16,17], who linked this behavior to the Lanczos series  $b_n$  obtained by using  $\gamma_{1,a}$  as the seed operator. In particular they found that the artificial single-particle Hamiltonian  $H_{\rm sp}$  from Eq. (6) resembles that of a dressed Su-Schrieffer-Heeger [53,54] (SSH) model with a vanishing staggering:

$$b_n = h_n + (-1)^n \tilde{h}_n. (10)$$

Here  $h_n$  is the positive monotonically increasing background hopping in Krylov subspace, and is expected to be present for any generic chaotic models [26], while  $\tilde{h}_n$  is the staggered component, which becomes trivial for some  $n > n^*$ . This structure has a strong influence on the possible form of the EDOS  $v_{\beta}^E(\omega)$ , Eq. (7).

Here we make use of the fact that the EDOS must to be of the form

$$\nu_{\beta}^{E}(\omega) = A(\beta) \frac{\gamma(\beta)/\pi}{\omega^{2} + \gamma(\beta)^{2}} + [1 - A(\beta)] \tilde{\nu}_{\beta}^{E}(\omega), \tag{11}$$

where  $\tilde{v}_{\beta}^{E}(\omega)$  defines an incoherent background density of states with a gap around zero energy. This incoherent background leads to fast short-time dynamics, while the asymptotic behavior is dominated by the Lorentzian line shape of width  $\gamma(\beta)$ .

In fact, the general model of Eq. (10) can be mapped by simple arguments to a new model consisting of a SSH chain of length  $N_{\rm eff}$  attached to a semi-infinite lead with homogeneous hopping. The Lorentzian peak results from the hybridization of the topological edge state of the SSH model with the gapless spectrum of the semi-infinite lead, while the bulk modes the SSH chain give rise to sidebands approximately described by semicircles:

$$2\tilde{\nu}_{\beta}^{E}(\omega) = \nu_{C}(E - E_{0}) + \nu_{C}(E + E_{0}),$$

$$\nu_{C}(\omega) = \frac{1}{\pi w^{*}} \sqrt{1 - \frac{\omega^{2}}{(2w^{*})^{2}}} \theta(2w^{*} - |\omega|).$$
(12)

See Appendix E for more details. We propose a simple model to capture all the dynamics of the ASZM at short and long times, involving four fitting parameters  $(A, \gamma, E_0, w^*)$ . In this model, the appearance of a narrow Lorentzian peak is the signature of an ASZM. From the EDOS, one can also recover the SZM limit as follows: since the Lorentzian contributes to the ACF as  $e^{-\gamma(\beta)t}$ , an infinite lifetime is recovered only for  $\gamma(\beta) \to 0$ . For this case, the Lorentzian function reduces to a delta function  $\delta(\omega)$ .

### III. MODEL

The explicit model studied in this work is that of spinless fermions defined by the creation/annihilation operators  $c_j^{\dagger}/c_j$  that reside on a chain of length L, and interact according to the Kitaev-Hubbard Hamiltonian

$$H = -w \sum_{j=1}^{L-1} (c_j^{\dagger} - c_j)(c_{j+1}^{\dagger} + c_{j+1})$$

$$+ U \sum_{i=1}^{L-1} p_j p_{j+1} - \frac{\mu}{2} \sum_{i=1}^{L} p_j.$$
(13)

Above  $p_j=2c_j^\dagger c_j-1$  defines the local parity of the site j. The quadratic part of this Hamiltonian (U=0) consists of the usual nearest-neighbor hopping term, a p-wave pair creation/annihilation process of neighboring particles, and a chemical potential  $\mu$  controlling the average density. For simplicity, we choose the pairing potential to be equal to the hopping amplitude and denote it by w. In order to break integrability, we introduce a nearest-neighbor Hubbard-like interaction of strength U. The Hamiltonian Eq. (13) commutes with the total fermionic parity  $P=\prod_j p_j$ , thus splitting the spectrum into two towers of even and odd parity.

In terms of the Majorana operators introduced in Sec. II D, the Hamiltonian (13) assumes the form

$$H = -w \sum_{j=1}^{L-1} i\gamma_{j,b}\gamma_{j+1,a} + \frac{\mu}{2} \sum_{j=1}^{L} i\gamma_{j,a}\gamma_{j,b}$$
$$- U \sum_{j=1}^{L-1} \gamma_{j,a}\gamma_{j,b}\gamma_{j+1,a}\gamma_{j+1,b}.$$

The Kitaev-Hubbard chain (13) possesses a rich phase diagram, sketched in Fig. 1, including an extended topological phase [9,11,55] characterized by a doubly degenerate ground-state manifold  $|\Omega_p\rangle$  with opposite fermion parity p, together with the appearance of edge-localized MZMs. While non-integrable for a generic choice of parameters, there are two exactly solvable limits. The first limit is the noninteracting case with U=0 where the model becomes quadratic in terms of the Majorana operators and is equivalent to the Kitaev chain [1]. The second limit corresponds to  $\mu=0$  but arbitrary interaction strengths U. In this case, the model is diagonalizable by defining a nonlocal unitary transformation of the original fermions  $c_i$ ; see Appendix C for more information.

In both cases one can construct a SZM analytically [1,21]. Away from these integrable limits, this is no longer possible. Nevertheless, the topological ground-state degeneracy does still allow for the existence of a MZM of the form  $\gamma_L = \sum_{j=1}^{N} \varphi_j \gamma_{j,a}$ ; see discussion in Sec. II D.

### IV. RESULTS

In this section we discuss the numerical results obtained for the temperature-dependent Lanczos series. Motivated by the analytical results for the SZM in the integrable limits of the Kitaev-Hubbard chain, Eq. (13), and the form of the MZM in the ground-state manifold, we choose the edge Majorana operator  $\gamma_{1,a}=c_1^{\dagger}+c_1$  as the seed operator for the Lanczos algorithm.

#### A. General behavior of the Lanczos series

We will start by considering the exemplary point  $\mu/w=1.2$ , U/w=0.1 to discuss the general features observed at finite temperatures. For all results we have chosen a fixed system size of L=22. We have checked that the resulting ACF has converged with respect to the system size; see also Appendix F 1. We start by discussing the general behavior of the temperature-dependent Lanczos series. The results are obtained by using the tensor network ansatz introduced in Sec. II C with a maximal bond dimension of  $\chi=2000$  for the matrix product operator. See Appendix F 1 for a detailed discussion on the convergence properties with the bond dimension. In Fig. 2 we show the coefficients  $b_n(\beta)$  for different inverse temperatures  $\beta=1/T$ . As a generic feature, we observe an increase of the coefficients with respect to n independent of  $\beta$ .

For small  $\beta$ , the increase follows a near-linear behavior  $b_n \sim n$  as expected for generic nonintegrable systems [26], before saturating to a plateau which depends on the system size; see Fig. 3(a). For larger  $\beta$ , the increase starts to deviate from this near linearity with a slightly stronger curvature,

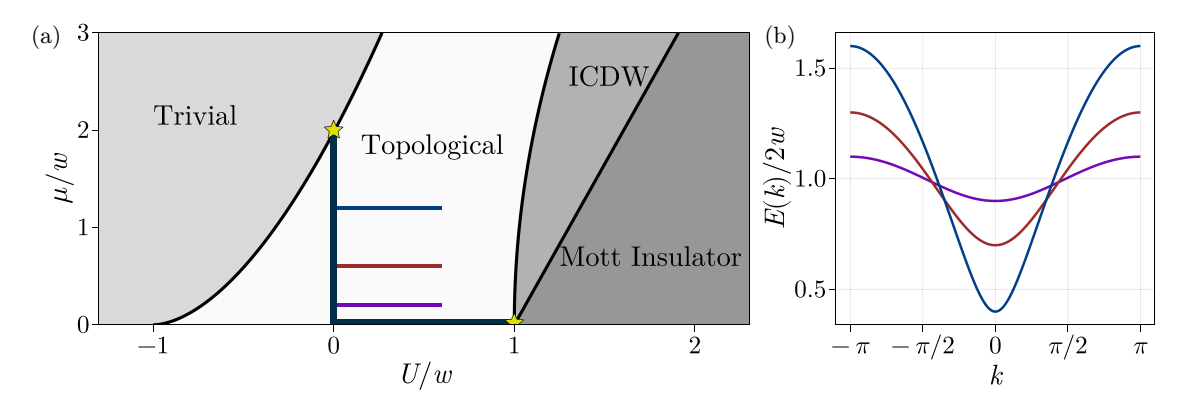


FIG. 1. (a) Sketch of the different phases of the Hamiltonian in Eq. (13) following [9,11,55]. For small  $\mu/w$  and U/w, there exists an extended region (white) showing a topological ground-state degeneracy. Increasing either  $\mu$  or U, one observes phase transitions into topologically trivial regions. For large  $\mu$ , the state is described by a trivial band insulator, while for a large U, one observes a transition into an incommensurate charge density wave phase, followed by a commensurate-incommensurate transition into a Mott insulating phase. The black lines denote the exactly solvable limits where it is possible to construct SZMs that commute with the Hamiltonian. These SZMs disappear at the phase transitions to the trivial regions, marked by yellow stars. Along the three cuts, marked by purple ( $\mu/w = 0.2$ ), red ( $\mu/w = 0.6$ ), and blue ( $\mu/w = 1.2$ ), we compute the effective energy scale  $\Delta_{\rm eff}$  in Sec. IV B. (b) Energy dispersion relations for U = 0 with the identification  $E(k = 0) = \Delta(U = 0)$ .

more like a power law behavior  $n^{\alpha}$ , a deeper analysis is left for future work. The system size dependence is greatly reduced at lower temperatures, as can be seen in Fig. 3(b). This is expected because as the temperature is lowered, the dynamics is projected to smaller regions of the Hilbert space.

In addition to this general increase, the series is dressed by a staggered component

$$\tilde{h}_n := (-1)^{n+1} (b_{n+1} - b_n).$$
 (14)

As can be seen by the inset of Fig. 2, for all temperatures this staggered component becomes trivial (i.e., either negative or oscillates around zero) for  $n > n^*$ . Increasing  $\beta$  has the effect of increasing  $\tilde{h}_n$ , while also shifting the point  $n^*$  at which  $\tilde{h}_n \approx 0$ , to larger values of n. The associated artificial single-particle Hamiltonian  $H_{\rm sp}$  is that of a dressed SSH chain in the topological regime with a vanishing staggering; see also the discussion in Sec. II D. We expect that at any finite

25  $w\beta = 0.0$  $w\beta = 0.8$  $-w\beta = 1.4$ 20  $w\beta = 2.0$  $w\beta = 2.35$ 15  $b_n$ 1.0 10 0.50.00.55 20 60 40 80 0 n50 100 150 200 n

FIG. 2. Lanczos coefficients for L=22 at various inverse temperatures  $w\beta=1/T$ . The insert shows the staggered component  $\tilde{h}_n$ , Eq. (14), averaged over seven sites to reduce the noise in the data.

temperature, the increase in the background,  $h_n$ , to have only a small influence on the lifetime of  $\gamma_{1,a}$  in contrast to the staggered component  $\tilde{h}_n$ .

This can be made more rigorous by considering the EDOS shown in Fig. 4. For all temperatures, the general shape of the EDOS is given by a narrow Lorentzian peak around  $\omega=0$ , with an additional incoherent background; see Eq. (11). Lowering the temperature has two effects: First, the Lorentzian peak becomes narrower, i.e., the width parameter  $\gamma(\beta)$  becomes smaller for larger  $\beta$ . Second, the incoherent part changes its form slightly. While the incoherent background shows a two-band structure separated by an energy gap for all temperatures, additional local extrema appear at higher energies, on lowering the temperature. We believe that the changes to the incoherent part of the DOS is mainly influenced

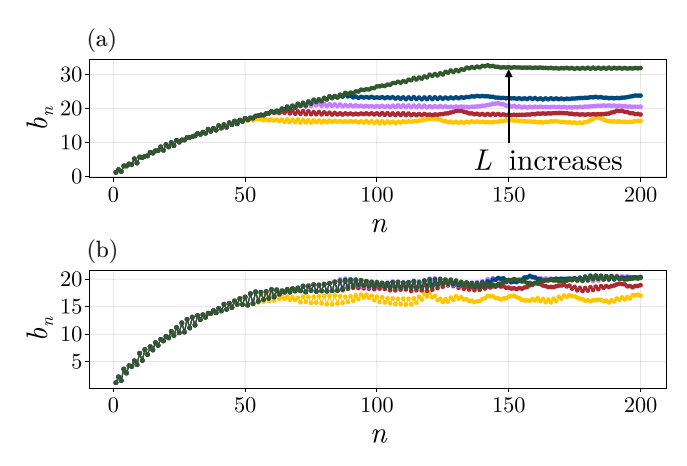


FIG. 3. (a) Comparison of the Lanczos series with increasing system sizes L=16, 18, 20, 22, 30 at infinite temperature. The final plateau value increases with system size. (b) The Lanczos sequence for the same L and for  $w\beta=2.35$ . In contrast to the infinite temperature sequence, the plateau value depends only weakly on the system size, with almost no difference between L=22 and L=30.

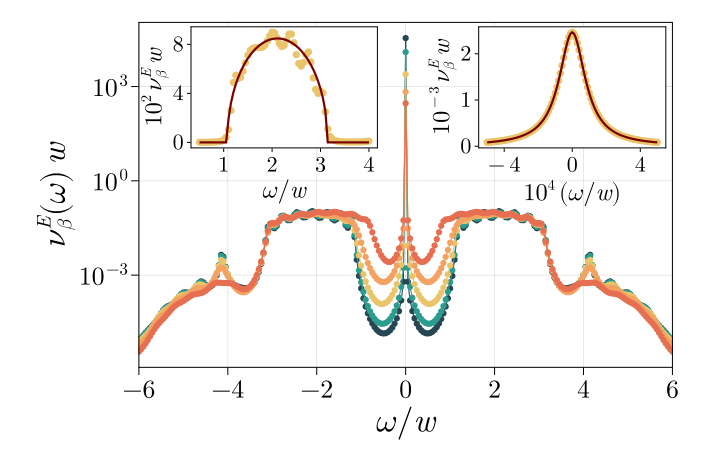


FIG. 4. EDOS obtained from the Lanczos coefficients at the finite temperatures shown in Fig. 2 and with the same color codes. The left inset shows a fit of the sidebands by the simplified model of Eq. (12). The right inset shows a fit of the central Lorentzian peak. Both insets are for  $w\beta = 1.4$ .

by the changes to the background values of the Lanczos coefficients  $h_n$ , while the decrease of  $\gamma(\beta)$  is directly related to the increase in the staggered component  $\tilde{h}_n$ .

Figure 5 shows the ACF (dots) obtained from the EDOS by the Fourier transform of Eq. (8). For all temperatures, one observes a transient decay at short timescales followed by a plateau. At timescales of order  $t \sim 1/\gamma(\beta)$ , one observes that the ACF decays further to zero.

Next, we test our simple model for describing the EDOS in terms of the four fitting parameters  $(A, \gamma, E_0, w^*)$ , where A and  $\gamma$  define the properties of the central Lorentzian and  $E_0$  and  $w^*$  define the incoherent sidebands by approximating them with semicircles; see Eqs. (11) and (12).

The inset of Fig. 4 shows an example of this simple four parameter fit. In particular, the left inset shows the semicircle

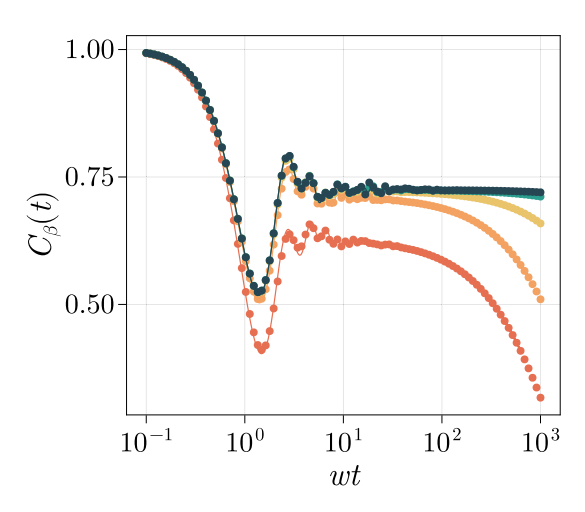


FIG. 5. ACR for different temperatures with the same color code as in Fig. 2. The dots represent the ACF obtained from the EDOS from Fig. 4. The lines are the analytical ACF from Eq. (15) with parameters obtained by fitting the EDOS with the simplified model (11) and (12).

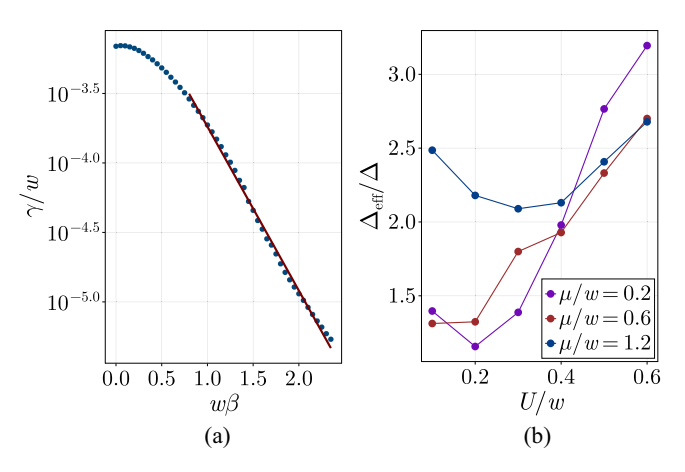


FIG. 6. (a) An example corresponding to  $\mu/w=1.2$  and U/w=0.1 of the extraction of the effective gap  $\Delta_{\rm eff}$  by fitting the lifetime to Eq. (16). (b) Effective gaps along the three cuts  $\mu/w=0.2, 0.6, 1.2$  as shown in Fig. 1 and normalized by the many-body gaps for each parameter point.

approximation of the incoherent side bands, while the right inset shows a fit to the central Lorentzian peak.

Using the exact ACF of the simplified model

$$C_{\beta}(\hat{O}, t) = Ae^{-\gamma t} + (1 - A)\frac{2}{\pi} \frac{J_1(2w^*t)}{2w^*t} \cos(E_0 t),$$
 (15)

where  $J_{\alpha}$  denotes the Bessel function of the first kind, we can compare the predictions from the four-parameter fit with the ACF obtained from the Lanczos series. We find that the simple four-parameter fit faithfully catches the short and long timescales of the ACF as can be seen in Fig. 5.

### B. Effective gaps

From general arguments, one expects that the lifetime of a local excitation obeys an exponential law [31]

$$\frac{1}{\tau(\beta)} := \gamma(\beta) = \gamma_0 e^{-\Delta_{\text{eff}}\beta} \tag{16}$$

for large  $\beta$ . For a local bulk excitation,  $\Delta_{\rm eff}$  is expected to be the many-body gap of the system. Figure 6(a) shows the temperature dependence of the inverse lifetime for  $\mu/w=1.2$  and U/w=0.1.

The large  $\beta$  regime shows the expected behavior, allowing a fit to be made. From this fit we obtain an effective energy gap  $\Delta_{\rm eff}/w \approx 2.7$ , which is significantly larger than the manybody gap of the system ( $\Delta/w \approx 1.09$ ); see Appendix F 4 for details on how the many-body gap was obtained. To check that this is not an accidental behavior of the point chosen, we performed the same analysis along the three cuts displayed in Fig. 1. The results of the different effective gaps are displayed in Fig. 6(b), normalized by the actual many-body gap  $\Delta$  of the system. For every parameter point we observe that the effective gap is larger than  $\Delta$  with a nontrivial dependence on the interaction strength U. We expect that due to the existence of a SZM that has infinite lifetime at infinite temperature for  $U=0,~\Delta_{\rm eff}/\Delta$  will diverge as  $U\to 0.$  The nonmonotonic behavior in U where  $\Delta_{\rm eff}/\Delta$  also increases at large U is intriguing and left for future study.

#### C. Exact diagonalization

To check if the effective energy gap obtained in the previous section is reflected in the low-energy part of the system, we study the model using exact diagonalization. For a given system size  $L \leq 16$ , we calculate the full spectrum  $\{|\psi_{n,p}\rangle, E_{n,p}\}$  of the Kitaev-Hubbard chain, with  $p=\pm$  being the parity of the state. From this, we construct an ASZM as follows [51]:

$$\Gamma = \sum_{n} g_n |\psi_{n,+}\rangle \langle \psi_{n,-}| + \text{H.c.}$$
 (17)

In the above equation,  $g_n \in \mathrm{U}(1)$  is a phase chosen such that  $g_n \langle \psi_{n,-} | \gamma_{1,a} | \psi_{n,+} \rangle \geqslant 0$ ; see also Appendix I for a more detailed discussion on the construction.

We can similarly construct an ASZM projected on the low-energy sector by

$$\Gamma_{\epsilon} = P_{\epsilon} \Gamma P_{\epsilon}$$

$$= \sum_{n}' g_{n} |\psi_{n,+}\rangle \langle \psi_{n,-}| + \text{H.c.}, \qquad (18)$$

with the projection operator

$$P_{\epsilon} |n, p\rangle = \begin{cases} |n, p\rangle, & \text{for } E_{n,p} - E_{0,p} \leqslant \epsilon \\ 0, & \text{for } E_{n,p} - E_{0,p} > \epsilon \end{cases}.$$

In Eq. (18) the primed sum means that compared to Eq. (17), we only keep the pairs of states with a maximum excitation energy  $\epsilon$  above the ground state. From  $\Gamma_\epsilon$  we can calculate the commutator with the Hamiltonian

$$||[H, \Gamma_{\epsilon}]||^2 = \sum_{n}' (E_{n,+} - E_{n,-})^2.$$

Another interesting quantity is the overlap of the  $\Gamma_{\epsilon}$  operator with the edge operator  $\gamma_{1,a}$ . This overlap is computed with respect to the infinite temperature scalar product, but not normalized by the dimension of the full Hilbert space, but with the dimensionality of the projected space  $P_{\epsilon}$ .

As an example, we consider  $\mu/w=1.2$ , U/w=0.1. In the previous section, from the temperature dependence of the Lanczos coefficients, we obtained an effective energy gap of  $\Delta_{\rm eff}/w\approx 2.7$ . In Fig. 7 we plot the commutator of the lowenergy projected ASZM for even system sizes  $4\leqslant L\leqslant 16$ . We find that for  $\epsilon/w<2.5$  the commutator shows an exponentially decaying behavior with L, with approximately the same slope. This behavior changes qualitatively for  $\epsilon/w>2.5$ , where the slope is much smaller, with the commutator reaching a L-independent plateau value. The behavior changes around  $\epsilon/w\sim 2.5$  close to the effective energy gap  $\Delta_{\rm eff}/w\approx 2.7$  obtained from the temperature analysis of the Lanczos coefficients.

Next, we consider the overlap of  $\Gamma_{\epsilon}$  with the edge operator  $\gamma_{1,a}$ . This overlap is plotted against the cutoff energy  $\epsilon$  in Fig. 8. If we do not impose any cutoff, i.e., considering the full ASZM  $\Gamma$ , we observe that the overlap decays with the system size. This is explicitly shown in Fig. 8(c). However, by reducing the cutoff energy, we observe that for  $\epsilon \lesssim \Delta_{\rm eff}$  the value of the overlap appears to converge with the system size. Combining the results for the commutator  $||[H, \Gamma_{\epsilon}]||^2$  with the results for the overlap  $\langle \Gamma_{\epsilon} | \gamma_{1,a} \rangle_0$ , we conclude that if we project the system to an energy below  $\Delta_{\rm eff}$ , we observe the

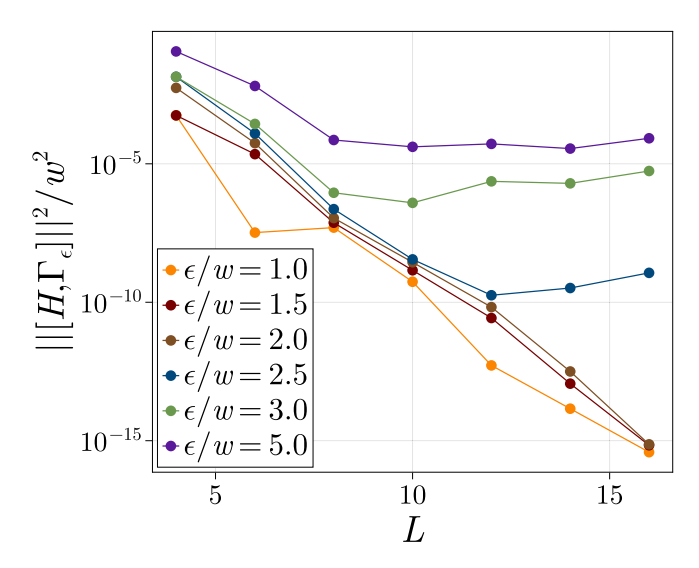


FIG. 7. Commutator of the Hamiltonian H with the low-energy projected ASZM  $\Gamma_{\epsilon}$ ; see Eq. (18) for  $\mu/w = 1.2$  and U/w = 0.1.

emergence of an operator  $\Gamma_{\epsilon}$  for which the commutator with the Hamiltonian H vanishes exponentially in the system size, while having a finite overlap with the edge operator  $\gamma_{1,a}$ . In that sense,  $\Gamma_{\epsilon}$  becomes a strong zero mode for the low-energy sector of the Kitaev-Hubbard chain.

#### V. CONCLUSIONS

An important topic both from a theoretical perspective as well as for practical realizations of quantum memories, is understanding the stability of topologically protected edge modes when interactions are present, and the system does not lie in the ground state sector. Our work takes a step in this direction by interpolating between zero temperature and infinite temperature. We find that, quite remarkably, the topological protection in the ground state manifold may not vanish immediately on raising the temperature, with stable edge modes present in an energy window which is of the order of, but systematically larger than the many-body gap. In arriving at this result, we have combined two methods for studying operator dynamics, Lanczos series expansions and tensor network ansatz, thus allowing us to access dynamics in the notoriously difficult regime of excited states, long times, and large systems.

While the particular example studied in this work was an interacting fermionic chain protected only by the  $\mathbb{Z}_2$  fermion parity, the approach can be easily extended to various other systems realizing stable edge modes. These include parafermionic systems [32–34] protected by general  $\mathbb{Z}_n$  symmetries and Floquet circuits, which host Majorana modes and the more exotic  $\pi$  modes [20,22,35–37]. Another interesting direction is the study of Majorana edge modes realized by quasi-one-dimensional fermionic ladder systems with strong pair hopping between the two ladders [34,38–40]. The topological phase in this ladder system occurs without breaking the total particle number conservation, opening the possibility for experimental realizations [41–45]. This additional global U(1) symmetry comes at the cost of gapless density

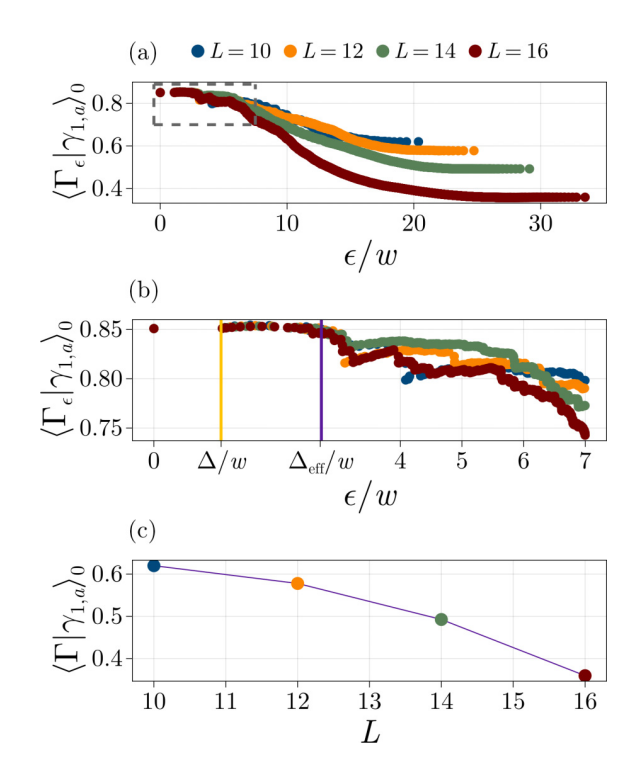


FIG. 8. Overlap of the projected ASZM  $\Gamma_{\epsilon}$  with the edge operator  $\gamma_{1,a}$  for  $\mu/w=1.2$  and U/w=0.1. (a) Varying the energy cutoff  $\epsilon$  over all scales. For large enough  $\epsilon$ , we observe a decay of the overlap with respect to the system size. (b) A detailed plot for all energies  $\epsilon/w<7$ , corresponding to the gray dotted box shown in (a). The effective energy gap  $\Delta_{\rm eff}$  is highlighted by a purple vertical line, while the thermodynamic many-body gap  $\Delta$  is denoted by the yellow vertical line. (c) Plot of the overlap with the full ASZM  $\Gamma$  for different system sizes. All three plots have the same color code for the system size L.

fluctuations [38,56,57] which makes the stability of these edge modes at finite temperatures questionable.

Other future directions include understanding the precise transition from absolutely stable SZMs at low energies to unstable but long-lived ASZMs at high energies. In this regard, it may be interesting to study the interplay of disorder and interactions, as it is possible that disorder increases the region of the spectrum that hosts SZMs [58], which is related to the phenomenology of many body localization. Finally, a fruitful direction of research is a more efficient construction of ASZMs by employing variational approaches tailored to directly target the low-energy space of a theory.

### **ACKNOWLEDGMENTS**

We acknowledge fruitful discussions with D. Alcalde, S. Diehl, R. Egger, G. Kells, A. Rosch, S. Trebst, and E. Weerda. N.T. and M.R. acknowledge the support from the DFG under Germany's Excellence Strategy-Cluster of Excellence Matter and Light for Quantum Computing (ML4Q) EXC 2004/1–390534769 and Project Grant No. 277101999 within the CRC network TR 183. A.M. acknowledges the support of the U.S. Department of Energy, Office of Science, Basic Energy Sciences, under Award No. DE-SC0010821. The authors

gratefully acknowledge the Gauss Centre for Supercomputing e.V. for funding this project by providing computing time through the John von Neumann Institute for Computing (NIC) on the GCS Supercomputer JUWELS [59] and through FZJ on JURECA [60] at Jülich Supercomputing Centre (JSC).

#### DATA AVAILABILITY

The simulations presented in this work were produced with a code based on the ITensor library [61]. Data and code are available at [62].

## APPENDIX A: FINITE TEMPERATURE SCALAR PRODUCT

In this paper, we consider a many-body Hilbert space  $\mathcal{H}$  defined on a finite chain. On this Hilbert space we consider the set of all operators  $\hat{O}: \mathcal{H} \to \mathcal{H}$ . Due to linearity, this set is itself a vector space denoted by  $\mathcal{H}^{\mathrm{op}}$ . It is also possible to define a scalar product on  $\mathcal{H}^{\mathrm{op}}$ . A general class of possible choices for a valid scalar product defined for a finite temperature  $T=1/\beta$  is given by [25]

$$\langle A|B\rangle_{\beta}^{g} := \frac{1}{\mathcal{Z}(\beta)} \int_{0}^{\beta} d\lambda \, g(\lambda) \text{Tr}[y^{\beta-\lambda} A^{\dagger} y^{\lambda} B].$$
 (A1)

Here

$$y := e^{-H}, \quad \mathcal{Z}(\beta) = \text{Tr}[e^{-\beta H}],$$

and  $g:[0,\beta]\to\mathbb{R}_+$  is a positive function with the properties

$$\frac{1}{\beta} \int_0^\beta d\lambda g(\lambda) = 1, \quad g(\beta - \lambda) = g(\lambda).$$

There are two important choices for the function  $g(\lambda)$ :

$$g_S(\lambda) = \frac{1}{2} [\delta(\lambda) + \lambda(\beta - \lambda)],$$
  
$$g_W(\lambda) = \delta(\beta/2 - \lambda),$$

leading to the two finite temperature scalar products:

$$\langle A|B\rangle_{\beta}^{S} = \frac{1}{2} \text{Tr}[\rho(\beta) \{A^{\dagger}B + BA^{\dagger}\}],$$

$$\langle A|B\rangle_{\beta}^{W} = \frac{1}{\mathcal{Z}(\beta)} \text{Tr}[e^{-\frac{\beta}{2}H}A^{\dagger}e^{-\frac{\beta}{2}H}B].$$
(A2)

Above  $\rho(\beta) = e^{-\beta H}/Z(\beta)$ . The first choice naturally appears in linear response theory while the second choice is related to Wightman correlation functions [25,26].

### APPENDIX B: JORDAN-WIGNER TRANSFORMATION

The Jordan-Wigner transformation [63,64] is a nonlocal unitary transformation of the Hilbert space that maps fermionic degrees of freedom to spins. Let  $\mathcal H$  again denote a many-body fermionic Hilbert space generated from the vacuum  $|0\rangle$  by the set of fermionic operators  $\{c_j\}$  obeying the canonical anticommutation relations.

The local Hilbert space  $\mathcal{H}_j^{\text{loc}}$  is formed by the two states  $|0\rangle_j$ , which is the vacuum, and  $|1\rangle_j = c_j^\dagger |0\rangle$ , which hosts one fermionic particle. The Jordan-Wigner transformation acts on this local Hilbert space by identifying the states

$$|0\rangle_{i} \rightarrow |\downarrow\rangle_{i}, \quad |1\rangle_{i} \rightarrow |\uparrow\rangle_{i},$$

together with the transformation of operators:

$$c_j = \frac{1}{2} (\sigma_j^x - i\sigma_j^y) \mathcal{S}_j, \quad c_j^{\dagger} = \frac{1}{2} (\sigma_j^x + i\sigma_j^y) \mathcal{S}_j,$$
 $n_j = \frac{1}{2} (\sigma_j^z + 1), \quad \mathcal{S}_j = \prod_{k < j} (-\sigma_k^z).$ 

Consider now the Kitaev-Hubbard chain with a general *p*-wave pairing potential

$$H = \sum_{j=1}^{L-1} -wc_{j}^{\dagger}c_{j+1} - \Delta c_{j}^{\dagger}c_{j+1}^{\dagger} + \text{H.c.}$$

$$+ U \sum_{j=1}^{L-1} p_{j}p_{j+1} - \frac{\mu}{2} \sum_{j=1}^{L} p_{j}, \tag{B1}$$

which reduces to Eq. (13) for  $\Delta = w$ .

Applying the Jordan-Wigner transformation to this Hamiltonian leads to the *XYZ* spin chain in a magnetic field

$$H = \sum_{j=1}^{L-1} \left[ J_x \sigma_j^x \sigma_{j+1}^x + J_y \sigma_j^y \sigma_{j+1}^y + J_z \sigma_j^z \sigma_{j+1}^z \right] + g \sum_{j=1}^{L} \sigma_j^z.$$
(B2)

The parameters are identified using

$$J_x = -\frac{w+\Delta}{2}$$
,  $J_y = -\frac{w-\Delta}{2}$ ,  
 $J_z = U$ ,  $g = -\mu/2$ .

Under the Jordan-Wigner transformation, the fermionic parity  $P = \exp(i\pi \sum_{j=1}^{L} n_j)$  becomes the product over all  $\sigma_j^z$ .

## APPENDIX C: SOLUTION OF THE KITAEV-HUBBARD CHAIN AT $\mu = 0$

In this Appendix, we discuss the transformation to diagonalize the Kitaev-Hubbard chain for  $\mu=0$ . The Hamiltonian of Eq. (13) reduces to

$$H = \sum_{j=1}^{L-1} -w(c_j^{\dagger} - c_j)(c_{j+1}^{\dagger} + c_{j+1}) + Up_j p_{j+1}.$$
 (C1)

Using the Jordan-Wigner transformation as described in Appendix B, this Hamiltonian becomes

$$H = \sum_{i=1}^{L-1} \left[ -w\sigma_{j}^{x}\sigma_{j+1}^{x} + U\sigma_{j}^{z}\sigma_{j+1}^{z} \right].$$
 (C2)

Now performing a second Jordan-Wigner transformation switches the role of  $\sigma_i^y$  with  $\sigma_i^z$ :

$$f_j = \frac{1}{2} (\sigma_j^x - i\sigma_j^z) \mathcal{S}_j', \quad \mathcal{S}_j' = \prod_{k < j} (-\sigma_k^y).$$

With this transformation, the Hamiltonian (C2) becomes

$$H = \sum_{j=1}^{L-1} -\tilde{w} f_j^\dagger f_{j+1} - \tilde{\Delta} f_j^\dagger f_{j+1}^\dagger + \text{H.c.},$$

which is again of type (B1) with zero chemical potential and interaction. One has  $\tilde{w} = w - U$  and  $\tilde{\Delta} = w + U$ . This

model is known to have a SZM, which for  $L \to \infty$  is

$$\Gamma = \mathcal{N} \sum_{k=1}^{\lfloor \frac{L+1}{2} \rfloor} \left( \frac{U}{w} \right)^{k-1} (f_{2k-1}^{\dagger} + f_{2k-1}),$$

$$\mathcal{N} = \sqrt{1 - (U/w)^2}.$$
(C3)

Let us now rewrite this in terms of the original fermions  $c_j$ . First, note that the Jordan-Wigner strings  $S'_{2k-1}$  are given in terms of the Majorana operators  $c_j = (\gamma_i^a - i \gamma_j^b)/2$  as

$$S'_{2k-1} = i^{k-1} \gamma_1^a \gamma_2^b \gamma_3^a \dots \gamma_{2k-2}^b,$$

which can be proven by induction. In the original fermions, the SZM is then given by

$$\Gamma = \mathcal{N} \sum_{k=1}^{\lfloor \frac{L+1}{2} \rfloor} \left( \frac{U}{w} \right)^{k-1} \mathcal{P}_k \gamma_{2k-1}^a, \tag{C4}$$

where  $\mathcal{P}_k$  is the string operator

$$\mathcal{P}_k = \mathcal{S}'_{2k-1} \mathcal{S}_{2k-1} = i^{k-1} \gamma_1^b \gamma_2^a \gamma_3^b \dots \gamma_{2k-2}^a.$$

## APPENDIX D: AUTOCORRELATION FUNCTION FROM THE GREEN'S FUNCTION

In this Appendix, we give more details on how the EDOS can be calculated efficiently by the continued fraction technique. The EDOS is defined as

$$v_{\beta}^{E}(\omega) = -\frac{1}{\pi} \lim_{\eta \to 0^{+}} \mathcal{I} \big[ G_{\beta}^{E}(\omega + i\eta) \big],$$

where  $\mathcal{I}[z]$  is the imaginary part of a complex number z and

$$G_{\beta}^{E}(z) = -i \langle 1 | \frac{1}{z\mathbb{1} - H_{\rm sp}} | 1 \rangle \tag{D1}$$

is the edge Green's function of the artificial single-particle Hamiltonian  $H_{\rm sp}$ . This expression for the EDOS is equivalent to Eq. (7).

We assume the following structure of  $H_{\rm sp}$ :

$$H_{SD} = H_0 + H_1 + V + V^{\dagger},$$

with

$$H_0 = \sum_{n=1}^{N-1} -t_n |n+1\rangle \langle n| + \text{H.c.},$$

$$H_1 = \sum_{n=N+1}^{\infty} -t_n |n+1\rangle \langle n| + \text{H.c.},$$

and  $V=-t_\star|N\rangle\langle N+1|$ . The part given by  $H_0$  contains all the hopping amplitudes obtained by the Lanczos series  $b_n=it_n$  as outlined in Sec. IIB. The second part  $H_1$  represents all the unknown hopping amplitudes which we interpolate by choosing a suitable model, and V represents the coupling between the two parts. As the Lanczos coefficients typically reach a plateau value for some  $n_\star$ , we choose  $t_n=t_\star=-ib_N$  for  $n>N>n_\star$ . Thus, we model the unknown Lanczos coefficients by a semi-infinite homogeneous chain.

To evaluate the edge Green's function (D1) we make use of the block inversion formula [65]

$$P_A \begin{pmatrix} H_1 & V \\ W & H_2 \end{pmatrix}^{-1} P_A = (H_1 - V H_2^{-1} W)^{-1},$$
 (D2)

with  $P_A$  being a projector on the first diagonal block. Applied to the edge Greens function one finds

$$iG_{\beta}^{E}(z) = (z\mathbb{1} - H_0 - |t_{\star}|^2 \tilde{G}_{\beta}^{E}(z) |N\rangle \langle N|)_{1,1}^{-1},$$
 (D3)

where  $\tilde{G}^{E}_{\beta}(z)$  is the EDOS of  $H_1$  and can be calculated analytically for the homogeneous chain

$$\tilde{G}_{\beta}^{E}(z) = \frac{1}{4|t_{\star}|^{2}} (z + \sqrt{z^{2} - 4|t_{\star}|^{2}}). \tag{D4}$$

Equation (D3) can now be evaluated by explicit inversion. Alternatively, one can again use the block inversion formula (D2) to further reduce the expression, obtaining the finite continued fraction:

$$iG_{\beta}^{E}(z) = \frac{1}{z - \frac{|t_{1}|^{2}}{z - \frac{|t_{2}|^{2}}{z - \frac{1}{z - |t_{\star}|^{2} \tilde{G}_{\beta}^{E}(z)}}},$$
 (D5)

which is numerically more stable and faster to compute than the explicit numerical inversion of  $z\mathbb{1} - H_0 - |t_{\star}|^2 \tilde{G}_{\beta}^E(z)$ .

## APPENDIX E: APPROXIMATE EDGE DENSITY OF STATES

In this Appendix we review the continuum approximation of the artificial Hamiltonian. The discussion mainly follows [17]. We will employ the continuum description reviewed here to motivate the phenomenological fit of Eq. (12).

We start from the artificial single-particle Hamiltonian

$$H = \sum_{n=0}^{N} ib_{n+1} |n+1\rangle \langle n| + \text{H.c.},$$

which gives the Schrödinger time evolution

$$i\partial_t \varphi_n(t) = ib_n \varphi_{n-1}(t) - ib_{n+1} \varphi_{n+1}(t), \tag{E1}$$

with  $\varphi_n(0) = \delta_{n,1}$ . We assume the form  $b_n = h_n + (-1)^n \tilde{h}_n$ , where the slowly varying k = 0,  $\pi$  components are  $h_n$  and  $\tilde{h}_n$ , respectively. This allows for a splitting of the wave function  $\varphi_n = \varphi_n^0 + (-1)^n \varphi_n^{\pi}$ . The k = 0,  $\pi$  components of the wave function can now be approximated by the envelope function

$$\varphi_n^k \approx \varphi^k(an),$$

which is assumed to be smooth and to vary slowly on the length scale of a, representing the lattice spacing between sites n and n+1. Introducing the Dirac spinor  $\Psi(x) = (\varphi^0(x), \varphi^\pi(x))^T$ , the Schrödinger equation (E1) can be approximated by the Dirac-like equation

$$i\partial_t \Psi = -a\{h(x), i\partial_x\}\sigma_z \Psi + m(x)\sigma_y \Psi,$$
 (E2)

with the mass term  $m(x) = 2\tilde{h}(x) + a\partial_x \tilde{h}(x)$ , and h(x) and  $\tilde{h}(x)$  are smooth approximations to  $h_n$  and  $\tilde{h}_n$ .

To remove the position dependence of the momentum operator, we consider the general coordinate transformation y = y(x), with

$$\partial_x y = \frac{1}{2h(x)}, \quad y(a) = a.$$
 (E3)

The initial condition is chosen so that the chain starts at the same point in both the original and transformed coordinates. This transformation is bijective as long as h(x) > 0. Defining the rescaled Dirac spinor  $\chi = \sqrt{h}\Psi$ , the transformed Dirac equation reads

$$i\partial_t \chi = [-ai\partial_v \sigma_z + \tilde{m}(v)\sigma_v]\chi$$
. (E4)

This equation now resembles a standard Dirac equation with the position-dependent mass term  $\tilde{m}(y) = 2\tilde{h}(y) + \frac{\partial_y \tilde{h}(y)}{[2h(y)]}$ .

We can now try to find a second lattice Hamiltonian  $\tilde{H}_{sp}$  which has the same continuum limit as given by Eq. (E4). For this consider

$$\tilde{H}_{\rm sp} = \sum_{\nu=0}^{\infty} -it_{n+1} |n+1\rangle \langle n| + \text{H.c.}, \tag{E5}$$

where  $t_n = t + (-1)^n \tilde{t}_n$ . Note that t is now a constant. The new staggered component  $\tilde{t}_n$  is again assumed to vary slowly. The continuum version of the Schrödinger equation given by  $\tilde{H}_{SD}$  is now

$$i\partial_t \chi = [-i2ta\partial_y \sigma_z + M(y)\sigma_y]\chi,$$
 (E6)

with  $M(y) = 2\tilde{t}(y) + \partial_y \tilde{t}(y)$ . Since t was a constant to start with, the momentum part has no additional position dependence.

Comparing Eqs. (E4) and (E6), we find both lead to the same time evolution if we set t = 1/2 and

$$2\tilde{t}(y) + \partial_y \tilde{t}(y) = 2\tilde{h}(y) + \partial_y \frac{\tilde{h}(y)}{2h(y)}.$$
 (E7)

We choose the initial condition to be  $\tilde{t}(a) = \tilde{h}_1$ . In general, this first-order differential equation has a unique solution that completely fixes  $\tilde{t}(x)$  by the parameters of the original model, h and  $\tilde{h}$ . An approximate solution can be found by discarding the derivatives on both sites of Eq. (E7):

$$\tilde{t}(y) = \tilde{h}[x(y)],$$

where x(y) is the inverse of the transformation defined in Eq. (E3). We can now set  $v(y) = 1/2 - \tilde{h}[x(y)]$  and  $w(y) = 1/2 + \tilde{h}[x(y)]$  such that the new lattice Hamiltonian  $\tilde{H}_{sp}$  reads

$$\tilde{H}_{sp} = \sum_{n} v(an) |n, a\rangle \langle n, b|$$

$$+ w(an) |n, b\rangle \langle n + 1, a| + \text{H.c.}$$

The single-particle Hamiltonian  $\tilde{H}_{\rm sp}$  is thus given by a SSH chain with position-dependent staggering of the hopping amplitudes centered around the constant value of 1/2. Within this approximation, knowing the solution of the Schrödinger equation for  $\chi$  derived from  $\tilde{H}_{\rm sp}$  is equivalent to knowing the solution of the original Schrödinger equation in terms of the variables  $\varphi_n(t)$ , and derived by  $H_{\rm sp}$ . Explicitly focusing on

the first site, one has

$$C(t) = \langle 1|e^{-itH_{\rm sp}}|1\rangle \approx \langle 1|e^{-it\tilde{H}_{\rm sp}}|1\rangle.$$

Furthermore, we find that the EDOS of  $H_{\rm sp}$  is the same as the EDOS of  $\tilde{H}_{\rm sp}$ .

We now consider a simple model with a constant staggering up to  $n_{\star}$ , and with the background h increasing linearly with n:

$$h(n) = \alpha + bn$$
,  $\tilde{h}_n = \rho \theta (n_{\star} - n)$ .

Here one finds for the transformed variables:

$$y = \frac{1}{b} \log \left( \frac{\alpha + bn}{\alpha + b} \right) + 1,$$
$$x = \frac{1}{b} [e^{b(y-1)}(\alpha + b) - \alpha].$$

The transformed model describes a short SSH chain in the topological regime  $v=1/2-\rho < w=1/2+\rho$  until it reaches the location  $y_\star=y(n_\star)$ , after which it becomes metallic. In such a situation, the topological edge mode in the SSH chain overlaps with the metallic bulk, leading to edge mode leakage. This leakage leads to a broadening of the delta peak at zero energy in the EDOS of a pure SSH chain. In contrast, the side bands of the EDOS describe the hybridization of the bulk bands of the SSH chain with the metallic states of the lead, and results in only small modifications of the density of states.

The exact EDOS of the SSH chain with hopping parameters v > 0 and w > 0 is given by

$$\begin{split} \nu_{E}(\omega) &= \frac{w^{2} - v^{2}}{w^{2}} \delta(\omega) \Theta(w - v) \\ &+ \frac{1}{2\pi \omega w^{2}} \sqrt{4v^{2}w^{2} - (\omega^{2} - v^{2} - w^{2})^{2}} \\ &\times \Theta(|\omega| - |v - w|) \Theta(|v + w| - |\omega|). \end{split} \tag{E8}$$

The first line of Eq. (E8) is due to the topological edge state present for v < w, while the second line describes the bulk contribution to the EDOS. The bulk gap of this SSH chain is given by  $\Delta = |v - w|$ , the bands are centered around  $\pm \bar{E}_0 = \pm \max(v, w)$ , and the bandwidth is given by  $\delta = \min(v, w)$ . In the large gap limit, the side bands are well approximated by simple semicircles

$$\nu_E(\omega) = \frac{A}{\pi \delta} \sqrt{1 - \frac{(|\omega| - \bar{E}_0)^2}{\delta^2}},\tag{E9}$$

for  $|v-w| \le |\omega| \le |v+w|$ . The factor A is associated with the spectral weight of the potential edge mode. One has  $A=(v/w)^2$  for v< w (topological) and A=1 for v> w (trivial). To demonstrate this behavior, we plot the EDOS of a short SSH chain attached to a homogeneous lead in Fig. 9, and compare it to the EDOS of a semi-infinite SSH chain, Eq. (E8), and to the semicircle approximation of Eq. (E9).

### APPENDIX F: FURTHER NUMERICAL RESULTS

In this Appendix we present additional numerical results.

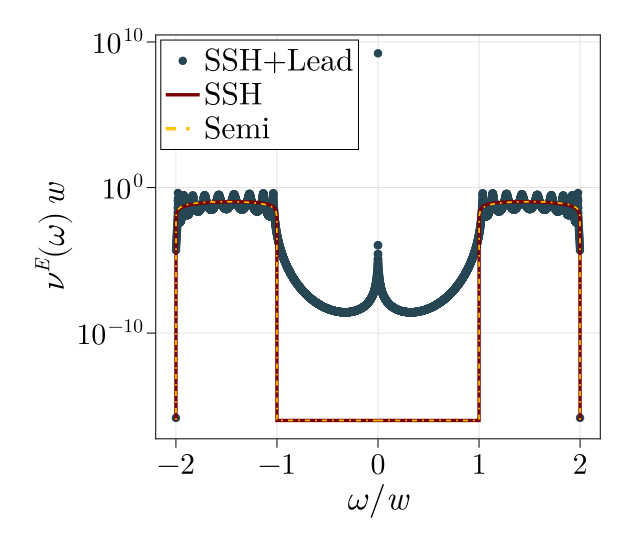


FIG. 9. EDOS obtained for a short SSH chain with v = 0.5, w = 1.5 of length L = 20 attached to a semi-infinite homogeneous chain with hopping t = 1. The red line is the bulk contribution of the EDOS of a semi-infinite SSH chain with the same parameters, the orange dashed line is the semicircle approximation of the side bands and it completely overlaps the red line of the SSH EDOS.

#### 1. Convergence properties

To calculate the EDOS and thus the lifetime of the edge modes at finite temperatures, we made two approximations: The truncation of the bond dimension of the matrix product operators, and the modeling of the unknown Lanczos coefficients by a semi-infinite homogeneous chain. In the following we discuss how these two approximations influence the results.

In Sec. II C we outlined that we approximate the orthonormal basis operators  $\mathcal{O}_n$  obtained from the Lanczos series by a matrix product operator with a finite bond dimension  $\chi$ . A finite bond dimension limits the amount of independent operators that can be present in  $\mathcal{O}_n$ . As a result, the sequence of Lanczos coefficients  $b_n$  is not precise, but only an approximation for any given value of  $\chi$ . Figure 10 shows the Lanczos coefficients for two different inverse temperatures  $t\beta = 0.4$  (left panel) and  $w\beta = 1.25$  (right panel), and for different

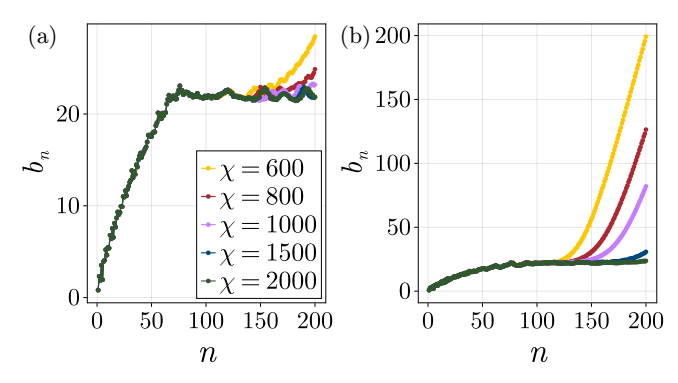


FIG. 10. Lanczos coefficients  $b_n$  obtained for  $\mu/w = 0.6$ , U/w = 0.3, and for a system of size L = 22, for different bond dimensions. Panel (a) [(b)] is for an inverse temperature  $w\beta = 0.4$  ( $w\beta = 1.25$ ).

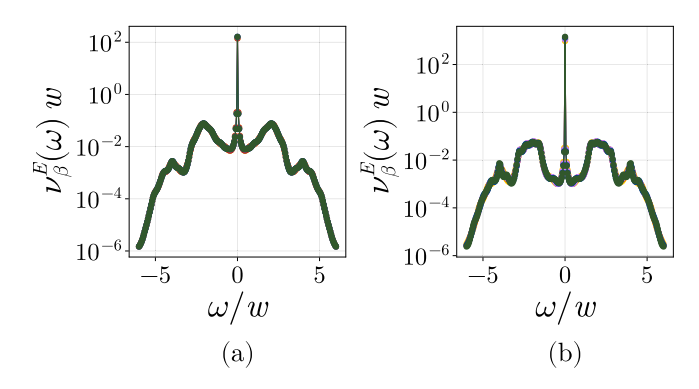


FIG. 11. EDOS obtained from the Lanczos series  $b_n$  from Fig. 10, with the same identification of color and bond dimension. Panel (a) [(b)] is for  $w\beta = 0.4$  ( $w\beta = 1.25$ ). To obtain meaningful results, we discarded all Lanczos coefficients for n larger than  $n_{\text{unstable}}$  as explained in the text. The collapse of all curves demonstrates the convergence of the EDOS with respect to the bond dimension.

bond dimensions, for the parameters  $\mu/w = 0.6$ , U/w = 0.3. At both temperatures we observe that the Lanczos series becomes unstable for some value of  $n_{\text{unstable}}$ . For larger  $\beta$ (smaller T) the instability occurs for a smaller value of  $n_{\text{unstable}}$ . This can be understood by noting that a large part of the Hilbert space has an exponentially small weight at sufficiently small temperatures. Small numerical errors can quickly accumulate and lead to instability of the Lanczos iteration. The situation is worst at strictly zero temperature, where the scalar product of Eq. (2) actually has a large null space. It is thus a pseudo scalar product instead of a real scalar product. At infinite precision, this null space should be projected out of the Lanczos series. However, small numerical errors can lead to large contributions within this null space. Increasing the bond dimension  $\chi$  reduces numerical errors, thereby shifting this instability to larger values of n. This is a generic feature obtained for every parameter combination  $(\mu/w, U/w)$  we have studied in this work.

To obtain any meaningful results from the  $b_n$ , it is therefore crucial to truncate the Lanczos series before the instability sets in. For example, for the  $\chi=400$  and  $w\beta=0.4$ , one truncates the  $b_n$  at  $n\sim100$ . However, it is crucial that the instability occurs at a value  $n_{\rm unstable}$  that is deep inside the plateau. In addition, in order to obtain a faithful result for the lifetime, the staggered component should already have decayed. In Fig. 11 we plot the EDOS obtained from the Lanczos series in Fig. 10, by removing all  $b_n$  for  $n>n_{\rm unstable}$ . We observe that, unlike the Lanczos series, the EDOS shows little dependence on the bond dimension. In addition, the central peak converges rapidly in the bond dimension  $\chi$ , and only small changes occur to the side bands.

This also implies that the lifetime  $\gamma(\beta)$  obtained by fitting the central Lorentzian converges rapidly in  $\chi$ , while only the short-time dynamics is modified by increasing the bond dimension.

We now discuss the second approximation, that involving the choice of the hopping parameter w for the semi-infinite chain. In all our results we have chosen  $w=ib_N$ , which is the last Lanczos coefficient before the instability sets in. Alternately, one could have averaged over the last K

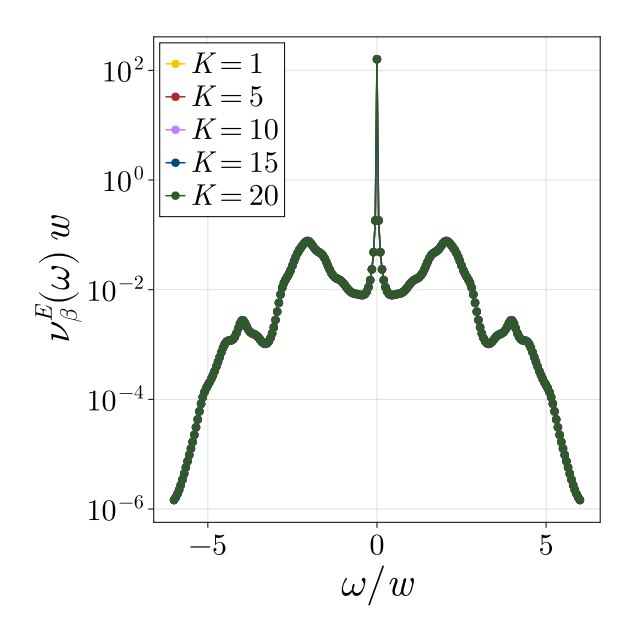


FIG. 12. EDOS obtained by varying the hopping strength w attaching the semi-infinite lead to the finite chain, with the latter described by the numerically obtained Lanczos coefficients  $b_n$ . The different hopping parameters w are obtained by varying the averaging window K according to equation (F1). The Lanczos coefficients are obtained for  $\mu/w = 0/6$ , U/w = 0.3, and  $w\beta = 0.4$ .

coefficients

$$w = i\frac{1}{K} \sum_{k=0}^{K-1} b_{N-k}.$$
 (F1)

In Fig. 12 we show the EDOS for different window sizes K. Since all the curves lie on top of each other, we conclude that the explicit value of w is not that important as long as w faithfully represents the plateau value.

Finally, we demonstrate the convergence of our results with respect to the system size L. For this, we calculate the EDOS for the two system sizes  $L_1 = 22$  and  $L_2 = 30$  from which we extract the relative error

$$\epsilon_{\nu}(\omega,\beta) := \left| \frac{\nu_{\beta}^{E}(\omega,L_{1}) - \nu_{\beta}^{E}(\omega,L_{2})}{\nu_{\beta}^{E}(\omega,L_{2})} \right|. \tag{F2}$$

Figure 13 shows this relative error for  $\mu/w = 1.2$ , U/w = 0.1 and the two inverse temperatures  $w\beta = 0.0$  and  $w\beta = 2.35$ . In both cases, the relative error is of order  $10^{-2}$  for all energy scales. This is also reflected in the width parameter

$$\left| \frac{\gamma(0, L_1) - \gamma(0, L_2)}{\gamma(0, L_2)} \right| \approx 0.05,$$

$$\left| \frac{\gamma(2.35, L_1) - \gamma(2.35, L_2)}{\gamma(2.35, L_2)} \right| \approx 0.007.$$
(F3)

As this study is not aiming to achieve the most precise values and due to the growth of computational resources with system size, we present results for L=22 as this system size is already sufficient for extracting reasonable numbers. A systematic study of the influence of the system size is left for future work.

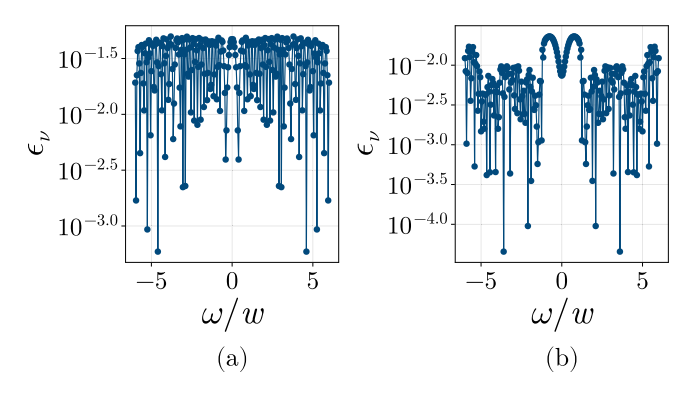


FIG. 13. Energy-resolved relative error  $\epsilon_{\nu}$  of the EDOS; see Eq. (F2). Panel (a) [(b)] shows the error for  $w\beta = 0$  ( $w\beta = 2.45$ ).

### 2. Wightman standard scalar product

In this Appendix we demonstrate that the Wightman finite temperature scalar product defined in Eq. (A2) in Appendix A gives qualitatively the same result as the standard scalar product which we have exclusively used throughout this paper. In Fig. 14 we plot the autocorrelation function obtained for  $\mu/w=1.2$  and U/w=0.1 for both choices of the scalar product. Both results are obtained for a system size of L=22, and for the inverse temperature  $w\beta=0.4$ . We see that both curves have the same overall behavior, although the standard scalar product has a smaller plateau value at intermediate times. The lifetime  $\tau$  at which the autocorrelation functions decay to zero is qualitatively the same for both choices of the scalar product.

### 3. TDVP versus Lanczos

In this Appendix we compare the autocorrelation function obtained from the Lanczos series with direct integration of the Heisenberg time evolution using the time dependent variational principle (TDVP) [28,29]. In the TDVP algorithm, we limit the bond dimension of the time-evolved operator  $\gamma_{1,a}(t)$  to  $\chi=512$ . To compare the TDVP with the Lanczos algorithm, we consider three different parameter points: (1)

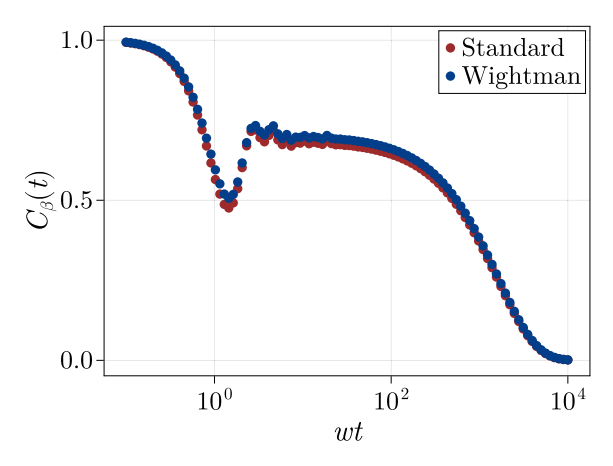


FIG. 14. Comparison between the autocorrelation function obtained using the scalar product (red) and the Wightman scalar product (blue).

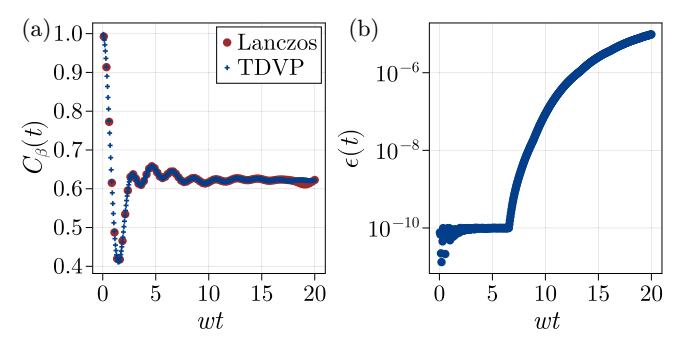


FIG. 15. Comparison between the autocorrelation function obtained from the Lanczos series (red dots) and the TDVP algorithm (blue crosses) at infinite temperature in the topological region  $(\mu/w=1.2, U/w=0.1)$ . (a) The truncated weight of the MPO of the TDVP simulation; (b) the autocorrelation function.

 $\mu/w = 1.2$ , U/w = 0.1, (2)  $\mu/w = 0.1$ , U/w = 1.5, and (3)  $\mu/w = 1.5$ , U/w = 0.1. For all three points we fixed L = 22 and considered infinite temperature ( $\beta = 0$ ). For (1) we fixed the bond dimension of the Lanczos series to  $\chi = 1500$ , while for (2) and (3) we used  $\chi = 1000$ . The first point is in the topological region of the model (see Fig. 1), while (2) and (3) are in the Mott insulating and trivial insulating phases, respectively. The results are shown in Figs. 15–17.

In general, we observe that the autocorrelation functions are consistent, even in the trivial and Mott insulating phase, where the correlation function decays rapidly. However, at late times we observe deviations of the TDVP results from the Lanczos series. This can be partially explained by the finite bond dimension of the MPO used in the TDVP algorithm, which leads to an error that increases with the simulated time *t*. However, since the discarded weight, panel (b) of Figs. 15–17, is relatively small up to the considered times, we expect this not to be the only effect.

Another aspect may be the finite size of the system itself. In the Lanczos algorithm, we approximated the unknown coefficients with a semi-infinite lead. This artificially extends the system to an infinite size, removing any kind of finite-size effects from reflected excitations. In the TDVP approach,

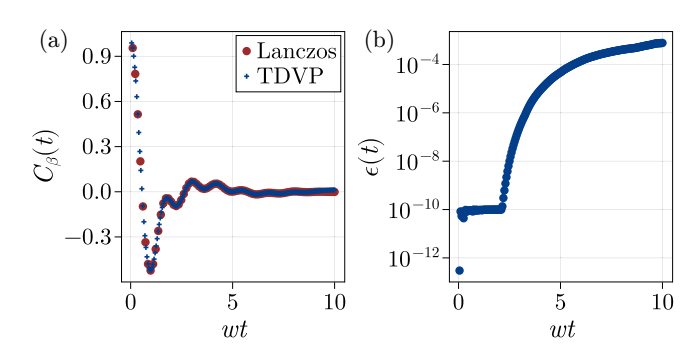


FIG. 16. Comparison between the autocorrelation function obtained from the Lanczos series (red dots) and the TDVP algorithm (blue crosses) at infinite temperature in the Mott insulating region ( $\mu/w=0.2,\,U/w=1.5$ ). Meaning of the panels is the same as in Fig. 15.

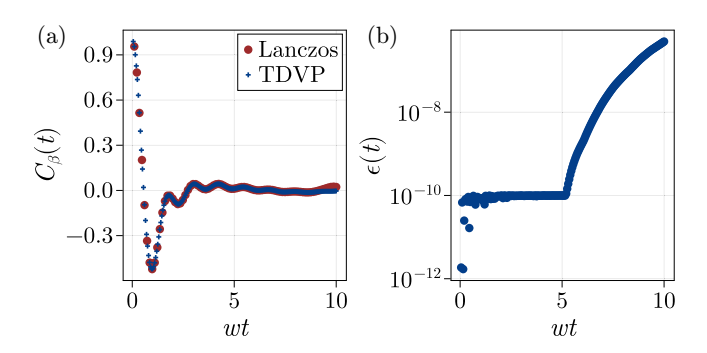


FIG. 17. Comparison between the autocorrelation function obtained from the Lanczos series (red dots) and the TDVP algorithm (blue crosses) at infinite temperature in the trivial insulating region  $(\mu/w=3,\ U/w=0.1)$ . Meaning of the panels is the same as in Fig. 15.

we cannot consider an infinitely extended chain and thus the deviation might originate from these finite-size effects.

We would also like to point out that the time required for the TDVP simulation is linear in the time steps and thus proportional to the final time. For the Lanczos simulation, this is not the case, since we only need to extract a few hundred coefficients to obtain a fairly good result for the time evolution, even at late times. This is especially important for the topological regime where we would like to access very large times  $wt \sim 10^3$  in order to extract the lifetime of the ASZM. For example, the TDVP simulation in Fig. 15 needed 12 hr on a AMD EPYC 74F3 with 24 cores. In the last steps, the time consumption per TDVP iteration saturated around 700 sec. A direct interpolation would give an estimate of ~80 days to complete a TDVP simulation with  $\chi = 512$  up to times of  $wt \sim 10^3$ . Moreover, it is certainly necessary to increase the bond dimension of the TDVP ansatz for these long times in order to obtain reasonable results. For comparison, the Lanczos series with  $\chi = 2000$  (used in Figs. 15–17) took only three days to compute.

#### 4. Gap extraction

We extracted the gaps of the many-body spectrum of the Kitaev-Hubbard model (13) using the density matrix renormalization group (DMRG) [66,67]. With the DMRG we extracted the ground state of the Hamiltonian for the even and odd parity sectors, together with the first excited states within each parity sector. For the extraction of the states we chose a matrix product state ansatz with a maximal bond dimension of  $\chi=200$ . This allows for a good enough estimator of the gap in the thermodynamic limit. However, we observe that for larger system sizes the ansatz is not sufficient to capture the first excited states with very high precision; see Fig. 18.

From the eigenstates  $|\psi_{n,p}\rangle$ , one can obtain the energy for every system size L

$$E_{n,p}(L) = \langle \psi_{n,p} | H | \psi_{n,p} \rangle$$
.

In Fig. 18 we plot the gap :=  $|E_{n,+1} - E_{n,-1}|$  between opposite parity sectors of the ground states n = 0, and the first excited states n = 1, showing that this gap vanishes exponentially in the system size L.

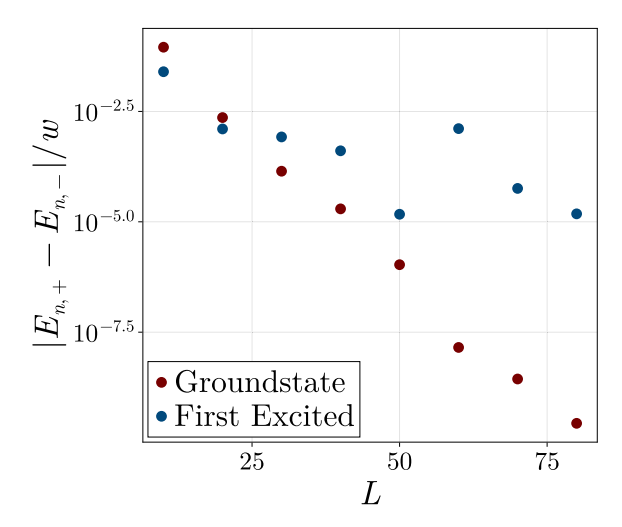


FIG. 18. Energy gaps between different parity sectors for  $\mu/w = 1.2$ , U/w = 0.6, and for various system sizes L. The energy difference between the two ground states of opposite parity vanishes exponentially with the system size. Similarly, the energy difference between the two excited states of opposite parity, vanishes exponentially for smaller system sizes. The noise for larger system sizes can be reduced by increasing the bond dimension.

Next we consider the mass gap  $m_p(L) = E_{1,p}(L) - E_{0,p}(L)$ . From general finite-size scaling one expects

$$m_p(L) = A/L^{\alpha} + \Delta_{\infty},$$
 (F4)

which can be fitted using linear regression in combination with an integral transformation [68]. In Fig. 19 we show that our extracted data shows the desired behavior. By fitting this algebraic decay, we can then extract the thermodynamic energy gap  $\Delta_{\infty}$ .

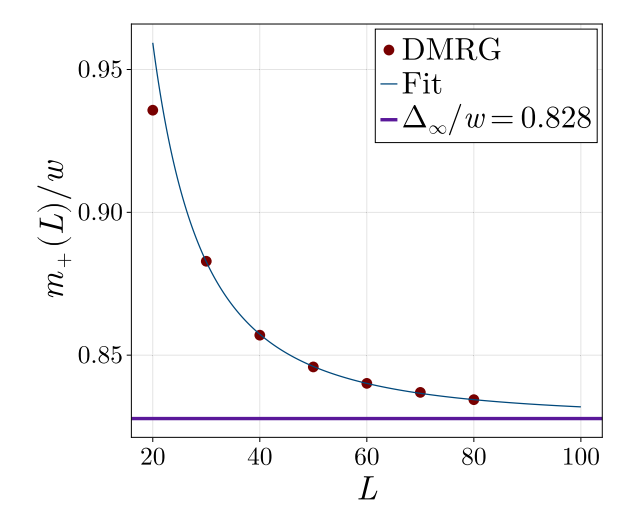


FIG. 19. Energy gap between the ground state and the first excited state in the even parity sector (red dots) for  $\mu/w=1.2$ , U/w=0.6. The blue line is a fit to Eq. (F4), and the horizontal purple line represents the thermodynamic limit of the gap  $\Delta_{\infty}$  extracted from this fit.

## APPENDIX G: DETAILS OF THE IMPLEMENTATION OF THE TRUNCATION

The truncation of the application of  $\mathcal{L}$  on the MPO  $\mathcal{O}_n$  is implemented by truncating the reduced density matrices [49] of the full network  $\mathcal{LO}_n = H\mathcal{O}_n - \mathcal{O}_nH$ . This can easily be understood by rewriting the MPO as a MPS by combining the domain and codomain into a single Hilbert space. This resembles the isomorphism on the local Hilbert space

$$|\sigma'\rangle\langle\sigma|\rightarrow|\sigma',\sigma\rangle:=|\tau\rangle$$
,

which is antilinear in the ket space, and linear in the bra space. We denote the MPS obtained from  $\mathcal{O}_n$  by this isomorphism as  $|\mathcal{O}_n\rangle$ . Under this isomorphism, the commutator  $\mathcal{L}$  becomes a standard MPO with bond dimension K.

Let  $|\Phi\rangle = \mathcal{L} |\mathcal{O}_n\rangle$  denote the MPS one formally obtains by a full contraction of the network given by the right-hand side. The maximal bond dimension of  $|\Phi\rangle$  is  $K*\chi$ , with  $\chi$  being the bond dimension of  $|\mathcal{O}\rangle$  and we would like to determine the most optimal truncation of  $|\Psi\rangle$  back to a bond dimension of  $\chi$ . For this, we start by calculating the reduced density matrix of the last site:

$$\rho_L := \operatorname{Tr}_{L-1}[|\Phi\rangle \langle \Phi|],$$

where  $\operatorname{Tr}_{L-1}$  is the trace over all sites 1 to L-1. In graphical notation

This also defines the environment  $E_k$  containing all the contractions to the left. This environment can be computed iteratively based on the previous environment  $E_{k-1}$ ,

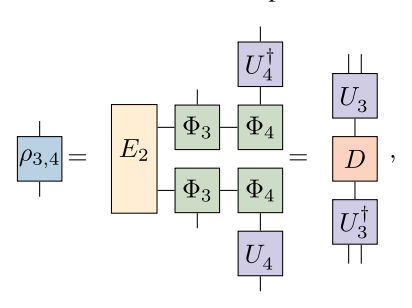
$$E_k = \sum_{\tau} \left( \Phi_k^{\tau} \right)^{\dagger} E_{k-1} \Phi_k^{\tau},$$

where  $\Phi_k^{\tau}$  is the MPS tensor on the *k*th site. This density matrix is now diagonalized, where we keep only at most  $\chi$  eigenstates,

$$\rho = \tilde{U}_L^{\dagger} D \tilde{U}_L,$$

with  $\tilde{U}_L \tilde{U}_L^{\dagger} = 1$ .

The matrix  $\tilde{U}_L^\dagger$  can be seen as the most optimal projection of the physical Hilbert space to at most  $\chi$  degrees of freedom and is the last tensor in our new truncated MPS. We can now construct the two-site reduced density matrix, with the last site transformed into the virtual Hilbert space



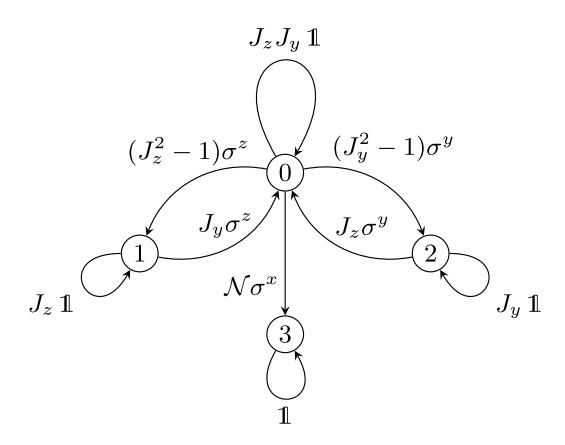


FIG. 20. Finite state machine representation of the SZM of the XYZ model.

which is again diagonalized, followed by truncation of the eigenspace to at most  $\chi$  states.

We can now continue by successively constructing the new reduced density matrix for the sites L-2 to L by projecting the sites L-1 and L onto the virtual Hilbert space. This density matrix is again diagonalized and truncated. We iterate until we reach the last point of the chain, which we simply keep as the last tensor in the new truncated MPS.

Note that the entire iteration does not require a full contraction of  $\mathcal{L} | \mathcal{O}_n \rangle$ , but only the environments, and this can be computed efficiently. Also, the whole procedure does not require an explicit transformation of the MPO into an MPS, and one can work directly with the MPO.

## APPENDIX H: MPO REPRESENTATION OF THE STRONG ZERO MODE IN THE XYZ MODEL

In Ref. [21], Fendley showed that the (integrable) XYZ model without a magnetic field [i.e., Eq. (B2) with g=0] hosts a SZM. Here we present a rewriting of the original rather complicated expression in terms of a MPO with bond dimension four and simple polynomial coefficients [69]. Without loss of generality, we set  $J_x=1$  and assume  $J_y, J_z<1$ : the SZM is then

$$\Gamma = \left( M_{\kappa_{1}',\kappa_{1}}^{0,\alpha_{1}} M_{\kappa_{j}',\kappa_{2}}^{\alpha_{1},\alpha_{2}} \dots M_{\kappa_{N},\kappa_{N}}^{\alpha_{N-1},3} \right) \left| \left\{ \kappa_{j}' \right\} \right\rangle \left\langle \left\{ \kappa_{j} \right\} \right|, \tag{H1}$$

with the operator-valued matrix  $M^{\alpha,\alpha'}$  being

$$M = \begin{pmatrix} J_z J_y 1 & (J_z^2 - 1)\sigma_z & (J_y^2 - 1)\sigma_y & \mathcal{N}\sigma_x \\ 0 & J_z 1 & 0 & J_y \sigma_z \\ 0 & 0 & J_y 1 & J_z \sigma_y \\ 0 & 0 & 0 & 1 \end{pmatrix},$$

and  $\mathcal{N}^2 = (1 - J_y^2)(1 - J_z^2)$ . A graphical representation in terms of a finite-state machine is displayed in Fig. 20. For  $J_z = J_y = 0$ , it reduces to the familiar  $\Gamma = \sigma_1^x$  for the Ising model.

## APPENDIX I: CONSTRUCTION OF STRONG ZERO MODE FROM SPECTRAL DATA

In this Appendix, we review the construction of an (almost) strong zero mode operator  $\Gamma$  from the full set of eigenstates

and eigenenergies of the Hamiltonian H [51]. Because of the parity symmetry, all eigenstates  $|\psi_{n,p}\rangle$  and eigenenergies  $E_{n,p}$  are labeled by their associated parity  $p=\pm 1$ . A general Majorana operator can now be written in this eigenbasis as

$$\Gamma = \sum_{n,m} g_{n,m} |\psi_{n,+1}\rangle \langle \psi_{m,-1}| + \text{H.c.},$$

where  $g \in U(\dim(\mathcal{H})/2)$  is a unitary matrix and  $\mathcal{H}$  is the underlying Hilbert space of the problem. This operator anticommutes with the parity operator and is Hermitian  $\Gamma^{\dagger} = \Gamma$ . Further, one has

$$\begin{split} \Gamma^2 &= \sum_{n,m} (g \, g^\dagger)_{m,n} \, |\psi_{m,+1}\rangle \, \langle \psi_{n,+1}| \\ &+ (g^\dagger g)_{m,n} \, |\psi_{m,-1}\rangle \, \langle \psi_{n,-1}| = \mathbb{1}, \end{split}$$

where the last equality follows from the g being a unitary matrix. Plugging this ansatz into  $\|[\Gamma, H]\|^2$ , one finds

$$\|[\Gamma, H]\|^2 = \sum_{n,m} |g_{n,m}|^2 (\epsilon_n - \epsilon_m)^2.$$

Assuming no degeneracies, this is minimized by  $g_{nm} = g_n \delta_{n,m}$  with  $g_n \in U(1)$  being an arbitrary phase. The fact that the operator is only specified up to some phases also reflects the gauge freedom to redefine states by arbitrary phases  $|\tilde{\psi}_{n,p}\rangle = \exp(i\varphi_{n,p}) |\psi_{n,p}\rangle$ . To obtain a gauge-independent result, the phases  $g_n$  must transform in a certain way when the gauge

is changed:

$$\tilde{g}_n = e^{-i(\varphi_{n,+1} - \varphi_{n,-1})} g_n.$$

We now fix the gauge of each eigenstate by calculating the argument of the overlap with the operator  $\gamma_{1,a} = c_1 + c_1^{\dagger} = X_1$ 

$$\alpha_n := \operatorname{Arg}(\langle \psi_{n,+1} | X_1 | \psi_{n,-1} \rangle),$$

and redefining the states as

$$|\tilde{\psi}_{n,+1}\rangle = e^{i\alpha_n} |\psi_{n,+1}\rangle, \quad |\tilde{\psi}_{n,-1}\rangle = |\psi_{n,-1}\rangle.$$

By fixing the phase of the eigenvectors in this way, the transition operator  $|\tilde{\psi}_{n,+1}\rangle \langle \tilde{\psi}_{n,-1}|$  becomes gauge independent and the Majorana operator minimizing the commutator with the Hamiltonian reads

$$\Gamma = \sum_{n} g_n |\tilde{\psi}_{n,+1}\rangle \langle \tilde{\psi}_{n,-1}| + \text{H.c.}, \quad g_n \in U(1).$$
 (I1)

For any choice of the phases  $g_n$ , Eq. (I1) defines a valid operator with minimal commutator. This reflects the possibility to dress a solution with unitaries generated by a polynomial of the Hamiltonian P(H):

$$\tilde{\Gamma} := e^{iP(H)} \Gamma e^{-iP(H)}.$$

To find a unique solution, we fix the phases by requiring a maximal overlap with the operator  $\gamma_{1,a}$ . This is achieved by setting  $g_n = 1$  for all n. If the spectrum is perfect degenerate between the two parity sectors  $E_{n,p} = E_n$ , the operator  $\Gamma$  has a vanishing commutator with the Hamiltonian. In this case,  $\Gamma$  is a true zero mode.

- [1] A. Y. Kitaev, Unpaired Majorana fermions in quantum wires, Phys. Usp. 44, 131 (2001).
- [2] D. A. Ivanov, Non-Abelian statistics of half-quantum vortices in *p*-wave superconductors, Phys. Rev. Lett. **86**, 268 (2001).
- [3] C. Nayak, S. H. Simon, A. Stern, M. Freedman, and S. Das Sarma, Non-Abelian anyons and topological quantum computation, Rev. Mod. Phys. **80**, 1083 (2008).
- [4] J. Alicea, Y. Oreg, G. Refael, F. von Oppen, and M. P. A. Fisher, Non-Abelian statistics and topological quantum information processing in 1D wire networks, Nat. Phys. 7, 412 (2011).
- [5] S. D. Sarma, M. Freedman, and C. Nayak, Majorana zero modes and topological quantum computation, npj Quantum Inf. 1, 15001 (2015).
- [6] A. Altland and M. R. Zirnbauer, Nonstandard symmetry classes in mesoscopic normal-superconducting hybrid structures, Phys. Rev. B 55, 1142 (1997).
- [7] S. Ryu, A. P. Schnyder, A. Furusaki, and A. W. W. Ludwig, Topological insulators and superconductors: Tenfold way and dimensional hierarchy, New J. Phys. 12, 065010 (2010).
- [8] E. M. Stoudenmire, J. Alicea, O. A. Starykh, and M. P. A. Fisher, Interaction effects in topological superconducting wires supporting Majorana fermions, Phys. Rev. B 84, 014503 (2011).
- [9] H. Katsura, D. Schuricht, and M. Takahashi, Exact ground states and topological order in interacting Kitaev/Majorana chains, Phys. Rev. B 92, 115137 (2015).
- [10] S. Jevtic and R. Barnett, Frustration-free Hamiltonians supporting Majorana zero edge modes, New J. Phys. **19**, 103034 (2017).

- [11] I. Mahyaeh and E. Ardonne, Study of the phase diagram of the Kitaev-Hubbard chain, Phys. Rev. B **101**, 085125 (2020).
- [12] J. Kemp, N. Y. Yao, C. R. Laumann, and P. Fendley, Long coherence times for edge spins, J. Stat. Mech. (2017) 063105.
- [13] D. V. Else, P. Fendley, J. Kemp, and C. Nayak, Prethermal strong zero modes and topological qubits, Phys. Rev. X 7, 041062 (2017).
- [14] D. E. Parker, R. Vasseur, and T. Scaffidi, Topologically protected long edge coherence times in symmetry-broken phases, Phys. Rev. Lett. 122, 240605 (2019).
- [15] J. Kemp, N. Y. Yao, and C. R. Laumann, Symmetry-enhanced boundary qubits at infinite temperature, Phys. Rev. Lett. 125, 200506 (2020).
- [16] D. J. Yates, A. G. Abanov, and A. Mitra, Lifetime of almost strong edge-mode operators in one-dimensional, interacting, symmetry protected topological phases, Phys. Rev. Lett. 124, 206803 (2020).
- [17] D. J. Yates, A. G. Abanov, and A. Mitra, Dynamics of almost strong edge modes in spin chains away from integrability, Phys. Rev. B 102, 195419 (2020).
- [18] H.-C. Yeh, G. Cardoso, L. Korneev, D. Sels, A. G. Abanov, and A. Mitra, Slowly decaying zero mode in a weakly nonintegrable boundary impurity model, Phys. Rev. B 108, 165143 (2023).
- [19] C. T. Olund, N. Y. Yao, and J. Kemp, Boundary strong zero modes, arXiv:2305.16382 [quant-ph] (2023).
- [20] M. Thakurathi, A. A. Patel, D. Sen, and A. Dutta, Floquet generation of Majorana end modes and topological invariants, Phys. Rev. B **88**, 155133 (2013).

- [21] P. Fendley, Strong zero modes and eigenstate phase transitions in the *XYZ*/interacting Majorana chain, J. Phys. A: Math. Theor. **49**, 30LT01 (2016).
- [22] D. J. Yates, F. H. L. Essler, and A. Mitra, Almost strong  $(0, \pi)$  edge modes in clean interacting one-dimensional Floquet systems, Phys. Rev. B **99**, 205419 (2019).
- [23] E. Vernier, H.-C. Yeh, L. Piroli, and A. Mitra, Strong zero modes in integrable quantum circuits, Phys. Rev. Lett. 133, 050606 (2024).
- [24] R. Orús, A practical introduction to tensor networks: Matrix product states and projected entangled pair states, Ann. Phys. 349, 117 (2014).
- [25] V. Viswanath and G. Müller, *The Recursion Method: Application to Many Body Dynamics*, Lecture Notes in Physics Monographs (Springer, Berlin, 1994).
- [26] D. E. Parker, X. Cao, A. Avdoshkin, T. Scaffidi, and E. Altman, A universal operator growth hypothesis, Phys. Rev. X 9, 041017 (2019).
- [27] A. E. Feiguin and S. R. White, Finite-temperature density matrix renormalization using an enlarged Hilbert space, Phys. Rev. B 72, 220401(R) (2005).
- [28] J. Haegeman, J. I. Cirac, T. J. Osborne, I. Pižorn, H. Verschelde, and F. Verstraete, Time-dependent variational principle for quantum lattices, Phys. Rev. Lett. 107, 070601 (2011).
- [29] J. Haegeman, C. Lubich, I. Oseledets, B. Vandereycken, and F. Verstraete, Unifying time evolution and optimization with matrix product states, Phys. Rev. B 94, 165116 (2016).
- [30] I. A. Maceira and F. Mila, Infinite coherence time of edge spins in finite-length chains, Phys. Rev. B **97**, 064424 (2018).
- [31] S. Sachdev, Quantum Phase Transitions, 2nd ed. (Cambridge University Press, Cambridge, 2011).
- [32] P. Fendley, Parafermionic edge zero modes in  $Z_n$ -invariant spin chains, J. Stat. Mech. (2012) P11020.
- [33] J. Alicea and P. Fendley, Topological phases with parafermions: Theory and blueprints, Annu. Rev. Condens. Matter Phys. 7, 119 (2016).
- [34] F. Iemini, C. Mora, and L. Mazza, Topological phases of parafermions: A model with exactly solvable ground states, Phys. Rev. Lett. **118**, 170402 (2017).
- [35] F. Harper, R. Roy, M. S. Rudner, and S. Sondhi, Topology and broken symmetry in Floquet systems, Annu. Rev. Condens. Matter Phys. 11, 345 (2020).
- [36] D. J. Yates and A. Mitra, Strong and almost strong modes of Floquet spin chains in Krylov subspaces, Phys. Rev. B 104, 195121 (2021).
- [37] A. Matthies, J. Park, E. Berg, and A. Rosch, Stability of Floquet Majorana box qubits, Phys. Rev. Lett. 128, 127702 (2022).
- [38] M. Cheng and H.-H. Tu, Majorana edge states in interacting two-chain ladders of fermions, Phys. Rev. B 84, 094503 (2011).
- [39] C. V. Kraus, M. Dalmonte, M. A. Baranov, A. M. Läuchli, and P. Zoller, Majorana edge states in atomic wires coupled by pair hopping, Phys. Rev. Lett. 111, 173004 (2013).
- [40] N. Lang and H. P. Büchler, Topological states in a microscopic model of interacting fermions, Phys. Rev. B 92, 041118(R) (2015).
- [41] F. Iemini, L. Mazza, L. Fallani, P. Zoller, R. Fazio, and M. Dalmonte, Majorana quasiparticles protected by z<sub>2</sub> angular momentum conservation, Phys. Rev. Lett. 118, 200404 (2017).

- [42] F. T. Lisandrini and C. Kollath, Majorana edge modes in a spinful-particle conserving model, Phys. Rev. B 106, 245121 (2022).
- [43] N. Tausendpfund, S. Diehl, and M. Rizzi, Majorana zero modes in fermionic wires coupled by Aharonov-Bohm cages, Phys. Rev. B 107, 035124 (2023).
- [44] A. Defossez, L. Vanderstraeten, L. P. Gavensky, and N. Goldman, Dynamic realization of Majorana zero modes in a particle-conserving ladder, arXiv:2412.14886 [quant-ph] (2024).
- [45] B. Michen, T. Pokart, and J. C. Budich, Adiabatic preparation of a number-conserving atomic Majorana phase, arXiv:2412.15286 [cond-mat.quant-gas] (2024).
- [46] P. Nandy, A. S. Matsoukas-Roubeas, P. Martínez-Azcona, A. Dymarsky, and A. del Campo, Quantum dynamics in Krylov space: Methods and applications, Phys. Rep. 1125, 1 (2025).
- [47] We underline that, for a chain with open boundaries, complex phases of hopping coefficients do not play any role.
- [48] F. Verstraete, J. J. García-Ripoll, and J. I. Cirac, Matrix product density operators: Simulation of finite-temperature and dissipative systems, Phys. Rev. Lett. 93, 207204 (2004).
- [49] I. P. McCulloch, From density-matrix renormalization group to matrix product states, J. Stat. Mech. (2007) P10014.
- [50] A. S. Jermyn, R. S. K. Mong, J. Alicea, and P. Fendley, Stability of zero modes in parafermion chains, Phys. Rev. B 90, 165106 (2014).
- [51] G. Kells, Many-body Majorana operators and the equivalence of parity sectors, Phys. Rev. B 92, 081401(R) (2015).
- [52] G. Kells, Multiparticle content of Majorana zero modes in the interacting *p*-wave wire, Phys. Rev. B **92**, 155434 (2015).
- [53] W. P. Su, J. R. Schrieffer, and A. J. Heeger, Solitons in polyacetylene, Phys. Rev. Lett. 42, 1698 (1979).
- [54] W. P. Su, J. R. Schrieffer, and A. J. Heeger, Soliton excitations in polyacetylene, Phys. Rev. B 22, 2099 (1980).
- [55] F. Hassler and D. Schuricht, Strongly interacting Majorana modes in an array of Josephson junctions, New J. Phys. 14, 125018 (2012).
- [56] J. D. Sau, B. I. Halperin, K. Flensberg, and S. Das Sarma, Number conserving theory for topologically protected degeneracy in one-dimensional fermions, Phys. Rev. B 84, 144509 (2011).
- [57] L. Fidkowski, R. M. Lutchyn, C. Nayak, and M. P. A. Fisher, Majorana zero modes in one-dimensional quantum wires without long-ranged superconducting order, Phys. Rev. B 84, 195436 (2011).
- [58] G. Kells, N. Moran, and D. Meidan, Localization enhanced and degraded topological order in interacting *p*-wave wires, Phys. Rev. B 97, 085425 (2018).
- [59] Jülich Supercomputing Centre, JUWELS Cluster and Booster: Exascale pathfinder with modular supercomputing architecture at JSC, J. Large-Scale Res. Facilities 7, A183 (2021).
- [60] Jülich Supercomputing Centre, JURECA: Data Centric and Booster modules implementing the modular supercomputing architecture at JSC, J. Large-Scale Res. Facilities 7, A182 (2021).
- [61] M. Fishman, S. R. White, and E. M. Stoudenmire, The ITensor software library for tensor network calculations, SciPost Phys. Codebases, 4 (2022).

- [62] N. Tausendpfund, A. Mitra, and M. Rizzi, Data and code associated to the paper "Almost strong zero modes at finite temperature" [Data set], Zenodo (2025), https://doi.org/10.5281/ zenodo.14752714.
- [63] P. Jordan and E. Wigner, Über das paulische Äquivalenzverbot, Z. Phys. **47**, 631 (1928).
- [64] E. Lieb, T. Schultz, and D. Mattis, Two soluble models of an antiferromagnetic chain, Ann. Phys. 16, 407 (1961).
- [65] Karim M. Abadir, Jan R. Magnus, and Peter C. B. Phillips, Rank, inverse, and determinant, in *Matrix Algebra*, Econometric Exercises (Cambridge University Press, Cambridge, 2005), pp. 97–130.
- [66] S. R. White, Density matrix formulation for quantum renormalization groups, Phys. Rev. Lett. **69**, 2863 (1992).
- [67] U. Schollwöck, The density-matrix renormalization group in the age of matrix product states, Ann. Phys. **326**, 96 (2011).
- [68] J. Jacquelin, Régressions et Équations Intégrales (2009), https://www.scribd.com/doc/14674814/Regressions-etequations-integrales.
- [69] In a private communication, Paul Fendley mentioned a more general family of nontrivial MPOs of bond dimension-four commuting with the *XYZ* Hamiltonian, of which the SZM is a special case.

# Almost Strong Zero Mode in Number Conserving Kitaev Chains

In this chapter, we apply the algorithm developed in Chapter IV to the class of Hamiltonians that realizes the Symmetry-Protected Topological Phase (SPTP) of unpaired Majorana Zero Mode (MZM) without breaking particle conservation. For example, the model studied in Chapter I belongs to this class. We explore how the additional U(1) symmetry and the emergence of gapless density fluctuations influence the behavior of the Almost Strong Zero Mode (ASZM).

### V.1 Introduction

The model used in Chapter IV to test the tensor-network algorithm for extracting the temperature-dependent lifetime of the ASZM was the Kitaev-Hubbard Model (KHM) of spinless fermions from Eq. (1.110). This model breaks particle number conservation owing to the creation and annihilation of pairs of spinless fermions  $\Delta c_j c_{j+1} + \text{h.c.}$ .

Compared to the Kitaev chain in Eq. (1.87), the presence of the additional Hubbard interaction  $U\hat{n}_j\hat{n}_{j+1}$  breaks integrability. When tuned to the correct parameter regime, see also Fig.(1) of [148], the KHM enters a topological phase protected by the fermionic parity  $\hat{P}$  with a doubly degenerate ground state and the emergence of MZMs. As found in Chapter IV, the MZMs extend to ASZMs at finite temperatures with long but finite lifetimes. In particular, the lifetime diverges exponentially when approaching the zero-temperature limit.

In contrast, the model proposed in Chapter I does not break the conservation of particles, and the  $\overline{\text{SPTP}}$  is instead realized by the existence of coherent pair-tunneling between two fermionic species a and b described by

$$H_{\text{pair}} = W \sum_{j=1}^{N-1} a_j^{\dagger} a_{j+1}^{\dagger} b_{j+1} b_j + \text{h.c.}.$$
 (V.1)

As a result, the total symmetry group of this model is  $G = U(1) \times \mathbb{Z}_2$ , where the U(1) is the conservation of the total density, and the  $\mathbb{Z}_2$  is the conservation of the

parity of the a flavored fermions. The two conserved operators are given by

$$\hat{P}_a = e^{i\pi \sum_{j=1}^N \hat{n}_j^a}, \quad \hat{N} = \sum_{j=1}^N \hat{n}_j^a + \hat{n}_j^b.$$
 (V.2)

As shown by Kraus et al. [160], a simple model of two chains coupled by the pair hopping term of Eq. (V.1) according to

$$H = -t \sum_{j=1}^{N-1} a_{j+1}^{\dagger} a_j + b_{j+1}^{\dagger} b_j + \text{h.c.} + H_{\text{pair}}$$
 (V.3)

can enter the SPTP with MZMs emerging at the edges for the correct choice of parameter.

From a low-energy analysis of this class of number-conserving Kitaev chains, it is found that local fluctuations of the total density are described by a gapless Tomonaga-Luttinger Liquid (TLL); see also Section 1.3 for a detailed review of the TLL. The question arises as to how this additional gapless part of the theory influences the lifetimes of edge excitations associated with the MZM and whether there is an ASZM in these number-conserving Kitaev chains, similar to the KHM, or whether the MZM exists only in the ground-state manifold. This is of particular interest if the model is realized in a dynamical way, for example, by Floquet engineering as proposed by the authors of [297], or by an adiabatic preparation protocol as proposed in [165].

To approach this question, we chose the one-parameter group of Hamiltonians proposed by Iemini et al. in [166] given by

$$\begin{split} H_{\lambda} &= -4w \sum_{j=1}^{N-1} \sum_{\alpha = a,b} \left[ \left( \alpha_{j}^{\dagger} \alpha_{j+1} + \text{h.c.} \right) - \left( \hat{n}_{j}^{\alpha} + \hat{n}_{j+1}^{\alpha} \right) + \lambda \, \hat{n}_{j}^{\alpha} \hat{n}_{j+1}^{\alpha} \right] \\ &- 2w \lambda \sum_{j=1}^{N-1} \left[ \left( \hat{n}_{j}^{a} + \hat{n}_{j+1}^{a} \right) \left( \hat{n}_{j}^{b} + \hat{n}_{j+1}^{b} \right) - \left( a_{j}^{\dagger} a_{j+1} b_{j}^{\dagger} b_{j+1} \right. \right. \\ &\left. + a_{j}^{\dagger} a_{j+1} b_{j+1}^{\dagger} b_{j}^{\dagger} - 2 a_{j}^{\dagger} a_{j+1}^{\dagger} b_{j+1} b_{j} + \text{h.c.} \right) \right] \,, \end{split}$$
 (V.4)

where w is an arbitrary energy scale. This group of Hamiltonians commutes with the two symmetry operators from Eq. (V.2), and thus has the correct symmetry group  $G = U(1) \times \mathbb{Z}_2$ .

Compared to the simpler pair-hopping Hamiltonian in Eq. (V.3) discussed by Kraus et al. in [160], or the effective model derived in Chapter I, the Hamiltonian from Eq. (V.4) has more complex coupling terms<sup>1</sup>. However, Iemini et al. [298] showed that this model is in the SPTP for all  $\lambda \leq 1$ , independent of the total density of particles in the chain. Furthermore, they demonstrated that for  $\lambda = 1$ , the ground state of this Hamiltonian can be solved analytically, allowing for writing down the exact MZM emerging in the ground-state manifold.

This MZM has a finite overlap with the operator

$$\hat{X}_1 = i \left( a_1^{\dagger} b_1 - b_1^{\dagger} a_1 \right) , \qquad (V.5)$$

which we will use as a seed operator for the generation of the Lanczos sequence, as discussed in Section 1.5 and Chapter IV. The phase diagram of this model is shown in Fig. V.1.

<sup>&</sup>lt;sup>1</sup> See Figure (8) in our publication [33] for a sketch relating the three different models.

V.2. RESULTS 193

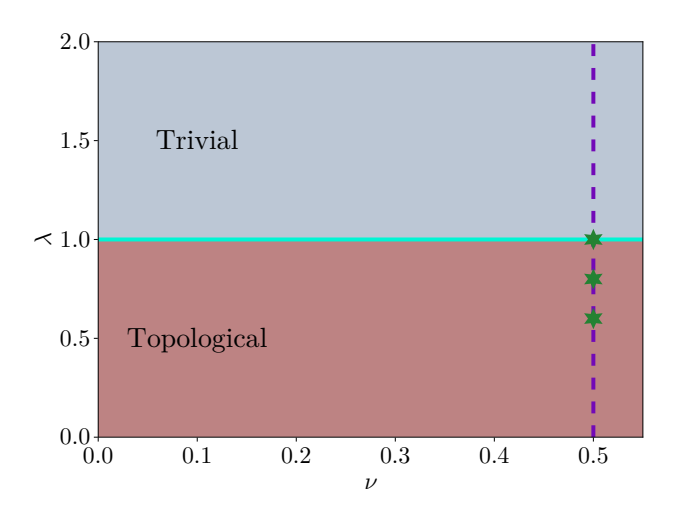


Figure V.1: Phase diagram of the Hamiltonian in Eq. (V.4) following [166] as a function of the coupling  $\lambda$  and the density  $\nu \coloneqq (N^a + N^b)/(2N)$ . The line  $\lambda = 1$  represents an exactly solvable line. For  $\lambda > 1$ , the model enters a trivial phase, while it is topological for all  $\lambda \le 1$  and all densities  $\nu \ne 0, 1$ . The phase diagram is symmetric with respect to  $\nu = 0.5$ . The green stars represent the three parameters considered in this study.

### V.2 Results

To determine whether this operator also yields an ASZM, we calculate the Lanczos series at various temperatures, similar to the findings presented in Chapter IV. Specifically, we compute the Lanczos series of the Hamiltonian in Eq. (V.4) at three exemplary points,  $\lambda/w=0.6,0.8,1.0$ , for a system size of N=24, utilizing the tensor network ansatz introduced in Chapter IV. For the Matrix Product Operators (MPOs) that approximate the Lanczos operators, we selected a maximum bond dimension of  $\chi=2000$ .

The generic properties of the obtained series are similar to the results obtained in the case of the KHM in Chapter IV. These properties are explained in the following using  $\lambda = 0.8w$ . Figure V.2 shows the first 50 Lanczos coefficients for different inverse temperatures  $\beta = 1/T$ . For all temperatures, the Lanczos coefficients show

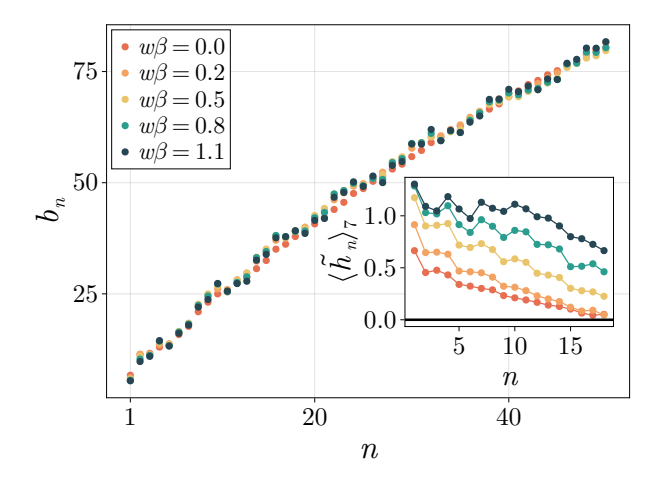


Figure V.2: Lanczos coefficients for N=24 at various inverse temperatures  $\beta=1/T$ . The inset shows the staggered component  $\tilde{h}_n$  from Eq. (V.7).

the universal increasing trend  $b_n \sim n$ . In contrast, for the KHM considered in Chap-

ter IV it was found that the increase becomes slower with decreasing temperature. This difference can be interpreted as follows: lowering the temperature effectively projects the operator dynamics onto a low-energy Hilbert space. In the KHM, the finite many-body gap ensures that this projection leads to a decreasing number of states that are relevant for the dynamics. In contrast, the Hamiltonian in Eq. (V.4) features a dense spectrum without a many-body gap, and projecting the operator dynamics onto a low-energy Hilbert space encompasses an infinite number of states. Consequently, the Lanczos series embodies the full complexity of a non-integrable many-body system, aligning with the universal operator growth hypothesis [222, 223], as discussed in Section 1.5. Another difference between the Hamiltonian considered here and the KHM considered in Chapter IV is that the Lanczos series does not saturate to a plateau value in the first 50 Lanczos coefficients. This behavior is anticipated for any finite-size many-body Hamiltonian and is expected to persist with a larger number of coefficients in this model as well.

In addition to this background increase, the series is dressed by a staggered component  $\tilde{h}_n$  defined in Eq. (1.186), repeated here for completeness

$$b_n \approx h_n + (-1)^n \tilde{h}_n \,, \tag{V.6}$$

where  $h_n$  is the monotonically increasing background. To isolate the staggered component  $\tilde{h}_n$ , we model the background using a linear function,  $h_n \approx An + B$ , for values of n greater than 20. The staggering component is then approximated by

$$\tilde{h}_n \approx (-1)^{n+1} (b_{n+1} - b_n - A)/2$$
. (V.7)

The inset of Fig. V.2 shows the extracted staggered component. For all temperatures,  $\tilde{h}_n$  is a decreasing function of n, which eventually becomes zero at  $n^\star$ . After this point, the staggering component becomes trivial, that is, either negative or oscillates around zero. Increasing  $\beta$  results in an overall increase in the staggered component, while simultaneously shifting the point  $n^\star$ , at which the staggered component becomes trivial, to higher values of n. As discussed in Section 1.5, and also in Chapter IV, the artificial single particle Hamiltonian associated to this Lanczos series given by

$$H_{\rm sp} = \sum_{n=0}^{\infty} i b_{n+1} |n+1\rangle \langle n| + \text{h.c.},$$
 (V.8)

see also Eq. (1.180), is that of a dressed Su–Schrieffer–Heeger Model (SSHM). Because the background is constant for all the different temperatures, the main influence on the Edge Density of States (EDOS) of this artificial single-particle Hamiltonian is given by the staggered component. As a reminder, the EDOS  $\nu_{\beta}^{E}(\omega)$ , as defined in Eq. (1.182), represents the density of states of the artificial Hamiltonian projected onto the first site. This density of states entirely determines the Autocorrelation Function (ACF) of the edge operator  $\hat{X}_{1}$  through Eq. (1.183)

$$C_{\beta}(\hat{X}_{1}, t) = \int_{-\infty}^{\infty} d\omega \, \nu_{\beta}^{E}(\omega) \cos(\omega t). \tag{V.9}$$

The EDOS is calculated from the obtained Lanczos series by applying the same methods as in Chapter IV.

Figure V.3(a) shows the EDOS for the Lanczos coefficients of Fig. V.2. For all temperatures, the EDOS has a sharp Lorentzian peak around zero energy, combined with an incoherent, exponential decreasing background

$$\nu^E_\beta = A(\beta) \frac{\gamma(\beta)/\pi}{\omega^2 + \gamma^2} + (1 - A(\beta)) \tilde{\nu}_\beta(\omega) \,. \label{eq:nu_beta}$$

V.2. RESULTS 195

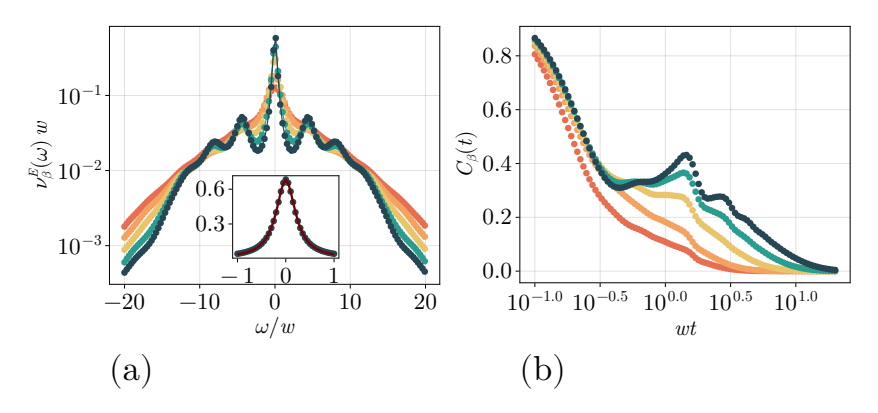


Figure V.3: (a) EDOS obtained from the Lanczos coefficients at the finite temperatures from Fig. V.2 with the same color codes. The inset in the middle shows a fit of the central Lorentzian peak for  $w\beta = 1.1$ . (b) ACF reconstructed from the EDOS from panel (a).

Increasing  $\beta$  only slightly affects the shape of the background, with the emergence of additional sidebands at some finite energy. On the other hand, the Lorentzian peak becomes narrower with  $\gamma(\beta)$  decreasing for  $\beta \to \infty$ . However, the initial width  $\gamma(\beta=0)$  is a few orders of magnitude smaller than that in the case of the KHM studied in Chapter IV. Even for the largest  $\beta$  considered in Fig. V.3(a), the width parameter is only of order one. Consequently, the ASZM is extremely weak, and to observe a long coherence time for the edge operator  $\hat{X}_1$ , Eq. (V.5), it is necessary to reach very low temperatures.

This can be seen more directly by looking at the ACF reconstructed from the EDOS using Eq. (V.9), as shown in Fig. V.3(b). In the infinite temperature limit  $\beta \to 0$ , the ACF has only a very weak intermediate plateau after the initial transient decay and reaches zero at time scales of order unity. Lowering the temperatures leads to the formation of a clearer plateau; however, the smallness of  $\gamma(\beta)$  still leads to the decay of the ACF after a time  $t^* \sim 10w$ .

The temperature dependence of the width parameter can be studied more quantitatively by fitting the central Lorentzian and extracting the temperature dependence of  $\gamma(\beta)$ . An example of such a fit is shown in the inset of Fig. V.3(a).

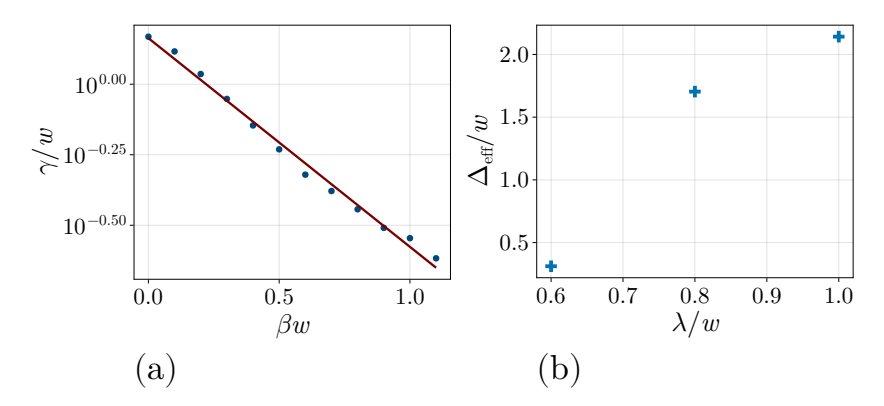


Figure V.4: (a) Extraction of the effective energy gap  $\Delta_{\text{eff}}$  by fitting the width parameter to Eq. (V.10), shown for  $\lambda = 0.8w$ . (b) Effective gaps for three different parameters  $\lambda/w = 0.6, 0.8, 1.0$ .

Figure V.4(a) shows the extracted values of the width parameter at the simulated temperatures. From this plot, it is clear that  $\gamma(\beta)$  decays exponentially with the

inverse temperature

$$\gamma(\beta) = \gamma_0 e^{-\Delta_{\text{eff}}\beta} \tag{V.10}$$

similar to the case of the KHM studied in Chapter IV. Although the width remains relatively narrow at high and intermediate temperatures, this indicates an exponential divergence in the lifetime  $\tau(\beta) = 1/\gamma(\beta)$  for excitations produced by the operator  $\hat{X}_1$  as the temperature approaches zero. While this behavior is anticipated for local excitations in gapped many-body Hamiltonians [299], it is not immediately clear that a similar principle applies to the gapless Hamiltonian in Eq. (V.4). The quantity  $\Delta_{\rm eff}$  can be understood as an effective gap for the ASZM. By fitting the exponential decay, the red line in Fig. V.4(a), this effective gap is found to be  $\Delta_{\rm eff} \approx 1.7 w$  with  $\gamma_0 \approx 1.4 w$ .

The same behavior is observed also for the other parameters,  $\lambda=0.6w$  and  $\lambda=w$ , and the extracted effective gaps for these three parameters are shown in Fig. V.4(b). It is observed that  $\Delta_{\rm eff}$  has a non-trivial dependence on the coupling parameter  $\lambda$ , reaching its maximum for  $\lambda=w$ .

### V.3 Conclusion

We demonstrated that the MZMs emerging in a number-conserving setup extend to ASZM at finite temperatures. However, this ASZM is very weak compared to their counterparts found in models that break the conservation of fermions, such as the KHM, in the sense that their lifetime is comparable to generic bulk excitations at large and intermediate temperatures. The main reason for the decrease of the lifetime is probably the coupling of the MZM to the gapless charge excitations at higher energies.

In future research, it would be interesting to extend the results presented here by considering a broader range of parameters. Furthermore, the low-energy description of the model predicts the MZM to appear in the anti-bonding sector, Eq. (1.143), of the theory. Therefore, it would be worthwhile to compare the effective energy gap  $\Delta_{\rm eff}$  with the gap directly in the anti-bonding sector. This comparison can be conducted relatively easily using the techniques developed in Subsection 2.2.2, similar to the results obtained in Chapter II.

Furthermore, the results presented only consider one specific bond dimension  $\chi$  for the MPO ansatz. As the computation of the Lanczos series is considerably harder for the coupled wire system, with the bond dimension quickly reaching this limit, considering larger bond dimensions was out of reach for this study. To strengthen the results obtained here, it would be beneficial to examine how the lifetime depends on the selected bond dimension. For instance, as discussed in Chapter IV, the lifetime of the ASZM in the KHM was only marginally affected by increasing the bond dimension of the MPO ansatz for the Lanczos operators. Here, it remains unclear how the gapless mode impacts the convergence of the lifetime concerning the bond dimension. Because  $\chi=2000$  is already a large bond dimension, a first check would be to lower the bond dimension and monitor the change in the lifetime. Performing such a large-scale numerical simulation is left for future studies.

# Variational Ansatz for Strong Zero Modes

In this chapter, we develop a variational ansatz that can be used to search for Strong Zero Modes (SZMs) and Almost Strong Zero Modes (ASZMs) in arbitrary models. The ansatz is a unitary circuit tailored to directly operate on the correct manifold of Majorana operators.

### VI.1 Introduction

Consider an open quantum chain of length N, populated by spinless fermions and described by a Hamiltonian H that commutes only with the fermionic parity  $\hat{P}$ . As detailed in Subsection 1.5.1, this Hamiltonian has a SZM if there exists a Hermitian operator  $\Gamma$  that fulfills the conditions

- C.1 Normalizability:  $\Gamma^2 = 1$
- C.2 Anti-commutation with the parity operator:  $\{\Gamma, \hat{P}\} = 0$
- C.3 Localized at position 1
- C.4 Commuting with the Hamiltonian for  $N \to \infty$ :  $[H, \Gamma] = \hat{R}$ ,  $||\hat{R}|| \sim e^{-\lambda N}$

The existence of such SZM was explicitly demonstrated in the integrable limits of the Kitaev-Hubbard Model (KHM) by solving the linear equation

$$\mathcal{L}(\Gamma) := [H, \Gamma] = 0 \tag{VI.1}$$

for an operator that meets the conditions C.1-C.3 [84, 224].

Rather than directly solving the linear equation (VI.1), the task of identifying an SZM within a model can alternatively be formulated as a minimization problem over the constrained set of operators

$$\mathcal{M} = \left\{ \Gamma: \mathcal{H} \to \mathcal{H} \mid \Gamma^\dagger = \Gamma \,, \ \Gamma^2 = \mathbb{1} \,, \ \{\hat{P}, \Gamma\} = 0 \right\} \,. \tag{VI.2}$$

This set, referred to as the Majorana manifold hereafter, incorporates conditions C.1 and C.2, which define  $\Gamma$  as a Majorana operator. The cost function to be minimized is the commutator functional

$$\mathcal{F}(\Gamma) = \frac{1}{2^{N}} \operatorname{Tr} \left[ \mathcal{L} \left( \Gamma \right)^{\dagger} \mathcal{L} \left( \Gamma \right) \right] = \left\langle \mathcal{L}(\Gamma), \mathcal{L}(\Gamma) \right\rangle, \Gamma \in \mathcal{M}, \tag{VI.3}$$

where  $\langle \hat{O}, \hat{K} \rangle$  represents the Frobenius scalar product, as defined in Eq. (1.9). We aim to find solutions that are localized to the first site of the chain to satisfy condition C.3. Because this functional represents the inner product of the left-hand side of Eq. (VI.1), it is positive semi-definite,  $\mathcal{F}(\Gamma) \geq 0$ , and is minimized by the SZM, provided such an operator exists.

Note that condition C.1,  $\Gamma^2=1$ , is important for obtaining an operator that acts on the entire many-body Hilbert space. Let  $|\Omega_{\pm}\rangle$  be the two ground states of the fermionic chain of opposite parity, dropping this condition allows for the definition of a pseudo-Majorana operator

$$\tilde{\Gamma} = |\Omega_{+}\rangle \langle \Omega_{-}| + |\Omega_{-}\rangle \langle \Omega_{+}| , \qquad (VI.4)$$

that minimizes Eq. (VI.3) if the model has a degenerate ground-state manifold, as in the case of an Symmetry-Protected Topological Phase (SPTP). This pseudo-Majorana operator anti-commutes with the parity operator,  $\{\tilde{\Gamma}, \hat{P}\} = 0$ , and is Hermitian, as indicated by  $\tilde{\Gamma}^{\dagger} = \tilde{\Gamma}$ . Furthermore, if the degeneracy arises from an SPTP, this operator is localized to the first site; see also the discussion at the end of Subsection 1.2.3 and Eq. (1.109), thereby satisfying all conditions C.2–C.4. However, when squared, it becomes the projector on the ground-state manifold, expressed as  $\tilde{\Gamma}^2 = |\Omega_+\rangle \langle \Omega_+| + |\Omega_-\rangle \langle \Omega_-|$ .

In the next section, we present a tensor-network ansatz that directly operates in the Majorana manifold to solve the numerical minimization of the commutator functional. This ansatz is motivated by the observation that the SZM in the integrable limits of the KHM is efficiently represented by a Matrix Product Operator (MPO) with a small, finite bond dimension; see also Appendix H of our publication [37]. Away from the integrable limits, the SZM becomes an ASZM [214, 217, 218] that only approximately commutes with the Hamiltonian. In this case, the variational minimization of the functional in Eq. (VI.3) should saturate to a small, constant value  $\mathcal{F}_0$  which depends on the microscopic details of the model.

## VI.2 Matrix Product Operator Ansatz

A general, but naive, MPO ansatz for the ASZM reads

As discussed before, the operator  $\Gamma$  should be a Majorana operator, and explicitly, it should square to the identity  $\Gamma^2 = \mathbb{1}$  (condition C.1). At the level of the MPO, this requires that the operator  $\Gamma$  is a special matrix product unitary [300, 301], and changing a tensor locally can easily destroy the unitary nature of  $\Gamma$ .

A straightforward solution might be to drop condition C.1. The ansatz can then be directly employed to minimize the commutator functional  $\mathcal{F}(\Gamma)$  from Eq. (VI.3) by iteratively minimizing the local tensors until a fixed point is reached, akin to the Density-Matrix Renormalization Group [60]. This method, as used in [38], has the drawback that the operator derived from this algorithm is not necessarily required to

act on the entire many-body Hilbert space because pseudo-Majorana operators, such as those in Eq. (VI.4) are allowed. As a transition between the two ground states, the operator in Eq. (VI.4) is anticipated to have a small MPO bond dimension  $\chi=2\tilde{\chi}$ , where  $\tilde{\chi}$  is the bond dimension needed to accurately represent the two ground states  $|\Omega_{\pm}\rangle$ , and the algorithm might erroneously converge to this operator during minimization. Moreover, iterative minimization may not produce operators that are necessarily localized at the edge of the chain, as required by condition C.3.

To circumvent this issue, we opted for an alternative strategy that directly incorporates all the conditions in the ansatz, albeit necessitating more sophisticated methods to determine the minimum of the commutator functional  $\mathcal{F}(\Gamma)$ . The idea is to selecting a seed operator  $\Gamma_0 \in \mathcal{M}$  and dressing it with a unitary  $\mathcal{U}$  that commutes with the parity operator P according to

$$\Gamma(\mathcal{U}) = \mathcal{U}\Gamma_0 \mathcal{U}^{\dagger}, \quad [\mathcal{U}, \hat{P}] = 0.$$
 (VI.6)

By construction, this operator is in the Majorana manifold, as the unitary  $\mathcal{U}$  preserves the global properties of the seed operator  $\Gamma_0$ . The commutation functional of Eq. (VI.3) becomes a functional of the unitary  $\mathcal{U}$  and its conjugated  $\mathcal{U}^{\dagger}$ 

$$\frac{1}{2}\mathcal{F}(\mathcal{U},\mathcal{U}^{\dagger}) = \langle H_{\rm KH}, H_{\rm KH} \rangle - \langle H_{\rm KH} \mathcal{U} \Gamma_0 \mathcal{U}^{\dagger}, \mathcal{U} \Gamma_0 \mathcal{U}^{\dagger} H_{\rm KH} \rangle \geq 0 \,. \tag{VI.7}$$

A suitable seed operator<sup>1</sup> is given by  $\sigma_1^x$  which can be written as an exact tensor network of bond dimension  $\chi = 1$ 

Furthermore, this operator is localized to the first site of the chain, thus fulfilling condition C.3.

The final step is to approximate the full many-body unitary  $\mathcal U$  using a circuit composed of two-body unitaries. This circuit consists of  $n_{\text{Laver}}$  layers

$$\mathcal{U} = \prod_{l=1}^{n_{\mathrm{Layer}}} \mathcal{U}_{n_{\mathrm{Layer}}-l+1} = \mathcal{U}_{n_{\mathrm{Layer}}} \mathcal{U}_{n_{\mathrm{Layer}}-1} \dots \mathcal{U}_2 \mathcal{U}_1 \,,$$

where each layer  $\mathcal{U}_l$  has the structure of a ladder<sup>2</sup>

$$\mathcal{U}_l = \begin{array}{|c|c|} \hline u_{3,4}^l \\ \hline u_{2,3}^l \\ \hline u_{1,2}^l \\ \hline \end{array} \quad \cdots \quad . \tag{VI.9}$$

The two-body unitary is denoted by  $u_{j,j+1}^l$ , where  $(s_j, s_{j+1})$  is the pair of indices on which the unitary acts. Every layer of this unitary circuit has the property of being

 $<sup>\</sup>sigma_1^x$  becomes  $\gamma_1^a$  in the fermionic picture under Jordan-Wigner transformation.

<sup>&</sup>lt;sup>2</sup> It may be more natural to use a brick-wall circuit instead of the ladder structure proposed here. However, because the seed operator in Eq. (VI.8) only acts non-trivially on the first site, most of the unitary matrices appearing in the brick wall circuit would cancel, and the effective structure that remains is the circuit proposed here.

local in the sense that  $\mathcal{U}_l \sigma_1^x \mathcal{U}_l^{\dagger}$  remains localized to the first site, as long as the first two-body unitary has a finite identity component  $u_{1,2}^l = a \, \mathbbm{1} + \dots$ , a > 0. Thus, if the circuit consists of only a finite number of layers, the ansatz in Eq. (VI.6) still fulfills the localization condition  $\mathbb{C}.3$ .

To ensure that the global unitary U preserves the parity,  $[\hat{P}, \mathcal{U}] = 0$ , the local unitary matrices are chosen to individually commute with the parity  $[\hat{P}, u^l_{j,j+1}] = 0$ . On the level of the tensors, this is explicitly enforced by using symmetric tensors that transform under the parity as

$$\frac{\left(\begin{array}{c} \sigma^{z} \\ \sigma^{z} \end{array}\right)}{\left(\begin{array}{c} u_{j,j+1}^{l} \\ \sigma^{z} \end{array}\right)} = \frac{\left(\begin{array}{c} u_{j,j+1}^{l} \\ \sigma^{z} \end{array}\right)}{\left(\begin{array}{c} \sigma^{z} \\ \sigma^{z} \end{array}\right)}$$

as discussed in Subsection 2.2.3.

Applying this circuit to the  $\Gamma_0$  in Eq. (VI.8), without truncation results in an MPO of bond dimension

$$\chi = 4^{n_{\text{Layer}}}. (VI.10)$$

This allows us to control the expressible power of the ansatz by tuning the number of layers.

In the following, we test the proposed ansatz exemplary on the KHM defined in Eq. (1.110) for  $\Delta_p = w$ , similar to Chapter IV. To formulate the tensor network, it is beneficial to consider the spin dual of the KHM obtained after using the Jordan-Wigner transformation introduced in Subsection 1.1.5. In the spin language, the KHM becomes

$$H_{\rm KH} = \sum_{j=1}^{N-1} -w \sigma_j^x \sigma_{j+1}^x + U \sigma_j^z \sigma_{j+1}^z + \frac{\mu}{2} \sum_{j=1}^{N-1} \sigma_j^z, \qquad (VI.11)$$

which commutes with the parity operator  $\hat{P} = \prod_{j} (-\sigma_{j}^{z})$ .

## VI.3 Exact Solution in the Integrable Limits

In the limit of U=0, the KHM becomes a non-interacting Kitaev chain that exhibits an SZM for  $|\mu| < 2w$ . The SZM, after the Jordan-Wigner transformation, can be represented by an MPO of bond dimension  $\chi=2$  given by the tensors

$$W^{j} = \begin{pmatrix} \frac{\mu}{2w} \sigma^{z} & \mathcal{N}\sigma^{x} \\ 0 & \mathbb{1} \end{pmatrix}, \quad W^{1} = \begin{pmatrix} \frac{\mu}{2w} \sigma^{z} & \mathcal{N}\sigma^{x} \end{pmatrix}, \quad W^{N} = \begin{pmatrix} \mathcal{N}\sigma^{x} \\ \mathbb{1} \end{pmatrix}$$
(VI.12)

in the notation of Chapter 2. Here,  $\mathcal{N}$  is an overall normalization constant that ensures  $\Gamma^2 = \mathbb{1}$ . The tensor network ansatz of Eq. (VI.6) should reproduce this exact MPO with  $n_{\text{Layer}} = 1$ , based on Eq. (VI.10). A direct calculation, see Appendix D for the details, shows that this is true and can be achieved by parameterizing the unitary  $u_{i,i+1}^1$  as

$$u_{j,j+1}^1 = e^{i\alpha_j\sigma_j^y\sigma_{j+1}^x} = \cos(\alpha_j)\,\mathbbm{1} + i\sin(\alpha_j)\sigma_j^y\sigma_{j+1}^x \tag{VI.13}$$

where the rotation angle is defined by  $(j \leq N-1)$ 

$$\tan(2\alpha_j)^2 = \frac{\rho^2}{1-\rho^2} \left(1-\rho^{2(N-j)}\right), \quad \rho = \frac{\mu}{2w}.$$
 (VI.14)

In the thermodynamic limit  $N \to \infty$ , the angles  $\alpha_j$  become position-independent, and every unitary in the circuit has the same shape.

In the other integrable limit  $\mu = 0$ , the SZM can be represented by an MPO with a bond-dimension  $\chi = 3$ 

$$W^{j} = \begin{pmatrix} 0 & \sigma^{y} & \mathcal{N}\sigma^{x} \\ -\frac{U}{w}\sigma^{y} & 0 & 0 \\ 0 & 0 & 1 \end{pmatrix}, \quad W^{1} = \begin{pmatrix} 0 & \sigma^{y} & \mathcal{N}\sigma^{x} \end{pmatrix}, \quad W^{N} = \begin{pmatrix} \mathcal{N}\sigma^{x} \\ 0 \\ 1 \end{pmatrix}. \tag{VI.15}$$

Similar to the U=0 case, an ansatz with  $n_{\text{Layer}}=1$  should be sufficient to reproduce this MPO. Again, a direct calculation, presented in Appendix D, shows that this is true. However, in contrast to the U=0 case, the unitary circuit has an alternating structure of unitaries acting differently on the odd-even index pairs (2j-1,2j) and even-odd index pairs (2j,2j+1). The two different rotations are defined by

$$\begin{split} u^{1}_{2j-j,2j} &= e^{i\alpha_{j}\sigma^{z}_{2j-1}\sigma^{z}_{2j}} = \cos(\alpha_{j}) \, \mathbb{1} + i \sin(\alpha_{j})\sigma^{z}_{j}\sigma^{z}_{j+1} \\ u^{1}_{2j,2j+1} &= e^{i\frac{\pi}{4}\sigma^{x}_{2j}\sigma^{x}_{2j+1}} = \frac{1}{\sqrt{2}} \left( \mathbb{1} + i\sigma^{x}_{j}\sigma^{x}_{j+1} \right) \,. \end{split} \tag{VI.16}$$

The angles  $\alpha_j$  with  $1 \leq j < \left\lfloor \frac{N+1}{2} \right\rfloor$  defining the rotation on the odd-even index pairs are fixed by the set of equations

$$\tan(2\alpha_j)^2 = \frac{\rho^2}{1-\rho^2} \left(1-\rho^{2(\lfloor\frac{N+1}{2}\rfloor-j)}\right)\,, \quad \rho = \frac{U}{w}\,. \tag{VI.17}$$

Similar to U=0, the angles become independent of the position in the chain for  $N\to\infty$ .

### VI.4 Numerical Minimization

The ansatz of Eq. (VI.6) can be used to numerical minimize the commutator functional  $\mathcal{F}(\mathcal{U},\mathcal{U}^\dagger)$  from Eq. (VI.7). This minimization is performed directly on the manifold of the unitaries  $u^l_{j,j+1}$  using Riemannian optimization, as explained for example in [302]. In short, Riemannian optimization uses the bare gradients  $\nabla_{u^{(\dagger)}_{j,j+1}}\mathcal{F}$ , evaluated by treating the unitary  $u^{(\dagger)}_{j,j+1}$  as a normal matrix, and projects them to the tangent space of the manifold of unitary matrices. The next update step is then determined by varying the unitary along a path in this manifold in the direction of the projected gradient.

The unitaries  $\boldsymbol{u}_{j,j+1}^l$  are initialized close to the identity using

$$u_{j,j+1}^l = e^{i\alpha V_{j,j+1}^l}$$

where  $V_{j,j+1}^l$  is a random Hermitian operator acting on the two sites  $(s_j, s_{j+1})$  with unit norm that commutes with the parity operator  $\hat{P}$ , and  $\alpha \ll 1$  is a small rotation angle.

The bare gradients  $\nabla_{u^{(\dagger)}_{j,j+1}} \mathcal{F}$  are calculated using automatic differentiation [303], and the cost function is minimized with respect to all the unitaries  $u^l_{j,j+1}$  in the circuit simultaneously. Optimizing all unitaries simultaneously requires the contraction of the full network every time the cost function  $\mathcal{F}(\mathcal{U},\mathcal{U}^{\dagger})$  is evaluated. This becomes very expensive for a larger number of layers, and a strategy that optimizes the tensors locally by fixing the rest is the preferred strategy, an approach that was taken, for example, by the authors of [304] and [305] to find the full spectrum of a many-body localized Hamiltonian. To demonstrate the efficiency of the ansatz, the chains considered in this section and the number of layers are chosen to be small, such that a full global optimization is possible. A comprehensive examination of the ansatz and the most effective minimization strategy will be presented in a future publication. Specifically, we minimized the ansatz with  $n_{\text{Layer}} \leq 3$  for system sizes  $N \leq 18$  in the integrable limits, and  $N \leq 16$  in the non-integrable limits. In all considered cases, the time required to evaluate the quantum circuit was less than 3 minutes, still allowing us to find the variational optimum within a few days.

### VI.4.1 Integrable Points

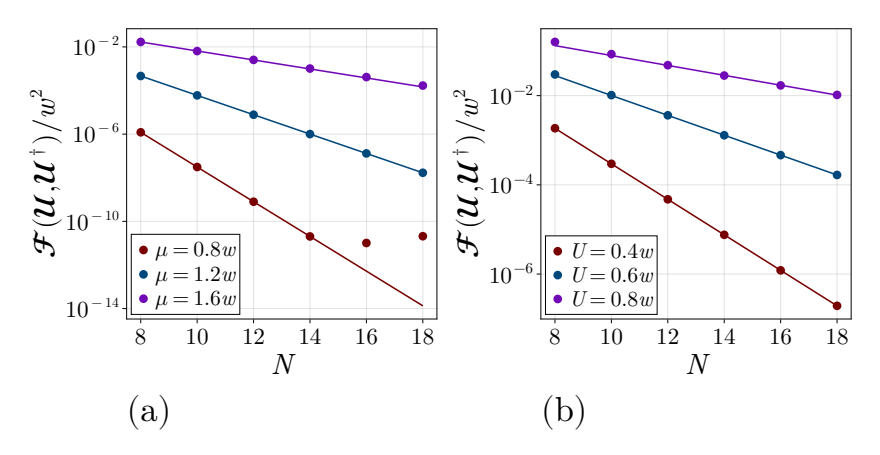


Figure VI.1: Commutator functional  $\mathcal{F}(\mathcal{U},\mathcal{U}^\dagger)$  from Eq. (VI.7) against the system size for U=0 (panel (a)) and  $\mu=0$  (panel (b)). In panel (a) for  $\mu=0.8$ , the commutator functional hits the sensitivity threshold set by the norms of the gradient, leading to a saturation of the values. The lines are obtained by fitting the points with the function  $f(N)=f_0e^{-2\lambda_{\rm fit}N}$ , with the results for  $\lambda_{\rm fit}$  reported in Table. VI.1.

As a first proof of concept, we test the numerical minimization of the ansatz for the ASZM in the integrable limits of the KHM from Eq. (VI.11)

I 
$$U = 0, |\mu| < 2w$$

II 
$$\mu = 0$$
,  $|U| < w$ , and  $w \neq 0$ 

In both cases, the ASZM becomes a SZM that commutes with the Hamiltonian in the thermodynamic limit and can be represented by an MPO of small bond dimension. For every finite system size, it is expected that the commutator cost function from equation Eq. (VI.3) vanishes exponentially with the system size

$$\mathcal{F}(\Gamma) \sim e^{-2\lambda N}$$
, (VI.18)

where  $\lambda$  defines the localization length of the SZM. From the exact form of the SZM, the localization length can be found to be

$$\lambda_{\text{exact}} = \begin{cases} -\log\left(\frac{\mu}{2w}\right) & \text{for } U = 0\\ -\frac{1}{2}\log\left(\frac{U}{w}\right) & \text{for } \mu = 0 \end{cases}$$
 (VI.19)

Because the exact MPO for both cases from Eqs. (VI.12) and (VI.15) are of bond dimension  $\chi < 4$ , it is expected that a circuit with only one layer from Eq. (VI.6) is sufficient to represent the exact MPO. The dependency of the commutator functional  $\mathcal{F}(\mathcal{U},\mathcal{U}^{\dagger})$  on the system length is shown for various parameters in Figure VI.1, where panel (a) shows the case of U = 0 and panel (b) shows the case of  $\mu = 0$ . In both instances, the unitary circuit with a single layer was variationally minimized until the gradient of  $\mathcal{F}(\mathcal{U},\mathcal{U}^{\dagger})$  fell below  $10^{-10}$ , establishing a natural cutoff for the precision of the commutator functional at the tenth digit.

$\mu/w$	$\lambda_{ m exact}$	$\lambda_{ m fit}$
0.8	0.91629	0.91627(7)
1.2	0.5108	0.5111(1)
1.6	0.223	0.237(3)

U/w	$\lambda_{ m exact}$	$\lambda_{ m fit}$
0.4	0.458145	0.458158(6)
0.6	0.2554	0.2565(3)
0.8	0.111	0.127(3)

Table VI.1: Extracted localization length of the SZM for U = 0 (a) and  $\mu = 0$  (b) by fitting the exponential decay of the commutator functional from Fig. VI.1.

For all parameters, the commutator functional vanishes exponentially with the system size, as expected, up to the precision determined by the gradient convergence. The localization length  $\lambda$  obtained from fitting this exponential decay is compatible with the exact value from Eq. (VI.19), as shown in Table VI.1.

Next, we examine the distance  $^3$  between the numerically minimized tensor network and the exact SZM given by

$$d(\Gamma, \Gamma_{\rm exact}) = \sqrt{2 \left(1 - \langle \Gamma, \Gamma_{\rm exact} \rangle \right)} \,. \tag{VI.20} \label{eq:VI.20}$$

Here,  $\Gamma_{\rm exact}$  is either the MPO from Eq. (VI.12) for U=0 or Eq. (VI.15) for  $\mu=0$ . This distance is shown in Fig. VI.2, where panel (a) shows the case U=0 and panel (b) shows the case  $\mu=0$ . For all parameters, the distance exponentially vanishes with respect to the system size, up to the precision determined by the gradient convergence. Performing the same analysis with an ansatz containing two layers,  $n_{\rm Layer}=2$ , reproduces the same results within numerical precision. Therefore, the initial assumption that  $n_{\rm Layer}=1$  is sufficient to represent the exact MPO is correct, and the results presented here clearly demonstrate that the unitary circuit can represent the exact SZM in the integrable limits.

### VI.4.2 General Case

Away from the integrable points discussed in the previous subsection, the KHM, Eq. (VI.11), is expected to exhibit only a ASZM at generic parameter points in the

 $<sup>^3</sup>$  The distance between two operators d(A,B) is induced by the Frobenius scalar product, Eq. (1.9), and given by  $d(A,B) = \sqrt{\langle (A-B)^\dagger, (A-B)\rangle}$ . Inserting  $A=\Gamma$  and  $B=\Gamma_{\rm exact}$ , and using  $\Gamma^2=\Gamma_{\rm exact}^2=\mathbbm{1}$  and  $\langle \Gamma, \Gamma_{\rm exact}\rangle=\langle \Gamma_{\rm exact}, \Gamma\rangle$  leads to Eq. (VI.20).

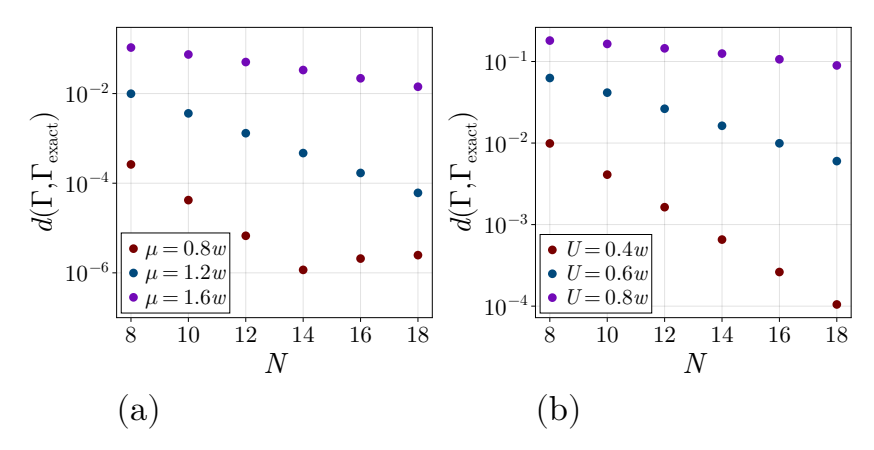


Figure VI.2: Distance between the numerical minimized tensor network and the exact MPO, as defined in Eq. (VI.20) against the system size. Panel (a) shows the case of U=0 with  $\Gamma_{\rm exact}$  given by the MPO in Eq. (VI.12), and panel (b) the case of  $\mu=0$  where  $\Gamma_{\rm exact}$  is given by the MPO from Eq. (VI.15).

SPTP. As discussed in Subsection 1.5, the existence of a ASZM implies prolonged lifetimes of excitations generated by the edge operator  $\sigma_1^x$ , even at infinite temperatures. At the level of the commutator functional from Eq. (VI.3), this suggests the existence of an edge localized Majorana operator  $\Gamma \in \mathcal{M}$  with a finite overlap  $\langle \Gamma, \sigma_1^x \rangle$  that minimizes  $\mathcal{F}(\Gamma)$ . In contrast to the integrable points, this minimum should become independent of the system size  $\mathcal{F}(\Gamma) \xrightarrow{N \to \infty} \mathcal{F}_0(U, \mu, w)$ , with this constant mainly defining the lifetime of edge excitations induced by  $\sigma_1^x$  [214].

In the following discussion, we present initial results obtained by minimizing the commutator functional in Eq. (VI.7) with respect to the unitary circuit described in Eq. (VI.9) for various numbers of layers. For all results presented below, optimization was performed until the gradients fell below  $10^{-6}$ . However, for  $n_{\text{Layer}} = 3$ , this threshold was not achieved for N = 14 and N = 16, leading to the exclusion of these datasets from the subsequent discussion. Additionally, the chemical potential was held constant at  $\mu = 0.2w$ , while the interaction parameter varied from U = 0.2w to U = 0.8w, ensuring that all considered parameter points remained within the SPTP.

Figure VI.3(a) presents the commutator functional of the numerically obtained  $\Gamma(\mathcal{U})$  against the number of sites N, exemplified for  $\mu=0.2w$ , U=0.4w. For every fixed  $n_{\text{Layer}}$ , the minimal commutator obtained saturates with the system size at approximately N=12. Compared to the exactly solvable limits shown in Fig. VI.1, this saturation suggests that the operator we have identified is not an SZM, indicating that edge excitations possess a finite lifetime. By fixing the number of system sites, the commutator functional is reduced by increasing the number of layers. By plotting the final value of the commutator functional against  $n_{\text{Layer}}$ , inset of Fig. VI.3(a), it is observed that this value converges in the number of layers. Because the unitary circuit is local, reaching a saturation within a finite number of layers indicates that the ASZM is localized to the edge of the system, exhibiting a finite penetration depth.

The overlap between the numerically determined  $\Gamma((U))$  and the edge operator  $\sigma_1^x$ , as illustrated in Figure VI.3(b) for  $\mu = 0.2w$ , U = 0.4w, further demonstrates this point. Similar to the commutator functional, the overlap saturates for a fixed number

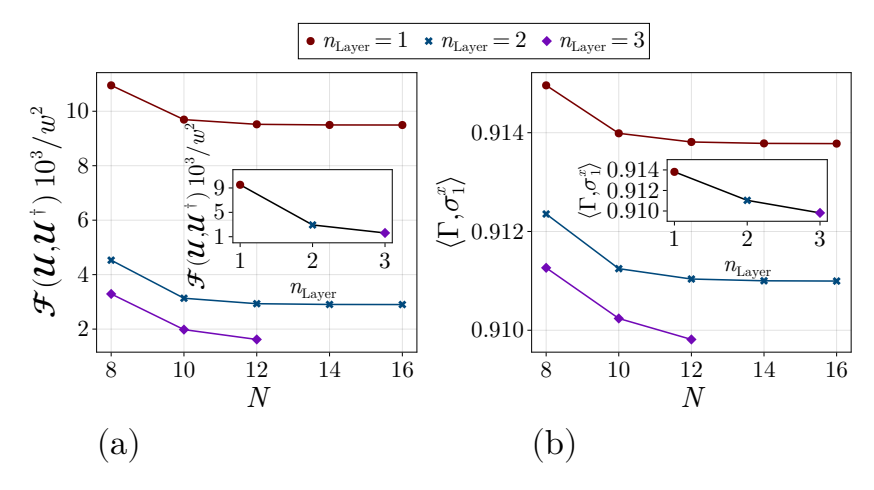


Figure VI.3: (a) Commutator functional  $\mathcal{F}(\mathcal{U}, \mathcal{U}^{\dagger})$  obtained from numerical minimization at  $\mu = 0.2w$  and U = 0.4w for an increasing number of layers in the unitary circuit. (b) Overlap of the numerically obtained ASZM with the edge operator  $\sigma_1^x$  for the same parameter point as in panel (a). The inset in both panels shows the convergence of the cost function (panel (a)) and the overlap (panel (b)) with respect to the number of layers for N = 12.

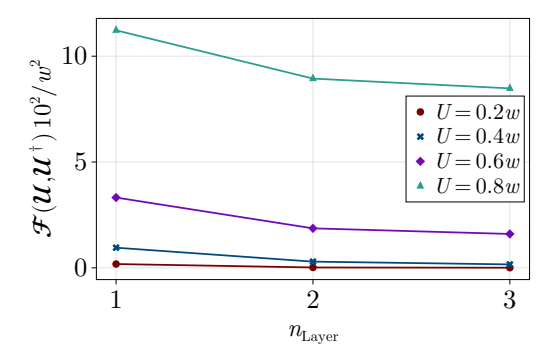


Figure VI.4: Commutator functional  $\mathcal{F}(\mathcal{U}, \mathcal{U}^{\dagger})$  as a function of the number of layers and for different interaction strengths at  $\mu = 0.2w$  for a chain of N = 12 sites.

of layers with respect to the system size and decreases slightly with an increase in the number of layers, see the inset of Fig. VI.3(b). This finite overlap indicates that  $\Gamma(\mathcal{U})$  functions as a boundary operator of finite depth, allowing the edge operator  $\sigma_1^x$  to be expanded as

$$\sigma_1^x = A\Gamma + \sqrt{1-A^2}\,\tilde{\Gamma}\,,\quad A = \langle \Gamma, \sigma_1^x \rangle \ ,$$

where  $\tilde{\Gamma}$  is a remaining Majorana operator that anti-commutes with  $\Gamma$ . Given that  $\mathcal{F}(\sigma_1^x) \sim w^2$  is valid for a generic point and  $\Gamma$  possesses a small commutator functional, it follows that the residual operator must also satisfy  $\mathcal{F}(\tilde{\Gamma}) \sim w^2 \gg \mathcal{F}(\Gamma)$ . As a consequence, the long-time properties of the edge excitation are defined by the ASZM  $\Gamma$ , and in particular the Autocorrelation Function, introduced in Section 1.5, has the asymptotic form [214]

$$C_{\beta=0}(\sigma_1^x,t)\approx A^2e^{-t/\tau}\,,\quad \tau=\frac{Bw}{\mathcal{F}_0(U,\mu,w)}\,,$$

where B is a constant of order one<sup>4</sup>.

<sup>&</sup>lt;sup>4</sup> The short-time dynamics of  $\sigma_1^x$  are more complex and related to the residual operator  $\tilde{\Gamma}$ . However, owing to the large commutator with the Hamiltonian, this contribution decays at time scales  $t^* \sim w$ .

The same convergence behavior in the commutator and overlap was also observed for other interaction strengths. This is explicitly shown in Fig. VI.4, where the commutator functional is plotted against the number of layers for various interaction strengths for a system with N=12 lattice sites. For all interaction values, the commutator becomes smaller as the number of layers increases; however, it displays a saturating behavior. This saturation value shows a non-trivial behavior on the interaction strength.

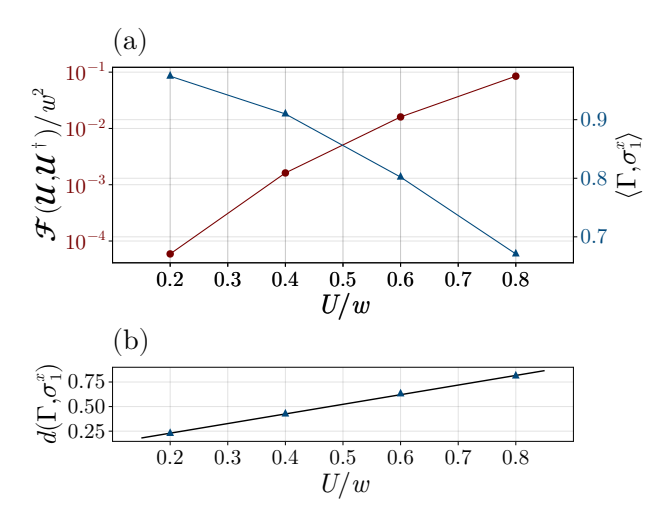


Figure VI.5: (a) Dependence of the commutator functional (red circles) and overlap with the seed operator  $\Gamma_0$  (blue triangles) on the interaction strength for  $\mu=0.2w$  and a chain of N=12 sites. (b) Distance, Eq. (VI.21), of the numerical obtained ASZM from the seed operator  $\Gamma_0$ . The black line is a linear fit of the form  $f(U)=\delta U/w+d_0$  with  $\delta=0.97(2)$  and  $d_0=0.033(9)$ .

To quantify this non-trivial dependence, we investigated how the commutator functional and overlap change with the interaction strength. Figure VI.5(a) shows the behavior of both quantities for a chain of size N=12 and three layers of the quantum circuit. Both quantities have a remarkable symmetry with respect to the interaction strength: while the logarithm commutator increases with increasing interaction strength, the overlap decreases. It is observed that the distance, compare also Eq. (VI.20), of the final ASZM  $\Gamma(\mathcal{U})$  with the edge operator  $\sigma_1^x$  defined as

$$d(\Gamma, \sigma_1^x) = \sqrt{2\left(1 - \langle \Gamma, \sigma_1^x \rangle\right)}, \qquad (\text{VI}.21)$$

has a simple linear dependence on the interaction strength U

$$d(\Gamma, \sigma_1^x) = \delta \frac{U}{w} + d_0.$$
 (VI.22)

This dependency is shown in Fig. VI.5(b), together with a fit of the above linear form. Based on the mirror symmetry of Fig. VI.5(a), a similar form can be found for the commutator functional

$$\mathcal{F}(U, \mu, w) \sim w^2 e^{-\frac{(\tilde{A}(1-U/w)+\tilde{f}_0)^2}{2}}$$

for the intermediate interactions considered in this study. We emphasize that this functional behavior is incorrect for small values of U, as the commutator must vanish exponentially with the system size when U = 0, as shown in Eq. (VI.18).

### VI.5 Conclusion

In this chapter, we presented a variational ansatz for the SZM and ASZM. This ansatz is based on a unitary circuit applied to a local seed operator and is tailored for direct operation in the correct manifold of Majorana operators. We demonstrated analytically and numerically that this ansatz is sufficient to reproduce the correct SZM in the integrable limits of the KHM. Furthermore, we extended the analysis to a set of generic parameter points inside the SPTP of the KHM. First initial results were presented, showing that the ansatz can be used to search for edge-localized Majorana operators that almost commute with the Hamiltonian. Because the value of the commutator functional defines the lifetime of the ASZM, this ansatz can be used to study how the lifetime changes across the phase diagram.

In future research, it would be interesting to consider a broader range of parameters and study how the commutator functional changes as a function of U and  $\mu$  in the entire SPTP. In particular, it would be of interest how the ASZM disappears while approaching the phase boundaries.

Another interesting direction is to consider other models that can host more exotic ASZM, such as a parafermionic chain with a  $\mathbb{Z}_3$  symmetry[298, 306, 307]. The variational ansatz presented here can easily be extended to such a parafermionic chain by simply replacing the seed operator  $\Gamma_0$  by an operator matching the conditions of a parafermionic ASZM.

Finally, the results presented for the non-integrable case display convergence with respect to the number of layers and sites. However, to obtain more conclusive results, a comprehensive study on convergence is required. In this study, it is also possible to consider a different form of the quantum circuit, such as replacing the two-body unitary operators with n-body unitary operators, while keeping the number of layers low, similar to the approach chosen by [305].

### Conclusion

In this thesis, we explored various exotic phases of correlated one-dimensional quantum matter. We proposed several models that can be tuned to achieve novel phases of interest for both theoretical and experimental purposes and studied their static properties. In addition, we examined the non-equilibrium dynamics of spatially localized objects, including edge modes in one-dimensional chains and domain walls in two-dimensional quantum magnets. After a general introduction to the field of one-dimensional quantum matter in the first part, we present the findings of this thesis in Chapters I–VI.

In Chapter I, we discussed a coupled wire model of fermions that realizes the Symmetry-Protected Topological Phase (SPTP) of unpaired Majorana Zero Modes (MZMs) while preserving the number of total fermions. Specifically, the model consists of four wires arranged around a cylinder, enabling the particles to traverse in the short direction of the cylinder. By applying a magnetic field along the cylinder's long axis, tuned to induce a  $\pi$ -flux, fermions begin to negatively interfere along various paths around the cylinder, resulting in all single-particle tunneling processes between two wires on opposite sides of the cylinder being precisely zero. We have shown that introducing generic two-body interaction terms to this coupled wire system gives rise to coherent pair tunneling processes, which mimic a p-wave pairing potential for one of the wires. Through analytical methods and extensive numerical studies using finite-size tensor networks, we demonstrated that this wire system transitions into the SPTP phase.

The second result presented in Chapter II explores the emergence of the Tricritical Ising (TCI) model within a network of superconducting islands interconnected by Josephson junctions. To engineer the TCI phase, we introduced a novel triple-junction element as a fundamental building block, which was arranged linearly to create a full quantum ladder model. We demonstrated that the anharmonicity of this triple junction reproduces the potential landscape necessary for the emergence of the TCI phase. In addition, we confirmed the semi-classical expectation through extensive numerical tensor network simulations of both finite and infinite systems. This allowed us to demonstrate that the TCI emerges in the full quantum model.

In Chapter III, we explore the dynamic phase transition of a domain wall within a two-dimensional quantum magnet described by the Transverse Field Ising Model. Previous research has indicated that a domain wall, which is a one-dimensional quantum object, can experience a continuous quantum phase transition in equilibrium. Our work has demonstrated the existence of a dynamic counterpart to this equilibrium transition, where the domain wall remains stable during time evolution, even over extended time scales below a critical coupling. To achieve this, we identified an effective non-perturbative one-dimensional Hamiltonian that characterizes the isolated dynamics of the domain wall and developed a corresponding observable to

210 CONCLUSION

capture the dynamical phase transition. By extending this observable to the entire two-dimensional quantum magnet, we have shown that below the critical coupling, the results of the full two-dimensional and effective one-dimensional dynamics are consistent with each other. Our study revealed a novel mechanism by which a quantum many-body system can avoid thermalization up to mesoscopic timescales, with the domain wall remaining a well-defined, one-dimensional quantum object.

In Chapter IV, we revisited the SPTP of unpaired MZMs, a topic also explored in Chapter I. Here, we focused on examining the non-equilibrium properties of emergent MZMs at finite temperatures. To this end, we considered a model that realizes this phase by breaking the particle number conservation, in contrast to the model considered in Chapter I. Previous research has found that within the SPTP, the MZM, typically defined in the ground-state manifold, becomes an Almost Strong Zero Mode (ASZM), an operator with a significantly extended but finite lifetime compared to typical bulk operators. While earlier studies concentrated on infinite temperatures, we developed an algorithm based on tensor-network methods to investigate the non-equilibrium properties of the ASZM at any finite temperature. Utilizing this algorithm, we demonstrated that the ASZM is smoothly connected to the MZM emerging in the ground-state manifold as the temperature is tuned from infinity to zero. Additionally, through exact diagonalization, we associated the prolonged lifetime of the ASZM with an extended degeneracy in the energy spectrum beyond the ground-state manifold.

In Chapters V and VI, we presented unpublished results that extend the findings discussed in Chapter IV. Specifically, in Chapter V, we applied the tensor-network algorithm developed in Chapter IV to a class of coupled fermionic wire models that realize the SPTP without breaking particle conservation, similar to the model considered in Chapter I. As demonstrated in Chapter I, this class of models exhibits additional gapless density wave excitations, raising the question of whether these long-wavelength excitations could undermine the existence of the ASZM in these models. We found that this class of models does indeed have an emerging ASZM; however, unlike the standard models considered in Chapter IV, this ASZM is quite weak at high temperatures but shows an exponential increase in lifetime with respect to the inverse temperature. This allows for the observation of the MZM if the temperature is sufficiently low, even in the presence of the gapless mode.

In Chapter VI, we introduced a general variational ansatz for the ASZM that is applicable to generic fermionic models. This ansatz is tailored to represent the relevant variational manifold. We have shown that it can accurately reproduce the form of the ASZM in the integrable limits, both analytically and numerically. Additionally, we presented preliminary findings for generic, non-integrable points. These findings reveal the presence of a localized operator that almost commutes with the Hamiltonian, indicating that the excitations generated by this edge operator have a long, but finite lifetime.

In conclusion, there are multiple possible directions for extending the findings of this thesis. Implementing the proposed models on a real physical platform would allow for new perspectives to observe these novel phases of matter. However, because the results presented in this thesis are mainly proofs of concept, such a device implementation would require a large-scale scan of the phase diagrams to identify possible parameter regions that realize the desired phase that are reachable with the quantum simulator. Second, the results presented in Chapters V and VI are preliminary. In particular, extending the investigation from Chapter V of the lifetime of the ASZM in the class of number-conserving Hamiltonians is important to understand how these platforms can be used to observe this novel SPTP. On the other hand, the variational algorithm presented in Chapter VI can be straightforwardly generalized to more exotic cases, such as parafermions. This can be used to search for possible Strong Zero Mode (SZM) in such models, where it is still an open question whether such a mode can exist or not.

# Appendix

## Basics of Linear Algebra

This appendix provides a brief review of vector spaces and linear maps, including the most important matrix decompositions used in the context of tensor networks. Since all vector spaces encountered in the context of this thesis are finite dimensional, this will be assumed throughout this appendix. For proofs and further details, the reader is referred to some standard books on linear algebra, such as [308].

### A.1 Linear Maps

### A.1.1 Vector Spaces

A vector space  $\mathcal{V}$  over the field  $\mathbb{C}$  is a set of vectors  $|v\rangle \in \mathcal{V}$  and the properties

$$z|v_1\rangle \in \mathcal{V}$$
,  $|v_1\rangle + |v_2\rangle \in \mathcal{V}$ 

for  $|v_j\rangle\in\mathcal{V}$  and  $z\in\mathbb{C}.$  If a vector  $|v\rangle$  can be expressed as a linear combination of other vectors

$$|v\rangle = \sum_{n} \lambda_n |v_n\rangle , \qquad (A.1)$$

it is called linear dependent. The maximal set of linearly independent vectors  $|v_m\rangle$  for  $m=1,\ldots,N$  is called a basis of  $\mathcal V$  and N is the dimension of  $\mathcal V$ . Every vector in  $\mathcal V$  can be expressed in this basis as in Eq. (A.1) with  $\lambda_n\in\mathbb C$ .

On the vector space  $\mathcal{V}$  it is possible to define an inner product

$$(|v_1\rangle, |v_2\rangle) \in \mathbb{C}$$

which is anti-linear in the first argument

$$(z|v_1\rangle + |v_2\rangle, |v_3\rangle) = \bar{z}(|v_1\rangle, |v_3\rangle) + (|v_2\rangle, |v_3\rangle),$$

and linear in the second argument

$$(|v_1\rangle, z|v_2\rangle + |v_3\rangle) = z(|v_1\rangle, |v_2\rangle) + (|v_1\rangle, |v_3\rangle),$$

where  $\bar{z}$  defines the complex conjugate of z. A vector space with an inner product is called a Hilbert space.

The existence of the inner product allows for choosing a basis which is orthonormal with respect to this inner product

$$(\left|v_{n}\right\rangle,\left|v_{m}\right\rangle)=\delta_{n,m}\,,$$

and the expansion coefficients from Eq. (A.1) for a generic state  $|v\rangle \in \mathcal{V}$  are given by

$$\lambda_n = \left( \left| v_n \right\rangle, \left| v \right\rangle \right).$$

This basis can be generated iteratively from N linearly independent vectors using general algorithms such as the Gram-Schmidt process [308, p. 88 – 91].

The space of all linear maps from  $\mathcal V$  to  $\mathbb C$  is called  $\overline{\mathcal V}$ 

$$\langle v|w\rangle\in\mathbb{C}$$
,

which also forms a linear vector space of dimension N. Using the inner product this set is naturally identified with  $\mathcal{V}$  itself

$$\langle v_1 | v_2 \rangle \equiv (|v_1\rangle, |v_2\rangle)$$
.

Given an orthonormal basis of  $\mathcal{V}$ , this duality directly results in an orthonormal dual basis of  $\overline{\mathcal{V}}$  that fulfills

$$\langle v_n | v_m \rangle = \delta_{n,m} \,. \tag{A.2}$$

### A.1.2 Linear Maps

A linear map between two Hilbert spaces  $\mathcal{V}$  and  $\mathcal{W}$ , with dimension  $N_V$  and  $N_W$  respectively, is a transformation

$$\mathcal{A}(\alpha \left| v_1 \right\rangle + \left| v_2 \right\rangle) = \alpha \mathcal{A}(\left| v_1 \right\rangle) + \mathcal{A}(\left| v_2 \right\rangle) \in \mathcal{W} \,.$$

By choosing an orthonormal basis  $|v_n\rangle\in\mathcal{V}$  and  $|w_n\rangle\in\mathcal{W}$  on the two Hilbert spaces, the linear map can be expressed as

$$\mathcal{A} = \sum_{n=1}^{N_{V}} \sum_{m=1}^{N_{W}} A_{m,n} \left| w_{m} \right\rangle \left\langle v_{n} \right|$$

where  $A_{m,n}$  forms a complex  $N_W \times N_V$  matrix. This can be naturally extended to multi-linear maps of L Hilbert spaces to R new Hilbert spaces, which are defined in the local basis as

$$\mathcal{A} = \sum_{n_1, \dots, n_L} \sum_{m_1, \dots, m_R} A_{(n_1, \dots, n_L), (m_1, \dots, m_R)} \left| w_1, \dots, w_R \right\rangle \left\langle v_1, \dots, v_L \right|$$

where  $A_{(n_1,\dots,n_L),(m_1,\dots,m_R)}$  forms a complex tensor, and the total number of indices is called the tensor rank.

### A.2 Matrix Decomposition

The tensors of complex multi-linear maps are the building blocks of tensor networks. These tensors can be manipulated by decomposing them into other tensors with special properties. This can be used, for example, to decompose a high-rank tensor into lower-rank constituents or to define compression methods. Typically, the decomposition is based on matrix decompositions and extended to tensors by combining indices into super-indices.

### A.2.1 QR Decomposition

The QR decomposition [308, p. 139 – 142] is a decomposition of a rectangular matrix  $M \in \operatorname{Mat}(\mathbb{C}, n, m)$  into an  $n \times n$  unitary Q and an upper rectangular matrix R of size  $n \times m$ 

$$M = QR, Q^{\dagger}, \quad Q = QQ^{\dagger} = \mathbb{1}.$$
 (A.3)

In the case of n > m, only the upper  $m \times m$  part of the rectangular matrix R is non-trivial, with the remaining (n-m) rows being plain zeros. It is possible to define a reduced QR decomposition by writing

$$M = \begin{pmatrix} Q_1 & Q_2 \end{pmatrix} \begin{pmatrix} R_1 \\ 0 \end{pmatrix} = Q_1 R_1 , \qquad (A.4)$$

and storing only the relevant part  $(Q_1,R_1)$ . Here, the two matrices  $Q_j$  are two isometries of size  $m\times m$  and  $(n-m)\times m$  for j=1 and j=2 respectively, with  $Q_jQ_j^\dagger=\mathbbm{1}$  and  $Q_j^\dagger Q_j^\dagger=\mathbbm{1}$ . In particular, the matrix  $P_j=Q_j^\dagger Q_j$  is a projector  $P_j^2=P_j$  on the subspace of the two blocks with  $P_1+P_2=\mathbbm{1}$  on the full  $n\times n$  space. For m>n such a decomposition is not possible if M has full rank and  $Q=Q_1$  is a full unitary. In general, the isometry (unitary)  $Q_1$  is not unique. However, by fixing the phase of the diagonals of  $R_1$  to be on the real positive line, the QR decomposition becomes unique.

In analogy to the QR decomposition, one can also define an LQ decomposition M = LQ, where L is a lower rectangular matrix. The LQ decomposition can be obtained from the QR decomposition by

$$M = (M^{\dagger})^{\dagger} \stackrel{\mathrm{QR}}{=} {}^{M^{\dagger}} (QR)^{\dagger} = R^{\dagger} Q^{\dagger} := L\tilde{Q}. \tag{A.5}$$

In the last step, it was used that the  $Q^{\dagger}$  is again a unitary matrix and  $R^{\dagger}$  becomes a lower rectangular matrix. Figure A.1(a) shows the QR decomposition using the graphical notation of tensor networks introduced in Chapter2.

$$(a)$$

$$-M - = Q - R - = -L - \tilde{Q} -$$

Figure A.1: Graphical representation of the QR (LQ) decomposition. (a) Splitting a rectangular matrix into a unitary Q and an upper (lower) triangular matrix R (L), as explained in the text. (b) QR decomposition of a multi-linear map by grouping the indices  $j_l$ ,  $j_u$  and  $j_d$  into one combined index  $J = (j_u, j_l, j_d)$  and treating the multi-linear map as a matrix.

The QR decomposition is generalized to multi-linear maps represented by the tensor  $A_{j_1,\ldots,j_N}$ . In this case, the indices are collected in two super indices  $J=(j_{l_1},\ldots j_{l_n})$  and  $K=(j_{k_1},\ldots j_{k_{N-n}})$  such that  $A_{J,K}$  forms a rectangular matrix that can be used to perform the QR decomposition. Here,  $l_i$  enumerates a subset of all N indices in an arbitrary order, and  $k_i$  enumerates the remaining indices. Figure A.1(b) shows an example of such a fusion operation for a tensor with four indices.

### A.2.2 Singular Value Decomposition

The Singular-Value Decomposition (SVD) [308, p. 209 – 220] is a decomposition of a rectangular matrix  $M \in \operatorname{Mat}(\mathbb{C}, n, m)$  into three matrices U,  $\Sigma$  and V, where U and V are unitary matrices of size  $n \times n$  and  $m \times m$  respectively, and  $\Sigma$  is a rectangular matrix of size  $n \times m$  with only real positive values on the diagonal. The non-zero elements in  $\Sigma$  are called singular values  $\sigma_j$  of the matrix M which are assumed to be ordered  $\sigma_1 \geq \sigma_2 \geq \dots$ . The decomposition reads

$$M = U\Sigma V^{\dagger}$$
.

The column vectors of U(V) are the left (right) singular vectors  $u_j(v_j)$ , and the number of non-zero singular values  $\sigma_j$  defines the rank of the matrix M.

Similar to the reduced QR decomposition defined in Eq. (A.4), it is possible to reduce the number of stored parameters using a compact SVD. By assuming again n > m, this reduced form is defined by

$$M = \begin{pmatrix} U_1 & U_2 \end{pmatrix} \begin{pmatrix} \Sigma_1 \\ 0 \end{pmatrix} V^\dagger = U_1 \Sigma_1 V^\dagger \tag{A.6}$$

where  $\Sigma_1$  is an  $m \times m$  diagonal matrix storing all the singular values  $\sigma_j$ , and the remaining part of the singular matrix is a  $(n-m) \times m$  matrix filled with zeros. The two matrices  $U_j$  are isometries with properties similar to those in the case of the QR decomposition.

One way to compute the SVD is to perform two eigenvalue decompositions on the matrices  $A_1 = M^{\dagger}M$  and  $A_2 = MM^{\dagger}$ . The singular values are the square roots of the eigenvalues of the two matrices  $A_i$ .

Truncating the singular matrix  $\Sigma_1$  to only contain m' < m singular values and discarding the corresponding columns in  $U_1$  and V, the compressed matrix  $M' = U_1'\Sigma'V'$  is the best low-rank approximation with respect to the Frobenius scalar product

$$||M - M'||^2 = \text{Tr} \left[ M - M' \right] = \sum_{j=m'+1}^M \sigma_j^2 \,.$$

#### A.2.3 Eigenvalue decomposition

If for a square matrix  $M \in \operatorname{Mat}(\mathbb{C},n,n)$  there exists an invertable matrix J such that

$$J^{-1}MJ = D (A.7)$$

such that D is a diagonal matrix with complex entries, the matrix M is called diagonalizable, and Eq. (A.7) is called the eigenvalue decomposition. The elements  $\lambda_j$  of D are the eigenvalue, and the columns of J are the eigenvectors  $v_j$  of M which fulfill

$$Mv_j = \lambda_j v_j \,, v_j^{\dagger} v_k = \delta_{j,k} \,.$$

There are special cases that allow for a stricter condition on the diagonalization matrix J. If the matrix M is Hermitian,  $M^{\dagger} = M$ , the matrix J can be chosen to be unitary  $J^{\dagger} = J^{-1}$  and the eigenvalues are real.

By discarding the smallest eigenvalues, the square matrix can be compressed, similar to the SVD compression.

# APPENDIX B

# Derivation of the Jordan-Wigner Transformation

This appendix provides details on the derivation of the Jordan-Wigner transformation, which maps local one-dimensional models of fermions to spins. For simplicity, only the case of spinless fermions described by the annihilation (creation) operators  $a_j^{(\dagger)}$  is considered here. The local fermionic Hilbert space is two-dimensional and is spanned by the occupation basis  $|0\rangle$  and  $|1\rangle$  which are the eigenstates of the fermionic number operator  $\hat{n}_j$ . On the level of many-body states, the local occupation basis is identified with the two-dimensional Hilbert space of a spin-1/2 degree of freedom according to

$$|0\rangle \cong |\downarrow\rangle$$
,  $|1\rangle \cong |\uparrow\rangle$ ,

and the local number operator becomes

$$\hat{n}_j = \frac{1}{2}(\mathbb{1} + \sigma_j^z) \,. \label{eq:nj}$$

To derive the mapping of the fermionic ladder operators into the spin basis, consider the improper annihilation and creation operators from Eq. (1.31)

$$\tilde{a}_j^\dagger = \frac{1}{2}(\sigma_j^x + i\sigma_j^y) \coloneqq \sigma_j^+ \,, \quad \tilde{a}_j = \frac{1}{2}(\sigma_j^x - i\sigma_j^y) \coloneqq \sigma_j^- \tag{B.1}$$

This set of operators have the correct anti-commutation relation onside

$$\left\{ \tilde{a}_{i}^{\dagger},\tilde{a}_{i}\right\} =1\,,\quad \left\{ \tilde{a}_{i}^{(\dagger)},\tilde{a}_{i}^{(\dagger)}\right\} =0$$

due to the commutation relations of Pauli matrices. However, they commute on different sites and do not fulfill the Canonical Anti-Commutation Relations (CAR); see also Eq. (1.28).

A way to restore the CAR is to dress the improper operators (B.1) by non-local unitaries

$$a_j = U_1(j) \, \tilde{a}_j \, U_2^\dagger(j) \,, \quad a_j^\dagger = U_2(j) \, \tilde{a}_j^\dagger \, U_1^\dagger(j) \,, \quad U_k^\dagger(j) U_k(j) = U_k(j) U_k^\dagger(j) = \mathbbm{1} \,\,.$$

By requiring that the local number operator is preserved under this dressing

$$n_j = a_j^\dagger a_j = \tilde{a}_j^\dagger \tilde{a}_j = \frac{1}{2} (\mathbb{1} + \sigma_j^z) \,, \label{eq:nj}$$

it is possible to choose  $U_2(j)=\mathbb{1}$  and  $U_1(j)=U(j)$  as non-trivial unitaries, which are fixed by the anti-commutation relations.

To find the correct expression for U(j), consider first the anti-commutator of two annihilation operators acting on the same site. From

$$\left\{a_{j},a_{j}\right\} = \left\{U(j)\,\tilde{a}_{j},U(j)\,\tilde{a}_{j}\right\} = 0$$

it follows

$$U(j)\,\tilde{a}_{\,i}\,U(j)\,\tilde{a}_{\,j}=0\,.$$

This equation is solved by requiring  $[U(j), \tilde{a}_j] = 0$ . Using the anti-commutator of  $a_j^{\dagger}$  and  $a_j$ , it follows  $[U(j), \tilde{a}_j^{\dagger}] = 0$ .

The anti-commutator of two annihilation operators at position j and k < j evaluates to

$$\begin{split} \left\{a_{j}, a_{k}\right\} &= \left\{U(j) \, \tilde{a}_{j}, U(k) \, \tilde{a}_{k}\right\} \\ &= U(k) \left[\tilde{a}_{k}, U(j)\right] \tilde{a}_{j} + U(k) U(j) \left[\tilde{a}_{k}, \tilde{a}_{j}\right] \\ &+ \left[U(k), U(j)\right] \tilde{a}_{j} \tilde{a}_{k} + U(j) \left\{U(k), \tilde{a}_{j}\right\} \tilde{a}_{k} \,, \end{split}$$

which follows from  $\{AB,C\}=A[B,C]+\{A,C\}B$  and [A,BC]=[A,B]C+B[A,C]. Since  $\{a_j,a_k\}=0$ , it follows that the all the terms on the right have to vanish individually

$$[U(j), \tilde{a}_k] = 0, \quad [U(j), U(k)] = 0, \quad \{\tilde{a}_j, U(k)\} = 0.$$

By considering the anti-commutator of two creation operators, a similar set of equations can be derived for  $U^{\dagger}(k)$ 

The first and second equation are fulfilled by choosing the operator  $U_j$  to consists of a string of local unitaries acting to the left of site j

$$U(j) \coloneqq \mathcal{J}_j = \prod_{k < j} p_k \,, \quad p_k^\dagger p_k = \mathbb{1}$$

and the last equation states that  $p_k$  must be an operator that anti-commutes with the local annihilation (creation) of a particle. An operator that has this sensitivity to the change in the local occupation is the local parity of site k. By setting  $p_k = \exp(i\pi\hat{n}_k) = -\sigma_j^z$ , the complete non-local mapping of the ladder operators to the spin operators becomes

$$a_j^{(\dagger)} = \mathcal{J}_j \, \tilde{a}_j^{(\dagger)} = \prod_{k < j} e^{i\pi \hat{n}_j} \, \tilde{a}_j^{(\dagger)} = \prod_{j < k} \left( -\sigma_j^z \right) \tilde{a}_j^{(\dagger)} \,. \tag{B.2} \label{eq:B.2}$$

This is the Jordan-Wigner transformation [82]. Note that the transformation is not unique, and other mappings are possible.

## Derivation of the Majorana Zero Modes

This appendix presents a detailed derivation of the expression of the Majorana Zero Mode (MZM) from Eq. (1.97). The starting point is the Kitaev chain model in the Majorana form from Eq. (1.89) given by

$$\begin{split} H_{\text{Kitaev}} &= \sum_{j=1}^{N-1} \left[ \lambda_x \, i \gamma_{j,b} \gamma_{j+1,a} + \lambda_y \, i \gamma_{j,a} \gamma_{j+1,b} \right] + g \sum_{j=1}^{N} i \gamma_{j,a} \gamma_{j,b} \\ \lambda_x &= -\frac{(w+\Delta_p)}{2} \,, \quad \lambda_y = \frac{(w-\Delta_p)}{2} \,, \quad g = -\frac{\mu}{2} \,. \end{split} \tag{C.1}$$

A suitable ansatz for the MZM is given by the two Majorana operators

$$\Gamma_a = \sum_{l=1}^N \rho_l^a \gamma_{l,a} \,, \quad \Gamma_b = \sum_{l=1}^N \rho_l^b \gamma_{l,b} \tag{C.2}$$

only involving one of the two Majorana types. The normalization condition  $\Gamma_{\alpha}^2 = \mathbb{1}$  requires

$$\sum_{j=1}^{N} (\rho_j^{\alpha})^2 = 1.$$

Taking the convention  $\rho_0^{\alpha} = \rho_{N+1}^{\alpha} = 0$ , the commutator of these two operators with the Hamiltonian of Eq. (C.1) is given by

$$\begin{split} [H,\Gamma_a] &= 2i\sum_{l=1}^N \left(\lambda_x \rho_{l+1}^a - g\rho_l^a - \lambda_y \rho_{l-1}^a\right) \gamma_{l,b} \\ [H,\Gamma_b] &= 2i\sum_{l=1}^N \left(-\lambda_x \rho_{l-1}^b + g\rho_l^b + \lambda_y \rho_{l+1}^b\right) \gamma_{l,a} \,. \end{split} \tag{C.3}$$

Note that the commutator of H with either of the two operators involves only Majorana operators of the other type. This is a direct consequence of the chiral symmetry of the Hamiltonian, as expressed in Eq. (1.101). If the two Majorana operators  $\Gamma_{a/b}$  are zero modes of the Hamiltonian, their commutator must vanish. By Eq. (C.3) this results in the two recursion relations

$$\xi \rho_{l+1}^a + \rho_l^a + \delta \rho_{l-1}^a = 0 \tag{C.4}$$

$$\xi \rho_{l-1}^b + \rho_l^b + \delta \rho_{l+1}^b = 0 \tag{C.5}$$

where the two parameters

$$\xi = -\frac{\lambda_x}{q}, \quad \delta = \frac{\lambda_y}{q}$$

were defined. These recursion relations must fulfill the boundary conditions  $\rho_0^{\alpha} = \rho_{N+1}^{\alpha} = 0$ . A way to solve a recursive equation as the two given by Eq. C.4 and C.4 is in terms of a generating function. As an example, consider the equation for  $\Gamma_a$ . The generating function is a real valued function F(x) defined by<sup>1</sup>

$$F(x) = \sum_{j=1}^{N} \rho_j^a x^{-j} \,. \tag{C.6}$$

Applying the recursion from Eq. (C.4) one obtains

$$\begin{split} F(x) = & \rho_1^a x^{-1} + \sum_{j=2}^{N-1} \rho_j^a x^{-1} + \rho_N^a x^{-N} \\ \stackrel{\text{(C.4)}}{=} & - \left( \xi \rho_2^a x^{-1} + \sum_{j=2}^{N-1} (\xi \rho_{j+1}^a + \delta \rho_{j-1}^a) x^{-j} + \delta \rho_{N-1}^a x^{-N} \right) \\ & = & - \left( \xi x \left[ \sum_{j=1}^N \rho_j^a x^{-j} - \rho_1^a x^{-1} \right] + \frac{\delta}{x} \left[ \sum_{j=1}^N \rho_j^a x^{-j} - \rho_N^a x^{-N-1} \right] \right) \\ & = & - \left( \frac{\delta}{x} + \xi x \right) F(x) + \rho_1^a \xi + \delta \rho_N^a x^{-N-1} \,. \end{split}$$

As the solution should be localized to the left site of the system, a reasonable approximation is  $\rho_N^a \approx 0$ . Solving the previous equation for F(x) results in

$$\begin{split} F(x) &= \frac{\rho_1^a \xi x}{\xi x^2 + x + \delta} = \frac{\rho_1^a \xi x}{(x - \rho_+)(x - \rho_-)} = \frac{\rho_1 \xi}{\rho_- - \rho_+} \left( \frac{1}{1 - \rho_+/x} - \frac{1}{1 - \rho_-/x} \right) \\ &= \mathcal{N} \sum_{j=0}^N (\rho_+^j - \rho_-^j) x^{-j} \,, \end{split}$$

where  $\mathcal{N}$  collects all constants and the  $\rho_{\pm}$  are the roots of the polynomial  $f(x) = \xi x^2 + x + \delta$  given by

$$\rho_{\pm} = -\frac{1}{2\xi} \pm \sqrt{\frac{1}{4\xi^2} - \frac{\delta}{\xi}} = \frac{\mu \pm \sqrt{\mu^2 - 4t^2 + 4\Delta_p^2}}{2(t + \Delta_p)}.$$
 (C.7)

A direct comparison with Eq. (C.6) gives the desired result

$$\rho_i^a = \mathcal{N} \left( \rho_+^{-j} - \rho_-^{-j} \right). \tag{C.8}$$

The constant  $\mathcal{N}$  is fixed by the condition  $\Gamma_a^2 = 1$ . The expression for  $\rho_j^b$  is derived in the same way, but with the modified generating function

$$\tilde{F}(x) = \sum_{j=1}^{N} \rho_j^b x^j \,.$$

This concludes the derivation of the MZM.

<sup>&</sup>lt;sup>1</sup> The ansatz chosen here leads to a result which is valid for all parameters  $\mu, t, \Delta_p > 0$ .

# Strong Zero Mode from Quantum Circuit

In this appendix, the unitary quantum circuit is derived that rotates the seed operator  $\Gamma_0 = \gamma_1^a$  to the Strong Zero Mode (SZM) of the two integrable points of the Kitaev-Hubbard Model (KHM). Under the Jordan-Wigner transformation, the model is given by

$$H_{\rm KH} = \sum_{j=1}^{N-1} -w \sigma_j^x \sigma_{j+1}^x + U \sigma_j^z \sigma_{j+1}^z + \frac{\mu}{2} \sum_{j=1}^{N-1} \sigma_j^z \,, \tag{D.1} \label{eq:KH}$$

and the two integrable points are defined by

I 
$$U = 0, |\mu| < 2w$$

II 
$$\mu = 0, |U| < w$$

The seed operator becomes  $\Gamma_0 = \sigma_1^x$  under the Jordan-Wigner transformation, and the SZM is given by

$$\Gamma_{\rm I} = \mathcal{N}(N) \sum_{j=1}^N \rho^{j-1} \left( \prod_{k < j} \sigma_k^z \right) \sigma_j^x \,, \quad \mathcal{N}(N) = \sqrt{\frac{1 - \rho^2}{1 - \rho^{2N}}} \,, \quad \rho = \frac{\mu}{2w} \tag{D.2}$$

for case I [84] and

$$\begin{split} \Gamma_{\mathrm{II}} &= \mathcal{N}(N) \sum_{j=1}^{\left \lfloor \frac{N+1}{2} \right \rfloor} (-\rho)^{j-1} \left( \prod_{k < j} \sigma_{2k-1}^y \sigma_{2k}^y \right) \sigma_{2j-1}^x \,, \\ \mathcal{N}(N) &= \sqrt{\frac{1-\rho^2}{1-\rho^2 \lfloor \frac{N+1}{2} \rfloor}} \,, \quad \rho = \frac{U}{w} \end{split} \tag{D.3}$$

for case II [224], respectively.

The aim is to find a unitary rotation represented by the quantum circuit

such that  $\Gamma_{\sigma} = U_{\sigma}\Gamma_{0}U_{\sigma}^{\dagger}$  for  $\sigma$  either I or II. As explained in Chapter VI, the local unitary matrices  $u_{j,j+1}^{\sigma}$  are chosen to commute with the parity operator  $\hat{P} = \prod_{j} (-\sigma_{j}^{z})$ . This requires that the total sum of the Pauli-X and Pauli-Y operators is conserved when acting on a pair of Pauli operators. In particular, by representing  $u_{j,j+1}^{\sigma}$  as the matrix exponential of an Hermitian operator  $V_{j,j+1}$  through

$$u_{j,j+1}^{\sigma} = e^{iV_{j,j+1}}$$
,

this operator can only be of the form

$$\begin{split} V_{j,j+1} &= \alpha_0 \, \mathbb{1} + \alpha_1 \sigma_j^z + \alpha_2 \sigma_{j+1}^z + \alpha_3 \sigma_j^z \sigma_{j+1}^z \\ &+ \alpha_4 \sigma_j^x \sigma_{j+1}^x + \alpha_5 \sigma_j^y \sigma_{j+1}^y + \alpha_6 \sigma_j^x \sigma_{j+1}^y + \alpha_7 \sigma_j^y \sigma_{j+1}^x \,, \end{split}$$

with  $\alpha_j \in \mathbb{R}$ .

### **D.1** Case I: U = 0

This section considers case I where the Hubbard interaction is zero. The model from Eq. (D.1) reduces to the Transverse Field Ising Model, and the SZM is given by Eq. (D.2). Below, two equivalent derivations of the unitary circuit U are presented.

### D.1.1 Algebraic Derivation

As the operator  $\Gamma_{\rm I}$  from Eq. (D.2) is a sum over strings of the type  $(\prod_{k < j} \sigma_k^z) \sigma_j^x$ , the two-body unitary should encode the transformation

$$\sigma_j^x \xrightarrow{u_{j,j+1}^I} \xi_1 \, \sigma_j^x + \xi_2 \, \sigma_j^z \sigma_{j+1}^x \,, \quad \xi_1^2 + \xi_2^2 = 1 \,.$$

In this way, the Pauli-X operator is shifted to the right owing to the ladder structure of the quantum circuit, generating the desired string structure.

An operator generating this transformation is given by

$$u_{i,j+1}^{\mathbf{I}} = e^{i\alpha_j \sigma_j^y \sigma_{j+1}^x} = \cos(\alpha_i) \, \mathbb{1} + i \sin(\alpha_i) \sigma_i^y \sigma_{j+1}^x \tag{D.5}$$

with  $\xi_1 = \cos(2\alpha_i)$  and  $\xi_2 = \sin(2\alpha_i)$ .

Applying the full unitary circuit to the seed operator  $\Gamma_0 = \sigma_1^x$  leads to

$$U_{\rm I}\,\Gamma_0 U_{\rm I}^\dagger = \sum_{j=1}^{N-1} \cos(2\alpha_j) \left(\prod_{k=1}^{j-1} \sin(2\alpha_k) \sigma_k^z\right) \sigma_j^x + \left(\prod_{k=1}^{N-1} \sin(2\alpha_k) \sigma_k^z\right) \sigma_N^x. \tag{D.6}$$

Compared to the expression of the SZM in Eq. (D.2), the angles have to fulfill the conditions

$$\begin{split} \gamma_{j} &= \cos(2\alpha_{j}) \prod_{k=1}^{j-1} \sin(2\alpha_{k}) = \mathcal{N}(N) \rho^{j-1} = \sqrt{\frac{1-\rho^{2}}{1-\rho^{2N}}} \rho^{j-1} \quad \forall \quad 0 < j < N \\ \gamma_{N} &= \prod_{k=1}^{N-1} \sin(2\alpha_{k}) = \mathcal{N}(N) \rho^{N-1} = \sqrt{\frac{1-\rho^{2}}{1-\rho^{2N}}} \rho^{N-1} \; . \end{split} \tag{D.7}$$

Dividing  $\gamma_N$  by  $\gamma_{N-1}$  results in

$$\frac{\gamma_N}{\gamma_{N-1}} = \tan(2\alpha_{N-1}) = \rho\,,$$

defining the last rotation angle  $\alpha_{N-1}$ . To find the result for the remaining N-2 angles, consider the relation

$$\sum_{l=0}^r \gamma_{N-l}^2 = \prod_{k=1}^{N-r-1} \sin(2\alpha_k)^2 = \mathcal{N}(N)^2 \sum_{l=0}^r \rho^{2(N-l-1)} \,,$$

which can be proven by induction. Dividing this square sum by  $\gamma_{N-r-1}^2$  results in

$$\frac{\sum_{l=0}^{r}\gamma_{N-l}^{2}}{\gamma_{N-r-1}^{2}} = \tan(2\alpha_{N-r-1})^{2} = \frac{\sum_{l=0}^{r}\rho^{2(N-l-1)}}{\rho^{2(N-r-2)}}\,,$$

and by setting j=N-r-1 gives the solution for all the angles for  $1\leq j\leq N-2$ 

$$\tan(2\alpha_j)^2 = \rho^2 \sum_{l=0}^{N-j-1} \rho^{2(N-j-1-l)} = \rho^2 \sum_{k=0}^{N-j-1} \rho^{2k} \,,$$

where the last step follows after a simple change in the summation variable k = N - j - 1 - l. Putting everything together, the solution for all angles can be written as

$$\tan(2\alpha_j)^2 = \rho^2 \sum_{k=0}^{N-j-1} \rho^{2k} = \frac{\rho^2}{1-\rho^2} \left(1 - \rho^{2(N-j)}\right). \tag{D.8}$$

### D.1.2 Derivation Using a Matrix Product Operator

An alternative derivation of the same result can be performed using tensor networks. The SZM  $\Gamma$  from Eq. (D.2) can be written as a homogeneous Matrix Product Operator (MPO) of bond dimension  $\chi = 2$ 

$$W^{j} = \begin{pmatrix} \rho \sigma^{z} & \mathcal{N} \sigma^{x} \\ 0 & \mathbb{1} \end{pmatrix}, \quad W^{1} = \begin{pmatrix} \rho \sigma^{z} & \mathcal{N} \sigma^{x} \end{pmatrix}, \quad W^{N} = \begin{pmatrix} \mathcal{N} \sigma^{x} \\ \mathbb{1} \end{pmatrix}$$
 (D.9)

in the notation of Chapter 2. Similar, the seed operator can be represented as a bond dimension  $\chi=2$  MPO by

$$\tilde{W}^{j} = \begin{pmatrix} 0 & \sigma^{x} \\ 0 & \mathbb{1} \end{pmatrix}, \quad \tilde{W}^{1} = \begin{pmatrix} 0 & \sigma^{x} \end{pmatrix}, \quad \tilde{W}^{N} = \begin{pmatrix} \sigma^{x} \\ \mathbb{1} \end{pmatrix}.$$
 (D.10)

Let  $\operatorname{contr}(A, B)$  be the operation of contracting two tensors sharing one vertical link. The contraction of two neighboring  $\tilde{W}^j$  tensors along the vertical direction yields

$$\tilde{W}^{j,j+1} := \operatorname{contr}(W^j, W^{j+1}) = \begin{pmatrix} 0 & \sigma^x \otimes \mathbb{1} \\ 0 & \mathbb{1} \otimes \mathbb{1} \end{pmatrix} ,$$

and a two-body unitary acts on this contracted tensor as

$$\begin{split} u^{\mathrm{I}}_{j,j+1} \tilde{W}^{j,j+1} (u^{\mathrm{I}}_{j,j+1})^\dagger &= \begin{pmatrix} 0 & u^{\mathrm{I}}_{j,j+1} \left(\sigma^x \otimes \mathbb{1}\right) (u^{\mathrm{I}}_{j,j+1})^\dagger \\ 0 & \mathbb{1} \otimes \mathbb{1} \end{pmatrix} \\ &= \begin{pmatrix} 0 & \cos(2\alpha_j) \, \mathbb{1} \otimes \mathbb{1} + \sin(2\alpha_j) \, \mathbb{1} \otimes \sigma^x \\ 0 & \mathbb{1} \otimes \mathbb{1} \end{pmatrix} \,. \end{split}$$

The action on the left side of this equation is to be understood for every combination of horizontal indices, and the second line uses the parameterization of the unitary from Eq. (D.5).

Setting

$$u_{j,j+1}^{\mathrm{I}} \tilde{W}^{j,j+1} (u_{j,j+1}^{\mathrm{I}})^{\dagger} = \operatorname{contr}(T \tilde{W}^{j+1}), \quad T = \begin{pmatrix} A & B \\ C & D \end{pmatrix}$$

defines a splitting where the new right tensor is again the generating tensor of the seed operator  $\Gamma_0$ , allowing the application of the next two-body unitary in the same way. Writing out the right site of this equation, it is found

$$\begin{pmatrix} 0 & A \otimes \sigma^x + B \otimes \mathbb{1} \\ 0 & C \otimes \sigma^x + D \otimes \mathbb{1} \end{pmatrix} = \begin{pmatrix} 0 & \cos(2\alpha_j)\sigma^x \otimes \mathbb{1} + \sin(2\alpha_j)\sigma^z \otimes \sigma^x \\ 0 & \mathbb{1} \otimes \mathbb{1} \end{pmatrix}.$$

This set of matrix equations is uniquely solved by

$$A = \sin(2\alpha_i)\sigma^z$$
,  $B = \cos(2\alpha_i)\sigma^x$ ,  $C = 0$ ,  $D = 1$ ,

and the tensor T is the generating tensor of the  $\Gamma$  from Eq. (D.9) if the angles  $\alpha_j$  are chosen as in Eq. (D.8).

### D.2 Case II: $\mu = 0$

This section considers case II where the chemical potential is zero. The SZM is given by Eq. (D.3). Below, only the algebraic derivation is presented. The derivation using the MPO formalism is similar to that in case I.

Similar to case I, the operator  $\Gamma_{\text{II}}$  in Eq. (D.3) is a sum over strings of the form  $(\prod_{k< l} \sigma_k^y) \sigma_l^x$ , but the sum runs only over all odd sites l=2j-1 of the chain. This requires considering the combined action of two adjacent unitary matrices in the circuit of Eq. (D.4) acting on sites (2j-1,2j) and (2j,2j+1). A possible chain of parity conserving transformations is given by

$$\sigma_{2j-1}^{x} \xrightarrow{u_{2j-1,2j}^{\text{II}}} \xi_{1} \, \sigma_{2j-1}^{x} + \xi_{2} \, \sigma_{2j-1}^{y} \sigma_{2j}^{z} \xrightarrow{u_{2j,2j+1}^{\text{II}}} \xi_{1} \, \sigma_{2j-1}^{x} + \xi_{2} \, \sigma_{2j-1}^{y} \sigma_{2j}^{y} \sigma_{2j+1}^{x} \,, \quad (\text{D.11})$$

with the constrain  $\xi_1^2 + \xi_2^2 = 1$ . If this chain of transformation exists, the ladder structure ensures that the Pauli-X operator is shifted to the right by two lattice sites while generating the desired string structure, similar to case I.

Consider the first transformation

$$\sigma^x_{2j-1} \xrightarrow{u^{\rm II}_{2j-1,2j}} \; \xi_1 \, \sigma^x_{2j-1} + \xi_2 \sigma^y_{2j-1} \sigma^z_{2j} \, .$$

A unitary that preforms this rotation of Pauli matrices is given by

$$u^{\mathrm{II}}_{2j-1,2j} = e^{i\alpha_j\sigma^z_{2j-1}\sigma^z_{2j}} = \cos(\alpha_j)\,\mathbbm{1} + i\sin(\alpha_j)\sigma^z_{2j-1}\sigma^z_{2j} \tag{D.12}$$

with  $\xi_1 = \cos(2\alpha_i)$  and  $\xi_2 = -\sin(2\alpha_i)$ .

The second transformation acting as

$$\sigma_{2j}^z \xrightarrow{u_{2j,2j+1}^{\text{II}}} \sigma_{2j}^y \sigma_{2j+1}^x \,,$$

is generated by the unitary matrix

$$u_{2j,2j+1}^{\text{II}} = e^{i\frac{\pi}{4}\sigma_{2j}^x \sigma_{2j+1}^x} = \frac{1}{\sqrt{2}} \left( \mathbb{1} + i\sigma_{2j}^x \sigma_{2j+1}^x \right) . \tag{D.13}$$

Combining the two unitary matrices from Eqs. (D.12) and (D.13), the transformation chain from Eq. (D.11) is obtained.

Assume that  $N=2\tilde{N}+1$  is odd, and the full unitary circuit of Eq. (D.4) consists of an even number of two-body unitary transformations. The case of even sites can be treated equivalently, but requires a slightly modified two-body unitary transformation on the last two sites. Applying the full unitary circuit to the seed operator  $\Gamma_0 = \sigma_1^x$  leads to

$$\begin{split} U_{\text{II}} \Gamma_0 U_{\text{II}}^\dagger &= \sum_{j=1}^{\tilde{N}} (-1)^{j-1} \cos(2\alpha_j) \left( \prod_{k=1}^{j-1} \sin(2\alpha_k) \sigma_{2k-1}^y \sigma_{2k}^y \right) \sigma_{2j-1}^x \\ &+ (-1)^{\tilde{N}} \left( \prod_{k=1}^{\tilde{N}} \sin(2\alpha_k) \sigma_{2k-1}^y \sigma_{2k}^y \right) \sigma_{2\tilde{N}+1}^x \,. \end{split} \tag{D.14}$$

Compared to the expression of the SZM in Eq. (D.3), the angles have to fulfill the conditions

$$\begin{split} \gamma_{j} &= \cos(2\alpha_{j}) \prod_{k=1}^{j-1} \sin(2\alpha_{k}) = \mathcal{N}(N) \rho^{j-1} = \sqrt{\frac{1-\rho^{2}}{1-\rho^{2(\tilde{N}+1)}}} \rho^{j-1} \quad \forall \quad 0 < j \leq \tilde{N} \\ \gamma_{\tilde{N}+1} &= \prod_{k=1}^{\tilde{N}} \sin(2\alpha_{k}) = \mathcal{N}(N) \rho^{\tilde{N}} = \sqrt{\frac{1-\rho^{2}}{1-\rho^{2(\tilde{N}+1)}}} \rho^{\tilde{N}} \,. \end{split} \tag{D.15}$$

This set of equations is very similar to the set of equations (D.7) found in case I, and can thus be solved in a similar manner. The solution for the angles is given by for all  $1 \le j \le \tilde{N}$ 

$$\tan(2\alpha_j)^2 = \rho^2 \sum_{k=0}^{\tilde{N}-j} \rho^{2k} = \frac{\rho^2}{1-\rho^2} \left(1 - \rho^{2(\tilde{N}+1-j)}\right) \,. \tag{D.16}$$

## Matrix Product Operator from Finite State Machines

This appendix discusses the construction of a Matrix Product Operator (MPO) for a spin Hamiltonian consisting only interactions of finite range written as

$$H = \sum_{k}^{M} h_k \,.$$

The condition that the  $h_k$  are interactions of finite range implies that they only act non-trivially in a finite window of size  $n_k$  of the spin chain. Consequently, it can be written as

$$h_k = \mathbb{1} \otimes \cdots \otimes \mathbb{1} \otimes \hat{O}_1 \otimes \hat{O}_2 \cdots \otimes \hat{O}_{n_k} \otimes \mathbb{1} \cdots \otimes \mathbb{1}$$
 (E.1)

where  $\hat{O}$  and  $\hat{O}_{n_k}$  are non-trivial operators acting on sites j and  $n_k+j-1$ , respectively. The remaining operators between the two sites are either identity or non-trivial operators. This string of operators can be interpreted as the transition of a machine initialized in the state  $\mathcal{I}$  into a final state  $\mathcal{F}$  and a finite number of intermediate states. The transitions of the machine are labeled by the operators that appear in the string. For example, the only transition allowed from the final state  $\mathcal{F}$  is into  $\mathcal{F}$  itself, labeled by the identity  $\mathbb{1}$ , and the transitions allowed from the state  $\mathcal{I}$  are either transitions into  $\mathcal{I}$  itself, labeled by  $\mathbb{1}$ , or into the first non-trivial state 1 labeled by  $\hat{O}_1$ .

In this language, the string of operators can be written as the transition path

$$\mathbb{1} \stackrel{\hat{O}_1}{\longrightarrow} \mathbb{1} \stackrel{\hat{O}_2}{\longrightarrow} \mathbb{2} \stackrel{\hat{O}_3}{\longrightarrow} \cdots \stackrel{\hat{O}_{n_k}}{\longrightarrow} \mathbb{1}$$
(E.2)

where the term of Eq. (E.1) corresponds to a path through this graph, where the transition  $\mathcal{I} \to \mathcal{I}$  is taken exactly j-1 times. Moreover, collecting all terms in a sum generated by this graph by starting in node  $\mathcal{I}$  and ending in  $\mathcal{F}$  of length N generates the sum structure typical for local Hamiltonians.

By expanding this to include multiple terms, every finite-range Hamiltonian can be expressed as such a finite-state machine. Taking the Transverse Field Ising Model (TFIM) as an example. The TFIM is described by the Hamiltonian

$$H_{\text{Ising}} = -J \sum_{j=1}^{N-1} \sigma_j^x \sigma_{j+1}^x - g \sum_{j=1}^{N} \sigma_j^z.$$
 (E.3)

Applying the above described recipe, the TFIM is described by the finite state machine with three states

The direct connection of the initial  $\mathcal{I}$  and final  $\mathcal{F}$  nodes creates the transverse field contributions, and the transition of the intermediate node 1 creates the XX interactions.

Constructing the MPO representation based on the finite state machine is straightforward in terms of the transition matrix associated with the transition graph of the finite state machine. Therefore, the transition matrix is a matrix in which each column and row index represents one of the possible states of the finite state machine, and the entries are either zero, with no allowed transition, or carry the operator symbol of the transition. For the TFIM, the finite state machine has three internal states, and thus, the transition matrix is a  $3 \times 3$  matrix with entries

$$W = \begin{pmatrix} 1 & \sigma^x & -g\sigma^z \\ 0 & 0 & -J\sigma^x \\ 0 & 0 & 1 \end{pmatrix} . \tag{E.5}$$

By interpreting the entries of the transition matrix W as operators acting along the vertical direction, W becomes the MPO tensor of the TFIM. The boundary tensors for j=1 and j=N are thereby found by using the initial and final condition of the finite state machine, compactly written as the vectors

$$v_{\mathcal{I}} = \begin{pmatrix} 1 \\ 0 \\ 0 \end{pmatrix}, \quad v_{\mathcal{F}} = \begin{pmatrix} 0 \\ 0 \\ 1 \end{pmatrix},$$

with the boundary tensors given by

$$W^1 = v_{\mathcal{I}}^T W, \quad W^N = W v_{\mathcal{F}} .$$

This formalism can simply be extended to include exponentially decaying interactions. Taking, for example, the TFIM with an exponential decaying interaction term

$$H'_{\text{Ising}} = -J \sum_{j=1}^{N-1} \sum_{k=j+1}^{N} \lambda^{k-j-1} \sigma_j^x \sigma_k^x - g \sum_{j=1}^{N} \sigma_j^z.$$
 (E.6)

The transition graph of the finite state machine is a simple extension of the graph in Eq. (E.4) and given by

The finite state machine is now allowed to spend arbitrary time in the intermediate state 1, generating a long-ranged exponentially decaying interaction term.

Using the transition matrix of this finite state machine, the  $\overline{\text{MPO}}$  tensors are readily found as

$$W = \begin{pmatrix} \mathbb{1} & \sigma^x & -g\sigma^z \\ 0 & \lambda \, \mathbb{1} & -J\sigma^x \\ 0 & 0 & \mathbb{1} \end{pmatrix} . \tag{E.8}$$

The boundary tensors are the same as those for the standard TFIM.

### **Bibliography**

- [1] P.W. Shor. "Algorithms for quantum computation: discrete logarithms and factoring." In: *Proceedings 35th Annual Symposium on Foundations of Computer Science*. 1994, pp. 124–134. doi: 10.1109/SFCS.1994.365700.
- [2] Richard P. Feynman. "Simulating physics with computers." In: *International Journal of Theoretical Physics* 21.6 (June 1982), pp. 467–488. issn: 1572-9575. doi: 10.1007/BF02650179.
- [3] Lincoln D. Carr, David DeMille, Roman V Krems, and Jun Ye. "Cold and ultracold molecules: science, technology and applications." In: *New Journal of Physics* 11.5 (May 2009), p. 055049. doi: 10.1088/1367-2630/11/5/055049.
- [4] Maciej Lewenstein, Anna Sanpera, and Verònica Ahufinger. *Ultracold Atoms in Optical Lattices: Simulating quantum many-body systems*. Oxford University Press, Mar. 2012. isbn: 9780199573127. doi: 10.1093/acprof:oso/9780199573127.001.0001.
- [5] Immanuel Bloch and Peter Zoller. "Chapter 5 Ultracold Atoms and Molecules in Optical Lattices." In: *Ultracold Bosonic and Fermionic Gases*. Ed. by Kathryn Levin, Alexander L. Fetter, and Dan M. Stamper-Kurn. Vol. 5. Contemporary Concepts of Condensed Matter Science. Elsevier, 2012, pp. 121–156. doi: https://doi.org/10.1016/B978-0-444-53857-4.00005-2.
- [6] R. Blatt and C. F. Roos. "Quantum simulations with trapped ions." In: Nat. Phys. 8.4 (Apr. 2012), pp. 277–284. issn: 1745-2481. doi: 10.1038/nphys2252.
- [7] H. Häffner, C. F. Roos, and R. Blatt. "Quantum computing with trapped ions." In: *Physics Reports* 469.4 (2008), pp. 155–203. issn: 0370-1573. doi: https://doi.org/10.1016/j.physrep.2008.09.003.
- [8] Markus Greiner, Olaf Mandel, Theodor W. Hnsch, and Immanuel Bloch. "Collapse and revival of the matter wave field of a Bose–Einstein condensate." In: *Nature* 419.6902 (Sept. 2002), pp. 51–54. issn: 1476-4687. doi: 10.1038/nature00968.
- [9] Esteban A. Martinez et al. "Real-time dynamics of lattice gauge theories with a few-qubit quantum computer." In: *Nature* 534.7608 (June 2016), pp. 516–519. issn: 1476-4687. doi: 10.1038/nature18318.
- [10] Hannes Bernien et al. "Probing many-body dynamics on a 51-atom quantum simulator." In: *Nature* 551.7682 (Nov. 2017), pp. 579–584. issn: 1476-4687. doi: 10.1038/nature24622.
- [11] Matthew T. Bell, Benoît Douçot, Michael E. Gershenson, Lev B. Ioffe, and Aleksandra Petković. "Josephson ladders as a model system for 1D quantum phase transitions." en. In: *Comptes Rendus. Physique* 19.6 (2018), pp. 484–497. doi: 10.1016/j.crhy.2018.09.002.

[12] C. G. L. Bøttcher, F. Nichele, M. Kjaergaard, H. J. Suominen, J. Shabani, C. J. Palmstrøm, and C. M. Marcus. "Superconducting, insulating and anomalous metallic regimes in a gated two-dimensional semiconductor–superconductor array." In: *Nat. Phys.* 14.11 (Nov. 2018), pp. 1138–1144. issn: 1745-2481. doi: 10.1038/s41567-018-0259-9.

- [13] J. Shabani et al. "Two-dimensional epitaxial superconductor-semiconductor heterostructures: A platform for topological superconducting networks." In: *Phys. Rev. B* 93.15 (Apr. 2016), p. 155402. doi: 10.1103/PhysRevB.93.155402.
- [14] Matteo M. Wauters, Lorenzo Maffi, and Michele Burrello. "Engineering a Josephson junction chain for the simulation of the quantum clock model." In: *Phys. Rev. B* 111 (4 Jan. 2025), p. 045418. doi: 10.1103/PhysRevB.111.045418.
- [15] L. Banszerus, C. W. Andersson, W. Marshall, T. Lindemann, M. J. Manfra, C. M. Marcus, and S. Vaitiekėnas. "Hybrid Josephson Rhombus: A Superconducting Element with Tailored Current-Phase Relation." In: *Phys. Rev.* X 15.1 (Feb. 2025), p. 011021. doi: 10.1103/PhysRevX.15.011021.
- [16] L. Banszerus, W. Marshall, C. W. Andersson, T. Lindemann, M. J. Manfra, C. M. Marcus, and S. Vaitiekėnas. "Voltage-Controlled Synthesis of Higher Harmonics in Hybrid Josephson Junction Circuits." In: *Phys. Rev. Lett.* 133.18 (Oct. 2024), p. 186303. doi: 10.1103/PhysRevLett.133.186303.
- [17] Markus Greiner, Olaf Mandel, Tilman Esslinger, Theodor W. Hänsch, and Immanuel Bloch. "Quantum phase transition from a superfluid to a Mott insulator in a gas of ultracold atoms." In: *Nature* 415.6867 (Jan. 2002), pp. 39–44. issn: 1476-4687. doi: 10.1038/415039a.
- [18] Jae-yoon Choi, Sebastian Hild, Johannes Zeiher, Peter Schauß, Antonio Rubio-Abadal, Tarik Yefsah, Vedika Khemani, David A. Huse, Immanuel Bloch, and Christian Gross. "Exploring the many-body localization transition in two dimensions." In: Science 352.6293 (2016), pp. 1547–1552. doi: 10.1126/science.aaf8834. eprint: https://www.science.org/doi/pdf/10.1126/science.aaf8834.
- [19] E. M. Stoudenmire, David J. Clarke, Roger S. K. Mong, and Jason Alicea. "Assembling Fibonacci anyons from a  $\mathbb{Z}_3$  parafermion lattice model." In: *Phys. Rev. B* 91.23 (June 2015), p. 235112. doi: 10.1103/PhysRevB.91.235112.
- [20] Tobias Meng. "Coupled-wire constructions: a Luttinger liquid approach to topology." In: *The European Physical Journal Special Topics* 229.4 (Feb. 2020), pp. 527–543. issn: 1951-6401. doi: 10.1140/epjst/e2019-900095-5.
- [21] Aditi Mitra. "Quantum Quench Dynamics." In: Annual Review of Condensed Matter Physics 9.Volume 9, 2018 (2018), pp. 245–259. issn: 1947-5462. doi: https://doi.org/10.1146/annurev-conmatphys-031016-025451.
- [22] Joshua M. Deutsch. "Eigenstate thermalization hypothesis." In: Reports on Progress in Physics 81.8 (July 2018), p. 082001. doi: 10.1088/1361-6633/aac9f1.
- [23] Bela Bauer and Chetan Nayak. "Area laws in a many-body localized state and its implications for topological order." In: *Journal of Statistical Mechanics:* Theory and Experiment 2013.09 (Sept. 2013), P09005. doi: 10.1088/1742-5468/2013/09/P09005.

[24] Rahul Nandkishore and David A. Huse. "Many-Body Localization and Thermalization in Quantum Statistical Mechanics." In: *Annual Review of Condensed Matter Physics* 6 (2015), pp. 15–38. issn: 1947-5462. doi: https://doi.org/10.1146/annurev-conmatphys-031214-014726.

- [25] Romain Vasseur and Joel E. Moore. "Nonequilibrium quantum dynamics and transport: from integrability to many-body localization." In: *Journal of Statistical Mechanics: Theory and Experiment* 2016.6 (June 2016), p. 064010. doi: 10.1088/1742-5468/2016/06/064010.
- [26] C. J. Turner, A. A. Michailidis, D. A. Abanin, M. Serbyn, and Z. Papić. "Weak ergodicity breaking from quantum many-body scars." In: Nature Physics 14.7 (July 2018), pp. 745–749. issn: 1745-2481. doi: 10.1038/s41567-018-0137-5.
- [27] Maksym Serbyn, Dmitry A. Abanin, and Papić Zlatko. "Quantum manybody scars and weak breaking of ergodicity." In: *Nat. Phys.* 17.6 (June 2021), pp. 675–685. issn: 1745-2481. doi: 10.1038/s41567-021-01230-2.
- [28] Cheng-Ju Lin, Vladimir Calvera, and Timothy H. Hsieh. "Quantum manybody scar states in two-dimensional Rydberg atom arrays." In: *Phys. Rev. B* 101.22 (June 2020), p. 220304. doi: 10.1103/PhysRevB.101.220304.
- [29] Ammar Ali, Hanjing Xu, William Bernoudy, Alberto Nocera, Andrew D. King, and Arnab Banerjee. "Quantum quench dynamics of geometrically frustrated Ising models." In: *Nature Communications* 15.1 (Dec. 2024), p. 10756. issn: 2041-1723. doi: 10.1038/s41467-024-54701-4.
- [30] A. Zenesini, A. Berti, R. Cominotti, C. Rogora, I. G. Moss, T. P. Billam, I. Carusotto, G. Lamporesi, A. Recati, and G. Ferrari. "False vacuum decay via bubble formation in ferromagnetic superfluids." In: *Nature Physics* 20.4 (Apr. 2024), pp. 558–563. issn: 1745-2481. doi: 10.1038/s41567-023-02345-4.
- [31] Morteza Aghaee et al. "Interferometric single-shot parity measurement in InAs-Al hybrid devices." In: *Nature* 638.8051 (Feb. 2025), pp. 651–655. issn: 1476-4687. doi: 10.1038/s41586-024-08445-2.
- [32] Henry F. Legg. Comment on "Interferometric single-shot parity measurement in InAs-Al hybrid devices", Microsoft Quantum, Nature 638, 651-655 (2025). 2025. arXiv: 2503.08944 [cond-mat.mes-hall].
- [33] Niklas Tausendpfund, Sebastian Diehl, and Matteo Rizzi. "Majorana zero modes in fermionic wires coupled by Aharonov-Bohm cages." In: *Phys. Rev. B* 107.3 (Jan. 2023), p. 035124. doi: 10.1103/PhysRevB.107.035124.
- [34] Bernard Field and Tapio Simula. "Introduction to topological quantum computation with non-Abelian anyons." In: Quantum Science and Technology 3.4 (July 2018), p. 045004. doi: 10.1088/2058-9565/aacad2.
- [35] Lorenzo Maffi, Niklas Tausendpfund, Matteo Rizzi, and Michele Burrello. "Quantum Simulation of the Tricritical Ising Model in Tunable Josephson Junction Ladders." In: *Phys. Rev. Lett.* 132.22 (May 2024), p. 226502. doi: 10.1103/PhysRevLett.132.226502.
- [36] Wladislaw Krinitsin, Niklas Tausendpfund, Matteo Rizzi, Markus Heyl, and Markus Schmitt. "Roughening Dynamics of Interfaces in the Two-Dimensional Quantum Ising Model." In: Phys. Rev. Lett. 134.24 (June 2025), p. 240402. doi: 10.1103/9bsk-x9rw.

[37] Niklas Tausendpfund, Aditi Mitra, and Matteo Rizzi. "Almost strong zero modes at finite temperature." In: *Phys. Rev. Res.* 7.2 (June 2025), p. 023245. doi: 10.1103/PhysRevResearch.7.023245.

- [38] G. Kells, N. Moran, and D. Meidan. "Localization enhanced and degraded topological order in interacting *p*-wave wires." In: *Phys. Rev. B* 97.8 (Feb. 2018), p. 085425. doi: 10.1103/PhysRevB.97.085425.
- [39] Niklas Tausendpfund. Additional Data and Scripts for the PhD Thesis "On the Design and Characterization of Exotic Phases in One Dimension". July 2025. doi: 10.5281/zenodo.15809310.
- [40] Alexander L. Fetter and John D. Walecka. Quantum Theory of Many-Particle Systems. Dover Publications, June 2003.
- [41] Alexei A. Abrikosov. Fundamentals of the theory of metals. Dover Publications, 1988.
- [42] John W. Negele and Henri Orland. Quantum many-particle systems. CRC Press, 1998. doi: https://doi.org/10.1201/9780429497926.
- [43] Steven M. Girvin and Kun Yang. *Modern Condensed Matter Physics*. Cambridge University Press, 2019.
- [44] Sin-itiro Tomonaga. "Remarks on Bloch's Method of Sound Waves applied to Many-Fermion Problems." In: *Progress of Theoretical Physics* 5.4 (July 1950), pp. 544–569. issn: 0033-068X. doi: 10.1143/ptp/5.4.544. eprint: https://academic.oup.com/ptp/article-pdf/5/4/544/5430161/5-4-544.pdf.
- [45] Joaquin M. Luttinger. "An Exactly Soluble Model of a Many-Fermion System." In: Journal of Mathematical Physics 4.9 (Sept. 1963), pp. 1154–1162. issn: 0022-2488. doi: 10.1063/1.1704046. eprint: https://pubs.aip.org/aip/jmp/article-pdf/4/9/1154/19057386/1154\\_1\\_online.pdf.
- [46] F. Duncan M. Haldane. "'Luttinger liquid theory' of one-dimensional quantum fluids. I. Properties of the Luttinger model and their extension to the general 1D interacting spinless Fermi gas." In: *Journal of Physics C: Solid State Physics* 14.19 (July 1981), p. 2585. doi: 10.1088/0022-3719/14/19/010.
- [47] Thierry Giamarchi. Quantum Physics in One Dimension. Oxford University Press, Dec. 2003. isbn: 9780198525004. doi: 10.1093/acprof:oso/9780198525004.001.0001.
- [48] Herbert Wagner. "Long-wavelength excitations and the Goldstone theorem in many-particle systems with "broken symmetries"." In: Z. Phys. 195.3 (June 1966), pp. 273–299. issn: 0044-3328. doi: 10.1007/BF01325630.
- [49] N. David Mermin and Herbert Wagner. "Absence of Ferromagnetism or Antiferromagnetism in One- or Two-Dimensional Isotropic Heisenberg Models." In: *Phys. Rev. Lett.* 17.22 (Nov. 1966), pp. 1133–1136. doi: 10.1103/PhysRevLett.17.1133.
- [50] Pierre C. Hohenberg. "Existence of Long-Range Order in One and Two Dimensions." In: Phys. Rev. 158.2 (June 1967), pp. 383–386. doi: 10.1103/PhysRev.158.383.
- [51] Frank Pollmann, Ari M. Turner, Erez Berg, and Masaki Oshikawa. "Entanglement spectrum of a topological phase in one dimension." In: *Phys. Rev. B* 81.6 (Feb. 2010), p. 064439. doi: 10.1103/PhysRevB.81.064439.

[52] Xie Chen, Zheng-Cheng Gu, and Xiao-Gang Wen. "Classification of gapped symmetric phases in one-dimensional spin systems." In: *Phys. Rev. B* 83.3 (Jan. 2011), p. 035107. doi: 10.1103/PhysRevB.83.035107.

- [53] Ari M. Turner, Frank Pollmann, and Erez Berg. "Topological phases of onedimensional fermions: An entanglement point of view." In: *Phys. Rev. B* 83.7 (Feb. 2011), p. 075102. doi: 10.1103/PhysRevB.83.075102.
- [54] Xie Chen, Zheng-Cheng Gu, and Xiao-Gang Wen. "Complete classification of one-dimensional gapped quantum phases in interacting spin systems." In: *Phys. Rev. B* 84.23 (Dec. 2011), p. 235128. doi: 10.1103/PhysRevB.84.235128.
- [55] Valerie Coffman, Joydip Kundu, and William K. Wootters. "Distributed entanglement." In: *Phys. Rev. A* 61.5 (Apr. 2000), p. 052306. doi: 10.1103/PhysRevA.61.052306.
- [56] Tobias J. Osborne and Frank Verstraete. "General Monogamy Inequality for Bipartite Qubit Entanglement." In: Phys. Rev. Lett. 96.22 (June 2006), p. 220503. doi: 10.1103/PhysRevLett.96.220503.
- [57] Hans Bethe. "Zur Theorie der Metalle." In: Z. Phys. 71.3 (Mar. 1931), pp. 205–226. doi: 10.1007/BF01341708.
- [58] Jan von Delft and Herbert Schoeller. "Bosonization for beginners refermionization for experts." In: *Annalen der Physik* 510.4 (1998), pp. 225—305. doi: https://doi.org/10.1002/andp.19985100401. eprint: https://onlinelibrary.wiley.com/doi/pdf/10.1002/andp.19985100401.
- [59] D. Sénéchal. "An Introduction to Bosonization." In: Theoretical Methods for Strongly Correlated Electrons. Ed. by David Sénéchal, André-Marie Tremblay, and Claude Bourbonnais. New York, NY: Springer New York, 2004, pp. 139– 186. isbn: 978-0-387-21717-8. doi: 10.1007/0-387-21717-7\_4.
- [60] Steven R. White. "Density matrix formulation for quantum renormalization groups." In: *Phys. Rev. Lett.* 69.19 (Nov. 1992), pp. 2863–2866. doi: 10.1103/PhysRevLett.69.2863.
- [61] Román Orús. "A practical introduction to tensor networks: Matrix product states and projected entangled pair states." In: *Annals of Physics* 349 (Oct. 2014), pp. 117–158. issn: 0003-4916. doi: https://doi.org/10.1016/j.aop.2014.06.013.
- [62] Ulrich Schollwöck. "The density-matrix renormalization group in the age of matrix product states." In: *Annals of Physics* 326.1 (Jan. 2011). January 2011 Special Issue, pp. 96–192. issn: 0003-4916. doi: https://doi.org/10.1016/j.aop.2010.09.012.
- [63] Jutho Haegeman, J. Ignacio Cirac, Tobias J. Osborne, Iztok Pižorn, Henri Verschelde, and Frank Verstraete. "Time-Dependent Variational Principle for Quantum Lattices." In: *Phys. Rev. Lett.* 107.7 (Aug. 2011), p. 070601. doi: 10.1103/PhysRevLett.107.070601.
- [64] Jutho Haegeman, Bogdan Pirvu, David J. Weir, J. Ignacio Cirac, Tobias J. Osborne, Henri Verschelde, and Frank Verstraete. "Variational matrix product ansatz for dispersion relations." In: *Phys. Rev. B* 85.10 (Mar. 2012), p. 100408. doi: 10.1103/PhysRevB.85.100408.
- [65] Matthew B. Hastings and Tohru Koma. "Spectral Gap and Exponential Decay of Correlations." In: Commun. Math. Phys. 265.3 (Aug. 2006), pp. 781–804. issn: 1432-0916. doi: 10.1007/s00220-006-0030-4.

[66] Bruno Nachtergaele and Robert Sims. "Lieb-Robinson Bounds in Quantum Many-Body Physics." In: *Entropy and the Quantum* 529 (Apr. 2010), pp. 141–176. doi: 10.1090/conm/529/10429.

- [67] P. Di Francesco, P. Mathieu, and D. Senechal. Conformal Field Theory. New York, NY, USA: Springer-Verlag, 1997. isbn: 978-1-4612-2256-9. doi: 10. 1007/978-1-4612-2256-9.
- [68] Eugene Paul Wigner. Group theory and its application to the quantum mechanics of atomic spectra. Pure Appl. Phys. Trans. from the German. New York, NY: Academic Press, 1959.
- [69] Pietro Silvi, Ferdinand Tschirsich, Matthias Gerster, Johannes Jünemann, Daniel Jaschke, Matteo Rizzi, and Simone Montangero. "The Tensor Networks Anthology: Simulation techniques for many-body quantum lattice systems." In: SciPost Phys. Lect. Notes (2019), p. 8. doi: 10.21468/SciPostPhysLectNotes.8.
- [70] Oleg Derzhko. Jordan-Wigner fermionization for spin-1/2 systems in two dimensions: A brief review. 2001. arXiv: cond-mat/0101188 [cond-mat].
- [71] Sergey B. Bravyi and Alexei Yu. Kitaev. "Fermionic Quantum Computation." In: *Annals of Physics* 298.1 (2002), pp. 210–226. issn: 0003-4916. doi: https://doi.org/10.1006/aphy.2002.6254.
- [72] F. Verstraete and J. I. Cirac. "Mapping local Hamiltonians of fermions to local Hamiltonians of spins." In: *Journal of Statistical Mechanics: Theory and Experiment* 2005.09 (Sept. 2005), P09012. doi: 10.1088/1742-5468/2005/09/P09012.
- [73] Hermann Weyl. "Quantenmechanik und Gruppentheorie." In: Z. Phys. 46.1 (Nov. 1927), pp. 1–46. issn: 0044-3328. doi: 10.1007/BF02055756.
- [74] Dieter Jaksch and Peter Zoller. "The cold atom Hubbard toolbox." In: Annals of Physics 315.1 (2005). Special Issue, pp. 52–79. issn: 0003-4916. doi: https://doi.org/10.1016/j.aop.2004.09.010.
- [75] Rosario Fazio and Herre van der Zant. "Quantum phase transitions and vortex dynamics in superconducting networks." In: *Physics Reports* 355.4 (2001), pp. 235–334. issn: 0370-1573. doi: https://doi.org/10.1016/S0370-1573(01)00022-9.
- [76] Leon N. Cooper. "Bound Electron Pairs in a Degenerate Fermi Gas." In: *Phys. Rev.* 104.4 (Nov. 1956), pp. 1189–1190. doi: 10.1103/PhysRev.104.1189.
- [77] John Bardeen, Leon N. Cooper, and John R. Schrieffer. "Theory of Superconductivity." In: *Phys. Rev.* 108.5 (Dec. 1957), pp. 1175–1204. doi: 10.1103/PhysRev.108.1175.
- [78] Joseph B. Krieger and Gerald J. Iafrate. "Time evolution of Bloch electrons in a homogeneous electric field." In: *Phys. Rev. B* 33.8 (Apr. 1986), pp. 5494–5500. doi: 10.1103/PhysRevB.33.5494.
- [79] Kurt Schönhammer. "Newton's law for Bloch electrons, Klein factors, and deviations from canonical commutation relations." In: *Phys. Rev. B* 63 (24 May 2001), p. 245102. doi: 10.1103/PhysRevB.63.245102.
- [80] Kurt Schönhammer. "Canonically conjugate pairs and phase operators." In: Phys. Rev. A 66 (1 July 2002), p. 014101. doi: 10.1103/PhysRevA.66. 014101.

[81] Wolfgang Pauli. "Über den Zusammenhang des Abschlusses der Elektronengruppen im Atom mit der Komplexstruktur der Spektren." In: Z. Phys. 31.1 (Feb. 1925), pp. 765–783. issn: 0044-3328. doi: 10.1007/BF02980631.

- [82] P. Jordan and E. Wigner. "über das Paulische Äquivalenzverbot." In: *Z. Phys.* 47.9 (Sept. 1928), pp. 631–651. issn: 0044-3328. doi: 10.1007/BF01331938.
- [83] Glen Bigan Mbeng, Angelo Russomanno, and Giuseppe E. Santoro. "The quantum Ising chain for beginners." In: *SciPost Phys. Lect. Notes* (2024), p. 82. doi: 10.21468/SciPostPhysLectNotes.82.
- [84] A. Yu Kitaev. "Unpaired Majorana fermions in quantum wires." In: *Physics-Uspekhi* 44.10S (Oct. 2001), p. 131. doi: 10.1070/1063-7869/44/10S/S29.
- [85] Felix Bloch. "Über die Quantenmechanik der Elektronen in Kristallgittern." In: Zeitschrift für Physik 52.7 (July 1929), pp. 555–600. issn: 0044-3328. doi: 10.1007/BF01339455.
- [86] Y. Aharonov and D. Bohm. "Significance of Electromagnetic Potentials in the Quantum Theory." In: *Phys. Rev.* 115.3 (Aug. 1959), pp. 485–491. doi: 10.1103/PhysRev.115.485.
- [87] Y. Aharonov and D. Bohm. "Further Considerations on Electromagnetic Potentials in the Quantum Theory." In: Phys. Rev. 123.4 (Aug. 1961), pp. 1511–1524. doi: 10.1103/PhysRev.123.1511.
- [88] Rudolf Peierls. "Zur Theorie des Diamagnetismus von Leitungselektronen." In: Z. Phys. 80.11 (Nov. 1933), pp. 763–791. issn: 0044-3328. doi: 10.1007/BF01342591.
- [89] Douglas R. Hofstadter. "Energy levels and wave functions of Bloch electrons in rational and irrational magnetic fields." In: *Phys. Rev. B* 14.6 (Sept. 1976), pp. 2239–2249. doi: 10.1103/PhysRevB.14.2239.
- [90] Albert Einstein. "Quantentheorie des einatomigen idealen Gases." In: Königliche Preußische Akademie der Wissenschaften. Sitzungsberichte (July 1924), pp. 261–267.
- [91] Lewi Tonks. "The Complete Equation of State of One, Two and Three-Dimensional Gases of Hard Elastic Spheres." In: *Phys. Rev.* 50.10 (Nov. 1936), pp. 955–963. doi: 10.1103/PhysRev.50.955.
- [92] M. Girardeau. "Relationship between Systems of Impenetrable Bosons and Fermions in One Dimension." In: Journal of Mathematical Physics 1.6 (Nov. 1960), pp. 516–523. issn: 0022-2488. doi: 10.1063/1.1703687. eprint: https://pubs.aip.org/aip/jmp/article-pdf/1/6/516/19055341/516\\_1\\_online.pdf.
- [93] A. Gold and A. Ghazali. "Exchange effects in a quasi-one-dimensional electron gas." In: Phys. Rev. B 41.12 (Apr. 1990), pp. 8318–8322. doi: 10.1103/PhysRevB.41.8318.
- [94] U. Meirav, M. A. Kastner, and S. J. Wind. "Single-electron charging and periodic conductance resonances in GaAs nanostructures." In: *Phys. Rev. Lett.* 65.6 (Aug. 1990), pp. 771–774. doi: 10.1103/PhysRevLett.65.771.
- [95] Roman M. Lutchyn, Jay D. Sau, and S. Das Sarma. "Majorana Fermions and a Topological Phase Transition in Semiconductor-Superconductor Heterostructures." In: *Phys. Rev. Lett.* 105.7 (Aug. 2010), p. 077001. doi: 10.1103/PhysRevLett.105.077001.

[96] Yuval Oreg, Gil Refael, and Felix von Oppen. "Helical Liquids and Majorana Bound States in Quantum Wires." In: Phys. Rev. Lett. 105.17 (Oct. 2010), p. 177002. doi: 10.1103/PhysRevLett.105.177002.

- [97] Cristina Bena, Smitha Vishveshwara, Leon Balents, and Matthew P. A. Fisher. "Measuring Fractional Charge in Carbon Nanotubes." In: Journal of Statistical Physics 103.3 (May 2001), pp. 429–440. issn: 1572-9613. doi: 10.1023/A:1010376929353.
- [98] A. R. Goñi, A. Pinczuk, J. S. Weiner, J. M. Calleja, B. S. Dennis, L. N. Pfeiffer, and K. W. West. "One-dimensional plasmon dispersion and dispersionless intersubband excitations in GaAs quantum wires." In: *Phys. Rev. Lett.* 67.23 (Dec. 1991), pp. 3298–3301. doi: 10.1103/PhysRevLett.67.3298.
- [99] Yoshino K. Fukai, Hayato Nakano, Shunji Nakata, Seigo Tarucha, and Kunihiro Arai. "Transition from weak to strong spin-orbit scattering regime in diffusive InGaAs/InAlAs quantum wires." In: Solid State Communications 94.9 (1995), pp. 757–761. issn: 0038-1098. doi: https://doi.org/10.1016/0038-1098(95)00103-4.
- [100] Zhen Yao, Henk W. Ch. Postma, Leon Balents, and Cees Dekker. "Carbon nanotube intramolecular junctions." In: *Nature* 402.6759 (Nov. 1999), pp. 273–276. issn: 1476-4687. doi: 10.1038/46241.
- [101] Marc Bockrath, David H. Cobden, Jia Lu, Andrew G. Rinzler, Richard E. Smalley, Leon Balents, and Paul L. McEuen. "Luttinger-liquid behaviour in carbon nanotubes." In: *Nature* 397.6720 (Feb. 1999), pp. 598–601. issn: 1476-4687. doi: 10.1038/17569.
- [102] C. Menotti, M. Lewenstein, T. Lahaye, and T. Pfau. "Dipolar interaction in ultra-cold atomic gases." In: AIP Conf. Proc. 970.1 (Jan. 2008), pp. 332–361. issn: 0094-243X. doi: 10.1063/1.2839130.
- [103] Leonardo Mazza, Alejandro Bermudez, Nathan Goldman, Matteo Rizzi, Miguel Angel Martin-Delgado, and Maciej Lewenstein. "An optical-latticebased quantum simulator for relativistic field theories and topological insulators." In: New Journal of Physics 14.1 (Jan. 2012), p. 015007. doi: 10.1088/1367-2630/14/1/015007.
- [104] S. Baier, M. J. Mark, D. Petter, K. Aikawa, L. Chomaz, Z. Cai, M. Baranov, P. Zoller, and F. Ferlaino. "Extended Bose-Hubbard models with ultracold magnetic atoms." In: Science 352.6282 (2016), pp. 201-205. doi: 10.1126/ science.aac9812. eprint: https://www.science.org/doi/pdf/10.1126/ science.aac9812.
- [105] Jeong Ho Han, Jin Hyoun Kang, and Y. Shin. "Band Gap Closing in a Synthetic Hall Tube of Neutral Fermions." In: *Phys. Rev. Lett.* 122.6 (Feb. 2019), p. 065303. doi: 10.1103/PhysRevLett.122.065303.
- [106] Aurélien Fabre, Jean-Baptiste Bouhiron, Tanish Satoor, Raphael Lopes, and Sylvain Nascimbene. "Laughlin's Topological Charge Pump in an Atomic Hall Cylinder." In: *Phys. Rev. Lett.* 128.17 (Apr. 2022), p. 173202. doi: 10.1103/ PhysRevLett.128.173202.
- [107] Martin Leijnse and Karsten Flensberg. "Parity qubits and poor man's Majorana bound states in double quantum dots." In: Phys. Rev. B 86.13 (Oct. 2012), p. 134528. doi: 10.1103/PhysRevB.86.134528.

[108] Athanasios Tsintzis, Rubén Seoane Souto, and Martin Leijnse. "Creating and detecting poor man's Majorana bound states in interacting quantum dots." In: Phys. Rev. B 106.20 (Nov. 2022), p. L201404. doi: 10.1103/PhysRevB. 106.L201404.

- [109] Maximilian Nitsch, Lorenzo Maffi, Virgil V. Baran, Rubén Seoane Souto, Jens Paaske, Martin Leijnse, and Michele Burrello. "Poor Man's Majorana Tetron." In: PRX Quantum 6.3 (Sept. 2025), p. 030365. doi: 10.1103/r75t-jv32.
- [110] Rubén Seoane Souto, Virgil V. Baran, Maximilian Nitsch, Lorenzo Maffi, Jens Paaske, Martin Leijnse, and Michele Burrello. "Majorana modes in quantum dots coupled via a floating superconducting island." In: *Phys. Rev. B* 111.17 (May 2025), p. 174501. doi: 10.1103/PhysRevB.111.174501.
- [111] S. Nadj-Perge, I. K. Drozdov, B. A. Bernevig, and Ali Yazdani. "Proposal for realizing Majorana fermions in chains of magnetic atoms on a superconductor." In: *Phys. Rev. B* 88.2 (July 2013), p. 020407. doi: 10.1103/PhysRevB. 88.020407.
- [112] Falko Pientka, Leonid I. Glazman, and Felix von Oppen. "Topological superconducting phase in helical Shiba chains." In: *Phys. Rev. B* 88.15 (Oct. 2013), p. 155420. doi: 10.1103/PhysRevB.88.155420.
- [113] Jelena Klinovaja, Peter Stano, Ali Yazdani, and Daniel Loss. "Topological Superconductivity and Majorana Fermions in RKKY Systems." In: *Phys. Rev. Lett.* 111.18 (Nov. 2013), p. 186805. doi: 10.1103/PhysRevLett.111.186805.
- [114] Hiroyuki Shiba. "Classical Spins in Superconductors." In: Progress of Theoretical Physics 40.3 (Sept. 1968), pp. 435-451. issn: 0033-068X. doi: 10. 1143/PTP.40.435. eprint: https://academic.oup.com/ptp/articlepdf/40/3/435/5185550/40-3-435.pdf.
- [115] Gerbold C. Ménard et al. "Coherent long-range magnetic bound states in a superconductor." In: *Nat. Phys.* 11.12 (Dec. 2015), pp. 1013–1016. issn: 1745-2481. doi: 10.1038/nphys3508.
- [116] Leo P. Kadanoff. "Scaling laws for ising models near  $T_c$ ." In: *Physics Physique Fizika* 2.6 (June 1966), pp. 263–272. doi: 10.1103/PhysicsPhysiqueFizika. 2.263.
- [117] J.I. Cirac, D. Pérez-García, N. Schuch, and F. Verstraete. "Matrix product density operators: Renormalization fixed points and boundary theories." In: *Annals of Physics* 378 (2017), pp. 100–149. issn: 0003-4916. doi: https://doi.org/10.1016/j.aop.2016.12.030.
- [118] J. Ignacio Cirac, David Pérez-García, Norbert Schuch, and Frank Verstraete. "Matrix product states and projected entangled pair states: Concepts, symmetries, theorems." In: *Rev. Mod. Phys.* 93 (4 Dec. 2021), p. 045003. doi: 10.1103/RevModPhys.93.045003.
- [119] Xie Chen, Zheng-Cheng Gu, and Xiao-Gang Wen. "Local unitary transformation, long-range quantum entanglement, wave function renormalization, and topological order." In: *Phys. Rev. B* 82.15 (Oct. 2010), p. 155138. doi: 10.1103/PhysRevB.82.155138.
- [120] Aron J. Beekman, Louk Rademaker, and Jasper van Wezel. "An introduction to spontaneous symmetry breaking." In: *SciPost Phys. Lect. Notes* (2019), p. 11. doi: 10.21468/SciPostPhysLectNotes.11.

[121] T. Senthil. "Symmetry-Protected Topological Phases of Quantum Matter." In: Annual Review of Condensed Matter Physics 6. Volume 6, 2015 (2015), pp. 299–324. issn: 1947-5462. doi: https://doi.org/10.1146/annurev-conmatphys-031214-014740.

- [122] János K. Asbóth, László Oroszlány, and András Pályi. A Short Course on Topological Insulators. Cham, Switzerland: Springer International Publishing, 2016. isbn: 978-3-319-25607-8. doi: 10.1007/978-3-319-25607-8\_1.
- [123] Haruki Watanabe, Hosho Katsura, and Jong Yeon Lee. "Critical Spontaneous Breaking of U(1) Symmetry at Zero Temperature in One Dimension." In: *Phys. Rev. Lett.* 133.17 (Oct. 2024), p. 176001. doi: 10.1103/PhysRevLett. 133.176001.
- [124] Eduardo Fradkin. Field Theories of Condensed Matter Physics. 2nd ed. Cambridge University Press, 2013.
- [125] Amit Dutta, Gabriel Aeppli, Bikas K. Chakrabarti, Uma Divakaran, Thomas F. Rosenbaum, and Diptiman Sen. Quantum Phase Transitions in Transverse Field Spin Models: From Statistical Physics to Quantum Information. Cambridge University Press, 2015.
- [126] Subir Sachdev. Quantum Phases of Matter. Cambridge University Press, 2023.
- [127] Press release: The Nobel Prize in Physics 2016. Accessed: 5. May 2025. 2016.
- [128] Chetan Nayak, Steven H. Simon, Ady Stern, Michael Freedman, and Sankar Das Sarma. "Non-Abelian anyons and topological quantum computation." In: *Rev. Mod. Phys.* 80.3 (Sept. 2008), pp. 1083–1159. doi: 10.1103/RevModPhys. 80.1083.
- [129] Sumathi Rao. "Introduction to abelian and non-abelian anyons." In: *Topology* and Condensed Matter Physics. Ed. by Somendra Mohan Bhattacharjee, Mahan Mj, and Abhijit Bandyopadhyay. Singapore: Springer Singapore, 2017, pp. 399–437. isbn: 978-981-10-6841-6. doi: 10.1007/978-981-10-6841-6\_16.
- [130] Gregory Moore and Nicholas Read. "Nonabelions in the fractional quantum hall effect." In:  $Nuclear\ Physics\ B\ 360.2\ (1991)$ , pp. 362–396. issn: 0550-3213. doi: https://doi.org/10.1016/0550-3213(91)90407-0.
- [131] M. Milovanović and N. Read. "Edge excitations of paired fractional quantum Hall states." In: *Phys. Rev. B* 53.20 (May 1996), pp. 13559–13582. doi: 10.1103/PhysRevB.53.13559.
- [132] M. Storni, R. H. Morf, and S. Das Sarma. "Fractional Quantum Hall State at  $\nu=\frac{5}{2}$  and the Moore-Read Pfaffian." In: *Phys. Rev. Lett.* 104.7 (Feb. 2010), p. 076803. doi: 10.1103/PhysRevLett.104.076803.
- [133] Yi Zhou, Kazushi Kanoda, and Tai-Kai Ng. "Quantum spin liquid states." In: Rev. Mod. Phys. 89.2 (Apr. 2017), p. 025003. doi: 10.1103/RevModPhys. 89.025003.
- [134] C. Broholm, R. J. Cava, S. A. Kivelson, D. G. Nocera, M. R. Norman, and T. Senthil. "Quantum spin liquids." In: Science 367.6475 (2020), eaay0668. doi: 10.1126/science.aay0668. eprint: https://www.science.org/doi/pdf/10.1126/science.aay0668.
- [135] Jacob Shapiro. "The bulk-edge correspondence in three simple cases." In: Reviews in Mathematical Physics 32.03 (2020), p. 2030003. doi: 10.1142/S0129055X20300034. eprint: https://doi.org/10.1142/S0129055X20300034.

[136] Alexei Kitaev. "Periodic table for topological insulators and superconductors." In: AIP Conference Proceedings 1134.1 (May 2009), pp. 22–30. issn: 0094-243X. doi: 10.1063/1.3149495. eprint: https://pubs.aip.org/aip/acp/article-pdf/1134/1/22/11584243/22\\_1\\_online.pdf.

- [137] Shinsei Ryu, Andreas P. Schnyder, Akira Furusaki, and Andreas W. W. Ludwig. "Topological insulators and superconductors: tenfold way and dimensional hierarchy." In: *New Journal of Physics* 12.6 (June 2010), p. 065010. doi: 10.1088/1367-2630/12/6/065010.
- [138] Alexander Altland and Martin R. Zirnbauer. "Nonstandard symmetry classes in mesoscopic normal-superconducting hybrid structures." In: *Phys. Rev. B* 55.2 (Jan. 1997), pp. 1142–1161. doi: 10.1103/PhysRevB.55.1142.
- [139] Lukasz Fidkowski and Alexei Kitaev. "Effects of interactions on the topological classification of free fermion systems." In: *Phys. Rev. B* 81.13 (Apr. 2010), p. 134509. doi: 10.1103/PhysRevB.81.134509.
- [140] A. J. Heeger, S. Kivelson, J. R. Schrieffer, and W.-P. Su. "Solitons in conducting polymers." In: Rev. Mod. Phys. 60.3 (July 1988), pp. 781–850. doi: 10.1103/RevModPhys.60.781.
- [141] János K. Asbóth, László Oroszlány, and András Pályi. "The Su-Schrieffer-Heeger (SSH) Model." In: A Short Course on Topological Insulators: Band Structure and Edge States in One and Two Dimensions. Cham: Springer International Publishing, 2016, pp. 1–22. isbn: 978-3-319-25607-8. doi: 10.1007/978-3-319-25607-8\_1.
- [142] J. G. Valatin. "Comments on the theory of superconductivity." In: Il Nuovo Cimento (1955-1965) 7.6 (Mar. 1958), pp. 843-857. issn: 1827-6121. doi: 10. 1007/BF02745589.
- [143] N. N. Bogoljubov. "On a new method in the theory of superconductivity." In: Il Nuovo Cimento (1955-1965) 7.6 (Mar. 1958), pp. 794–805. issn: 1827-6121. doi: 10.1007/BF02745585.
- [144] Liang Fu and C. L. Kane. "Josephson current and noise at a superconductor/quantum-spin-Hall-insulator/superconductor junction." In: *Phys. Rev. B* 79.16 (Apr. 2009), p. 161408. doi: 10.1103/PhysRevB.79.161408.
- [145] E. M. Stoudenmire, Jason Alicea, Oleg A. Starykh, and Matthew P.A. Fisher. "Interaction effects in topological superconducting wires supporting Majorana fermions." In: *Phys. Rev. B* 84.1 (July 2011), p. 014503. doi: 10.1103/PhysRevB.84.014503.
- [146] Fabian Hassler and Dirk Schuricht. "Strongly interacting Majorana modes in an array of Josephson junctions." In: New Journal of Physics 14.12 (Dec. 2012), p. 125018. doi: 10.1088/1367-2630/14/12/125018.
- [147] Hosho Katsura, Dirk Schuricht, and Masahiro Takahashi. "Exact ground states and topological order in interacting Kitaev/Majorana chains." In: *Phys. Rev. B* 92.11 (Sept. 2015), p. 115137. doi: 10.1103/PhysRevB.92.115137.
- [148] Iman Mahyaeh and Eddy Ardonne. "Study of the phase diagram of the Kitaev-Hubbard chain." In: Phys. Rev. B 101.8 (Feb. 2020), p. 085125. doi: 10.1103/PhysRevB.101.085125.
- [149] G. Kells. "Multiparticle content of Majorana zero modes in the interacting p-wave wire." In: Phys. Rev. B 92.15 (Oct. 2015), p. 155434. doi: 10.1103/PhysRevB.92.155434.

[150] L. Mazza, M. Rizzi, M. D. Lukin, and J. I. Cirac. "Robustness of quantum memories based on Majorana zero modes." In: *Phys. Rev. B* 88 (20 Nov. 2013), p. 205142. doi: 10.1103/PhysRevB.88.205142.

- [151] Matteo Ippoliti, Matteo Rizzi, Vittorio Giovannetti, and Leonardo Mazza. "Quantum memories with zero-energy Majorana modes and experimental constraints." In: *Phys. Rev. A* 93 (6 June 2016), p. 062325. doi: 10.1103/PhysRevA.93.062325.
- [152] Jason Alicea. "New directions in the pursuit of Majorana fermions in solid state systems." In: Reports on Progress in Physics 75.7 (June 2012), p. 076501. doi: 10.1088/0034-4885/75/7/076501.
- [153] Yu. A. Bychkov and E. I. Rashba. "Properties of a 2D electron gas with lifted spectral degeneracy." In: *Journal of Experimental and Theoretical Physics Letters* 39.2 (Jan. 1984), p. 66.
- [154] G. Bihlmayer, O. Rader, and R. Winkler. "Focus on the Rashba effect." In: New Journal of Physics 17.5 (May 2015), p. 050202. doi: 10.1088/1367-2630/17/5/050202.
- [155] Lukasz Fidkowski, Roman M. Lutchyn, Chetan Nayak, and Matthew P. A. Fisher. "Majorana zero modes in one-dimensional quantum wires without long-ranged superconducting order." In: *Phys. Rev. B* 84.19 (Nov. 2011), p. 195436. doi: 10.1103/PhysRevB.84.195436.
- [156] Liang Fu and C. L. Kane. "Superconducting Proximity Effect and Majorana Fermions at the Surface of a Topological Insulator." In: *Phys. Rev. Lett.* 100.9 (Mar. 2008), p. 096407. doi: 10.1103/PhysRevLett.100.096407.
- [157] Tudor D. Stanescu, Jay D. Sau, Roman M. Lutchyn, and S. Das Sarma. "Proximity effect at the superconductor—topological insulator interface." In: *Phys. Rev. B* 81.24 (June 2010), p. 241310. doi: 10.1103/PhysRevB.81.241310.
- [158] J. A. Sauls. "Andreev bound states and their signatures." In: Philosophical Transactions of the Royal Society A: Mathematical, Physical and Engineering Sciences 376.2125 (2018), p. 20180140. doi: 10.1098/rsta.2018.0140. eprint: https://royalsocietypublishing.org/doi/pdf/10.1098/rsta.2018.0140.
- [159] Francesco Zatelli et al. "Robust poor man's Majorana zero modes using Yu-Shiba-Rusinov states." In: *Nature Communications* 15.1 (Sept. 2024), p. 7933. issn: 2041-1723. doi: 10.1038/s41467-024-52066-2.
- [160] Christina V. Kraus, Marcello Dalmonte, Mikhail A. Baranov, Andreas M. Läuchli, and P. Zoller. "Majorana Edge States in Atomic Wires Coupled by Pair Hopping." In: *Phys. Rev. Lett.* 111.17 (Oct. 2013), p. 173004. doi: 10.1103/PhysRevLett.111.173004.
- [161] Anna Keselman and Erez Berg. "Gapless symmetry-protected topological phase of fermions in one dimension." In: *Phys. Rev. B* 91.23 (June 2015), p. 235309. doi: 10.1103/PhysRevB.91.235309.
- [162] F. Iemini, L. Mazza, L. Fallani, P. Zoller, R. Fazio, and M. Dalmonte. "Majorana Quasiparticles Protected by Z₂ Angular Momentum Conservation." In: Phys. Rev. Lett. 118.20 (May 2017), p. 200404. doi: 10.1103/PhysRevLett. 118.200404.

[163] Tommy Li, Michele Burrello, and Karsten Flensberg. "Coulomb-interaction-induced Majorana edge modes in nanowires." In: *Phys. Rev. B* 100.4 (July 2019), p. 045305. doi: 10.1103/PhysRevB.100.045305.

- [164] Franco T. Lisandrini and Corinna Kollath. "Majorana edge modes in a spinful-particle conserving model." In: *Phys. Rev. B* 106.24 (Dec. 2022), p. 245121. doi: 10.1103/PhysRevB.106.245121.
- [165] Benjamin Michen, Tim Pokart, and Jan Carl Budich. "Adiabatic preparation of a number-conserving atomic Majorana phase." In: *Phys. Rev. B* 112.4 (July 2025), p. 045112. doi: 10.1103/dqsb-nzx1.
- [166] Fernando Iemini, Leonardo Mazza, Davide Rossini, Rosario Fazio, and Sebastian Diehl. "Localized Majorana-Like Modes in a Number-Conserving Setting: An Exactly Solvable Model." In: *Phys. Rev. Lett.* 115.15 (Oct. 2015), p. 156402. doi: 10.1103/PhysRevLett.115.156402.
- [167] Adilet Imambekov and Leonid I. Glazman. "Universal Theory of Nonlinear Luttinger Liquids." In: *Science* 323.5911 (2009), pp. 228–231. doi: 10.1126/science.1165403.
- [168] Ananda Roy, Dirk Schuricht, Johannes Hauschild, Frank Pollmann, and Hubert Saleur. "The quantum sine-Gordon model with quantum circuits." In: Nuclear Physics B 968 (2021), p. 115445. issn: 0550-3213. doi: https://doi.org/10.1016/j.nuclphysb.2021.115445.
- [169] John Cardy. "Conformal Field Theory and Statistical Mechanics." In: Les Houches Summer School: Session 89: Exacts Methods in Low-Dimensional Statistical Physics and Quantum Computing. July 2008. arXiv: 0807.3472 [cond-mat.stat-mech].
- [170] Giuseppe Mussardo. Statistical Field Theory. Oxford, England, UK: Oxford University Press, Mar. 2020.
- [171] A. Einstein, B. Podolsky, and N. Rosen. "Can Quantum-Mechanical Description of Physical Reality Be Considered Complete?" In: *Phys. Rev.* 47.10 (May 1935), pp. 777–780. doi: 10.1103/PhysRev.47.777.
- [172] J. S. Bell. "On the Einstein Podolsky Rosen paradox." In: *Physics Physique Fizika* 1.3 (Nov. 1964), pp. 195–200. doi: 10.1103/PhysicsPhysiqueFizika. 1.195.
- [173] Alain Aspect, Philippe Grangier, and Gérard Roger. "Experimental Tests of Realistic Local Theories via Bell's Theorem." In: *Phys. Rev. Lett.* 47.7 (Aug. 1981), pp. 460–463. doi: 10.1103/PhysRevLett.47.460.
- [174] Alain Aspect, Jean Dalibard, and Gérard Roger. "Experimental Test of Bell's Inequalities Using Time-Varying Analyzers." In: Phys. Rev. Lett. 49.25 (Dec. 1982), pp. 1804–1807. doi: 10.1103/PhysRevLett.49.1804.
- [175] Stuart J. Freedman and John F. Clauser. "Experimental Test of Local Hidden-Variable Theories." In: *Phys. Rev. Lett.* 28.14 (Apr. 1972), pp. 938–941. doi: 10.1103/PhysRevLett.28.938.
- [176] Daniel M. Greenberger, Michael A. Horne, and Anton Zeilinger. "Going Beyond Bell's Theorem." In: Bell's Theorem, Quantum Theory and Conceptions of the Universe. Ed. by Menas Kafatos. Dordrecht: Springer Netherlands, 1989, pp. 69–72. isbn: 978-94-017-0849-4. doi: 10.1007/978-94-017-0849-4\_10.

[177] Daniel M. Greenberger, Michael A. Horne, Abner Shimony, and Anton Zeilinger. "Bell's theorem without inequalities." In: American Journal of Physics 58.12 (Dec. 1990), pp. 1131–1143. issn: 0002-9505. doi: 10.1119/1.16243. eprint: https://pubs.aip.org/aapt/ajp/article-pdf/58/12/1131/11479397/1131\\_1\\_online.pdf.

- [178] Erhard Schmidt. "Zur Theorie der linearen und nichtlinearen Integralgleichungen." In: Math. Ann. 63.4 (Dec. 1907), pp. 433–476. issn: 1432-1807. doi: 10.1007/BF01449770.
- [179] Artur Ekert and Peter L. Knight. "Entangled quantum systems and the Schmidt decomposition." In: Am. J. Phys. 63.5 (May 1995), pp. 415–423. issn: 0002-9505. doi: 10.1119/1.17904.
- [180] Ingo Peschel and Viktor Eisler. "Reduced density matrices and entanglement entropy in free lattice models." In: Journal of Physics A: Mathematical and Theoretical 42.50 (Dec. 2009), p. 504003. doi: 10.1088/1751-8113/42/50/ 504003.
- [181] Daniele Contessi, Alessio Recati, and Matteo Rizzi. "Phase diagram detection via Gaussian fitting of number probability distribution." In: *Phys. Rev. B* 107.12 (Mar. 2023), p. L121403. doi: 10.1103/PhysRevB.107.L121403.
- [182] Andreas M. Läuchli. Operator content of real-space entanglement spectra at conformal critical points. 2013. arXiv: 1303.0741 [cond-mat.stat-mech].
- [183] Rui-Zhen Huang, Long Zhang, Andreas M. Läuchli, Jutho Haegeman, Frank Verstraete, and Laurens Vanderstraeten. "Emergent Conformal Boundaries from Finite-Entanglement Scaling in Matrix Product States." In: *Phys. Rev. Lett.* 132.8 (Feb. 2024), p. 086503. doi: 10.1103/PhysRevLett.132.086503.
- [184] Vincenzo Alba, Masudul Haque, and Andreas M. Läuchli. "Boundary-Locality and Perturbative Structure of Entanglement Spectra in Gapped Systems." In: Phys. Rev. Lett. 108.22 (May 2012), p. 227201. doi: 10.1103/PhysRevLett.108.227201.
- [185] Don N. Page. "Average entropy of a subsystem." In: *Phys. Rev. Lett.* 71.9 (Aug. 1993), pp. 1291–1294. doi: 10.1103/PhysRevLett.71.1291.
- [186] S. K. Foong and S. Kanno. "Proof of Page's conjecture on the average entropy of a subsystem." In: *Phys. Rev. Lett.* 72.8 (Feb. 1994), pp. 1148–1151. doi: 10.1103/PhysRevLett.72.1148.
- [187] Jorge Sánchez-Ruiz. "Simple proof of Page's conjecture on the average entropy of a subsystem." In: *Phys. Rev. E* 52.5 (Nov. 1995), pp. 5653–5655. doi: 10.1103/PhysRevE.52.5653.
- [188] Siddhartha Sen. "Average Entropy of a Quantum Subsystem." In: *Phys. Rev. Lett.* 77.1 (July 1996), pp. 1–3. doi: 10.1103/PhysRevLett.77.1.
- [189] Michael M. Wolf, Frank Verstraete, Matthew B. Hastings, and J. Ignacio Cirac. "Area Laws in Quantum Systems: Mutual Information and Correlations." In: *Phys. Rev. Lett.* 100.7 (Feb. 2008), p. 070502. doi: 10.1103/ PhysRevLett.100.070502.
- [190] M. B. Hastings. "An area law for one-dimensional quantum systems." In: Journal of Statistical Mechanics: Theory and Experiment 2007.08 (Aug. 2007), P08024. doi: 10.1088/1742-5468/2007/08/P08024.
- [191] Mark Srednicki. "Entropy and area." In: Phys. Rev. Lett. 71.5 (Aug. 1993), pp. 666–669. doi: 10.1103/PhysRevLett.71.666.

[192] J. Eisert, M. Cramer, and M. B. Plenio. "Colloquium: Area laws for the entanglement entropy." In: *Rev. Mod. Phys.* 82.1 (Feb. 2010), pp. 277–306. doi: 10.1103/RevModPhys.82.277.

- [193] Nicolas Laflorencie. "Quantum entanglement in condensed matter systems." In: *Physics Reports* 646 (2016). Quantum entanglement in condensed matter systems, pp. 1–59. issn: 0370-1573. doi: https://doi.org/10.1016/j.physrep.2016.06.008.
- [194] G. Vidal, J. I. Latorre, E. Rico, and A. Kitaev. "Entanglement in Quantum Critical Phenomena." In: *Phys. Rev. Lett.* 90.22 (June 2003), p. 227902. doi: 10.1103/PhysRevLett.90.227902.
- [195] Pasquale Calabrese and John Cardy. "Entanglement entropy and quantum field theory." In: *Journal of Statistical Mechanics: Theory and Experiment* 2004.06 (June 2004), P06002. doi: 10.1088/1742-5468/2004/06/P06002.
- [196] Vincenzo Alba, Maurizio Fagotti, and Pasquale Calabrese. "Entanglement entropy of excited states." In: *Journal of Statistical Mechanics: Theory and Experiment* 2009.10 (Oct. 2009), P10020. doi: 10.1088/1742-5468/2009/10/P10020.
- [197] Lluís Masanes. "Area law for the entropy of low-energy states." In: *Phys. Rev.* A 80.5 (Nov. 2009), p. 052104. doi: 10.1103/PhysRevA.80.052104.
- [198] Jutho Haegeman, Spyridon Michalakis, Bruno Nachtergaele, Tobias J. Osborne, Norbert Schuch, and Frank Verstraete. "Elementary Excitations in Gapped Quantum Spin Systems." In: *Phys. Rev. Lett.* 111.8 (Aug. 2013), p. 080401. doi: 10.1103/PhysRevLett.111.080401.
- [199] A. Bijl, J. de Boer, and A. Michels. "Properties of liquid helium II." In: *Physica* 8.7 (1941), pp. 655–675. issn: 0031-8914. doi: https://doi.org/10.1016/S0031-8914(41)90422-6.
- [200] Richard P. Feynman. "Atomic Theory of the Two-Fluid Model of Liquid Helium." In: *Phys. Rev.* 94.2 (Apr. 1954), pp. 262–277. doi: 10.1103/PhysRev. 94.262.
- [201] Richard P. Feynman and Michael Cohen. "Energy Spectrum of the Excitations in Liquid Helium." In: *Phys. Rev.* 102.5 (June 1956), pp. 1189–1204. doi: 10.1103/PhysRev.102.1189.
- [202] P. W. Anderson. "An Approximate Quantum Theory of the Antiferromagnetic Ground State." In: *Phys. Rev.* 86.5 (June 1952), pp. 694–701. doi: 10.1103/PhysRev.86.694.
- [203] Claire Lhuillier. Frustrated Quantum Magnets. 2005. arXiv: cond-mat/0502464 [cond-mat.str-el].
- [204] Yoichiro Nambu. "Quasi-Particles and Gauge Invariance in the Theory of Superconductivity." In: *Phys. Rev.* 117.3 (Feb. 1960), pp. 648–663. doi: 10. 1103/PhysRev.117.648.
- [205] Jeffrey Goldstone. "Field theories with "superconductor" solutions." In: Nuovo Cimento 19 (1961), pp. 154–164. doi: 10.1007/BF02812722.
- [206] Jeffrey Goldstone, Abdus Salam, and Steven Weinberg. "Broken Symmetries." In: Phys. Rev. 127.3 (Aug. 1962), pp. 965–970. doi: 10.1103/PhysRev.127.965.

[207] Michael M. Wolf. "Violation of the Entropic Area Law for Fermions." In: *Phys. Rev. Lett.* 96.1 (Jan. 2006), p. 010404. doi: 10.1103/PhysRevLett. 96.010404.

- [208] Dimitri Gioev and Israel Klich. "Entanglement Entropy of Fermions in Any Dimension and the Widom Conjecture." In: *Phys. Rev. Lett.* 96.10 (Mar. 2006), p. 100503. doi: 10.1103/PhysRevLett.96.100503.
- [209] Alexei Kitaev and John Preskill. "Topological Entanglement Entropy." In: Phys. Rev. Lett. 96.11 (Mar. 2006), p. 110404. doi: 10.1103/PhysRevLett. 96.110404.
- [210] J. Ignacio Cirac, Didier Poilblanc, Norbert Schuch, and Frank Verstraete. "Entanglement spectrum and boundary theories with projected entangled-pair states." In: *Phys. Rev. B* 83.24 (June 2011), p. 245134. doi: 10.1103/PhysRevB.83.245134.
- [211] Hui Li and F. D. M. Haldane. "Entanglement Spectrum as a Generalization of Entanglement Entropy: Identification of Topological Order in Non-Abelian Fractional Quantum Hall Effect States." In: *Phys. Rev. Lett.* 101.1 (July 2008), p. 010504. doi: 10.1103/PhysRevLett.101.010504.
- [212] Erik Lennart Weerda and Matteo Rizzi. "Fractional quantum Hall states with variational projected entangled-pair states: A study of the bosonic Harper-Hofstadter model." In: *Phys. Rev. B* 109.24 (June 2024), p. L241117. doi: 10.1103/PhysRevB.109.L241117.
- [213] Jack Kemp, Norman Y. Yao, Christopher R. Laumann, and Paul Fendley. "Long coherence times for edge spins." In: *Journal of Statistical Mechanics:* Theory and Experiment 2017.6 (June 2017). issn: 17425468. doi: 10.1088/1742-5468/aa73f0.
- [214] Dominic V. Else, Paul Fendley, Jack Kemp, and Chetan Nayak. "Prethermal Strong Zero Modes and Topological Qubits." In: *Phys. Rev. X* 7.4 (Dec. 2017), p. 041062. doi: 10.1103/PhysRevX.7.041062.
- [215] Daniel E. Parker, Romain Vasseur, and Thomas Scaffidi. "Topologically Protected Long Edge Coherence Times in Symmetry-Broken Phases." In: *Phys. Rev. Lett.* 122.24 (June 2019), p. 240605. doi: 10.1103/PhysRevLett.122.240605.
- [216] Jack Kemp, Norman Y. Yao, and Chris R. Laumann. "Symmetry-Enhanced Boundary Qubits at Infinite Temperature." In: *Phys. Rev. Lett.* 125.20 (Nov. 2020), p. 200506. doi: 10.1103/PhysRevLett.125.200506.
- [217] Daniel J. Yates, Alexander G. Abanov, and Aditi Mitra. "Lifetime of Almost Strong Edge-Mode Operators in One-Dimensional, Interacting, Symmetry Protected Topological Phases." In: *Phys. Rev. Lett.* 124.20 (May 2020), p. 206803. doi: 10.1103/PhysRevLett.124.206803.
- [218] Daniel J. Yates, Alexander G. Abanov, and Aditi Mitra. "Dynamics of almost strong edge modes in spin chains away from integrability." In: *Phys. Rev. B* 102.19 (Nov. 2020), p. 195419. doi: 10.1103/PhysRevB.102.195419.
- [219] Hsiu-Chung Yeh, Gabriel Cardoso, Leonid Korneev, Dries Sels, Alexander G. Abanov, and Aditi Mitra. "Slowly decaying zero mode in a weakly nonintegrable boundary impurity model." In: *Phys. Rev. B* 108.16 (Oct. 2023), p. 165143. doi: 10.1103/PhysRevB.108.165143.

[220] Christopher T. Olund, Norman Y. Yao, and Jack Kemp. "Boundary strong zero modes." In: Phys. Rev. B 111.20 (May 2025), p. L201114. doi: 10.1103/ PhysRevB.111.L201114.

- [221] V.S. Viswanath and G. Müller. *The Recursion Method: Application to Many Body Dynamics*. 1st ed. Lecture Notes in Physics Monographs. Springer Berlin Heidelberg, Nov. 1994. isbn: 978-3-540-48651-0.
- [222] Daniel E. Parker, Xiangyu Cao, Alexander Avdoshkin, Thomas Scaffidi, and Ehud Altman. "A Universal Operator Growth Hypothesis." In: *Physical Review X* 9.4 (Oct. 2019). issn: 21603308. doi: 10.1103/PhysRevX.9.041017.
- [223] Pratik Nandy, Apollonas S. Matsoukas-Roubeas, Pablo Martínez-Azcona, Anatoly Dymarsky, and Adolfo del Campo. "Quantum dynamics in Krylov space: Methods and applications." In: *Physics Reports* 1125-1128 (2025). Quantum dynamics in Krylov space: Methods and applications, pp. 1–82. issn: 0370-1573. doi: https://doi.org/10.1016/j.physrep.2025.05.001.
- [224] Paul Fendley. "Strong zero modes and eigenstate phase transitions in the XYZ/interacting Majorana chain." In: *Journal of Physics A: Mathematical and Theoretical* 49.30 (June 2016). issn: 17518121. doi: 10.1088/1751-8113/49/30/30LT01.
- [225] A. N. Kirillov and N. Yu Reshetikhin. "Exact solution of the integrable XXZ Heisenberg model with arbitrary spin. I. The ground state and the excitation spectrum." In: *Journal of Physics A: Mathematical and General* 20.6 (Apr. 1987), p. 1565. doi: 10.1088/0305-4470/20/6/038.
- [226] G. Vidal. "Entanglement Renormalization." In: *Phys. Rev. Lett.* 99.22 (Nov. 2007), p. 220405. doi: 10.1103/PhysRevLett.99.220405.
- [227] G. Vidal. "Class of Quantum Many-Body States That Can Be Efficiently Simulated." In: *Phys. Rev. Lett.* 101.11 (Sept. 2008), p. 110501. doi: 10.1103/PhysRevLett.101.110501.
- [228] F. Verstraete and J. I. Cirac. Renormalization algorithms for Quantum-Many Body Systems in two and higher dimensions. 2004. arXiv: cond-mat/0407066 [cond-mat.str-el].
- [229] J. Jordan, R. Orús, G. Vidal, F. Verstraete, and J. I. Cirac. "Classical Simulation of Infinite-Size Quantum Lattice Systems in Two Spatial Dimensions." In: *Phys. Rev. Lett.* 101.25 (Dec. 2008), p. 250602. doi: 10.1103/PhysRevLett. 101.250602.
- [230] Steven R. White and Adrian E. Feiguin. "Real-Time Evolution Using the Density Matrix Renormalization Group." In: *Phys. Rev. Lett.* 93.7 (Aug. 2004), p. 076401. doi: 10.1103/PhysRevLett.93.076401.
- [231] Michael Zwolak and Guifré Vidal. "Mixed-State Dynamics in One-Dimensional Quantum Lattice Systems: A Time-Dependent Superoperator Renormalization Algorithm." In: *Phys. Rev. Lett.* 93.20 (Nov. 2004), p. 207205. doi: 10.1103/PhysRevLett.93.207205.
- [232] Jutho Haegeman, Christian Lubich, Ivan Oseledets, Bart Vandereycken, and Frank Verstraete. "Unifying time evolution and optimization with matrix product states." In: *Phys. Rev. B* 94.16 (Oct. 2016), p. 165116. doi: 10.1103/PhysRevB.94.165116.

[233] Raghavendra Dheeraj Peddinti, Stefano Pisoni, Alessandro Marini, Philippe Lott, Henrique Argentieri, Egor Tiunov, and Leandro Aolita. "Quantum-inspired framework for computational fluid dynamics." In: *Communications Physics* 7.1 (Apr. 2024), p. 135. issn: 2399-3650. doi: 10.1038/s42005-024-01623-8.

- [234] Erika Ye and Nuno F. Loureiro. "Quantized tensor networks for solving the Vlasov–Maxwell equations." In: *Journal of Plasma Physics* 90.3 (2024), p. 805900301. doi: 10.1017/S0022377824000503.
- [235] Raj G. Patel et al. Quantum-Inspired Tensor Neural Networks for Option Pricing. 2024. arXiv: 2212.14076 [q-fin.PR].
- [236] Nozomu Kobayashi, Yoshiyuki Suimon, and Koichi Miyamoto. *Time series generation for option pricing on quantum computers using tensor network*. 2024. arXiv: 2402.17148 [quant-ph].
- [237] Roger Penrose. "Applications of negative dimensional tensors." In: Combinatorial Mathematics and its Applications, Academic Press. Academic Press, 1971, pp. 221–244.
- [238] David Pérez-García, Frank Verstraete, Michael Wolf, and J. Cirac. "Matrix Product State Representations." In: *Quantum Information & Computation* 7 (July 2007), pp. 401–430. doi: 10.26421/QIC7.5-6-1.
- [239] Thomas H. Seligman and Tomaž Prosen. "Third quantization." In: *AIP Conference Proceedings* 1323.1 (Dec. 2010), pp. 296–300. issn: 0094-243X. doi: 10.1063/1.3537859. eprint: https://pubs.aip.org/aip/acp/article-pdf/1323/1/296/11999212/296\\_1\\_online.pdf.
- [240] Ian P. McCulloch. "From density-matrix renormalization group to matrix product states." In: *Journal of Statistical Mechanics: Theory and Experiment* 2007.10 (Oct. 2007), P10014. doi: 10.1088/1742-5468/2007/10/P10014.
- [241] Gregory M. Crosswhite and Dave Bacon. "Finite automata for caching in matrix product algorithms." In: *Phys. Rev. A* 78 (1 July 2008), p. 012356. doi: 10.1103/PhysRevA.78.012356.
- [242] Gregory M. Crosswhite, A. C. Doherty, and Guifré Vidal. "Applying matrix product operators to model systems with long-range interactions." In: *Phys. Rev. B* 78.3 (July 2008), p. 035116. doi: 10.1103/PhysRevB.78.035116.
- [243] Sebastian Paeckel, Thomas Köhler, and Salvatore R. Manmana. "Automated construction of U(1)-invariant matrix-product operators from graph representations." In:  $SciPost\ Phys.\ 3\ (2017)$ , p. 035. doi: 10.21468/SciPostPhys. 3.5.035.
- [244] Daniel E. Parker, Xiangyu Cao, and Michael P. Zaletel. "Local matrix product operators: Canonical form, compression, and control theory." In: *Phys. Rev. B* 102.3 (July 2020), p. 035147. doi: 10.1103/PhysRevB.102.035147.
- [245] G. Vidal. "Classical Simulation of Infinite-Size Quantum Lattice Systems in One Spatial Dimension." In: *Phys. Rev. Lett.* 98.7 (Feb. 2007), p. 070201. doi: 10.1103/PhysRevLett.98.070201.
- [246] Laurens Vanderstraeten, Jutho Haegeman, and Frank Verstraete. "Tangent-space methods for uniform matrix product states." In: SciPost Phys. Lect. Notes (2019), p. 7. doi: 10.21468/SciPostPhysLectNotes.7.

[247] V. Zauner, D. Draxler, L. Vanderstraeten, M. Degroote, J. Haegeman, M. M. Rams, V. Stojevic, N. Schuch, and F. Verstraete. "Transfer matrices and excitations with matrix product states." In: New Journal of Physics 17.5 (May 2015), p. 053002. doi: 10.1088/1367-2630/17/5/053002.

- [248] Marek M. Rams and Bogdan Damski. "Quantum Fidelity in the Thermodynamic Limit." In: *Phys. Rev. Lett.* 106.5 (Feb. 2011), p. 055701. doi: 10.1103/PhysRevLett.106.055701.
- [249] Davide Rossini and Ettore Vicari. "Ground-state fidelity at first-order quantum transitions." In: *Phys. Rev. E* 98.6 (Dec. 2018), p. 062137. doi: 10.1103/PhysRevE.98.062137.
- [250] M. Fannes, B. Nachtergaele, and R. F. Werner. "Finitely correlated states on quantum spin chains." In: Communications in Mathematical Physics 144.3 (Mar. 1992), pp. 443–490. issn: 1432-0916. doi: 10.1007/BF02099178.
- [251] F. Verstraete and J. I. Cirac. "Matrix product states represent ground states faithfully." In: *Phys. Rev. B* 73 (9 Mar. 2006), p. 094423. doi: 10.1103/ PhysRevB.73.094423.
- [252] Norbert Schuch, Michael M. Wolf, Frank Verstraete, and J. Ignacio Cirac. "Entropy Scaling and Simulability by Matrix Product States." In: *Phys. Rev. Lett.* 100.3 (Jan. 2008), p. 030504. doi: 10.1103/PhysRevLett.100.030504.
- [253] L. Tagliacozzo, Thiago. R. de Oliveira, S. Iblisdir, and J. I. Latorre. "Scaling of entanglement support for matrix product states." In: *Phys. Rev. B* 78 (2 July 2008), p. 024410. doi: 10.1103/PhysRevB.78.024410.
- [254] Frank Pollmann, Subroto Mukerjee, Ari M. Turner, and Joel E. Moore. "Theory of Finite-Entanglement Scaling at One-Dimensional Quantum Critical Points." In: *Phys. Rev. Lett.* 102.25 (June 2009), p. 255701. doi: 10.1103/PhysRevLett.102.255701.
- [255] Philipp Schmoll, Sukhbinder Singh, Matteo Rizzi, and Román Orús. "A programming guide for tensor networks with global SU(2) symmetry." In: *Annals of Physics* 419 (2020), p. 168232. issn: 0003-4916. doi: https://doi.org/10.1016/j.aop.2020.168232.
- [256] Steven R. White. "Density matrix renormalization group algorithms with a single center site." In: *Phys. Rev. B* 72.18 (Nov. 2005), p. 180403. doi: 10.1103/PhysRevB.72.180403.
- [257] C. Hubig, I. P. McCulloch, U. Schollwöck, and F. A. Wolf. "Strictly single-site DMRG algorithm with subspace expansion." In: *Phys. Rev. B* 91.15 (Apr. 2015), p. 155115. doi: 10.1103/PhysRevB.91.155115.
- [258] V. Zauner-Stauber, L. Vanderstraeten, M. T. Fishman, F. Verstraete, and J. Haegeman. "Variational optimization algorithms for uniform matrix product states." In: *Phys. Rev. B* 97.4 (Jan. 2018), p. 045145. doi: 10.1103/PhysRevB. 97.045145.
- [259] Y.-Y. Shi, L.-M. Duan, and G. Vidal. "Classical simulation of quantum many-body systems with a tree tensor network." In: *Phys. Rev. A* 74.2 (Aug. 2006), p. 022320. doi: 10.1103/PhysRevA.74.022320.
- [260] L. Tagliacozzo, G. Evenbly, and G. Vidal. "Simulation of two-dimensional quantum systems using a tree tensor network that exploits the entropic area law." In: *Phys. Rev. B* 80.23 (Dec. 2009), p. 235127. doi: 10.1103/PhysRevB. 80.235127.

[261] Timo Felser. Tree tensor networks for high-dimensional quantum systems and beyond. 2021. doi: http://dx.doi.org/10.22028/D291-35211.

- [262] M. Gerster, P. Silvi, M. Rizzi, R. Fazio, T. Calarco, and S. Montangero. "Unconstrained tree tensor network: An adaptive gauge picture for enhanced performance." In: *Phys. Rev. B* 90.12 (Sept. 2014), p. 125154. doi: 10.1103/ PhysRevB.90.125154.
- [263] M. Gerster, M. Rizzi, P. Silvi, M. Dalmonte, and S. Montangero. "Fractional quantum Hall effect in the interacting Hofstadter model via tensor networks." In: *Phys. Rev. B* 96.19 (Nov. 2017), p. 195123. doi: 10.1103/PhysRevB.96.195123.
- [264] Timo Felser, Simone Notarnicola, and Simone Montangero. "Efficient Tensor Network Ansatz for High-Dimensional Quantum Many-Body Problems." In: Phys. Rev. Lett. 126.17 (Apr. 2021), p. 170603. doi: 10.1103/PhysRevLett. 126.170603.
- [265] Giovanni Cataldi, Giuseppe Magnifico, Pietro Silvi, and Simone Montangero. "Simulating (2+1)D SU(2) Yang-Mills lattice gauge theory at finite density with tensor networks." In: *Phys. Rev. Res.* 6.3 (July 2024), p. 033057. doi: 10.1103/PhysRevResearch.6.033057.
- [266] Benedikt Kloss, David R. Reichman, and Yevgeny Bar Lev. "Studying dynamics in two-dimensional quantum lattices using tree tensor network states." In: SciPost Phys. 9 (2020), p. 070. doi: 10.21468/SciPostPhys.9.5.070.
- [267] Luka Pavešić, Daniel Jaschke, and Simone Montangero. "Constrained dynamics and confinement in the two-dimensional quantum Ising model." In: *Phys. Rev. B* 111.14 (Apr. 2025), p. L140305. doi: 10.1103/PhysRevB.111. L140305.
- [268] Wladislaw Krinitsin, Niklas Tausendpfund, Markus Heyl, Matteo Rizzi, and Markus Schmitt. "Time evolution of the quantum Ising model in two dimensions using tree tensor networks." In: *Phys. Rev. B* 112.13 (Oct. 2025), p. 134310. doi: 10.1103/kj16-sqcm.
- [269] Jan Naumann, Erik L. Weerda, Jens Eisert, Matteo Rizzi, and Philipp Schmoll. "Variationally optimizing infinite projected entangled-pair states at large bond dimensions: A split corner transfer matrix renormalization group approach." In: *Phys. Rev. B* 111.23 (June 2025), p. 235116. doi: 10.1103/PhysRevB.111.235116.
- [270] Daniel Alcalde Puente, Erik Lennart Weerda, Konrad Schröder, and Matteo Rizzi. "Efficient optimization and conceptual barriers in variational finite projected entangled pair states." In: *Phys. Rev. B* 111.19 (May 2025), p. 195120. doi: 10.1103/PhysRevB.111.195120.
- [271] Meng Cheng and Hong-Hao Tu. "Majorana edge states in interacting two-chain ladders of fermions." In: *Phys. Rev. B* 84.9 (Sept. 2011), p. 094503. doi: 10.1103/PhysRevB.84.094503.
- [272] Julien Vidal, Rémy Mosseri, and Benoît Douçot. "Aharonov-Bohm Cages in Two-Dimensional Structures." In: *Phys. Rev. Lett.* 81.26 (Dec. 1998), pp. 5888–5891. doi: 10.1103/PhysRevLett.81.5888.
- [273] Julien Vidal, Patrick Butaud, Benoît Douçot, and Rémy Mosseri. "Disorder and interactions in Aharonov-Bohm cages." In: *Phys. Rev. B* 64.15 (Sept. 2001), p. 155306. doi: 10.1103/PhysRevB.64.155306.

[274] Matthew Fishman, Steven R. White, and E. Miles Stoudenmire. "The ITensor Software Library for Tensor Network Calculations." In: *SciPost Phys. Codebases* (Aug. 2022), p. 4. doi: 10.21468/SciPostPhysCodeb.4.

- [275] Lorenzo Maffi, Niklas Tausendpfund, Matteo Rizzi, and Michele Burrello. Data and Code associated to the paper "Quantum simulation of the tricritical Ising model in tunable Josephson junction ladders". Nov. 2023. doi: 10.5281/zenodo.10225786.
- [276] Yichen Hu and C. L. Kane. "Fibonacci Topological Superconductor." In: Phys. Rev. Lett. 120.6 (Feb. 2018), p. 066801. doi: 10.1103/PhysRevLett. 120.066801.
- [277] Tingyu Gao, Niklas Tausendpfund, Erik L. Weerda, Matteo Rizzi, and David F. Mross. *Triangular lattice models of the Kalmeyer-Laughlin spin liquid from coupled wires*. 2025. arXiv: 2502.13223 [cond-mat.str-el].
- [278] Armin Rahmani, Xiaoyu Zhu, Marcel Franz, and Ian Affleck. "Emergent Supersymmetry from Strongly Interacting Majorana Zero Modes." In: *Phys. Rev. Lett.* 115.16 (Oct. 2015), p. 166401. doi: 10.1103/PhysRevLett.115.166401.
- [279] Edward O'Brien and Paul Fendley. "Lattice Supersymmetry and Order-Disorder Coexistence in the Tricritical Ising Model." In: *Phys. Rev. Lett.* 120.20 (May 2018), p. 206403. doi: 10.1103/PhysRevLett.120.206403.
- [280] P. Krogstrup, N. L. B. Ziino, W. Chang, S. M. Albrecht, M. H. Madsen, E. Johnson, J. Nygård, C. M. Marcus, and T. S. Jespersen. "Epitaxy of semiconductor-superconductor nanowires." In: *Nature Materials* 14.4 (Apr. 2015), pp. 400–406. issn: 1476-4660. doi: 10.1038/nmat4176.
- [281] C. G. L. Bøttcher, F. Nichele, J. Shabani, C. J. Palmstrøm, and C. M. Marcus. "Dynamical vortex transitions in a gate-tunable two-dimensional Josephson junction array." In: *Phys. Rev. B* 108.13 (Oct. 2023), p. 134517. doi: 10.1103/PhysRevB.108.134517.
- [282] C. G. L. Bøttcher, F. Nichele, J. Shabani, C. J. Palmstrøm, and C. M. Marcus. "Berezinskii-Kosterlitz-Thouless transition and anomalous metallic phase in a hybrid Josephson junction array." In: *Phys. Rev. B* 110.18 (Nov. 2024), p. L180502. doi: 10.1103/PhysRevB.110.L180502.
- [283] Ananda Roy. "Quantum electronic circuits for multicritical Ising models." In: *Phys. Rev. B* 108.23 (Dec. 2023), p. 235414. doi: 10.1103/PhysRevB.108.
- [284] Gábor Zsolt Tóth. "A nonperturbative study of phase transitions in the multi-frequency sine-Gordon model." In: *Journal of Physics A: Mathematical and General* 37.41 (Sept. 2004), p. 9631. doi: 10.1088/0305-4470/37/41/003.
- [285] G. Delfino and G. Mussardo. "Non-integrable aspects of the multi-frequency sine-Gordon model." In: *Nuclear Physics B* 516.3 (1998), pp. 675–703. issn: 0550-3213. doi: https://doi.org/10.1016/S0550-3213(98)00063-7.
- [286] C. W. J. Beenakker. "Universal limit of critical-current fluctuations in mesoscopic Josephson junctions." In: *Phys. Rev. Lett.* 67.27 (Dec. 1991), pp. 3836–3839. doi: 10.1103/PhysRevLett.67.3836.
- [287] Niklas Tausendpfund, Wladislaw Krinitsin, Markus Schmitt, and Matteo Rizzi. TTN.jl A tree tensor network library for calculating groundstates and solving time evolution. Version 0.1. Dec. 2024. doi: 10.5281/zenodo. 14421855.

[288] Wladislaw Krinitsin, Niklas Tausendpfund, Matteo Rizzi, Markus Heyl, and Schmitt Markus. Data and Code associated to the paper "Roughening dynamics of interfaces in two-dimensional quantum matter". Jan. 2025. doi: 10.5281/zenodo.14705609.

- [289] S. T. Chui and J. D. Weeks. "Phase transition in the two-dimensional Coulomb gas, and the interfacial roughening transition." In: *Phys. Rev. B* 14.11 (Dec. 1976), pp. 4978–4982. doi: 10.1103/PhysRevB.14.4978.
- [290] Eduardo Fradkin. "Roughening transition in quantum interfaces." In: *Phys. Rev. B* 28.9 (Nov. 1983), pp. 5338–5341. doi: 10.1103/PhysRevB.28.5338.
- [291] Henk van Beijeren. "Exactly Solvable Model for the Roughening Transition of a Crystal Surface." In: *Phys. Rev. Lett.* 38.18 (May 1977), pp. 993–996. doi: 10.1103/PhysRevLett.38.993.
- [292] W. K. Burton, N. Cabrera, F. C. Frank, and Nevill Francis Mott. "The growth of crystals and the equilibrium structure of their surfaces." In: *Philosophical Transactions of the Royal Society of London. Series A, Mathematical and Physical Sciences* 243.866 (1951), pp. 299–358. doi: 10.1098/rsta.1951.0006. eprint: https://royalsocietypublishing.org/doi/pdf/10.1098/rsta.1951.0006.
- [293] John D. Weeks, George H. Gilmer, and Harry J. Leamy. "Structural Transition in the Ising-Model Interface." In: *Phys. Rev. Lett.* 31.8 (Aug. 1973), pp. 549–551. doi: 10.1103/PhysRevLett.31.549.
- [294] Niklas Tausendpfund, Aditi Mitra, and Matteo Rizzi. Data and Code associated to the paper "Almost Strong Zero Modes at Finite Temperature". Jan. 2025. doi: 10.5281/zenodo.14752714.
- [295] F. Verstraete, J. J. García-Ripoll, and J. I. Cirac. "Matrix Product Density Operators: Simulation of Finite-Temperature and Dissipative Systems." In: Phys. Rev. Lett. 93.20 (Nov. 2004), p. 207204. doi: 10.1103/PhysRevLett. 93.207204.
- [296] Adrian E. Feiguin and Steven R. White. "Finite-temperature density matrix renormalization using an enlarged Hilbert space." In: *Phys. Rev. B* 72.22 (Dec. 2005), p. 220401. doi: 10.1103/PhysRevB.72.220401.
- [297] Anaïs Defossez, Laurens Vanderstraeten, Lucila Peralta Gavensky, and Nathan Goldman. "Dynamic realization of Majorana zero modes in a particle-conserving ladder." In: *Phys. Rev. Res.* 7.2 (May 2025), p. 023183. doi: 10.1103/PhysRevResearch.7.023183.
- [298] Fernando Iemini, Christophe Mora, and Leonardo Mazza. "Topological Phases of Parafermions: A Model with Exactly Solvable Ground States." In: *Phys. Rev. Lett.* 118.17 (Apr. 2017), p. 170402. doi: 10.1103/PhysRevLett.118.170402.
- [299] Subir Sachdev. Quantum Phase Transitions. 2nd ed. Cambridge University Press, 2011.
- [300] J. Ignacio Cirac, David Pérez-García, Norbert Schuch, and Frank Verstraete. "Matrix product unitaries: structure, symmetries, and topological invariants." In: Journal of Statistical Mechanics: Theory and Experiment 2017.8 (Aug. 2017), p. 083105. doi: 10.1088/1742-5468/aa7e55.

[301] Sujeet K. Shukla. "A simple and general equation for matrix product unitary generation." In: Journal of Mathematical Physics 66.10 (Oct. 2025), p. 101901. issn: 0022-2488. doi: 10.1063/5.0262317. eprint: https://pubs.aip.org/aip/jmp/article-pdf/doi/10.1063/5.0262317/20721814/101901\_1\_5.0262317.pdf.

- [302] Markus Hauru, Maarten Van Damme, and Jutho Haegeman. "Riemannian optimization of isometric tensor networks." In: *SciPost Phys.* 10 (2021), p. 040. doi: 10.21468/SciPostPhys.10.2.040.
- [303] "Calculating Derivatives." In: *Numerical Optimization*. New York, NY: Springer New York, 2006, pp. 193–219. isbn: 978-0-387-40065-5. doi: 10.1007/978-0-387-40065-5\_8.
- [304] Frank Pollmann, Vedika Khemani, J. Ignacio Cirac, and S. L. Sondhi. "Efficient variational diagonalization of fully many-body localized Hamiltonians." In: *Phys. Rev. B* 94.4 (July 2016), p. 041116. doi: 10.1103/PhysRevB.94.041116.
- [305] Thorsten B. Wahl, Arijeet Pal, and Steven H. Simon. "Efficient Representation of Fully Many-Body Localized Systems Using Tensor Networks." In: Phys. Rev. X 7.2 (May 2017), p. 021018. doi: 10.1103/PhysRevX.7.021018.
- [306] Paul Fendley. "Parafermionic edge zero modes in Zn-invariant spin chains." In: Journal of Statistical Mechanics: Theory and Experiment 2012.11 (Nov. 2012), P11020. doi: 10.1088/1742-5468/2012/11/P11020.
- [307] Jason Alicea and Paul Fendley. "Topological Phases with Parafermions: Theory and Blueprints." In: *Annual Review of Condensed Matter Physics* 7.Volume 7, 2016 (2016), pp. 119–139. issn: 1947-5462. doi: https://doi.org/10.1146/annurev-conmatphys-031115-011336.
- [308] Nathaniel Johnston. Advanced Linear and Matrix Algebra. Springer International Publishing, 2021. isbn: 978-3-030-52815-7. doi: 10.1007/978-3-030-52815-7.

## Acknowledgment

The last few years of research have been an exciting but demanding journey. During my time writing this thesis, I was pleased to meet many interesting and enlightening people and make new friends who helped me on my journey. I would like to extend my appreciation to everyone who has been with me during this period. Especially I would like to thank the following people:

First of all, Metteo Rizzi for giving me the opportunity to work on all these interesting problems and for being a scientific mentor for over six years since my master thesis. I am very grateful for the freedom I enjoyed during my thesis and for the ambitious supervision I received for this long time.

The entire group in Jülich and Cologne for all the scientific discussions and fun moments we had together. Especially, I want to thank my office colleagues Erik L. Weerda, Daniel Alcalde Puente, who started with me this exciting journey during the Covid pandamic, as well as Jan Reuter, David Korbany, Junaid Akhter and Patrick Geraghty, who I also want to thank for reading this thesis and providing helpful comments.

All my collaborators with whom I have worked on many exciting projects. I especially want to thank Wladislaw Krinitsin and Lorenzo Maffi for their great work and fruitful discussions.

All my friends, both within the university and outside, for being with me and enhancing my life. I am especially thankful to all my fellow students for supporting each other. Specifically, I want to thank the *PropellerflugzeugClub* for our weekly meetings discussing interesting questions in physics, mathematics, finance, and beyond.

My family for always having my back and supporting me throughout this time. In particular, I want to thank my parents and my brother for all their encouragement and love. Without your support, my studies and this thesis would not have been possible. Furthermore, I would like to thank Christel and Karl-Heinz Schwertel for always providing me with coffee and cake during the long days of studying and writing.

Finally, I would like to thank Annika Schwertel for all the love, care, and support. I am grateful for all the great memories we have shared and for all the good and bad times we have experienced together. I am happy to be with you for this long time, and I look forward to a bright future with you.